Multiscale Modeling of Electrolytes for Energy Storage and Conversion

A Dissertation Presented for the

Doctor of Philosophy

Degree

The University of Tennessee, Knoxville

Fatemeh Sepehr

December 2016

DEDICATION

This dissertation is dedicated to my husband, my parents, and my sibling who have supported and encouraged me throughout my life and academic career.

ACKNOWLEDGEMENTS

I would like to express my sincere gratitude to my advisor, Dr. Stephen J. Paddison, for his tremendous support throughout my Ph.D. studies at the University of Tennessee. His guidance played an important role in my research as well as my professional growth. I sincerely thank the efforts of knowledgeable faculty whom I learned from during my academic endeavor. I would also like to extend my thanks to Dr. Chen Wang, Dr. Jeffrey Clark, Dr. Hongjuan Zhu, Dr. Jun He, Dr. Hongjun Liu, Dr. Dongsheng Wu, Mr. Vincent Hall, and Mr. Xubo Luo for their help. The financial support from the National Science Foundation (NSF) and the TNSCORE program is greatly appreciated and valued.

ABSTRACT

Fuel cells, redox flow batteries, and secondary ion batteries are under active investigation to fulfill the requirements of efficient and sustainable energy storage and conversion technologies. The discovery of high-performance stable electrolytes that are relatively cheap and versatile is crucial to the commercialization of these electrochemical devices and necessitates a comprehensive understanding of the materials (i.e., from the atomistic to continuum levels). This dissertation is on multiscale modeling and simulations of several electrolytes under consideration in vanadium redox flow batteries (VRFBs), alkaline fuel cells (AFCs), or secondary magnesium batteries.

The hydrated structure and associated solvation Gibbs energies were determined for vanadium cations at four oxidation states using first principles based electronic structure calculations and quasi-chemical theory. The effect of sulfuric and trifluoromethanesulfonic (triflic) acids on the local structures of the hydrated vanadium cations was explored by employing hybrid density functional theory (DFT) in conjunction with a continuum solvation model. The results indicate that the hydration structure of vanadium at the oxidation state of three was the most perturbed in acidic media and that the oxo-group of vanadate may be protonated by either acid.

Dissipative particle dynamics (DPD) simulations were undertaken and a novel parametrization method developed to study the meso-scale behavior and hydrated morphology of proton and anion exchange membranes (PEMs and AEMs). The results for hydrated Nafion with the absorbed vanadium species indicate that the hydrated cations increase the aggregation of the sulfonate groups and that this effect is a function of both the cation charge and the degree of hydration. It was also observed that the simulated morphology and the size of the water domains in AEMs based on triblock copolymers depend on the hydration level and the anion type.

Vibrational frequencies of model clusters were calculated using DFT for two ionic liquid-based electrolytes and their experimental IR and Raman spectra were assigned. Moreover, the hydration of ten acids commonly used in electrolytes was investigated using DFT in order to provide a fundamental understanding of their hydrated acidity and proton transfer.

TABLE OF CONTENTS

Chapter 1 Introduction 1

1.1 Redox Flow Batteries 1

1.1.1 Vanadium Redox Flow Batteries (VRFBs) 2

1.1.2 Electrolytes for VRFBs 4

1.2 Fuel Cells 6

1.2.1 Proton Exchange Membrane Fuel Cells (PEMFCs) 6

1.2.2 Electrolytes for PEMFCs 8

1.2.3 Alkaline Fuel Cells (AFCs) 12

1.2.4 Electrolytes for Anion Exchange Membrane Fuel Cells 13

1.3 Secondary Magnesium Batteries 16

1.3.1 Electrolytes Based on Ionic Liquids 18

1.4 Research Overview 19

Chapter 2 Computational Methods 22

2.1 Multiscale Modeling 22

2.2 Quantum Chemical Calculations 24

2.2.1 Time-Independent Schrödinger Equation 25

2.2.2 Hartree-Fock Method 28

2.2.3 Density Functional Theory 31

2.2.4 Basis Sets 35

2.2.5 Continuum Solvation Models 37

2.2.6 Vibrational Frequencies 40

2.3 Quasi-Chemical Approach 42

2.3.1 Potential Distribution Theory 43

2.3.2 Basic Quasi-Chemical Formula 49

2.3.3 Chemical Equilibrium and Quasi-Chemical Description 51

2.4 Dissipative Particle Dynamics 53

2.4.1 Determining the Interaction Parameters 55

Chapter 3 PFSA Electrolytes with V^{n+} 59

3.1 Hydration and Thermodynamics of the V^{n+} Cations 60

3.1.1 Hydration Structures 60

3.1.2 Gibbs Energies of Hydration 63

3.2 Effect of Sulfuric and Triflic Acids on the Hydration of V^{n+} 67

3.2.1 The V^{2+} Cation 68

3.2.2 The V^{3+} Cation 70

3.2.3 The VO^{2+} Cation 72

3.2.4 The VO_2^{+} Cation 74

3.2.5 Partial Atomic Charges 76

3.3 Approach to Parameterize Dissipative Particle Dynamics 79

3.4 Morphology of the Membrane Electrolyte 83

3.4.1 Coarse-Graining of Particles 84

3.4.2 Conservative Interaction Parameters 85

3.4.3 Bonded Interaction Parameters 87

3.4.4 Simulations 89

Chapter 4 Anion Exchange Electrolytes 94

4.1 Coarse-Grained Model 94
4.1.1 Coarse-Graining of the Particles 94
4.1.2 Conservative Interaction Parameters 96
4.1.3 Bonded Interaction Parameters 98
4.1.4 Simulations 99
4.2 Morphology of SEBS Triblock Copolymer 100
4.3 Morphology of SEBS-Based Electrolytes 102
4.3.1 The Effect of Hydration 104
4.3.2 The Effect of Anion (OH^- versus Cl^-) 109
Chapter 5 SDAPP Electrolytes 116
5.1 Coarse-Graining of Particles 116
5.2 Conservative Interaction Parameters 118
Chapter 6 EMIm-Based Electrolytes 120
6.1 Structure of $EMImAlX_4$ and $EMImAl_2X_7$ with MgX_2 (X = Cl, I) 120
6.2 Vibrational Spectra of the Electrolytes 124
6.2.1 $(EMImCl/(AlCl_3)_{1.5})/(\delta\text{-}MgCl_2)_x$ System 124
6.2.2 $(EMImAlI_4)/(\delta\text{-}MgI_2)_x$ System 127
Chapter 7 Mixed Acid Electrolytes 129
7.1 Hydration of the Acids 129
7.2 Proton Transfer 144
Chapter 8 Conclusions 152
References 158
Appendices 196

Appendix A Computer Programs and Routines 197

Appendix B List of Presentations and Publications 216

Appendix C Reprints of Publications 218

Vita 358

LIST OF TABLES

Table 3.1. Average vanadium-oxygen distances for optimized structures shown in Figure 3.1.[a] 61

Table 3.2. Binding energies of water ligands to central vanadium cations calculated at B3LYP/6-311G** and B3LYP/6-311+G** (in parenthesis) level of theory (all in kcal/mol). 63

Table 3.3. Calculated Gibbs energy of hydration of vanadium cations using the quasi-chemical approach compared with available experimental information (all in kcal/mol). 64

Table 3.4. Average vanadium-oxygen distances for optimized structures shown in Figures 3.3 to 3.6.[a] 70

Table 3.5. Computed atomic partial charges on vanadium, oxygen, and water molecules in the primary hydration shell using ChelpG scheme. 77

Table 3.6. Selected bead types, their structures, and volumes. 84

Table 3.7. Calculated conservative interaction parameters. 86

Table 3.8. Bonded interaction parameters obtained by fitting to the structures from classical MD simulations. 87

Table 4.1. Selected bead types, their chemical structures, and volumes 96

Table 4.2. Calculated conservative interaction parameters. 97

Table 4.3. Bonded interaction parameters for simulating the SEBS triblock copolymer and hydrated AEMs. The first four rows define the bonded parameters of the SEBS and all for the AEM. 99

Table 4.4. Diffusivities of W, OH^-, and Cl^- beads at various hydration levels for the hydrated AEMs at the alkaline and chloride forms. Diffusivities are in $cm^2/s \times 10^4$. 114

Table 5.1. Selected bead types, their structures, and volumes. 117

Table 5.2. Calculated conservative interaction parameters. 119

Table 7.1. The number of water molecules required to effect dissociation of a proton in the gas phase and SMD solvated systems. The acids are ordered based on the acid strength (i.e., pK_a values and gas phase acidities).....132

LIST OF FIGURES

Figure 1.1. Schematic illustration of a VRFB during the discharge and charge processes (taken from reference 10). (a) Discharging: the V^{2+} cation oxidizes to V^{3+} and produces electrons that are transferred via an external circuit. The hydronium ion is transferred from the anolyte to the catholyte and the VO_2^+ cation reduces to VO^{2+}. (b) Charging: the V^{3+} cation reduces to V^{2+} and the VO^{2+} cation oxidizes to VO_2^+. The hydronium ion is transferred in a direction opposite to the discharge process. 3

Figure 1.2. Schematic representation of a PEMFC (taken from reference 62). Hydrogen and oxygen gases are inserted at the anode and cathode, respectively. Hydrogen gas produces protons and electrons. An external circuit transfers the electrons to the cathode and the protons permeate through the membrane electrolyte. At the cathode the oxygen and protons react and produce water. 7

Figure 1.3. The chemical structure of Nafion ionomer. The values of y and x determine the molecular weight and equivalent weight (molecular weight per ionic group), respectively. 9

Figure 1.4. Schematic representation of an alkaline fuel cell with a polymer electrolyte membrane. Hydrogen and oxygen gases insert at the anode and cathode, respectively. Hydrogen gas reacts with hydroxide at the anode generating water and electrons. The electrons are transferred through an external circuit to the cathode, where oxygen reacts with water to generate hydroxide ions. 13

Figure 1.5. Chemical structures of common functional groups used in AEMs. (a) pyridinium; (b) quaternary ammonium; (c) phosphonium; (d) sulfonium; (e) guanidinium; and (f) imidazolium (taken from reference 98).....14

Figure 1.6. The chemical structures of: (a) the SEBS triblock copolymer; and (b) the synthesized AEM ionomer obtained by functionalization of the SEBS copolymer with quaternary ammonium groups (taken from reference 112). The two end blocks of the SEBS consist of polystyrene, a rigid polymer, while the midblock is hydrogenated polybutadiene, an elastomer. 15

Figure 2.1. Classification of several computational methods in chemistry and materials science as a function of length and time scales. The methods at larger length scales probe longer times but lack any small scale information.....22

Figure 2.2. Coarse-graining of Nafion, a PFSA ionomer. Different mesoscopic particles are defined to represent chemically distinct subunits of the polymer (taken from reference 173).....23

Figure 2.3. Illustration of the conformational coordinate notation, R^n (taken from reference 195). 47

Figure 3.1. First hydration shell structures of vanadium ions at the B3LYP6-311+G**/SMD level of theory: (a) V^{2+}; (b) V^{3+}; (c) VO^{2+}; (d) VO_2^+, octahedral; and (e) VO_2^+, bipyramidal. Color scheme: oxygen (red), hydrogen (white), vanadium (purple). Two-tone solid lines present covalent bonds and dashed lines show coordinate bonds and hydrogen bonds (hydrogen bond criterion 1.1 Å < O···H < 2.5 Å). 61

Figure 3.2. Quasi-chemical contributions of the solvation free energy of aqueous V^{2+}, V^{3+}, VO^{2+}, and VO_2^+ versus *n* number of water molecules inside the inner-shell structure. The calculations performed at the B3LYP/6-311+G(2d,p)//B3LYP/6-311G** level of theory and the outer-shell contributions are assessed using the SMD dielectric continuum model. Triangles represent inner-shell contributions and squares are outer-shell contributions to the total free energy of solvation. Circles are the total free energy of solvation predicting $n = 6$ as the most probable inner-shell occupancy for V^{2+} and V^{3+}, $n = 4$ for VO^{2+} and $n = 2$ for VO_2^+.....66

Figure 3.3. Fully optimized configurations at B3LYP/6-311G**/SMD level of theory for the hydrated V^{2+} cation in proximity to: (a) H_2SO_4; (b) HSO_4^-; (c) SO_4^{2-}; (d) CF_3SO_3H; and (e) $CF_3SO_3^-$. The atomic color scheme is: oxygen (red), hydrogen (white), vanadium (purple), sulfur (yellow), carbon (grey), and fluorine (cyan). Distances are represented in Å, two-tone solid lines present covalent bonds, and dashed lines show coordinate bonds and hydrogen bonds (hydrogen bond criterion 1.1 Å < O···H < 2.5 Å). 69

Figure 3.4. Fully optimized configurations at B3LYP/6-311G**/SMD level of theory for the hydrated V^{3+} cation in proximity to: (a) H_2SO_4; (b) HSO_4^-; (c) SO_4^{2-}; (d) CF_3SO_3H; and (e) $CF_3SO_3^-$. Color scheme as described in Figure 3.3. 71

Figure 3.5. Fully optimized configurations at the B3LYP/6-311G**/SMD level of theory for the hydrated VO^{2+} cation in proximity to: (a) H_2SO_4; (b) HSO_4^-; (c) SO_4^{2-}; (d) CF_3SO_3H; and (e) $CF_3SO_3^-$. Color scheme as described in Figure 3.3. 73

Figure 3.6. Fully optimized configurations at B3LYP/6-311G**/SMD level of theory for the hydrated VO_2^+ cation in proximity to: (a) H_2SO_4; (b) HSO_4^-; (c) SO_4^{2-}; (d) CF_3SO_3H; and (e) $CF_3SO_3^-$. Color scheme as described in Figure 3.3. 75

Figure 3.7. The six degrees of freedom that contribute different configurations to the two objects (beads). The atomic structures of the beads i and j are arbitrary. The angles can vary as $0° \leq \theta \leq 180°$ and $0° \leq \varphi \leq 360°$ for each configuration. The lower limit for the r_{ij} is when the beads start to overlap and the upper limit is the cut off distance r_c. 81

Figure 3.8. Distribution of: (a) the bond distance between connected A beads; (b) the angle between three consecutive A beads; and (c) the distance between two neighboring C beads in each Nafion chain. In order to compare atomistic chain structures from MD simulations to those of DPD, each Nafion chain was dissected into fragments equivalent to the selected beads and the center of

mass of each fragment was considered as the position of the representing bead. The solid lines are the results from the MD simulation. The dashed lines are the corresponding DPD system with conservative interaction parameters from Table 3.7 and the default set of bonded interactions ($f_i^{Bonded} = 4.0r_b$). The dash-dots are the corresponding DPD system with both bonded and non-bonded interactions from Table 3.7 and 3.8. 88

Figure 3.9. RDFs of vanadium and C^- beads for hydrated Nafion systems at different hydration levels and EW = 1115. (a) V^{n+}–V^{n+} RDFs at λ = 6; (b) V^{n+}–V^{n+} RDFs at λ = 18; (c) C^-– C^- RDFs at λ = 6; and (d) C^-– C^- RDFs at λ = 18. Color code: violet-V^{2+}; green-V^{3+}; blue-VO^{2+}; yellow-VO_2^+; black-hydrated Nafion.....90

Figure 3.10. Radial distribution functions of the water beads at EW = 1115 and two different hydration levels: (a) $\lambda = 6$; and (b) $\lambda = 18$. The insets are magnification of the first peak in each graph. The solid line is for the system of hydrated Nafion, the dashed line has absorbed V^{2+}, and the dotted line has absorbed V^{3+}. 91

Figure 3.11. Calculated vanadium and water diffusivities at different hydration levels in hydrated Nafion with an EW = 1115. (a) V^{n+} beads; and (b) W beads. The V^{3+} and VO_2^+ beads show the lowest and the highest diffusivities, respectively. The effect of vanadium cations on the diffusivity of the water beads is insignificant.....92

Figure 3.12. RDFs and diffusivities for hydrated Nafion systems at different equivalent weights and λ = 12. (a) W–W RDFs; (b) VO^{2+}– C^- RDFs; (c) VO^{2+}– VO^{2+} RDFs; and (d) diffusivities of W and VO^{2+} beads. The cation-anion interactions are increased by increasing the EWs, whereas the vanadium diffusivity is decreased.....93

Figure 4.1. Coarse-grained model of: (a) SEBS triblock copolymer; and (b) hydrated AEM in alkaline form. Each circle represents the selected chemical group or collection of atoms for a

particular bead and is distinguished with a different color. The midblock of SEBS is modeled as polyethylene instead of the poly(ethylene-co-butylene) for simplicity (see Figure 1.5).....95

Figure 4.2. Simulated morphology of the SEBS triblock copolymer. Only the polystyrene end blocks, i.e., the Bs and Ph beads, are shown for clarity. (a) and (b) show two different views of the hexagonal cylindrical morphology. $R_{cylinder}$ is the cylinder radius and $d_{cylinder}$ is the intercylinder distance. The orange and mauve spheres illustrate the Bs and Ph beads, respectively. The simulation box is shown in blue. 100

Figure 4.3. The polystyrene (i.e., BsPh – BsPh) RDF of the SEBS triblock copolymer. The position of the second point with the unit function value is twice the cylinder radius ($2R_{cylinder}$) and the position of the next peak is the intercylinder distance ($d_{cylinder}$).....101

Figure 4.4. Simulated morphology of the hydrated AEM in the alkaline form at $\lambda = 8$. Each figure shows a specific bead type for clarity: (a) all beads; (b) Bs, Ph, TMM, and TMA^+; (c) Bm; (d) TMA^+; (e) OH^-; and (f) W. (a) shows a strong phase separation between the functionalized polystyrene end blocks and the midblocks that are shown separately in (b) and (c). (d) and (e) illustrate the distribution of ionic species and (d) shows that the majority of water are in the polystyrene phase with a few distributed in the midblock phase. Color code: Bs and Bm (orange); Ph (mauve); TMM (green); TMA^+ (purple); OH^- (cyan); and W (blue).....102

Figure 4.5. RDFs of the hydrated AEM in the alkaline form at $\lambda = 8$. The inset shows a magnification at short distances. Color scheme: BsPh – BsPh (blue); BsPh – Bm (red); Bm – Bm (orange); and TMA^+ – TMA^+ (purple). 103

Figure 4.6. Simulated morphology of the hydrated AEM in the alkaline form for $\lambda =$: (a) 4; (b) 8; (c) 12; (d) 16; and (e) 20. All beads are shown and the color scheme is the same as in Figure 4.4. The ionomer phase separates into hydrophilic and hydrophobic phases at all hydration levels.

As the hydration increases the morphology changes from perforated and interconnected lamellae ($\lambda = 4$ and 8) to perfect lamellae ($\lambda = 12$) and then to disordered bicontinuous domains ($\lambda = 16$ and 20). Domains exclusively consisting of water are formed within the hydrophilic phase at the two highest water contents only.....105

Figure 4.7. Polystyrene RDFs for the hydrated AEM in the alkaline form at five levels of hydration. Increasing the water content increases the intensity of the first peak and decreases that of the second. The distance at which the RDF reaches one increases through hydration indicating that the hydrophilic phase swells.....106

Figure 4.8. Cross sections of the morphologies (shown in Figures 4.6 (d) and (e)) in the xy, yz, and xz planes (top to bottom). (a) $\lambda = 16$; and (b) $\lambda = 20$. The exclusive water domains are within the hydrophilic phase and larger at the higher level of hydration. The cross sections reveal that the water domains are three dimensional.....107

Figure 4.9. W – W RDFs for the hydrated AEM in the alkaline form at various degrees of hydration. Clearly, increasing the hydration intensifies the peaks. The distance at which the RDF reaches one is the same for $\lambda = 8$ and 12 and increases for $\lambda = 16$ and 20. This is due to the formation of domains that exclusively contain water. There are not sufficient W beads in the simulation box at $\lambda = 4$ to form a smooth curve and therefore this data is not shown. 108

Figure 4.10. (a) TMA^+ – OH^- RDFs for the hydrated AEM in the alkaline form at various levels of hydration. (b) An expanded view of the first peak seen in (a). (c) The integrated number of the OH^- beads around the TMA^+ beads. There is one OH^- in the immediate vicinity of each TMA^+. At a higher degree of hydration there are fewer numbers of OH^- around TMA^+ at r > 5 Å. 109

Figure 4.11. Simulated morphology of the hydrated AEM in the chloride form at $\lambda = 8$. Each figure shows a specific bead type for clarity: (a) all beads; (b) TMA^+; (c) Cl^-; and (d) W. The AEM

ionomer shows phase separation similar to the alkaline form. Color code: Bs and Bm (orange); Ph (mauve); TMM (green); TMA^+ (purple); Cl^- (shamrock green); and W (blue).....110

Figure 4.12. Simulated morphology of the hydrated AEM in the chloride form for $\lambda =$: (a) 4; (b) 8; (c) 12; (d) 16; and (e) 20. All beads are shown and the color scheme is the same as in Figure 4.11. The ionomer phase separates into hydrophilic and hydrophobic phases at all hydration levels. Similar to the alkaline form, the morphology changes by increasing the water content and exclusive domains of water are formed within the hydrophilic phase at the two highest values of λ.....111

Figure 4.13. W – W RDFs for the hydrated AEM in the alkaline (solid lines) and chloride (dashed lines) forms at various levels of hydration. Changing the anion from OH^- to Cl^- results in negligible changes at $\lambda = 8$ and 12, however it significantly increases the peaks at $\lambda = 16$ and 20. The distance at which the RDF reaches one substantially increases at $\lambda = 16$. 112

Figure 4.14. Cross sections of the hydrated AEM morphologies in the: xy (top), yz (middle), and xz (bottom) planes at $\lambda = 16$. (a) Alkaline form; and (b) chloride form. Changing the anion from OH^- to Cl^- results in larger exclusive domains of water. 113

Figure 5.1. The repeat unit of the SDAPP ionomer. The number of sulfonate groups per monomer depends on the level of sulfonation which is controlled by the reaction time (taken from reference 74). 116

Figure 5.2. The coarse-graining scheme for the SDAPP ionomer. (a) The monomer without sulfonation; and (b) two sulfonate groups per monomer. Different ratios of (a) and (b) may be combined to represent sulfonation levels ranging from 0 to 2. Different bead types are shown by colored ovals. Color code: P1 (red), P2 (blue), P3 (green).....118

Figure 6.1. Optimized geometries of the ionic liquid complexes determined at the B3LYP/6-311G** level of theory. (a) $EMImAlCl_4$; (b) $EMImAlCl_4$ with $MgCl_2$; (c) $EMImAlCl_4$ with

($MgCl_2$)$_2$; (d) $EMImAl_2Cl_7$; (e) $EMImAl_2Cl_7$ with $MgCl_2$; and (f) $EMImAl_2Cl_7$ with ($MgCl_2$)$_2$. Color code: chlorine (green), aluminum (pink), magnesium (yellow), nitrogen (blue), hydrogen (white), carbon (grey). Distances between chlorine and hydrogen are only shown when less than 3 Å.....122

Figure 6.2. Optimized geometries of the ionic liquid complexes determined at the B3LYP/6-311G** level of theory. (a) $EMImAlI_4$; (b) $EMImAlI_4$ with MgI_2; (c) $EMImAlI_4$ with (MgI_2)$_2$; (d) $EMImAl_2I_7$; (e) $EMImAl_2I_7$ with MgI_2; and (f) $EMImAl_2I_7$ with (MgI_2)$_2$. Color code: iodine (orange), aluminum (pink), magnesium (yellow), nitrogen (blue), hydrogen (white), carbon (grey).....123

Figure 6.3. Electrostatic potential map on the total electron density isosurface. (a) $[AlCl_4MgCl_2]^-$; (b) $[Al_2Cl_7MgCl_2]^-$; (c) $[AlCl_4(MgCl_2)_2]^-$; and (d) $[Al_2Cl_7(MgCl_2)_2]^-$ complexes. These maps show a more negative electrostatic potential and therefore more electron rich area on $MgCl_2$ rather than aluminium chloride. Color code: chlorine (green), aluminum (pink), magnesium (yellow).....124

Figure 6.4. Vibrational spectra of ([EMIm]Cl/($AlCl_3$)$_{1.5}$)/(δ-$MgCl_2$)$_x$ electrolytes with $0 \leq x \leq 0.20$. (a) Raman spectra in the region between 100 and 480 cm^{-1}, the intensity of the band corresponding to the stretching of the monomeric species $AlCl_4^-$ (blue) increases at higher concentrations of the Mg salt, whereas the intensity of the band attributed to the stretching of the dimeric species $Al_2Cl_7^-$ (yellow) decreases; and (b) far IR spectra, the intensities of the bands corresponding to the vibrations of polymeric $MgCl_2$ species (green) and Mg–Cl–Al stretching modes (blue and yellow) increase at higher concentrations of the Mg salt.....126

Figure 6.5. Vibrational spectra of ($EMImAlI_4$)/(δ-MgI_2)$_x$ electrolyte with $0 \leq x \leq 0.023$. (a) Raman spectra with band assignments based on DFT calculations, the intensity of the band assigned to the

stretching of AlI_4^- (blue) increases with the δ-MgI_2 concentration while that of $Al_2I_7^-$ (orange) decreases; and (b) far IR spectra. 127

Figure 7.1. Fully optimized structures of CF_3SO_3H with from zero to five water molecules at the B3LYP/6-311G** level of theory: (a) gas phase structures, proton dissociation occurs after three water molecules are added; (b) structures with the SMD model, proton dissociates after only one water molecule is added. The atomic color scheme in Figures 7.1 to 7.10 is: oxygen (red), hydrogen (white), sulfur (yellow), carbon (gray), fluorine (cyan), nitrogen (blue), phosphor (orange). 131

Figure 7.2. Fully optimized structures of FSO_3H with from zero to five water molecules at the B3LYP/6-311G** level of theory: (a) gas phase structures, proton dissociation occurs after three water molecules are added; (b) structures with the SMD model, proton dissociates after only one water molecule is added. 133

Figure 7.3. Fully optimized structures of CH_3SO_3H with from zero to five water molecules at the B3LYP/6-311G** level of theory: (a) gas phase structures, proton dissociation occurs after three water molecules are added; (b) structures with the SMD model, proton dissociates after only two water molecules are added. 134

Figure 7.4. Fully optimized structures of H_2SO_4 with from zero to five water molecules at the B3LYP/6-311G** level of theory: (a) gas phase structures, proton dissociation occurs after four water molecules are added; (b) structures with the SMD model, proton dissociates after three water molecules are added. In all structures, the water molecules bind to one side of the acid. The only exception is the gas phase with three water molecules. 136

Figure 7.5. Fully optimized structures of HNO_3 with from zero to five water molecules at the B3LYP/6-311G** level of theory: (a) gas phase structures, proton dissociation occurs after five

water molecules are added; (b) structures with the SMD model, proton dissociates after only three water molecules are added. 137

Figure 7.6. Fully optimized structures of HF with from zero to five water molecules at the B3LYP/6-311G** level of theory: (a) gas phase structures; (b) structures with the SMD model. No proton dissociation occurs in agreement with the weak acidity of HF. 138

Figure 7.7. Fully optimized structures of H_3PO_2 with from zero to five water molecules at the B3LYP/6-311G** level of theory: (a) gas phase structures; (b) structures with the SMD model. No proton dissociation occurs, except in the gas phase with five added water molecules…...140

Figure 7.8. Fully optimized structures of H_3PO_3 with from zero to five water molecules at the B3LYP/6-311G** level of theory: (a) gas phase structures; (b) structures with the SMD model. No proton dissociation occurs.....141

Figure 7.9. Fully optimized structures of H_3PO_4 with from zero to five water molecules at the B3LYP/6-311G** level of theory: (a) gas phase structures; (b) structures with the SMD model. No proton dissociation occurs.....142

Figure 7.10. Fully optimized structures of $CF_3SO_2NHSO_2CF_3$ with from zero to five water molecules at the B3LYP/6-311G** level of theory: (a) gas phase structures, proton dissociation occurs after three water molecules are added (nitrogen is not involved in the hydrogen bond network); (b) structures with the SMD model, proton dissociates after only two water molecules are added (nitrogen is involved in the hydrogen bond network). 143

Figure 7.11. The relative energy profiles of PES scans for: CF_3SO_3H, FSO_3H, and CH_3SO_3H. The gas phase results are shown in the left panel and the results with the SMD model are displayed in the right panel. The extremum plots in the gas phase correspond to the back transfer events indicating that the molecular acid is more stable than the ionized form. The gas phase results are

similar, because the proton dissociation occurs after three water molecules are added. The SMD results for CF_3SO_3H and FSO_3H are similar to each other and different to those for CH_3SO_3H, as the formers require only one water molecule to effect proton dissociation. The right panel scans do not show a back transfer of a proton, because the formed hydronium ion is stabilized by the continuum solvation model.....146

Figure 7.12. The relative energy profiles of PES scans for: H_2SO_4, HNO_3, and HF. The gas phase results are shown in the left panel and the results with the SMD model are displayed in the right panel. The gas phase results exhibit back transfer of a proton indicating that the molecular acid is more stable than the ionized form. The energy barrier to move a proton away from the acid is inversely related to the number of water molecules and the acid strength. The weakest acid, HF, has the highest energy barriers. The relative energy axis is plotted from 0 to 18 kcal/mol for all acids except for HF (from 0 to 35 kcal/mol).....148

Figure 7.13. The relative energy profiles of PES scans for: H_3PO_2, H_3PO_3, and H_3PO_4. The gas phase results are shown in the left panel and the results with the SMD model are displayed in the right panel. Only a back transfer or an increasing scan is observed, because the proton dissociation is not favored by any of these weak acids. The proton transfer energetics are similar for these acids in agreement with their similar acidity and pK_a values listed in Table 7.1.....149

Figure 7.14. The relative energy profiles of PES scans for $CF_3SO_2NHSO_2CF_3$. The gas phase results are shown in the left panel and the results with the SMD model are displayed in the right panel. In the gas phase with one water molecule, the secondary proton is transferred to an oxygen atom of the acid. The gas phase structure of this acid with three water molecules does not involve hydrogen bonding with nitrogen as shown in Figure 7.10 (a). Hence the proton was transferred to an oxygen atom of the acid, i.e., the orange plot in the left panel shows OH distance rather than

NH. The proton dissociation occurs after two water molecules are added to the SMD solvated structures, however the proton transfer energetics is negligible with one water molecule. 150

Chapter 1 Introduction

Recent interest in replacing fossil fuels with renewable green energy sources such as solar and wind has significantly increased as a result of the perceived consequences to the environment. One of the limiting factors for the utilization of renewable sources in either the electric distribution grid or smart grid is the intermittent nature of these sources which requires the employment of electrical energy storage devices.[1] The conversion of energy by clean, efficient, and sustainable means such as fuel cells is another challenge in the replacement of fossil fuels. Lead acid, Ni-Cd, lithium-ion/air, and magnesium batteries along with fuel cells and redox flow batteries constitute the majority of the current energy storage and conversion technologies.[2] The specific systems of interest in this body of work are the all-vanadium redox flow battery, the alkaline fuel cell, and the secondary magnesium battery.

1.1 Redox Flow Batteries

Redox Flow Batteries (RFBs) are among the promising large-scale (grid size) electrical energy storage systems and have received attention due to their superior properties. These include: long lifespan; simple installation; low maintenance cost; the possibility of instant charging through the replacing of the electrolytes; and the ability to repeatedly store and convert electrical energy to chemical energy and vice versa.[1]

A RFB stores energy in two electrolyte solution tanks containing different redox couples. The liquid electrolyte solutions flow through the electrochemical cell, where electrochemical reactions occur. The two electrolytes are separated by an ion exchange membrane within the cell. The energy storage capacity is determined by the size of the electrolyte tanks, and the power is a dependent upon the size of the cell stacks. Thus, the power and energy of a RFB are decoupled.[3] Various

redox couples have been employed in RFBs, including but not limited to: Cr^{2+}/Cr^{3+} vs. Fe^{2+}/Fe^{3+};[4-5] S_2^{2-}/S_4^{2-} vs. Br^-/Br_2;[6-7] Zn/Zn^{2+} vs. Br^-/Br_2;[8] and V^{2+}/V^{3+} vs. V^{4+}/V^{5+}.[9] The last mentioned in this list is referred to as the vanadium redox flow battery as it uses all-vanadium electrolytes.

1.1.1 Vanadium Redox Flow Batteries (VRFBs)

The VRFB demonstrates the greatest commercial prospects among the many reported RFBs, due to its high energy efficiency, long cycle-life, and reversibility.[3,9] Having all the active species from one element at different oxidation states, makes the regeneration of the electrolytes relatively easy. The VRFB consists of a V^{2+}/V^{3+} sulfate solution as the negative electrolyte (i.e., anolyte) and a VO^{2+}/VO_2^+ sulfate solution as the positive electrolyte (i.e., catholyte) and are separated by an ion selective membrane that permits the transport of protons. A schematic of the VRFB system is illustrated in Figure 1.1.

Figure 1.1 (a) shows the VRFB during the discharge process where the VO_2^+ is reduced to VO^{2+} and the V^{2+} cation is oxidized to V^{3+}. The hydronium ion is transferred from the anolyte to the catholyte to complete the circuit and generate electricity. The same reactions take place during the charging (see Figure 1.1 (b)) but in the opposite direction, i.e., the VO_2^+ and V^{2+} cations are oxidized and reduced, respectively and the hydronium ion is transferred from the catholyte to the anolyte. The half-cell reaction during charging for the negative electrolyte is:

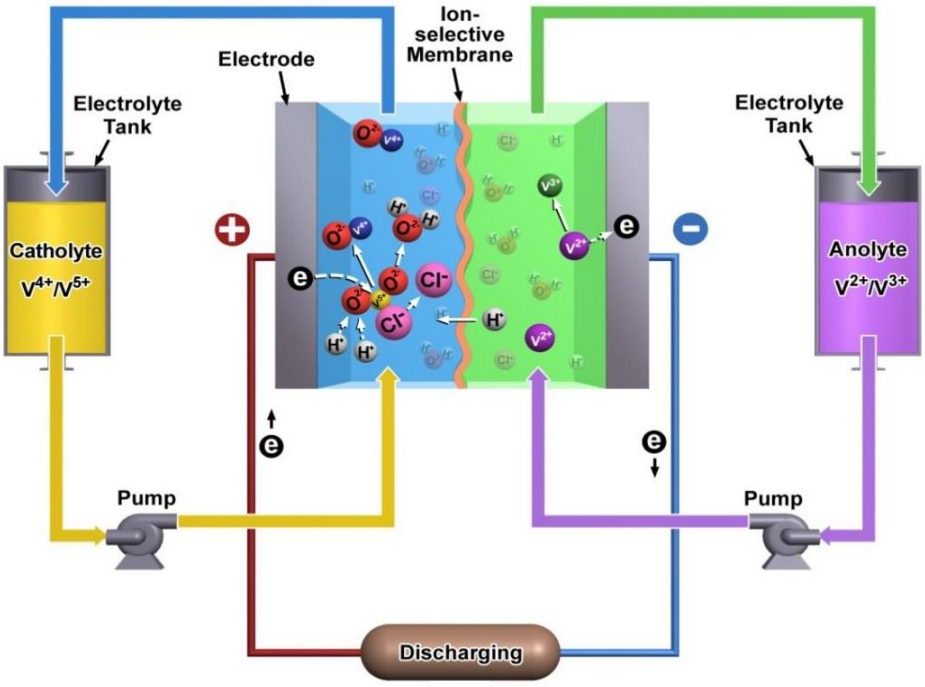
$$V^{3+} + e^- \longrightarrow V^{2+}\,; \tag{1.1}$$

and for the positive electrolyte is:

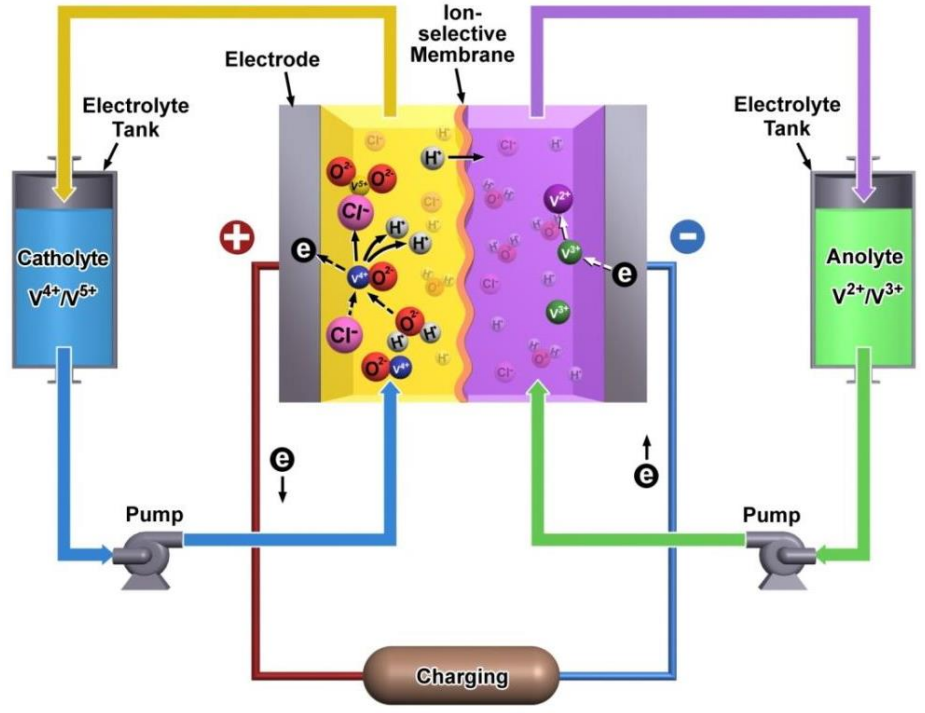
$$VO^{2+} + H_2O \longrightarrow VO_2^+ + 2H^+ + e^-\,. \tag{1.2}$$

Hence, the total cell reaction may be written as:

$$VO^{2+} + H_2O + V^{3+} \longrightarrow VO_2^+ + 2H^+ + V^{2+}\,. \tag{1.3}$$



(a)



(b)

Figure 1.1. Schematic illustration of a VRFB during the discharge and charge processes (taken from reference 10). (a) Discharging: V^{2+} is oxidized to V^{3+} and produces electrons that are transferred via an external circuit. The hydronium ion is transferred from the anolyte to the catholyte and the VO_2^+ cation is reduced to VO^{2+}. (b) Charging: the V^{3+} cation is reduced to V^{2+} and the VO^{2+} cation is oxidized to VO_2^+. The hydronium ion is transferred in a direction opposite to the discharge process.

The discharge process obeys the same reactions, but in the opposite direction. The wide difference in the reduction potentials of the two half-cells produces a standard voltage of 1.25 V, which is comparable to other types of RFBs.[10]

1.1.2 Electrolytes for VRFBs

The energy density of the battery depends on the concentration of the electrolyte solutions. VRFBs have low energy density and therefore need large electrolyte tanks which limit their application to stationary storage.[1,11] Hence, increasing the vanadium concentration results in an increase in the energy density of the battery. However, the concentration of the vanadium ions is limited by the stability of the electrolytes and precipitation of the four vanadium cations. The stability of the electrolytes is determined by the concentration of sulfuric acid, solution temperature, and the state of charge of the battery.[12-14] The stability of VO_2^+ (in H_2SO_4) is compromised by V_2O_5 precipitation which occurs at high temperature (> 40 °C) and high vanadium concentration (> 2 M).[15] Although, the VO_2^+ concentration can be increased by the addition of sulfuric acid to the solution, the increase in acid concentration is limited by the stability of the VO^{2+} species, as both VO_2^+ and VO^{2+} species are present in the positive electrolyte.[14] In contrast to VO_2^+, the V^{2+}, V^{3+}, and VO^{2+} solutions are stabilized by increasing the temperature and decreasing the sulfuric acid concentration,[12,14] which makes the design of VRFB electrolytes challenging. Inorganic and organic agents have been added in an effort to stabilize the electrolytes.[13,16-19] The stability of the vanadyl solution V(IV) at low temperatures can be improved through the addition of stabilizing agents, however the effect of the stabilizers must be considered on both the V(IV) and V(V) solutions as they co-exist in the positive electrolyte. Furthermore, since the crossover of stabilizing agents through the membrane is possible, their effects need to be considered on all four vanadium cations simultaneously.[13,18]

Under the high ionic strength condition of a VRFB, understanding the hydration of the vanadium cations and their interaction with the solvent and membrane is crucial in optimizing the design and modification of the electrolytes and membranes. Vanadium complexes have been subject to both experimental and theoretical investigations.[20-28] However, the structure of hydrated vanadium ions, the oxidation state of the ions, and their interaction with sulfuric acid and/or a hydrated perfluorosulfonic acid (PFSA) ionomer are not understood.[29] Hence, a molecular-level investigation on the interaction of vanadium cations in a VRFB electrolyte is warranted.

Membranes used in VRFBs are classified as either cation exchange or anion exchange depending on the type of ion that is permeated. Both types of membranes must exhibit low permeability to the vanadium ions, high proton or sulfate conductivity, good thermal and chemical stability, substantial mechanical integrity, and low cost.[3,11] Typically, the imperfect ion selectivity of the cation exchange membrane results in vanadium cation crossover that causes electrolyte contamination and capacity loss of the battery as well as a decrease in conductivity of the membrane.[3,30-32] The diffusion of sulfuric acid into Nafion has also been observed.[33-35] Hence, there is ongoing research on the development of new membranes and membrane treatments to decrease solvent and vanadium ion transport across the membrane.[36-39] One of the most widely used cation exchange membranes for VRFBs is the PFSA membrane, Nafion.[40] Nafion phase separates when hydrated into nano-dimensioned regions containing water associated with the sulfonic acid groups surrounded by the polytetrafluoroethylene backbone of the ionomer.[41-45] Protons and vanadium cations permeate through the membrane (via the water domains). Although, the mobility of the vanadium cations is much lower than that of a proton, over time the crossover of vanadium cations results in significant capacity loss and electrolyte contamination.[30,46-47]

Understanding the diffusion of vanadium cations through the membrane and the morphology evolution, from a meso-scale perspective, is another important aspect in the design of a VRFB, due to impact on electrolyte contamination, battery capacity, and the hydration and conductivity of the membrane. The dynamics and morphological properties of hydrated Nafion have been simulated extensively,[48-53] however the effect of the absorbed vanadium cations are not known. There is a recent molecular dynamics (MD) study on the effect of the absorbed V^{2+} and V^{3+} species on the hydrated Nafion,[54] and more investigations are required to understand their effects.

1.2 Fuel Cells

Fuel cells are an important sustainable energy conversion devices. These devices convert chemical energy into electrical energy through electrochemical reactions of a gaseous fuel (e.g. hydrogen or methanol) and an oxidant gas (e.g. oxygen from the air) producing water.[55] Energy conversion via fuel cells is pollution free and more efficient than other conventional thermo-mechanical technologies.[55-56] Fuel cells may be classified into five major groups based on the type of the electrolyte: alkaline fuel cells (AFCs), proton-exchange membrane fuel cells (PEMFCs), solid oxide fuel cells (SOFCs), phosphoric acid fuel cells (PACFs) and molten carbonate fuel cells (MCFCs).[57] PEMFCs and AFCs have received significant attention due to their application and commercialization potential[58-60] and are further described below.

1.2.1 Proton Exchange Membrane Fuel Cells (PEMFCs)

The first PEMFC was designed and developed in 1955 at General Electric (GE).[61] PEMFCs use a solid polymer electrolyte that results in safer and easier cell operation and handling. PEMFCs may be utilized in automotive vehicles due to their quick start up and high power density. Despite many advantages they are restricted to operating temperatures below 100 °C and also require expensive platinum catalysts.[56]

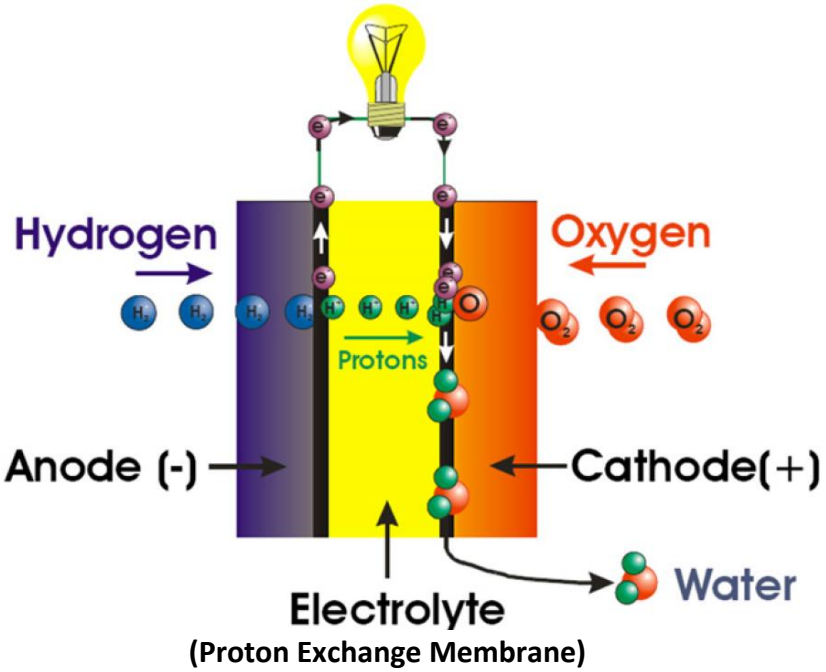


Figure 1.2. Schematic representation of a PEMFC (taken from reference 62). Hydrogen and oxygen gases are inserted at the anode and cathode, respectively. Hydrogen gas is oxidized producing protons and electrons. An external circuit transfers the electrons to the cathode and the protons permeate through the membrane electrolyte. At the cathode oxygen is reduced producing only water.

A schematic design of the PEMFC is illustrated in Figure 1.2. Hydrogen and oxygen gases are introduced at the anode and cathode, respectively. Hydrogen gas produces protons and electrons. An external circuit transfers the electrons to the cathode and the protons permeate through the electrolyte (membrane). At the cathode the oxygen and protons react and produce water. The electrochemical reaction at the anode is called the hydrogen oxidation reaction (HOR) and is written as:

$$H_2 \longrightarrow 2H^+ + 2e^- \; ; \tag{1.4}$$

and at the cathode the oxygen reduction reaction (ORR) takes place:

$$2H^+ + \frac{1}{2}O_2 + 2e^- \longrightarrow H_2O \; . \tag{1.5}$$

The overall cell reaction is:

$$H_2 + \frac{1}{2} O_2 \longrightarrow H_2O \ . \tag{1.6}$$

The ORR at the cathode is kinetically slow and requires relatively high platinum loading that results in high cell costs.[58,60]

1.2.2 Electrolytes for PEMFCs

The solid polymer electrolyte is the central component of the PEMFC and is required to possess high proton conductivity, adequate mechanical strength, high chemical stability, low fuel gas permeability, and low cost.[59] The membrane materials may be classified as follows:

- Perfluorinated ionomers
- Non-fluorinated ionomers
- Acid-base complexes
- Supported composites

The following provides a brief description and several examples for each group.

Perfluorinated Ionomers. The perfluorinated polymers functionalized by sulfonic acid groups, i.e., PFSA membranes, have been extensively studied and utilized in PEMFCs due to their high proton conductivity and substantial thermal and mechanical stability.[59] The high proton conductivity of PFSAs is due to the hydration and consequent proton dissociation of the strong acid groups. Nafion, originally developed by DuPont, is the most widely used PFSA ionomer as the cation exchange membrane for both PEMFCs and VRFBs.[40,56,63] Figure 1.3 shows the chemical structure of Nafion with the equivalent weight (EW) being the molecular weight per ionic group of the ionomer. The polytetrafluoroethylene (PTFE) backbone provides outstanding chemical stability in both basic and acidic environments.

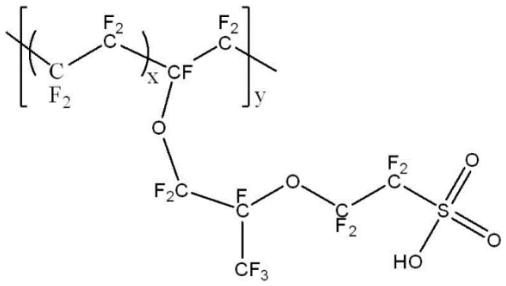


Figure 1.3. The chemical structure of Nafion ionomer. The values of y and x determine the molecular weight and equivalent weight (molecular weight per ionic group), respectively.

Despite many advantages, PFSA membranes have high costs, limited operating temperatures, permeability to methanol, complex water management, and environmental issues related to the recycling.[64] These challenges have led to significant research into finding alternative materials either by modifying the PFSAs or synthesizing and developing novel polymeric and composite materials.

One of the approaches to modifying the present PFSAs is to replace the sulfonic acid group with other protogenic groups. The bis[(trifluoromethane)sulfonyl]imide, $CF_3SO_2NHSO_2CF_3$, is one of the alternatives that shows higher proton conductivity at intermediate hydration levels when substituted for the sulfonic acid group in Nafion.[65] This sulfonyl imide is one of the strongest superacids[66] and may be used under more extreme conditions.[67-68] Phosphonic acid group is another alternative owing to its good thermal and oxidative stability.[69] Although phospho-acids (phosphoric, phosphonic, and phosphinic) are not as strong as sulfonic acids under certain conditions they may exhibit even higher proton conductivity. Phosphoric acid is an outstanding proton conductor as a neat liquid.[70-72] If transferrable to phosphonic acid this may lead to improved conductivities over the PFSAs at very low hydrations and anhydrous conditions. Burton *et al.* prepared perfluorophosphonic acid ionomers that showed good thermal stability and equal or lower conductivities to that of Nafion control.[73]

Non-Fluorinated Ionomers. The non-fluorinated hydrocarbon polymers have received tremendous attention as low-cost alternatives to PFSAs.[62,64] These membranes are typically made from aromatic or heterocyclic repeat units to enhance the stability at elevated temperatures. Polysulfones (PSU), poly(ether sulfone) (PES), poly(ether ketone)s (PEK) with varying number of ether and ketone functionalities (e.g., PEEK, PEKK, PEEKK), and polybenzimidazole (PBI) are some examples of this group. These polymers are inherently insulating and therefore need to be modified for application in PEMFCs. Several approaches have been developed to add the ion conducting functional groups to the polymers including: acid or base doping; direct sulfonation of the backbone; grafting of a sulfonated or phosphonated functional group; and synthesis from the sulfonated monomer.[64] The characteristics of the final membrane depend on the chemical nature of the polymer backbone, the molecular weight of the polymer, the distribution of the molecular weight, and the degree of functionalization.

A competitive hydrocarbon-based ionomer is a sulfonated Diels-Alder poly(phenylene) (SDAPP) polymer.[74] SDAPP can achieve comparable conductivity to Nafion and has been shown to outperform it when used in VRFBs.[75-77] Transmission electron microscopy (TEM) imaging shows that the ionic domains in SDAPP are roughly 0.5 nm in diameter compared to Nafion where the average dimension of the water domains are approximately 2 nm when fully hydrated.[76] It is important to understand the factors controlling the size of the ionic domains in the hydrated ionomer in order to enhance both ionic conductivity and selectivity.

Acid-Base Complexes. This class of membranes incorporates acid components into an alkaline polymer base to promote proton conduction without humidification at high temperatures.[59,62] The phosphoric acid-doped polybenzimidazole (PBI/H_3PO_4) is a successful example showing high proton conductivity and excellent mechanical properties at temperatures up to 200 °C.[78] Acid-base

polymer blends are also promising materials exhibiting low water uptake, high proton conductivity, good mechanical and thermal stability. The improved properties of these blends are related to the acid-base interactions between the polymer chains, specifically, ionic interactions and hydrogen bonding.[79] The polymer blend of sulfonated poly(ether ether ketone) as the acidic compound and polybenzimidazole as the basic compound, i.e., sPEEK/PBI, is an example with good proton conductivity and excellent thermal stabilities.[80]

Supported Composites. These membranes are obtained by combining polymers with inorganic materials; either the polymer or the inorganic component or both may be ion conducting. Composites incorporate the advantages of both polymers (e.g., flexibility and ionic conductivity) and inorganic materials (e.g., thermal and mechanical stability) plus the synergistic effects due to their interactions.[81] The composite membranes offer higher thermal stability, enhanced proton conductivity, water retention at high temperatures, and mechanical support when compared to the pure polymer membranes.[62] Metal oxides, metal phosphates, phosphosilicates, porous inorganic materials (e.g., zeolite, activated carbon, and metal organic framework (MOF)), and carbon nanotubes are some of the common inorganic materials used.

The preparation technique controls the final properties of the composites because it directly affects the particle dispersion (determines the isotropy) and interfacial adhesion (relates to the synergism).[81] The following preparation methods: infiltration; recasting; and electrospinning may be utilized depending on the compositions of the mixing components and the desired characteristics. The first two methods incorporate inorganic particles into the polymer by swelling or dissolution in a solvent. The last technique involves electrospinning of a non-conductive or less conductive phase into a mat and then adding a highly proton conducting component.[82-85] The

inverse, i.e., electrospinning a conductive phase and then enforcing it with a non-conductive material has also been done.[86-89]

1.2.3 Alkaline Fuel Cells (AFCs)

The AFC is one of the oldest fuel cells and was first described by Reid in 1903.[90-91] It uses an aqueous electrolyte solution of potassium hydroxide (KOH), because it is the most conducting of all alkaline hydroxides.[57] Hydrogen gas reacts with hydroxide anions at the anode generating water and electrons. The electrons are transferred through an external circuit to the cathode, where oxygen reacts with water to generate hydroxide ions.[57] The half-cell reaction at the anode may be written as:

$$H_2 + 2OH^- \longrightarrow 2H_2O + 2e^- ; \tag{1.7}$$

and at the cathode:

$$O_2 + 2H_2O + 4e^- \longrightarrow 4OH^- . \tag{1.8}$$

The overall cell reaction is the same as in a PEMFC, i.e.:

$$2H_2 + O_2 \longrightarrow 2H_2O . \tag{1.9}$$

Some of the advantages of the AFC over other fuel cells include: lower operating temperature (≈ 23 – 70 °C), higher reaction kinetics at the electrodes resulting in higher cell voltages, and much lower noble metal catalyst loading. The ORR in AFC is more facile than in PEMFC due to the basic environment. Thus, AFC may operate with little or no platinum catalyst reducing the cost of the cell. It has been shown that non-precious metals (silver, nickel, and cobalt)[92-93] and transition metal oxides[94-95] may successfully be used as the catalyst.

One of the main drawbacks in the AFC is the sensitivity of the KOH solution to CO_2.[96] This necessitates the use of a pure feed oxidant stream instead of air. It is difficult to purify the fuel stream and consequently limits the commercialization of AFCs. The KOH solution may be

replaced with an anion-conducting polymer electrolyte.[97] This relatively new design has an anion exchange membrane (AEM) functioning as both the separator and the conductive support between the electrodes and is shown in Figure 1.4. No solid crystals of the metal carbonate are formed that would block the gas diffusion electrodes, because there are no mobile cations (K^+) and hence, the efficiency and lifetime of AFC are improved.

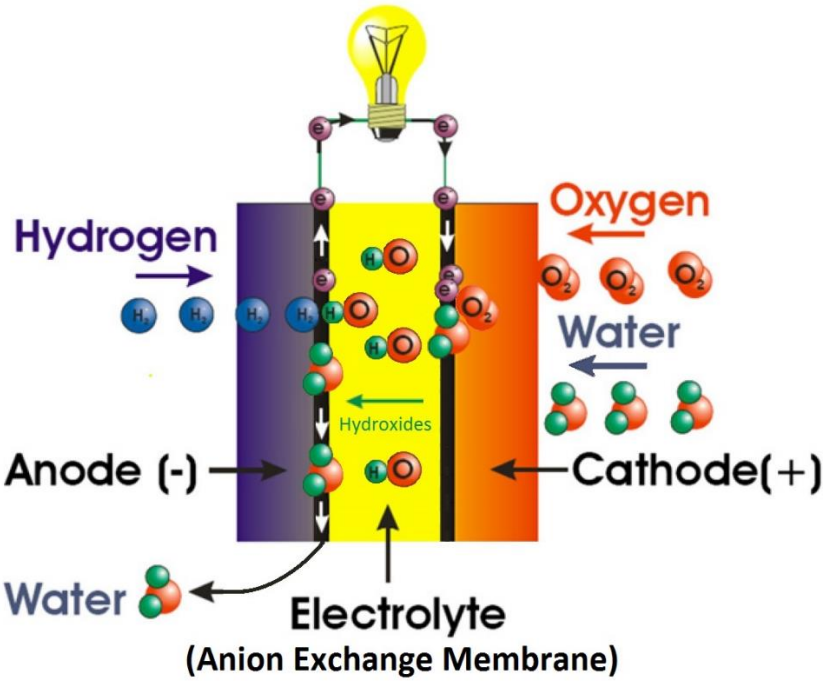


Figure 1.4. Schematic representation of an alkaline fuel cell with a polymer electrolyte membrane. Hydrogen and oxygen gases are introduced at the anode and cathode, respectively. Hydrogen gas reacts with hydroxide at the anode generating water and electrons. The electrons are transferred through an external circuit to the cathode, where oxygen reacts with water to generate hydroxide ions.

1.2.4 Electrolytes for Anion Exchange Membrane Fuel Cells

AEMs must have high ionic conductivity (but not electron conducting), low gas permittivity, and high thermal and mechanical stability.[57,98] They are generally polymers functionalized by cationic groups capable of conducting hydroxide ions (OH^-). A few anion-exchange groups are depicted in Figure 1.5. Benzyl trimethyl quaternary ammonium (Figure 1.5 (b) with R = $–CH_3$) is one of the most widely used cation exchange groups in AEMs.[99]

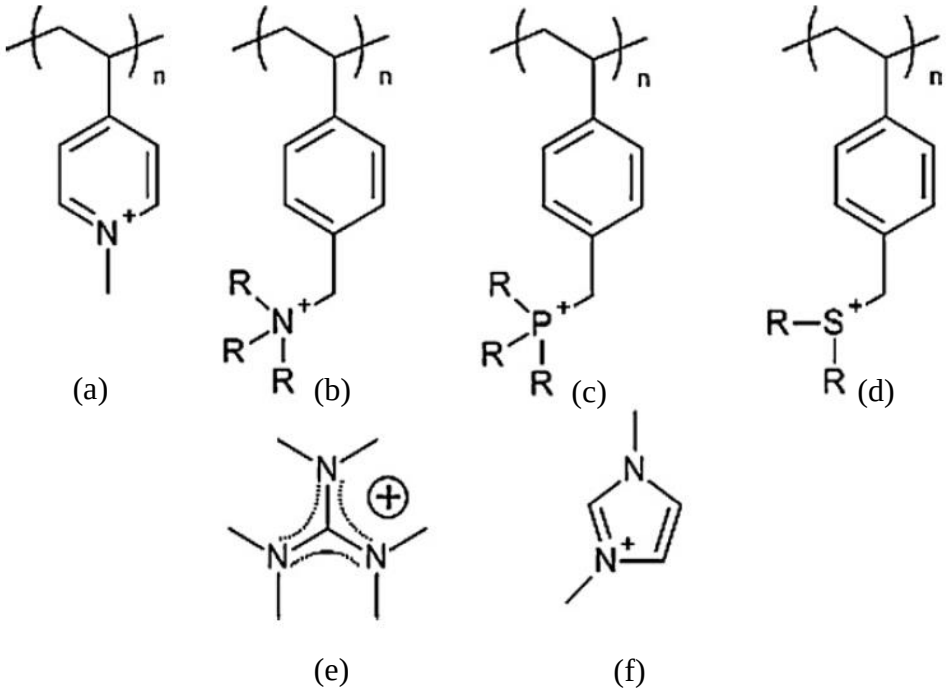
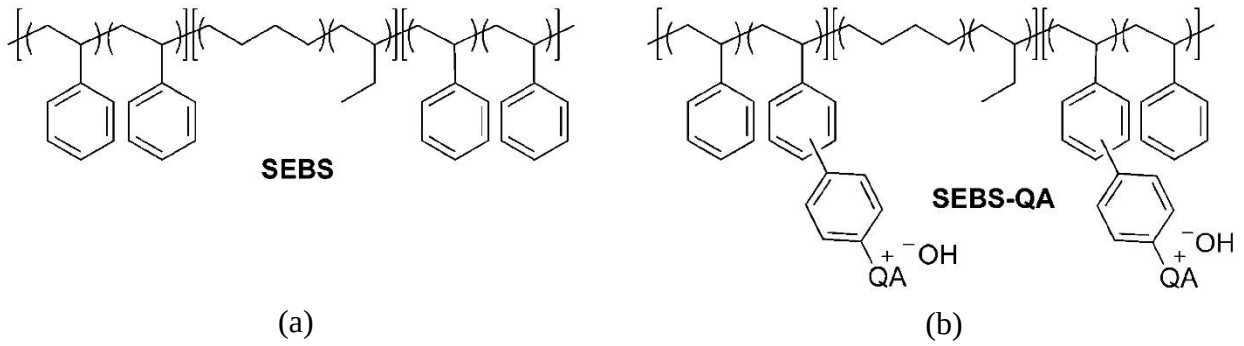


Figure 1.5. Chemical structures of common functional groups used in AEMs. (a) pyridinium; (b) quaternary ammonium; (c) phosphonium; (d) sulfonium; (e) guanidinium; and (f) imidazolium (taken from reference 98).

The conductivity of AEMs is generally lower than PEMs, because: (1) the hydroxide ion has a lower mobility than that of the proton;[100] and (2) some AEMs lack the microphase separation between the hydrophilic and hydrophobic phases that facilitate ion transport.[60,101-102] A main problem with AEMs is the limited chemical and thermal stability under highly corrosive alkaline conditions. The cationic groups may be decomposed by OH^- that results in degradation of the polymer, reduced ion exchange capacity, and lower conductivity of the membrane. It has been determined that the stability of an AEM strongly depends on the chemical nature of the cationic functional groups and the main chain structure.[60] The alkaline stability may be improved by using stable cation structures,[103-107] imposing steric hindrance and electronic effects,[106,108-109] and crosslinking.[110-111]

Several chemically stable AEMs using the triblock copolymer: polystyrene-b-poly(ethylene-co-butylene)-b-polystyrene (SEBS), functionalized by various benzyl- and alkyl-substituted quaternary ammonium groups have been recently developed.[112-114] The chemical structures of the SEBS and SEBS functionalized by a quaternary ammonium group (SEBS-QA) are shown in Figure 1.6. The SEBS backbone provides good chemical and mechanical stability to the membrane due to its robust structure, high molecular weight, and elastomeric units. It is known that the morphology of the SEBS copolymer depends on the block compositions.[115-118] Hence, the phase-separated morphology of SEBS-based AEMs may be tailored to achieve high anion conductivity by varying the block composition in the SEBS copolymer.



(a) (b)

Figure 1.6. The chemical structures of: (a) the SEBS triblock copolymer; and (b) the synthesized AEM ionomer obtained by functionalization of the SEBS copolymer with quaternary ammonium groups (taken from reference 112). The two end blocks of the SEBS consist of polystyrene, a rigid polymer, while the midblock is hydrogenated polybutadiene, an elastomer.

Fundamental understanding of transport in AEMs is still in its infancy,[119] in contrast to PEMs which have been systematically studied for many years.[120] Quantum chemical calculations[121-123] and molecular dynamics simulations[124-127] have previously been used to determine the structure and stability of the anion exchange functional groups as well as the transport mechanism of hydroxide in AEMs, similar to what has been done for PEMs.[128-132] These techniques provide

valuable information at the atomic and molecular scales, however they are inadequate to explore the morphological aspects due to the length and time scale limitations. Meso-scale simulations may provide a relative understanding of the morphological features of AEMs as they previously did for PEMs.[48-49,133-134] The effect of other anions including chlorine and bromine may also be studied, because the membranes are usually prepared and characterized in a halogen precursor form.[112,114]

1.3 Secondary Magnesium Batteries

Secondary batteries are of great interest to industry as they may offer solutions to the current technical and cost barriers as well as the safety and environmental concerns associated with portable energy storage.[2] Magnesium based batteries are deemed particularly promising if advancements in materials and manufacturing technologies are achieved.[2,135-136] These batteries show advantages over other competing types (i.e., lithium and sodium ion batteries) owing to the abundance of Mg in the earth's crust and the issues concerning disposal and waste. They also have a broad operating temperature range and their capacity loss over time is quite small. The magnesium cation is, of course, divalent thereby providing twice the charge per ion as monovalent ions such as lithium. This results in a theoretical volumetric capacity of 3832 mAh/cm^{-3} (in contrast to Li which has a capacity of 2061 mAh/cm^{-3}).[135] It is also more stable and less chemically reactive than either Li or Na, and consequently, large scale magnesium electrical energy storage devices are simpler to design.[2] A practical magnesium rechargeable battery was pioneered by Aurbach *et al.* with an energy density of 60 Wh/kg which was operated for more than 2000 cycles with little fade.[137] Proper design and architecture may lead to even higher gravimetric energy densities of 150 − 200 Wh/kg and operating voltages between 2 and 3 volts.[2,138]

The anode is usually made of commercially pure magnesium (99.9% or higher) in different forms such as foil, ribbon, or coupon.[2,137] At the cathode, where the electrons are transferred to the host material, Mg^{2+} ions must be inserted and extracted from a solid host to the electrolyte solution without causing any electrode destruction. Many materials fail to serve as the cathode for magnesium batteries due to the difficulty of intercalating magnesium ions.[137] Cathodes made of chevrel phases (CPs), $M_xMo_6T_8$ (M = metal, T = S, Se, Te) a unique class of host materials, exhibit fast and reversible intercalation.[137,139] Other cathodes have been developed based on V_2O_5, MoO_3, transition metal oxide/sulfide/boride, and NASICON-type materials.[2] Recently, Muldoon and coworkers developed a new class of cathodes based on the conversion cathode reaction of metallic magnesium with elemental sulfur, referred to as the magnesium/sulfur conversion cathode.[136,140] The combination of a magnesium anode and a sulfur cathode can theoretically deliver a high energy density (~ 4000 Wh/l). However, the greater challenge is to identify suitable electrolytes which are compatible with sulfur.

A critical roadblock towards practical Mg-based energy storage is the lack of reversible electrolytes that are safe and electrochemically stable. The choice of the electrolyte and its properties also affects the class of cathodes utilized. Magnesium has a unique electrochemistry which prohibits its reversible deposition in aprotic solvents due to the formation of a passivation layer which prohibits conduction of Mg^{2+} ions.[141] Ethereal solutions of Grignard reagents and magnesium organohaloaluminates may surpass this problem.[139,142-143] However, these solutions are hazardous due to their volatility and flammability.

Existing electrolytes[136,144-146] based on liquid solvents are inadequate for meeting the needs of functional devices for portable electronics and transportation applications due to their high volatility and corrosiveness.[135,138] The volatility issue may be relieved by using polymers, however,

the possibility of synthesizing high-performance polymer electrolytes with the α and β forms of $MgCl_2$ had been ruled out due to the high lattice energy of the salt.[147] $MgCl_2$ may be prepared in a form called δ-$MgCl_2$ that is characterized by high crystallographic disorder, reactivity, and solubility.[148] The non-conventional properties of this salt are due to the presence of a metastable nanoribbon or polymeric structure with concatenating $MgCl_2$ repeating units, in which the Mg atoms are bridged *via* chloride bridges. The preparation of polymer electrolytes using this salt has yielded Mg^{2+}-conducting materials with conductivities as high as 10^{-4} $S \cdot cm^{-1}$ at room temperature. These studies lead to the first Mg-polymer batteries.[149] The use of the δ-form of $MgCl_2$ with ionic liquids as the electrolyte is a significant milestone in the search for high-performance stable electrolytes.

1.3.1 Electrolytes Based on Ionic Liquids

Ionic liquids (ILs) have been examined in the preparation of electrolytes for Mg batteries because, in addition to being endowed with high thermal and electrochemical stability, they exhibit negligible vapor pressure and are non-flammable.[150-151] However, it was determined that magnesium electrodes are generally reactive toward imidazolium-based ILs.[152] Magnesium appears to develop a blocking passivation layer impervious to the transport of ions in the few ILs that are electrochemically stable. These observations dampened earlier interest in EMImCl/$AlCl_3$ melts (EMImCl: 1-ethyl-3-methylimidazolium chloride) partially neutralized with conventional $MgCl_2$[153-154] which were carefully studied due to their intriguing Lewis acid-base properties defined in terms of the ratio $R = n_{AlCl_3}/n_{EMImCl}$. A melt is classified as basic, neutral, or acidic, if *R* is less, equal to, or more than 1, respectively.

High-performance electrolytes based on EMImCl doped with $AlCl_3$ and highly amorphous $MgCl_2$ have recently been developed.[138] These systems have the general formula: (EMImCl/$(AlCl_3)_{1.5}$)/(δ-

$MgCl_2)_x$, with molar ratio $x = n_{\delta-MgCl_2}/n_{IL}$, $0 \leq x \leq 0.2$, and exhibit an initial capacity of 80 mAh/g with a steady-state voltage of 2.3 V when discharged in a coin cell set up. The structural characteristics and the properties of the resulting electrolyte are tied to the ion-ion interactions within the IL. This development seems very promising, however the key to improvement and success of these new materials is identification of the structure.

Experimental IR and Raman spectra of the electrolyte systems with the general formula $(EMImCl/(AlCl_3)_{1.5})/(\delta\text{-}MgCl_2)_x$ reveals peaks which are indicative of the formation of new species and structural changes over the pristine IL, i.e., $EMImCl/(AlCl_3)_{1.5}$. Changing the halide from chloride to the iodide also affects the electrolyte properties. EMIm-based ILs have been studied extensively.[155-159] However, the effect of the Mg-halide salt on their structure and properties has not been explored. Quantum chemical calculations were undertaken previously to determine the structure of small clusters of molecules and assignment of the experimental vibrational spectra in various ILs including: EMImCl;[160-162] $EMImCl/AlCl_3$;[160] EMImBr;[163] $EMImBF_4$;[163-164] and $EMImPF_6$.[163] Hence, molecular-level investigations were undertaken in this work to understand the ionic structure and experimentally observed properties of these EMIm-based electrolytes.

1.4 Research Overview

The research undertaken and reported in this dissertation aims to understand various structural and dynamical aspects of a variety of electrolytes used in energy storage and conversion technologies. Several modeling techniques at different length scales were utilized to elucidate how the molecular structure determines the properties of these materials.

The hydration of the four vanadium cations (V^{2+}, V^{3+}, VO^{2+}, and VO_2^+) present in VRFB electrolytes was determined via electronic structure calculations. The Gibbs energies of hydration

of the four vanadium cations were calculated using quasi-chemical theory. Electronic structure calculations determined the local interactions of the hydrated vanadium cations with sulfuric acid (H_2SO_4) and trifluoromethanesulfonic acid (CF_3SO_3H) employing a continuum solvation model to account for the solvent/liquid phase effects. A parameterization method based on *ab initio* calculations was developed to compute interaction parameters utilized in dissipative particle dynamics (DPD) simulations of hydrated Nafion membrane with absorbed vanadium cations. The hydrated morphology of Nafion was investigated to determine the effects of absorbed vanadium cations.

Microstructure/morphology relationships in the AEM systems based on SEBS was explored at the meso-scale via DPD simulations employing the developed parameterization scheme. The SEBS triblock copolymer was first benchmarked and then hydrated AEM systems were simulated to probe the effect of the degree of hydration and anion type (OH^- vs Cl^-) on the morphology.

A coarse-graining scheme was proposed for the SDAPP membrane electrolyte systems. This was followed by electronic structure calculations in order to provide the atomic scale information required for the parameterization of the DPD interactions (utilizing the method developed in this work).

Two recent EMIm-based electrolyte materials for magnesium batteries were investigated using density functional theory (DFT). The $EMImCl/(AlCl_3)_{1.5}$ and $EMImAlI_4$ ILs were studied at the proximity of MgX_2 (X = Cl and I, respectively) to investigate the effect of the magnesium salt. The calculated vibrational frequencies were compared to the experimental IR and Raman spectra to assign the vibrational peaks and reveal the speciation of the electrolyte systems.

The hydration and dissociation of ten acid molecules that are commonly utilized in electrolytes: CF_3SO_3H; FSO_3H; CH_3SO_3H; H_2SO_4; HNO_3; HF; H_3PO_2; H_3PO_3; H_3PO_4; and $CF_3SO_2NHSO_2CF_3$

were studied via the electronic structure calculations. The hydrated structures were further explored for proton transfer by performing potential energy surface scans in both gas phase and with a dielectric continuum model. These calculations aimed to provide a fundamental understanding of the relative acidities and to serve the purpose of designing novel electrolytes featuring one or more of these acids in either the solution or tethered to an ionomer.

The theoretical background for the various techniques employed in this work are summarized in Chapter 2. A discussion of the results is presented in Chapters 3 – 7: Chapter 3, multiscale modeling of VRFB electrolytes with quantum chemical calculations, quasi-chemical theory, and DPD simulations; Chapter 4, morphological investigations of SEBS-based AEMs coarse-grained DPD simulations; Chapter 5, a meso-scale study of SDAPP membranes; Chapter 6, structural and vibrational frequency analysis of EMIm-based electrolytes; and Chapter 7, DFT calculations of the hydration and proton transfer of several acids. The summary of the significant findings and concluding remarks are given in Chapter 8.

Chapter 2 Computational Methods

2.1 Multiscale Modeling

Any physical phenomena may be viewed from different scales and levels of complexity depending on the application and properties of interest. For example, in engineering problems where the macroscopic behavior of materials is important, continuum models are often used with little or no appeal to molecular scale information. In contrast, in quantum physics the materials behavior is often described by the atomic and electronic level processes.[165]

Figure 2.1 shows a classification of various computational methods in chemistry and materials science as functions of length and time scales: quantum mechanics; atomistic; mesoscopic; and macroscopic. Decreasing the length scale usually increases the computational expense and thereby decreases the time scale.

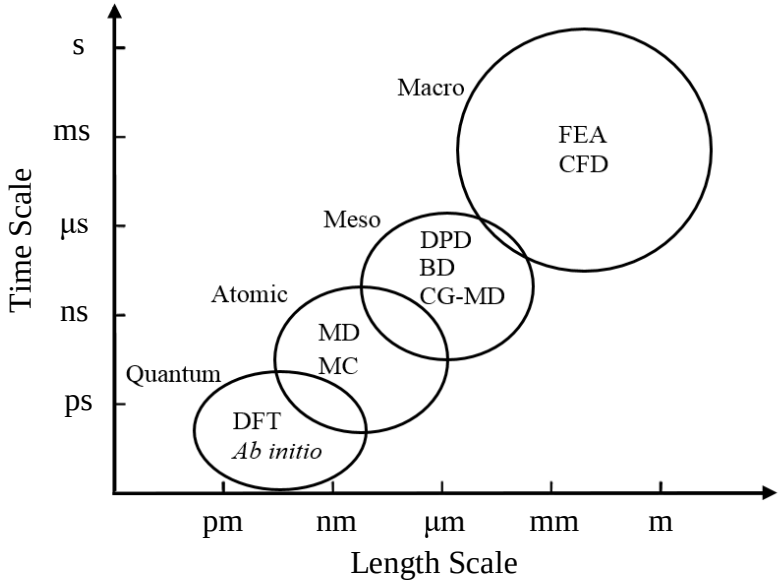


Figure 2.1. Classification of several computational methods in chemistry and materials science as a function of length and time scales. The methods at larger length scales probe longer times but lack any small scale information.

Macroscopic scale methods (e.g. finite element calculations) assume that the materials of interest are continuous and ignore the microscopic and atomic resolution. The effects of the smaller scales may be implicitly introduced in these methods through constitutive equations that are often empirical and based on simple considerations such as symmetry, linearization, or Taylor series expansions.[165] Empirical constitutive models are typically highly successful in engineering applications, however they are inadequate in cases where the system is complex and lack the ability to connect information between the microstructure and macroscale behavior.

Dissipative particle dynamics (DPD), Brownian dynamics (BD), and coarse-grained molecular dynamics (CG-MD) are meso-scale simulation techniques that have been extensively employed[48-50,54,133,166] and improved[167-172] in recent years due to their computational efficiency. In these methods, several atoms or molecules are replaced with a representing mesoscopic particle (or bead) and a mesoscopic force field assumed to define the interactions between the particles. The mesoscopic force fields are critical to the coarse-grained models. Figure 2.2 shows a schematic of a coarse-grained model for the PFSA ionomer, Nafion.

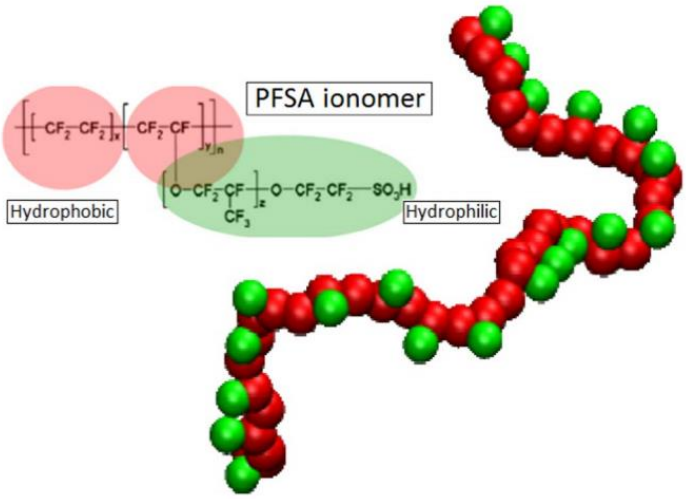


Figure 2.2. Coarse-graining of Nafion, a PFSA ionomer. Different mesoscopic particles are defined to represent chemically distinct subunits of the polymer (taken from reference 173).

Classical molecular dynamics and Monte Carlo (MC) are atomic scale simulation techniques that consider full atomistic resolution. The atoms and molecules interact with each other based on force fields that are obtained either empirically or by fitting to quantum mechanical data.[174-175] However, these methods do not consider electrons and subatomic particles and therefore do not effectively describe electronic effects including chemical reactions, breaking and forming of covalent bonds, and to some extent even hydrogen bonding.

The methods at the finest scale shown in Figure 2.1 rest on the principles of quantum mechanics to determine the electronic structure of the matter. First principles (i.e., *ab initio*) calculations are the most accurate and computationally expensive methods and therefore limited to very small systems consisting of hundreds of atoms or several molecules. The application of quantum mechanics to the problems in chemistry is referred to as quantum chemistry.[176]

In what follows, a brief description of quantum chemical calculations and some approximation techniques are presented. Next, a statistical mechanical approach that describes the thermodynamics of ion solvation phenomena, quasi-chemical theory, is presented. The statistical mechanical derivations and practical formulations required for the calculation of Gibbs energies are presented. The meso-scale simulation method, DPD, is then described and several parameterization methods for obtaining the coarse-grained interactions are reviewed.

2.2 Quantum Chemical Calculations

The insufficiency of Newtonian mechanics in describing the behavior of very small particles such as electrons and atoms nuclei led to the development of quantum mechanics. This branch of physics considers the discreteness of energy, the wave-particle duality of light and matter, and spin of a particle that Newtonian mechanics fails to describe. In quantum mechanics, the state of a physical system at a given time is postulated to be described in the form of a function

of the particles' coordinates and spin, namely the wave function Ψ.[176] The state of a system changes with time and therefore the wave function is also time dependent. The time evolution of the system is described by the Schrödinger equation that predicts the future state of the system.

$$i\hbar\frac{\partial}{\partial t}\Psi = \hat{H}\Psi \tag{2.1}$$

Here t is time, $i = \sqrt{-1}$ is the imaginary unit, $\hbar$ is the plank's constant divided by 2π, and $\hat{H}$ is the Hamiltonian operator that describes the total energy of the system. If the system experiences no time-dependent external forces and the potential energy is not a function of time, Ψ may be written as $\Psi = \mathrm{f(t)}\psi$, i.e., the product of a function of time, f(t), and a function of particles' coordinates and spin, ψ. In these cases the Schrödinger equation reduces to a time-independent form for ψ. Such states are called stationary states and do not change with time.

Static *ab initio* electronic structures are based on the solution of the time-independent Schrödinger equation for a physical system of interest. However, the exact solution to this equation is only available for a single-particle system. Hence, different approximation methods are developed and used. The time-independent Schrödinger equation is introduced along with approximate solution methods including Hartree-Fock (HF) and density functional theory (DFT).[176-177] Later the basis sets, a brief introduction to continuum solvation models, and vibrational frequencies are explained.

2.2.1 Time-Independent Schrödinger Equation

In quantum mechanics the stationary state of a physical system is described by wave function, a function of the particles' coordinates and spin. Every measurable physical quantity is described by a Hermitian operator (i.e., $\hat{A} = \hat{A}^{\dagger}$). The operator corresponding to the total energy of the system

is the Hamiltonian operator, $\hat{H}$. It is also postulated that the measurement of a physical quantity gives an eigenvalue of its operator, and therefore the physical quantity can be calculated by solving an eigenvalue problem. The time-independent Schrödinger equation is an eigenvalue problem for the total energy of the system:

$$\hat{H}\psi = E\psi \,, \tag{2.2}$$

where ψ is the space and spin wave function/eigenfunction, and E is the energy/eigenvalue. The wave function itself does not have any physical interpretation. However the product of ψ with its complex conjugate ψ^*, which is $|\psi^*\psi| = |\psi|^2$ is the probability of finding the system in the state ψ, provided that the normalization condition:

$$\int |\psi|^2 \, d\tau = 1 \,, \tag{2.3}$$

is satisfied. The τ is coordinates and spin of all particles and the $\int d\tau$ integrates over all the coordinates and spin in which the system and its Hamiltonian are defined.

The Hamiltonian is simply the sum of the kinetic and potential energies of all the particles in the system.

$$\hat{H} = \hat{T}_e + \hat{T}_n + \hat{V}_{ee} + \hat{V}_{nn} + \hat{V}_{en} \tag{2.4}$$

Here $\hat{T}$ and $\hat{V}$ represent the operators of kinetic and potential energies, respectively and the subscripts e and n refer to electron and nucleus, respectively. The operator $\hat{V}_{ee}$ represents the potential energy due to the electron-electron interactions and similarly $\hat{V}_{nn}$ and $\hat{V}_{ne}$ are the operators corresponding to the nucleus-nucleus and nucleus-electron interactions. The expanded form of the Hamiltonian operator in atomic units for N_e electrons and N_n nuclei is:

$$\hat{H} = -\frac{1}{2}\sum_{i}^{N_e}\nabla_i^2 - \sum_{k}^{N_n}\frac{1}{2M_k}\nabla_k^2 + \sum_{i}^{N_e}\sum_{j>i}^{N_e}\frac{1}{r_{ij}} + \sum_{k}^{N_n}\sum_{l>k}^{N_n}\frac{Z_k Z_l}{r_{kl}} - \sum_{i}^{N_e}\sum_{k}^{N_n}\frac{Z_k}{r_{ik}} \qquad (2.5)$$

where i and j denote electrons, k and l denote nuclei, M_k is the ratio of the mass of the k^{th} nucleus to the mass of an electron, ∇^2 is the Laplacian operator, Z is the atomic number of the nucleus, and $r_{ij} = |r_i - r_j|$ and $r_{kl} = |r_k - r_l|$.

The mass of the nuclei is far greater than that of electrons, implying that the time scale of nuclear motion is significantly smaller than the electrons and hence their motion may be decoupled. Thus, in the study of the motion of electrons, the nuclei can be considered at fixed positions. This is the **Born-Oppenheimer (BO) approximation** and permits the neglecting of the kinetic energy of the nuclei in electronic structure calculations. Because the position of the nuclei are no longer variables, the nuclear-nuclear repulsion becomes a constant which solely depends on the positions of the nuclei. Hence, the Hamiltonian operator becomes:

$$\hat{H} = \hat{H}_{elec} + V_{nn} \qquad (2.6)$$

where, $\hat{H}_{elec}$ is the electronic Hamiltonian. This may be further simplified by introducing the compact notation for the one- and two- electron terms:

$$\hat{H}_{elec} = \sum_{i}^{N_e} h_i + \sum_{i}^{N_e}\sum_{j>i}^{N_e} g_{ij}\,. \qquad (2.7)$$

Here, $h_i = -\frac{1}{2}\nabla_i^2 - \sum_k^{N_n}\frac{Z_k}{r_{ik}}$ is the one-electron operator corresponding to the kinetic energy and coulombic attraction of electron i in the field of all the nuclei, and $g_{ij} = \frac{1}{r_{ij}}$ is the two-electron operator describing the electron-electron repulsion. The electronic version of the Schrödinger equation may be written as follows:

$$\hat{H}_{elec}\psi_{elec} = E_{elec}\psi_{elec}\,, \qquad (2.8)$$

where ψ_{elec} and E_{elec} are the electronic wave function and electronic energy, respectively.

2.2.2 Hartree-Fock Method

The difficulty in evaluating an analytic solution of the time-independent Schrödinger equation is the coulombic electron-electron repulsion term which prevents independent treatment of the electrons. To overcome the problem associated with electron correlation it is assumed that each electron moves in an orbital within the average field generated by all the other electrons. This approximation[178] leads to a simple form of the many-electron wave function. The *N*-electron wave function is expressed as the product of *N* independent single particle wave functions. However, the electronic wave function must be antisymmetric in order to satisfy the Pauli Exclusion Principle, which states that each electron in a system has a unique quantum state, i.e., the probability of finding two electrons in the same state is zero. To satisfy the antisymmetric requirement the wave function is expressed as a Slater determinant (SD):

$$\psi^{SD}(x_1, x_2, \dots, x_N) = \frac{1}{\sqrt{N!}} \begin{vmatrix} \chi_1(x_1) & \chi_2(x_1) & \cdots & \chi_N(x_1) \\ \chi_1(x_2) & \chi_2(x_2) & \cdots & \chi_N(x_2) \\ \vdots & \vdots & \ddots & \vdots \\ \chi_1(x_N) & \chi_2(x_N) & \cdots & \chi_N(x_N) \end{vmatrix}, \qquad (2.9)$$

where x_i is the space-spin coordinate for the i^{th} electron, $x_i \equiv [r_i, \omega_i]$ (r_i and ω_i are the spatial and spin coordinates, respectively) and χ_i is the spin orbital. The spin orbitals must be orthonormal, i.e., $\langle \chi_i | \chi_j \rangle = \delta_{ij}$ and therefore the prefactor $1/\sqrt{N!}$ ensures the normalization of the wave function.

Using the SD and Equation (2.7) the electronic HF energy of the system may be calculated as:

$$E_{elec}^{HF} = \langle \psi^{SD} | \hat{H}_{elec} | \psi^{SD} \rangle = \langle \psi^{SD} | \sum_i \hat{h}_i | \psi^{SD} \rangle + \langle \psi^{SD} | \sum_i \sum_{j>i} \hat{g}_{ij} | \psi^{SD} \rangle . \qquad (2.10)$$

By substituting a simpler form of the SD, using the orthonormality of the spin orbitals, and knowing the electronic HF energy can be written as the sum of one- and two- electron terms as:

$$E_{elec}^{HF} = \sum_{i}^{N} h_i + \frac{1}{2}\sum_{i}^{N}\sum_{j}^{N}(J_{ij} - K_{ij}) \,, \tag{2.11}$$

where the one-electron term h_i is the expectation value of its operator, i.e., $\langle \psi^{SD} | \hat{h}_i | \psi^{SD} \rangle = h_i$, and corresponds to the kinetic energy and coulombic attraction of electron *i* in the field of all the nuclei. The term J_{ij} is called the Coulomb integral as it represents the coulombic repulsion between the two *i* and *j* electrons ($J_{ij} = \langle \chi_i(x_i)\chi_j(x_j) | \hat{g}_{ij} | \chi_i(x_i)\chi_j(x_j) \rangle$) and K_{ij} is the exchange integral and unlike the Coulomb integral has no physical analog ($K_{ij} = \langle \chi_i(x_i)\chi_j(x_j) | \hat{g}_{ij} | \chi_j(x_i)\chi_i(x_j) \rangle$). The exchange integral is the result of the antisymmetric requirement of the wave function.

If the spin orbitals and consequently the SD (the wave function) are known the energy of the system can be calculated accordingly. Unfortunately, the mathematical form of the wave function is unknown in almost all cases. The practice is to apply a variational method and to make use of a trial wave function to calculate the energy of the system. This trial wave function is then optimized until the energy of the system reaches a minimum. The energy obtained via the trial wave function is always greater than the ground state energy unless the wave function is exact. The HF method applies the variational principle to determine the spin orbitals that minimize the energy (the expectation value of the Hamiltonian). The method of Lagrange multipliers under the constraint of orthonormal orbitals is applied to the energy expression in Equation (2.11). This leads to the HF equation for an arbitrary electron:

$$\hat{F}(1)\chi_i(1) = \varepsilon_i \chi_i(1) \,, \tag{2.12}$$

where $\hat{F}$ is the Fock operator defined as:

$$\hat{F}(1) = \hat{h}_1 + \sum_{j}^{N} \left(\hat{J}_j(1) - \hat{K}_j(1) \right) , \tag{2.13}$$

which is the single electron operator describing the energy of an electron involved in the interaction with all other electrons and the nuclei. The first term of the Fock operator is associated with the kinetic energy of an electron and its attractive interaction with all the nuclei. The second term describes the electron-electron repulsion due to the presence of all other electrons. Both Coulomb and exchange operators depend on all the spin orbitals and hence the Fock operator itself. Thus, the Fock operator can be determined only if all other occupied orbitals are known. The consequence of this dependency is that the HF equation becomes a non-linear eigenvalue problem, which involves iterative procedures with an initial guess of the orbitals to solve. The iteration is usually continued until the change in the energy is less than a predetermined value. This iterative approach is referred to as the self-consistent field (SCF) method.

The term ε_i in the Equation (2.12) can be interpreted as the energy of the i^{th} molecular orbital, $\chi_i(1)$. The molecular orbitals are usually expressed as a linear combination of atomic orbitals (LCAO) that are expanded as:

$$\chi_i = \sum_a C_{ai}\varphi_a \,, \tag{2.14}$$

where φ_a is the atomic orbital of atom a (known) and C_{ai} is the expansion coefficient (unknown). The HF equations cast in matrix form under the LCAO approximation are the Hartree-Fock-Roothaan equations:

$$FC = SC\varepsilon \,, \tag{2.15}$$

where F and S are the Fock and basis function overlap matrices, respectively ($\hat{F}_{ab} = \langle\varphi_a|\hat{F}(1)|\varphi_b\rangle$ and $S_{ab} = \langle\varphi_a|\varphi_b\rangle$). C is the coefficient matrix and ε is a diagonal matrix of the orbital energies. A first set of coefficients along with the atomic basis functions are used as an initial guess to find the orbital energies in Equation (2.12) via the SCF method.

HF theory assumes a single-determinantal form for the wave function and neglects part of the correlation between the electrons. The electrons are subject to an average non-local potential arising from the other electrons, which can lead to a poor description of the electronic structure. Although the HF method provides a base for other more sophisticated post HF methods such as Møller-Plesset (MP) perturbation theory and configuration interaction (CI), but its accuracy is questionable. Post HF methods generally provide a better description of the electron correlation and consequently a more accurate description of the system, however they are considerably more computationally expensive.

2.2.3 Density Functional Theory

DFT has been widely used in recent years to overcome the electron correlation deficiency and computational cost of the HF and post HF methods. In this approach the molecular electronic energy is obtained from the molecular electron probability density rather than the molecular wave function. This significantly decreases the number of variables, since the molecular electron probability density is a function of only 3 spatial coordinates for all the electrons, whereas the molecular wave function depends on 3*N* spatial and *N* spin coordinates.

The central idea to DFT was first introduced by Hohenberg and Kohn in 1964.[179] They developed two theorems in which the electronic energy could be obtained exactly from the electron density. In the first theorem, called the **existence theorem**, they proved that for a system of electrons in an external potential with a non-degenerate ground state, the ground state electron probability density has a one to one relationship with the ground state molecular energy, wave function, and all other molecular electronic properties. Thus, the ground state electronic energy, E_0, can be written as a function of the ground state electron probability density, ρ_0, as:

$$E_0 = E_v[\rho_0] = T_e[\rho_0] + V_{ee}[\rho_0] + V_{ne}[\rho_0] \tag{2.16}$$

where the square brackets denote a functional relation and the subscript υ emphasizes the dependence of E_0 on the external potential. The T_e and V_{ee} are the ground state kinetic energy and electron-electron repulsion energy functionals, respectively. The V_{ne} functional is associated with the attraction between the electrons and the nuclei and is only a function of the coordinates of the electrons (the nuclei are fixed due to the BO approximation). This potential is considered external in DFT, since it is produced by the nuclei external to the system of electrons. If the electron density is known the $V_{ne}[\rho_0]$ can be determined, however the other two functionals, $T_e[\rho_0]$ and $V_{ee}[\rho_0]$, are unknown.

The second Hohenberg and Kohn theorem, the **variational theorem**, states that the exact ground state electron density should minimize the energy functional which is in fact the application of the variational principle (similar to the HF method). Thus,

$$E_\upsilon[\rho_{trial}] \geq E_\upsilon[\rho_0] \tag{2.17}$$

and the trial density must satisfy the $\int \rho_{trial}(r)d(r) = N$ and $\rho_{trial}(r) \geq 0$ conditions. Although the Hohenberg-Kohn theorems provide the possibility to calculate all the ground state molecular properties from ρ_0, they neither explain how to determine E_0 without knowing the kinetic and repulsion potential energy functionals nor how to find ρ_0 without first knowing the form of the wave function.

Kohn and Sham devised a practical method to utilize the Hohenberg-Kohn formalism.[180] They considered a hypothetical system, denoted by subscript s, consisted of *N* non-interacting electrons that each experience the same external potential energy function, where this potential is such as to make the ground state electron density of the hypothetical system equal to the ground state electron density of the real system, i.e. $\rho_s = \rho_0$ (the density subscript will be dropped for simplicity in what

follows). To facilitate analysis of the unknown functionals in Equation (2.16), the energy functional may be rewritten as:

$$E_v[\rho] = \int \rho(r)v(r)dr + T_s[\rho] + \frac{1}{2}\iint \frac{\rho(r_1)\rho(r_1)}{r_{12}} dr_1 dr_2 + E_{xc}[\rho]\,, \qquad (2.18)$$

where the first term is the external attraction potential energy, T_s is the kinetic energy functional of the non-interacting system, the double integral term is the self-repulsion of a classical charge distribution, and the last is the exchange-correlation energy functional, $E_{xc}[\rho]$. The exchange-correlation functional includes not only the effects of exchange and correlation embedded in $V_{ee}[\rho]$, but also the correction for the classical self-interaction energy (the double integral term) and for the difference in kinetic energy between the fictitious non-interacting system and the real one ($\Delta T[\rho]$).

Determining the electron density for the hypothetical non-interacting system is easy because there is no electron-electron repulsion term and the electronic Hamiltonian can be easily expanded as the sum of one-electron operators and the eigenfunction is the SD of the individual one electron eigenfunctions. Rewriting the energy expression as:

$$E[\rho] = -\sum_{i=1}^{N} \left\langle \chi_i \middle| \sum_{k=1}^{N_n} \frac{Z_k}{r_{ik}} \middle| \chi_i \right\rangle - \sum_{i=1}^{N} \left\langle \chi_i \middle| \frac{1}{2}\nabla_i^2 \middle| \chi_i \right\rangle + \sum_{i=1}^{N} \left\langle \chi_i \middle| \frac{1}{2}\int \frac{\rho(r_j)}{r_{ij}} dr_j \middle| \chi_i \right\rangle + E_{xc}[\rho]\,, \quad (2.19)$$

where the density is $\rho = \sum_{i=1}^{N} \langle \chi_i | \chi_i \rangle$. In order to find χ_i a similar approach to the HF method is used. The method of Lagrange multipliers is applied to minimize the energy expression in this equation and results in the central KS DFT equations:

$$\hat{h}_i^{KS} \chi_i = \varepsilon_i \chi_i\,, \qquad (2.20)$$

where $\hat{h}_i^{KS}$ is the one-electron KS Hamiltonian:

$$\hat{h}_i^{KS} = -\frac{1}{2}\nabla_i^2 - \sum_k^{N_n} \frac{Z_k}{r_{ik}} + \int \frac{\rho(r_j)}{r_{ij}} dr_j + V_{xc} \,. \tag{2.21}$$

V_{xc} is the functional derivative:

$$V_{xc} = \frac{\delta E_{xc}}{\delta \rho} \,. \tag{2.22}$$

The KS equations are solved iteratively, similar to the SCF method. The key difference between the HF method and DFT is that the former simplifies the problem by approximations and attempts to solve the approximate equations exactly, whereas the latter is an exact theory but one of its key operators is unknown and must be solved approximately.

If the exact $E_{xc}[\rho]$ functional form is known, the calculated KS DFT energy would be exact, however it is not and instead approximations are used. The local density approximation (LDA) is the simplest approximation to $E_{xc}[\rho]$, in which the value of the exchange correlation functional is computed exclusively from the value of the density at that position, i.e., the local value of the density. LDA assumes that the α and β spin electrons have equal densities. In general, the local spin density approximation (LSDA) is used where the density of the α and β spin electrons may differ.

The LDA and LSDA are developed based on a uniform electron gas model and are limited to systems with small spatial variations in the density. A simple correction is to include both the density and its gradient as the variables of the integrand of the exchange correlation functional. This leads to the generalized gradient approximation (GGA) and the functional is expressed as:

$$E_{xc}^{GGA}[\rho^\alpha, \rho^\beta] = \int f\left(\rho^\alpha(r), \rho^\beta(r), \nabla\rho^\alpha(r), \nabla\rho^\beta(r)\right) dr \,, \tag{2.23}$$

which may be decomposed into exchange and correlation functionals similar to LDA:

$$E_{xc}^{GGA} = E_x^{GGA} + E_c^{GGA} \,. \tag{2.24}$$

One of the popular gradient-corrected exchange functionals, E_x^{GGA}, is B88 and was developed by Becke in 1988.[181] The gradient-corrected correlation functional that is often used in conjunction with Becke's exchange functional is the Lee-Yang-Parr (LYP)[182] functional and the combination is called BLYP.

More accurate functionals are obtained by adding a fraction of exchange energy calculated by the HF method (the SD is composed of KS orbitals for the non-interacting system) to those of DFT exchange correlation functionals. These combinations are called hybrid functionals. One of the most popular hybrid functionals is B3LYP and is defined as:[183-184]

$$E_{xc}^{B3LYP} = (1-a)E_x^{LSDA} + aE_x^{HF} + b\Delta E_x^{B88} + (1-c)E_c^{LSDA} + cE_c^{LYP}\ , \qquad (2.25)$$

where the three parameters $a = 0.20$, $b = 0.72$, and $c = 0.81$ are determined by fitting to the experimental molecular atomization energies.

2.2.4 Basis Sets

The molecular orbitals in most quantum chemistry methods (e.g. HF, Post HF, DFT, and etc.) are usually expressed as a linear combination of known mathematical functions that are called basis functions. The set of mathematical/basis functions from which the wave function is constructed is called a basis set with the coefficients are to be determined in the calculation. Larger basis sets more accurately approximate the orbitals as there are fewer restrictions on the location of the electrons, however the computational cost increases.

The LCAO approximation is widely used in the construction of the basis sets. The atomic orbitals are either expressed by Slater type orbitals (STOs) or Gaussian type orbitals (GTOs). The STOs are exponential functions of radial distance from the atom center and better describe the true behavior of atomic wave functions but are computationally more demanding and limited. In

contrast GTOs are easy to work with but do not show the cusp at the nucleus. The general form of a GTO in atom-centered Cartesian coordinates is:

$$\phi(x,y,z) = N(i,j,k,\alpha)x^i y^j z^k e^{-\alpha\left(x^2+y^2+z^2\right)}, \quad (2.26)$$

where *N* is a normalization constant, α is an exponent controlling the width of the GTO, and *i*, *j*, and *k* are non-negative integers that dictate the nature of the orbital. For example, if all three *i*, *j*, and *k* are zero the GTO has spherical symmetry and is called an s-type GTO. A linear combination of GTOs shown in the Equation (2.26), also called primitive Gaussians, may be used to better resemble the true wave function and get the desired cusp. Such combination is referred to as a contracted Gaussian basis function. The degree of contraction refers to the total number of primitives used to make the contracted functions.

The basis set consisted of STOs approximated by linear combination of primitive Gaussians and the degree of contraction *M* is referred to STO-*M*G. Hehre, Stewart, and Pople discovered that the combination of three primitive Gaussians (STO-3G) result in optimum speed and accuracy (comparing to STOs).[185] The STO-3G is known as a single-zeta or 'minimal' basis set because there is one and only one basis contracted Gaussian basis function for each orbital of each atom. Single-zeta basis sets are computationally inexpensive; however they do not provide accurate results. Larger basis sets such as double- or triple-zeta with two and three functions for each atomic orbitals, respectively, are more accurate but they increase the computational cost. Split-valence basis sets are computationally more efficient. They use fewer basis functions to describe the core orbitals (as they are weakly affected by chemical bonding) than the valence orbitals. The most widely used split-valence basis sets are those of Pople *et al.* including but not limited to: 3-21G, 6-31G, and 6-311G.[186-190] The first number indicates the number of primitive Gaussians used in the contracted core functions and the ones after the hyphen refer to the numbers of primitives used

in the valence functions. For example 6-311G is a split-valence-triple-zeta basis set which uses one contracted Gaussian consisting of six primitives for the core orbitals and three contracted Gaussians for the valence orbitals, the first contracted consisting of three primitives and the second and third with one primitive.

In a molecular system the orbitals require more flexibility than do the atoms due to the overlap of atomic orbitals and chemical bonding. This flexibility is added in the form of a polarization function that are basis functions corresponding to one quantum number of higher angular momentum than the valence orbitals. Thus, for the hydrogen and first-row atoms the most useful polarization functions are p and d GTOs, respectively. For Pople basis sets the use of '*' (pronounced 'star') or d and p at the end of the basis set indicates the polarization functions, e.g. 6-311G** or 6-311G(d,p) has d-type polarization functions on heavy atoms and p-type on hydrogen atoms. A single star denotes d-type polarization functions.

Anions, highly excited electronic states, and loose supermolecular complexes tend to have much more spatially diffused molecular orbitals at large distances from the nuclei. To add the required flexibility for a weakly bound electron to localize far from the remaining density, the standard basis sets are often augmented with diffuse basis functions. In general, diffuse functions have an exponent about a factor of four smaller than the smallest valence exponent. In the Pople family of basis sets, the diffuse functions are indicated by '+' or '++' in the basis set name. Thus, 6-31+G(d) indicates the addition of s and p type diffuse functions on all atoms except for hydrogen, while 6-31++G(d) has an extra s-type diffuse function for the hydrogen atom.

2.2.5 Continuum Solvation Models

The electronic structure calculation of an isolated molecule in vacuum was discussed previously. The results are only applicable to gas phase materials at low pressure and not liquid phase or high

pressure. The interaction of a solute with the solvent induces polarization in the solvent and the polarized solvent generates an electric field, called the reaction field, at each solute molecule. The reaction field distorts the solute's molecular electronic wave function and induces a dipole moment that further polarizes the solvent; and so on. Thus, the liquid phase/solution molecular electronic wave function and other molecular properties differ from those of them in the gas phase. This makes the inclusion of solvent effects essential in many real molecular systems.

The explicit inclusion of solvent molecules in quantum chemical calculations is impractical due to the system size and computational limits. The common way of considering the solvent effects is via a continuum solvation model which ignores the solvent molecular structure and treats it as a continuous dielectric of infinite extent characterized by its experimental dielectric constant, ε. The solute molecule *M*, is placed inside a cavity surrounded by the solvent and then treated either classically or quantum mechanically. In a classical treatment the solute is a collection of charges that interacts with the dielectric and in the quantum chemical approach the interaction between the solute and the surrounding dielectric continuum is modeled by a term $\hat{V}_{int}$ that is added to the molecular electronic Hamiltonian of the solute in vacuum, $\hat{H}_M^{(0)}$. The electronic wave function and probability density of the solute molecule are changed until a self-consistency between the charge distribution of solute and the solvent's reaction field is achieved. Such a treatment is called a **self-consistent reaction field (SCRF)** model. In fact, the solvent effect is represented as a perturbation to the Hamiltonian of the solute. Different SCRF models are defined depending on the choice of the size and shape of the solute's cavity and the calculation of $\hat{V}_{int}$.

The simplest SCRF model is the **quantum-Onsager method** which considers a sphere of radius *a* as the solute's cavity and the solute-solvent interaction (the interaction between the molecular charge distribution of solute and the reaction field) is calculated by approximating the molecular

charge distribution as an electric dipole located at the cavity center.[191-192] The quantum-Onsager SCRF method is unable to consider the solvent effect on a solute molecule that is uncharged and has no permanent dipole moment, because it ignores the quadruple and higher moments of the solute which interact with the solvent. The use of a spherical cavity for the solute molecular shape is also a crude approximation.

The **polarizable continuum model (PCM)**[193] is one of the most commonly used continuum solvation models. PCM uses a more realistic molecular shape for the solute via a set of overlapping spheres centered on the nuclei positions with a radius 1.2 times the van der Waals radius of the atom. As a result, a numerical method is used to find the potential energy of the interaction between the solute's charge distribution and the surrounding continuum dielectric ($\hat{V}_{int}$). The reaction field is represented by an apparent surface charge (ASC) model customized through point charges located on the surface of the molecular cavity. Using the integral equation formulation of the Poisson problem, relating the reaction field to the molecular electrostatic potential, the ASC is obtained. The molecular Gibbs energy of solvation is computed as the sum of three terms: the electrostatic $G_{estatic}$, dispersion-repulsion$G_{dis-rep}$, cavitation energyG_{cav}, and thermal motion $G_{thermal}$. The electrostatic term considers the electrostatic interactions between the solute and the solvent. The dispersion energy results from the London dispersion attraction between the solute and the solvent, while the repulsion contribution is from the quantum mechanical exchange repulsion between the solute and solvent molecules. The cavitation energy is the work needed to create a cavity of the solute size in the solvent and the thermal contribution includes the changes in molecular motions on going from the gas to the solution. The PCM method tries to include all of these contributions in the Gibbs energy of the solvation, however it fails to directly calculate the cavitation and dispersion-repulsion energies.

The **density based solvation model (SMD)** is a variant of the PCM model that was developed recently.[194] This model considers two main components for the solvation Gibbs energy. The first component is the bulk electrostatic contribution arising from the SCRF treatment that involves the integral equation formalism of PCM. The second component is called the cavity-dispersion-solvent-structure (CDS) term and is the contribution arising from short-range interactions between the solute and solvent molecules in the first solvation shell.

The SMD model contains two types of parameters: (1) intrinsic atomic Coulomb radii for the bulk electrostatic calculation; and (2) atomic surface tension coefficients for the CDS contribution. The intrinsic atomic Coulomb radii refers to the systematically optimized atomic radii that are used in the construction of the solute cavity. The atomic surface tension coefficients are geometry dependent proportionality constants. These empirical parameters strongly depend on the intrinsic Coulomb radii, whereas the intrinsic Coulomb radii slightly depend on the atomic surface tensions. The SMD model has been rigorously parameterized with the solvation free energy data from more than two thousand ionic and neutral solutes in both aqueous and non-aqueous solvents. This model employs a single set of parameters that are optimized with six different electronic structure methods. It has been shown that SMD provides the solvation free energies with negligible error and is the best method to calculate the free energy of solvation. This universal continuum solvation model is applicable to any charged or uncharged solute in a solvent or liquid medium.

2.2.6 Vibrational Frequencies

A consequence of the uncertainty principle is that polyatomic molecules, even at absolute zero, must vibrate.[177] The vibration of a molecule can be considered as a superposition of a number of basic vibrations. These vibrations are called normal modes and are molecular vibrations in a defined manner with the same vibrational frequency. A linear molecule with N atoms has $3N - 5$

normal modes while a nonlinear molecule has $3N-6$.[176] The normal modes are independent of each other and each normal mode involves simultaneous vibrations of different or all parts of the molecule.

The quantum mechanical description of the vibration of a diatomic molecule has a potential-energy term that can be approximated by a harmonic oscillator. In the harmonic-oscillator approximation, the quantum mechanical energy levels of a polyatomic molecule is:[176]

$$E_{vib} = \sum_i \left(n_i + \frac{1}{2}\right) h\upsilon_i \,, \tag{2.27}$$

where the υ_i is the vibration frequency of the i^{th} normal mode of the molecule and n_i is the vibrational quantum number of the i^{th} normal mode. Each n takes on the values $0, 1, 2, \ldots$ independently of the values of the other vibrational quantum numbers.

The normal mode frequencies for polyatomic molecules are usually obtained from the Hessian matrix. The Hessian matrix consists of the second derivatives of the energy with respect to the coordinates of the nuclei. The Hessian should only be evaluated at stationary points, and its elements are defined as:

$$H_{ij} = \frac{\partial^2 E}{\partial r_i \partial r_j}, \tag{2.28}$$

where E is the sum of the electronic and nuclei energy and r_i and r_j are the atomic coordinates for the i^{th} and j^{th} atoms, respectively. The order of the differentiation does not matter and therefore the Hessian is symmetric. To calculate the vibrational frequencies the Hessian matrix is mass-weighted ($\frac{H_{ij}}{\sqrt{m_i m_j}}$) and then diagonalized to give the eigenvalues. Each eigenvalue corresponds to the force constant of a normal mode and consequently to the vibrational frequency of that normal mode.

Absorption of a quantum of energy excites a molecular vibration corresponding to the vibration's frequency ($E = h\upsilon$). Transitions in molecular vibrational energy levels typically occur within the IR range of the frequency spectrum. The SI unit for spectroscopic frequencies is the *hertz* (Hz), defined by $1\ Hz \equiv 1\ s^{-1}$. However, the infrared spectra are usually specified by *wavenumber* $\tilde{\upsilon}$, defined as:

$$\tilde{\upsilon} \equiv \frac{1}{\lambda} = \frac{\upsilon}{c}\ , \tag{2.29}$$

where λ is the wavelength and c is the speed of light. The vibration of a molecule can be probed using infrared (IR) or Raman spectroscopies. IR spectroscopy is developed based on the absorption of light by the vibrating molecules, whereas Raman relies on the scattering of the light by the vibrating molecules. A vibration is IR active if the dipole moment of the molecule changes due to the vibration and is Raman active if the polarizability changes. These two techniques are complementary and in conjunction can provide useful structural information.

2.3 Quasi-Chemical Theory

The quasi-chemical theory (QCT) is a method that uses high resolution computations in conjunction with low resolution descriptions to give an accurate model for the thermodynamics of solutions.[195] Having a strong statistical mechanical context, the QCT may be used to calculate the hydration free energy of ions. The term “quasi-chemical: was acquired from the work of Guggenheim[196-197] because the strong solute-solvent interactions (relative to the thermal energy) are characterized as chemical associations, although they may not be covalent. In this theory, the most primitive idea is to identify an inner-shell region from the rest of the neighborhood of a distinguished solute, and then to rely on a careful treatment of the inner shell with full molecular resolution. The remainder of the neighborhood of that distinguished solute (the outer-shell region) can be given an alternative statistical description, and then a proper matching of results for inner

and outer shells is accomplished.[195,198-202] In the present study, the inner shell, where chemical effects are important, is treated quantum mechanically. The outer-shell contributions to the solvation of ions are including using the SMD dielectric continuum solvation model.

The following section presents the statistical mechanical foundation required for QCT, i.e., the potential distribution theory. This theory is a simple and effective perspective on the statistical thermodynamics of molecular solutions. This section is followed by the derivation of the excess chemical potential within the quasi-chemical approach. Only a minimum foundation required for the application of QCT is presented in this work and extensive derivations and associated contents may be found elsewhere.[195]

2.3.1 Potential Distribution Theory

The potential distribution theory (PDT) is a useful statistical mechanics theory and has many applications in equilibrium states. The general principle was introduced by B. Widom in 1963.[203] The PDT presents a partition function for the evaluation of the excess chemical potential of a molecular component in a general thermodynamic system. The excess chemical potential of a component α is part of the Gibbs chemical potential that vanishes in the absence of intermolecular interactions. This chemical potential is important to a molecular based consideration of complex solutions.

Simple Solute. The simple solute is defined as a solute with no internal structure and no internal degrees of freedom. For a system of $N-1$ particles in a volume, V, the canonical partition function may be written as:

$$Q_{N-1} = \frac{1}{(N-1)!\,h^{3(N-1)}} \int \dots \int \int_V \dots \int_V e^{-\beta H_{N-1}} d\tau_1 \dots d\tau_{N-1} dp_1 \dots dp_{N-1}\,, \quad (2.30)$$

where H_{N-1} is the Hamiltonian of the $N-1$ particles, τ_i is the coordinate of the i^{th} particle, p_i is its conjugate momentum, h is Plank's constant, and $\beta = 1/k_B T$. If the kinetic energy and intermolecular potentials are assumed to be separable, then the Hamiltonian may be written as:

$$H_{N-1} = H_{translational} + H_{interaction} = \sum_{i=1}^{N-1} \frac{p_i^2}{2m_i} + U_{N-1} \,. \tag{2.31}$$

Substituting this into the partition function equation and realizing that U_{N-1} depends only on the coordinates, the integrals over all conjugate momenta can be integrated with all $m_i = m$.

$$Q_{N-1} = \frac{1}{(N-1)!\,\Lambda^{3(N-1)}} \int_V \dots \int_V e^{-\beta U_{N-1}} d\tau_1 \dots d\tau_{N-1} \tag{2.32}$$

The term $\Lambda = \sqrt{\frac{h^2\beta}{2\pi m}}$ is the thermal deBroglie wavelength. This form of the partition function contains the configurational partition function, Q_{N-1}^{conf}, defined by:

$$Q_{N-1}^{conf} = \frac{1}{(N-1)!} \int_V \dots \int_V e^{-\beta U_{N-1}} d\tau_1 \dots d\tau_{N-1} \,, \tag{2.33}$$

therefore:

$$Q_{N-1} = \frac{Q_{N-1}^{conf}}{\Lambda^{3(N-1)}} \,. \tag{2.34}$$

It is assumed that the configurational partition function of a system of *N* particles in a volume V is:[203-204]

$$Q_N^{conf} = \frac{1}{(N-1)!\,N_\alpha!} V \int_V \dots \int_V e^{-\beta(U_{N-1}+\Delta U_\alpha)} d\tau_1 \dots d\tau_{N-1} \,, \tag{2.35}$$

where U_{N-1} is the energy of interaction of particles $1, \dots, N-1$ as a function of their configuration, and N_α denotes the number of solutes which is unity for one test particle. ΔU_α is the additional interaction energy due to the presence of the N^{th} particle (the test particle or solute α) at an arbitrary fixed point in the fluid. The solute effect may be considered as a perturbation

to the $N-1$ particles system via $\lambda\Delta U_\alpha$ ($\lambda = 0$ or 1). The two sides of Equation (2.35) may be divided by Q_{N-1}^{conf} to obtain:

$$\frac{Q_N^{conf}}{Q_{N-1}^{conf}} = \frac{V(N-1)!}{(N-1)!\,N_\alpha} \frac{\int_V \dots \int_V e^{-\beta(U_{N-1}+\Delta U_\alpha)} d\tau_1 \dots d\tau_{N-1}}{\int_V \dots \int_V e^{-\beta U_{N-1}} d\tau_1 \dots d\tau_{N-1}}$$

$$= \frac{1}{\rho_\alpha} \frac{\int_V \dots \int_V e^{-\beta(U_{N-1}+\Delta U_\alpha)} d\tau_1 \dots d\tau_{N-1}}{\int_V \dots \int_V e^{-\beta U_{N-1}} d\tau_1 \dots d\tau_{N-1}}\ , \tag{2.36}$$

where $\rho_\alpha = N_\alpha/V$ is the number density of particle α in the system. The right hand side of this equation contains a canonical average and may be simplified as follows:

$$\frac{Q_N^{conf}}{Q_{N-1}^{conf}} = \frac{1}{\rho_\alpha} \langle e^{-\beta\Delta U_\alpha} \rangle_0\ . \tag{2.37}$$

The notation $\langle \dots \rangle$ is the canonical average in the $N-1$ particle system and the subscript zero indicates the averaging condition in which the configurations of the $N-1$ particles are not influenced by the presence of the test particle.

Hence, the partition function for the N particles system may be written as:

$$Q_N = \frac{Q_N^{conf}}{\Lambda_\alpha^3 \Lambda^{3(N-1)}}, \tag{2.38}$$

that results in the following:

$$\frac{Q_N}{Q_{N-1}} = \frac{Q_N^{conf}}{Q_{N-1}^{conf}} \frac{\Lambda^{3(N-1)}}{\Lambda_\alpha^3 \Lambda^{3(N-1)}} = \frac{Q_N^{conf}}{Q_{N-1}^{conf}} \frac{1}{\Lambda_\alpha^3}\,. \tag{2.39}$$

The aim is to calculate the chemical potential for such a system. The Helmholtz energy may be evaluated from the canonical partition function:

$$A = -\frac{1}{\beta} \ln Q \tag{2.40}$$

and the chemical potential can be calculated from:

$$\mu = \left[\frac{\partial A}{\partial N}\right]_{V,T} = \lim_{N\to\infty}\left[\frac{A_N - A_{N-1}}{N-(N-1)}\right] \tag{2.41}$$

Combining Equations (2.39), (2.40), and (2.41) the chemical potential for the distinguished solute molecule is obtained from:

$$\mu_\alpha = \left[\frac{\partial A}{\partial N_\alpha}\right]_{V,T,N-N_\alpha} = -\frac{1}{\beta}\ln\frac{Q_N}{Q_{N-1}} = -\frac{1}{\beta}\ln\left(\frac{Q_N^{conf}}{Q_{N-1}^{conf}}\frac{1}{\Lambda_\alpha^3}\right). \tag{2.42}$$

Substituting Equation (2.37) into (2.42) gives:

$$\mu_\alpha = -\frac{1}{\beta}\ln\left(\frac{\langle e^{-\beta\Delta U_\alpha}\rangle_0}{\rho_\alpha\Lambda_\alpha^3}\right). \tag{2.43}$$

This equation can be rewritten into the following form which consists of two parts: the ideal chemical potential (the first term $\beta\mu_\alpha^{ideal}$); and the excess chemical potential (the second term $\beta\mu_\alpha^{excess}$):

$$\beta\mu_\alpha = \ln(\rho_\alpha\Lambda_\alpha^3) - \ln\langle e^{-\beta\Delta U_\alpha}\rangle_0\,. \tag{2.44}$$

This equation clearly shows that the excess chemical potential is only due to the interactions between the solute and solvent and vanishes in the absence of such interactions ($\Delta U_\alpha = 0$).

The absolute activity may be obtained from:

$$Z_\alpha \equiv e^{\beta\mu_\alpha} = \frac{\rho_\alpha\Lambda_\alpha^3}{\langle e^{-\beta\Delta U_\alpha}\rangle_0}. \tag{2.45}$$

The most useful relation obtained from the PDT may be viewed as follows:

$$\beta\mu_\alpha^{ex} = -\ln\langle e^{-\beta\Delta U_\alpha}\rangle_0\,. \tag{2.46}$$

The superscripts *excess* and *ex* denote the same concept and are used interchangeably. Having the interaction potential between the solute and solvent, the excess chemical potential for the solute may be computed. This result is obtained by assuming that the kinetic energy and intermolecular

potentials are separable and the presence of the solute does not change the thermal configurations of the solvent.

Solute with Internal Degrees of Freedom. If the solute molecule is not simple and has some internal degrees of freedom, e.g. a protein molecule, then different conformations of the solute should be considered. If it is assumed that the kinetic energy and the intra-molecular, and inter-molecular potentials are separable, the Hamiltonian may be written as:

$$H_{N-1} = H_{translational} + H_{intera-molecular} + H_{inter-molecular}\,, \tag{2.47}$$

and the partition function for the N particle system becomes:

$$Q_N = \frac{1}{\Lambda^{3N}} \cdot q_{int}^{N} \cdot Q_N^{conf}\,. \tag{2.48}$$

Here, q_{int} is the internal partition function for each particle and is unity for a simple particle.

A new notation, R^n, is defined to enter the effect of solute internal degrees of freedom and ease the derivation. The $R^n = \{r_1, r_2, \dots, r_n\}$ is the conformation of the solute consisting of n particles as illustrated in Figure 2.3. The $S_\alpha^{(0)}(R^n)$ is the conformation distribution of the solute in the absence of any interactions with the solvent.

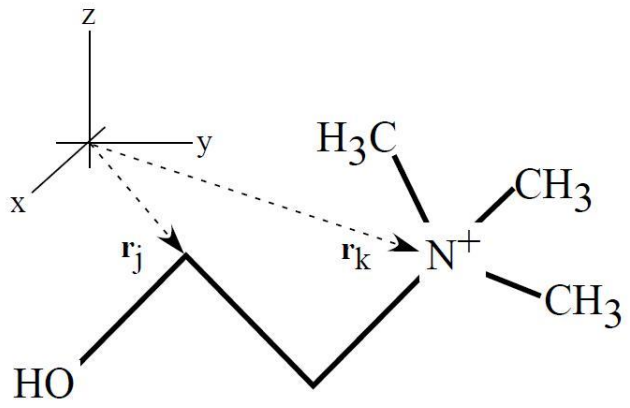


Figure 2.3. Illustration of the conformational coordinate notation, R^n (taken from reference 195).

The conformational distribution of the single molecule is sampled in the absence of the interactions with the solvent using suitable simulation procedures and appropriate coordinates. The normalization adopted in this development can be viewed as follows:

$$\int S_{\alpha}^{(0)}(R^n)d(R^n) = V\,. \tag{2.49}$$

To obtain the partition function the solvent thermal degrees of freedom are averaged over a specific solute conformation, then a weighted averaging is performed over all possible conformations of the solute. The latter is expressed by the following notation:

$$\langle\langle \dots \rangle\rangle_0 = \frac{1}{V}\int \langle \dots | R^n \rangle_0 S_{\alpha}^{(0)}(R^n)d(R^n)\,. \tag{2.50}$$

The subscript zero indicates that the averaging is performed with the condition that the solute conformations and solvent configurations are decoupled. Using the Widom's particle insertion method, described above, the configurational partition function is:

$$Q_N^{conf} = \frac{1}{V}\int \left[\frac{V}{(N-1)!\,N_{\alpha}!}\int_V \dots \int_V \left(e^{-\beta(U_{N-1}+\Delta U_{\alpha})}\middle| R^n\right) d\tau_1 \dots d\tau_{N-1}\right] S_{\alpha}^{(0)}(R^n)d(R^n)\,. \tag{2.51}$$

Hence:

$$\frac{Q_N^{conf}}{Q_{N-1}^{conf}} = \frac{1}{V}\int \left[\frac{\frac{V}{(N-1)!\,N_{\alpha}!}\int_V \dots \int_V \left(e^{-\beta(U_{N-1}+\Delta U_{\alpha})}\middle| R^n\right) d\tau_1 \dots d\tau_{N-1}}{\frac{1}{(N-1)!}\int_V \dots \int_V e^{-\beta U_{N-1}} d\tau_1 \dots d\tau_{N-1}}\right] S_{\alpha}^{(0)}(R^n)d(R^n)$$

$$= \frac{1}{V}\int \left[\frac{V}{N_{\alpha}}\left\langle e^{-\beta\Delta U_{\alpha}}\middle| R^n\right\rangle_0\right] S_{\alpha}^{(0)}(R^n)d(R^n)\,. \tag{2.52}$$

The double bracket may also be written as:

$$\frac{Q_N^{conf}}{Q_{N-1}^{conf}} = \frac{1}{\rho_{\alpha}}\langle\langle e^{-\beta\Delta U_{\alpha}}\rangle\rangle_0\,. \tag{2.53}$$

This result is similar to that of the simple solute except for the additional averaging over the different conformations of the solute. The chemical potential is therefore:

$$\mu_\alpha = -\frac{1}{\beta}\ln\frac{Q_N}{Q_{N-1}} = -\frac{1}{\beta}\ln\left(\frac{Q_N^{conf}}{Q_{N-1}^{conf}}\frac{q_{int}^{N-1}q_\alpha^{int}}{q_{int}^{N-1}}\frac{\Lambda^{3(N-1)}}{\Lambda_\alpha^3\Lambda^{3(N-1)}}\right)$$

$$= -\frac{1}{\beta}\ln\left(\frac{Q_N^{conf}}{Q_{N-1}^{conf}}\frac{q_\alpha^{int}}{\Lambda_\alpha^3}\right), \tag{2.54}$$

and so:

$$\beta\mu_\alpha = \ln\left(\frac{\rho_\alpha\Lambda_\alpha^3}{q_\alpha^{int}}\right) - \ln\langle\langle e^{-\beta\Delta U_\alpha}\rangle\rangle_0 . \tag{2.55}$$

The first term is $\beta\mu_\alpha^{ideal}$ and the second term is $\beta\mu_\alpha^{excess}$. As explained above the $\langle\langle \dots \rangle\rangle_0$ notation denotes averaging over the thermal motion of the solute and the solvent molecules, conditioned that they are decoupled, i.e.,

$$\langle\langle e^{-\beta\Delta U_\alpha}\rangle\rangle_0 = \frac{1}{V}\int\left\langle e^{-\beta\Delta U_\alpha}\middle|R^n\right\rangle_0 S_\alpha^{(0)}(R^n)d(R^n) . \tag{2.56}$$

The term $\left\langle e^{-\beta\Delta U_\alpha}\middle|R^n\right\rangle_0$ is averaging over solvent configurations conditioned on the R^n conformation of the solute. Hence, the excess chemical potential and absolute activity of the solute may be written as:

$$\beta\mu_\alpha^{ex} = -\ln\langle\langle e^{-\beta\Delta U_\alpha}\rangle\rangle_0 , \tag{2.57}$$

where:

$$Z_\alpha \equiv e^{\beta\mu_\alpha} = \frac{\rho_\alpha\Lambda_\alpha^3}{q_\alpha^{int}}\frac{1}{\langle\langle e^{-\beta\Delta U_\alpha}\rangle\rangle_0} . \tag{2.58}$$

2.3.2 Basic Quasi-Chemical Formula

The solute-solvent interactions are not necessarily covalent, however they are strong relative to the thermal energy, kT, and can be characterized as chemical associations. These interactions are typically short-ranged and structurally specific. Thus, an inner shell around the solute can be

identified with strong associating solvent molecules and an outer shell region that corresponds to the bulk solvent. In the case of the solvation of an ion in water; the first hydration shell is the inner shell and the remainder of the system volume is the outer shell. An indicator function $b_\alpha(j)$ is used to specify the inner shell, such that when the solvent molecule *j* occupies the inner shell of the distinguished molecule α then $b_\alpha(j) = 1$ and when this solvent molecule is outside that region $b_\alpha(j) = 0$. Using this definition and the PDT the outer shell contribution to the solute excess chemical potential may be written as:

$$\beta\mu_\alpha^{ex}|_{outer} = -\ln\langle\langle e^{-\beta\Delta U_\alpha}\prod_j[1 - b_\alpha(j)]\rangle\rangle_0 . \tag{2.59}$$

The additional factor within the average, $\prod_j[1 - b_\alpha(j)]$, would be zero for those solvent configurations that have a solvent molecule inside the inner shell. This equation can be used to calculate the fraction of those configurations:

$$\frac{\langle\langle e^{-\beta\Delta U_\alpha}\prod_j[1 - b_\alpha(j)]\rangle\rangle_0}{\langle\langle e^{-\beta\Delta U_\alpha}\rangle\rangle_0} . \tag{2.60}$$

The excess chemical potential is the sum of the inner and outer shell contributions:

$$\beta\mu_\alpha^{ex} = -\ln\left[\frac{\langle\langle e^{-\beta\Delta U_\alpha}\rangle\rangle_0}{\langle\langle e^{-\beta\Delta U_\alpha}\prod_j[1 - b_\alpha(j)]\rangle\rangle_0}\right] - \ln\langle\langle e^{-\beta\Delta U_\alpha}\prod_j[1 - b_\alpha(j)]\rangle\rangle_0 . \tag{2.61}$$

Here, the first term is the inner shell contribution and the second term is the outer shell contribution. This separation allows simpler physical approximations to be used for the outer shell expression and the inner shell can be considered with high resolution. The ratio of the averages in the inner shell contribution can alternatively be viewed as $1/x_0$, where x_0 is the probability of those configurations that have no solvent molecules inside the inner shell:

$$\beta\mu_\alpha^{excess} = -\ln\left[\frac{1}{x_0}\right] - \ln\langle\langle e^{-\beta\Delta U_\alpha}\prod_j[1 - b_\alpha(j)]\rangle\rangle_0 . \tag{2.62}$$

2.3.3 Chemical Equilibrium and Quasi-Chemical Description

The inner shell population can be described by a stoichiometric model for a chemical equilibrium which provides a correct description of x_0. Consider the following reaction at equilibrium in the inner shell that contains the number of solvent molecules inside the inner shell, n:

$$\alpha + nW \rightleftarrows \alpha W_n \,, \tag{2.63}$$

where α indicates the solute and W indicates the solvent molecule (e.g. water). If $n = 0$ there are no solvent particles in the inner shell. This is equivalent to the case where x_0 is calculated. The concentration ratio for the case with $n = 0$ to the sum of all cases with $n = 0, 1, 2, \ldots$ gives x_0:

$$x_0 \equiv \frac{\rho_{\alpha W_0}}{\sum_{n\geq 0} \rho_{\alpha W_n}} \,. \tag{2.64}$$

Based on this definition, the chemical equilibrium constant may be written as follows:

$$K_n \equiv \frac{\rho_{\alpha W_n}}{\rho_\alpha \rho_W^n} = \frac{\rho_{\alpha W_n}}{\rho_{\alpha W_0} \rho_W^n} \,. \tag{2.65}$$

ρ_α is simply equal to the $\rho_{\alpha W_0}$. Hence, the relationship between x_0 and the equilibrium constant becomes:

$$x_0 = \frac{\rho_{\alpha W_0}}{\rho_{\alpha W_0} + \sum_{n\geq 1} \rho_{\alpha W_n}} = \frac{\rho_{\alpha W_0}}{\rho_{\alpha W_0} + \sum_{n\geq 1} K_n \rho_{\alpha W_0} \rho_W^n} = \frac{1}{1 + \sum_{n\geq 1} K_n \rho_W^n} \,. \tag{2.66}$$

The excess chemical potential may be calculated from:

$$\beta \mu_\alpha^{ex} = -\ln\left[1 + \sum_{n\geq 1} K_n \rho_W^n\right] - \ln \langle\langle e^{-\beta \Delta U_\alpha} \prod_j [1 - b_\alpha(j)] \rangle\rangle_0 \,. \tag{2.67}$$

To simplify this equation the summation is approximated and replaced by its largest term, denoted as $\bar{n}$. This gives for the excess chemical potential:

$$\beta \mu_\alpha^{ex} \approx -\ln[K_{\bar{n}} \rho_W^{\bar{n}}] + \beta \mu_\alpha^{ex}|_{outer} \,. \tag{2.68}$$

Replacing the summation with the largest term makes a negligible difference, because the succeeding terms in the summation reflect chemical energy differences. A slight difference in the chemical energy implies that the lower energy term dominates all the others on a thermal energy scale. Moreover, there are only several finite terms in the sum and therefore no significant accumulation of entropic contributions, e.g., if there are two similar terms in the sum then the resulting error is $kT \ln 2$, which is negligible.

The equilibrium constant can be related to the average of the interaction potential obtained from the PDT. The Gibbs free energies at equilibrium are:

$$\mu_\alpha + n\mu_W = \mu_{\alpha W_n} . \tag{2.69}$$

Hence, the relation between their absolute activities is:

$$e^{-\beta\mu_\alpha} . e^{-\beta n\mu_W} = e^{-\beta\mu_{\alpha W_n}} . \tag{2.70}$$

The absolute activities may be written from Equation (2.58):

$$\frac{\rho_\alpha \Lambda_\alpha^3}{q_\alpha^{int}\langle\langle e^{-\beta\Delta U_\alpha}\rangle\rangle_0}\left(\frac{\rho_W \Lambda_W^3}{q_W^{int}\langle\langle e^{-\beta\Delta U_W}\rangle\rangle_0}\right)^n = \frac{\rho_{\alpha W_n}\Lambda_{\alpha W_n}^3}{q_{\alpha W_n}^{int}\langle\langle e^{-\beta\Delta U_{\alpha W_n}}\rangle\rangle_0} . \tag{2.71}$$

The equilibrium constant is obtained by rearranging this equation to give the concentration ratio of the products to the reactants:

$$K_n = \frac{\frac{q_{\alpha W_n}^{int}}{\Lambda_{\alpha W_n}^3}}{\frac{q_\alpha^{int}}{\Lambda_\alpha^3}\left(\frac{q_W^{int}}{\Lambda_W^3}\right)^n}\frac{\langle\langle e^{-\beta\Delta U_{\alpha W_n}}\rangle\rangle_0}{\langle\langle e^{-\beta\Delta U_\alpha}\rangle\rangle_0(\langle\langle e^{-\beta\Delta U_W}\rangle\rangle_0)^n} = {K_n}^{(0)} e^{-\beta(\mu_{\alpha W_n}^{ex} - \mu_\alpha^{ex} - \mu_W^{ex})} , \tag{2.72}$$

where ${K_n}^{(0)}$ denotes the ideal equilibrium constant at standard conditions, i.e., at 1 atm and 298.15 K. There is no solvent-solute interaction in an ideal solution and so ΔU_α is zero and the excess terms vanish. Therefore, ${K_n}^{(0)}$ may be considered as the ideal equilibrium constant.

The density in Equation (2.68) is the actual density of liquid water ($1\,\mathrm{g/cm^3}$ @ STP). ${K_n}^{(0)}$ is calculated for an ideal gas at standard state, hence the effect of the actual density is a replacement contribution calculated as follows:

$$-\frac{n}{\beta}\ln\left(\frac{\rho_{W(aq)}}{\rho_{W(gas)}}\right) = -\frac{n}{\beta}\ln\left(\frac{\frac{1\,{}^{g}/_{cm^3}}{18.01\,{}^{g}/_{mol}}}{\frac{1atm}{82.06\,{}^{atm.cm^3}/_{Kmol}\times 298.15K}}\right)$$

$$= -\frac{n}{\beta}ln(1354) = -4.27n\left(\frac{Kcal}{mol}\right). \qquad (2.73)$$

This amounts to the contribution of $-4.27\,\mathrm{kcal/mol}$ per ligand. The replacement contribution is added to Equation (2.68) and then combined with Equation (2.71) to give:

$$\beta\mu_\alpha^{excess} \approx -\ln {K_n}^{(0)} - \bar{n}\ln(1354) + \beta\mu_{\alpha W_{\bar{n}}}^{ex} - \beta\mu_\alpha^{ex} - \bar{n}\beta\mu_W^{ex} + \beta\mu_\alpha^{ex}|_{outer}\,. \qquad (2.74)$$

The contribution $\beta\mu_\alpha^{ex}$ is precisely the outer-shell contribution $\beta\mu_\alpha^{ex}|_{outer}$ obtained before, and therefore these two terms will cancel, giving the final result:

$$\beta\mu_\alpha^{excess} \approx -\ln {K_{\bar{n}}}^{(0)} - \bar{n}\ln(1354) + \beta\mu_{\alpha W_{\bar{n}}}^{ex} - \bar{n}\beta\mu_W^{ex}\,. \qquad (2.75)$$

This equation is an applicable form of the quasi-chemical approach and was used in this work.

2.4 Dissipative Particle Dynamics

DPD is a meso-scale simulation technique that was first introduced by Hoogerbrugge and Koelman.[205] Further developments by Español and Warren included the stochastic differential equations and conservation of energy.[206-207] The method describes the system in terms of soft particles, or beads, whose motion is governed by certain collision rules.[208] The soft particles, or beads, represent groups of atoms or molecules in the system. The use of simplified potentials and the grouping of the atoms into particles permit simulations of large systems over long time scales that are either impossible or difficult to perform in all atom methods such as classical molecular

dynamics simulations.[209] DPD has been successfully applied to a large variety of systems including: block copolymers,[210-211] surfactant solutions,[212] bilayer membranes,[213] and ionomers.[48-50,133,214-215]

The following presents an overview of the method, however more detailed description may be found elsewhere.[205-208,216-217] The time evolution of the interacting particles is governed by Newton's equations of motion which are integrated using a modified velocity-Verlet algorithm.[208] The dimensionless equations of motion are:

$$\frac{dr_i}{dt} = v_i \quad and \quad \frac{dv_i}{dt} = f_i \,, \tag{2.76}$$

where r_i and v_i are the position and velocity of the i^{th} particle, respectively, and f_i is the net force acting on the i^{th} particle. The net force contains three non-bonded terms. Bonded terms may also be included in order to make the simulation of macromolecules viable:

$$f_i = \sum_{j \neq i} (F_{ij}^C + F_{ij}^D + F_{ij}^R) + f_i^{bonded} \,. \tag{2.77}$$

The first three terms in the summation: F_{ij}^C, F_{ij}^D, and F_{ij}^R are conservative, dissipative, and random forces which are the non-bonded components and are typically formulated as follows:

$$F_{ij}^C = a_{ij}\left(1 - r_{ij}\right)n_{ij} \tag{2.78}$$

$$F_{ij}^D = -\gamma_{ij}\left(1 - r_{ij}\right)^2\left(n_{ij}.v_{ij}\right)n_{ij} \tag{2.79}$$

$$F_{ij}^R = \sigma_{ij}\left(1 - r_{ij}\right)\xi_{ij}\frac{1}{\sqrt{\Delta t}}n_{ij} \tag{2.80}$$

These forces are pairwise and in the direction of $n_{ij} = (r_i - r_j)/|r_{ij}|$ which towards the centers of particles i and j. The cut off distance for all the non-bonded forces is r_c, the length scale, which is linked to physical units based on the system of study and the degree of coarse-graining. The relative position and velocities are defined as $r_{ij} = r_i - r_j$ and $v_{ij} = v_i - v_j$. a_{ij} is the interaction

parameter between two beads and is material or chemical compositional specific and therefore must be determined for each system. The dissipation constant, γ_{ij}, and the noise amplitude, σ_{ij}, are related by $\sigma_{ij} = \sqrt{\gamma_{ij} 2k_B T}$ to control the temperature fluctuations as dictated by the fluctuation-dissipation theorem.[206] The noise amplitude has a typical value of 3.0 that gives a reasonable compromise between fast temperature equilibration, fast and stable simulation, and a physically meaningful system.[48-49,208] ξ_{ij} is a symmetric Gaussian random number with zero mean and unit variance chosen independently for each pair of interacting particles at each time step (Δt). The last term in Equation (2.77) comes from the bonded potentials defined to describe polymeric systems. Beads of a polymer are usually connected to their nearest neighbor beads by harmonic springs.[208,210] However, another spring term to describe the second nearest neighbor beads or an angle potential may also be added in order to improve the structural properties of a polymer chain.[50,218-219] In this formulation, the only material parameters to be determined for the system of interest are the conservative interaction parameters, a_{ij}, and bonded potentials if present.

2.4.1 Determining the Interaction Parameters

The reliability of DPD simulations depends on the proper translation of the atomic scale into the meso-scale through the interaction parameters. There are different methods to obtain the interaction parameters in order to link the chemical composition of the system to the fictitious DPD particles.[50,167,220-224]

The most widely used method was introduced by Groot and Warren.[208] In order to obtain the repulsion parameters for like species, they simulated pure water. The amplitude of the conservative force was varied and the system pressure was measured as a function of the conservative interaction parameter. A quadratic equation of state was observed for a wide range of densities:

$$p = \rho k_B T + 0.101 a \rho^2 . \qquad (2.81)$$

where, p is pressure, ρ is density, and a is the conservative force amplitude. Hence, the dimensionless compressibility corresponding to this equation of state is:

$$\kappa^{-1} = 1 + \frac{0.202a\rho}{k_B T}. \tag{2.82}$$

Substituting the experimentally known compressibility of water, $\kappa^{-1} \approx 16$, it is found that $a\rho/k_B T \approx 75$. The density is a free parameter, but is linearly related to the number of interactions for each particle and therefore constrained by the computational expense. Groot and Warren obtained $\rho = 3$ as a reasonable choice to achieve the highest efficiency while satisfying the scaling relations. Therefore, $a = 25k_B T$ corresponds to the compressibility of water and $\rho = 3$.

Groot and Warren used the Flory-Huggins χ-parameter to define the interactions between dissimilar beads. They established a link between the χ-parameter and the difference in the repulsion of like and dislike beads, i.e., $a_{ij} - a_{ii}$. The χ-parameter was measured from DPD simulation results for a binary mixture, varying the difference in the repulsion parameters. The following linear relationship was determined between the Flory-Huggins χ-parameter and the repulsion parameters difference:

$$\chi = (0.286 \pm 0.002)\Delta a. \tag{2.83}$$

Here, $\Delta a = a_{ij} - a_{ii}$ and is only applicable to $\rho = 3$.

The χ-parameter may be determined experimentally and is related to the solubility.[225] It may also be approximated from mixing energy calculations using a Monte Carlo approach.[48-49] However, the experimental value of χ is not available for every substance, and there are cases where the calculations via mixing energy are not valid. For instance, if the beads contain a net electrostatic charge both the solubility and mixing energy approximations fail to give a suitable value for χ and consequently the interaction parameters.

Some authors have set the parameters based on the nature of the chemical groups that are contained in each bead or the phase separation behavior of the system.[220-222] This technique requires a thorough understanding of the materials, specific experimental, and simulation results. Others started with MD simulations and extracted an effective coarse-grained potential, requiring the meso-scale simulations to match the structural data or pair-correlation functions obtained from atomistic simulations.[50,223-224]

Maiti and McGrother further developed the method of Groot and Warren by including the bead size in their formulation.[226] They suggested that the interaction parameter between dissimilar beads should depend on the bead size and degree of coarse-graining, whereas the interaction parameter between similar beads does not depend on the bead size. Recently, Kacar *et al.* studied mixtures of DPD beads with different sizes.[169] They presented a general approach to parameterize DPD interactions for mixtures with variable (local) densities.

Lee *et al.* presented a method for parameterization of chain molecules based on a combination of top-down and bottom-up approaches.[227] In their approach the interaction parameter between dissimilar beads are obtained from the fitting of the infinite dilution activity coefficients in binary solutions of reference compounds to the results of MC simulations of the respective DPD fluids. The bonded potential parameters are determined by fitting to atomistic MD simulations. They demonstrated the consistency and transferability of their proposed method for a system of nonionic surfactants.

Groot developed a smeared-charge approach for the treatment of electrostatic interactions in which the charge is distributed within a sphere rather than being only on a point.[167] The inclusion of this long-range interaction increases the computational cost and violates the basic principle of DPD (that only considers short range interactions).

Overall, it is important to provide a method for defining the interaction parameters that is versatile, doesn't rely on the experimental information, and still fits into the simple original DPD framework to ensure high computational efficiency. Hence, a novel parameterization method was developed in this work that is capable of capturing any types of interactions including strong electrostatics and preserves the simple form of the DPD potentials.[228] This method is presented in Chapter 3 section 3.3 and is further utilized in the DPD simulations performed to investigate the electrolytes.

The following chapters present the results and discussion on various electrolyte systems that were investigated using the techniques described in this chapter. The results and findings for each electrolyte system are presented in a separate chapter that encompasses several sections corresponding to different aspects.

Chapter 3 PFSA Electrolytes with V^{n+}

This chapter is based on the following publications:[228-230]

- Sepehr, F.; Paddison, S. J., The solvation structure and thermodynamics of aqueous vanadium cations. *Chemical Physics Letters* **2013,** *585*, 53-58.
- Sepehr, F.; Paddison, S. J., Effect of sulfuric and triflic acids on the hydration of vanadium cations: An *ab initio* study. *Journal of Physical Chemistry A* **2015,** *119*, 5749-5761.
- Sepehr, F.; Paddison, S. J., Dissipative particle dynamics interaction parameters from *ab initio* calculations. *Chemical Physics Letters* **2016,** *645*, 20-26.

This chapter presents the multiscale modeling of electrolyte systems for VRFBs. The electronic structures on the hydration of four vanadium cations (V^{2+}, V^{3+}, VO^{2+}, and VO_2^{+}) are presented and discussed. The Gibbs energies of hydration of vanadium cations calculated using the quasi-chemical approach are also reported and compared to the experimental values. The effect of sulfuric and triflic acids and their conjugate anions on the hydrated structures of vanadium cations are discussed because they mimic the electrolytes in VRFBs. Understanding the effect of the diffused vanadium cations on the morphology of VRFB membrane from a meso-scale perspective is of importance and requires larger length and time scales than those achievable in electronic structure calculations. Hence, DPD (a meso-scale simulation method) was selected to study the dynamics and morphological properties of hydrated Nafion with absorbed vanadium cations. A parameterization approach was developed to enable DPD simulation of these systems and is fully described later in this chapter. This pragmatic parameterization method was utilized to calculate the parameters for the system of hydrated Nafion with absorbed vanadium cations. The simulation results exploring the effects of vanadium cations are presented and discussed.

3.1 Hydration and Thermodynamics of the V^{n+} Cations

Hydration structure of the V^{2+}, V^{3+}, VO^{2+}, and VO_2^+ cations is of importance in the study of the VRFB electrolyte properties and stability as discussed in Chapter 1. The following presents the results of atomic scale investigations on the hydration of the vanadium cations and the calculation of Gibbs energies in bulk water that are taken from the published letter.[229]

3.1.1 Hydration Structures

The hydrated structures of the four vanadium cations were obtained by performing electronic structure calculations using the GAUSSIAN 09 suite of programs.[231] This program enables electronic structure modeling and its theoretical background is presented in Chapter 2. Geometries were optimized using DFT with Becke's 3-parameter hybrid functional (B3LYP)[181-184] and the 6-31G** split valence basis set[188] without imposing any symmetry constraints. The SMD solvation model[194] was subsequently utilized to obtain optimized structures with water selected as the solvent ($\varepsilon = 78$). The resulting structures were then further refined at the B3LYP/6-311G** level.[190] Frequency calculations at a similar level of theory (B3LYP/6-311G**) were performed to confirm local minima. Partial charges distributions and electrostatic potentials for each of the hydrated vanadium ions were determined using the ChelpG scheme.[232]

The structure of the first hydration shell for each vanadium cation was obtained using an unbiased approach to limit the effect of the initial structure on the final structures. The procedure involved adding water molecules to each cation incrementally followed by a geometry optimization at each step, until one of the water molecules was forced out of the first hydration shell. Hence, the optimized geometries obtained from the step with the largest number of waters allowed in the first hydration shell was chosen to be the equilibrium hydrated structure for the specific central cation.

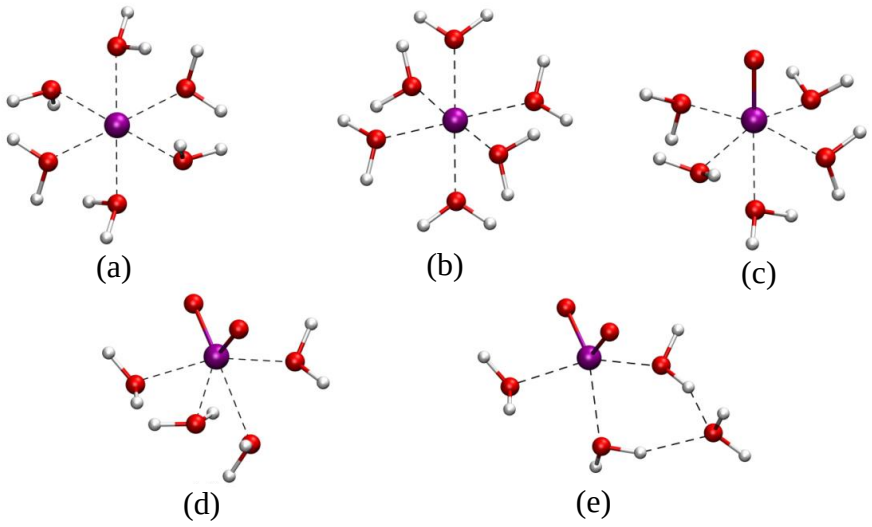


Figure 3.1. First hydration shell structures of vanadium ions at the B3LYP6-311+G**/SMD level of theory: (a) V^{2+}; (b) V^{3+}; (c) VO^{2+}; (d) VO_2^+, octahedral; and (e) VO_2^+, bipyramidal. Color scheme: oxygen (red), hydrogen (white), vanadium (purple). Two-tone solid lines present covalent bonds and dashed lines show coordinate bonds and hydrogen bonds (hydrogen bond criterion 1.1 Å < O···H < 2.5 Å).

The first hydration shell structures for the vanadium ions obtained with this approach are shown in Figure 3.1. The V^{2+} and V^{3+} cations (Figure 3.1(a) and (b)) are hydrated with six water molecules and both have an octahedral structure that agrees favorably with previous studies.[22,233] The gas-phase structures for V^{2+} and V^{3+} show T_h and S_6 point group symmetries, respectively. However, the solution phase structures are all slightly distorted and are C_1. Further structural analysis revealed that the trivalent vanadium complex is more distorted in comparison to the divalent undoubtedly due to higher charge density.

Table 3.1. Average vanadium-oxygen distances for optimized structures shown in Figure 3.1.[a]

V^{2+}	V^{3+}	VO^{2+} [b]	VO_2^+ [c]	VO_2^+ [d]
2.19	2.09	2.10	2.20	2.11

[a] Values are in Å; [b] Only the equatorial bonds are averaged; [c] Bipyramidal; [d] Octahedral.

The first hydration shell of VO^{2+} (Figure 3.1(c)) consists of only five water molecules with an octahedral structure. The distance of the axial water molecule from the central vanadium cation is

2.35 Å and is greater than the average distance to the equatorial water molecules which is 2.10 Å (see Table 3.1). Moreover, the equatorial plane in VO^{2+} is distorted as a result of the repulsion from the oxo-oxygen atoms.

There are two different local minimum energy structures for VO_2^+: one with a first hydration shell consisting of four water molecules and exhibiting an octahedral structure (Figure 3.1(d)) and the other with three water molecules within the first hydration shell and one water molecule outside of the shell (Figure 3.1(e)). This latter structure is bipyramidal and its Gibbs energy at 298 K was determined to be 7.3 kcal/mol lower than that of the octahedral complex (B3LYP/6-311G** level of theory, 8.6 kcal/mol with the inclusion of diffuse functions). Hence, the bipyramidal structure is the most stable. However, this does not imply that the octahedral structure doesn't exist in solution, but that there is a population distribution for the bipyramidal and octahedral structures at 298 K in agreement with previous Car-Parrinello molecular dynamics (CPMD) simulations.[24]

The average calculated bond lengths for all four cations as reported in Table 3.1 were found to be in close agreement with the available literature values. The experimental bond lengths are slightly shorter than the computational values in almost all of these aqua-complexes,[229] but this probably due to the fact that the X-ray diffraction (XRD) measurements were done in the solid phase and our calculations were performed in solution. It may also be due to the effect of the counter ion which is not considered in these *ab initio* calculations.

The binding energies of the water molecules to the central vanadium cations is calculated for the above structures and presented in Table 3.2. As expected, the binding energies for V^{3+} is larger and twice that of V^{2+} as a result of the higher atomic charge density on V^{3+} ion. The value for VO^{2+} is close to V^{2+} while the lowest binding energy belongs to the two VO_2^+ complexes. Also, the

similarities in the binding energies of the bipyramidal and octahedral structures of VO_2^+ may promote the interchange between the two structures in solution as mentioned previously.

Table 3.2. Binding energies of water ligands to central vanadium cations calculated at B3LYP/6-311G** and B3LYP/6-311+G** (in parenthesis) level of theory (all in kcal/mol).

Structure	$-\Delta E^a$	$-\Delta E_{ZPE}{}^b$
$[V(H_2O)_6]^{2+}$	58.52(54.10)	56.06(51.73)
$[V(H_2O)_6]^{3+}$	113.77(108.27)	110.99(105.58)
$[VO(H_2O)_5]^{2+}$	67.44(62.34)	64.68(59.66)
$[VO_2(H_2O)_3]^{+}$	50.20(45.51)	47.41(42.74)
$[VO_2(H_2O)_4]^{+}$	42.83(37.88)	40.12(35.23)

[a] Binding energy based on uncorrected total electronic energies; [b] Binding energy based on ZPE corrected total electronic energies.

Partial atomic charge calculations show that the charge on V^{2+} is 1.72 (1.93 when diffuse function are included) which is close to its formal charge. But for V^{3+} it is 2.05 (1.77 with diffuse function) which is only two thirds of its formal charge. The inclusion of the diffuse functions on the V^{2+} complex resulted in higher atomic charges on all the atoms, while it had a reverse effect on the V^{3+} complex.[229] The following presents the calculation of Gibbs energy of hydration based on the optimized structures of the vanadium cations using the quasi-chemical theory.

3.1.2 Gibbs Energies of Hydration

The Gibbs energies of hydration were estimated using the quasi-chemical theory which was presented in Chapter 2. The inner-shell was considered to follow an equilibrium reaction between the cation and the water molecules of the first hydration shell. The ion clusters obtained from the electronic structure calculations were used as the inner-shell structures. Single point energies were calculated at the B3LYP/6-311+G(2d,p) level on each of the optimized gas phase structures. The outer-shell contribution to the solvation of the ions was determined using the SMD model.

We chose the most stable aqua-complex for each cation and used it as the inner-shell structure in the calculation of the Gibbs energy of solvation in the quasi-chemical approach. Hence, the octahedral structure for V^{2+} and V^{3+} which contained six water molecules, the five water coordinated structure for VO^{2+}, and the three water coordinated trigonal bipyramidal structure for VO_2^+ were selected.

Table 3.3. Calculated Gibbs energy of hydration of vanadium cations using the quasi-chemical approach compared with available experimental information (all in kcal/mol).

cation	$-\Delta G_{calc.}$	$-\Delta G_{exp.}$
V^{2+}	440.0	436.2[a]
V^{3+}	1018.8	1008.6[a]
VO^{2+}	457.2	[b]
VO_2^+	184.4	[b]

[a] Taken from reference 234; [b] Not reported in the literature.

Table 3.3 shows the calculated and experimental Gibbs energies of hydration (where available). The calculated values for V^{2+} and V^{3+} are in good agreement with the experimental values (i.e., ~ 1%). Previous quasi-chemical calculations of the solvation Gibbs energies of cations, including the first transition row metals, have also reported a good agreement with experiments.[202,235-236] Despite the fact that the calculated and experimental values are in the same range and in good agreement, one should notice that the solvation Gibbs energy of the highly charged species may have significant uncertainty.[237] As there was no experimental information for the hydration energies of VO^{2+} and VO_2^+, the calculated values may be used as estimates.

The ion's excess chemical potential versus its coordination number may be monitored by progressively adding water molecules to the inner-shell structure (molecular *aufbau* approach[238]). This approach determines the coordination state at which the dominant contribution to the thermodynamics of hydration is obtained.[239] The results of the *aufbau* approach using the quasi-

chemical theory on the four vanadium cations are presented in Figure 3.2. This figure shows that the Gibbs energy of cations (showed by circles) changes as the number of water molecules inside the inner-shell varies. This signifies the importance of chemical structure around the cation in its solvation phenomena.

Figure 3.2 shows that for both V^{2+} and V^{3+} cations the octahedral structure is the most stable form in solution and contributes the most to the hydration thermodynamics. This coordination number is consistent with our *ab initio* results presented above. However, the prediction of quasi-chemical theory for the coordination number of VO^{2+} and VO_2^{+} ions is 4 and 2, respectively, which differs than our *ab initio* results by one. This result signifies that the majority of the solvation thermodynamics is captured by $VO^{2+}(H_2O)_4$ and $VO_2^{+}(H_2O)_2$, while it is the hexa-hydrate structures for V^{2+} and V^{3+} cations. Previous studies[240] show that the compatibility of the *aufbau* approach and *ab initio* results usually occurs for ions with high charge densities, in our case V^{2+} and V^{3+} and not for VO^{2+} and VO_2^{+}.

The portion of each contribution to the total Gibbs energy of solvation may also be derived. The chemical contribution to the total Gibbs energy of solvation (triangles in Figure 3.2) comes from the inner-shell structure. This contribution is increased by the addition of water molecules to the cluster. In contrast, the outer-shell contribution (squares in Figure 3.2) is decreased by adding water molecules to the coordination shell. Previous studies explain that the ligand desolvation energy is the reason for this decrease.[241-242] The chemical portion of the Gibbs energy of hydration for the most stable structure is about 64% for V^{2+}, 59% for V^{3+}, 60% for VO^{2+}, and 67% for VO_2^{+}. Hence, the local chemical effects form more than half of the hydration phenomena for the structures with the most stable coordination number. As the major contribution to the ion solvation is due to the inner-shell structure, there may be a relationship between the binding energies of the ligands and the free energy of solvation.

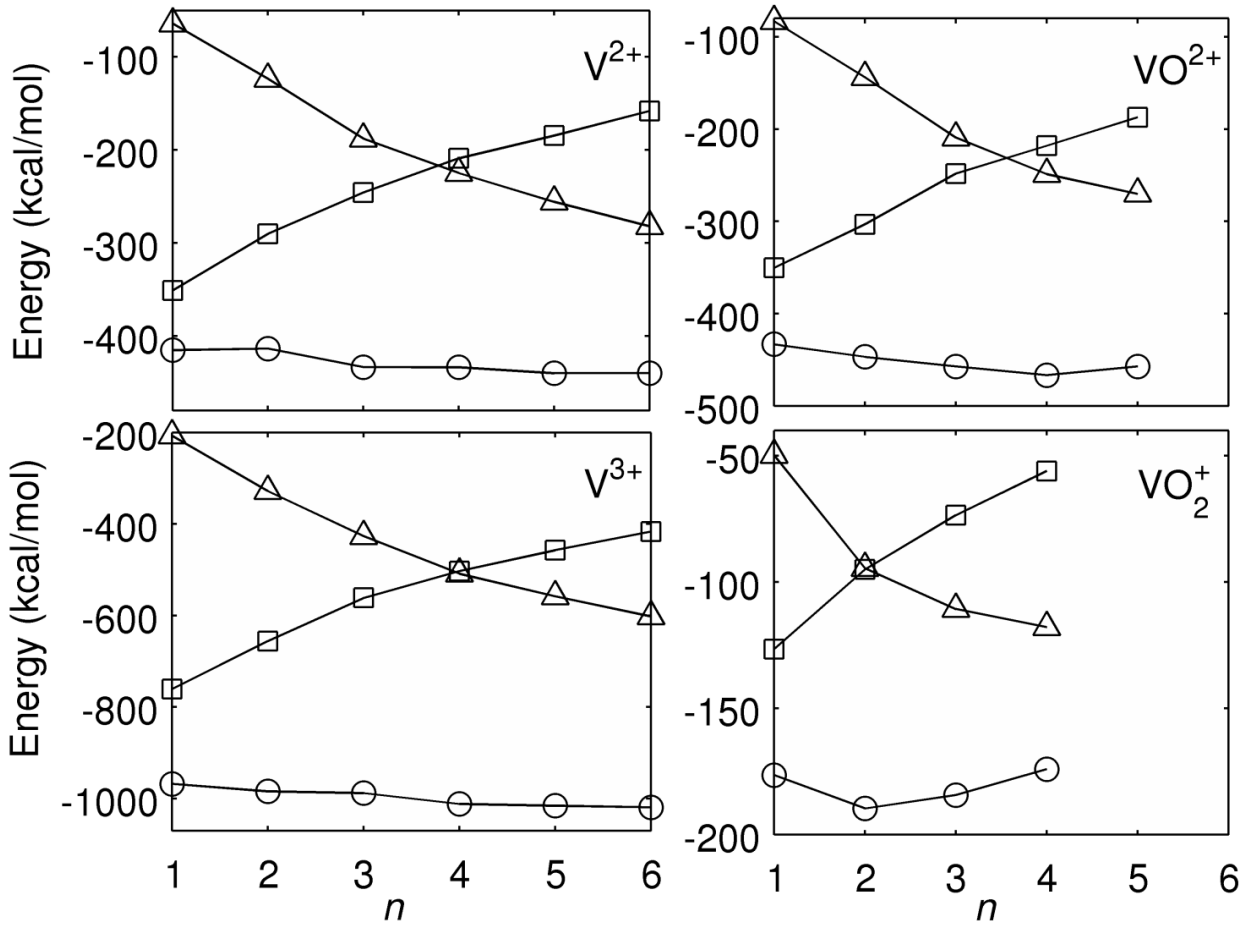


Figure 3.2. Quasi-chemical contributions of the solvation free energy of aqueous V^{2+}, V^{3+}, VO^{2+}, and VO_2^+ versus *n* number of water molecules inside the inner-shell structure. The calculations performed at the B3LYP/6-311+G(2d,p)//B3LYP/6-311G** level of theory and the outer-shell contributions are assessed using the SMD dielectric continuum model. Triangles represent inner-shell contributions and squares are outer-shell contributions to the total free energy of solvation. Circles are the total free energy of solvation predicting $n = 6$ as the most probable inner-shell occupancy for V^{2+} and V^{3+}, $n = 4$ for VO^{2+} and $n = 2$ for VO_2^+.

3.2 Effect of Sulfuric and Triflic Acids on the Hydration of V^{n+}

The effects of sulfuric and triflic (CF_3SO_3H) acids were examined on the hydration of vanadium species as they mimic the electrolyte environment and functional group of PFSA membranes in VRFBs. The results and discussion presented in this section are taken from the published work.[230] Electronic structure calculations were performed on each of the hydrated cations in the presence of an acid molecule. The introduction of an acid to each of the four vanadium cations was performed beginning from three different initial starting positions. In the first set of geometry optimizations, the acid molecule was placed adjacent to the hydrated vanadium cation. In the second set, one of the water molecules of the hydration shell was replaced by an acid molecule and placed at a different position in the cluster. Under the third set of conditions the acid molecule was forced to coordinate with the central vanadium cation, while all the water molecules in the first hydration shell remained coordinated with the vanadium cation. The total number of initial starting geometries generated for each set of conditions typically exceeded several hundred due to the steric and symmetry of the ions and molecules.

After generating the initial geometries, optimizations were performed without symmetry constraints at the B3LYP/6-31G** level and then refined at the B3LYP/6-311G** level followed by a frequency calculation. The SMD solvation model was subsequently utilized to determine all structures within a solvent dielectric of water. The V^{2+} and V^{3+} cations were considered to be of high spin state in all open shell calculations.[243-244] The B3LYP/6-311G** model chemistry along with the SMD continuum solvation model was chosen because of the success in predicting the structures of the vanadium cations in bulk water and the associated hydration Gibbs energies.[229] The structures with the lowest energy were selected among all the optimized structures obtained from the many different initial geometries as the global minimum. Optimizations were performed

using MP2 on V^{3+} in proximity to sulfuric acid in order to test whether a different quantum mechanical treatment of the dispersion forces would affect the results. The results were identical to B3LYP with minor structural changes. Only single point MP2 calculations were performed on the B3LYP optimized structures for the other clusters. It was found that even with MP2 the B3LYP determined global minimum energy structures are still the lowest energy configurations.

The dissociation of the proton in water is expected as both H_2SO_4 and CF_3SO_3H are very strong acids. The hydration and proton transfer behaviors of these acids relative to each other are examined using quantum chemical calculations and presented in Chapter 7. Therefore, in the calculations not only the acids (H_2SO_4, CF_3SO_3H) but also their conjugate anions (HSO_4^-, SO_4^{2-}, $CF_3SO_3^-$) were considered. Moreover, due to the high proton concentrations in the electrolyte of a VRFB, the local interactions between the hydrated proton and the vanadium cations were also investigated.

3.2.1 The V^{2+} Cation

The fully optimized configuration of a hydrated V^{2+} ion in proximity to: (a) sulfuric acid; (b) bisulfate; (c) sulfate; (d) triflic acid; (e) triflate; and (f) sulfate are shown in Figure 3.3. The average $V\cdots OH_2$ distance for the water molecules of the primary hydration shell are reported in Table 3.4. The V^{2+} adopts a hexa-coordinated octahedral structure in the presence of all the acids and anions with a slight angle deviation (< 3°) from 90°. No covalent bonds formed between the vanadium cation and any of the acids or anions as shown in Figure 3.3. The metal cation acts as a Lewis acid accepting electron density from the oxygen atom of either a water or acid molecule (the latter acting as a Lewis base). Since the shared electrons are only from the Lewis base, the bonds are dipolar or coordinate and may undergo ligand substitution reactions.

The calculations indicate that in the presence of the molecular acids (see Figures 3.3(a) and (d)) one of the water molecules in the primary hydration shell is replaced by the acid. However, the

direct interaction of the oxygen atom of the acid with the cation does not change the hexa-coordinated octahedral structure of the V^{2+} ion. The interaction between the molecular acids and the V^{2+} ion affects the extent of dissociation of the triflic acid. This is due to the fact that CF_3SO_3H is a stronger acid than H_2SO_4 and hence has a higher propensity to transfer a proton (see the mixed acid electrolytes section for further detail).

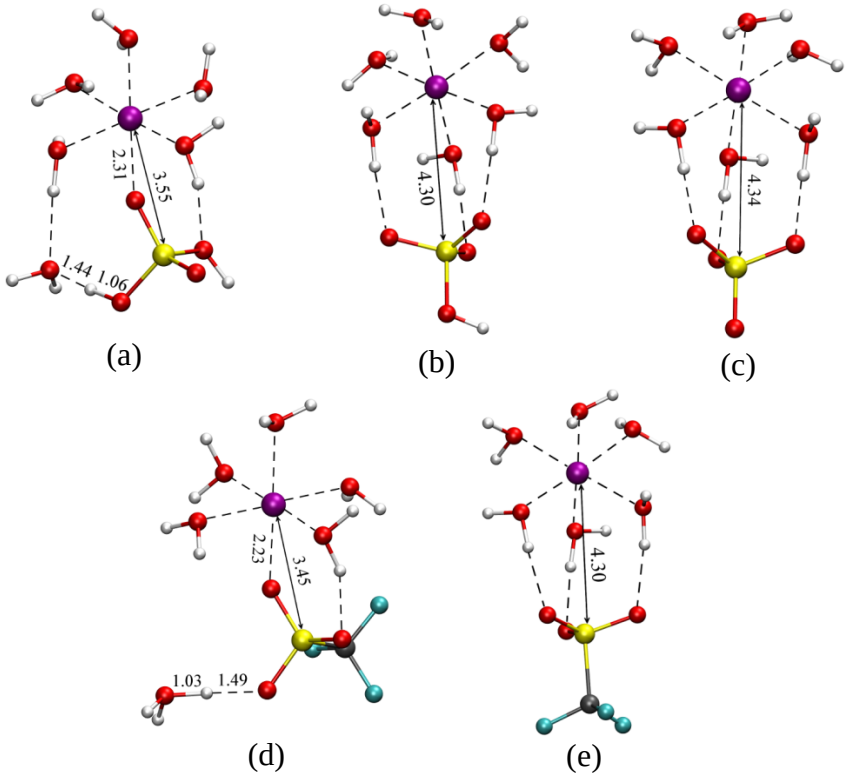


Figure 3.3. Fully optimized configurations at B3LYP/6-311G**/SMD level of theory for the hydrated V^{2+} cation in proximity to: (a) H_2SO_4; (b) HSO_4^-; (c) SO_4^{2-}; (d) CF_3SO_3H; and (e) $CF_3SO_3^-$. The atomic color scheme is: oxygen (red), hydrogen (white), vanadium (purple), sulfur (yellow), carbon (grey), and fluorine (cyan). Distances are represented in Å, two-tone solid lines present covalent bonds, and dashed lines show coordinate bonds and hydrogen bonds (hydrogen bond criterion 1.1 Å < O···H < 2.5 Å).

The global minimum energy structures for the interaction of the bisulfate, sulfate, and triflate anions with hydrated V^{2+} are shown in Figures 3.3(b), (c), and (e). The primary hydration shell consists of all six water molecules and the anions do not enter and are only hydrogen bonded to the primary hydration shell, in contrast to the two acid conformations (Figures 3.3(a) and (d)).

Obviously, the $S\cdots V^{2+}$ distance is greater for the anions (4.3 Å) than for the acids (ca. 3.5 Å) because the anions do not directly interact with the cation and only interact with V^{2+} through the primary hydration shell.

A closer association of the anions to V^{2+} is anticipated from a consideration of the electrostatics. The most stable structures in the absence of a solvation model (i.e. gas phase) are with the anions occupying the primary hydration shell and directly interacting with V^{2+}. However, the presence of the high dielectric constant solvent (i.e. $\varepsilon = 78$) and the hydrogen bonds between the anions and hydration shell increase the structural stability resulting in the dissociation of the hydrated V^{2+} cation from the anions preventing the formation of contact ion pairs.

Table 3.4. Average vanadium-oxygen distances for optimized structures shown in Figures 3.3 to 3.6.[a]

Species	V^{2+}	V^{3+}	VO^{2+}			VO_2^+	
	$V\cdots O(H_2O)$	$V\cdots O(H_2O)$	$V–O_{oxo}$	$V\cdots O^b$	$V\cdots O^c$	$V–O_{oxo}$	$V\cdots O(H_2O)$
H_2SO_4	2.18	2.07	1.56	2.07	3.57	1.64	2.04
CF_3SO_3H	2.19	2.07	1.56	2.08	7.76	1.64	2.05
HSO_4^-	2.20	2.08	1.56	2.06	3.94	1.60	2.10
$CF_3SO_3^-$	2.19	2.07	1.56	2.06	3.58	1.60	2.10
SO_4^{2-}	2.19	2.09	1.57	2.09	3.26	1.61	1.92
Water	2.19	2.09	1.57	2.10	2.35	1.60[d,e]	2.11[d], 2.20[e]

[a] Values are in Å; [b] Equatorial bonds; [c] Axial bond; [d] Bipyramidal; [e] Octahedral.

3.2.2 The V^{3+} Cation

Results for the V^{3+} cation are shown in Figure 3.4. Similar to V^{2+}, V^{3+} also exhibits a hexa-coordinated octahedral structure, however the octahedral angles deviate more significantly from 90° indicating that the presence of the acids/anions have a more signified effect in comparison to V^{2+}.

Both acid molecules (H_2SO_4 and CF_3SO_3H) displace a single H_2O from the primary hydration shell (see Figures 3.4(a) and (d)). Both sulfuric and triflic acid associate more closer to V^{3+} due to a stronger electrostatic interaction. Proton dissociation occurs with both H_2SO_4 and CF_3SO_3H in proximity to the V^{3+} cation forming H_3O^+ (see Figures 3.3(a) and (d)). This is in contrast to their interaction with the V^{2+} cation where only the stronger acid, CF_3SO_3H, dissociates. This is due to the higher charge transfer to the ligands for V^{3+} than V^{2+} and facilitates proton dissociation by both acids.

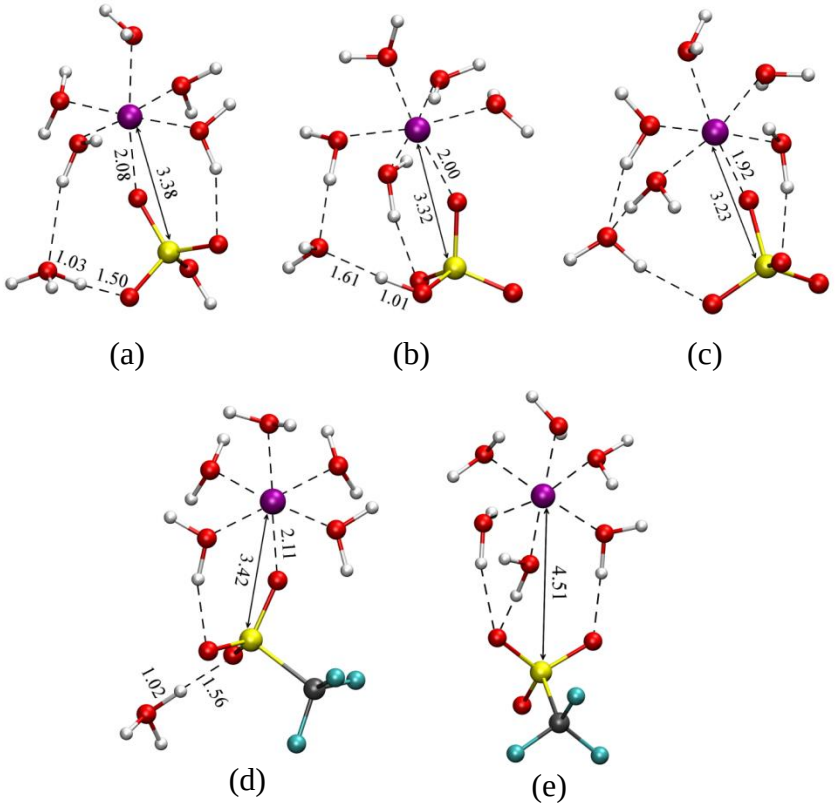


Figure 3.4. Fully optimized configurations at B3LYP/6-311G**/SMD level of theory for the hydrated V^{3+} cation in proximity to: (a) H_2SO_4; (b) HSO_4^-; (c) SO_4^{2-}; (d) CF_3SO_3H; and (e) $CF_3SO_3^-$. Color scheme as described in Figure 3.3.

Figures 3.4(b), (c), and (e) show the interaction of the anions with the hydrated V^{3+} cation. The results indicate that the HSO_4^- and SO_4^{2-} enter the hydration shell and coordinate directly with the

metal cation, but $CF_3SO_3^-$ does not enter the shell preferring to form hydrogen bonds with the water molecules. The formation of contact ion pairs between V^{3+} and SO_4^{2-} has been observed previously, both experimentally and computationally.[245] The structure of the V^{3+} cation with triflate as the counter anion is in agreement with the solid state crystallography results of Cotton *et al.*[246] and NMR studies of Hugi *et al.* in solution.[247]

The anions did not form contact ion pairs when interacting with V^{2+}. We primarily attribute this to the ability of the solvent to stabilize the ions. However, in the case of the V^{3+} cation, two out of the three anions (i.e. bisulfate and sulfate) form contact ion pairs. This suggests that the high electrostatic interaction between the positive and negative ions may overcome the solvent effect. The triflate does not form contact ion pairs because it is the conjugate base of a very strong acid (see the section on the mixed acid electrolytes) owing to the electron withdrawing by the trifluoromethyl group.

3.2.3 The VO^{2+} Cation

Figure 3.5 shows the results of the VO^{2+} cation in proximity to the acids and anions. The aqua-vanadyl ion adopts a hexa-coordinated structure in pure water.[23,27,229] However, our results (Figures 3.5, all panels except (c)) reveal that in close proximity to the acids or anions, the axial water in the *trans* position (relative to VO^{2+}) is replaced with either an acid or anion. Vanadium is penta-coordinated (i.e., vanadyl ion is tetra-hydrated), because the acids or anions in the axial position are more than 4 Å from VO^{2+}. Hence the acids or anions are not directly coordinating with vanadyl. The interaction of VO^{2+} with sulfate (Figure 3.5(c)) results in a rather different structure which has the SO_4^{2-} ion in one of the equatorial positions. This structure is similar to the crystallographic measurements of Ballhausen *et al.*[21] Only the sulfate formed an ion pair with VO^{2+}.

The solidity of the VO_{oxo} entity in Figure 3.5 is in accordance with the fact that vanadyl is the most stable diatomic ion[248] in either solution or solid phases with a strong covalent bond between vanadium and the oxo-oxygen.[249-250] In Figure 3.5 there are no interactions with the oxo-oxygen and also none of the minimum energy structures obtained for the VO^{2+} show any interactions within a distance of 3 Å from the oxo-oxygen. The molecular orbital bonding scheme proposed by Ballhausen and Gray explains the high stability and absence of any interactions of the oxo-oxygen observed in our results.[249]

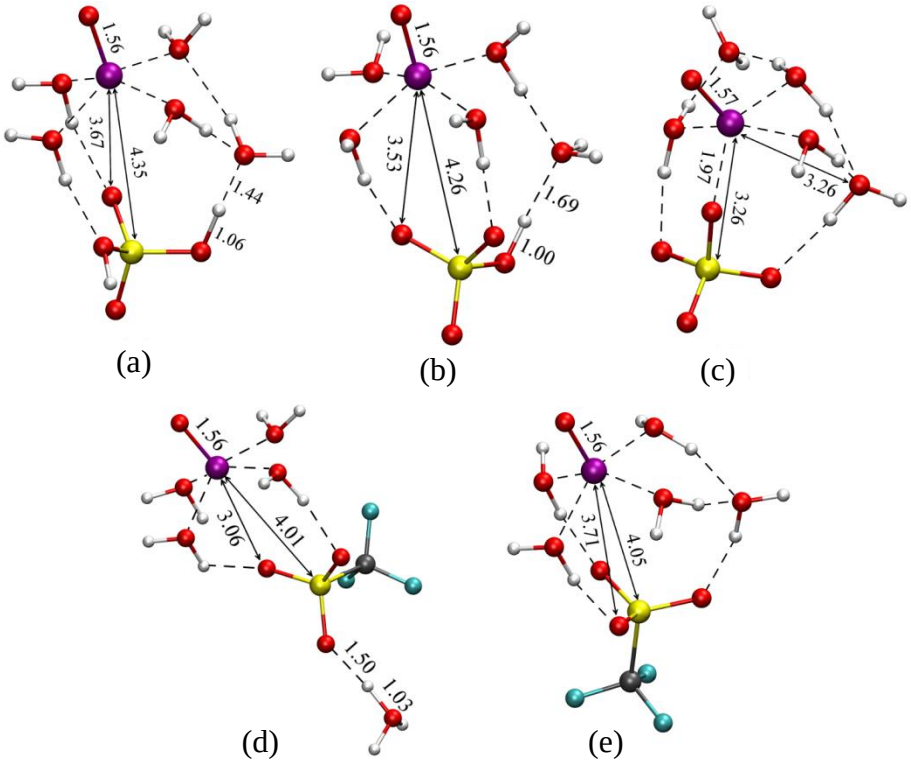


Figure 3.5. Fully optimized configurations at the B3LYP/6-311G**/SMD level of theory for the hydrated VO^{2+} cation in proximity to: (a) H_2SO_4; (b) HSO_4^-; (c) SO_4^{2-}; (d) CF_3SO_3H; and (e) $CF_3SO_3^-$. Color scheme as described in Figure 3.3.

The extent of dissociation of the acids when in proximity to VO^{2+} (Figures 3.5(a) and (d)) is similar to that of the V^{2+} cation. Triflic acid again dissociates completely forming a hydronium ion,

whereas the sulfuric acid does not dissociate. The triflic and triflate associate closer to the VO^{2+} cation than either sulfuric acid or the sulfate anion. The same trend was followed by the V^{2+} cation in Figure 3.3, however the V···S distances were shorter as a result of stronger interactions and the formation of contact ion pairs. Based on our previous work, the V^{2+} and VO^{2+} cations have very similar hydration Gibbs energies (–440.0 and –457.2 kcal/mol, respectively) and binding energies to the water molecules (–56.1 and –64.7 kcal/mol, respectively).[229] Thus, despite the fact that V^{2+} and VO^{2+} have quite different structures they have very similar hydration Gibbs energies, binding energies, and proton dissociation behavior.

The four equatorial ligands in Figure 3.5 are located in a plane beneath the vanadium atom, similar to the hydrated VO^{2+} in pure water or dilute solutions.[23,28,229] Our results show that the angles between the oxo-oxygen, vanadium, and the oxygen atoms of the equatorial ligands, $\angle O_{oxo}VO$, are increased by 5 – 6° in the presence of the acids or anions.[230] These observations are similar to recent experimental results,[28] where the authors reported that the presence of a space demanding oxygen-donor ligand removes the axial ligand and reduces the vanadium coordination number to five thereby increasing the $\angle O_{oxo}VO$.

3.2.4 The VO_2^+ Cation

Figure 3.6 shows the results of the VO_2^+ cation (vanadate) in proximity to the studied acids and anions. It is known that the solution acidity and total concentration of vanadium determine the form of the vanadium species in the +5 oxidation state.[251] In highly acidic solutions it generally exists in the form of a hydrated VO_2^+ cation, consistent with the results shown in Figure 3.6. Both penta- and hexa-hydrated structures have been reported for the hydrated VO_2^+.[24,229,252-254] However, the results from the electronic structure calculations (Figure 3.6) suggest that VO_2^+ mostly adopts a penta-coordinated bipyramidal structure. Among all the determined local minima, those clusters

with an octahedral conformation (not shown) were observed to have an energy at least 7 kcal/mol higher than those with bipyramidal structures. The higher stability of the penta-coordinated VO_2^+ in comparison to the octahedral structure was also reported in previous electronic structure calculations[15,24,229,255] and CPMD simulations.[252]

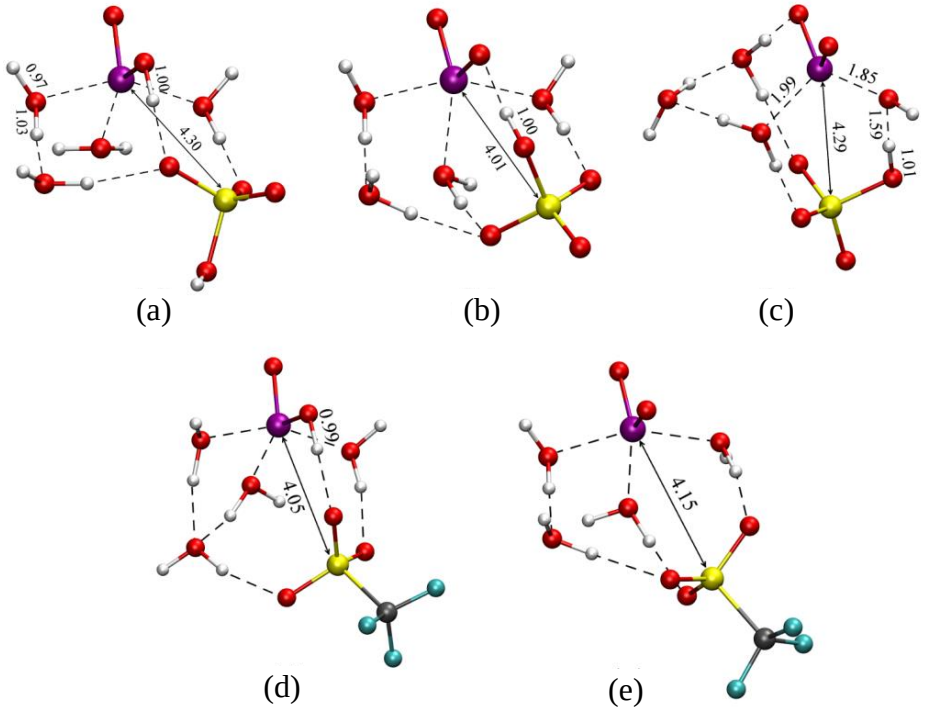


Figure 3.6. Fully optimized configurations at B3LYP/6-311G**/SMD level of theory for the hydrated VO_2^+ cation in proximity to: (a) H_2SO_4; (b) HSO_4^-; (c) SO_4^{2-}; (d) CF_3SO_3H; and (e) $CF_3SO_3^-$. Color scheme as described in Figure 3.3.

The acidic proton fully dissociates and protonates one of the oxo-oxygen atoms to form $[VO(OH)(H_2O)_3]^{2+}$ and the conjugate anion as shown in Figures 3.6(a) and (d). The protonation of the positively charged oxo-species is unique to the VO_2^+ cation (i.e., the oxo-vanadium(IV) is not protonated). Protonation of other vanadium(V) species under moderate acidic solutions is well studied experimentally,[254,256] but for the VO_2^+ species the protonation is only observed in simulations.[230,252] A stretched hydrogen-oxygen bond of 1.03 Å length is observed for one of the

water ligands in Figure 3.6(a). Deprotonation of the hydrated dioxovanadium cation and formation of a OH^- group may eventually result in inorganic polymerization and precipitation.[15,251-252]

The interaction of VO_2^+ with the bisulfate anion is shown in Figure 3.6(b). The cation has a penta-coordinated bipyramidal structure. The bisulfate anion is hydrogen bonded to VO_2^+ and no dissociation of HSO_4^- or protonation of VO_2^+ occurs. The cation with the triflate anion adopts a bipyramidal hydration structure and $CF_3SO_3^-$ does not enter the primary hydration shell of the dioxo-vanadium(V) (see Figure 3.6(e)). A tetra-coordinated vanadium structure is obtained for the sulfate anion (see Figure 3.6(c)). This structure has two oxo-oxygen atoms, one water ligand at 1.99 Å, and a hydroxide ion at 1.85 Å from the vanadium cation. The OH^- is formed by deprotonation of a water ligand and transfer of the dissociated proton to the sulfate to form the bisulfate anion shown in Figure 3.6(c). The other two water molecules are expelled from the primary hydration shell. The water deprotonation in proximity to the sulfate anion (now bisulfate) results in the formation of a reactive hydroxide ion that can be followed by oxolation condensation and formation of precipitates.[15,252,257] Therefore, the interaction of VO_2^+ with SO_4^{2-} ions and the formation of the complex illustrated in Figure 3.6(c) could be the initiation of precipitation reactions.

3.2.5 Partial Atomic Charges

The partial atomic charges on vanadium, water molecules, and oxo-oxygen atoms are reported in Table 3.5. The partial charge on the vanadium atom in V^{2+} clusters varies from + 1.7 to 1.8 which is less than its formal charge of +2. The neighboring water molecules are not charge neutral and carry a slight positive partial charge.

Table 3.5. Computed atomic partial charges on vanadium, oxygen, and water molecules in the primary hydration shell using ChelpG scheme.

Environment		V^{2+}	V^{3+}	VO^{2+}	VO_2^{+}
H_2SO_4	V	1.778	1.851	1.850	1.825
	H_2O[a]	0.036	0.184	0.176	0.228
	O_{oxo}	–	–	–0.605	–0.777[b], –0.455
CF_3SO_3H	V	1.749	1.995	1.792	1.940
	H_2O[a]	0.044	0.169	0.178	0.208
	O_{oxo}	–	–	–0.574	–0.774[b], –0.465
HSO_4^-	V	1.700	1.889	1.816	1.798
	H_2O[a]	0.026	0.159	0.146	0.163
	O_{oxo}	–	–	–0.612	–0.771, –0.631
$CF_3SO_3^-$	V	1.799	2.057	2.031	1.861
	H_2O[a]	0.025	0.139	0.129	0.153
	O_{oxo}	–	–	–0.652	–0.745, –0.692
SO_4^{2-}	V	1.729	2.044	1.899	1.810
	H_2O[a]	0.011	0.098	0.093	0.139
	O_{oxo}	–	–	–0.666	–0.776, –0.740
Water	V	1.719	2.054	1.801	1.805[c], 1.703[d]
	H_2O[a]	0.047	0.158	0.179[e], 0.097[f]	0.161[c], 0.167[d]
	O_{oxo}	–	–	–0.615	(–0.702, –0.697)[c], (–0.702, –0.671)[d]

[a] Average total charge on water molecules in the primary hydration shell of vanadium; [b] Protonated oxo-oxygen; [c] Bipyramidal; [d] Octahedral; [e] Equatorial water molecules; [f] Axial water molecule.

The atomic charge on V^{3+} varies from + 1.9 to 2.1 (formal charge of +3) and is therefore slightly greater than the V^{2+} ion. Consequently, the electron donor ligands around the V^{3+} carry a relatively high positive charge to compensate the difference between the formal charge of the V^{3+} ion and the actual charge residing on the atom. The charge on the water molecules as reported in Table 3.5 vary from + 0.1 to 0.18 and are an order of magnitude greater than those of V^{2+}. The observed charge transfer indicates that the coordinate bonds between the metal and the ligands for the V^{3+} cation are stronger resulting in the closer association of the acids to V^{3+}.

The partial atomic charge on vanadium in the VO^{2+} clusters ranges from + 1.8 to 2.0 which is significantly lower than its formal charge of +4. The charge on the oxo-oxygen atom is about –0.6 which results in a total charge of + 1.2 to 1.4 on the VO_{oxo} instead of its formal charge of +2. Hence, the water ligands are positively charged as observed for the V^{2+} and V^{3+} cations. The charge on the water ligands around VO^{2+} is similar to that observed for V^{3+} and almost an order of magnitude greater than that of V^{2+}.

The partial atomic charge on vanadium in the VO_2^+ clusters varies from + 1.7 to 1.9 and the water molecules in the hydration shell, as expected, are not charge neutral and carry the highest positive charge when coordinating with VO_2^+.

Understanding the effect of the diffused vanadium cations on the membrane and the morphology evolution from a meso-scale perspective is another important aspect of the VRFB design. Probing the dynamic behaviors including the diffusion of ionic species and the morphology evolution require larger length and time scales than those achievable in electronic structure calculations. Hence, DPD was selected to study the dynamics and morphological properties of hydrated Nafion with absorbed vanadium cations.

DPD simulations require meso-scale parameters to describe the interactions between various species of the system as explained in Chapter 2. The conventional parameterization methods discussed earlier failed to give proper parameters for the DPD simulation of the desired system (hydrated Nafion with absorbed vanadium cations). Hence, a parameterization approach was developed based on the electronic structure calculations to overcome this problem. The following presents this pragmatic parameterization method. The application of the developed method on the system of interest is discussed later in this chapter and further in the electrolyte systems of AEMs and SDAPP in Chapters 4 and 5, respectively.

3.3 Approach to Parameterize Dissipative Particle Dynamics

The formulation and basic principles of DPD are presented in Chapter 2. The following presents the parameterization approach that was developed in this work to describe the conservative force interactions in the system of VRFB electrolyte. The developed parameterization method is published and may be found elsewhere.[228]

The conservative interaction potential is assumed to consist of two terms in the quadratic form:

$$U_{ij}^{C} = U_{ij}^{R} + U_{ij}^{ex} = \begin{cases} \frac{a_{ij}}{2}(1 - r_{ij})^2 & , \ r_{ij} < 1 \\ 0 & , \ r_{ij} \geq 1 \end{cases}, \tag{3.1}$$

where:

$$U_{ij}^{R} = \frac{a^{R}}{2}(1 - r_{ij})^2 , \tag{3.2}$$

and:

$$U_{ij}^{ex} = \frac{a_{ij}^{ex}}{2}(1 - r_{ij})^2 . \tag{3.3}$$

This implies $a_{ij} = a^R + a_{ij}^{ex}$. The first term is the reference potential and is related to the compressibility of a reference material. The second term is the excess interaction and contains the information regarding the relative interactions among the beads excess to the reference. The intention is to reproduce the experimental compressibility of one pure reference material and then to obtain all the other interactions (either like or unlike) relative to this reference. The reference bead is a charge neutral species in the system with known experimental compressibility. The a^R is then obtained by matching the simulated compressibility of pure reference to that of the experiment, similar to the remarkable work by Groot and Warren (see section IV of their work).[208] The excess energy may be related to the interaction energy of the two beads which may be computed from electronic structure calculations.

$$U_{ij}^{int} = U_{(i+j)} - \left[U_{(i)} + U_{(j)}\right], \tag{3.4}$$

where U_{ij}^{int} is the interaction energy and is obtained by subtracting the total electronic energy of the isolated beads (i.e., $U_{(i)}$ and $U_{(j)}$) from that of the interacting beads (i.e., $U_{(i+j)}$; the total electronic energy of a system containing the two interacting beads *i* and *j*). In order to correctly sample the interaction energy, $U_{(i+j)}$ should be calculated and averaged over many different spatial configurations of the two beads. Figure 3.7 illustrates the six spatial degrees of freedom that are varied in order to consider all the probable configurations of two objects in a three dimensional space. By varying these six geometric parameters, many different configurations are generated and consequently the interaction energies are fitted to a quadratic function of r_{ij} (the distance between the centers of mass of beads *i* and *j*). Overall, the procedure is similar to the derivation of classical two-body pair potentials from quantum chemical calculations.[243,258-259] However, in this case the calculations are performed on two large clusters of atoms or molecules

(the selected beads with full atomistic resolution) instead of two atoms or small molecules and also the functional form of the potential is only a simple quadratic from.

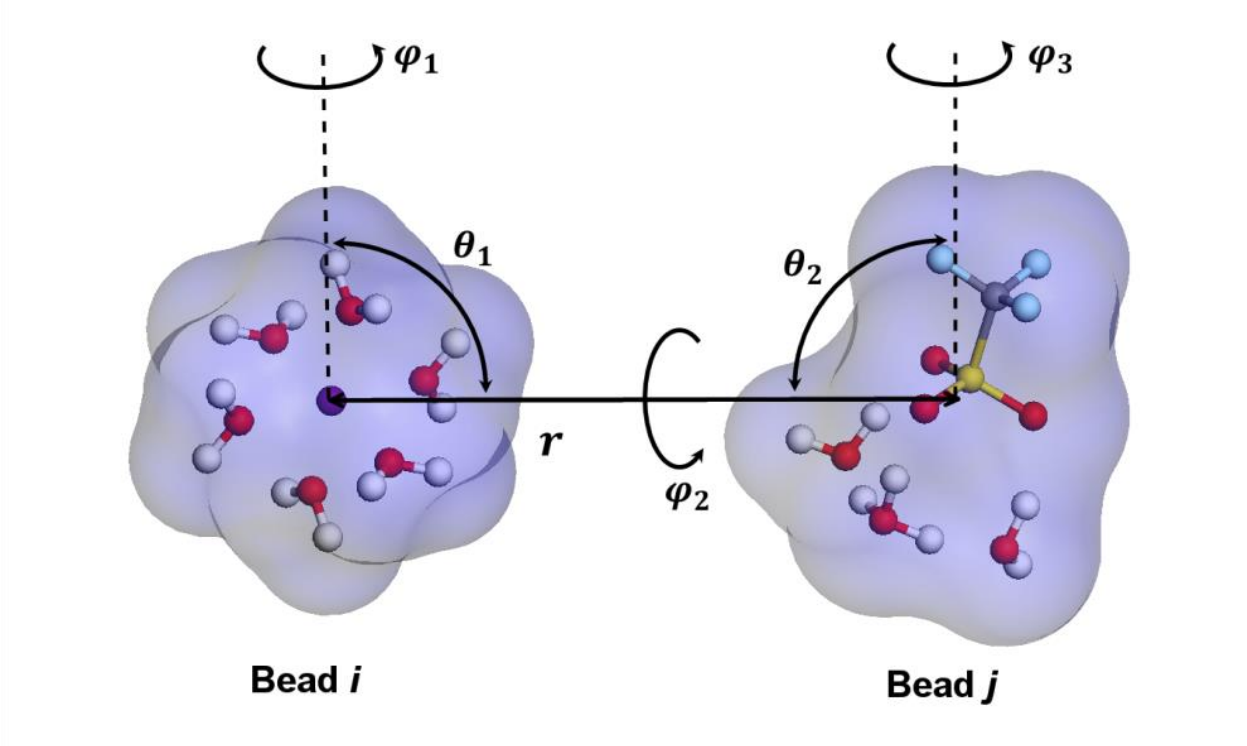


Figure 3.7. The six degrees of freedom that contribute different configurations to the two objects (beads). The atomic structures of the beads i and j are arbitrary. The angles can vary as $0° \leq \theta \leq 180°$ and $0° \leq \varphi \leq 360°$ for each configuration. The lower limit for the r_{ij} is when the beads start to overlap and the upper limit is the cut off distance r_c.

The least squares method is used to fit the calculated interaction energies onto the quadratic functional form. A high-quality fit is not expected to be achieved because the simple quadratic form of the potential is not sufficient to completely explain the interaction of the two clusters of atoms. However, the use of more sophisticated potentials is not utilized in order to maintain the linear functional form of the conservative force and consequently the high speed and efficiency of the DPD simulations. In practice, the addition of a constant to the quadratic form improves the fit

quality. This improvement is significant and necessary for the charged beads and minor for those that are charge neutral. Hence, the practical form of the interaction energy becomes:

$$U_{ij}^{int} = \frac{a_{ij}^{int}}{2}(1 - r_{ij})^2 + b_{ij}^{int} . \tag{3.5}$$

Because b_{ij}^{int} is usually negligible for charge neutral beads but has a large value for charged beads, it may be considered as the contribution due to electrostatic interactions.

The next step is to map the fitted parameters, a_{ij}^{int} and b_{ij}^{int}, to the meso-scale parameter a_{ij}^{ex}. The excess parameter of the reference bead should go to zero because the excess energy is defined as the excess to the reference. Hence, the calculated a_{RR}^{int} is scaled to a negligible value. The fitted parameters for all the beads (either like or unlike) are also scaled with this factor in order to maintain the correlation between the calculated energies and the phase behavior of the system. The fitted parameter, b_{ij}^{int}, vanishes in the derivative of energy and consequently in the force. In order to keep its effect in the final force we assume that this interaction decays quadratically from the center of particle, becoming zero at the cut off distance, similar to the U_{ij}^{R} and U_{ij}^{ex} potentials. Hence:

$$a_{ij}^{ex} = a_{ij}^{int^*} + b_{ij}^{int^{**}} , \tag{3.6}$$

where the stars indicate that the fitted parameters are scaled. The double star in the superscript of b_{ij}^{int} denotes that its scaling differs to that of a_{ij}^{int} by r_c^2, as their units are different. This equation applies to both $i = j$ and $i \neq j$; and so depending on the values of $a_{ii}^{int^*}$ and $b_{ii}^{int^{**}}$, the like-bead interactions (a_{ii}) differ for different bead types. The importance of having different like-bead interactions has been substantiated recently.[169,260]

The treatment of electrostatics via the $b_{ij}^{int^{**}}$ parameter in the conservative force with a cut off distance at r_c does not violate the domain decomposition scheme of the DPD method. However,

this assumption is only reasonable when the charge screening effect is strong (i.e., short Debye length and high ionic strength) and as a result the long range electrostatic interactions vanish at distances around the cut off. This limitation is only important for systems with charged beads. For other systems this constraint is irrelevant. It is also important to note that the excess energy is a meso-scale quantity corresponding to both overlapping and non-overlapping configurations of the two beads. During the mapping we relate it to the atomistic interaction energy in the inter-bead distance where two beads are not overlapping and up to the cut off distance, r_c. Because the electronic energy of an overlapping configuration is either impossible to converge or extremely high (i.e., far beyond the soft particle treatment) the excess energy in the overlapping region is covered by extrapolating the energy of the non-overlapping configurations.

The reliability of the parameterization method was further evaluated by applying it to a system of interest. The following presents the calculation of DPD parameters for a hydrated PFSA ionomer, Nafion, with absorbed vanadium cations using the developed method. This system was selected because it mimics the membrane environment of the VRFB electrolytes.

3.4 Morphology of the Membrane Electrolyte

Nafion is the most widely used PFSA ionomer in VRFBs. The membrane of a VRFB is designed to only permeate hydronium, however vanadium cations cross over due to the imperfect permeability of Nafion.[30] Therefore, investigation of the morphology, phase separation and diffusion of vanadium cations is critical to the improved design of these electrochemical systems. The morphology of hydrated Nafion with absorbed vanadium cations was determined using DPD simulations. The interaction parameters between the DPD beads were calculated using the developed method described in the previous section.

3.4.1 Coarse-Graining of Particles

The choice of the particles is based on the requirement for similar volumes and the preserving distinct chemical nature of the various beads. Selected bead types, their structure, and corresponding volume are listed in Table 3.6. The structure of all bead types were optimized by employing DFT at the B3LYP/6-311G** level[181-184,190] using the GAUSSIAN 09 suite of programs.[231]

Table 3.6. Selected bead types, their structures, and volumes.

Bead Type	Structure[a]	Volume[b] (Å^3)
A	[F]$(CF_2)_6$[F]	291.8
B	[CF_3]$OCF_2CF(CF_3)OCF_2$[F]	279.7
C	[F]$CF_2SO_3^-$ + H_3O^+ $(H_2O)_2$	224.0
C^-	[F]$CF_2SO_3^-$ $(H_2O)_3$	225.1
W	$(H_2O)_8$	241.1
H^+	H_3O^+ $(H_2O)_7$	229.2
V^{2+}	V^{2+} $(H_2O)_6$	212.8
V^{3+}	V^{3+} $(H_2O)_6$	203.0
VO^{2+}	VO^{2+} $(H_2O)_5$	193.4
VO_2^+	VO_2^+ $(H_2O)_4$	178.3

[a] The atoms in brackets are added to stabilize the structures and facilitate DFT calculations. Only fluorine and carbon atoms are added to prevent changes in the chemical nature of selected beads; [b] Volumes are calculated by creating Connolly surfaces with the Atom Volumes & Surfaces tool in Materials Studio.[261]

The backbone of Nafion ionomer was represented by a bead consisting of six CF_2, i.e., $(CF_2)_6$, and designated A. The side chain was represented by two different bead types: a B bead representing the perfluoroether link, and a C bead representing the protogenic group. The C bead, a sulfonic acid group with three water molecules, was selected similar to the previous work on hydrated PFSA membranes.[48] A negatively charged particle, C^- bead, was introduced that consists of a sulfonate anion and three water molecules. The water bead, W, was taken to consist of eight water

molecules. Considering the common value for the density, $\rho r_c^3 = 3$, and the volume of each water molecule as 30 Å^3, the length scale is determined to be $r_c \cong 8.96$ Å.

Distinct bead types were defined for each of the oxidation states of the vanadium cations (V^{2+}, V^{3+}, VO^{2+}, and VO_2^+). All vanadium cation beads contained the first hydration shell of the cation according to our previous study.[229] The number of positively and negatively charged beads may interchange in order to maintain the electroneutrality in a simulation system.

3.4.2 Conservative Interaction Parameters

The presence of charged vanadium species inside the Nafion requires special treatment of the conservative interactions. The parameterization method presented in section 3.1.3 was developed and utilized to define the conservative interactions.[228] the interaction energies were calculated using DFT at the B3LYP/3-21G* level[182-183,186,262-263] and the excess energies were obtained for all pairs of beads. The counterpoise method of Boys and Bernardi[264] was employed to compute the effect of basis set superposition error on the computed energies of each pair of beads. The calculated error was determined to be less than 3% of the computed excess energy and therefore negligible. Over 16000 different configurations were considered for each pair. The calculated energies were fitted using the least squares method (see Equation (3.5) to obtain a_{ij}^{int} and b_{ij}^{int}. The energies were equally weighted during the least squares procedure, however values above an energy threshold were excluded as they correspond to the overlapping configurations. The water was selected as the reference material and a^R was set to 25 based on the experimental compressibility.[208] The a_{WW}^{int} was scaled to a negligible value. The scaling factor was chosen to be r_c^{-3} and the a_{ij}^{int} and b_{ij}^{int} values were scaled accordingly. The calculated a_{ij} values for the selected bead types are reported in Table 3.7. Some of the interactions are not calculated as the simulated systems does not include the pair.

Table 3.7 shows the like bead interaction between the W beads, $a_{WW} = 24.9$, which is essentially identical to the desired value of 25.0. The interaction parameters between the A, B, and C beads are in qualitative agreement with those of Wu *et al.*[48] which were related to the Flory-Huggins χ-parameter (they calculated χ using the Blends module in Materials Studio which approximates it from the mixing energy calculated using a Monte Carlo approach). The self-repulsion is calculated as 33.1, 56.6, and 96.3 for the H^+, V^{2+}, and V^{3+} beads, respectively. This suggests that the like-bead repulsion increases as the charge of the bead increases. Note that the b_{ij}^{int**} is almost negligible for neutral beads and has a large value for the charged beads, confirming that it models the electrostatics. Overall, the derived interaction parameters are physically meaningful and compare favorably with previous literature values.

Table 3.7. Calculated conservative interaction parameters.

a_{ij}	A	B	C	C^-	W	H^+	V^{2+}	V^{3+}	VO^{2+}	VO_2^+
A	34.6									
B	32.0	28.4								
C	38.5	31.7	29.9							
C^-	39.7	33.7	32.9	43.7						
W	37.9	28.4	25.9	27.6	24.9					
H^+	37.0	27.5	25.7	19.1	25.4	33.1				
V^{2+}	34.9	25.3	24.4	7.3	24.3	40.4	56.6			
V^{3+}	27.4	23.8	19.6	–13.1	18.0	46.8	–	96.3		
VO^{2+}	29.6	25.1	24.4	6.5	24.5	40.2	–	–	55.8	
VO_2^+	29.4	25.4	25.0	16.6	24.7	32.6	–	–	–	32.5

It is worth noting that by increasing the number of molecules within a single bead the repulsion parameter generally increases.[208-209] However, we selected $a^R = 25$ (derived for a bead consisting of only 1 H_2O) for our system of interest to prevent the solidification artifact that occurs in large

degrees of coarse-graining.[265] This also increases the simulation speed as the time step for soft beads may be much larger. The use of soft beads is a common practice[48,50,214] and it is known that only the relative magnitude of the interactions actually matters to the behavior of the system.[266-267] Hence, the use of a smaller a^R is acceptable and it does not affect the rest of the mapping and relative interactions.

3.4.3 Bonded Interaction Parameters

Two types of bonded potentials are introduced: (*i*) a harmonic spring potential between neighboring connected beads; and (*ii*) an angular potential between three consecutive beads, $f_i^{Bonded} = f_i^S + f_i^A$. The spring force experienced by bead i is $f_i^S = -\partial U^S / \partial r_i$, where U^S is the total spring potential, whose form is given by:

$$U^S = \sum_{all\ bonds} \frac{1}{2} K_b (r_b - r_b^0)^2 \tag{3.7}$$

where K_b, r_b, and r_b^0 are the spring modulus, bond length, and equilibrium bond length, respectively. Similarly, the angle force derives from the total angular potential defined as:

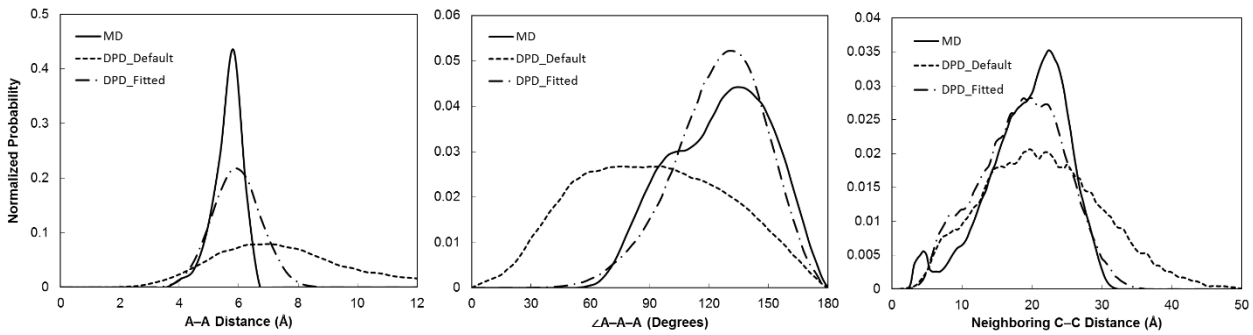
$$U^A = \sum_{all\ angles} K_a (1 - \cos(\theta_a - \theta_a^0)) \tag{3.8}$$

where θ is the angle between three consecutively bonded beads.

Table 3.8. Bonded interaction parameters obtained by fitting to the structures from classical MD simulations.

Bond	K_b	r_b^0	Angle	K_a	θ_a^0
A–A	100	0.65	A–A–A	5	135
A–B	100	0.55	A–A–B	10	100
B–C	100	0.5	A–B–C	10	135
B–C$^-$	100	0.5	A–B–C$^-$	10	135

The structure of a Nafion chain was matched to that of a corresponding classical MD simulation in order to find the bonded interaction parameters: K_b, K_a, r_b^0, and θ_a^0; similar to previous work.[50,268] A smaller system is chosen as the prototype because the classical MD simulations are limited by time and length scales. MD simulations were undertaken for a three dimensional periodic system of hydrated Nafion in an NVT ensemble. The number of water molecules in the system corresponded to the hydration level $\lambda = \frac{H_2O}{-SO_3^-} = 18$ and the Nafion chains contained 15 repeating units. Further details on the MD simulations may be found in Cui and Paddison.[54] The DPD bonded parameters were tuned until the structure of the coarse-grained molecules were close to those of the MD results. Table 3.8 summarizes the bonded parameters obtained from the fitting to the MD simulations.



(a) (b) (c)

Figure 3.8. Distribution of: (a) the bond distance between connected A beads; (b) the angle between three consecutive A beads; and (c) the distance between two neighboring C beads in each Nafion chain. In order to compare atomistic chain structures from MD simulations to those of DPD, each Nafion chain was dissected into fragments equivalent to the selected beads and the center of mass of each fragment was considered as the position of the representing bead. The solid lines are the results from the MD simulation. The dashed lines are the corresponding DPD system with conservative interaction parameters from Table 3.7 and the default set of bonded interactions ($f_i^{Bonded} = 4.0r_b$). The dash-dots are the corresponding DPD system with both bonded and non-bonded interactions from Table 3.7 and 3.8.

Figure 3.8 shows the structural improvements obtained from the fitted parameters over the default bonded potential used in previous simulations.[48,133-134,208,214] The stiffness parameters are

deliberately set to values that qualitatively match the bond distance and angles. If we decide to exactly replicate the results from the MD simulations the K_b and K_a values become too large which consequently requires much shorter time steps and decreases simulation efficiency.[50,268] Hence, a reasonable bond and angle distribution is deemed to be suitable.

3.4.4 Simulations

A three dimensional periodic unit cell of side length 40 (35.8 nm^3) was chosen; using a density of 3 there were 192000 DPD particles in a simulation box. The time step was set to 0.02 (136 fs) and the systems were equilibrated for at least 30000 steps (13.7 ns). The simulations were performed using the DPD module in Materials Studio.[261] Nafion chains were selected to have the molecular weight of 124928 g/mol and equivalent weights (EW) of 944, 1115, and 1244. Systems contained Nafion, water, vanadium cation and/or sulfuric acid. Three hydration levels of 6, 12, and 18 were examined. Each of the vanadium oxidation states was included at a time to prevent inter-cation interactions. Such interactions are not considered because vanadium species may be chemically reactive to each other which are beyond the scope of this study. In order to keep the electro-neutrality of the system upon addition of the vanadium cations, hydronium ions have been removed and C beads were replaced by C^-.

Figure 3.9 shows the radial distribution functions (RDFs) for hydrated Nafion systems. The vanadium RDFs (shown in Figures 3.9(a) and (b)) illustrate that the system with V^{3+} has the highest first peak and the most right shifted onset of the curve. This suggests that the V^{3+} species has the strongest self-repulsion among all vanadium species. The least self-repulsion is for VO_2^+ which has the lowest total charge. The effects are more significant at lower hydration levels.

The sulfonate RDFs in Figures 3.9(c) and (d) show that the C^- beads are brought closer together, i.e., the aggregation of sulfonate groups is increased, in the presence of the cationic species with the effects being the most significant for V^{3+}. Note that the effects decrease at higher hydration levels. Similar behavior was also reported in the MD simulations.[54]

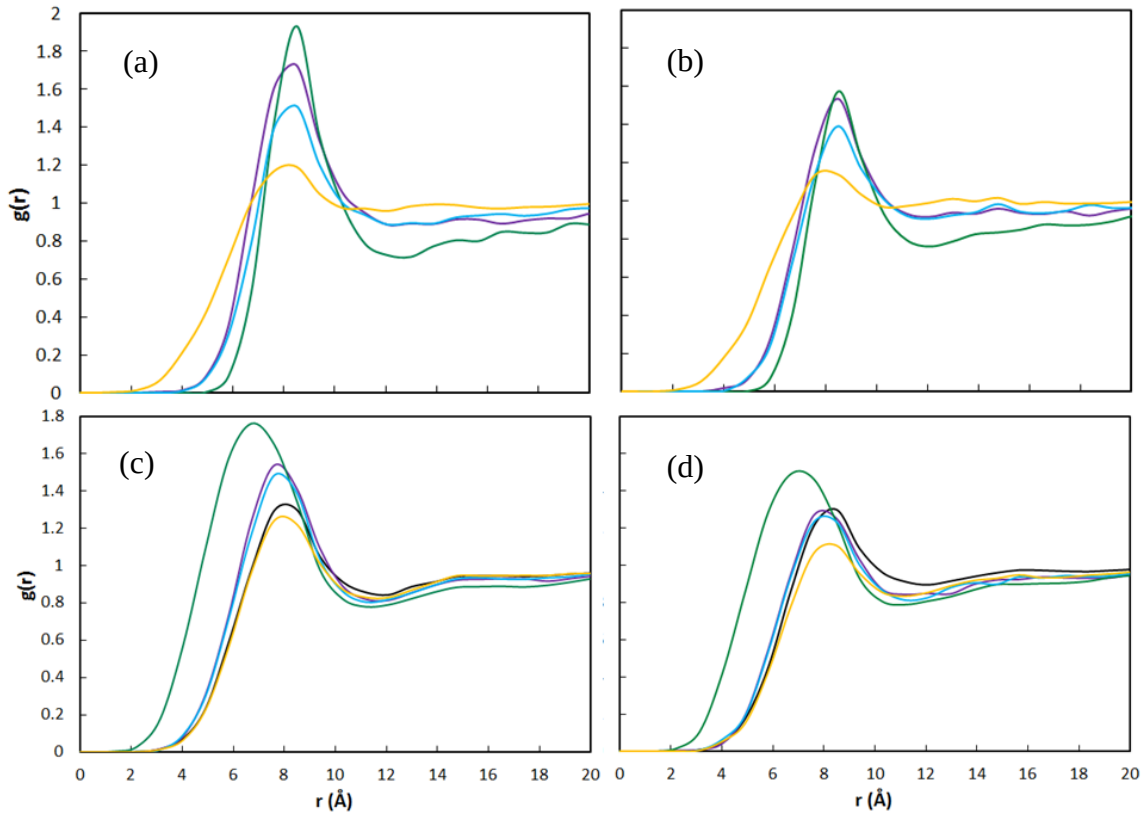


Figure 3.9. RDFs of vanadium and C^- beads for hydrated Nafion systems at different hydration levels and EW = 1115. (a) $V^{n+} - V^{n+}$ RDFs at $\lambda = 6$; (b) $V^{n+} - V^{n+}$ RDFs at $\lambda = 18$; (c) $C^- - C^-$ RDFs at $\lambda = 6$; and (d) $C^- - C^-$ RDFs at $\lambda = 18$. Color code: violet-V^{2+}; green-V^{3+}; blue-VO^{2+}; yellow-VO_2^+; black-hydrated Nafion.

The RDFs of the water beads are shown in Figure 3.10. The first peak of the system containing V^{3+} is slightly stronger than V^{2+} and both are more prominent than the pure hydrated Nafion system. The presence of the vanadium cations also shifts the peak to the left. Hence, water clusters tend to be more compact and structured in the systems containing V^{2+} and V^{3+}. This effect is evident at the lowest hydration level but is hardly noticeable at the highest level. Similar

behavior was recently observed in MD simulations.[54] The pair correlation functions were stronger and shifted to the left for water molecules with vanadium cations in the system. They also reported decreasing peak height with increasing water content. However, the peaks are much stronger in MD than in DPD. This is due to the coarse-graining effect and the use of large DPD beads which screens some of the effects. However, the observed behavior in the DPD simulation results is still outstanding.

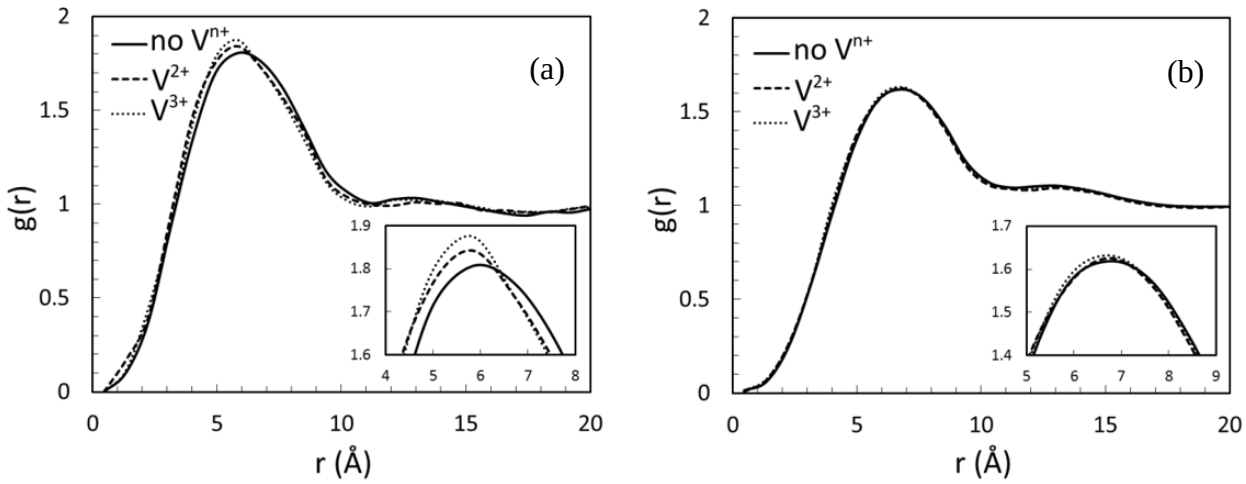


Figure 3.10. Radial distribution functions of the water beads at EW = 1115 and two different hydration levels: (a) $\lambda = 6$; and (b) $\lambda = 18$. The insets are magnification of the first peak in each graph. The solid line is for the system of hydrated Nafion, the dashed line has absorbed V^{2+}, and the dotted line has absorbed V^{3+}.

Figure 3.11 illustrates the diffusivities of vanadium and water beads. The diffusivities are obtained from the mean square displacements calculated over the last 20000 steps for each simulation. The DPD results indicate that V^{3+} is the slowest moving cation, and that VO_2^+ is the fastest. The V^{2+} and VO^{2+} beads have similar diffusivities. The experimental results are inconsistent with some authors' measurements indicating that V^{2+} diffuses the fastest[269] and that V^{3+} is the slowest; others researchers measured the reverse.[270] The discrepancy in the experimentally reported values

warrants more experimental and simulations. The presence of vanadium species slightly affects the diffusivity of the water beads (see Figure 3.11(b)).

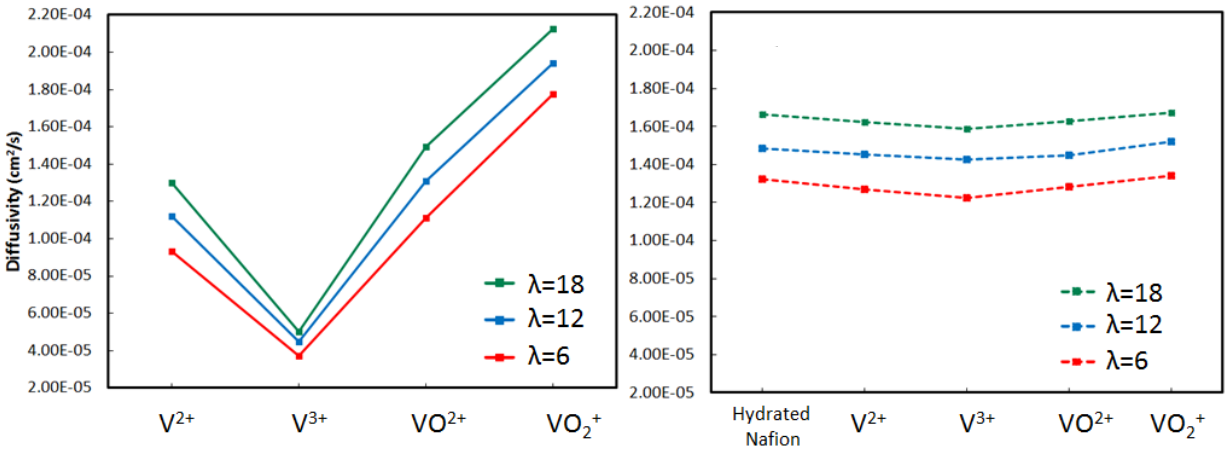


Figure 3.11. Calculated vanadium and water diffusivities at different hydration levels in hydrated Nafion with an EW = 1115. (a) V^{n+} beads; and (b) W beads. The V^{3+} and VO_2^+ beads show the lowest and the highest diffusivities, respectively. The effect of vanadium cations on the diffusivity of the water beads is insignificant.

The distributions of the water beads and vanadium-sulfonate beads are affected when the equivalent weight of Nafion is increased from 944 to 1244, but keeping the molecular weight constant. Figure 3.12 illustrates the RDFs and diffusivities for hydrated Nafion system with diffused VO^{2+} cation at $\lambda = 12$. The W–W and VO^{2+}– C^- RDFs become stronger and more structured as the equivalent weight is increased. However, the vanadium RDFs (VO^{2+}– VO^{2+}) do not significantly change. The results indicate stronger cation-anion interaction for the higher EWs which consequently decreases the vanadium diffusivity. The diffusivities of water and vanadium beads are both increased by decreasing the EW, however the increase in the water diffusivity is greater.

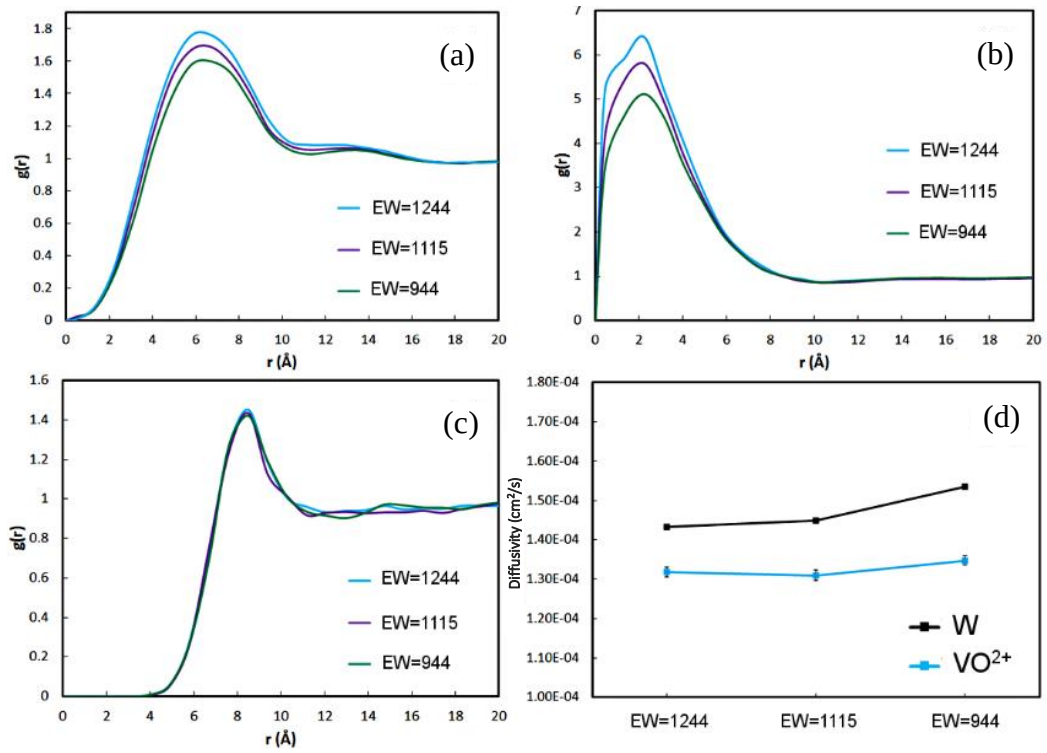


Figure 3.12. RDFs and diffusivities for hydrated Nafion systems at different equivalent weights and λ = 12. (a) W – W RDFs; (b) VO^{2+} – C^{-} RDFs; (c) VO^{2+} – VO^{2+} RDFs; and (d) diffusivities of W and VO^{2+} beads. The cation-anion interactions are increased by increasing the EWs, whereas the vanadium diffusivity is decreased.

The following chapter presents the results and discussion on the AEM electrolytes based on SEBS triblock copolymer. These systems were investigated using DPD simulations employing the developed parameterization method presented in the previous section.

Chapter 4 Anion Exchange Electrolytes

This chapter is based on the following manuscript to be submitted for publication:

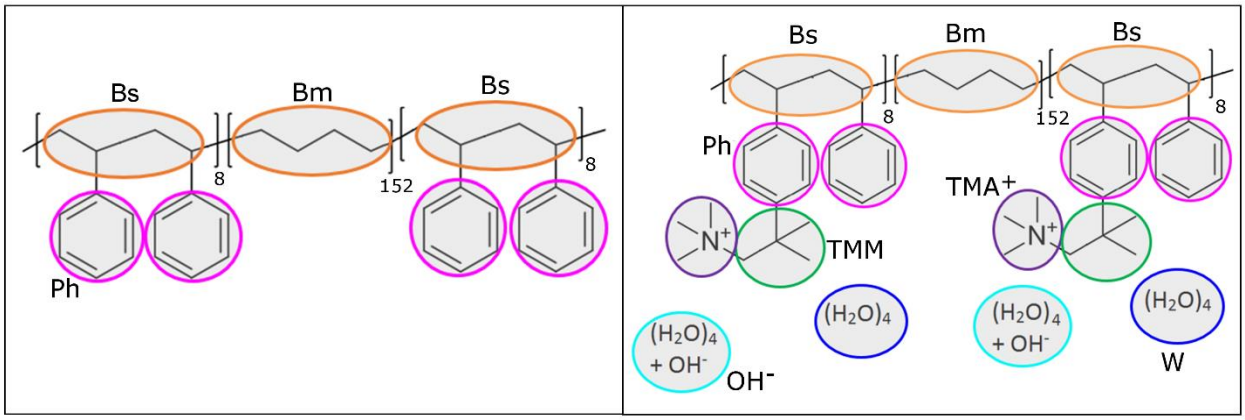
- Sepehr, F.; Liu, H; Bae, C; Tuckerman, M. E.; Hickner, M. A.; and Paddison, S. J., Meso-scale simulations of anion exchange membranes based on quaternary ammonium tethered triblock copolymers. *Macromolecules,* to be submitted.

This chapter presents the study of a chemically stable AEM, quaternary ammonium-functionalized SEBS triblock copolymer, at meso-scale using dissipative particle dynamics (DPD) simulations in order to understand the relationships between the microstructure and morphology. A broad range of hydration levels was examined and the effect of another anion (Cl^-) was studied in addition to OH^-, as membranes are usually prepared and tested in a halogen precursor form. The chemical structures of SEBS and synthesized AEMs were briefly introduced in Chapter 1. The theoretical background of the DPD method is provided in Chapter 2. The following presents the coarse-graining scheme, parameterization of DPD interactions (conservative and bonded), simulations set up, and the results and discussions.

4.1 Coarse-Grained Model

4.1.1 Coarse-Graining of Particles

Similar volume particles corresponding to distinct chemical groups were selected. Figure 4.1 shows the coarse-grained models of the SEBS triblock copolymer and the hydrated AEM in the alkaline form. Selected bead types, their chemical structure, and corresponding volume are listed in Table 4.1. This level of coarse-graining was chosen to enable future examination of various desired microstructural changes. The SEBS was also modeled in order to benchmark the bonded interaction parameters for the DPD simulations.



(a) (b)

Figure 4.1. Coarse-grained model of: (a) SEBS triblock copolymer; and (b) hydrated AEM in alkaline form. Each circle represents the selected chemical group or collection of atoms for a particular bead and is distinguished with a different color. The midblock of SEBS is modeled as polyethylene instead of the poly(ethylene-co-butylene) for simplicity (see Figure 1.5).

The polystyrene end block of the SEBS copolymer was modeled by two different bead types: a Bs bead representing two polymerized vinyl groups, $(CH_2CH_2)_2$; and a Ph bead representing the phenyl group. The midblock was considered to be polyethylene instead of the poly(ethylene-co-butylene) for simplicity and was modeled with a Bm bead consisting of two vinyl groups (identical to Bs). Although the Bs and Bm beads are chemically identical, one of them represents the backbone of a more rigid polymer (polystyrene) and the other a flexible elastomer. The model incorporates these characteristic properties through the careful choice of the bonded parameters distinguishing the flexibility of the end and mid block polymers (see the following section on the bonded interaction parameters).

The TMA^+ bead represents the trimethyl ammonium (TMA) cationic group and bears a single positive charge. Methyl imidazolium cation was considered as the MIm^+ bead to explore the effect of the cationic group type in future work. Two negatively charged particles: OH^- bead to model the alkaline form; and Cl^- bead for the chloride precursor form were introduced in the system to be simulated. . The OH^- bead consists of a hydroxide ion and four water molecules (i.e., OH^-

$(H_2O)_4$), while the Cl^- bead consists of a chloride anion and three water molecules (i.e., Cl^- $(H_2O)_3$). The hydrated structures of the OH^- and Cl^- beads were taken from structures reported in the literature,[271-272] and satisfying the similar volume criterion. A water bead, W, was taken to consist of four water molecules.

Table 4.1. Selected bead types, their chemical structures, and volumes.

Bead Type	Structure[a]	Volume[b] ($Å^3$)
Bs, Bm	$[H](CH_2CH_2)_2[H]$	125.5
Ph	$C_6H_4[H_2]$	129.7
TMM	$[H]C(CH_3)_2CH_2[H]$	124.8
TMA^+	$[H]N(CH_3)_3^+$	121.8
W	$(H_2O)_4$	120.1
OH^-	OH^- $(H_2O)_4$	134.6
Cl^-	Cl^- $(H_2O)_3$	125.0
MIm^+	$[H]C_3N_2H_3CH_3$	130.9

[a] The atoms in brackets were added to stabilize the structures and facilitate DFT calculations. Only hydrogen atom was added to prevent changes in the chemical nature of the beads; [b] Volumes were calculated by creating Connolly surfaces with the Atom Volumes & Surfaces tool in Materials Studio.[261]

4.1.2 Conservative Interaction Parameters

The developed parameterization method[228] presented earlier in Chapter 3 was utilized to derive the meso-scale conservative interactions. The structure of all bead types were optimized by employing DFT at the B3LYP/6-311G** level[181-184,190] using the GAUSSIAN 09 suite of programs.[231] The interaction energies were calculated at the B3LYP/6-31G* level and the excess energies were obtained for all pairs of beads. Over 2000 different configurations were considered for each pair. The DPD particles in this chapter represent half the volume size of the particles used in the VRFB simulations (see Chapter 3). Therefore, a larger basis set and fewer number of configurations were considered. The calculated energies were fitted using the least squares method to obtain a_{ij}^{int} and b_{ij}^{int}. The energies were equally weighted, however

values above an energy threshold were excluded as they correspond to the overlapping configurations.

The water was selected as the reference material and a^R was set to 25 based on the experimental compressibility.[208] The a_{WW}^{int} was scaled to a negligible value. The scaling factor was chosen to be $(2.28 \times r_c^2)^{-1}$ and the remainder of the a_{ij}^{int} and b_{ij}^{int} values were scaled accordingly. Utilizing the common value for the density, $\rho r_c^3 = 3$, and taking the volume of each water molecule as 30 Å^3, the length scale was determined to be: $r_c \cong 7.11$ Å. The a_{ij} values were calculated for the selected bead types are their values are reported in Table 4.2. Interaction parameters were not calculated if the simulated systems did not contain the specific pair of beads.

Table 4.2. Calculated conservative interaction parameters.

a_{ij}	Bs, Bm	Ph	TMM	TMA^+	MIm^+	W	OH^-	Cl^-
Bs, Bm	30.28							
Ph	35.02	30.53						
TMM	29.24	27.74	26.03					
TMA^+	27.52	27.31	25.59	65.79				
MIm^+	32.59	34.42	26.70	–	71.97			
W	35.57	33.44	27.46	26.61	31.27	25.01		
OH^-	34.80	30.05	27.88	–15.02	–12.12	27.34	65.68	
Cl^-	32.22	30.50	29.34	–16.65	–12.53	28.17	–	73.99

Table 4.2 shows a strong repulsive interaction between the SEBS copolymer beads (i.e., Bs, Ph, and Bm) and the W bead consistent with their hydrophobic nature. The self-repulsion between the charged beads, i.e., TMA^+, OH^-, and Cl^- is very strong and varies from 65 to 74. These values are in the same order indicating the chemical structure of the ions has little effect on their conservative

interaction parameters. This suggests that the interaction between the charged beads is predominantly controlled by their charge and electrostatic interactions.

The identical chemical structures of the Bs and Bm beads results in the same conservative interaction parameters. The Bs bead represents the backbone of a more rigid polymer (polystyrene), whereas the Bm bead models a flexible elastomer. This was incorporated into the model by careful choice of the bonded parameters distinguishing the flexibility of the end and mid block polymers (see the following).

4.1.3 Bonded Interaction Parameters

Harmonic spring and angular potentials were considered between the connected beads of polymer similar to the earlier DPD simulations on VRFB electrolytes. Among all the possible angles only four and six angles were considered for the simulation of the SEBS and hydrated AEMs, respectively (see Table 4.3).

Several initial values for the bonded potential parameters (K_b, K_a, r_b^0, and θ_a^0) were used based on the flexibility of the polymers. The polystyrene end blocks are stiffer than the elastomeric midblocks, hence more rigid parameters were used for the former. The parameters were further refined until the expected experimental morphology of SEBS, i.e., hexagonal cylindrical,[115,273] was reproduced. The first four rows of Table 4.3 report the bonded interaction parameters corresponding to the hexagonal cylindrical morphology of SEBS that were also used in the simulation of the hydrated AEMs.

The AEM ionomer has cationic functional groups attached to the end blocks and therefore two additional types of bonds and angles were required for the coarse-grained model. There were no structural information to benchmark these parameters, hence values close to those of SEBS were selected.

Table 4.3. Bonded interaction parameters for simulating the SEBS triblock copolymer and hydrated AEMs. The first four rows define the bonded parameters of the SEBS and all for the AEM.

Bond	K_b	r_b^0	Angle	K_a	θ_a^0
Bs – Bs	30	0.7	Bs – Bs – Bs	15	150
Bs – Ph	30	0.7	Bs – Bs – Bm	10	150
Bs – Bm	30	0.7	Bs – Bm – Bm	1	90
Bm – Bm	20	0.7	Bm – Bm – Bm	1	90
Ph – TMA^+	30	0.7	Bs – Ph – TMM	1	90
TMM – TMA^+	20	0.7	Ph – TMM – TMA^+	1	90

4.1.4 Simulations

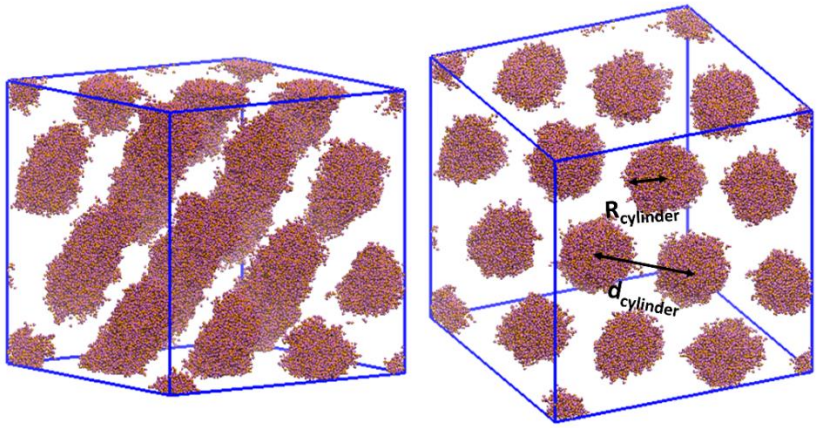
The large scale atomic/molecular massively parallel simulator (LAMMPS) software package[274] employing DPD style was used to perform all the simulations. The PACKMOL package[275] and VMD program[276] were used to generate random initial configurations and visualize the results, respectively. A three dimensional periodic unit cell of end length 60 in DPD length unit (42.7 nm^3) was chosen; using a density of 3 there were 648000 DPD particles in a simulation box. The time step was set to 0.01 in DPD time unit (38 fs) and systems were equilibrated for 70 million steps (2.68 μs).

The SEBS macromolecules were selected to have a molecular weight of 11840 g/mol with the composition of polystyrene, i.e., end blocks, being 29.63 mol%. All chains had equal molecular weight or a polydispersity index of 1.0. This simulated system is quite similar to molecular weight property of experimental SEBS except for chain length. For example, a commercial SEBS synthesized by anionic polymerization has M_n = 105,000 g/mol, a polydispersity index of 1.04, and polystyrene content of 30 mol%.[112] In the pure SEBS system there were 3240 macromolecules of SEBS and therefore, only Bs, Ph, and Bm beads were placed in the simulation box.

The AEM ionomers had the same number of repeating units as SEBS, but 50% of the styrene was functionalized with the TMM and TMA^+ beads. Every other styrene group was functionalized as shown in Figure 4.1 (b), however in experiment they are randomly functionalized. The effect of water content was explored by simulating various degrees of hydration. The hydration level in these systems ranged from λ = 4 – 20, where $\lambda \equiv \frac{H_2O}{TMA^+}$, i.e., water molecules per cationic functional group. The systems consisted of water, OH^- or Cl^- anions, and more than 2000 macromolecules depending on the hydration level. The number of positively and negatively charged beads were set to maintain the electroneutrality of the system.

4.2 Morphology of SEBS Triblock Copolymer

The SEBS triblock copolymer was initially simulated in order to benchmark the bonded interaction parameters for DPD simulations of the hydrated AEMs. Figure 4.2 presents the simulated morphology of the SEBS copolymer. Only the polystyrene end blocks (those modeled with Bs and Ph beads) are shown in this figure for clear illustration of the morphology. The midblocks are modeled by the Bm beads (not shown in the figure) and occupy the empty spaces between the cylinders.



(a) (b)

Figure 4.2. Simulated morphology of the SEBS triblock copolymer. Only the polystyrene end blocks, i.e., the Bs and Ph beads, are shown for clarity. (a) and (b) show two different views of the hexagonal cylindrical morphology. $R_{cylinder}$ is the cylinder radius and $d_{cylinder}$ is the intercylinder distance. The orange and mauve spheres illustrate the Bs and Ph beads, respectively. The simulation box is shown in blue.

The end and mid blocks of the SEBS clearly phase separate. The polystyrene units form cylinders in a hexagonal orientation and are contained within the matrix of the midblocks. The simulated hexagonal cylindrical morphology is in agreement with the previous experimental and simulation studies.[115-118,273,277]

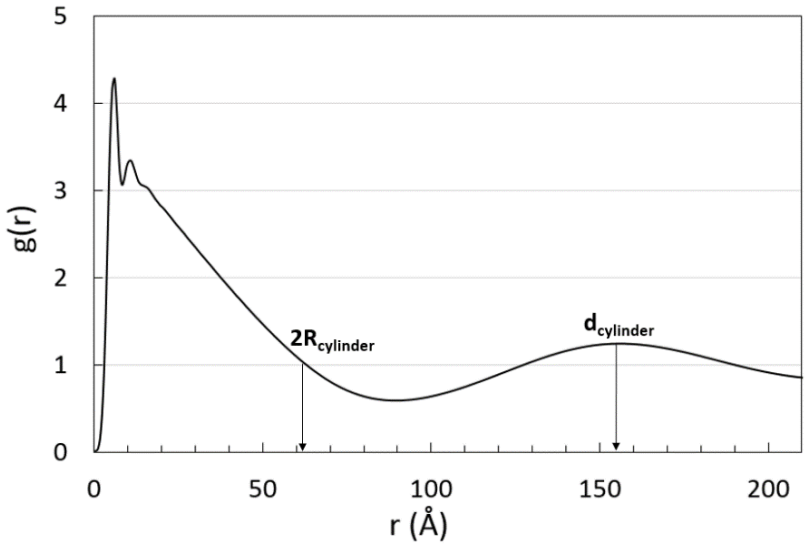


Figure 4.3. The polystyrene (i.e., BsPh – BsPh) RDF of the SEBS triblock copolymer. The position of the second point with the unit function value is twice the cylinder radius ($2R_{cylinder}$) and the position of the next peak is the intercylinder distance ($d_{cylinder}$).

The polystyrene radial distribution function (RDF) is shown in Figure 4.3. . The distance at which the RDF reaches one for the second time is considered to be twice the cylinder radius ($2R_{cylinder}$) and the position of the next peak is the intercylinder distance ($d_{cylinder}$).[117] The DPD simulation results suggest that $R_{cylinder} = 3.1$ nm and $d_{cylinder} = 15.6$ nm (see Figure 4.3). Experimental measurements based on small angle X-ray scattering (SAXS) determined $R_{cylinder} = 7.5$ nm and $d_{cylinder} = 29.5$ nm.[115] The difference between the values from the DPD simulations and the scattering experiments may be due to the selected molecular weight of the macromolecule. The molecular weight of the real SEBS macromolecule is about an order of

magnitude larger than that simulated. The ratio of the cylinder radius to the intercylinder distance for the DPD simulations is 0.20 and compares favorably with the experimental value of 0.25.

4.3 Morphology of SEBS-Based Electrolytes

Figure 4.4 shows the simulated morphology of the hydrated ionomer, the SEBS triblock copolymer functionalized by TMA cationic groups, in the alkaline form at a hydration level where $\lambda = 8$. The AEM ionomer strongly phase separates into a lamellae morphology with alternating layers of the functionalized polystyrene end blocks (consisting of Bs, Ph, TMM, and TMA^+) and the polyethylene midblocks (Bm). The lamellae morphology is generally perforated and interconnected.

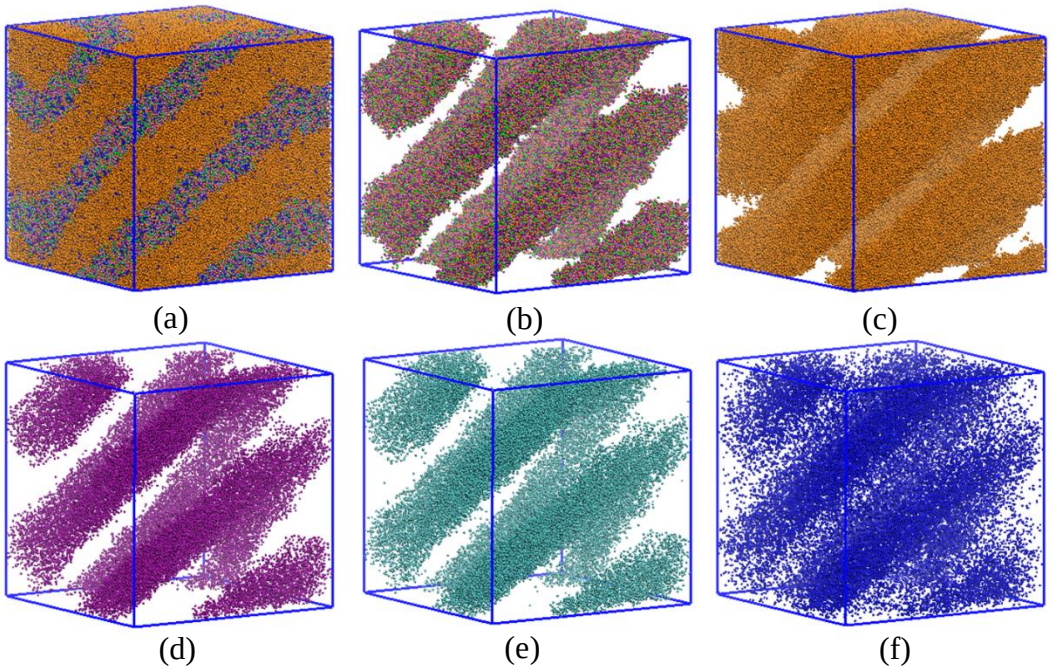


Figure 4.4. Simulated morphology of the hydrated AEM in the alkaline form at $\lambda = 8$. Each figure shows a specific bead type for clarity: (a) all beads; (b) Bs, Ph, TMM, and TMA^+; (c) Bm; (d) TMA^+; (e) OH^-; and (f) W. (a) shows a strong phase separation between the functionalized polystyrene end blocks and the midblocks that are shown separately in (b) and (c). (d) and (e) illustrate the distribution of ionic species and (d) shows that the majority of water are in the polystyrene phase with a few distributed in the midblock phase. Color code: Bs and Bm (orange); Ph (mauve); TMM (green); TMA^+ (purple); OH^- (cyan); and W (blue).

Figures 4.4 (d) and (e) show the distribution of the ionic species, i.e., the TMA^+ and OH^- beads. The distribution of the TMA^+ beads resembles that of the polystyrene end blocks in Figure 4 (b) which is expected as they are chemically bonded to each other. The oppositely charged beads, i.e., OH^-, are similarly distributed due to their strong attraction to the cationic sites.

The ionic species and the majority of the water are in the functionalized polystyrene phase, with some water also distributed throughout the polyethylene phase. This distribution suggests that the hydrated AEM phase separates into a hydrophilic phase consisting of the end blocks and a hydrophobic phase consisting of the midblocks.

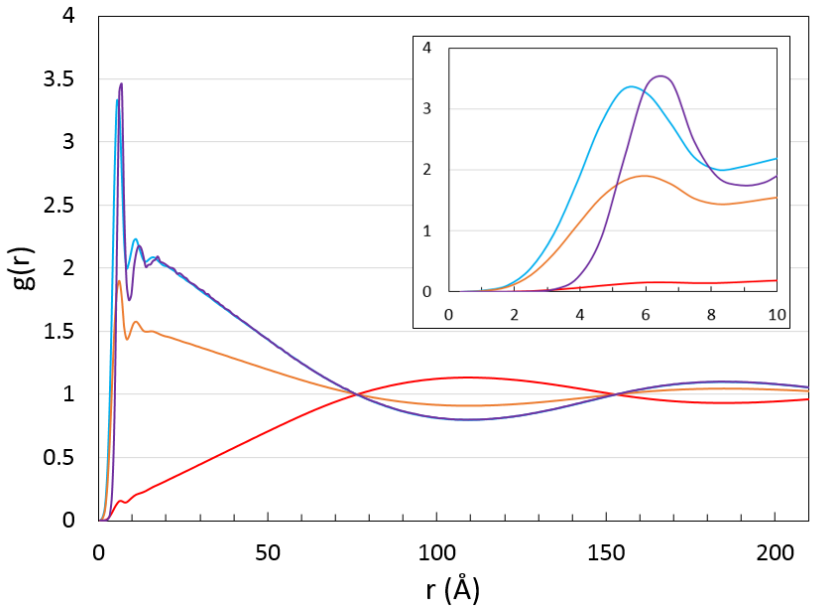


Figure 4.5. RDFs of the hydrated AEM in the alkaline form at $\lambda = 8$. The inset shows a magnification at short distances. Color scheme: BsPh – BsPh (blue); BsPh – Bm (red); Bm – Bm (orange); and TMA^+ – TMA^+ (purple).

The computed RDFs are shown in Figure 4.5. The blue line is the BsPh – BsPh RDF corresponding to the polystyrene end blocks. The orange line corresponds to the midblocks and hence the hydrophobic phase. The RDF of the hydrophilic and hydrophobic phases is in

red and shows a strong repulsion between the two phases as clearly shown in Figure 4.4. The TMA^+ beads result in a similar RDF to the end blocks. The RDFs of the hydrophilic phase and TMA^+ closely resemble each other at distances greater than 20 Å, confirming that the TMA^+ groups are distributed within the hydrophilic phase. The TMA^+ – TMA^+ RDF (purple curve) is shifted to the right at very short distances in comparison to the hydrophilic phase (blue curve) (see the inset in Figure 4.5). This is due to the strong self-repulsion between the positively charged beads.

4.3.1 The Effect of Hydration

Figure 4.6 shows the morphology of the hydrated AEM in the alkaline form at five different hydration levels: $\lambda = 4, 8, 12, 16,$ and 20. It is clear that the AEM ionomer sharply phase separates into hydrophilic and hydrophobic phases at all degrees of hydration. More importantly is the qualitative change in the morphology with increasing hydration. A perforated and interconnected lamellae morphology is exhibited at the lower water contents where $\lambda = 4$ and 8. The morphology is perfectly lamellae at $\lambda = 12$ and then becomes a disordered bicontinuous morphology at the highest hydration ($\lambda = 16$ and 20).

Figure 4.7 shows the polystyrene RDFs for the systems displayed in Figure 4.6. It is clear that increasing the level of hydration increases the intensity of the first peak and decreases that of the second. This suggests that the polystyrene end blocks become more structured as the water is added. The distance at which the RDF reaches unity (which was previously related to the size of the domains[48]) increases through hydration indicating that the size of the hydrophilic phase grows. Recently, Sun *et al.* characterized the morphology of a similar SEBS-based ionomer functionalized with quaternary ammonium groups through atomic force microscopy (AFM) phase imaging.[114] They observed a clear phase separation between the hydrophilic functional styrene blocks and the hydrophobic ethylene/butylene blocks. Their results revealed that the hydrophilic domains swell and become larger upon hydration in agreement with the results displayed in Figure 4.6.

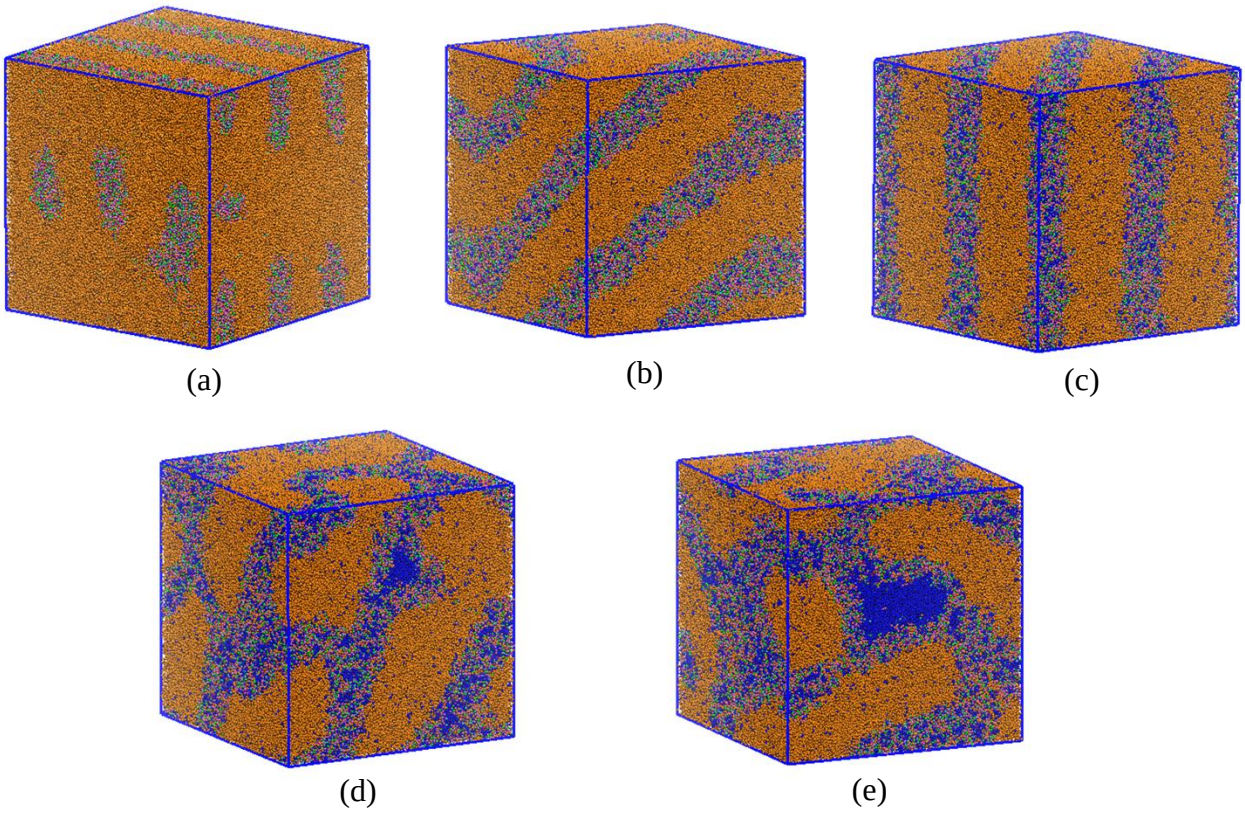


Figure 4.6. Simulated morphology of the hydrated AEM in the alkaline form for $\lambda =$: (a) 4; (b) 8; (c) 12; (d) 16; and (e) 20. All beads are shown and the color scheme is the same as in Figure 4.4. The ionomer phase separates into hydrophilic and hydrophobic phases at all hydration levels. As the hydration increases the morphology changes from perforated and interconnected lamellae ($\lambda = 4$ and 8) to perfect lamellae ($\lambda = 12$) and then to disordered bicontinuous domains ($\lambda = 16$ and 20). Domains exclusively consisting of water are formed within the hydrophilic phase at the two highest water contents only.

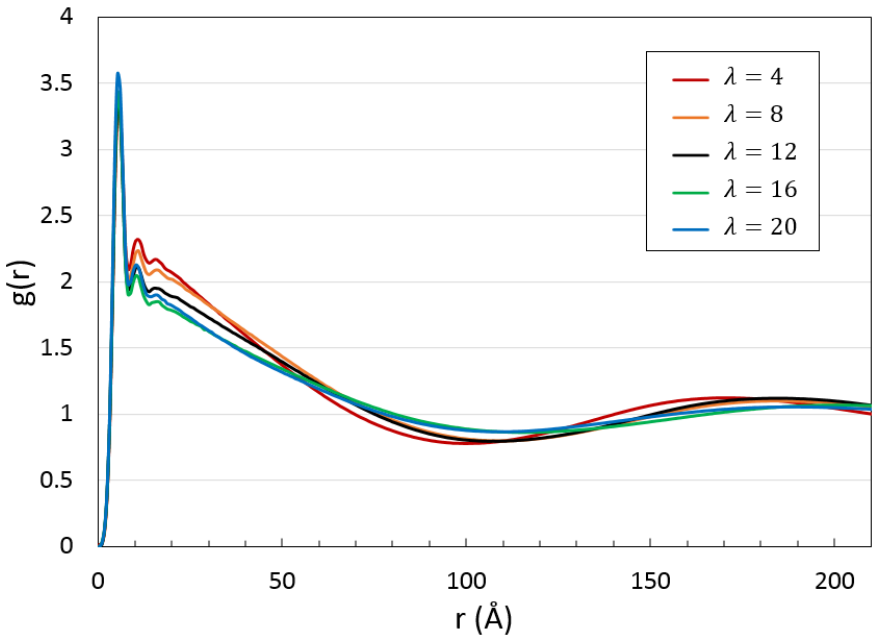


Figure 4.7. Polystyrene RDFs for the hydrated AEM in the alkaline form at five levels of hydration. Increasing the water content increases the intensity of the first peak and decreases that of the second. The distance at which the RDF reaches one increases through hydration indicating that the hydrophilic phase swells.

The blue domains observed in Figures 4.6 (d) and (e) correspond to the domains that only contain water (i.e., exclusively the W beads). Cross sections of the morphologies at $\lambda = 16$ and 20 are shown in Figure 4.8 for better visualization of the 3D extent. Several small domains of water are observed at $\lambda = 16$ and there is one large domain at $\lambda = 20$. The cross sections show that these clusters are three dimensional. The SAXS measurements of the sulfonated SEBS ionomers by Weiss *et al.* exhibited the formation of nano-scale ionic clusters dispersed within larger polystyrene domains that themselves were dispersed in a continuous elastomeric phase.[278] Their experimental finding compares well with our simulations results. They both show the formation of nano domains within the polystyrene end block phase, although their ionomer was sulfonated and our system is functionalized with TMA.

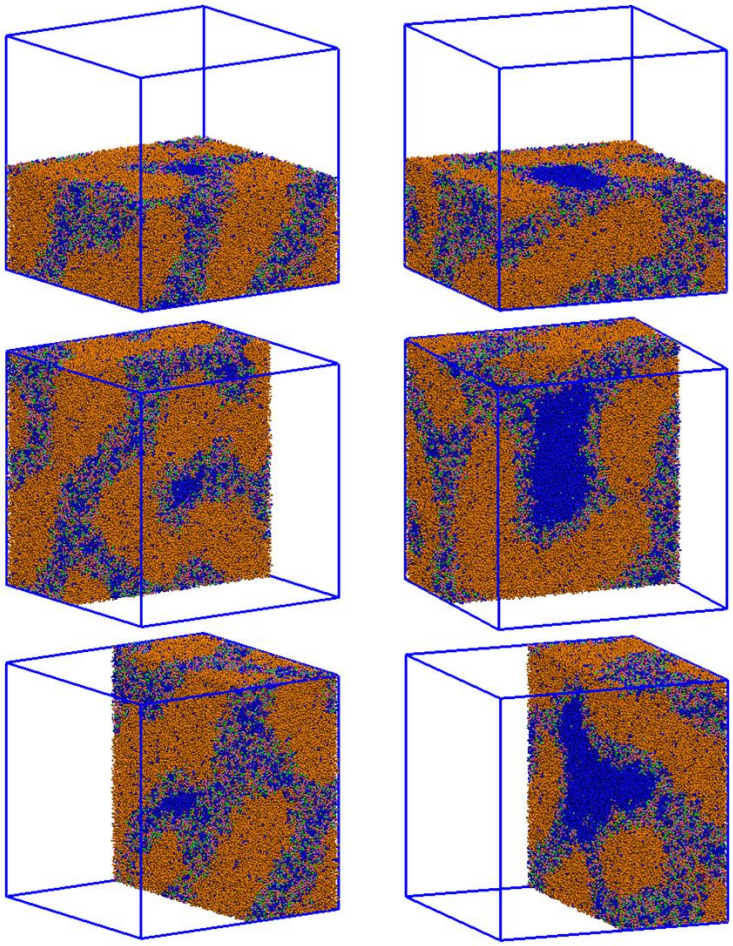


Figure 4.8. Cross sections of the morphologies (shown in Figures 4.6 (d) and (e)) in the xy, yz, and xz planes (top to bottom). (a) $\lambda = 16$; and (b) $\lambda = 20$. The exclusive water domains are within the hydrophilic phase and larger at the higher level of hydration. The cross sections reveal that the water domains are three dimensional.

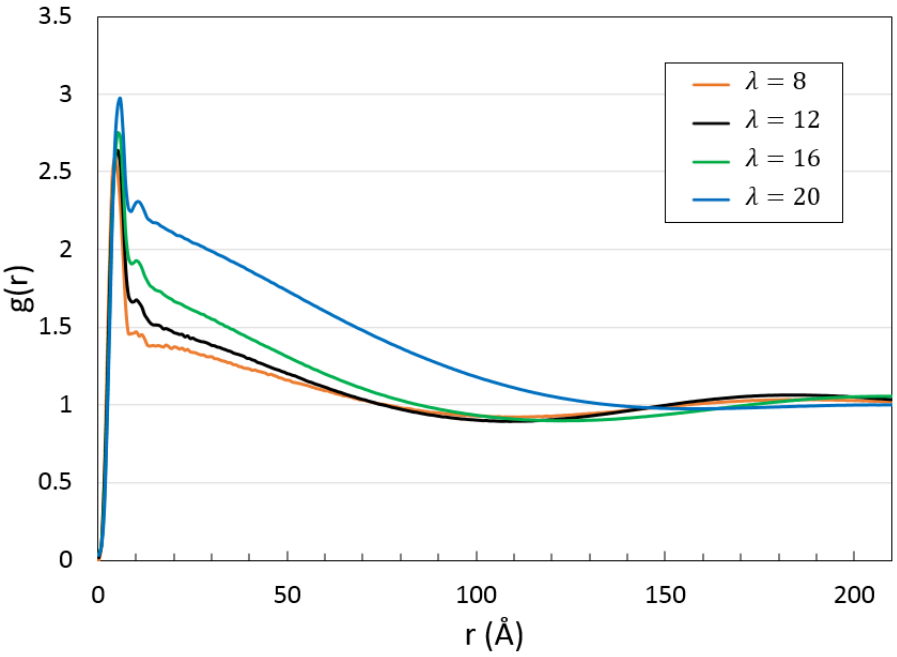


Figure 4.9. W – W RDFs for the hydrated AEM in the alkaline form at various degrees of hydration. Clearly, increasing the hydration intensifies the peaks. The distance at which the RDF reaches one is the same for $\lambda = 8$ and 12 and increases for $\lambda = 16$ and 20. This is due to the formation of domains that exclusively contain water. There are not sufficient W beads in the simulation box at $\lambda = 4$ to form a smooth curve and therefore this data is not shown.

The W –W RDFs at various levels of hydration are shown in Figure 4.9. The intensity of both peaks increases as the hydration increases suggesting that the water becomes more structured. The distance at which the RDF reaches a value of one is the same for $\lambda = 8$ and 12 which hardly showed any exclusive domains of water. However, it increases for $\lambda = 16$ and 20 as a result of the formation of exclusive water domains at these two levels of hydration. The formation of large water domains and the extension of the RDF tail at the highest water contents were also observed in the 3M perfluorosulfonic acid ionomers.[48]

The TMA^+ – OH^- RDFs for the hydrated AEM are shown in Figure 4.10. The intensity of the first peak increases with increasing hydration, whereas the second and third peaks decrease. Figure 4.10 (c) shows that the integrated number of OH^- is one at the vicinity of each TMA^+ bead and

independent of the hydration level. This suggests that each TMA^+ bead is paired with one OH^- in its immediate vicinity. This value monotonically increases at longer distances (> 5 Å), however the rate of increase is lower at higher levels of hydration. This suggests that there are fewer number of OH^- beads around the TMA^+ cations as the water content is increased and that the ionic pairs disperse throughout the hydrophilic phase as the ionomer swells upon hydration.

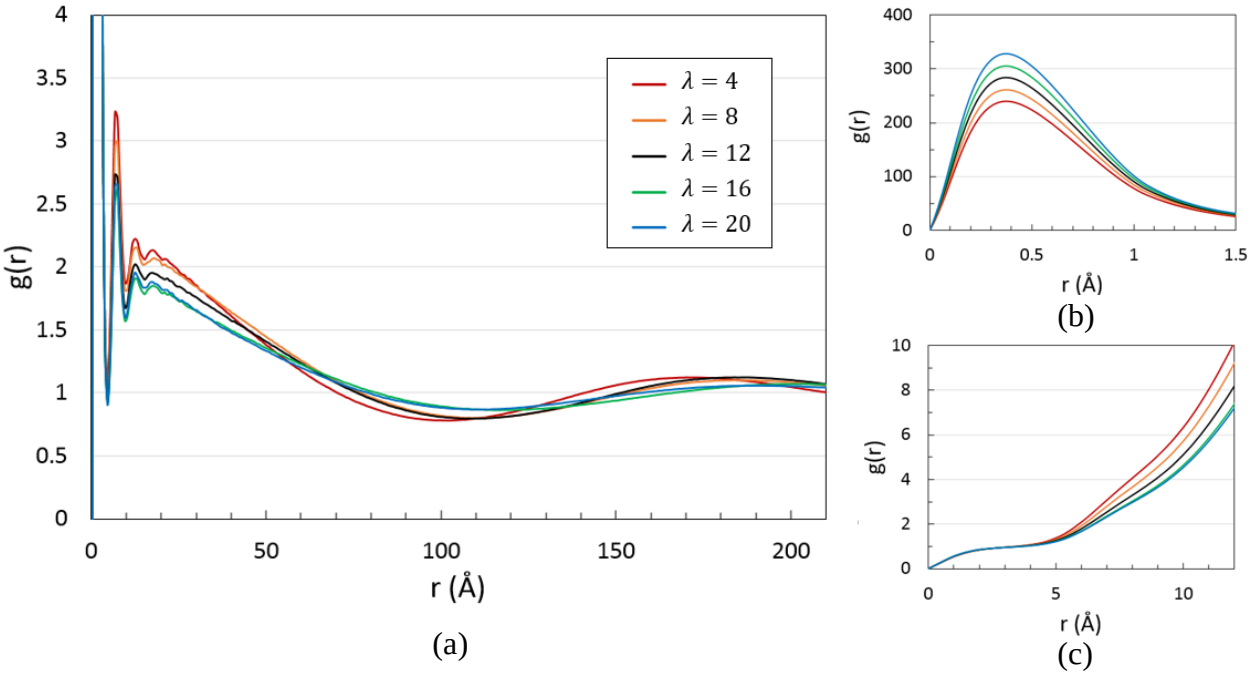


Figure 4.10. (a) TMA^+ – OH^- RDFs for the hydrated AEM in the alkaline form at various levels of hydration. (b) An expanded view of the first peak seen in (a). (c) The integrated number of the OH^- beads around the TMA^+ beads. There is one OH^- in the immediate vicinity of each TMA^+. At a higher degree of hydration there are fewer numbers of OH^- around TMA^+ at r > 5 Å.

4.3.2 The Effect of Anion (OH^- versus Cl^-)

The effect of changing the anion from hydroxide to chloride was also investigated, as the AEMs are usually prepared in a halogen precursor form, but tested in hydroxide form, so knowledge of both anions is informative. Similar simulations were performed using the Cl^- as the anion at five

levels of hydration. Figure 4.11 shows the simulated morphology of the hydrated AEM system in the Cl^- precursor form at $\lambda = 8$.

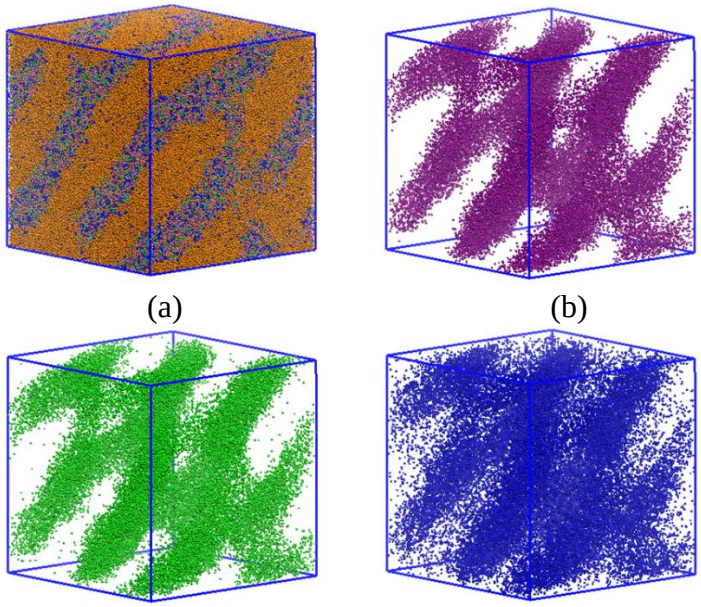


Figure 4.11. Simulated morphology of the hydrated AEM in the chloride form at $\lambda = 8$. Each figure shows a specific bead type for clarity: (a) all beads; (b) TMA^+; (c) Cl^-; and (d) W. The AEM ionomer shows phase separation similar to the alkaline form. Color code: Bs and Bm (orange); Ph (mauve); TMM (green); TMA^+ (purple); Cl^- (shamrock green); and W (blue).

The functionalized SEBS phase separates into a hydrophilic and a hydrophobic phase similar to the hydroxide form. Perforated interconnected lamellae morphology is formed and the Cl^- beads are positioned near the TMA^+ beads. The Cl^- precursor form shows similar morphological dependence to the water content as the hydroxide form (see Figure 4.12).

Figure 4.13 compares the W – W RDFs of the chloride and alkaline as a function of hydration. Increasing the hydration level increases the intensity of peaks in both chloride and alkaline forms. However, the RDF peaks have greater intensity with Cl^- in the system. The effect is more profound at the highest levels of hydration (i.e., $\lambda = 16$ and 20). The distance at which the RDF reaches a value of one substantially increases at $\lambda = 16$ indicating that much larger clusters of water are formed at this level of hydration in comparison to the hydroxide form.

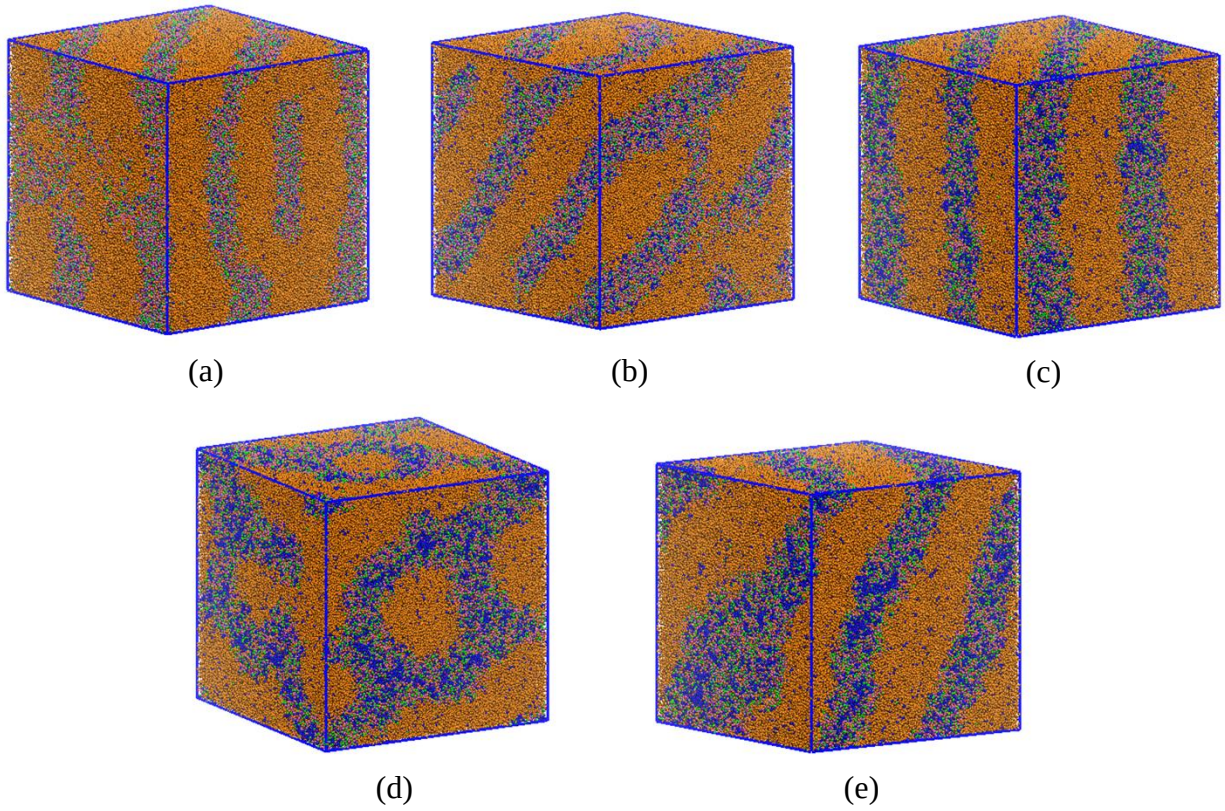


Figure 4.12. Simulated morphology of the hydrated AEM in the chloride form for $\lambda =$: (a) 4; (b) 8; (c) 12; (d) 16; and (e) 20. All beads are shown and the color scheme is the same as in Figure 4.11. The ionomer phase separates into hydrophilic and hydrophobic phases at all hydration levels. Similar to the alkaline form, the morphology changes by increasing the water content and exclusive domains of water are formed within the hydrophilic phase at the two highest values of λ.

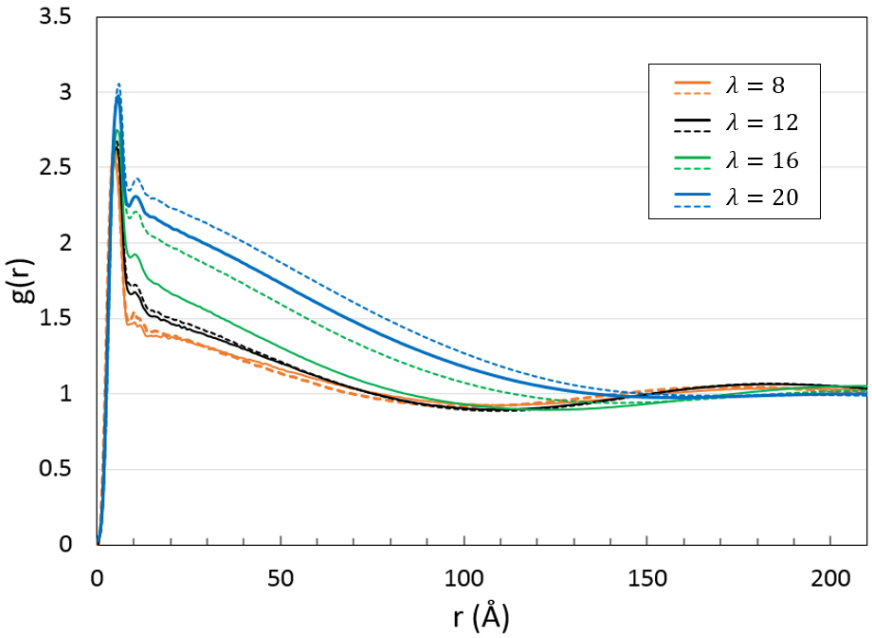


Figure 4.13. W – W RDFs for the hydrated AEM in the alkaline (solid lines) and chloride (dashed lines) forms at various levels of hydration. Changing the anion from OH^- to Cl^- results in negligible changes at $\lambda = 8$ and 12, however it significantly increases the peaks at $\lambda = 16$ and 20. The distance at which the RDF reaches one substantially increases at $\lambda = 16$.

Figure 4.14 confirms this finding as it clearly shows the presence of larger water domains in the chloride form. The chloride anion has higher preference for associating to TMA^+ when compared to the hydroxide (based on the *ab initio* calculated conservative interactions reported in Table 4.2) and OH^- prefers W more than Cl^- prefers W. The differences in the W and TMA^+ affinities affect the distribution of ions and water and results in larger water domains in the systems with chloride. Table 4.4 reports the diffusivities of the W, OH^-, and Cl^- beads at various levels of hydration calculated from the root mean square displacements. It is known that the DPD simulations are insufficient to quantitatively predict the diffusivities due to the intrinsic deficiencies of the method.[210] Hence, the values reported in this table may only serve as a qualitative or as a comparative measure in understanding the dynamics of the systems.

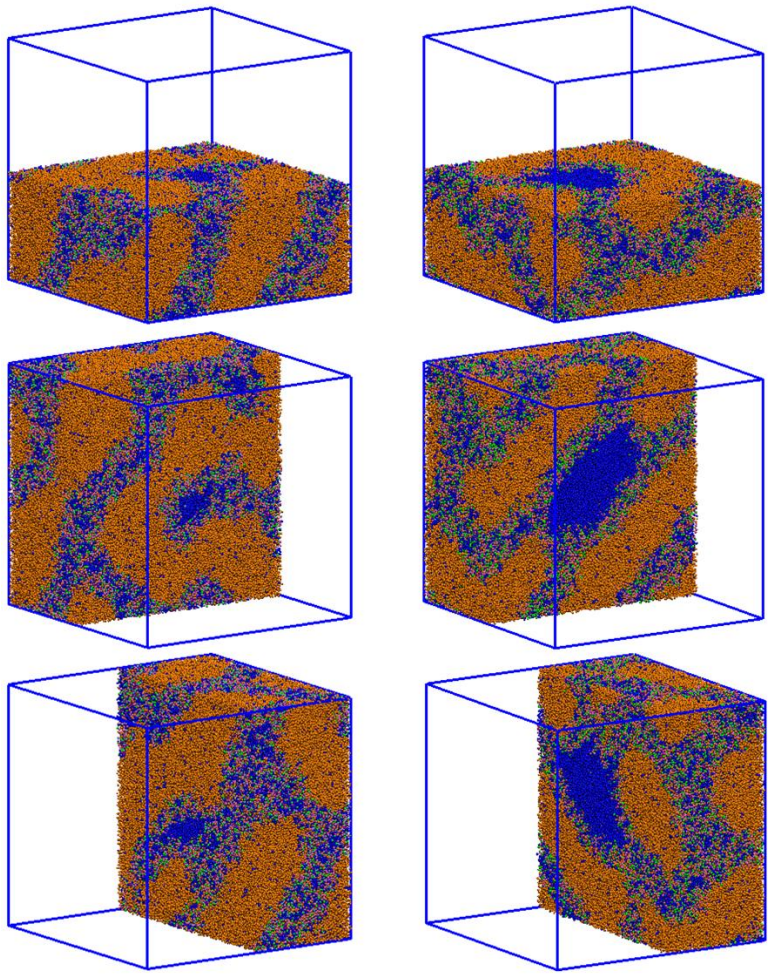


Figure 4.14. Cross sections of the hydrated AEM morphologies in the: xy (top), yz (middle), and xz (bottom) planes at $\lambda = 16$. (a) Alkaline form; and (b) chloride form. Changing the anion from OH^- to Cl^- results in larger exclusive domains of water.

Increasing the hydration level increases the diffusivities of both anions as expected. The simulation results indicate that the Cl^- beads have lower diffusivities than the OH^-. It is interesting that the DPD simulations correctly predicted the relative diffusivities of the OH^- and Cl^-, despite the fact that the transport mechanism of hydroxide ion[271,279] is obviously more complex than these simulations are able to capture. In fact, the deficiencies of the DPD model in including migration of the charge through individual proton transfer reactions were partially compensated by the derivation of meso-scale interactions obtained from the quantum chemical calculations.

The diffusivity of the W beads slightly decreases as the hydration level increases independent of the anion type. The diffusivities of both anions are lower than the W beads by an order of magnitude. However, the experimental diffusivities of OH^- in water[280-283] are larger than that of H_2O.[284-285] As indicated earlier, this discrepancy is due to the deficiencies of the mesoscopic model in capturing the structural changes, hydrogen bond reorientation, and proton shuttling or hopping involved in the water and ion transport.

Table 4.4. Diffusivities of W, OH^-, and Cl^- beads at various hydration levels for the hydrated AEMs at the hydroxise and chloride forms. Diffusivities are in $cm^2/s \times 10^4$.

Hydration Level (λ)	Hydroxide Form		Chloride Form	
	W	OH^-	W	Cl^-
4	1.72	0.31	1.73	0.27
8	1.67	0.34	1.70	0.29
12	1.62	0.35	1.66	0.30
16	1.62	0.36	1.61	0.31
20	1.56	0.38	1.53	0.31

The following chapter discusses the primary steps performed to study the morphology of SDAPP membranes using DPD simulations. A proposed coarse-graining scheme and the electronic

structure calculations performed to calculate the DPD conservative interaction parameters are discussed.

Chapter 5 SDAPP Electrolytes

DPD simulations may provide insight into the microstructure/morphology relationships and determine the key factors controlling the phase separation and the size of the ionic domains in the hydrated SDAPP membranes. A coarse-graining scheme and meso-scale interactions are required in order to undertake the DPD simulations, similar to the previous studies on VRFB and AEM electrolytes. In what follows, the proposed coarse-graining scheme and the calculated meso-scale interaction parameters are presented. The theoretical background for the DPD technique was described in Chapter 2. The developed parameterization method introduced earlier in Chapter 3 was utilized for calculating the conservative interactions.

5.1 Coarse-Graining of Particles

Figure 5.1 shows the repeating unit of the SDAPP ionomer. Similar volume particles corresponding to distinct chemical groups were selected to represent a monomer. The selected beads and the corresponding volumes are listed in Table 5.1 and the coarse-graining scheme is shown in Figure 5.2.

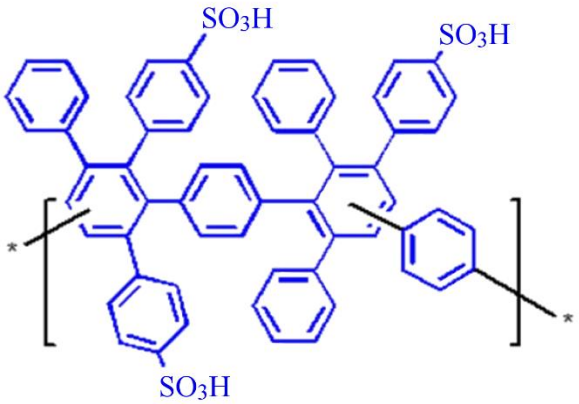


Figure 5.1. The repeat unit of the SDAPP ionomer. The number of sulfonate groups per monomer depends on the level of sulfonation which is controlled by the reaction time (taken from reference 74).

This level of coarse-graining was chosen to enable the study of the morphological properties at large enough length scales that would enable comparison with the hydrated Nafion system presented in Chapter 3. The structure of all bead types were optimized by employing DFT at the B3LYP/6-311G** level[181-184,190] using the GAUSSIAN 09 suite of programs.[231]

Table 5.1. Selected bead types, their structures, and volumes.

Bead Type	Structure	Volume[a] ($Å^3$)
P1	$(C_6H_5)_2$	259.8
P2	$(C_6H_5)C_2H_2(C_6H_5)$	309.3
P3	$(C_6H_5)SO_3^- + H_3O^+ (H_2O)_2$	298.7
W	$(H_2O)_8$	237.8

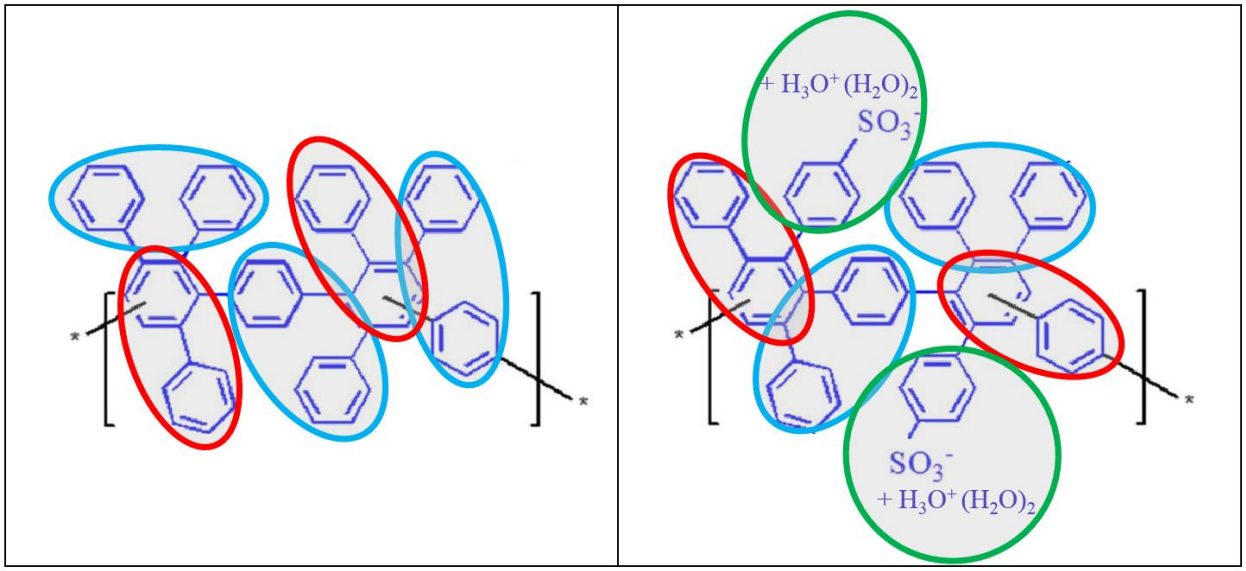
[a] Volumes were calculated by creating Connolly surfaces via Atom Volumes & Surfaces tool in Materials Studio.[261]

The P1 and P2 beads consist of two benzene groups and represent the backbone of the SDAPP ionomer. In the P1 bead, the two benzene groups are connected by a covalent bond, while in the P2 bead they are connected via a C_2H_2 linker (see Figure 5.2). The protogenic group was modeled with the P3 bead, a benzenesulfonic acid group with three water molecules. The water bead, W, was taken to consist of eight water molecules similar to the hydrated Nafion system presented earlier in Chapter 3.

The number of sulfonated groups per SDAPP monomer varies from 0.8 to 2.1 depending on the level of sulfonation.[74] Two course-grained models were considered to represent the SDAPP ionomer and are shown in Figure 5.2. Different ratios of these two coarse-grained monomers may be combined to model the ionomer at different sulfonation levels, i.e., from 0 to 2.0.

The linker between the benzene groups in the P2 bead, i.e., the C_2H_2 group, overlaps with the atoms associated with the P1 bead (as seen in Figure 5.2). This overlap was inevitable due to the

complex structure of the monomer, however the effects were reduced through a proper choice of the bonded parameters.



(a) (b)

Figure 5.2. The coarse-graining scheme for the SDAPP ionomer. (a) The monomer without sulfonation; and (b) two sulfonate groups per monomer. Different ratios of (a) and (b) may be combined to represent sulfonation levels ranging from 0 to 2. Different bead types are shown by colored ovals. Color code: P1 (red), P2 (blue), P3 (green).

5.2 Conservative Interaction Parameters

The conservative interactions between the mesoscopic beads were calculated using the parameterization method[228] presented in Chapter 3. The interaction energies were computed using DFT at the B3LYP/3-21G* level[182-183,186,262-263] and the excess energies were obtained for all pairs of beads. Over 16000 different configurations were considered for each pair. The calculated energies were fitted using the least squares method to obtain a_{ij}^{int} and b_{ij}^{int}. The energies were equally weighted during the least squares procedure, however values above an energy threshold were excluded as they correspond to the overlapping configurations. The water was selected as the reference material and a^R was set to 25 based on the experimental compressibility.[208] The a_{WW}^{int}

was scaled to a negligible value. The scaling factor was chosen to be $(1.87 \times r_c^2)^{-1}$ and the rest of a_{ij}^{int} and b_{ij}^{int} values were scaled accordingly. The calculated a_{ij} values for the selected bead types are reported in Table 5.2.

Table 5.2. Calculated conservative interaction parameters.

a_{ij}	P1	P2	P3	W
P1	29.00			
P2	30.97	34.13		
P3	28.90	30.68	28.16	
W	30.06	34.57	29.54	25.15

The strongest repulsive interaction shown in Table 5.2 is between the P2 and W beads ($a_{P2\,W} = 34.57$). The W – aromatic beads interactions are in the order: $a_{P2\,W} > a_{P1\,W} > a_{P3\,W}$, implying that P2 and P3 are the most and least hydrophobic beads, respectively. This was expected as the P2 bead is the largest fully aromatic bead and the P3 bead consists of hydrophobic (benzene) and hydrophilic (hydrated sulfonic acid group) sides.

A prototype system is currently under investigation using DPD simulations with the calculated conservative interaction parameters in order to find bonded parameters (similar to what has been done in Chapter 3). The following chapter presents the study of two EMIm-based electrolyte systems for the application in secondary magnesium batteries. Electronic structure calculations and vibrational frequency analyses are discussed and compared to the experimental IR and Raman spectra of these materials.

Chapter 6 EMIm-Based Electrolytes

This chapter is based on the following publications:[138,286]

- Bertasi, F.; Hettige, C.; Sepehr, F.; Bogle, X.; Pagot, G.; Vezzù, K.; Negro, E.; Paddison, S. J.; Greenbaum, S. G.; Vittadello, M.; Di Noto, V., A key concept in magnesium secondary battery electrolytes. *ChemSusChem* **2015,** *8,* 3069-3076.
- Bertasi, F.; Sepehr, F.; Pagot, G.; Paddison, S. J.; Di Noto, V., Toward a magnesium-iodine battery. *Advanced Functional Materials* **2016,** *26,* 4860-4865.

In what follows, electronic structure calculations and vibrational frequency analyses of two EMIm-based electrolytes: $EMImCl/(AlCl_3)_{1.5}$; and $EMImAlI_4$ with dissolved magnesium salt, are presented. Model clusters consisting of $EMImAlX_4$ and $EMImAl_2X_7$ with MgX_2 or $(MgX_2)_2$ (X = Cl, I) were used. The vibrational frequencies of the models were computed and compared to the experimental IR and Raman spectra of these electrolytes. The theoretical background on the quantum chemical calculations may be found in Chapter 2. The aforementioned publications also discuss several experimental techniques performed to characterize these chloroaluminate[138] and iodoaluminate electrolytes.[286]

6.1 Structure of $EMImAlX_4$ and $EMImAl_2X_7$ with MgX_2 (X = Cl, I)

The structure of the $EMIm^+$ cation interacting with AlX_4^-, $Al_2X_7^-$, and MgX_2 (X = Cl, I) was determined using DFT employing the B3LYP functional.[181-184] The 6-311G** split valence basis set[190] was used for H, C, N, Mg, and Al, and for I a supplemented all electrons 6-311G** basis set.[287] The optimizations were performed over all degrees of freedom with no symmetry constraints and tight convergence criteria. Frequency calculations at the same level of theory were done to confirm the resulting stationary points as local minima. The optimizations for each ionic

cluster were performed beginning from different initial starting positions. The lowest energy structure was selected for further investigations.

To minimize the effect of systematic errors in the calculated vibrational frequencies all frequencies were scaled by 1.04 except for the cationic vibrations which were not scaled. This is similar to the scaling factor previously utilized for organic molecules containing C, H, N, O, S, P, and Cl atoms.[288] As the effect of diffuse functions was determined to be negligible in the vibrational analysis, they were not included in the calculations in favor of computational efficiency.

Figures 6.1 and 6.2 show the optimized structures for the $EMIm^+$ cation interacting with AlX_4^-, $Al_2X_7^-$, and MgX_2. The results show that the anion is highly likely to occupy the front position around the imidazolium ring, rather than the side or back position. Upon addition of either MgX_2 or $(MgX_2)_2$ to the optimized structures, the nearest anion to $EMIm^+$ is the Mg halide rather than Al halide anions, in all cases. This is a consequence of the more polarized Mg–X bond compared to the Al–X bond, and is confirmed by the electrostatic potential maps on the electron isodensity surface of $[AlCl_4MgCl_2]^-$ and $[Al_2Cl_7MgCl_2]^-$ concatenated complexes. These maps, as illustrated in Figure 6.3, show a more negative electrostatic potential and, therefore, a more electron rich area on the Mg–Cl bonds rather than the Al–Cl bonds.

Analyzing the energetics of these systems, we find that the binding energy of MgX_2 to the $[EMIm]AlX_4$ structure is more than 5 kcal/mol lower than its binding to the $[EMIm]Al_2X_7$ structure after addition of one or two units of MgX_2. This indicates that in the presence of MgX_2 the AlX_4^- complexes are more energetically favored compared to those based on $Al_2X_7^-$.

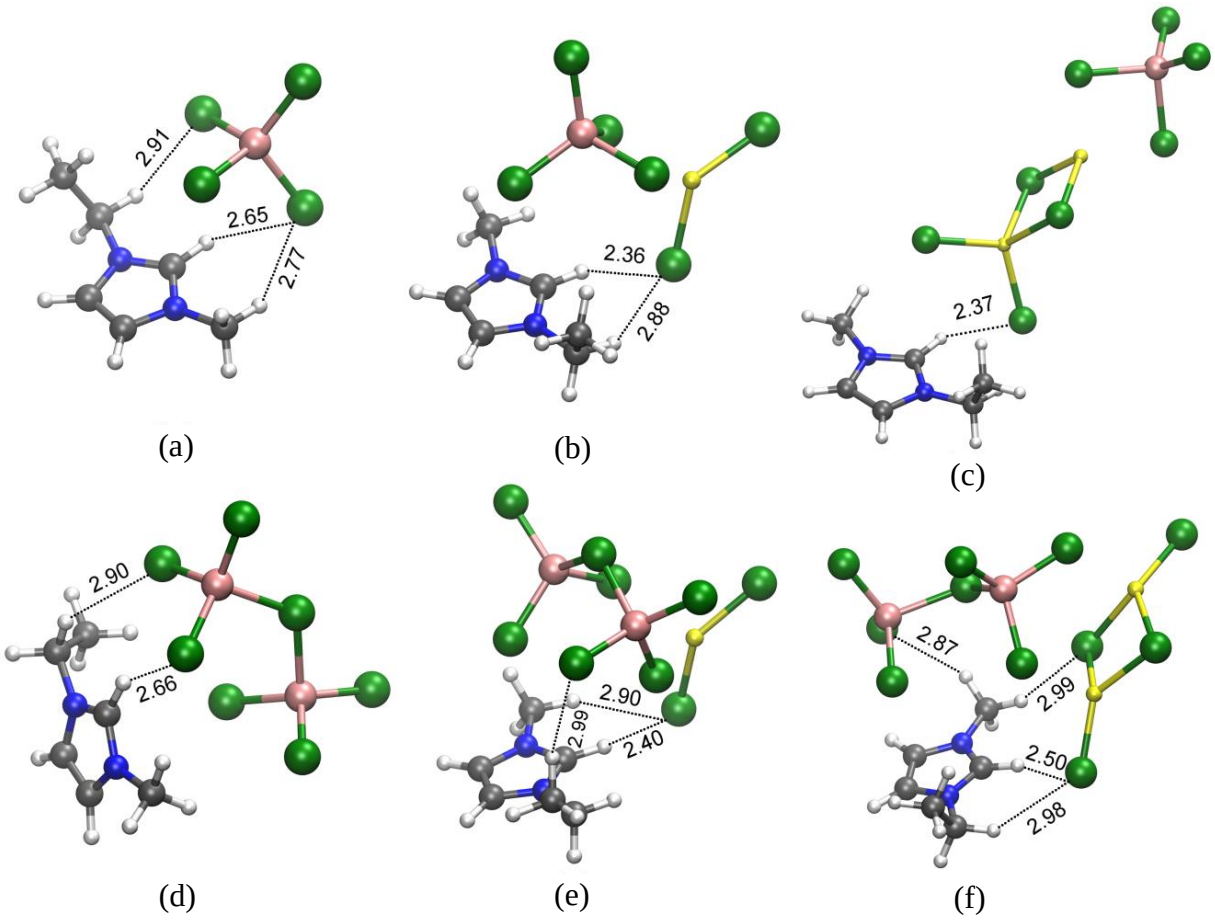


Figure 6.1. Optimized geometries of the ionic liquid complexes determined at the B3LYP/6-311G** level of theory. (a) $EMImAlCl_4$; (b) $EMImAlCl_4$ with $MgCl_2$; (c) $EMImAlCl_4$ with $(MgCl_2)_2$; (d) $EMImAl_2Cl_7$; (e) $EMImAl_2Cl_7$ with $MgCl_2$; and (f) $EMImAl_2Cl_7$ with $(MgCl_2)_2$. Color code: chlorine (green), aluminum (pink), magnesium (yellow), nitrogen (blue), hydrogen (white), carbon (grey). Distances between chlorine and hydrogen are only shown when less than 3 Å.

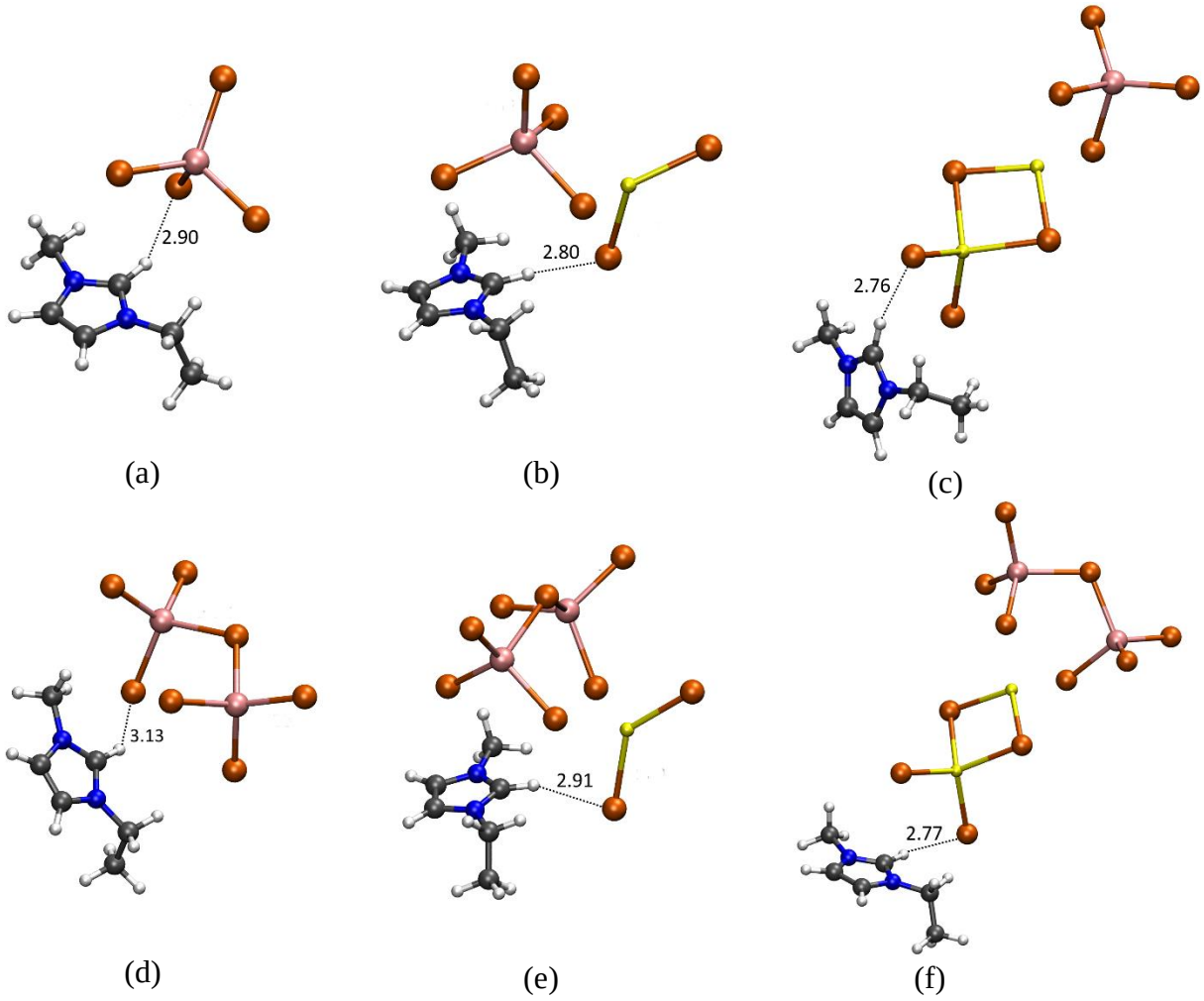


Figure 6.2. Optimized geometries of the ionic liquid complexes determined at the B3LYP/6-311G** level of theory. (a) $EMImAlI_4$; (b) $EMImAlI_4$ with MgI_2; (c) $EMImAlI_4$ with $(MgI_2)_2$; (d) $EMImAl_2I_7$; (e) $EMImAl_2I_7$ with MgI_2; and (f) $EMImAl_2I_7$ with $(MgI_2)_2$. Color code: iodine (orange), aluminum (pink), magnesium (yellow), nitrogen (blue), hydrogen (white), carbon (grey).

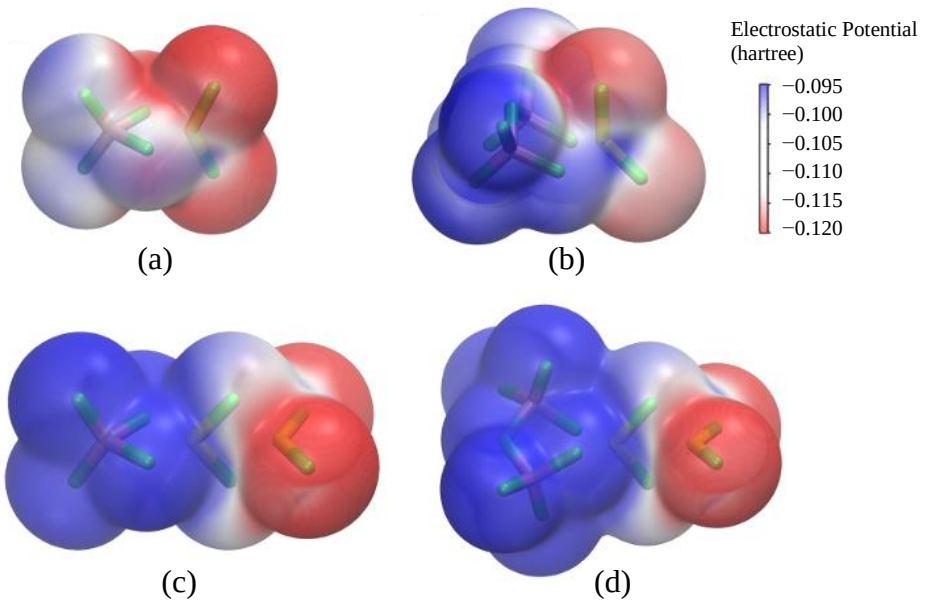


Figure 6.3. Electrostatic potential map on the total electron density isosurface. (a) $[AlCl_4MgCl_2]^-$; (b) $[Al_2Cl_7MgCl_2]^-$; (c) $[AlCl_4(MgCl_2)_2]^-$; and (d) $[Al_2Cl_7(MgCl_2)_2]^-$ complexes. These maps show a more negative electrostatic potential and therefore more electron rich area on $MgCl_2$ rather than aluminium chloride. Color code: chlorine (green), aluminum (pink), magnesium (yellow).

6.2 Vibrational Spectra of the Electrolytes

The global minimum structures obtained above were used to calculate the vibrational frequencies and assign the experimental spectra. Experimental IR and Raman spectra of $(EMImCl/(AlCl_3)_{1.5})/(\delta\text{-}MgCl_2)_x$ and $(EMImAlI_4)/(\delta\text{-}MgI_2)_x$ electrolytes, with x being the molar ratio $x = n_{\delta-MgCl_2}/n_{IL}$, are shown in Figures 6.4 and 6.5. The following discusses the analysis of these spectra for each electrolyte system based on the calculated vibrational frequencies.

6.2.1 $(EMImCl/(AlCl_3)_{1.5})/(\delta\text{-}MgCl_2)_x$ System

The Raman spectrum in Figure 6.4 (a) shows the intensity of the band at 350 cm^{-1} (blue peak) attributed to the stretching mode of $AlCl_4^-$ which increases with increasing concentration of the Mg salt. This is in contrast to the intensity of the band at 311 cm^{-1} (yellow peak), related to the Al–Cl–Al symmetrical stretching mode of $Al_2Cl_7^-$, which decreases. Osteryoung *et al.*[289] has previously established a direct

relationship between the peak intensities and concentrations of the chloroaluminate anions in IL melts. Hence, our results reveal that the concentration of $AlCl_4^-$ units prevails at higher x values, i.e., δ-$MgCl_2$ concentration.

The peak intensities at 156, 310, 331 and 385 cm^{-1} (all in the far IR region) decrease with increasing x (see Figure 6.4 (b)). These peaks are assigned to the calculated vibrational modes of the $Al_2Cl_7^-$ species. Hence, the concentration of the this species decreases with increasing the salt (in agreement with the above results from the Raman spectra). As the concentration of δ-$MgCl_2$ increases, new peaks appear in the far IR spectrum (highlighted blue, yellow, and green in Figure 6.4 (b)). Interestingly, the calculated frequencies for the structures containing $EMIm^+$, $AlCl_4^-$, $Al_2Cl_7^-$ and $MgCl_2$ (see Figure 6.1 (a), (b), (d), and (e)) do not show any vibrational modes between 242 and 296 cm^{-1}. However, the addition of a second or third concatenated $MgCl_2$ unit to the system (see Figure 6.1 (c) and (f)) results in the appearance of new vibrational modes for the magnesium chloride structures. Thus, the appearance of the green peaks in Figure 6.4 (b) is a result of the presence of $(MgCl_2)_n$, $n > 1$. Furthermore, the growth of the blue peak at 430 cm^{-1} and the appearance of the yellow peak at 450 cm^{-1} is attributed to the Mg–Cl–Al and Cl–Mg–Cl vibrational modes.

These results indicate that: (1) at low Mg concentrations ($x < 0.05$) both $AlCl_4^-$ and $Al_2Cl_7^-$ concatenated anionic complexes dominate; (2) at higher Mg concentration ($x = 0.05$) the equilibrium is shifted toward the $AlCl_4^-$ complexes because of a decrease in the concentration of $Al_2Cl_7^-$ and higher concentration of the concatenated complexes involving Al–Cl–Mg and Cl–Mg–Cl bridges; and (3) the electrolyte contains nanostructures of the magnesium salt, i.e., $(MgCl_2)_n$, $n > 1$.

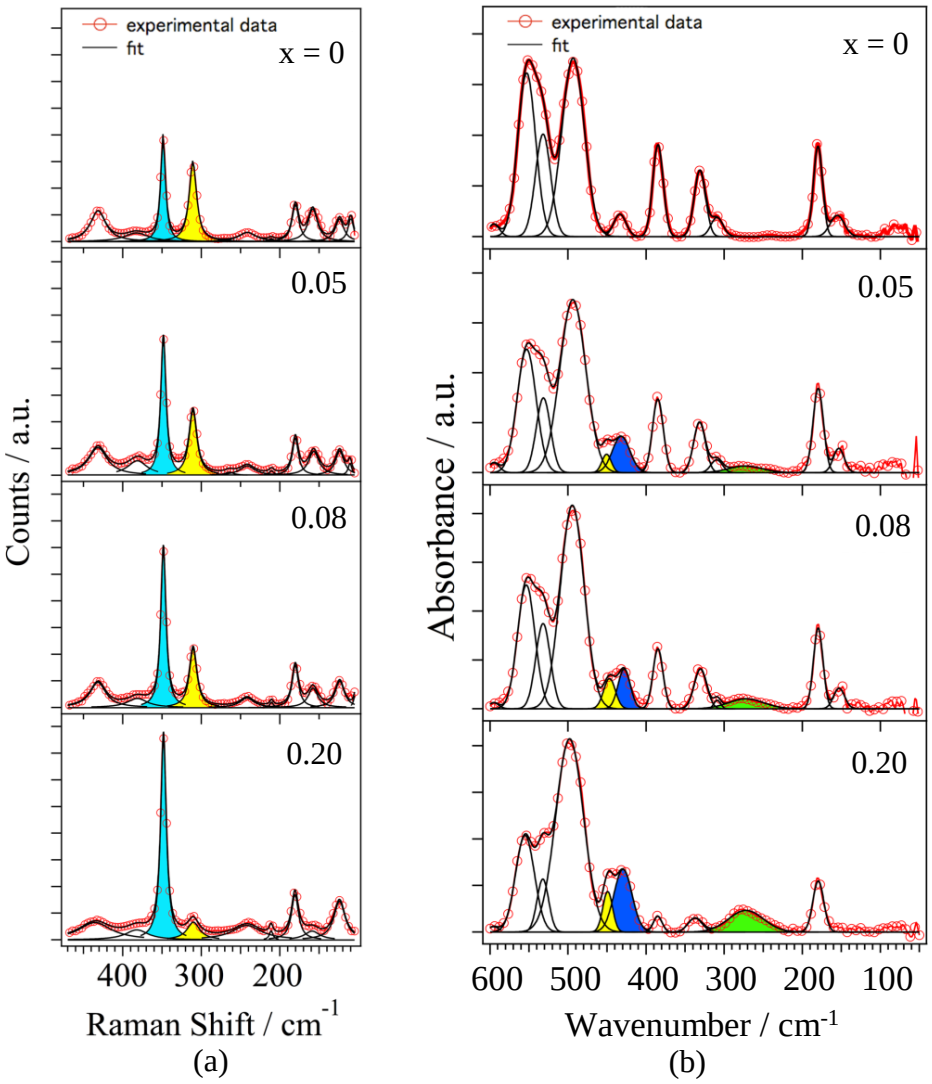


Figure 6.4. Vibrational spectra of $([EMIm]Cl/(AlCl_3)_{1.5})/(\delta\text{-}MgCl_2)_x$ electrolytes with $0 \leq x \leq 0.20$. (a) Raman spectra in the region between 100 and 480 cm^{-1}, the intensity of the band corresponding to the stretching of the monomeric species $AlCl_4^-$ (blue) increases at higher concentrations of the Mg salt, whereas the intensity of the band attributed to the stretching of the dimeric species $Al_2Cl_7^-$ (yellow) decreases; and (b) far IR spectra, the intensities of the bands corresponding to the vibrations of polymeric $MgCl_2$ species (green) and Mg–Cl–Al stretching modes (blue and yellow) increase at higher concentrations of the Mg salt.

6.2.2 (EMImAlI$_4$)/(δ-MgI$_2$)$_x$ System

The experimental Raman spectrum of pristine IL, EMImAlI$_4$, shows two strong peaks at 146 and 140 cm^{-1} (see Figure 6.5 (a)) which are characteristics of the AlI$_4^-$ and Al$_2$I$_7^-$ anions in agreement with the calculated vibrations and literature reports.[290-291] Hence, EMIm$^+$ cationic species and both AlI$_4^-$ and Al$_2$I$_7^-$ anions exist in the pristine IL despite the stoichiometric formulation of EMImAlI$_4$.

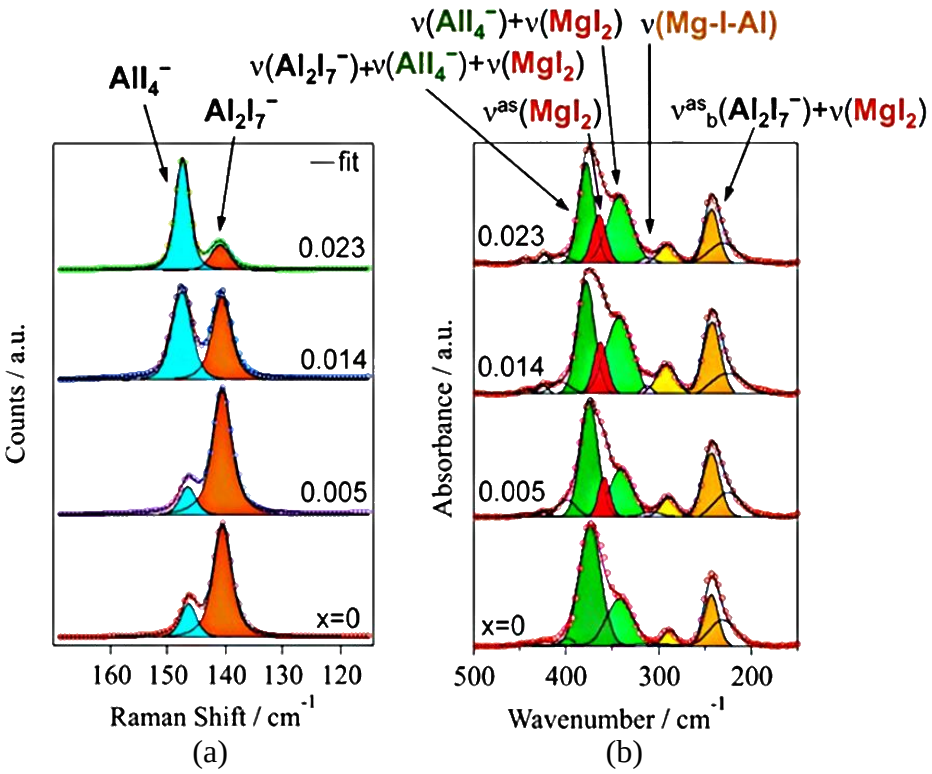


Figure 6.5. Vibrational spectra of (EMImAlI$_4$)/(δ-MgI$_2$)$_x$ electrolyte with $0 \leq x \leq 0.023$. (a) Raman spectra with band assignments based on DFT calculations, the intensity of the band assigned to the stretching of AlI$_4^-$ (blue) increases with the δ-MgI$_2$ concentration while that of Al$_2$I$_7^-$ (orange) decreases; and (b) far IR spectra.

This figure shows that the ratio of the peak intensity at 140 cm^{-1} to the one at 146 cm^{-1} increases upon addition of δ-MgI$_2$ salt. These two peaks, according to the DFT calculations, are still assigned to the vibrations of AlI$_4^-$ and Al$_2$I$_7^-$ anions even in the presence of MgI$_2$. Hence, the increase in the ratio of the two peak intensities suggests that the concentration of AlI$_4^-$ anions increases and

the equilibrium $Al_2I_7^- + I^- \Leftrightarrow 2AlI_4^-$ shifts to the right. The increase in the AlI_4^- concentration with x is associated with the formation of an anionic complex with bridging iodide atoms as witnessed by the presence of the stretching band ν(Mg–I–Al) at 312 cm^{-1} in the far IR spectra (Figure 6.5 (b)). Therefore, at low δ-MgI_2 concentration (x = 0.005) the $[Al_2I_7MgI_2]^-$ anionic complexes are predominant, while for x > 0.005 the concentration of the $[AlI_4MgI_2]^-$ anionic complexes increases together with the concentration of the Mg–I–Al bridges.

Both clusters containing $(MgI_2)_2$ species shown in Figure 6.2 (c) and (f) have vibrational modes with high intensity at wavenumbers that are inactive in the experimental IR and Raman spectra (at 268 cm^{-1} for $EMImAlI_4/(MgI_2)_2$ and at 258 and 261 cm^{-1} for $EMImAl_2I_7/(MgI_2)_2$). Similar high intensity bands appear in the vibrational spectra of $EMImAlI_4/(MgI_2)_3$ and $EMImAl_2I_7/(MgI_2)_3$ clusters. Hence, the computational frequency analysis disregards the presence of dimeric and trimeric magnesium iodide in the IL system. It is concluded that the MgI_2 salt interacts favorably with the IL in the form of a monomer in contrast to the $MgCl_2$ salt in the chlorine based electrolytes. The following chapter presents electronic structure calculations performed on ten different acids which are commonly used in the electrolytes of the energy storage and conversion devices. Hydration and proton transfer are studied in the vicinity of a few water molecules and the effect of a dielectric continuum solvation model is explored.

Chapter 7 Mixed Acid Electrolytes

This chapter is based on the following manuscript to be submitted for publication:

- Sepehr, F.; Paddison, S. J., The primary hydration and proton transfer of acids: an *ab initio* study. *Solid State Ionics*, to be submitted.

The electrolytes utilized in energy storage and conversion technologies often include acids dissolved in a solution or tethered to a polymer backbone. The properties of electrolyte membranes are directly related to the acid strength and propensity of the acidic groups to transfer the proton to the water absorbed within the membrane. Hence, the relative acidity and acid-base interactions[79] are influential in the design and performance of advanced electrolyte materials such as acid-base complexes and electrospun membranes that involve two or more types of acids (as described in Chapter 1). Hence, a comparative study of acid strength including the primary hydration structure is a first step in the design of electrolytes.

This chapter presents a first principles based study of the hydration of ten acid molecules commonly employed in electrolytes: CF_3SO_3H; FSO_3H; CH_3SO_3H; H_2SO_4; HNO_3; HF; H_3PO_2; H_3PO_3; H_3PO_4; and $CF_3SO_2NHSO_2CF_3$. Proton dissociation is discussed and the effect of a dielectric continuum solvation model is explored. The potential energy surface scans of the hydrated acids are analyzed to understand the relative proton transfer energetics establishing fundamental information that may serve the purpose of designing or screening novel electrolytes featuring one or more of these acids.

7.1 Hydration of the Acids

Electronic structure calculations (see Chapter 2) were performed using the GAUSSIAN 09 suite of programs.[231] Geometries were optimized using DFT with Becke's 3-parameter hybrid functional (B3LYP)[181-184] and the 6-31G** split valence basis set[188] without imposing any

symmetry constraints. The resulting structures were then refined with optimizations performed with the larger 6-311G** basis set.[190] Frequency calculations at the same level of theory were performed to confirm local minima. The SMD solvation model[194] was subsequently applied to all the optimized structures with water selected as the solvent.

The B3LYP functional and the Pople's split valence basis set were selected in this study to enable comparison of the results with previous computational studies of these acids.[128,131-132,292-302] This level of theory has proven successful in providing relative information on the primary hydration, proton dissociation, and interactions of various imide, sulfonic, and phosphonic acid groups.[292,294,303-304] This work does not evaluate the validity or preeminence of DFT over other computational methods, but rather seeks to provide a fundamental and relative understanding of the hydration and proton transfer of the acids.

Minimum energy structures of the ten acid molecules were obtained using the described methodology. One to five water molecules were subsequently added to the optimized structures of each acid from different initial starting positions and full optimizations (over all degrees of freedom) were performed. The lowest energy structure for each system was selected as the ground state hydrated structure for that particular acid. Figures 7.1 to 7.10 show the fully optimized structures for the ten acids in both gas phase and solvated with the SMD model. All distances are reported in Å and covalent bonds between hydrogen and oxygen atoms are shown when O−H ≤ 1.10 Å.

Figure 7.1 (a) shows that a single isolated triflic acid molecule does not dissociate in the gas phase until three water molecules are added to the cluster, in agreement with the computational studies by Paddison *et al.*[132,295] and other authors.[305] However, it dissociates in the vicinity of only one water molecule when the SMD model is applied on the hydrated system as shown in Figure 7.1 (b). This clearly reveals the effect of a dielectric medium on stabilizing the conjugate base ($CF_3SO_3^-$) and the propensity of the acid to dissociate.

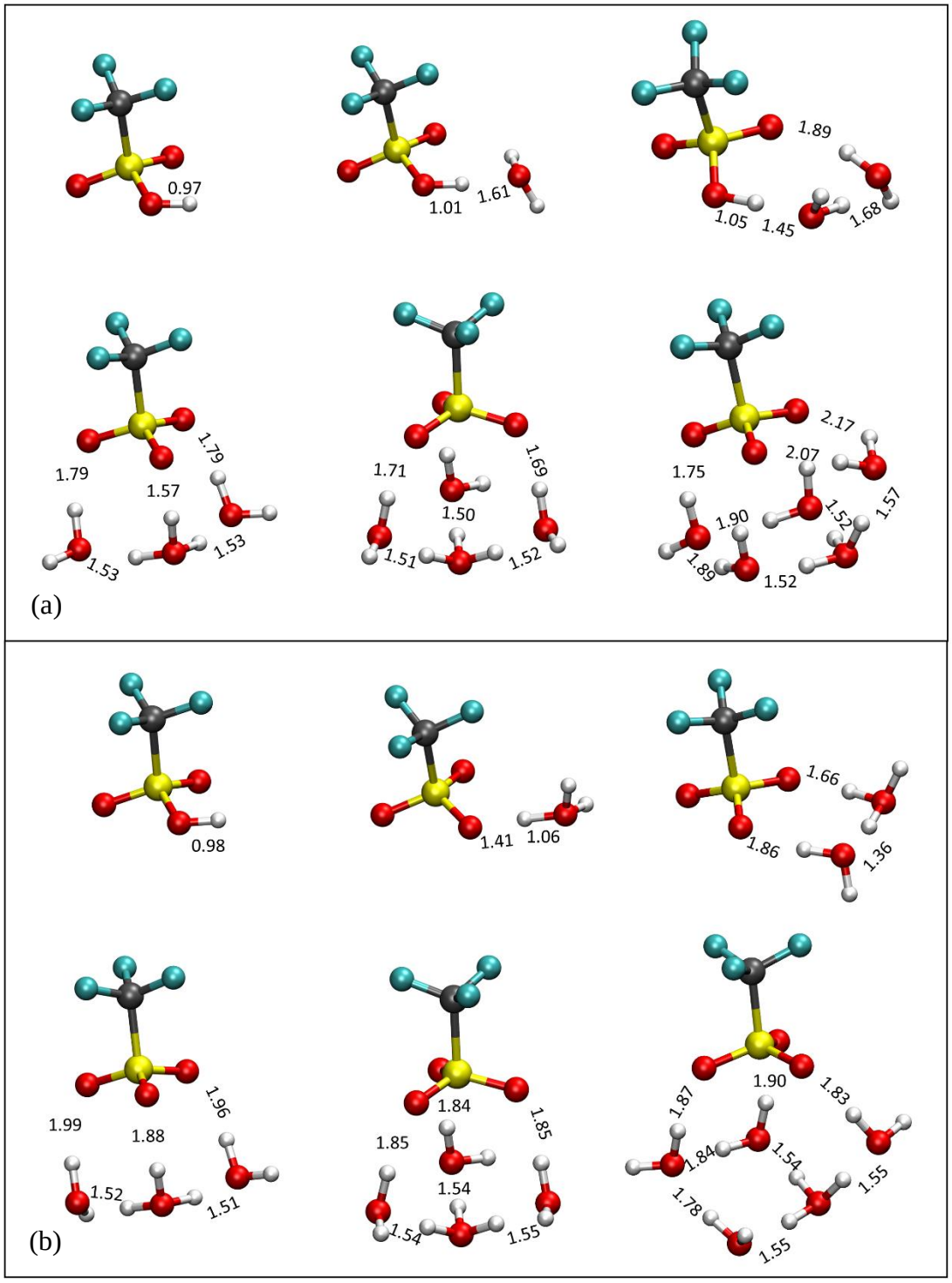


Figure 7.1. Fully optimized structures of CF_3SO_3H with from zero to five water molecules at the B3LYP/6-311G** level of theory: (a) gas phase structures, proton dissociation occurs after three water molecules are added; (b) structures with the SMD model, proton dissociates after only one water molecule is added. The atomic color scheme in Figures 7.1 to 7.10 is: oxygen (red), hydrogen (white), sulfur (yellow), carbon (gray), fluorine (cyan), nitrogen (blue), phosphor (orange).

Similar behavior is observed for the other acids, with dissociation occurring with a fewer number of water molecules when the dielectric continuum solvation model is included. Table 7.1 reports the number of water molecules required to first witness proton dissociation for each of the acids.

Table 7.1. The number of water molecules required to effect dissociation of a proton in the gas phase and SMD solvated systems. The acids are ordered based on the acid strength (i.e., pK_a values and gas phase acidities).

Acid	pK_a		Gas	SMD
	value	reference		
$CF_3SO_2NHSO_2CF_3$	[a]		3	2
CF_3SO_3H	−14.7	306	3	1
FSO_3H	−6.4	307	3	1
H_2SO_4	−3.0	308	4	3
CH_3SO_3H	−1.9	307,309	3	2
HNO_3	−1.3	308	5	3
H_3PO_2	+1.24	310	5	>5
H_3PO_3	+1.26	310	>5	>5
H_3PO_4	+2.15	310	>5	>5
HF	+3.17	311	>5	>5

[a] Not reported in the literature.

The three sulfonic acids shown in Figures 7.1 to 7.3 form similar hydrogen bond networks. In a prior study, Li *et al.*[300] performed quantum chemical calculations on the clusters of $XSO_3H{-}(H_2O)_n$, n = 1−4 and X = F, Cl, and Br, and reported accumulation of water molecules around the hydroxyl group of XSO_3H promoting the proton transfer and stabilizing the resulting hydronium cation. They also observed the spontaneous transfer of a proton from the acid to water with three or four water molecules in the gas phase in agreement with our results.

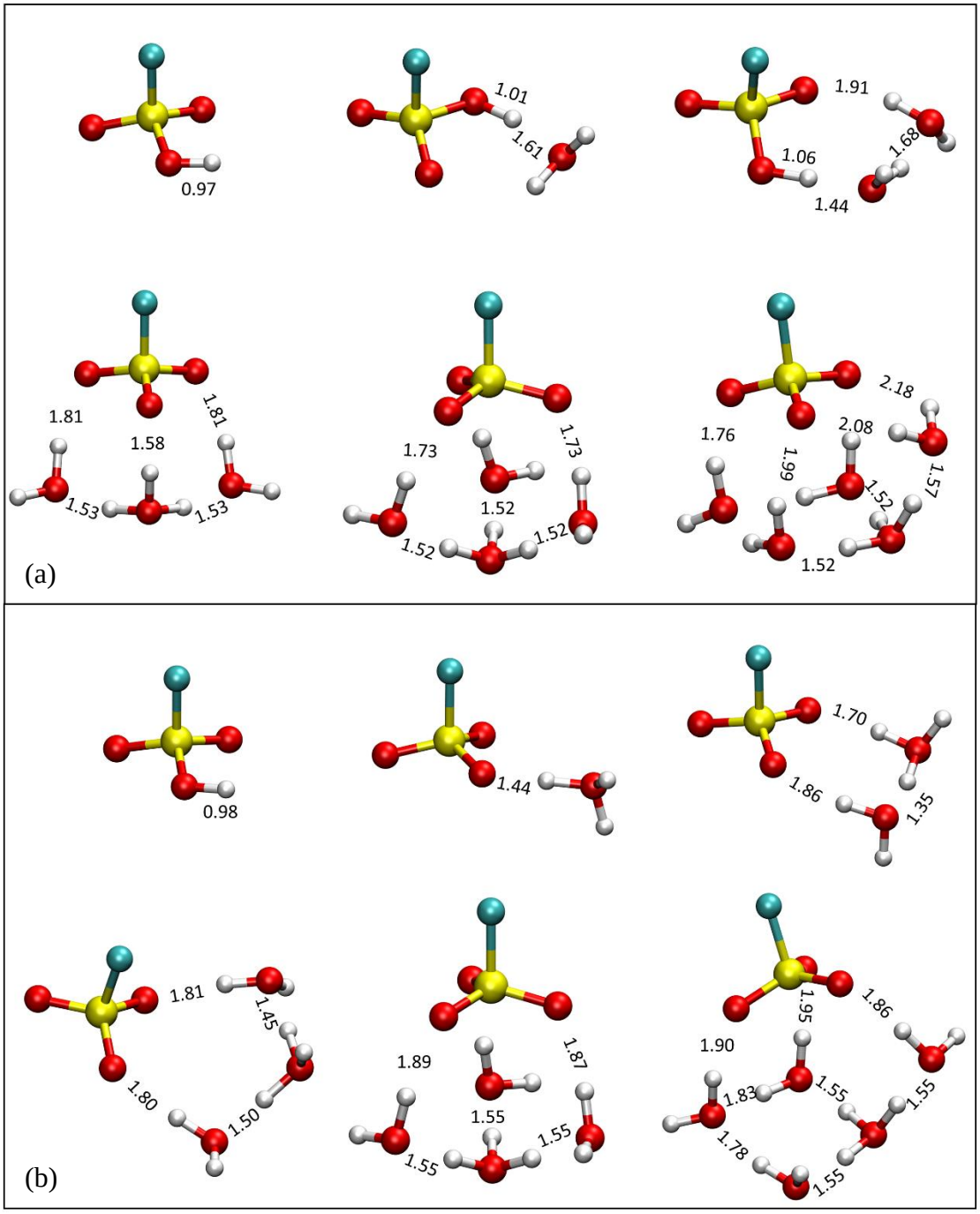


Figure 7.2. Fully optimized structures of FSO_3H with from zero to five water molecules at the B3LYP/6-311G** level of theory: (a) gas phase structures, proton dissociation occurs after three water molecules are added; (b) structures with the SMD model, proton dissociates after only one water molecule is added.

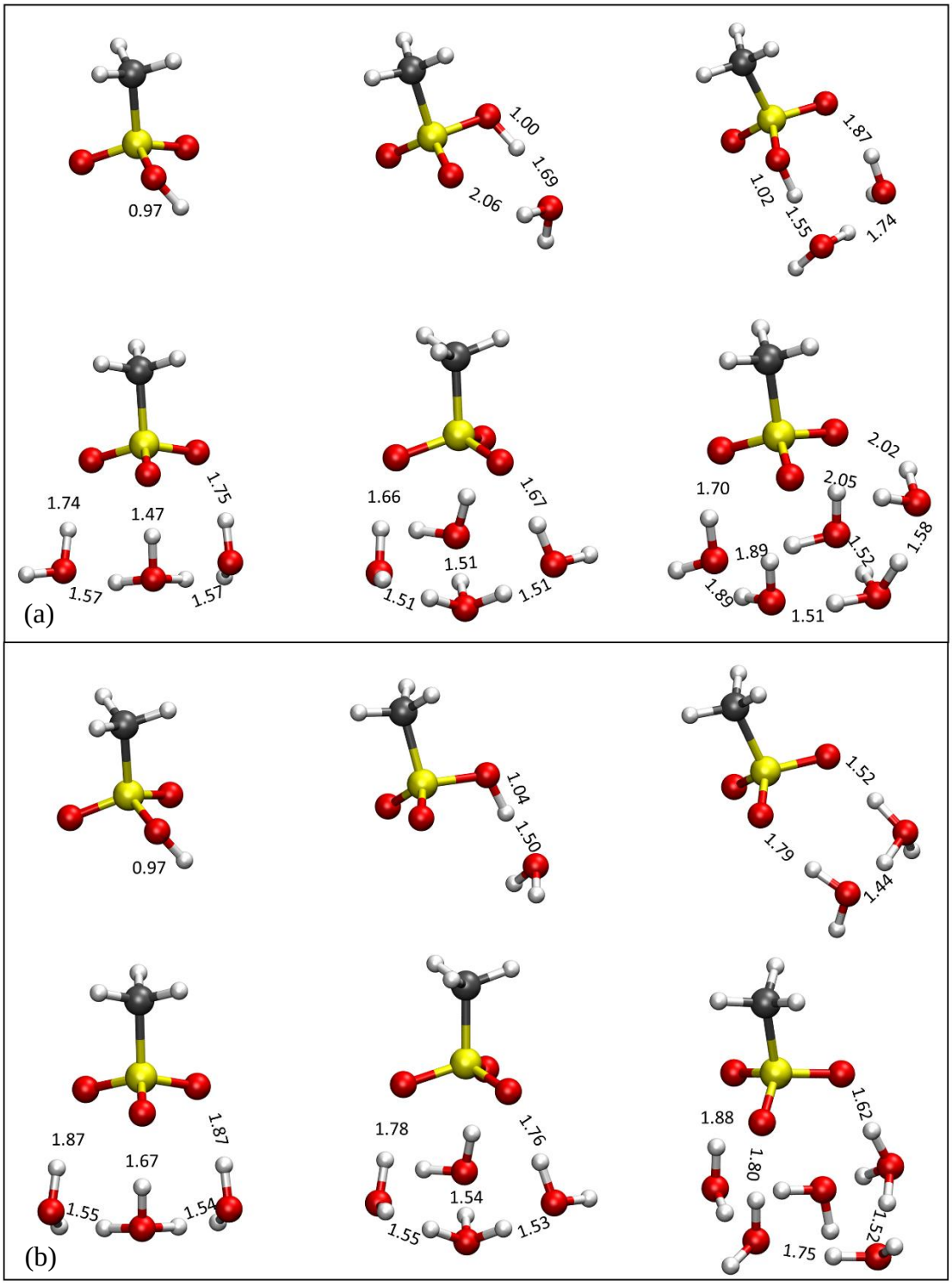


Figure 7.3. Fully optimized structures of CH_3SO_3H with from zero to five water molecules at the B3LYP/6-311G** level of theory: (a) gas phase structures, proton dissociation occurs after three water molecules are added; (b) structures with the SMD model, proton dissociates after only two water molecules are added.

A prior study of CH_3SO_3H with one to five water molecules using B3LYP/6-311++G** level of theory determined that proton transfer occurs when four water molecules are added in the gas phase.[299] Their results are confirmed with our calculations upon the addition of diffuse functions. The diffuse functions were not included in our calculations in favor of the computational efficiency and also because the effects were determined negligible on the confirmation of hydrated CF_3SO_3H[132] (the most widely used acid in electrolytes).

The hydrated structure of sulfuric acid shown in Figure 7.4 is in agreement with previous calculations.[312-313] There are some discrepancies in the literature regarding the position of the water molecules in the most stable hydrated clusters and whether the water molecules bind to the acid molecule from one side or both sides.[297,312,314] The structure of the $H_2SO_4(H_2O)_2$ cluster shown in Figure 7.4 (a) is in agreement with recent semiempirical calculations that reproduce the proton transfer observed in this system.[313] The authors in this work also found that the first proton transfer occurs in clusters consisting of four water molecules, in agreement with the present work.

Figure 7.5 shows the hydrated structures for HNO_3. Successive hydrogen bonds forming ring structure are observed in both the gas phase and SMD solvated molecules in agreement with previous computational work.[301,315] The acidic proton is transferred to water in the gas phase when five water molecules are in the cluster consistent with previous MP2 and B3LYP results.[301] The minimum energy structures in Figure 7.6 do not show a proton transfer as a result of the weak acidity of HF in water. Gas phase computational studies of hydrated clusters of HF employing DFT and MP2 indicate that more than seven[302] or ten[316] water molecules are required in order to first witness proton dissociation.

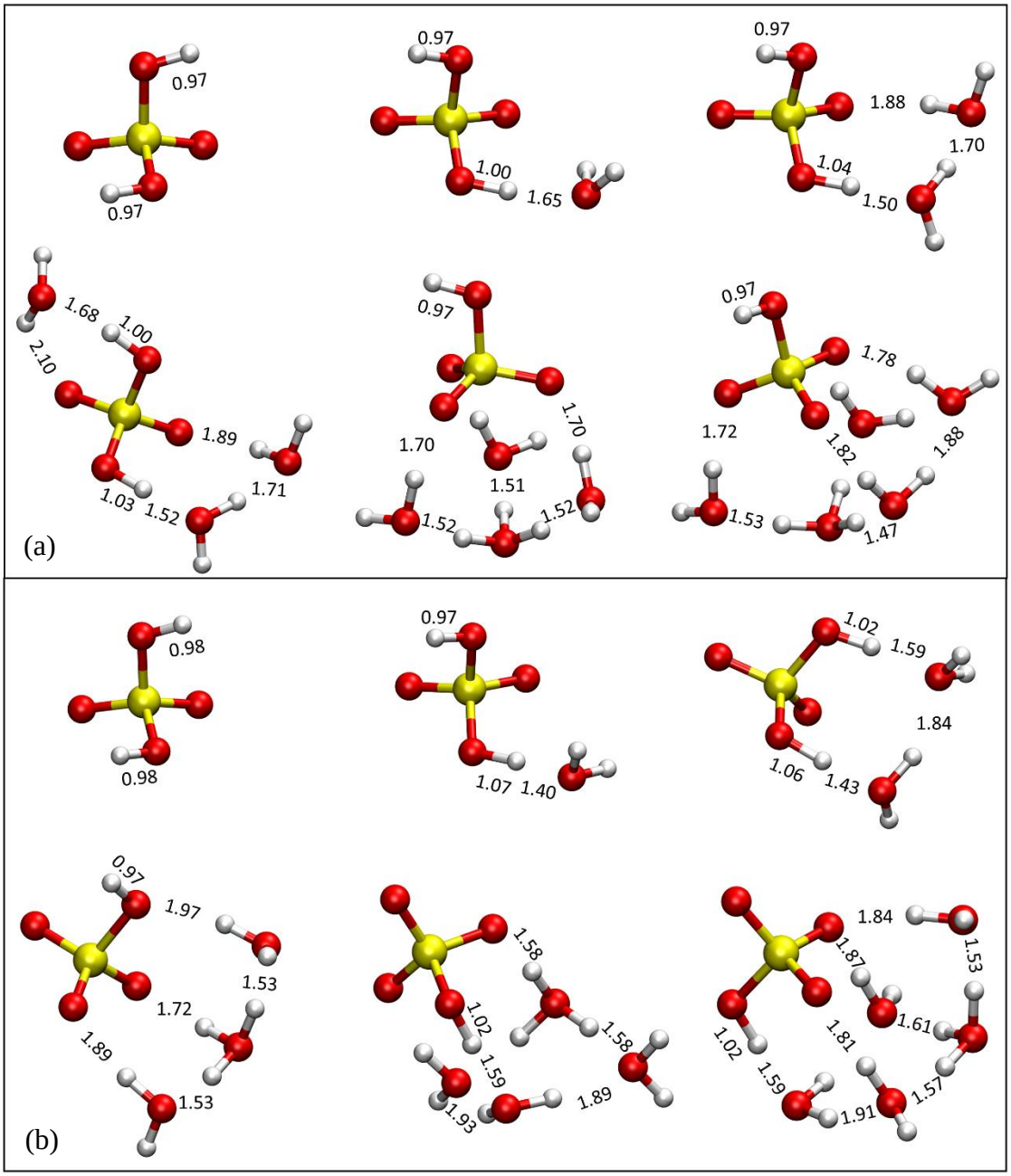


Figure 7.4. Fully optimized structures of H_2SO_4 with from zero to five water molecules at the B3LYP/6-311G** level of theory: (a) gas phase structures, proton dissociation occurs after four water molecules are added; (b) structures with the SMD model, proton dissociates after three water molecules are added. In all structures, the water molecules bind to one side of the acid. The only exception is the gas phase with three water molecules.

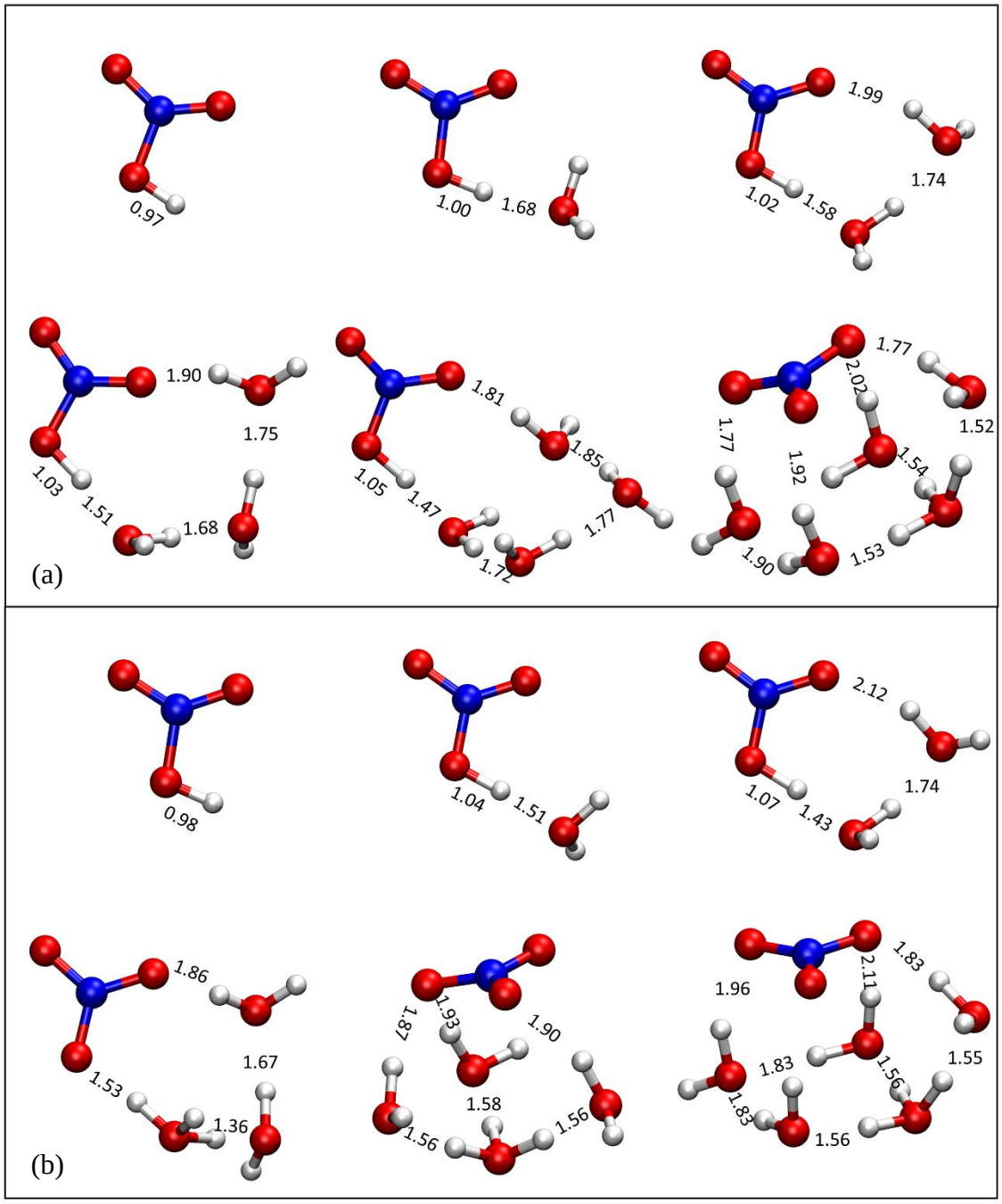


Figure 7.5. Fully optimized structures of HNO_3 with from zero to five water molecules at the B3LYP/6-311G** level of theory: (a) gas phase structures, proton dissociation occurs after five water molecules are added; (b) structures with the SMD model, proton dissociates after only three water molecules are added.

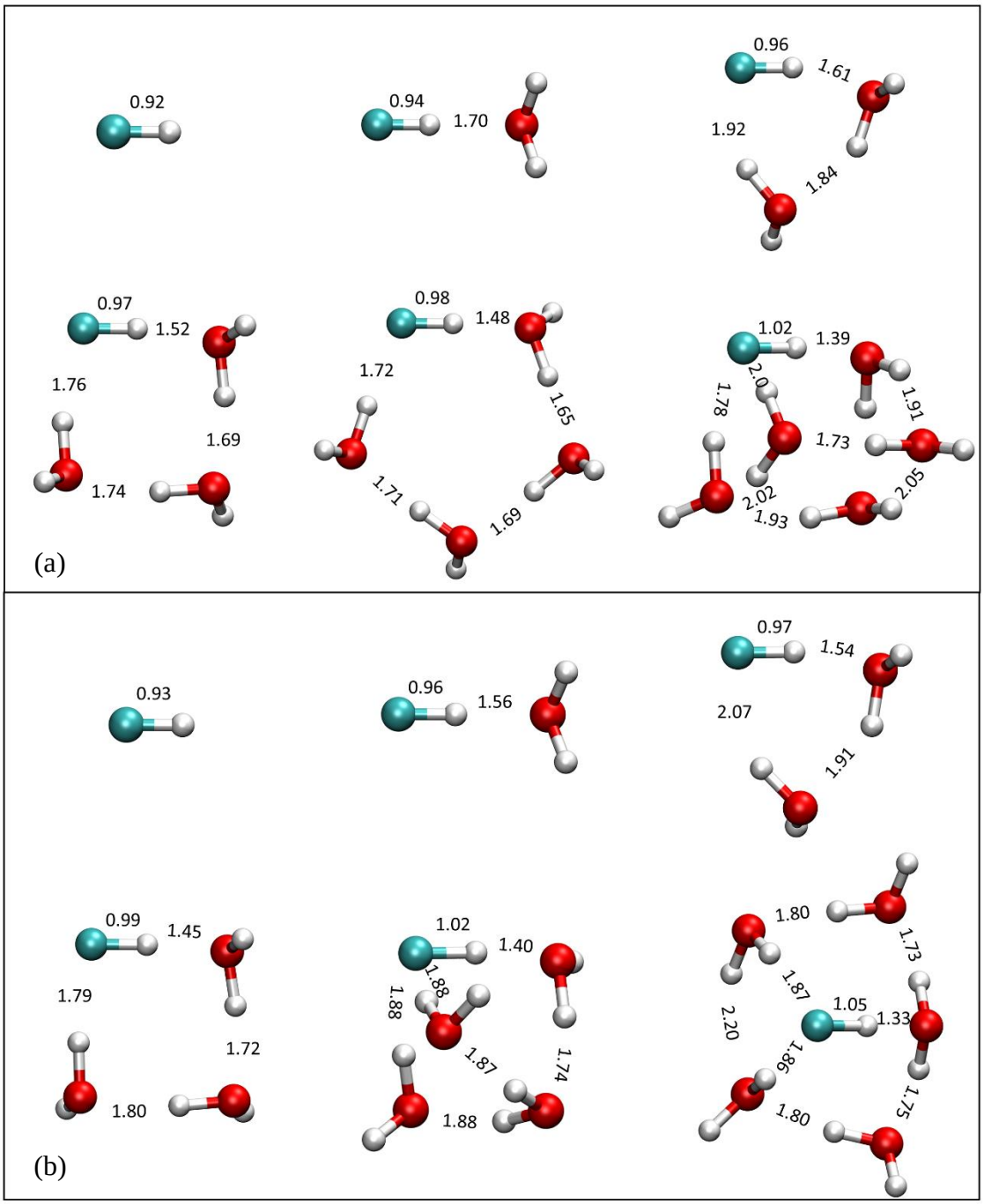


Figure 7.6. Fully optimized structures of HF with from zero to five water molecules at the B3LYP/6-311G** level of theory: (a) gas phase structures; (b) structures with the SMD model. No proton dissociation occurs in agreement with the weak acidity of HF.

An important observation is the relation between the acid strength and the number of water molecules required to effect proton dissociation forming the conjugate anion and hydrated proton. The gas phase acidities of the strong acids studied in this work may be ranked as follows: $CF_3SO_2NHSO_2CF_3$ > CF_3SO_3H > FSO_3H > H_2SO_4 > CH_3SO_3H > HNO_3, based on measurements using the pulsed FT ion cyclotron resonance (ICR) equilibrium constant method[66] and the pK_a values (see Table 7.1). The gas phase calculations are in agreement with this ranking except for H_2SO_4 which requires four water molecules to dissociate in the gas phase, more than that of the CH_3SO_3H acid. This may be due to the diprotic nature of the acid.

The weak acids in this study: H_3PO_2 > H_3PO_3 > H_3PO_4 > HF (ranked based on the pK_a values in Table 7.1) do not dissociate even with the addition of five water molecules. The only exception is H_3PO_2 which is the strongest among these weak acids. It dissociates in the gas phase when five water molecules are added (see Figure 7.7 (a)).

The hydrated structures for the $CF_3SO_2NHSO_2CF_3$ acid are shown in Figure 7.10. The gas phase structures dissociate when three or more water molecules are added to the system in agreement with the literature using the same level of theory.[292] Figure 7.10 (b) shows that in the SMD solvated clusters the proton is transferred to water in the vicinity of two or more water molecules. The experimental gas phase acidities indicate that this imide acid is stronger than either CF_3SO_3H or FSO_3H.[66] However, the calculations using the SMD solvation model show that CF_3SO_3H and FSO_3H require only one water molecule to transfer a proton. This may be due to the solvent effects that change the relative acid strengths, implying that the gas phase acidities are not transferable to the liquid phase or solvent.

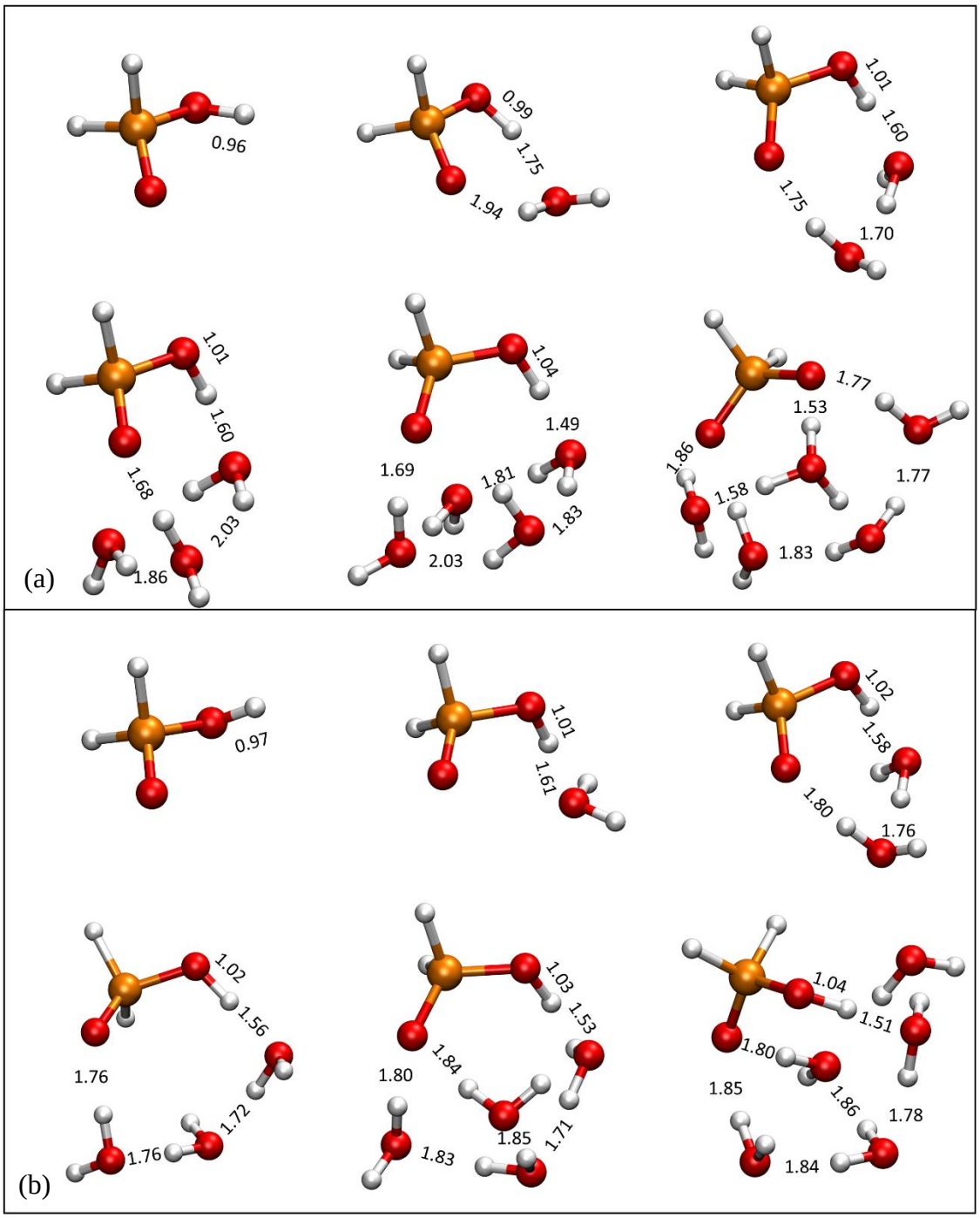


Figure 7.7. Fully optimized structures of H_3PO_2 with from zero to five water molecules at the B3LYP/6-311G** level of theory: (a) gas phase structures; (b) structures with the SMD model. No proton dissociation occurs, except in the gas phase with five added water molecules.

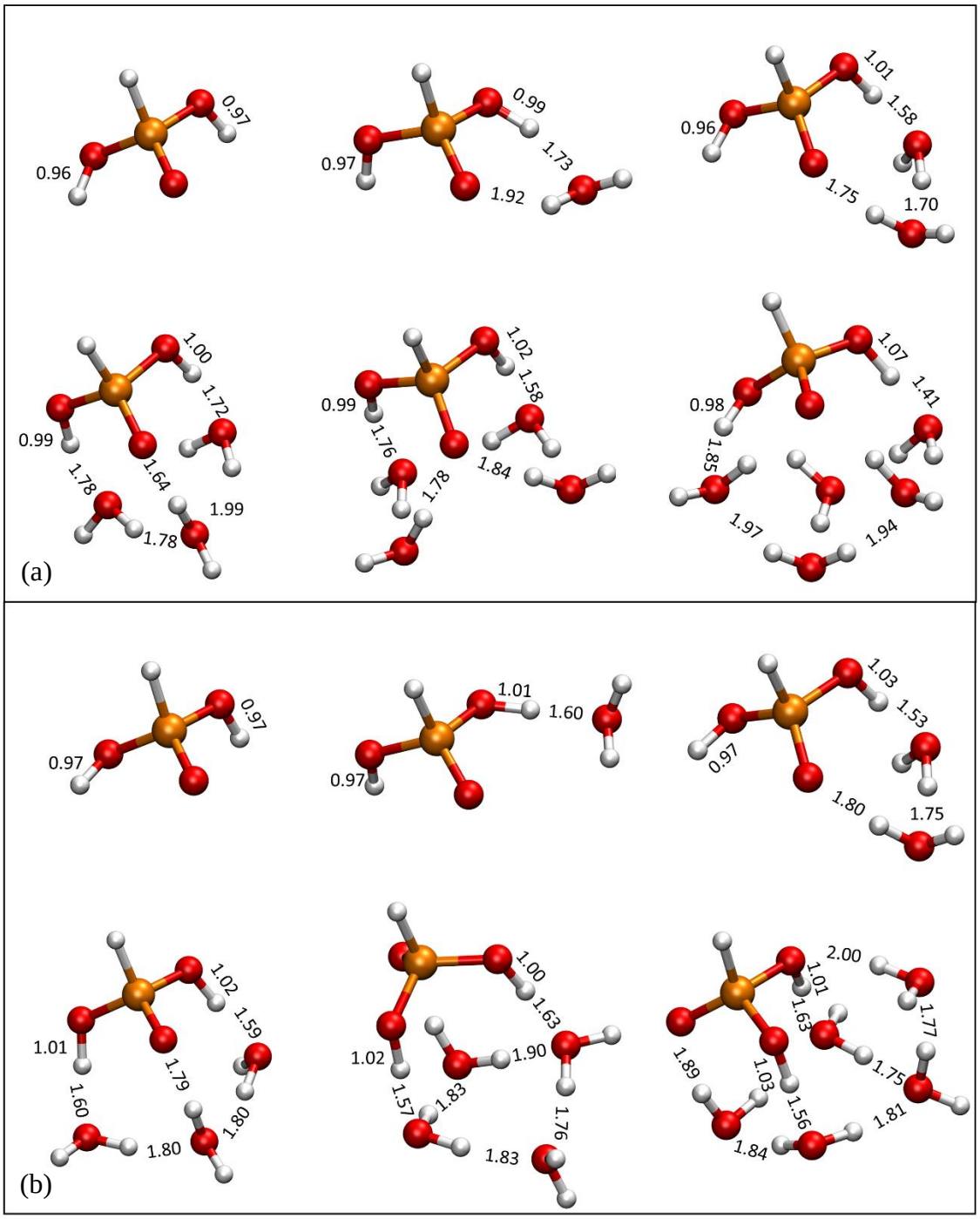


Figure 7.8. Fully optimized structures of H_3PO_3 with from zero to five water molecules at the B3LYP/6-311G** level of theory: (a) gas phase structures; (b) structures with the SMD model. No proton dissociation occurs.

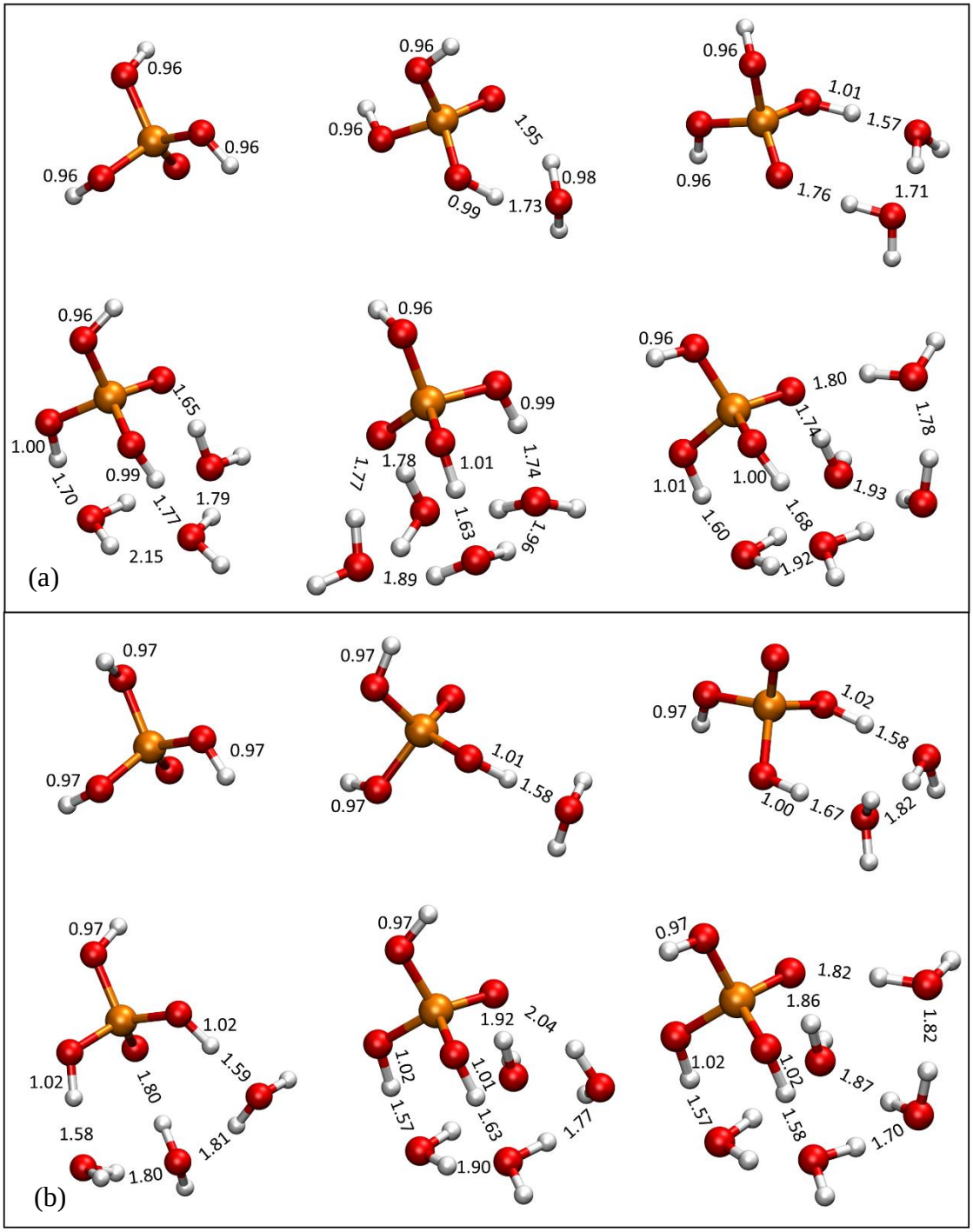


Figure 7.9. Fully optimized structures of H_3PO_4 with from zero to five water molecules at the B3LYP/6-311G** level of theory: (a) gas phase structures; (b) structures with the SMD model. No proton dissociation occurs.

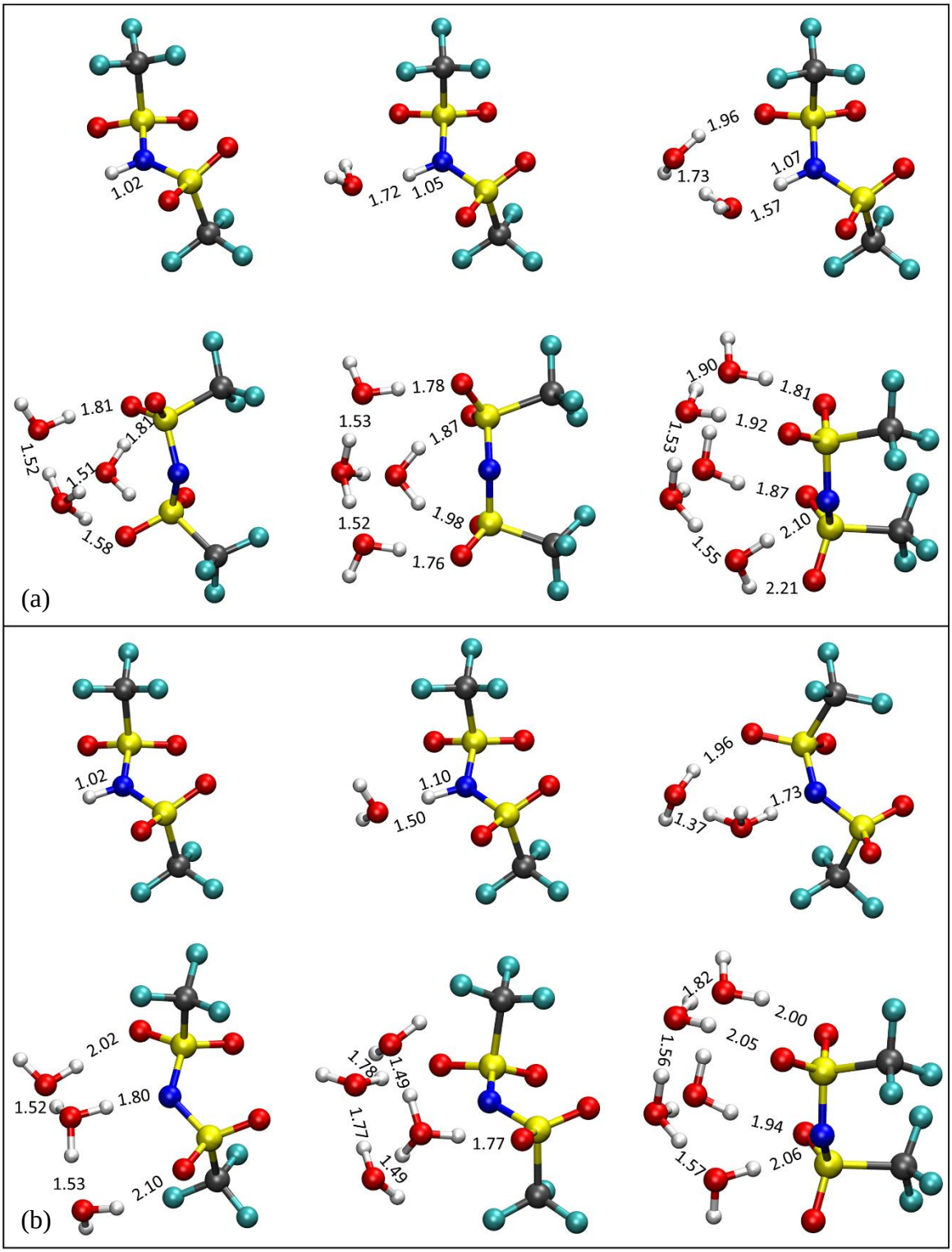


Figure 7.10. Fully optimized structures of $CF_3SO_2NHSO_2CF_3$ with from zero to five water molecules at the B3LYP/6-311G** level of theory: (a) gas phase structures, proton dissociation occurs after three water molecules are added (nitrogen is not involved in the hydrogen bond network); (b) structures with the SMD model, proton dissociates after only two water molecules are added (nitrogen is involved in the hydrogen bond network).

Adding more water molecules to the dissociated systems in the gas phase results in further separation of the hydronium ion from the conjugate anion. This implies that the solvent separated ion pairs are more stable than the contact ion pairs and reflects the propensity of the hydronium ion to delocalize the excess charge over the water molecules.[292,295] This behavior is also observed in the SMD solvated structures with some deviations.

The reported structures in this work may only serve as a relative measure of the propensity of the acids to dissociate and transfer a proton in the vicinity of a few water molecules and therefore may not be the exact hydration structures. Only one acid and a few water molecules were present in each cluster and therefore the findings are not general, because the presence of additional acid molecules or anhydrous conditions will certainly affect the results. One example is the energetics of proton transfer in anhydrous or neat phosphoric acid (the highest proton conducting substance) which decreases by increasing the number of phosphoric acids in the cluster.[71]

7.2 Proton Transfer

Potential energy surface (PES) scans were performed on the optimized structures of the acids with one to three water molecules. The length of the covalent OH bond between the transferring proton and the oxygen was increased incrementally in steps of 0.02 Å. In the case of $CF_3SO_2NHSO_2CF_3$ and HF the NH and FH bond lengths are scanned, respectively. The length of the OH bond (or NH or FH) was the only fixed parameter and the optimizations were performed over all other degrees of freedom without symmetry constraints at each step of the scan. A reverse set of scans were also performed by decreasing the OH bond with the same incremental steps starting from the geometry obtained at the last step of the original scan. The configuration with the lower energy at a similar OH bond length was selected from the original and reverse scans to plot the energy profiles.

Figures 7.11 to 7.14 show the relative energy profiles with respect to the optimized structures shown previously. The relative energy profiles are plotted as a function of the distance between the scanned proton and the oxygen/ nitrogen/ or fluorine atom of the acid. These plots may be categorized into four groups corresponding to the distinct behavior as the OH (or NH or FH) distance is increased: (1) the relative energy continuously increases from zero to a positive value; (2) the relative energy continuously decreases from a positive value to zero; (3) first the relative energy increases to an extremum and then decays; and (4) the changes in the relative energy are negligible (smaller than 2 kcal/mol).

The first type of scan occurs when the hydrated structure with the acid molecule is more stable than the dissociated form and as the proton is separated from the acid the configuration becomes energetically unfavorable. The opposite occurs in second class, i.e., the dissociated form is more stable than the molecular acid and when the proton is near the acid the relative energy is high and dramatically decreases when the proton is moved away from the acid. The third type of scans occur when the molecular acid is more stable (similar to the first case) but during the scan another proton is transferred to the acid, from either the hydronium ion or a water molecule. This secondary proton transfer is denoted a 'back transfer' in the literature.[303] The fourth type corresponds to the case where the energy difference between the dissociated and the molecular form is less than 2 kcal/mol. Hence, the energy penalty for transferring a proton from or to the acid is negligible.

Figure 7.11 compares the proton transfer scans for the three sulfonic acids with one to three water molecules. The three acids in the gas phase show back transfer of a proton with one and two water molecules (type 3) and a decreasing scan is observed with three water molecules (type 2). This is because of the acids do not dissociate in the gas phase until three water molecules are added.

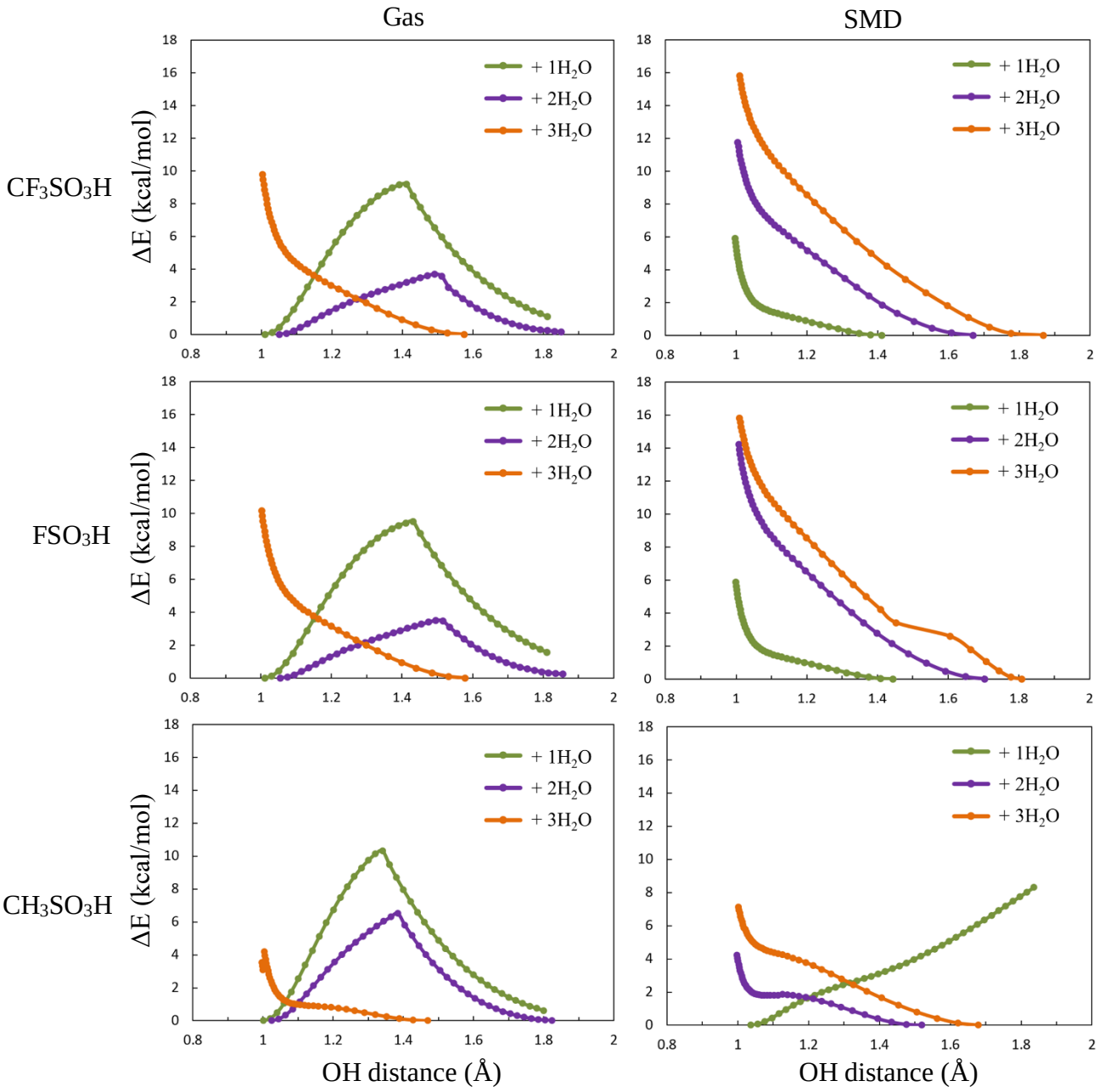


Figure 7.11. The relative energy profiles of PES scans for: CF_3SO_3H, FSO_3H, and CH_3SO_3H. The gas phase results are shown in the left panel and the results with the SMD model are displayed in the right panel. The extremum plots in the gas phase correspond to the back transfer events indicating that the molecular acid is more stable than the ionized form. The gas phase results are similar, because the proton dissociation occurs after three water molecules are added. The SMD results for CF_3SO_3H and FSO_3H are similar to each other and different to those for CH_3SO_3H, as the formers require only one water molecule to effect proton dissociation. The right panel scans do not show a back transfer of a proton, because the formed hydronium ion is stabilized by the continuum solvation model.

The solvated structures (the right panel in Figure 7.11) do not show a back transfer of a proton and the relative energy decreases as the OH distance is increased (type 2). The absence of a back transfer suggests that the formed hydronium ion is stabilized by the continuum solvation model. The CH_3SO_3H acid with one water molecule does not dissociate (see Figure 7.3 (b)) and therefore the energy simply increases with increasing OH distance (type 1). The energy penalty for moving the proton closer to the acid increases as the number of water molecules is increased in the SMD model scans. This implies that the clusters consisting of more water molecules have a higher propensity to remain in the ionized (dissociated) form.

Figure 7.12 shows the proton transfer scans for three of the inorganic acids: H_2SO_4; HNO_3; and HF. The gas phase scans show back transfer of a proton to the acids in all cases. An extra proton transfer scan for the HNO_3 acid with four water molecules was also performed for further verification. The energy barrier at the extremum points decreases as the number of water molecules is increased. The acid strength is inversely related to the energy barriers and hence the values for HF (the weakest acid) are much greater than those for H_2SO_4 and HNO_3.

The right panels in Figure 7.12 show that the transfer of a proton to one water molecule is unfavorable for all three acids (type 1) and as the acid strength decreases the energy penalty increases. The H_2SO_4 and HNO_3 acids with two water molecules show type 4 behavior, implying a negligible energy barrier to transfer a proton. As both H_2SO_4 and HNO_3 dissociate with three water molecules with the SMD model, the energy simply decreases with increasing OH distance (see the right panel of Figure 7.12). The weakest acid, HF, exhibits a back transfer with either two or three added water molecules and the energy barriers are lower than their corresponding values in the gas phase.

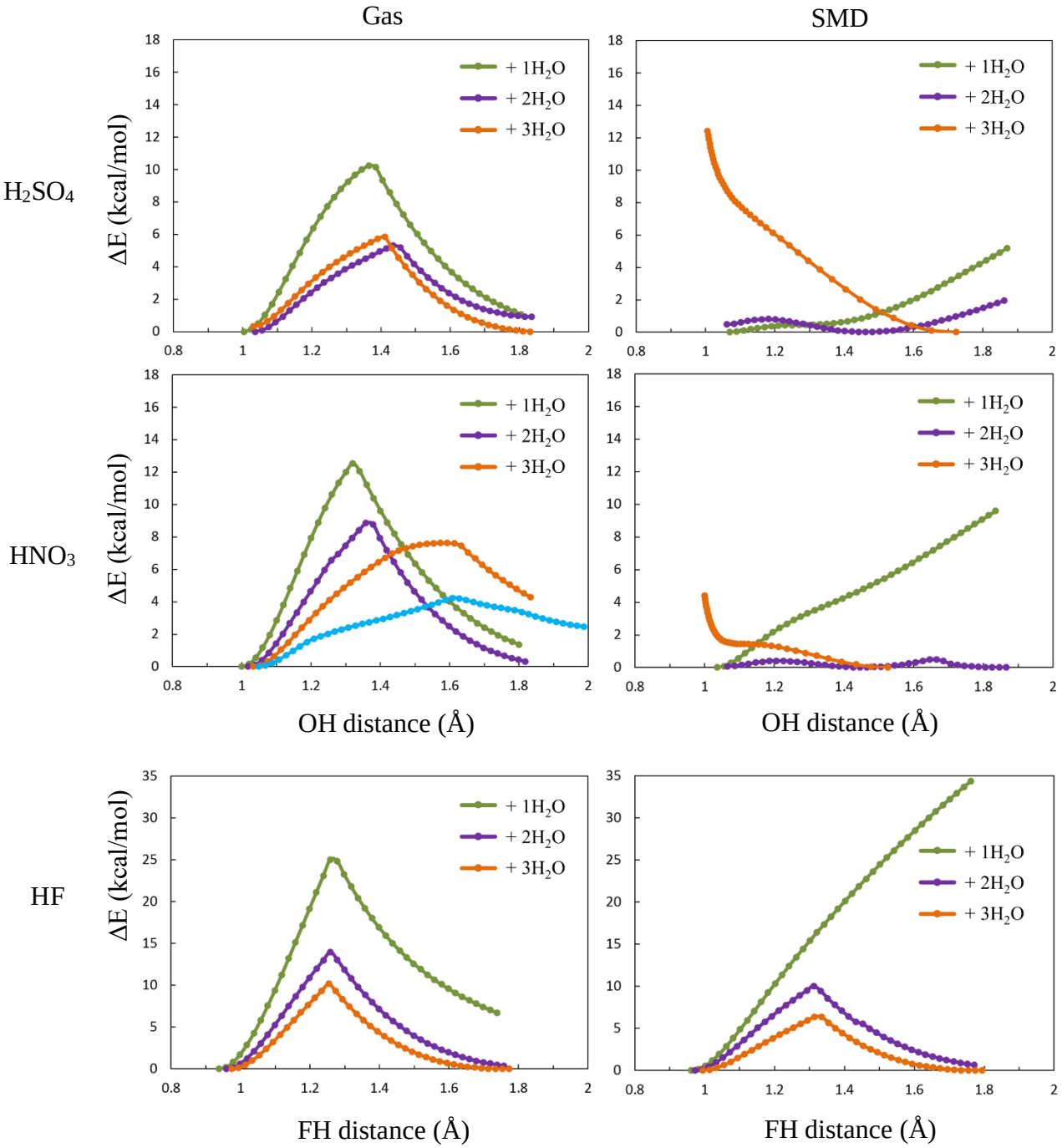


Figure 7.12. The relative energy profiles of PES scans for: H_2SO_4, HNO_3, and HF. The gas phase results are shown in the left panel and the results with the SMD model are displayed in the right panel. The gas phase results exhibit back transfer of a proton indicating that the molecular acid is more stable than the ionized form. The energy barrier to move a proton away from the acid is inversely related to the number of water molecules and the acid strength. The weakest acid, HF, has the highest energy barriers. The relative energy axis is plotted from 0 to 18 kcal/mol for all acids except for HF (from 0 to 35 kcal/mol).

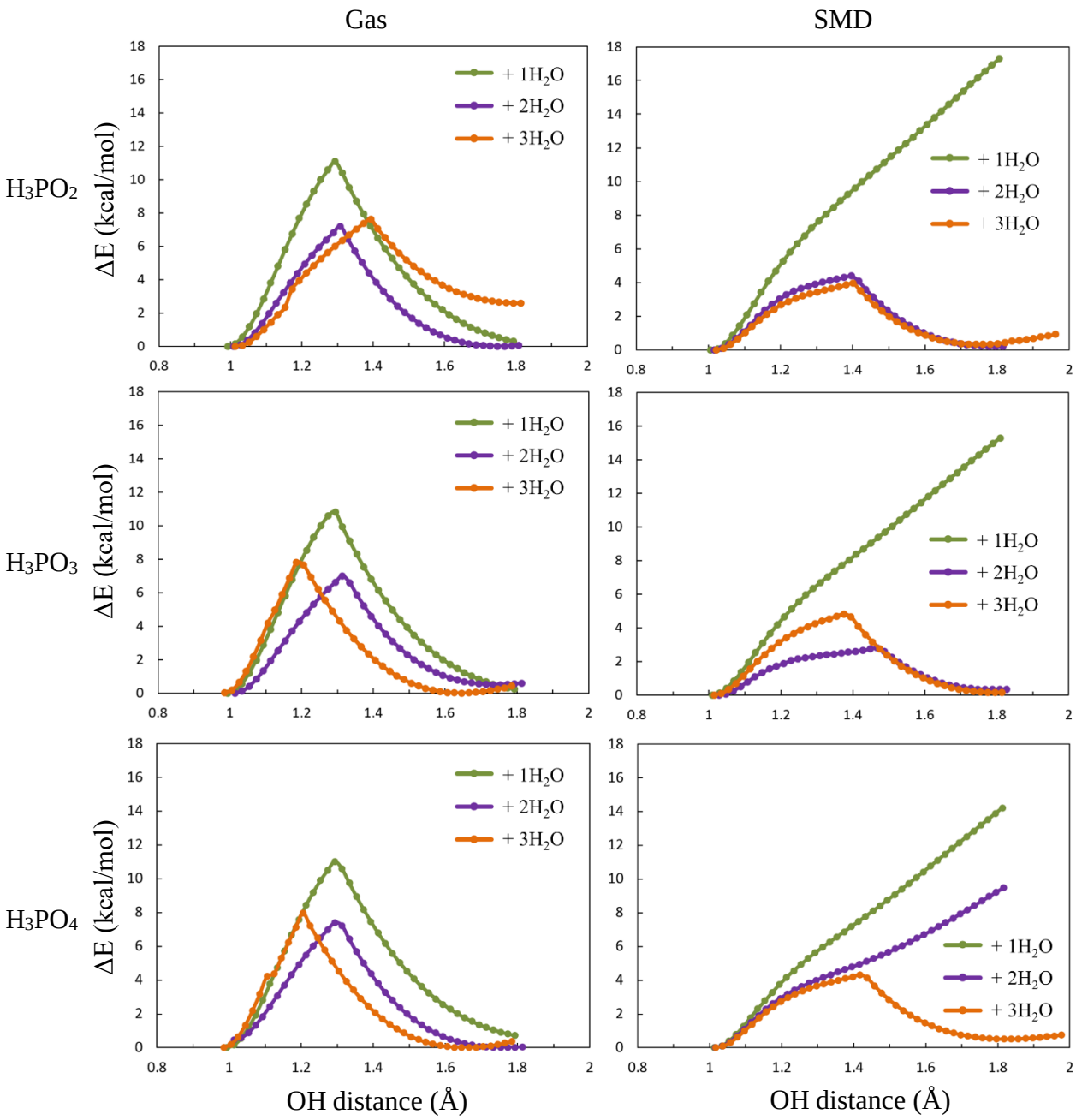


Figure 7.13. The relative energy profiles of PES scans for: H_3PO_2, H_3PO_3, and H_3PO_4. The gas phase results are shown in the left panel and the results with the SMD model are displayed in the right panel. Only a back transfer or an increasing scan is observed, because the proton dissociation is not favored by any of these weak acids. The proton transfer energetics are similar for these acids in agreement with their similar acidity and pK_a values listed in Table 7.1.

The scan plots of the three phosphor based acids are shown in Figure 7.13. These acids do not dissociate when up to three water molecules are added either in the gas phase or in a solvent. They all have a proton back transferred to them in the gas phase similar to the HF acid. The proton transfer behavior for the SMD solvated scans is also similar to those of HF. However, the energy barriers and penalties are much lower than HF.

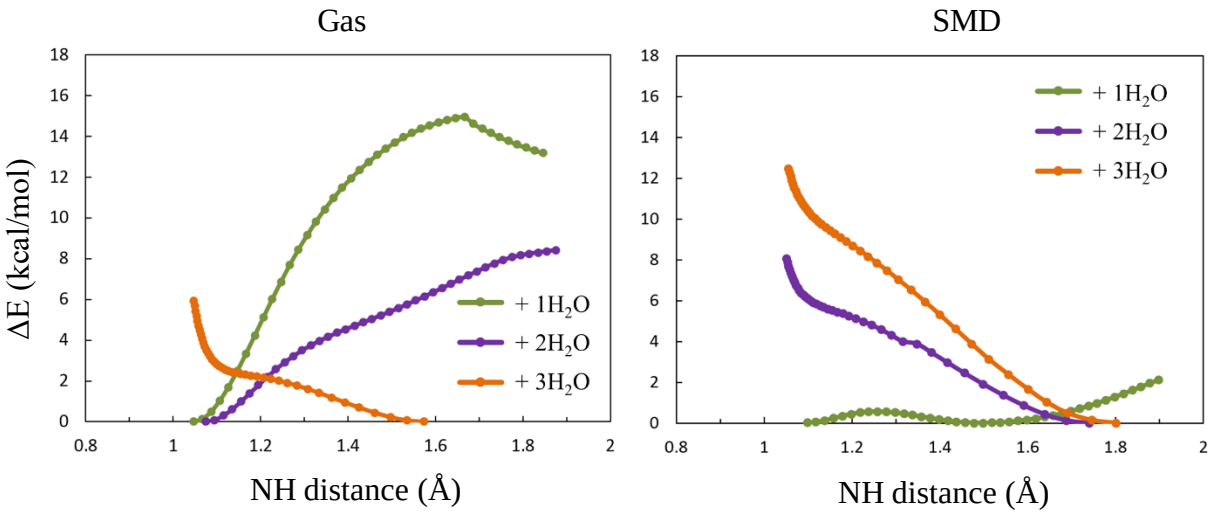


Figure 7.14. The relative energy profiles of PES scans for $CF_3SO_2NHSO_2CF_3$. The gas phase results are shown in the left panel and the results with the SMD model are displayed in the right panel. In the gas phase with one water molecule, the secondary proton is transferred to an oxygen atom of the acid. The gas phase structure of this acid with three water molecules does not involve hydrogen bonding with nitrogen as shown in Figure 7.10 (a). Hence the proton was transferred to an oxygen atom of the acid, i.e., the orange plot in the left panel shows OH distance rather than NH. The proton dissociation occurs after two water molecules are added to the SMD solvated structures, however the proton transfer energetics is negligible with one water molecule.

Figure 7.14 plots the proton transfer scans for the imide acid, $CF_3SO_2NHSO_2CF_3$. The acid with one water molecule shows a back transfer in the gas phase; the secondary proton is transferred to an oxygen atom of the acid. Type 2 behavior is observed for this strong acid with three water molecules in the gas phase and with two and three when solvated with the SMD model, consistent with the structures shown in Figure 7.10. The acid and three water molecules in the gas phase

form a hydrogen bond network that does not involve the nitrogen atom (see Figure 7.10 (a)). Hence, the proton transfer scan was performed by transferring a proton to the oxygen atom of the acid.

Chapter 8 Conclusions

The development of efficient and sustainable energy conversion and storage technologies is critical in the path to replacing fossil fuels with their detrimental environmental consequences. Electrochemical devices including metal ion batteries and fuel cells are under significant investigation and optimization for this purpose. The electrolytes used in all-vanadium redox flow batteries (VRFBs), fuel cells (anion and proton exchange membranes (AEMs and PEMs)), and secondary magnesium batteries have been the specific interest and focus in this dissertation. Multiscale modeling has been utilized to provide a molecular understanding of the structure, stability, morphology, and effective parameters of various electrolyte materials.

The first hydration shell structures of the four vanadium cations employed in VRFB electrolytes were determined using electronic structure calculations. The results indicate that the most stable structure for the V^{2+} and V^{3+} cations is hexa-aqua octahedral structure and for the VO^{2+} and VO_2^{+} cations the penta-aqua octahedral complex and tri-hydrated bipyramidal structure are the ground state, respectively. The solvation energies for the four vanadium cations in bulk water were determined using a quasi-chemical theory. The calculated Gibbs energies were in excellent agreement with experimental values for V^{2+} and V^{3+} and therefore the results may be used for VO^{2+} and VO_2^{+} ions for which no experimental information is currently available.

The local hydration structure of the four vanadium cations in proximity to H_2SO_4, CF_3SO_3H, HSO_4^{-}, SO_4^{2-}, and $CF_3SO_3^{-}$ were also elucidated through extensive quantum chemical calculations. It was determined that for all four species the vanadium cations do not bind covalently to any of the acids or anions. A contact ion pair may form in some of the complexes and is promoted in the vicinity of a proton. The presence of either an acid or anion in most cases decreased the $V\cdots O(H_2O)$ distance compared to that of the cation in bulk water. The structure of the V^{3+} ion

is more distorted than V^{2+} when in the presence of any of the acids or anions. No interaction of a proton with the oxo-group of the VO^{2+} cation was observed. However, the oxo-group of the VO_2^+ was protonated. The partial atomic charge on the vanadium atom for all oxidation states was computed to be between +1.7 and +2.0, significantly lower than the formal oxidation state. Our results indicate that the VO_2^+ species is stable in the presence of HSO_4^- while it forms new complexes with SO_4^{2-} that can deprotonate and form a hydroxide ion and subsequently precipitate. Hence, the stability of the VO_2^+ cation at low pH is linked to the proton concentration and the ratio of HSO_4^- to SO_4^{2-} in the solution.

The interaction of all four vanadium cations with CF_3SO_3H (the protogenic group of a PFSA ionomer) was found to be energetically favorable: all cations retained their primary hydration shell and did not form covalent bonds with the acid. However, in the vicinity of a hydrated proton the V^{2+} and V^{3+} cations formed contact ion pairs with CF_3SO_3H. The triflate anion, in general, did not form a contact ion pair with any of the vanadium cationic species.

A new method for the parameterization of DPD conservative interactions was developed. The conservative potential was assumed to be composed of two terms: reference and excess. The reference potential was obtained from the experimental compressibility of a selected reference material. The excess potential was related to the interaction energy of two beads computed quantum mechanically. Several different spatial configurations were considered to correctly sample the interaction energy. The quantum chemical energies were fitted onto a quadratic function of inter-particle distance. A mapping procedure was implemented to scale the fitted parameters and compute the conservative force parameters. The electrostatic interactions were considered implicitly through the conservative force parameters (i.e., the $b_{ij}^{int^{**}}$ term). The absence

of a separate electrostatic potential term significantly improves the computational efficiency over previous treatments.

The derived method was tested and applied to systems consisting of hydrated Nafion with dissolved vanadium cations (mimicking the membrane in VRFBs). The conservative interaction parameters were computed using the derived method and the bonded potentials were parameterized by comparing to a prototypical system using all atom classical MD simulations. The DPD simulations agreed well with recent MD simulations, confirming the credibility of the parameterization method. The results indicated that the V^{3+} species has the strongest self-repulsion among the four vanadium cations. The smallest self-repulsion was observed for VO_2^+ which has the lowest total charge. The sulfonate groups exhibited closer aggregation in the presence of the cationic species and the effects were more significant for V^{3+} and at low hydration levels ($\lambda = 6$). Diffusivities were calculated from the mean square displacements and indicated that V^{3+} is the slowest moving cation and VO_2^+ is the fastest. The results indicated stronger cation-anion interaction for high EW Nafion which decreased the vanadium diffusivity. The diffusivities of water and vanadium beads were both increased by decreasing the EW, however the increase in the water diffusivity was greater.

DPD simulations were performed to study the hydrated morphology and microstructure of an alkyl-substituted quaternary ammonium-functionalized SEBS triblock copolymer. The unfunctionalized SEBS base material was first simulated to benchmark the bonded interaction parameters by reproducing the experimental morphology of SEBS (i.e., hexagonal cylinders). The hydrated AEM was subsequently simulated employing a similar set of parameters and was observed to phase separate into a functionalized polystyrene-rich phase (hydrophilic) and a

polyethylene phase (hydrophobic). The ionic species and majority of the water were distributed throughout the former phase, while some water was also in the latter.

The morphology was observed to be controlled by the degree of hydration and was transformed from perforated and interconnected lamellae at low water content (i.e., $\lambda = 4$ and 8) to perfect lamellae ($\lambda = 12$) and then to disordered bicontinuous domains at the highest water contents (i.e., $\lambda = 16$ and 20). The hydrophilic phase swelled with hydration consistent with the AFM phase imaging of a similar SEBS-based ionomer. Domains exclusively consisting of water were formed at the high levels of hydration within the hydrophilic phase. Changing the associated anion from OH^- to Cl^- resulted in larger exclusive domains of water at the highest hydration levels.

The diffusivities of water and ionic species were calculated and reported only as a comparative measure, because DPD replaces the atoms with coarse-grained particles and therefore neglects the structural changes, hydrogen bond reorientation, and proton shuttling or hopping involved in the water and ion transport. The simulation results predict that the Cl^- ion is less mobile than OH^- with a slight increase in the diffusivity of both anions with increasing water content. This is an interesting result confirming the reliability of the DPD parameterization method.

A similar coarse-graining scheme was proposed for DPD simulations of the SDAPP membranes. The SDAPP ionomer was represented with two coarse-grained monomers: one representing the sulfonated monomer and the other with no degrees of sulfonation. This scheme was proposed to enable modeling of different sulfonation levels by combining different ratios of these two coarse-grained monomers. Electronic structure calculations were performed for further determination of the conservative interaction parameters following the developed parameterization method presented earlier in this work. Further progress to model and simulate the SDAPP membrane system is warranted.

Electronic structure calculations determined the atomic scale structures of the $EMIm^+$ cation interacting with AlX_4^-, $Al_2X_7^-$, and MgX_2 (X = Cl, I). The results showed that the anion is highly likely to occupy the front position around the imidazolium ring, and upon addition of MgX_2 and $(MgX_2)_2$ units to the optimized structures the Mg halide is the nearest anion to $EMIm^+$. Analysis of the binding energies revealed that in the presence of MgX_2, the AlX_4^- concatenated complexes are more energetically favored when compared to those containing $Al_2X_7^-$.

Vibrational frequencies were computed from the DFT calculations and enabled the assignment of the experimental IR and Raman spectra of $(EMImCl/(AlCl_3)_{1.5})/(\delta\text{-}MgCl_2)_x$ and $(EMImAlI_4)/(\delta\text{-}MgI_2)_x$ electrolytes (x relates to the concentration of the Mg salt). These results indicated that at low Mg salt concentration both the AlX_4^- and $Al_2X_7^-$ anionic species were present and at higher concentrations the equilibrium was shifted toward the AlX_4^- complexes because of a decrease in the concentration of $Al_2X_7^-$. It was also found that the $(EMImCl/(AlCl_3)_{1.5})/(\delta\text{-}MgCl_2)_x$ electrolytes contained nanostructures of the magnesium salt, i.e., $(MgCl_2)_n$, $n > 1$, however the MgI_2 salt in the $(EMImAlI_4)/(\delta\text{-}MgI_2)_x$ electrolytes interacted favorably with the IL in the form of a monomer.

The primary hydration of ten acids commonly employed in electrolytes was investigated using quantum chemical calculations in order to provide a fundamental understanding of their hydrated acidity and proton transfer in comparison to each other. It was determined that fewer number of water molecules were required to dissociate a proton from the stronger acids. The number of water molecules required to first witness proton dissociation was decreased upon the addition of a solvation model through stabilizing the conjugate ions. It was observed that the hydronium ion further separated from the conjugate anion as the number of water molecules was increased. This was explained by the solvent separated ion pairs being more stable than the contact ion pairs.

Potential energy surface scans were performed to analyze the relative proton transfer. It was determined that the proton transfer energetics are controlled by the structure of the hydrated acid, the acid strength, and the continuum solvation model. The energy barrier for moving a proton away from the acid was inversely related to the acid strength. The propensity of proton dissociation was higher when the solvation model was applied. This fundamental study may serve the purpose of designing novel electrolytes featuring one or more of these acids.

In summary, the multiscale findings from the electronic structure calculations, quasi-chemical theory, and the DPD simulations provided a better understanding of the electrolyte materials, structural and morphological information, and the effective parameters. These results increase the overall knowledge of such electrolyte systems and are deemed useful in better design and optimization of energy storage and conversion technologies.

References

1. Weber, A. Z.; Mench, M. M.; Meyers, J. P.; Ross, P. N.; Gostick, J. T.; Liu, Q. H., Redox flow batteries: A review. *Journal of Applied Electrochemistry* **2011,** *41*, 1137-1164.

2. Saha, P.; Datta, M. K.; Velikokhatnyi, O. I.; Manivannan, A.; Alman, D.; Kumta, P. N., Rechargeable magnesium battery: Current status and key challenges for the future. *Progress in Materials Science* **2014,** *66*, 1-86.

3. Skyllas-Kazacos, M., Secondary batteries – flow systems | vanadium redox-flow batteries. In *Encyclopedia of Electrochemical Power Sources*, Garche, J., Ed. Elsevier: Amsterdam, **2009**; pp 444-453.

4. de Leon, C. P.; Frias-Ferrer, A.; Gonzalez-Garcia, J.; Szanto, D. A.; Walsh, F. C., Redox flow cells for energy conversion. *Journal of Power Sources* **2006,** *160*, 716-732.

5. Bartolozzi, M., Development of redox flow batteries: A historical bibliography. *Journal of Power Sources* **1989,** *27*, 219-234.

6. Price, A.; Bartley, S.; Male, S.; Cooley, G., A novel approach to utility scale energy storage. *Power Engineering Journal* **1999,** *13*, 122-129.

7. Soloveichik, G. L., Flow Batteries: Current Status and Trends. *Chemical Reviews* **2015,** *115*, 11533-11558.

8. Clark, N.; Eidler, P.; Lex, P. *Development of zinc/bromine batteries for load-leveling applications: Phase 2 final report*; Sandia National Laboratories, Albuquerque, NM: 1999.

9. Skyllas-Kazacos, M.; Rychick, M.; Robins, R. All-vanadium redox battery. Unisearch Limited, Australia, US Patent 4,786,567, November 22, **1988**.

10. Li, L.; Kim, S.; Wang, W.; Vijayakumar, M.; Nie, Z.; Chen, B.; Zhang, J.; Xia, G.; Hu, J.; Graff, G.; Liu, J.; Yang, Z., A stable vanadium redox-flow battery with high energy density for large-scale energy storage. *Advanced Energy Materials* **2011,** *1*, 394-400.

11. Parasuraman, A.; Lim, T. M.; Menictas, C.; Skyllas-Kazacos, M., Review of material research and development for vanadium redox flow battery applications. *Electrochimica Acta* **2013,** *101*, 27-40.

12. Skyllas-Kazacos, M.; Menictas, C.; Kazacos, M., Thermal stability of concentrated V(V) electrolytes in the vanadium redox cell. *Journal of Electroanalytical Chemistry* **1996,** *143*, L86-L88.

13. Skyllas-Kazacos, M.; Peng, C.; Cheng, M., Evaluation of precipitation inhibitors for supersaturated vanadyl electrolytes for the vanadium redox battery. *Electrochemical and Solid-State Letters* **1999,** *2*, 121-122.

14. Rahman, F.; Skyllas-Kazacos, M., Vanadium redox battery: Positive half-cell electrolyte studies. *Journal of Power Sources* **2009,** *189*, 1212-1219.

15. Vijayakumar, M.; Li, L. Y.; Graff, G.; Liu, J.; Zhang, H. M.; Yang, Z. G.; Hu, J. A., Towards understanding the poor thermal stability of V^{5+} electrolyte solution in vanadium redox flow batteries. *Journal of Power Sources* **2011,** *196*, 3669-3672.

16. Skyllas-Kazacos, M.; Kazacos, M. Stabilized vanadium electrolyte solutions for all-vanadium redox cells and batteries. US Patent 6,562,514, May 13, **2003**.

17. Kazacos, M.; Skyllas-Kazacos, M. High energy density vanadium electrolyte solutions, methods of preparation thereof and all-vanadium redox cells and batteries containing high energy vanadium electrolyte solutions. US Patent 7,078,123, July 18, **2006**.

18. Zhang, J. L.; Li, L. Y.; Nie, Z. M.; Chen, B. W.; Vijayakumar, M.; Kim, S.; Wang, W.; Schwenzer, B.; Liu, J.; Yang, Z. G., Effects of additives on the stability of electrolytes for all-vanadium redox flow batteries. *Journal of Applied Electrochemistry* **2011,** *41*, 1215-1221.

19. Li, S.; Huang, K. L.; Liu, S. Q.; Fang, D.; Wu, X. W.; Lu, D.; Wu, T., Effect of organic additives on positive electrolyte for vanadium redox battery. *Electrochimica Acta* **2011,** *56*, 5483-5487.

20. Montgomery, H.; Chastain, R. V.; Natt, J. J.; Witkowska, A. M.; Lingafelter, E. C., Crystal structure of Tuttons salts. VI. Vanadium(II) iron(II) and cobalt(II) ammonium sulfate hexahydrates. *Acta Crystallographica* **1967,** *22*, 775-780.

21. Ballhausen, C. J.; Djurinskij, B. F.; Watson, K. J., The polarized absorption spectra of three crystalline polymorphs of $VOSO_4 \cdot 5H_2O$. *Journal of the American Chemical Society* **1968,** *90*, 3305-3309.

22. Cotton, F. A.; Falvello, L. R.; Murillo, C. A.; Pascual, I.; Schultz, A. J.; Tomas, M., Neutron and X-ray structural characterization of the hexaaquavanadium(II) compound $VSO_4.7H_2O$. *Inorganic Chemistry* **1994,** *33*, 5391-5395.

23. Grant, C. V.; Cope, W.; Ball, J. A.; Maresch, G. G.; Gaffney, B. J.; Fink, W.; Britt, R. D., Electronic structure of the aqueous vanadyl ion probed by 9 and 94 GHz EPR and pulsed ENDOR spectroscopies and density functional theory calculations. *Journal of Physical Chemistry B* **1999,** *103*, 10627-10631.

24. Bühl, M.; Parrinello, M., Medium effects on ^{51}V NMR chemical shifts: A density functional study. *Chemistry - A European Journal* **2001,** *7*, 4487-4494.

25. Benmelouka, M.; Messaoudi, S.; Furet, E.; Gautier, R.; Le Fur, E.; Pivan, J. Y., Density functional investigation of hydrated V(II) and V(III) ions: Influence of the second coordination sphere; water exchange mechanism. *Journal of Physical Chemistry A* **2003,** *107*, 4122-4129.

26. Kritayakornupong, C., Structural and dynamical properties of the V^{3+} ion in dilute aqueous solution: An *ab initio* QM/MM molecular dynamics simulation. *Journal of Computational Chemistry* **2009,** *30*, 2777-2783.

27. Vijayakumar, M.; Burton, S. D.; Huang, C.; Li, L. Y.; Yang, Z. G.; Graff, G. L.; Liu, J.; Hu, J. Z.; Skyllas-Kazacos, M., Nuclear magnetic resonance studies on vanadium(IV) electrolyte solutions for vanadium redox flow battery. *Journal of Power Sources* **2010,** *195*, 7709-7717.

28. Krakowiak, J.; Lundberg, D.; Persson, I., A coordination chemistry study of hydrated and solvated cationic vanadium ions in oxidation states +III, +IV, and +V in solution and solid state. *Inorganic Chemistry* **2012,** *51*, 9598-9609.

29. Vijayakumar, M.; Bhuvaneswari, M. S.; Nachimuthu, P.; Schwenzer, B.; Kim, S.; Yang, Z. G.; Liu, J.; Graff, G. L.; Thevuthasan, S.; Hu, J. Z., Spectroscopic investigations of the fouling process on Nafion membranes in vanadium redox flow batteries. *Journal of Membrane Science* **2011,** *366*, 325-334.

30. Wiedemann, E.; Heintz, A.; Lichtenthaler, R. N., Transport properties of vanadium ions in cation exchange membranes: Determination of diffusion coefficients using a dialysis cell. *Journal of Membrane Science* **1998,** *141*, 215-221.

31. Chen, J. Q.; Wang, B. B.; Yang, J. C., Adsorption and diffusion of $VO^{2+}$and VO_2^+ across cation membrane for all-vanadium redox flow battery. *Solvent Extraction and Ion Exchange* **2009,** *27*, 312-327.

32. Tang, Z.; Keith, R. E.; Aaron, D. S.; Lawton, J. S.; Papandrew, A. B.; Zawodzinski, T. A., Proton exchange membrane performance characterization in VRFB. *ECS Transactions* **2012,** *41*, 25-34.

33. Verbrugge, M. W.; Hill, R. F., Experimental and theoretical investigation of perfluorosulfonic acid membranes equilibrated with aqueous sulfuric acid solutions. *Journal of Physical Chemistry* **1988,** *92*, 6778-6783.

34. Verbrugge, M. W.; Hill, R. F., Ion and solvent transport in ion-exchange membranes. II. A radiotracer study of the sulfuric-acid, Nafion-117 system. *Journal of the Electrochemical Society* **1990,** *137*, 893-899.

35. Tang, Z. J.; Svoboda, R.; Lawton, J. S.; Aaron, D. S.; Papandrew, A. B.; Zawodzinski, T. A., Composition and conductivity of membranes equilibrated with solutions of sulfuric acid and vanadyl sulfate. *Journal of the Electrochemical Society* **2013,** *160*, F1040-F1047.

36. Mohammadi, T.; Skyllas-Kazacos, M., Characterization of novel composite membrane for redox flow battery applications. *Journal of Membrane Science* **1995,** *98*, 77-87.

37. Mohammadi, T.; Skyllas-Kazacos, M., Preparation of sulfonated composite membrane for vanadium redox flow battery applications. *Journal of Membrane Science* **1995,** *107*, 35-45.

38. Sukkar, T.; Skyllas-Kazacos, M., Modification of membranes using polyelectrolytes to improve water transfer properties in the vanadium redox battery. *Journal of Membrane Science* **2003,** *222*, 249-264.

39. Li, X. F.; Zhang, H. M.; Mai, Z. S.; Zhang, H. Z.; Vankelecom, I., Ion exchange membranes for vanadium redox flow battery (VRB) applications. *Energy & Environmental Science* **2011,** *4*, 1147-1160.

40. Prifti, H.; Parasuraman, A.; Winardi, S.; Lim, T. M.; Skyllas-Kazacos, M., Membranes for redox flow battery applications. *Membranes* **2012,** *2*, 275-306.

41. Kreuer, K. D.; Portale, G., A critical revision of the nano-morphology of proton conducting ionomers and polyelectrolytes for fuel cell applications. *Advanced Functional Materials* **2013,** *23,* 5390-5397.

42. Kreuer, K. D., Ion conducting membranes for fuel cells and other electrochemical devices. *Chemistry of Materials* **2014,** *26,* 361-380.

43. Rubatat, L.; Rollet, A. L.; Gebel, G.; Diat, O., Evidence of elongated polymeric aggregates in Nafion. *Macromolecules* **2002,** *35,* 4050-4055.

44. Li, J.; Park, J. K.; Moore, R. B.; Madsen, L. A., Linear coupling of alignment with transport in a polymer electrolyte membrane. *Nature Materials* **2011,** *10,* 507-511.

45. Wang, C.; Krishnan, V.; Wu, D. S.; Bledsoe, R.; Paddison, S. J.; Duscher, G., Evaluation of the microstructure of dry and hydrated perfluorosulfonic acid ionomers: Microscopy and simulations. *Journal of Materials Chemistry A* **2013,** *1*, 938-944.

46. Sukkar, T.; Skyllas-Kazacos, M., Water transfer behaviour across cation exchange membranes in the vanadium redox battery. *Journal of Membrane Science* **2003,** *222*, 235-247.

47. Mohammadi, T.; Chieng, S. C.; Skyllas-Kazacos, M., Water transport study across commercial ion exchange membranes in the vanadium redox flow battery. *Journal of Membrane Science* **1997,** *133,* 151-159.

48. Wu, D. S.; Paddison, S. J.; Elliott, J. A., A comparative study of the hydrated morphologies of perfluorosulfonic acid fuel cell membranes with mesoscopic simulations. *Energy & Environmental Science* **2008,** *1*, 284-293.

49. Yamamoto, S.; Hyodo, S. A., A computer simulation study of the mesoscopic structure of the polyelectrolyte membrane Nafion. *Polymer Journal* **2003,** *35,* 519-527.

50. Vishnyakov, A.; Neimark, A. V., Self-assembly in nafion membranes upon hydration: Water mobility and adsorption isotherms. *Journal of Physical Chemistry B* **2014,** *118*, 11353-11364.

51. Dorenbos, G.; Morohoshi, K., Percolation thresholds in hydrated amphiphilic polymer membranes. *Journal of Materials Chemistry* **2011,** *21*, 13503-13515.

52. Jorn, R.; Voth, G. A., Mesoscale simulation of proton transport in proton exchange membranes. *Journal of Physical Chemistry C* **2012,** *116*, 10476-10489.

53. Wescott, J. T.; Qi, Y.; Subramanian, L.; Capehart, T. W., Mesoscale simulation of morphology in hydrated perfluorosulfonic acid membranes. *Journal of Chemical Physics* **2006,** *124*.

54. Cui, S.; Paddison, S. J., A Molecular Dynamics Study of the Effects of V2+ and V3+ on the Local Structure of Hydrated Nafion. *Journal of Physical Chemistry C* **2015,** *119*, 12848-12855.

55. Stambouli, A. B.; Traversa, E., Fuel cells, an alternative to standard sources of energy. *Renewable & Sustainable Energy Reviews* **2002,** *6*, 295-304.

56. Kirubakaran, A.; Jain, S.; Nema, R. K., A review on fuel cell technologies and power electronic interface. *Renewable & Sustainable Energy Reviews* **2009,** *13*, 2430-2440.

57. Merle, G.; Wessling, M.; Nijmeijer, K., Anion exchange membranes for alkaline fuel cells: A review. *Journal of Membrane Science* **2011,** *377*, 1-35.

58. Shao, Y. Y.; Yin, G. P.; Wang, Z. B.; Gao, Y. Z., Proton exchange membrane fuel cell from low temperature to high temperature: Material challenges. *Journal of Power Sources* **2007,** *167*, 235-242.

59. Smitha, B.; Sridhar, S.; Khan, A. A., Solid polymer electrolyte membranes for fuel cell applications - a review. *Journal of Membrane Science* **2005,** *259*, 10-26.

60. Cheng, J.; He, G. H.; Zhang, F. X., A mini-review on anion exchange membranes for fuel cell applications: Stability issue and addressing strategies. *International Journal of Hydrogen Energy* **2015,** *40*, 7348-7360.

61. Cleveland, C. J.; Lawrence, T.; Grubb, W. T., In *Encyclopedia of Earth*, Cleveland, C. J., Ed. Washington, D.C, 2008.

62. Peighambardoust, S. J.; Rowshanzamir, S.; Amjadi, M., Review of the proton exchange membranes for fuel cell applications. *International Journal of Hydrogen Energy* **2010,** *35*, 9349-9384.

63. Wu, J. F.; Yuan, X. Z.; Martin, J. J.; Wang, H. J.; Zhang, J. J.; Shen, J.; Wu, S. H.; Merida, W., A review of PEM fuel cell durability: Degradation mechanisms and mitigation strategies. *Journal of Power Sources* **2008,** *184*, 104-119.

64. Roziere, J.; Jones, D. J., Non-fluorinated polymer materials for proton exchange membrane fuel cells. *Annual Review of Materials Research* **2003,** *33*, 503-555.

65. Creager, S. E.; Sumner, J. J.; Bailey, R. D.; Ma, J. J.; Pennington, W. T.; DesMarteau, D. D., Equivalent weight and crystallinity effects on water content and proton conductivity in bis[(perfluoroalkyl) sulfonyl]imide-based ionomers. *Electrochemical and Solid State Letters* **1999,** *2*, 434-436.

66. Koppel, I. A.; Taft, R. W.; Anvia, F.; Zhu, S. Z.; Hu, L. Q.; Sung, K. S.; Desmarteau, D. D.; Yagupolskii, L. M.; Yagupolskii, Y. L.; Ignatev, N. V.; Kondratenko, N. V.; Volkonskii, A. Y.; Vlasov, V. M.; Notario, R.; Maria, P. C., The Gas-Phase Acidities of Very Strong Neutral Bronsted Acids. *Journal of the American Chemical Society* **1994,** *116*, 3047-3057.

67. Razaq, M.; Razaq, A.; Yeager, E.; Desmarteau, D. D.; Singh, S., Oxygen Electroreduction in Perfluorinated Sulfonyl Imides. *Journal of Applied Electrochemistry* **1987,** *17*, 1057-1064.

68. Razaq, M.; Razaq, A.; Yeager, E.; Desmarteau, D. D.; Singh, S., Perfluorosulfonimide as an Additive in Phosphoric-Acid Fuel-Cell. *Journal of the Electrochemical Society* **1989,** *136*, 385-390.

69. Hamrock, S. J.; Yandrasits, M. A., Proton exchange membranes for fuel cell applications. *Polymer Reviews* **2006,** *46*, 219-244.

70. Greenwood, N. N.; Thompson, A., Proton-Switch as a Mechanism for Conduction in Anhydrous Phosphoric Acid. *Proceedings of the Chemical Society of London* **1958**, 352-353.

71. Vilciauskas, L.; Paddison, S. J.; Kreuer, K. D., Ab Initio Modeling of Proton Transfer in Phosphoric Acid Clusters. *Journal of Physical Chemistry A* **2009,** *113*, 9193-9201.

72. Vilciauskas, L.; Tuckerman, M. E.; Bester, G.; Paddison, S. J.; Kreuer, K. D., The mechanism of proton conduction in phosphoric acid. *Nature Chemistry* **2012,** *4*, 461-466.

73. Kotov, S. V.; Pedersen, S. D.; Qiu, W. M.; Qiu, Z. M.; Burton, D. J., Preparation of perfluorocarbon polymers containing phosphonic acid groups. *Journal of Fluorine Chemistry* **1997,** *82*, 13-19.

74. Fujimoto, C. H.; Hickner, M. A.; Cornelius, C. J.; Loy, D. A., Ionomeric poly(phenylene) prepared by diels-alder polymerization: Synthesis and physical properties of a novel polyelectrolyte. *Macromolecules* **2005,** *38*, 5010-5016.

75. Fujimoto, C.; Kim, S.; Stains, R.; Wei, X. L.; Li, L. Y.; Yang, Z. G., Vanadium redox flow battery efficiency and durability studies of sulfonated Diels Alder poly(phenylene)s. *Electrochemistry Communications* **2012,** *20*, 48-51.

76. Tang, Z. J.; Lawton, J. S.; Sun, C. N.; Chen, J. H.; Bright, M. I.; Jones, A. M.; Papandrew, A. B.; Fujimoto, C. H.; Zawodzinski, T. A., Characterization of sulfonated Diels-Alder

poly(phenylene) membranes for electrolyte separators in vanadium redox flow batteries. *Journal of the Electrochemical Society* **2014,** *161*, A1860-A1868.

77. Pezeshki, A. M.; Tang, Z. J.; Fujimoto, C.; Sun, C. N.; Mench, M. M.; Zawodzinski, T. A., Full Cell Study of Diels Alder Poly(phenylene) Anion and Cation Exchange Membranes in Vanadium Redox Flow Batteries. *Journal of the Electrochemical Society* **2016,** *163*, A5154-A5162.

78. Wang, J. T.; Savinell, R. F.; Wainright, J.; Litt, M.; Yu, H., A H-2/O-2 fuel cell using acid doped polybenzimidazole as polymer electrolyte. *Electrochimica Acta* **1996,** *41*, 193-197.

79. Wu, D.; Xu, T. W.; Wu, L.; Wu, Y. H., Hybrid acid-base polymer membranes prepared for application in fuel cells. *Journal of Power Sources* **2009,** *186*, 286-292.

80. Kerres, J.; Ullrich, A.; Meier, F.; Haring, T., Synthesis and characterization of novel acid-base polymer blends for application in membrane fuel cells. *Solid State Ionics* **1999,** *125*, 243-249.

81. Bakangura, E.; Wu, L.; Ge, L.; Yang, Z. J.; Xu, T. W., Mixed matrix proton exchange membranes for fuel cells: State of the art and perspectives. *Progress in Polymer Science* **2016,** *57*, 103-152.

82. Hasani-Sadrabadi, M. M.; Shabani, I.; Soleimani, M.; Moaddel, H., Novel nanofiber-based triple-layer proton exchange membranes for fuel cell applications. *Journal of Power Sources* **2011,** *196*, 4599-4603.

83. Molla, S.; Compan, V., Polyvinyl alcohol nanofiber reinforced Nafion membranes for fuel cell applications. *Journal of Membrane Science* **2011,** *372*, 191-200.

84. Shabani, I.; Hasani-Sadrabadi, M. M.; Haddadi-Asl, V.; Soleimani, M., Nanofiber-based polyelectrolytes as novel membranes for fuel cell applications. *Journal of Membrane Science* **2011,** *368*, 233-240.

85. Takemori, R.; Kawakami, H., Electrospun nanofibrous blend membranes for fuel cell electrolytes. *Journal of Power Sources* **2010,** *195*, 5957-5961.

86. Ballengee, J. B.; Pintauro, P. N., Morphological Control of Electrospun Nafion Nanofiber Mats. *Journal of the Electrochemical Society* **2011,** *158*, B568-B572.

87. Chen, H.; Snyder, J. D.; Elabd, Y. A., Electrospinning and solution properties of Nafion and poly(acrylic acid). *Macromolecules* **2008,** *41*, 128-135.

88. Subianto, S.; Cavaliere, S.; Jones, D. J.; Roziere, J., On Electrospinning of PFSA: A Comparison between Long and Short-Side Chain Ionomers. *Polymer Electrolyte Fuel Cells 11* **2011,** *41*, 1517-1520.

89. Yao, Y. F.; Guo, B. K.; Ji, L. W.; Jung, K. H.; Lin, Z.; Alcoutlabi, M.; Hamouda, H.; Zhang, X. W., Highly proton conductive electrolyte membranes: Fiber-induced long-range ionic channels. *Electrochemistry Communications* **2011,** *13*, 1005-1008.

90. Reid, J. H. Gass-battery. USA, US 757637, **1904**.

91. Reid, J. H. Process of generating electricity. USA, US 736016, **1903**.

92. Asazawa, K.; Yamada, K.; Tanaka, H.; Oka, A.; Taniguchi, M.; Kobayashi, T., A platinum-free zero-carbon-emission easy fuelling direct hydrazine fuel cell for vehicles. *Angewandte Chemie-International Edition* **2007,** *46*, 8024-8027.

93. Zhang, F. X.; Zhang, H. M.; Qu, C.; Ren, J. X., Poly(vinylidene fluoride) based anion conductive ionomer as a catalyst binder for application in anion exchange membrane fuel cell. *Journal of Power Sources* **2011,** *196*, 3099-3103.

94. Suntivich, J.; Gasteiger, H. A.; Yabuuchi, N.; Nakanishi, H.; Goodenough, J. B.; Shao-Horn, Y., Design principles for oxygen-reduction activity on perovskite oxide catalysts for fuel cells and metal-air batteries. *Nature Chemistry* **2011,** *3*, 546-550.

95. Miyazaki, K., Electrocatalysts and Triple-Phase Boundary for Anion-Exchange Membrane Fuel Cells. *Electrochemistry* **2014,** *82*, 730-735.

96. Gulzow, E.; Schulze, M., Long-term operation of AFC electrodes with CO2 containing gases. *Journal of Power Sources* **2004,** *127*, 243-251.

97. Agel, E.; Bouet, J.; Fauvarque, J. F., Characterization and use of anionic membranes for alkaline fuel cells. *Journal of Power Sources* **2001,** *101*, 267-274.

98. Couture, G.; Alaaeddine, A.; Boschet, F.; Ameduri, B., Polymeric materials as anion-exchange membranes for alkaline fuel cells. *Progress in Polymer Science* **2011,** *36*, 1521-1557.

99. Zha, Y. P.; Disabb-Miller, M. L.; Johnson, Z. D.; Hickner, M. A.; Tew, G. N., Metal-Cation-Based Anion Exchange Membranes. *Journal of the American Chemical Society* **2012,** *134*, 4493-4496.

100. Light, T. S.; Licht, S.; Bevilacqua, A. C.; Morash, K. R., The fundamental conductivity and resistivity of water. *Electrochemical and Solid State Letters* **2005,** *8*, E16-E19.

101. Yokota, N.; Ono, H.; Miyake, J.; Nishino, E.; Asazawa, K.; Watanabe, M.; Miyatake, K., Anion conductive aromatic block copolymers containing diphenyl ether or sulfide groups for application to alkaline fuel cells. *Acs Applied Materials & Interfaces* **2014,** *6*, 17044-17052.

102. Zhang, F. X.; Zhang, H. M.; Qu, C., Influence of Solvent on Polymer Prequaternization toward Anion-Conductive Membrane Fabrication for All-Vanadium Flow Battery. *Journal of Physical Chemistry B* **2012,** *116*, 9016-9022.

103. Jangu, C.; Long, T. E., Phosphonium cation-containing polymers: From ionic liquids to polyelectrolytes. *Polymer* **2014,** *55*, 3298-3304.

104. Lin, X. C.; Varcoe, J. R.; Poynton, S. D.; Liang, X. H.; Ong, A. L.; Ran, J.; Li, Y.; Xu, T. W., Alkaline polymer electrolytes containing pendant dimethylimidazolium groups for alkaline membrane fuel cells. *Journal of Materials Chemistry A* **2013,** *1*, 7262-7269.

105. Tomoi, M.; Yamaguchi, K.; Ando, R.; Kantake, Y.; Aosaki, Y.; Kubota, H., Synthesis and thermal stability of novel anion exchange resins with spacer chains. *Journal of Applied Polymer Science* **1997,** *64*, 1161-1167.

106. Hibbs, M. R., Alkaline Stability of Poly(phenylene)-Based Anion Exchange Membranes with Various Cations. *Journal of Polymer Science Part B-Polymer Physics* **2013,** *51*, 1736-1742.

107. Couture, G.; Ladmiral, V.; Ameduri, B., Methods to prepare quaternary ammonium groups-containing alternating poly(chlorotrifluoroethylene-alt-vinyl ether) copolymers. *Rsc Advances* **2015,** *5*, 10243-10253.

108. Wright, A. G.; Holdcroft, S., Hydroxide-Stable Ionenes. *Acs Macro Letters* **2014,** *3*, 444-447.

109. Thomas, O. D.; Soo, K. J. W. Y.; Peckham, T. J.; Kulkarni, M. P.; Holdcroft, S., A Stable Hydroxide-Conducting Polymer. *Journal of the American Chemical Society* **2012,** *134*, 10753-10756.

110. Park, A. M.; Turley, F. E.; Wycisk, R. J.; Pintauro, P. N., Electrospun and Cross-Linked Nanofiber Composite Anion Exchange Membranes. *Macromolecules* **2014,** *47*, 227-235.

111. Ni, J.; Zhao, C. J.; Zhang, G.; Zhang, Y.; Wang, J.; Ma, W. J.; Liu, Z. G.; Na, H., Novel self-crosslinked poly(aryl ether sulfone) for high alkaline stable and fuel resistant alkaline anion exchange membranes. *Chemical Communications* **2011,** *47*, 8943-8945.

112. Mohanty, A. D.; Ryu, C. Y.; Kim, Y. S.; Bae, C., Stable Elastomeric Anion Exchange Membranes Based on Quaternary Ammonium-Tethered Polystyrene-b-poly(ethylene-co-butylene)-b-polystyrene Triblock Copolymers. *Macromolecules* **2015,** *48*, 7085-7095.

113. Zeng, Q. H.; Liu, Q. L.; Broadwell, I.; Zhu, A. M.; Xiong, Y.; Tu, X. P., Anion exchange membranes based on quaternized polystyrene-block-poly(ethylene-ran-butylene)-block-polystyrene for direct methanol alkaline fuel cells. *Journal of Membrane Science* **2010,** *349*, 237-243.

114. Sun, L.; Guo, J. S.; Zhou, J.; Xu, Q. M.; Chu, D.; Chen, R. R., Novel nanostructured high-performance anion exchange ionomers for anion exchange membrane fuel cells. *Journal of Power Sources* **2012,** *202*, 70-77.

115. Heck, B.; Arends, P.; Ganter, M.; Kressler, J.; Stuhn, B., SAXS and TEM studies on poly(styrene)-block-poly(ethene-co-but-1-ene)-block-poly(styrene) in bulk and at various interfaces. *Macromolecules* **1997,** *30*, 4559-4566.

116. Matsen, M. W.; Thompson, R. B., Equilibrium behavior of symmetric ABA triblock copolymer melts. *Journal of Chemical Physics* **1999,** *111*, 7139-7146.

117. Tallury, S. S.; Spontak, R. J.; Pasquinelli, M. A., Dissipative particle dynamics of triblock copolymer melts: A midblock conformational study at moderate segregation. *Journal of Chemical Physics* **2014,** *141*.

118. Abu-Sharkh, B.; AlSunaidi, A., Morphology and conformation analysis of self-assembled triblock copolymer melts. *Macromolecular Theory and Simulations* **2006,** *15*, 507-515.

119. Marino, M. G.; Melchior, J. P.; Wohlfarth, A.; Kreuer, K. D., Hydroxide, halide and water transport in a model anion exchange membrane. *Journal of Membrane Science* **2014,** *464*, 61-71.

120. Kreuer, K. D.; Paddison, S. J.; Spohr, E.; Schuster, M., Transport in proton conductors for fuel-cell applications: Simulations, elementary reactions, and phenomenology. *Chemical Reviews* **2004,** *104*, 4637-4678.

121. Castaneda, S.; Ribadeneira, R., Theoretical Description of the Structural Characteristics of the Quaternized SEBS Anion-Exchange Membrane Using DFT. *Journal of Physical Chemistry C* **2015,** *119*, 28235-28246.

122. Chempath, S.; Boncella, J. M.; Pratt, L. R.; Henson, N.; Pivovar, B. S., Density Functional Theory Study of Degradation of Tetraalkylammonium Hydroxides. *Journal of Physical Chemistry C* **2010,** *114*, 11977-11983.

123. Long, H.; Pivovar, B. S., Hydroxide Degradation Pathways for Substituted Benzyltrimethyl Ammonium: A DFT Study. *Ecs Electrochemistry Letters* **2015,** *4*, F13-F16.

124. Chen, C.; Tse, Y. L. S.; Lindberg, G. E.; Knight, C.; Voth, G. A., Hydroxide Solvation and Transport in Anion Exchange Membranes. *Journal of the American Chemical Society* **2016,** *138*, 991-1000.

125. Han, K. W.; Ko, K. H.; Abu-Hakmeh, K.; Bae, C.; Sohn, Y. J.; Jang, S. S., Molecular Dynamics Simulation Study of a Polysulfone-Based Anion Exchange Membrane in Comparison with the Proton Exchange Membrane. *Journal of Physical Chemistry C* **2014,** *118*, 12577-12587.

126. Takaba, H.; Shimizu, N.; Hisabe, T.; Alam, M. K., Modeling of transport mechanisms of OH- in electrolyte of alkaline fuel cell. *Computational Studies on Battery and Fuel Cell Materials* **2014,** *61*, 63-69.

127. Zhang, W. W.; van Duin, A. C. T., ReaxFF Reactive Molecular Dynamics Simulation of Functionalized Poly(phenylene oxide) Anion Exchange Membrane. *Journal of Physical Chemistry C* **2015,** *119*, 27727-27736.

128. Wang, C.; Paddison, S. J., Hydration and Proton Transfer in Highly Sulfonated Poly(phenylene sulfone) Ionomers: An Ab Initio Study. *Journal of Physical Chemistry A* **2013,** *117*, 650-660.

129. Kumar, M.; Paddison, S. J., Side-chain degradation of perfluorosulfonic acid membranes: An ab initio study. *Journal of Materials Research* **2012,** *27*, 1982-1991.

130. Cui, S. T.; Liu, J. W.; Selvan, M. E.; Keffer, D. J.; Edwards, B. J.; Steele, W. V., A molecular dynamics study of a nafion polyelectrolyte membrane and the aqueous phase structure for proton transport. *Journal of Physical Chemistry B* **2007,** *111*, 2208-2218.

131. Elliott, J. A.; Paddison, S. J., Modelling of morphology and proton transport in PFSA membranes. *Physical Chemistry Chemical Physics* **2007,** *9*, 2602-2618.

132. Wang, C.; Clark, J. K.; Kumar, M.; Paddison, S. J., An ab initio study of the primary hydration and proton transfer of CF(3)SO(3)H and CF(3)O (CF(2))(2)SO(3)H: Effects of the hybrid functional and inclusion of diffuse functions. *Solid State Ionics* **2011,** *199*, 6-13.

133. Wang, C.; Paddison, S. J., Mesoscale modeling of hydrated morphologies of sulfonated polysulfone ionomers. *Soft Matter* **2014,** *10*, 819-830.

134. Wu, D. S.; Paddison, S. J.; Elliott, J. A., Effect of molecular weight on hydrated morphologies of the short-side-chain perfluorosulfonic acid membrane. *Macromolecules* **2009,** *42*, 3358-3367.

135. Mohtadi, R.; Mizuno, F., Magnesium batteries: Current state of the art, issues and future perspectives. *Beilstein Journal of Nanotechnology* **2014,** *5*, 1291-1311.

136. Muldoon, J.; Bucur, C. B.; Oliver, A. G.; Sugimoto, T.; Matsui, M.; Kim, H. S.; Allred, G. D.; Zajicek, J.; Kotani, Y., Electrolyte roadblocks to a magnesium rechargeable battery. *Energy & Environmental Science* **2012,** *5*, 5941-5950.

137. Aurbach, D.; Lu, Z.; Schechter, A.; Gofer, Y.; Gizbar, H.; Turgeman, R.; Cohen, Y.; Moshkovich, M.; Levi, E., Prototype systems for rechargeable magnesium batteries. *Nature* **2000,** *407*, 724-727.

138. Bertasi, F.; Hettige, C.; Sepehr, F.; Bogle, X.; Pagot, G.; Vezzù, K.; Negro, E.; Paddison, S. J.; Greenbaum, S. G.; Vittadello, M.; Di Noto, V., A key concept in magnesium secondary battery electrolytes. *ChemSusChem* **2015,** *8*, 3069-3076.

139. Aurbach, D.; Suresh, G. S.; Levi, E.; Mitelman, A.; Mizrahi, O.; Chusid, O.; Brunelli, M., Progress in rechargeable magnesium battery technology. *Advanced Materials* **2007,** *19*, 4260-4267.

140. Kim, H. S.; Arthur, T. S.; Allred, G. D.; Zajicek, J.; Newman, J. G.; Rodnyansky, A. E.; Oliver, A. G.; Boggess, W. C.; Muldoon, J., Structure and compatibility of a magnesium electrolyte with a sulphur cathode. *Nature Communications* **2011,** *2*, 427.

141. Brown, O. R.; Mcintyre, R., The magnesium and magnesium amalgam electrodes in aprotic organic solvents. A kinetic study. *Electrochimica Acta* **1985,** *30*, 627-633.

142. Genders, J. D.; Pletcher, D., Studies using microelectrodes of the Mg(II)/Mg couple in tetrahydrofuran and propylene carbonate. *Journal of Electroanalytical Chemistry* **1986,** *199*, 93-100.

143. Brenner, A., Note on electrodeposition of magnesium from an organic solution of a magnesium-boron complex. *Journal of the Electrochemical Society* **1971,** *118*, 99-100.

144. Aurbach, D.; Weissman, I.; Gofer, Y.; Levi, E., Nonaqueous magnesium electrochemistry and its application in secondary batteries. *Chemical Record* **2003,** *3*, 61-73.

145. Doe, R. E.; Han, R.; Hwang, J.; Gmitter, A. J.; Shterenberg, I.; Yoo, H. D.; Pour, N.; Aurbach, D., Novel electrolyte solutions comprising fully inorganic salts with high anodic stability for rechargeable magnesium batteries. *Chemical Communications* **2014,** *50*, 243-245.

146. Liebenow, C.; Yang, Z.; Lobitz, P., The electrodeposition of magnesium using solutions of organomagnesium halides, amidomagnesium halides and magnesium organoborates. *Electrochemistry Communications* **2000,** *2*, 641-645.

147. Yang, L. L.; Mcghie, A. R.; Farrington, G. C., Ionic-conductivity in complexes of poly(ethylene oxide) and $MgCl_2$. *Journal of the Electrochemical Society* **1986,** *133*, 1380-1385.

148. Vittadello, M.; Stallworth, P. E.; Alamgir, F. M.; Suarez, S.; Abbrent, S.; Drain, C. M.; Di Noto, V.; Greenbaum, S. G., Polymeric δ-$MgCl_2$ nanoribbons. *Inorganica Chimica Acta* **2006,** *359*, 2513-2518.

149. Di Noto, V.; Fauri, M. Magnesium-based primary (non rechargeable) and secondary (rechargeable) batteries. International Patent Application PCT/EP00/07221, 2447PTW0, July 29th, 1999, **2000**.

150. Kakibe, T.; Hishii, J. Y.; Yoshimoto, N.; Egashira, M.; Morita, M., Binary ionic liquid electrolytes containing organo-magnesium complex for rechargeable magnesium batteries. *Journal of Power Sources* **2012,** *203*, 195-200.

151. Nuli, Y. N.; Yang, J.; Wang, P., Electrodeposition of magnesium film from $BMImBF_4$ ionic liquid. *Applied Surface Science* **2006,** *252*, 8086-8090.

152. Amir, N.; Vestfrid, Y.; Chusid, O.; Gofer, Y.; Aurbach, D., Progress in nonaqueous magnesium electrochemistry. *Journal of Power Sources* **2007,** *174*, 1234-1240.

153. Fuller, J.; Carlin, R. T.; Osteryoung, R. A.; Koranaios, P.; Mantz, R., Anodization and speciation of magnesium in chloride-rich room temperature ionic liquids. *Journal of the Electrochemical Society* **1998,** *145*, 24-28.

154. Koronaios, P.; Osteryoung, R. A., $CaCl_2$ and $MgCl_2$ as buffering agents for room-temperature chloroaluminate ionic liquids. *Journal of the Electrochemical Society* **1999,** *146*, 2995-2999.

155. Wilkes, J. S.; Levisky, J. A.; Wilson, R. A.; Hussey, C. L., Dialkylimidazolium chloroaluminate melts: A new class of room-temperature ionic liquids for electrochemistry, spectroscopy, and synthesis. *Inorganic Chemistry* **1982,** *21*, 1263-1264.

156. Dymek, C. J.; Grossie, D. A.; Fratini, A. V.; Adams, W. W., Evidence for the presence of hydrogen-bonded ion-ion interactions in the molten-salt precursor, 1-methyl-3-ethylimidazolium chloride. *Journal of Molecular Structure* **1989,** *213*, 25-34.

157. Takahashi, S.; Curtiss, L. A.; Gosztola, D.; Koura, N.; Saboungi, M. L., Molecular-orbital calculations and Raman measurements for 1-ethyl-3-methylimidazolium chloroaluminates. *Inorganic Chemistry* **1995,** *34*, 2990-2993.

158. Schreiter, E. R.; Stevens, J. E.; Ortwerth, M. F.; Freeman, R. G., A room-temperature molten salt prepared from $AuCl_3$ and 1-ethyl-3-methylimidazolium chloride. *Inorganic Chemistry* **1999,** *38*, 3935-3937.

159. Salanne, M.; Siqueira, L. J. A.; Seitsonen, A. P.; Madden, P. A.; Kirchner, B., From molten salts to room temperature ionic liquids: Simulation studies on chloroaluminate systems. *Faraday Discussions* **2012,** *154*, 171-188.

160. Dieter, K. M.; Dymek, C. J.; Heimer, N. E.; Rovang, J. W.; Wilkes, J. S., Ionic Structure and Interactions in 1-Methyl-3-Ethyl-Imidazolium Chloride/Alcl3 Molten-Salts. *Journal of the Electrochemical Society* **1987,** *134*, C510-C510.

161. Turner, E. A.; Pye, C. C.; Singer, R. D., Use of ab initio calculations toward the rational design of room temperature ionic liquids. *Journal of Physical Chemistry A* **2003,** *107*, 2277-2288.

162. Hunt, P. A.; Gould, I. R., Structural characterization of the 1-butyl-3-methylimidazolium chloride ion pair using a initio methods. *Journal of Physical Chemistry A* **2006,** *110*, 2269-2282.

163. Katsyuba, S. A.; Zvereva, E. E.; Vidis, A.; Dyson, P. J., Application of density functional theory and vibrational spectroscopy toward the rational design of ionic liquids. *Journal of Physical Chemistry A* **2007,** *111*, 352-370.

164. Heimer, N. E.; Del Sesto, R. E.; Meng, Z. Z.; Wilkes, J. S.; Carper, W. R., Vibrational spectra of imidazolium tetrafluoroborate ionic liquids. *Journal of Molecular Liquids* **2006,** *124*, 84-95.

165. E., W., Principles of Multiscale Modeling. Cambridge University Press: 2011.

166. Pan, J.; Chen, C.; Li, Y.; Wang, L.; Tan, L. S.; Li, G. W.; Tang, X.; Xiao, L.; Lu, J. T.; Zhuang, L., Constructing ionic highway in alkaline polymer electrolytes. *Energy & Environmental Science* **2014,** *7*, 354-360.

167. Groot, R. D., Electrostatic interactions in dissipative particle dynamics-simulation of polyelectrolytes and anionic surfactants. *Journal of Chemical Physics* **2003,** *118*, 11265-11277.

168. Espanol, P.; Revenga, M., Smoothed dissipative particle dynamics. *Physical Review E* **2003,** *67*.

169. Kacar, G.; Peters, E. A. J. F.; de With, G., A generalized method for parameterization of dissipative particle dynamics for variable bead volumes. *Epl* **2013,** *102*, 40009.

170. Gonzalez-Melchor, M.; Mayoral, E.; Velazquez, M. E.; Alejandre, J., Electrostatic interactions in dissipative particle dynamics using the Ewald sums. *Journal of Chemical Physics* **2006,** *125*.

171. Saadat, A.; Khomami, B., Computationally efficient algorithms for incorporation of hydrodynamic and excluded volume interactions in Brownian dynamics simulations: A comparative study of the Krylov subspace and Chebyshev based techniques. *Journal of Chemical Physics* **2014,** *140*.

172. Saadat, A.; Khomami, B., Matrix-free Brownian dynamics simulation technique for semidilute polymeric solutions. *Physical Review E* **2015,** *92*.

173. Quiroga, M. A.; Malek, K.; Franco, A. A., A Multiparadigm Modeling Investigation of Membrane Chemical Degradation in PEM Fuel Cells. *Journal of the Electrochemical Society* **2016,** *163*, F59-F70.

174. Brooks, B. R.; Bruccoleri, R. E.; Olafson, B. D.; States, D. J.; Swaminathan, S.; Karplus, M., Charmm - a Program for Macromolecular Energy, Minimization, and Dynamics Calculations. *Journal of Computational Chemistry* **1983,** *4*, 187-217.

175. Jorgensen, W. L.; Maxwell, D. S.; TiradoRives, J., Development and testing of the OPLS all-atom force field on conformational energetics and properties of organic liquids. *Journal of the American Chemical Society* **1996,** *118*, 11225-11236.

176. Levine, I. N., *Quantum chemistry*. Pearson Education Inc., Upper Saddle River, NJ, **2000**.

177. Cramer, C. J., *Essentials of computational chemistry theories and models*. John Wiley & Sons Ltd., Chichester, West Sussex, UK, **2004**.

178. Hartree, D. R., The wave mechanics of an atom with a non-Coulomb central field. Part I. Theory and methods. *Proceedings of the Cambridge Philosophical Society* **1928,** *24*, 89-110.

179. Hohenberg, P.; Kohn, W., Inhomogeneous electron gas. *Physical Review* **1964,** *136*, B864.

180. Kohn, W.; Sham, L. J., Self-consistent equations including exchange and correlation effects. *Physical Review* **1965,** *140*, A1133.

181. Becke, A. D., Density-functional exchange-energy approximation with correct asymptotic behavior. *Physical Review A* **1988,** *38*, 3098-3100.

182. Lee, C. T.; Yang, W. T.; Parr, R. G., Development of the Colle-Salvetti correlation-energy formula into a functional of the electron density. *Physical Review B* **1988,** *37*, 785-789.

183. Becke, A. D., Density-functional thermochemistry. III. The role of exact exchange. *Journal of Chemical Physics* **1993,** *98*, 5648-5652.

184. Becke, A. D., A New Mixing of Hartree-Fock and Local Density-Functional Theories. *Journal of Chemical Physics* **1993,** *98*, 1372-1377.

185. Hehre, W. J.; Stewart, R. F.; Pople, J. A., Self-Consistent Molecular-Orbital Methods .I. Use of Gaussian Expansions of Slater-Type Atomic Orbitals. *Journal of Chemical Physics* **1969,** *51*, 2657-2664.

186. Binkley, J. S.; Pople, J. A.; Hehre, W. J., Self-Consistent Molecular-Orbital Methods .21. Small Split-Valence Basis-Sets for 1st-Row Elements. *Journal of the American Chemical Society* **1980,** *102*, 939-947.

187. Ditchfield, R.; Hehre, W. J.; Pople, J. A., Self-Consistent Molecular-Orbital Methods. IX. An Extended Gaussian-Type Basis for Molecular-Orbital Studies of Organic Molecules. *Journal of Chemical Physics* **1971,** *54*, 724-728.

188. Hariharan, P. C.; Pople, J. A., Influence of Polarization Functions on Molecular-Orbital Hydrogenation Energies. *Theoretica Chimica Acta* **1973,** *28*, 213-222.

189. Hehre, W. J.; Ditchfield, R.; Pople, J. A., Self-Consistent Molecular-Orbital Methods. 12. Further Extensions of Gaussian-Type Basis Sets for Use in Molecular-Orbital Studies of Organic-Molecules. *Journal of Chemical Physics* **1972,** *56*, 2257-2261.

190. McLean, A. D.; Chandler, G. S., Contracted Gaussian Basis Sets for Molecular Calculations. I. Second Row Atoms, Z=11-18. *Journal of Chemical Physics* **1980,** *72*, 5639-5648.

191. Kirkwood, J. G., Theory of Solutions of Molecules Containing Widely Separated Charges with Special Application to Zwitterions. *Journal of Chemical Physics* **1934,** *2*, 351-361.

192. Onsager, L., Electric moments of molecules in liquids. *Journal of the American Chemical Society* **1936,** *58*, 1486-1493.

193. Miertus, S.; Scrocco, E.; Tomasi, J., Electrostatic Interaction of a Solute with a Continuum - a Direct Utilization of Abinitio Molecular Potentials for the Prevision of Solvent Effects. *Chemical Physics* **1981,** *55*, 117-129.

194. Marenich, A. V.; Cramer, C. J.; Truhlar, D. G., Universal solvation model based on solute electron density and on a continuum model of the solvent defined by the bulk dielectric constant and atomic surface tensions. *Journal of Physical Chemistry B* **2009,** *113*, 6378-6396.

195. Beck, T. L.; Paulaitis, M. E.; Pratt, L. R., *The potential distribution theorem and the statistical thermodynamics of molecular solutions*. Cambridge University Press, **2006**.

196. Guggenheim, E. A., The statistical mechanics of regular solutions. *Proceedings of the Royal Society of London Series A Mathematical and Physical Sciences* **1935,** *148*, 0304-0312.

197. Guggenheim, E. A., The statistical mechanics of co-operative assemblies. *Proceedings of the Royal Society of London Series A Mathematical and Physical Sciences* **1938,** *169*, 0134-0148.

198. Pratt, L. R.; LaViolette, R. A., Quasi-chemical theories of associated liquids. *Molecular Physics* **1998,** *94*, 909-915.

199. Pratt, L. R.; Rempe, S. B., Quasi-chemical theory and implicit solvent models for simulations. *AIP Conf. Proc.* **1999,** *492*, 172-201.

200. Asthagiri, D.; Dixit, P. D.; Merchant, S.; Paulaitis, M. E.; Pratt, L. R.; Rempe, S. B.; Varma, S., Ion selectivity from local configurations of ligands in solutions and ion channels. *Chemical Physics Letters* **2010,** *485*, 1-7.

201. Rogers, D. M.; Jiao, D.; Pratt, L. R.; Rempe, S. B., Structural models and molecular thermodynamics of hydration of ions and small molecules. *Ann. Rep. Comp. Chem.* **2012,** *8*, 71-127.

202. Rempe, S. B.; Pratt, L. R.; Hummer, G.; Kress, J. D.; Martin, R. L.; Redondo, A., The hydration number of Li^+ in liquid water. *Journal of the American Chemical Society* **2000,** *122*, 966-967.

203. Widom, B., Some topics in theory of fluids. *Journal of Chemical Physics* **1963,** *39*, 2808-2812.

204. Widom, B., Potential-distribution theory and the statistical mechanics of fluids. *The Journal of Physical Chemistry* **1982,** *86*, 869-872.

205. Hoogerbrugge, P. J.; Koelman, J., Simulating microscopic hydrodynamic phenomena with dissipative particle dynamics. *Europhysics Letters* **1992,** *19*, 155-160.

206. Español, P.; Warren, P. B., Statistical mechanics of dissipative particle dynamics. *Europhysics Letters* **1995,** *30*, 191-196.

207. Español, P., Dissipative particle dynamics with energy conservation. *Europhysics Letters* **1997,** *40*, 631-636.

208. Groot, R. D.; Warren, P. B., Dissipative particle dynamics: Bridging the gap between atomistic and mesoscopic simulation. *Journal of Chemical Physics* **1997,** *107*, 4423-4435.

209. Groot, R. D.; Rabone, K. L., Mesoscopic simulation of cell membrane damage, morphology change and rupture by nonionic surfactants. *Biophysical Journal* **2001,** *81,* 725-736.

210. Groot, R. D.; Madden, T. J., Dynamic simulation of diblock copolymer microphase separation. *Journal of Chemical Physics* **1998,** *108,* 8713-8724.

211. Cao, X. R.; Xu, G. Y.; Li, Y. M.; Zhang, Z. Q., Aggregation of poly(ethylene oxide)-poly(propylene oxide) block copolymers in aqueous solution: DPD simulation study. *Journal of Physical Chemistry A* **2005,** *109,* 10418-10423.

212. Li, Y.; Zhang, P.; Dong, F. L.; Cao, X. L.; Song, X. W.; Cui, X. H., The array and interfacial activity of sodium dodecyl benzene sulfonate and sodium oleate at the oil/water interface. *Journal of Colloid and Interface Science* **2005,** *290,* 275-280.

213. Shillcock, J. C.; Lipowsky, R., The computational route from bilayer membranes to vesicle fusion. *Journal of Physics: Condensed Matter* **2006,** *18,* S1191-S1219.

214. Wu, D. S.; Paddison, S. J.; Elliott, J. A.; Hamrock, S. J., Mesoscale modeling of hydrated morphologies of 3M perfluorosulfonic acid-based fuel cell electrolytes. *Langmuir* **2010,** *26,* 14308-14315.

215. Elliott, J. A.; Wu, D. S.; Paddison, S. J.; Moore, R. B., A unified morphological description of Nafion membranes from SAXS and mesoscale simulations. *Soft Matter* **2011,** *7,* 6820-6827.

216. Moeendarbary, E.; Ng, T. Y.; Zangeneh, M., Dissipative particle dynamics: Introduction, methodology and complex fluid applications - a review. *International Journal of Applied Mechanics* **2009,** *1,* 737-763.

217. Moeendarbary, E.; Ng, T. Y.; Zangeneh, M., Dissipative particle dynamics in soft matter and polymeric applications - a review. *International Journal of Applied Mechanics* **2010,** *2,* 161-190.

218. Lee, M. T.; Vishnyakov, A.; Neimark, A. V., Calculations of critical micelle concentration by dissipative particle dynamics simulations: The role of chain rigidity. *Journal of Physical Chemistry B* **2013,** *117*, 10304-10310.

219. Vishnyakov, A.; Talaga, D. S.; Neimark, A. V., DPD simulation of protein conformations: From alpha-helices to beta-structures. *Journal of Physical Chemistry Letters* **2012,** *3*, 3081-3087.

220. Shillcock, J. C.; Lipowsky, R., Equilibrium structure and lateral stress distribution of amphiphilic bilayers from dissipative particle dynamics simulations. *Journal of Chemical Physics* **2002,** *117*, 5048-5061.

221. Yamamoto, S.; Maruyama, Y.; Hyodo, S., Dissipative particle dynamics study of spontaneous vesicle formation of amphiphilic molecules. *Journal of Chemical Physics* **2002,** *116*, 5842-5849.

222. Alexeev, A.; Uspal, W. E.; Balazs, A. C., Harnessing Janus nanoparticles to create controllable pores in membranes. *Acs Nano* **2008,** *2*, 1117-1122.

223. Reith, D.; Meyer, H.; Muller-Plathe, F., Mapping atomistic to coarse-grained polymer models using automatic simplex optimization to fit structural properties. *Macromolecules* **2001,** *34*, 2335-2345.

224. Tschop, W.; Kremer, K.; Batoulis, J.; Burger, T.; Hahn, O., Simulation of polymer melts. I. Coarse-graining procedure for polycarbonates. *Acta Polymerica* **1998,** *49*, 61-74.

225. Maiti, A.; Wescott, J.; Kung, P., Nanotube-polymer composites: Insights from Flory-Huggins theory and mesoscale simulations. *Molecular Simulation* **2005,** *31*, 143-149.

226. Maiti, A.; McGrother, S., Bead-bead interaction parameters in dissipative particle dynamics: Relation to bead-size, solubility parameter, and surface tension. *Journal of Chemical Physics* **2004,** *120*, 1594-1601.

227. Lee, M.-T.; Mao, R.; Vishnyakov, A.; Neimark, A. V., Parametrization of Chain Molecules in Dissipative Particle Dynamics. *The Journal of Physical Chemistry B* **2016**.

228. Sepehr, F.; Paddison, S. J., Dissipative particle dynamics interaction parameters from *ab initio* calculations. *Chemical Physics Letters* **2016,** *645*, 20-26.

229. Sepehr, F.; Paddison, S. J., The solvation structure and thermodynamics of aqueous vanadium cations. *Chemical Physics Letters* **2013,** *585*, 53-58.

230. Sepehr, F.; Paddison, S. J., Effect of sulfuric and triflic acids on the hydration of vanadium cations: An *ab initio* study. *Journal of Physical Chemistry A* **2015,** *119*, 5749-5761.

231. Frisch, M. J.; Trucks, G. W.; Schlegel, H. B.; Scuseria, G. E.; Robb, M. A.; Cheeseman, J. R.; Scalmani, G.; Barone, V.; Mennucci, B.; Petersson, G. A.; Nakatsuji, H.; Caricato, M.; Li, X.; Hratchian, H. P.; Izmaylov, A. F.; Bloino, J.; Zheng, G.; Sonnenberg, J. L.; Hada, M.; Ehara, M.; Toyota, K.; Fukuda, R.; Hasegawa, J.; Ishida, M.; Nakajima, T.; Honda, Y.; Kitao, O.; Nakai, H.; Vreven, T.; Montgomery, J. A.; Peralta, J. E.; Ogliaro, F.; Bearpark, M.; Heyd, J. J.; Brothers, E.; Kudin, K. N.; Staroverov, V. N.; Kobayashi, R.; Normand, J.; Raghavachari, K.; Rendell, A.; Burant, J. C.; Iyengar, S. S.; Tomasi, J.; Cossi, M.; Rega, N.; Millam, J. M.; Klene, M.; Knox, J. E.; Cross, J. B.; Bakken, V.; Adamo, C.; Jaramillo, J.; Gomperts, R.; Stratmann, R. E.; Yazyev, O.; Austin, A. J.; Cammi, R.; Pomelli, C.; Ochterski, J. W.; Martin, R. L.; Morokuma, K.; Zakrzewski, V. G.; Voth, G. A.; Salvador, P.; Dannenberg, J. J.; Dapprich, S.; Daniels, A. D.; Farkas; Foresman, J. B.; Ortiz, J. V.; Cioslowski, J.; Fox, D. J., Gaussian 09, Revision A.01. Gaussian 09, Revision A.01, Wallingford CT, 2009.

232. Breneman, C. M.; Wiberg, K. B., Determining atom-centered monopoles from molecular electrostatic potentials. The need for high sampling density in formamide conformational analysis. *Journal of Computational Chemistry* **1990,** *11*, 361-373.

233. Cotton, F. A.; Falvello, L. R.; Llusar, R.; Libby, E.; Murillo, C. A.; Schwotzer, W., Synthesis and characterization of four vanadium(II) compounds, including vanadium(II) sulfate hexahydrate and vanadium(II) saccharinates. *Inorganic Chemistry* **1986,** *25*, 3423-3428.

234. Marcus, Y., Thermodynamics of solvation of ions. Part 5. Gibbs free-energy of hydration at 298.15 K. *Journal of the Chemical Society, Faraday Transactions* **1991,** *87*, 2995-2999.

235. Asthagiri, D.; Pratt, L. R.; Paulaitis, M. E.; Rempe, S. B., Hydration structure and free energy of biomolecularly specific aqueous dications, including Zn^{2+} and first transition row metals. *Journal of the American Chemical Society* **2004,** *126*, 1285-1289.

236. Jiao, D.; Leung, K.; Rempe, S. B.; Nenoff, T. M., First principles calculations of atomic nickel redox potentials and dimerization free energies: A study of metal nanoparticle growth. *Journal of Chemical Theory and Computation* **2011,** *7*, 485-495.

237. Asthagiri, D.; Pratt, L. R., Quasi-chemical study of Be^{2+}(aq) speciation. *Chemical Physics Letters* **2003,** *371*, 613-619.

238. Merchant, S.; Asthagiri, D., Thermodynamically dominant hydration structures of aqueous ions. *Journal of Chemical Physics* **2009,** *130*, 195102.

239. Merchant, S.; Shah, J. K.; Asthagiri, D., Water coordination structures and the excess free energy of the liquid. *Journal of Chemical Physics* **2011,** *134*, 124514.

240. Merchant, S.; Dixit, P. D.; Dean, K. R.; Asthagiri, D., Ion-water clusters, bulk medium effects, and ion hydration. *Journal of Chemical Physics* **2011,** *135*, 054505.

241. Varma, S.; Rempe, S. B., Tuning ion coordination architectures to enable selective partitioning. *Biophysical Journal* **2007,** *93*, 1093-1099.

242. Varma, S.; Rempe, S. B., Structural Transitions in Ion Coordination Driven by Changes in Competition for Ligand Binding. *Journal of the American Chemical Society* **2008,** *130*, 15405-15419.

243. Loeffler, H. H.; Yague, J. I.; Rode, B. M., QM/MM-MD simulation of hydrated vanadium(II) ion. *Chemical Physics Letters* **2002,** *363*, 367-371.

244. Rotzinger, F. P., Performance of molecular orbital methods and density functional theory in the computation of geometries and energies of metal aqua ions. *Journal of Physical Chemistry B* **2005,** *109*, 1510-1527.

245. Vijayakumar, M.; Li, L. Y.; Nie, Z. M.; Yang, Z. G.; Hu, J. Z., Structure and stability of hexa-aqua V(III) cations in vanadium redox flow battery electrolytes. *Physical Chemistry Chemical Physics* **2012,** *14*, 10233-10242.

246. Cotton, F. A.; Fair, C. K.; Lewis, G. E.; Mott, G. N.; Ross, F. K.; Schultz, A. J.; Williams, J. M., Precise structural characterizations of the hexaaquovanadium(III) and diaquohydrogen ions. X-ray and neutron diffraction studies of $[V(H_2O)_6][H_5O_2](CF_3SO_3)_4$. *Journal of the American Chemical Society* **1984,** *106*, 5319-5323.

247. Hugi, A. D.; Helm, L.; Merbach, A. E., Water exchange on hexaaquavanadium(III): A variable-temperature and variable-pressure ^{17}O-NMR study at 1.4 and 4.7 Tesla. *Helvetica Chimica Acta* **1985,** *68*, 508-521.

248. Selbin, J., The chemistry of oxovanadium(IV). *Chemical Reviews* **1965,** *65*, 153-175.

249. Ballhausen, C. J.; Gray, H. B., The electronic structure of the vanadyl ion. *Inorganic Chemistry* **1962,** *1*, 111-122.

250. Winkler, J. R.; Gray, H. B., *Molecular electronic structures of transition metal complexes I*. Springer: **2011**; Vol. 142, p 17-28.

251. Greenwood, N. N.; Earnshaw, A., Vanadium, niobium and tantalum. In *Chemistry of the Elements*, Butterworth-Heinemann: Oxford, **1997**; pp 976-1001.

252. Sadoc, A.; Messaoudi, S.; Furet, E.; Gautier, R.; Le Fur, E.; Le Polles, L.; Pivan, J. Y., Structure and stability of VO_2^+ in aqueous solution: A Car-Parrinello and static *ab initio* study. *Inorganic Chemistry* **2007,** *46*, 4835-4843.

253. Harnung, S. E.; Larsen, E.; Pedersen, E. J., Structure of monovanadates in aqueous solution. *Acta Chemica Scandinavica* **1993,** *47*, 674-682.

254. Cruywagen, J. J.; Heyns, J. B. B.; Westra, A. N., Protonation equilibria of mononuclear vanadate: Thermodynamic evidence for the expansion of the coordination number in VO_2^+. *Inorganic Chemistry* **1996,** *35*, 1556-1559.

255. Zhang, Y. *Ab initio* study of low pH vanadium(V). M.S. Thesis, Saint Mary's University, Halifax, Canada, **March 2012**.

256. Gharib, F.; Sayadian, M.; Shame, A.; Mobasher-Moghaddam, M., Formation equilibria of vanadium(V) species in different ionic media: Salt effect and protonation constant. *Journal of Molecular Liquids* **2008,** *138*, 9-13.

257. Wang, Z. L.; Kang, Z. C., *Functional and smart materials: Structural evolution and structure analysis*. Plenum Press, New York, **1998**.

258. Inada, Y.; Mohammed, A. M.; Loeffler, H. H.; Rode, B. M., Hydration structure and water exchange reaction of Nickel(II) ion: Classical and QM/MM Simulations. *Journal of Physical Chemistry A* **2002,** *106*, 6783-6791.

259. Kritayakornupong, C.; Yague, J. I.; Rode, B. M., Molecular dynamics Simulations of the hydrated trivalent transition metal ions Ti3+, Cr3+, and Co3+. *Journal of Physical Chemistry A* **2002,** *106*, 10584-10589.

260. Travis, K. P.; Bankhead, M.; Good, K.; Owens, S. L., New parametrization method for dissipative particle dynamics. *Journal of Chemical Physics* **2007,** *127*, 014109.

261. MaterialsStudio *Materials Studio*, Accelrys Inc., San Diego, CA, USA, **2005**.

262. Dobbs, K. D.; Hehre, W. J., Molecular-Orbital Theory of the Properties of Inorganic and Organometallic Compounds .5. Extended Basis-Sets for 1st-Row Transition-Metals. *Journal of Computational Chemistry* **1987,** *8*, 861-879.

263. Gordon, M. S.; Binkley, J. S.; Pople, J. A.; Pietro, W. J.; Hehre, W. J., Self-Consistent Molecular-Orbital Methods .22. Small Split-Valence Basis-Sets for 2nd-Row Elements. *Journal of the American Chemical Society* **1982,** *104*, 2797-2803.

264. Boys, S. F.; Bernardi, F., Calculation of Small Molecular Interactions by Differences of Separate Total Energies - Some Procedures with Reduced Errors. *Molecular Physics* **1970,** *19*, 553-&.

265. Pivkin, I. V.; Karniadakis, G. E., Coarse-graining limits in open and wall-bounded dissipative particle dynamics systems. *Journal of Chemical Physics* **2006,** *124*.

266. Wijmans, C. M.; Smit, B.; Groot, R. D., Phase behavior of monomeric mixtures and polymer solutions with soft interaction potentials. *Journal of Chemical Physics* **2001,** *114*, 7644-7654.

267. Kranenburg, M.; Nicolas, J. P.; Smit, B., Comparison of mesoscopic phospholipid-water models. *Physical Chemistry Chemical Physics* **2004,** *6*, 4142-4151.

268. Ortiz, V.; Nielsen, S. O.; Discher, D. E.; Klein, M. L.; Lipowsky, R.; Shillcock, J., Dissipative particle dynamics simulations of polymersomes. *Journal of Physical Chemistry B* **2005,** *109*, 17708-17714.

269. Sun, C. X.; Chen, J.; Zhang, H. M.; Han, X.; Luo, Q. T., Investigations on transfer of water and vanadium ions across Nafion membrane in an operating vanadium redox flow battery. *Journal of Power Sources* **2010,** *195*, 890-897.

270. Xi, J. Y.; Wu, Z. H.; Teng, X. G.; Zhao, Y. T.; Chen, L. Q.; Qiu, X. P., Self-assembled polyelectrolyte multilayer modified Nafion membrane with suppressed vanadium ion crossover for vanadium redox flow batteries. *Journal of Materials Chemistry* **2008,** *18*, 1232-1238.

271. Tuckerman, M. E.; Marx, D.; Parrinello, M., The nature and transport mechanism of hydrated hydroxide ions in aqueous solution. *Nature* **2002,** *417*, 925-929.

272. Ge, L.; Bernasconi, L.; Hunt, P., Linking electronic and molecular structure: insight into aqueous chloride solvation. *Physical Chemistry Chemical Physics* **2013,** *15*, 13169-13183.

273. Sugimoto, M.; Sakai, K.; Aoki, Y.; Taniguchi, T.; Koyama, K.; Ueda, T., Rheology and Morphology Change with Temperature of SEBS/Hydrocarbon Oil Blends. *Journal of Polymer Science Part B-Polymer Physics* **2009,** *47*, 955-965.

274. Plimpton, S., Fast Parallel Algorithms for Short-Range Molecular-Dynamics. *Journal of Computational Physics* **1995,** *117*, 1-19.

275. Martinez, L.; Andrade, R.; Birgin, E. G.; Martinez, J. M., PACKMOL: A Package for Building Initial Configurations for Molecular Dynamics Simulations. *Journal of Computational Chemistry* **2009,** *30*, 2157-2164.

276. Humphrey, W.; Dalke, A.; Schulten, K., VMD: Visual molecular dynamics. *Journal of Molecular Graphics & Modelling* **1996,** *14*, 33-38.

277. Chantawansri, T. L.; Duncan, A. J.; Ilavsky, J.; Stokes, K. K.; Berg, M. C.; Mrozek, R. A.; Lenhart, J. L.; Beyer, F. L.; Andzelm, J. W., Phase Behavior of SEBS Triblock Copolymer Gels. *Journal of Polymer Science Part B-Polymer Physics* **2011,** *49*, 1479-1491.

278. Weiss, R. A.; Sen, A.; Pottick, L. A.; Willis, C. L., Block copolymer ionomers: thermoplastic elastomers possessing two distinct physical networks. *Polymer Communications* **1990,** *31*, 220-223.

279. Marx, D.; Chandra, A.; Tuckerman, M. E., Aqueous Basic Solutions: Hydroxide Solvation, Structural Diffusion, and Comparison to the Hydrated Proton. *Chemical Reviews* **2010,** *110*, 2174-2216.

280. Halle, B.; Karlstrom, G., Prototropic Charge Migration in Water .1. Rate Constants in Light and Heavy-Water and in Salt Solution from O-17 Spin Relaxation. *Journal of the Chemical Society-Faraday Transactions Ii* **1983,** *79*, 1031-1046.

281. Tuckerman, M. E.; Chandra, A.; Marx, D., Structure and dynamics of OH^-(aq). *Accounts of Chemical Research* **2006,** *39*, 151-158.

282. Atkins, P.; de Paula, J., *Atkins' Physical Chemistry*. 7th ed.; Oxford University Press, Oxford, **2002**.

283. Lee, S. H.; Rasaiah, J. C., Proton transfer and the mobilities of the H+ and OH- ions from studies of a dissociating model for water. *Journal of Chemical Physics* **2011,** *135*.

284. Mills, R., Self-Diffusion in Normal and Heavy-Water in Range 1-45 Degrees. *Journal of Physical Chemistry* **1973,** *77*, 685-688.

285. Krynicki, K.; Green, C. D.; Sawyer, D. W., Pressure and Temperature-Dependence of Self-Diffusion in Water. *Faraday Discussions* **1978,** *66*, 199-208.

286. Bertasi, F.; Sepehr, F.; Pagot, G.; Paddison, S. J.; Di Noto, V., Toward a magnesium-iodine battery. *Advanced Functional Materials* **2016,** *26*, 4860-4865.

287. Glukhovtsev, M. N.; Pross, A.; Mcgrath, M. P.; Radom, L., Extension of Gaussian-2 (G2) theory to bromine- and iodine-containing molecules: Use of effective core potentials. *Journal of Chemical Physics* **1995,** *103*, 1878-1885.

288. Katsyuba, S.; Vandyukova, E., Scaled quantum mechanical computations of vibrational spectra of organoelement molecules, containing the atoms P, S, and Cl. *Chemical Physics Letters* **2003,** *377*, 658-662.

289. Gale, R. J.; Gilbert, B.; Osteryoung, R. A., Raman-Spectra of Molten Aluminum-Chloride - 1-Butylpyridinium Chloride Systems at Ambient-Temperatures. *Inorganic Chemistry* **1978,** *17*, 2728-2729.

290. Begun, G. M.; Boston, C. R.; Torsi, G.; Mamantov, G., Raman Spectra of Molten Aluminum Trihalide-Alkali Halide Systems. *Inorganic Chemistry* **1971,** *10*, 886-889.

291. Manteghetti, A.; Potier, A., Vibrational Spectroscopy and Normal Coordinate Analysis of Mu-Halo Halo Hexahalodialuminates Ions Al2cl7,Al2br7,Al2i7 in Some Salts and in Friedel-Crafts Solutions. *Spectrochimica Acta Part a-Molecular and Biomolecular Spectroscopy* **1982,** *38*, 141-148.

292. Clark, J. K.; Paddison, S. J.; Eikerling, M.; Dupuis, M.; Zawodzinski, T. A., A Comparative Ab Initio Study of the Primary Hydration and Proton Dissociation of Various Imide and Sulfonic Acid Ionomers. *Journal of Physical Chemistry A* **2012,** *116*, 1801-1813.

293. Clark, J. K.; Paddison, S. J.; Hamrock, S. J., The effect of hydrogen bond reorganization and equivalent weight on proton transfer in 3M perfluorosulfonic acid ionomers. *Physical Chemistry Chemical Physics* **2012,** *14*, 16349-16359.

294. Paddison, S. J., The modeling of molecular structure and ion transport in sulfonic acid based ionomer membranes. *Journal of New Materials for Electrochemical Systems* **2001,** *4*, 197-207.

295. Eikerling, M.; Paddison, S. J.; Zawodzinski, T. A., Molecular orbital calculations of proton dissociation and hydration of various acidic moieties for fuel cell polymers. *Journal of New Materials for Electrochemical Systems* **2002,** *5*, 15-23.

296. Paddison, S. J.; Zawodzinski, T. A., Molecular modeling of the pendant chain in Nafion (R). *Solid State Ionics* **1998,** *113*, 333-340.

297. Bandy, A. R.; Ianni, J. C., Study of the hydrates of H2SO4 using density functional theory. *Journal of Physical Chemistry A* **1998,** *102*, 6533-6539.

298. Loerting, T.; Liedl, K. R., Water-mediated proton transfer: A mechanistic investigation on the example of the hydration of sulfur oxides. *Journal of Physical Chemistry A* **2001,** *105*, 5137-5145.

299. Li, S. J.; Qian, W.; Tao, F. M., Ionic dissociation of methanesulfonic acid in small water clusters. *Chemical Physics Letters* **2007,** *438*, 190-195.

300. Li, S. J.; Tao, F. M.; Gu, R. N., Theoretical study on the ionic dissociation of halosulfonic acids in small water clusters. *Chemical Physics Letters* **2006,** *426*, 1-7.

301. Scott, J. R.; Wright, J. B., Computational investigation of the solvation of nitric acid: Formation of the NO3- and H3O+ ion pair. *Journal of Physical Chemistry A* **2004,** *108*, 10578-10585.

302. Re, S. Y., Enhanced stability of non-proton-transferred clusters of hydrated hydrogen fluoride HF(H2O)(n) (n=1-7): A molecular orbital study. *Journal of Physical Chemistry A* **2001,** *105*, 9725-9735.

303. Wang, C.; Paddison, S. J., Proton transfer in functionalized phosphonic acid molecules. *Physical Chemistry Chemical Physics* **2010,** *12*, 970-81.

304. Paddison, S. J.; Kreuer, K. D.; Maier, J., About the choice of the protogenic group in polymer electrolyte membranes: Ab initio modelling of sulfonic acid, phosphonic acid, and imidazole functionalized alkanes. *Physical Chemistry Chemical Physics* **2006,** *8*, 4530-4542.

305. Ishimoto, T.; Ogura, T.; Koyama, M., Stability and hydration structure of model perfluorosulfonic acid compound systems, CF3SO3H(H2O)(n) (n=1-4), and its isotopomer by the direct treatment of H/D nuclear quantum effects. *Computational and Theoretical Chemistry* **2011,** *975*, 92-98.

306. Trummal, A.; Lipping, L.; Kaljurand, I.; Koppel, I. A.; Leito, I., Acidity of Strong Acids in Water and Dimethyl Sulfoxide. *Journal of Physical Chemistry A* **2016,** *120*, 3663-3669.

307. Guthrie, J. P., Hydrolysis of Esters of Oxy Acids - Pka Values for Strong Acids - Bronsted Relationship for Attack of Water at Methyl - Free-Energies of Hydrolysis of Esters of Oxy Acids - and a Linear Relationship between Free-Energy of Hydrolysis and Pka Holding over a Range of 20 Pk Units. *Canadian Journal of Chemistry-Revue Canadienne De Chimie* **1978,** *56*, 2342-2354.

308. Kolthoff, I. M., *Treatise on Analytical Chemistry*. Interscience Encyclopedia, Inc., New York, **1959**.

309. Albert, A.; Serjeant, E. P., *Ionization constants of acids and bases*. Methuen, London, **1962**.

310. Larson, J. W.; Pippin, M., Thermodynamics of Ionization of Hypophosphorous and Phosphorus-Acids - Substituent Effects on 2nd Row Oxy Acids. *Polyhedron* **1989,** *8*, 527-530.

311. Harris, D. C., *Quantitative Chemical Analysis (Eighth Edition)*. W. H. Freeman and Company, New York, **2010**.

312. Re, S.; Osamura, Y.; Morokuma, K., Coexistence of neutral and ion-pair clusters of hydrated sulfuric acid H2SO4(H2O)n (n=1-5) - A molecular orbital study. *Journal of Physical Chemistry A* **1999,** *103*, 3535-3547.

313. Sugawara, S.; Yoshikawa, T.; Takayanagi, T.; Shiga, M.; Tachikawa, M., Quantum Proton Transfer in Hydrated Sulfuric Acid Clusters: A Perspective from Semiempirical Path Integral Simulations. *Journal of Physical Chemistry A* **2011,** *115*, 11486-11494.

314. Arstila, H.; Laasonen, K.; Laaksonen, A., Ab initio study of gas-phase sulphuric acid hydrates containing 1 to 3 water molecules. *Journal of Chemical Physics* **1998,** *108*, 1031-1039.

315. McCurdy, P. R.; Hess, W. P.; Xantheas, S. S., Nitric acid-water complexes: Theoretical calculations and comparison to experiment. *Journal of Physical Chemistry A* **2002,** *106*, 7628-7635.

316. Odde, S.; Mhin, B. J.; Lee, K. H.; Lee, H. M.; Tarakeshwar, P.; Kim, K. S., Hydration and dissociation of hydrogen fluoric acid (HF). *Journal of Physical Chemistry A* **2006,** *110*, 7918-7924.

Appendices

Appendix A Computer Programs and Routines

MATLAB code to generate coordinates of one macromolecule of AEM ionomer type:

```
%%% generate structure of a chain
%%% topology: (B[S][S TMM TMA])8 (E)152 (B[S][S TMM TMA])8
clc
clear

nSblock=8; %%% number of B beads in one block
nEblock=152; %%% number of E beads
nBranch=2; %%% number of beads added to each B bead as a branch

data = fopen('SEBS_8_152_8.xyz', 'w');
fprintf(data, '%d\n \n', nEblock+nSblock*2+nSblock*4+2*nSblock*2);

for i=1:nSblock
    fprintf(data, '%s\t %f\t %f\t %f\n', 'B', i, 1, 0);
    fprintf(data, '%s\t %f\t %f\t %f\n', 'S', i, 2, 0);
    fprintf(data, '%s\t %f\t %f\t %f\n', 'S', i, 0, 0);
end

for i=nSblock+1:nEblock+nSblock
    fprintf(data, '%s\t %f\t %f\t %f\n', 'E', i, 1, 0);
end

for i=nEblock+nSblock+1:(nEblock+nSblock*2)
    fprintf(data, '%s\t %f\t %f\t %f\n', 'B', i, 1, 0);
    fprintf(data, '%s\t %f\t %f\t %f\n', 'S', i, 2, 0);
    fprintf(data, '%s\t %f\t %f\t %f\n', 'S', i, 0, 0);
end

for i=1:nSblock
```

```
    fprintf(data, '%s\t %f\t %f\t %f\n', 'M', i, 3, 0);
    fprintf(data, '%s\t %f\t %f\t %f\n', 'A', i, 4, 0);
end

for i=nEblock+nSblock+1:(nEblock+nSblock*2)
    fprintf(data, '%s\t %f\t %f\t %f\n', 'M', i, 3, 0);
    fprintf(data, '%s\t %f\t %f\t %f\n', 'A', i, 4, 0);
end

fclose(data);
```

MATLAB code to generate topological data files for a macromolecule of AEM ionomer type:

```
function Lammps_topology_file

clear
clc

tic
%%% topology
%%% (B[S][S TMM TMA])8 (E)152 (B[S][S TMM TMA])8
nmon=1;
nSblock=8;
nEblock=152;
nBB=nSblock*3*2+nEblock;

%%%%%%% Bonds
output_b  = fopen('bond.data', 'w');
for i=1:nSblock
    atom = (i-1)*3+1;
    fprintf(output_b, '%d   %d\n', atom, atom+3);
    fprintf(output_b, '%d   %d\n', atom, atom+1);
    fprintf(output_b, '%d   %d\n', atom, atom+2);
    fprintf(output_b, '%d   %d\n', atom+1, (i*2-1)+nBB);
    fprintf(output_b, '%d   %d\n', (i*2-1)+nBB, (i*2)+nBB);
end
for i= nSblock*3+1:nSblock*3+nEblock
    fprintf(output_b, '%d   %d\n', i, i+1);
end
for i= 1:(nSblock-1)
    atom = nSblock*3+nEblock+(i-1)*3+1;
    fprintf(output_b, '%d   %d\n', atom, atom+3);
    fprintf(output_b, '%d   %d\n', atom, atom+1);
    fprintf(output_b, '%d   %d\n', atom, atom+2);
    fprintf(output_b, '%d   %d\n', atom+1, (i*2-1)+nBB+nSblock*2);
```

```
    fprintf(output_b, '%d   %d\n', (i*2-1)+nBB+nSblock*2,
(i*2)+nBB+nSblock*2);
end
atom = nEblock+nSblock*6-2;
fprintf(output_b, '%d   %d\n', atom, atom+1);
fprintf(output_b, '%d   %d\n', atom, atom+2);
fprintf(output_b, '%d   %d\n', atom+1, nBB+nSblock*4-1);
fprintf(output_b, '%d   %d\n', nBB+nSblock*4-1, nBB+nSblock*4);

fclose(output_b);

%%%%%%% Angles
output_a  = fopen('angle.data', 'w');
% BBB
for i=1:(nSblock-2)
    atom=(i-1)*3+1;
    fprintf(output_a, '%d   %d   %d\n', atom, atom+3, atom+2*3);
end
%BBE
atom=(nSblock-2)*3+1;
fprintf(output_a, '%d   %d   %d\n', atom, atom+3, atom+6);
%BEE
fprintf(output_a, '%d   %d   %d\n', atom+3, atom+6, atom+7);

% EEE
for i=nSblock*3+1:nSblock*3+nEblock-2
    fprintf(output_a, '%d   %d   %d\n', i, i+1, i+2);
end

atom=nSblock*3+nEblock-1;
%EEB
fprintf(output_a, '%d   %d   %d\n', atom, atom+1, atom+2);
%EBB
fprintf(output_a, '%d   %d   %d\n', atom+1, atom+2, atom+5);
```

```
% BBB
EndE = nEblock+nSblock*3;
for i=1:(nSblock-2)
    atom=(i-1)*3+EndE+1;
    fprintf(output_a, '%d   %d   %d\n', atom, atom+3, atom+2*3);
end

% B-S-TMM
for i=1:nSblock
    atom=(i-1)*3+1;
    fprintf(output_a, '%d   %d   %d\n', atom, atom+1, (i*2-1)+nBB);
    fprintf(output_a, '%d   %d   %d\n', atom+EndE, atom+EndE+1, (i*2-
1)+nBB+nSblock*2);
end
% S-TMM-TMA
for i=1:nSblock
    atom=(i-1)*3+1;
    fprintf(output_a, '%d   %d   %d\n', atom+1, (i*2-1)+nBB,
(i*2)+nBB);
    fprintf(output_a, '%d   %d   %d\n', atom+EndE+1, (i*2-
1)+nBB+nSblock*2, (i*2)+nBB+nSblock*2);
end
fclose(output_b);

toc
end
```

FORTRAN code to generate LAMMPS data file:

```
       program generate
c
c     generate input configuration for hydrated AEM electrolyte system

      implicit none

      integer index,nm
      integer Nsys,nmol,Nbond,Nangle
      integer dex
      integer moltag
      integer ia1,ia2,ia3
      integer i,j,k,ii
      integer mol(2000000)
      integer atom(2000000)
      integer b1(1000),b2(1000),bond(1000)
      integer ha1(1000),ha2(1000),ha3(1000),angle(1000)

      double precision xlo,xhi
      double precision ylo,yhi
      double precision zlo,zhi
      double precision x(2000000),y(2000000),z(2000000)
      double precision q(2000000)

      CHARACTER (LEN=6) a1
      CHARACTER (LEN=2) a2
      CHARACTER (LEN=70) a3
      CHARACTER (LEN=1) a4


      dex=0
c     write(*,*) 'input Nsys, number of particles'
c     read(*,*) Nsys
```

```
      Nsys=648000
      moltag=1

      nm = 232                !number of beads per chain
      nmol = 2314                !number of chains
      Nbond = 231
      Nangle = 198

10    format (I2,  3(3x,f8.4))

      open(unit=10, file="mixtureAEM.xyz")
      read(10,*) a3
      read(10,*) a3


      do i=1,Nsys               !


         read(10,*) a4,x(i),y(i),z(i)
         if (a4.eq.'B') then
            atom(i)=1
         elseif (a4.eq.'S') then
            atom(i)=2
         elseif (a4.eq.'E') then
            atom(i)=3
         elseif (a4.eq.'M') then
            atom(i)=4
         elseif (a4.eq.'A') then
            atom(i)=5
         elseif (a4.eq.'O') then
            atom(i)=6
         elseif (a4.eq.'W') then
            atom(i)=7
         endif
```

```
         q(i)=0.0

      enddo


      write(*,*) "done with reading molecules"

      moltag=1


      do i=1,nmol
         do j=1,nm

            mol(dex+j)=moltag

         enddo
         moltag=moltag+1
         dex=dex+nm
      enddo

      do i =1, Nsys-nmol*nm
         mol(nmol*nm+i)= nmol+i
      enddo


!     stop
      xlo=0.
      ylo=0.
      zlo=0.
      xhi=240.
      yhi=240.
      zhi=240.


c     !write out the data file in lammps format
```

```
      open(unit=5, file="DPD.data", access= 'append')
      write(5,*) "LAMMPS Description"
      write(5,*)
      write(5,*) Nsys,    "   atoms"

      write(5,*)  Nbond*nmol, "   bonds"
      write(5,*)  Nangle*nmol,      "   angles"
      write(5,*) 0,      "   dihedrals"
      write(5,*) 0,      "   impropers"
      write(5,*)
      write(5,*) 7,    "   atom types"     !B,S,E
      write(5,*) 6,    "   bond types"     !BB, BS, BE, EE
      write(5,*) 6,    "   angle types"    !



      write(5,*) 0,    "   dihedral types"
      write(5,*) 0,    "   improper types"
      write(5,*)
      write(5,*)  xlo, xhi, "  xlo xhi"
      write(5,*)  ylo, yhi, "  ylo yhi"
      write(5,*)  zlo, zhi, "  zlo zhi"
      write(5,*)
      write(5,*) "Masses"
      write(5,*)
      write(5,*) 1, 1.0
      write(5,*) 2, 1.0
      write(5,*) 3, 1.0
      write(5,*) 4, 1.0
      write(5,*) 5, 1.0
      write(5,*) 6, 1.0
      write(5,*) 7, 1.0
c     write(5,*) 8, 1.0
```

```
c     ccccccccccccccccccc
c     output atoms data
c     ccccccccccccccccccc
      write(5,*)
      write(5,*) "Atoms"
      write(5,*)

      do i=1,Nsys
!     write(5,3) i, mol(i),atom(i), q(i), xpar(i),ypar(i),zpar(i)
!     3        format (4x, I4, 3x, I4, 3x, I2, 3x, f4.1, 3(3x,f8.4))
         write(5,3) i, mol(i),atom(i), q(i),  x(i),y(i),z(i)
 3       format (4x, I6, 3x, I6, 3x, I2, 3x, f8.4,  3(3x,f8.4))
      enddo


      open(unit=8, file="bond.data")

      do i=1,Nbond
         read(8,*) b1(i),b2(i)
         ia1=b1(i)
         ia2=b2(i)
         if(atom(ia1).eq.1.and.atom(ia2).eq.1) then
            bond(i)=1
         elseif(atom(ia1).eq.1.and.atom(ia2).eq.2) then
            bond(i)=2
         elseif(atom(ia1).eq.2.and.atom(ia2).eq.1) then
            bond(i)=2
         elseif(atom(ia1).eq.1.and.atom(ia2).eq.3) then
            bond(i)=3
         elseif(atom(ia1).eq.3.and.atom(ia2).eq.1) then
            bond(i)=3
         elseif(atom(ia1).eq.3.and.atom(ia2).eq.3) then
            bond(i)=4
         elseif(atom(ia1).eq.2.and.atom(ia2).eq.4) then
            bond(i)=5
```

```
         elseif(atom(ia1).eq.4.and.atom(ia2).eq.5) then
            bond(i)=6
         endif
        write(*,*) i, b1(i),b2(i),bond(i)
      enddo

      open(unit=9, file="angle.data")
      do i=1,Nangle
         read(9,*) ha1(i),ha2(i),ha3(i)
         ia1=ha1(i)
         ia2=ha2(i)
         ia3=ha3(i)

         if(atom(ia1).eq.1.and.atom(ia2).eq.1.and.atom(ia3).eq.1) then
            angle(i)=1
       elseif(atom(ia1).eq.1.and.atom(ia2).eq.1.and.atom(ia3).eq.3)
then
           angle(i)=2
       elseif(atom(ia1).eq.3.and.atom(ia2).eq.1.and.atom(ia3).eq.1)
then
           angle(i)=2
       elseif(atom(ia1).eq.1.and.atom(ia2).eq.3.and.atom(ia3).eq.3)
then
            angle(i)=3
       elseif(atom(ia1).eq.3.and.atom(ia2).eq.3.and.atom(ia3).eq.1)
then
            angle(i)=3
       elseif(atom(ia1).eq.3.and.atom(ia2).eq.3.and.atom(ia3).eq.3)
then
            angle(i)=4
       elseif(atom(ia1).eq.1.and.atom(ia2).eq.2.and.atom(ia3).eq.4)
then
            angle(i)=5
       elseif(atom(ia1).eq.2.and.atom(ia2).eq.4.and.atom(ia3).eq.5)
then
```

```
            angle(i)=6
         endif
         write(*,*) i, ha1(i),ha2(i),ha3(i),angle(i)
      enddo

c     ccccccccccccccccccc
c     output bond data
c     ccccccccccccccc
      write(5,*)
      write(5,*) "Bonds"
      write(5,*)

!     btype=1
      dex=0

      do ii=1,nmol
         do i=1,Nbond


            write(5,4) dex+i, bond(i),  b1(i)+(ii-1)*nm, b2(i)+(ii-
1)*nm
         enddo
         dex=dex+Nbond
 4       format(4x,I6,3x, I1, 3x, I6, 3x, I6)
      enddo

c     ccccccccccccccccccc
c     output angle data
c     ccccccccccccccccccccc
      write(5,*)
      write(5,*) "Angles"
      write(5,*)

!     atype=1
      dex=0
```

```
      do ii=1,nmol

         do i=1,Nangle


            write(5,5) dex+i, angle(i),  ha1(i)+(ii-1)*nm,
     &           ha2(i)+(ii-1)*nm, ha3(i)+(ii-1)*nm
         enddo
         dex=dex+Nangle

5        format(4x,I6,3x, I1, 3x, I6, 3x, I6, 3x, I6)
      enddo

      close(5)
      stop
      end
```

Sample LAMMPS input for DPD simulations:

```
boundary        p p p

units           lj
atom_style      full
bond_style      harmonic
angle_style     cosine/delta
variable        T equal  1.0
pair_style      dpd 1.0 3438752

# read data file or restart
#read_restart    restart.*
read_data       DPD.data

# define masses
mass            * 1
# define bonded interactions
bond_coeff      1  15.0  0.7
bond_coeff      2  15.0  0.7  # the rest of the interactions are
defined according to this syntax

angle_coeff     1  15.0  150.
angle_coeff     2  10.0  150.  # the rest of the interactions are
defined according to this syntax

special_bonds   lj 1.0 1.0 1.0

variable        gamma equal 4.5

# define conservative interactions
pair_coeff       1 1 30.28 4.5
pair_coeff       1 2 35.02 4.5  # the rest of the interactions are
defined according to this syntax
```

```
comm_modify     vel yes cutoff 2.0

neighbor        2.0 bin
neigh_modify    delay 0 every 1

timestep        0.01

fix             1 all nve

run             10000
change_box      all x scale 0.64 y scale 0.64 z scale 0.64 boundary p
p p remap units box
run             10000
change_box      all x scale 0.625 y scale 0.625 z scale 0.625 boundary
p p p remap units box
run             10000
change_box      all x scale 0.625 y scale 0.625 z scale 0.625 boundary
p p p remap units box
run             100000

dump            myDump6 all custom 1000000
Coordinates_every1M.lammpstrj id mol type x y z ix iy iz

thermo          100
thermo_style    one

fix             2 all ave/time 1 1 100 c_thermo_temp file temp.profile
fix             3 all ave/time 1 1 100 c_thermo_press file
press.profile

compute         1 all property/local batom1 batom2 btype
compute         2 all bond/local dist
compute         3 all property/local aatom1 aatom2 aatom3 atype
compute         4 all angle/local theta
```

```
dump            1 all local 1000000 btmp.*.dump index c_1[1] c_1[2]
c_1[3] c_2
dump            2 all local 1000000 atmp.*.dump index c_3[1] c_3[2]
c_3[3] c_3[4] c_4

# calculate MSD
group           But1 type 1
compute         myMSD1 But1 msd
fix             4 But1 ave/time 1 1 100 c_myMSD1[4] file
But1_MSD.profile

group           Benz type 2
compute         myMSD2 Benz msd
fix             5 Benz ave/time 1 1 100 c_myMSD2[4] file
Benz_MSD.profile

group           But3 type 3
compute         myMSD3 But3 msd
fix             6 But3 ave/time 1 1 100 c_myMSD3[4] file
But3_MSD.profile

group           TMM type 4
compute         myMSD4 TMM msd
fix             7 TMM ave/time 1 1 100 c_myMSD4[4] file
TMM_MSD.profile

group           TMA type 5
compute         myMSD5 TMA msd
fix             8 TMA ave/time 1 1 100 c_myMSD5[4] file
TMA_MSD.profile

group           OH type 6
compute         myMSD6 OH msd
fix             9 OH ave/time 1 1 100 c_myMSD6[4] file OH_MSD.profile
```

```
group           W type 7
compute         myMSD7 W msd
fix             10 W ave/time 1 1 100 c_myMSD7[4] file W_MSD.profile

restart         2000000 restart
run             20000000
```

MATLAB code to extract specific energies from scan calculations of GAUSSIAN output files:

```
function extract_data_folder

clear
clc

tic

lala=0;
dirlist = dir('C:\Users\fsepehr\Documents\Work\Input');
dirlist
f_cnt   = 0;
for f_it = 1:length(dirlist)
    f_name  = dirlist(f_it).name;

    if dirlist(f_it).isdir
        continue;
    end

    fprintf('Processing file: %s\t', f_name);
    f_cnt   = f_cnt + 1;
    data    = fopen(strcat('.\Input\', f_name), 'r');
    output  = fopen(strcat(f_name, '.txt'), 'w');
    str=0;
    while ~feof(data)
        strghabl=str;
        str = fgets(data);
        if (findstr(str, 'SCF Done')& findstr(strghabl, 'not met'))
            lala=lala+1;
        end
        if (findstr(str, 'SCF Done')& findstr(strghabl, 'a'))
            num = str2double(str(26:39));
            fprintf(output, '%f\n', num);

        end

        if (findstr(str, 'Error termination'))
            break;
        end
    end

    fprintf('Finished\n');
```

```
    fclose(data);
    fclose(output);

    end

toc

end
```

Appendix B List of Presentations and Publications

Presentations:

1. Sepehr, F.; Paddison, S. J. Morphology of Elastomeric Anion Exchange Membranes: A Dissipative Particle Dynamics Study. *230th ECS Meeting, Honolulu, HI,* Oct 2016.
2. Sepehr, F.; Bertasi, F.; Paddison, S. J.; Di Noto, V. Interplay between Vibrational Modes and Relaxations in Electrolytes for Secondary Magnesium Batteries Based on Haloaluminate Ionic Liquids. *227th ECS Meeting, Chicago, IL,* May 2015.
3. Sepehr, F.; Paddison, S. J. Meso-Scale Study of Hydrated Nafion with Diffused Vanadium Cations and Sulfuric Acid. *227th ECS Meeting, Chicago, IL,* May 2015.
4. Sepehr, F.; Paddison, S. J. Solvation of Vanadium Cations: Effects of Sulfuric and Triflic Acids. *AICHE Annual Meeting, Atlanta, GA,* Nov 2014.
5. Sepehr, F.; Paddison, S. J. Solvation of Vanadium Cations: Effects of Sulfuric and Triflic Acids. *TN-SCORE Annual Conference, Nashville, TN,* Jun 2014.
6. Sepehr, F.; Bertasi, F.; Di Noto, V.; Paddison, S. J. *Ab Initio* Study and Vibrational Spectroscopy of Imidazolium Based Ionic Liquids with Dissolved δ-$MgCl_2$. *225th ECS Meeting, Orlando, FL,* May 2014.
7. Sepehr, F.; Paddison, S. J. Solvation of Vanadium Cations in Sulfuric and Perfluorosulfonic Acids and Their Effect on the Morphology of PFSA Membranes. *225th ECS Meeting, Orlando, FL,* May 2014.
8. Sepehr, F.; Paddison, S. J. The Solvation of Aqueous Vanadium Cations in Bulk Water and Perfluorosulfonic Acid Systems. *SETCA 2013 Meeting, Auburn, AL,* May 2013.

Publications:

1. Sepehr, F.; Paddison, S. J., The Solvation Structure and Thermodynamics of Aqueous Vanadium Cations. *Chemical Physics Letters* **2013,** *585*, 53-58.
2. Sepehr, F.; Paddison, S. J., Effect of Sulfuric and Triflic Acids on the Hydration of Vanadium Cations: An *Ab Initio* Study. *Journal of Physical Chemistry A* **2015,** *119*, 5749-5761.
3. Bertasi, F.; Hettige, C.; Sepehr, F.; Bogle, X.; Pagot, G.; Vezzù, K.; Negro, E.; Paddison, S. J.; Greenbaum, S. G.; Vittadello, M.; Di Noto, V., A Key Concept in Magnesium Secondary Battery Electrolytes. *ChemSusChem* **2015,** *8*, 3069-3076.
4. Sepehr, F.; Paddison, S. J., Dissipative Particle Dynamics Interaction Parameters from *Ab Initio* Calculations. *Chemical Physics Letters* **2016,** *645*, 20-26.
5. Bertasi, F.; Sepehr, F.; Pagot, G.; Paddison, S. J.; Di Noto, V., Toward a Magnesium-Iodine Battery. *Advanced Functional Materials* **2016,** *26*, 4860-4865.

Manuscripts in preparation:

1. Sepehr, F.; Liu, H; Bae, C; Tuckerman, M. E.; Hickner, M. A.; and Paddison, S. J., Meso-Scale Simulations of Anion Exchange Membranes Based on Quaternary Ammonium Tethered Triblock Copolymers. *Macromolecules*, to be submitted.
2. Sepehr, F.; Paddison, S. J., The Primary Hydration and Proton Transfer of Acids: An *Ab Initio* Study. *Solid State Ionics*, to be submitted.

Appendix C Reprints of Publications

Reprinted with permission from Chemical Physics Letters 2013, 585, 53-58.
Copyright 2013 Elsevier B.V.

Chemical Physics Letters 585 (2013) 53–58

Contents lists available at ScienceDirect

Chemical Physics Letters

journal homepage: www.elsevier.com/locate/cplett

The solvation structure and thermodynamics of aqueous vanadium cations

Fatemeh Sepehr, Stephen J. Paddison *

Department of Chemical & Biomolecular Engineering, University of Tennessee, Knoxville, TN 37996, USA

ARTICLE INFO

Article history:
Received 15 July 2013
In final form 22 August 2013
Available online 30 August 2013

ABSTRACT

The present work seeks to understand the chemical structure and solvation thermodynamics of aqueous vanadium cations commonly employed in vanadium redox flow batteries. First principles based electronic structure calculations were performed to obtain the hydration structure and partial charges distributions of the cations in bulk water. The thermodynamics of solvation was determined within the context of a quasi-chemical theory of solution. The free energies of solvation for the V^{2+}, V^{3+}, VO^{2+}, and VO_2^+ cations were computed to be: −440.0, −1018.8, −457.2, and −184.4 kcal/mol, respectively, which agree well with available experimental values.

© 2013 Elsevier B.V. All rights reserved.

1. Introduction

The desire, in recent decades, to replace fossil fuel with renewable green energy sources such as solar and wind has significantly increasing as a result of environmental issues. One of the limiting factors for the utilization of renewable energy sources in the electrical supply grid is the intermittent nature of these sources which requires the employment of megawatt scale electrical energy storage devices. Redox flow batteries (RFBs) are among the promising large-scale electrical energy storage systems and have received significant attention due to their superior properties. RFBs provide long life-span, simple installation, the possibility of instant charging by replacing the electrolytes, and the ability to repeatedly store and convert electrical energy into chemical energy and vice versa. In addition, RFBs have the unique advantage of having power and energy decoupled due to the separation of the electrolyte reservoirs and the battery stacks [1,2]. Of the various RFBs currently under investigation, the vanadium redox flow battery (VRFB) demonstrates design flexibility, good electrochemical activity, reversibility, and low maintenance cost [3,4]. A VRFB consists of a V^{2+}/V^{3+} sulfate solution at the negative electrolyte and a VO^{2+}/VO_2^+ sulfate solution at the positive electrolyte separated by a proton exchange membrane (PEM). The wide span between the standard reduction potentials of the two half-cells in these batteries produces a standard voltage of 1.25 V, which is comparable to other types of RFBs [5].

Despite the numerous advantages of VRFBs, there still exist a number of issues that hinder the commercialization of these storage devices. For example, the poor stability of the VO_2^+ solution at high temperatures and high concentrations, results in precipitation of hydrated V_2O_5 and energy loss [6]. Although, the stability of the VO_2^+ ion may be increased by the addition of hydrochloric acid, eventually it will form a gel-type precipitate involving the V^{3+} cation [7]. It is therefore important to understand the chemistry and thermodynamics of solvation of vanadium cations in the electrolyte for design improvements. The other challenging area arises from the membranes used in these devices. The most widely used PEM in VRFBs is Nafion which degrades as a result of exposure to the highly acidic electrolytes. It has also been found that the low ion selectivity of PEMs allows permeation of vanadium cations and cross contamination of the electrolytes [8,9]. Hence, the nature of the cations diffusing within perfluorosulfonic acid (PFSA) membranes is of great importance, as the hydration behavior of the cations is crucial to their interaction with the sulfonic acid groups [10–12].

Vanadium complexes have been subject to both experimental and theoretical investigation [13–21]. However, the structure of hydrated vanadium ions, the oxidation state of the ions, and their interaction with sulfonic acid groups inside hydrated PFSA are not understood [22].

In this Letter we report the hydration structure, coordination number, and partial charges distribution of all four vanadium cations (V^{2+}, V^{3+}, VO^{2+}, and VO_2^+) in bulk water as determined by *ab initio* electronic structure calculations. The thermodynamics of solvation is also considered within the context of a quasi-chemical theory of solution [23,24], where the inner- and outer-shell contributions to the solvation of the cations are assessed separately. Consequently, the free energies of solvation for the four vanadium ions are calculated and compared with the available experimental information.

* Corresponding author. Fax: +1 865 974 2026.
E-mail address: spaddison@utk.edu (S.J. Paddison).

0009-2614/$ - see front matter © 2013 Elsevier B.V. All rights reserved.
http://dx.doi.org/10.1016/j.cplett.2013.08.089

Reprinted with permission from Chemical Physics Letters 2013, 585, 53-58.
Copyright 2013 Elsevier B.V.

2. Methodology

2.1. Ab initio calculations

Electronic structure calculations were performed using the Gaussian 09 suite of programs [25]. Geometries were optimized using density functional theory (DFT) with Becke's 3-parameter hybrid functional (B3LYP) [26] and the 6-31G** split valence basis set [27] without symmetry constraint. A universal solvation model [28] (implemented in Gaussian 09 as the SMD model) was subsequently applied to all the optimized structures with water as the solvent. The resulting structures were then refined with optimizations performed with a larger basis set 6-311G** [29] with and without the inclusion of diffuse functions for heavy atoms and the results of both are reported in Tables 1–5. In addition, frequency calculations at the same level of theory were performed to confirm local minima. For the V^{2+}, V^{3+}, and VO^{2+} open shell calculations were performed, while for VO_2^+ closed shell calculations were undertaken. Additionally, partial charges distributions and electrostatic potentials for each of the vanadium ion clusters were obtained according to the ChelpG scheme [30] with the inclusion of a dielectric medium.

To obtain the structure of the first hydration shell for each vanadium cation, an unbiased approach has been used to limit the effect on the final structures. The procedure involved adding water molecules to each central cation incrementally followed by a geometry optimization at each step, until one of the water molecules is forced to stay out of the first hydration shell. Therefore, the optimized geometries obtained from the step with the largest number of waters allowed in its first hydration shell was chosen to be the ground state hydrated structure of that particular central cation.

2.2. Quasi-chemical theory

In the quasi-chemical theory, the most primitive idea is to identify an inner-shell region from the rest of the neighborhood of a distinguished solute, and then to rely on a painstaking treatment of the inner shell, with full molecular resolution. The remainder of the neighborhood of that distinguished solute (the outer-shell region) can be given an alternative statistical description, and then a proper matching of results for inner and outer shells must be accomplished. The reader is referred to references [23,24,31–34] for overviews and more complete description of the quasi-chemical theory. In the present study, the inner shell, where chemical effects (water-vanadium interactions) are important, is treated quantum mechanically. The inner-shell structure is considered to be obtained from the following reaction:

$$\alpha + n\mathrm{H_2O} \rightleftarrows \alpha(\mathrm{H_2O})_n \tag{1}$$

where α indicates the solute, here it is any of the vanadium cations, and n is the number of water molecules inside the inner-shell structure. The equilibrium constant and free energy changes for this reaction were obtained using electronic structure calculations and considered as the inner-shell contribution to the total free energy change of ion solvation. The calculations were done using the Gaussian 09 suite of programs. The clusters were geometry optimized in the gas phase at the B3LYP/6-311G** level of theory and frequency calculations were performed to confirm a true minimum. Single point energies were calculated at the B3LYP/6-311+G(2d,p) level of theory on each of the optimized gas phase structures.

The outer-shell contributions to the solvation of ions are assessed using the SMD universal dielectric continuum model. The cavities for the bulk electrostatic calculation are defined by superposition of nuclear-centered spheres with the radii suggested by Truhlar et al. [28]. Therefore, the excess chemical potential of the ion in water is obtained from the expression [31]:

$$\beta\mu_\alpha^{\mathrm{ex}} \approx -\ln K_{\bar{n}}^{(0)} - \bar{n}\ln(1354) + \beta\mu^{\mathrm{ex}}_{[\alpha(\mathrm{H_2O})_{\bar{n}}]} - \bar{n}\beta\mu^{\mathrm{ex}}_{\mathrm{H_2O}} \tag{2}$$

where $K_{\bar{n}}^{(0)}$ is the equilibrium constant for the Eq. (1) in an ideal gas state, $\bar{n}$ the number of water molecules in the most stable cluster, and $\beta = 1/k_BT$. As $K_{\bar{n}}^{(0)}$ is calculated for an ideal gas at standard state, the effect of the actual liquid water density is included by a *replacement contribution* that involves the ln(1354) constant for each water molecule inside the inner-shell [35]. The last two terms of Eq. (2) are calculated using the SMD model for the cluster and each water molecule separately.

Table 2
Structural parameters of $[VO(H_2O)_5]^{2+}$ (all in Å).

Method	V…O(H_2O axial)	V…O(H_2O equatorial)[a]	V–O
B3LYP/6-311G**/SMD[b]	2.35	2.10	1.57
B3LYP/6-311+G**/SMD[b]	2.36	2.12	1.57
DFT[c]	2.17	2.03	1.57
DFT[d]	2.32	2.12	1.57
XRD[e]	2.22	2.04	1.59

[a] Average value of bond length between oxygen of water and vanadium.
[b] This work.
[c] Grant et al. [16].
[d] Vijayakumar et al. [20].
[e] Ballhausen et al. [14].

Table 1
Structural parameters of $[V(H_2O)_6]^{2+}$ and $[V(H_2O)_6]^{3+}$ (all in Å).

Method	$[V(H_2O)_6]^{2+}$ V…O(H_2O)[a]	$[V(H_2O)_6]^{3+}$ V…O(H_2O)[a]
B3LYP/6-311G**/SMD	2.19[b]	2.09[b]
B3LYP/6-311 + G**/SMD	2.21[b]	2.09[b]
Ab initio SCF	2.20[c]	2.06[c]
B3LYP/6-311G* on V and 6-31G* on O,H	2.15[d]	2.04[d]
QM/MM	–	1.99[e]
XRD	2.13[f]	1.99_3[g]
XRD	2.15(1)[h,i]	–

[a] Average value of bond length between oxygen atom of water and vanadium.
[b] This work.
[c] Akesson et al. [47].
[d] Benmelouka et al. [18].
[e] Kritayakornupong [19].
[f] Cotton et al. [36].
[g] Cotton et al. [48].
[h] Montgomery et al. [13].
[i] The value in parentheses is estimated standard deviation in the least significant digit.

Reprinted with permission from Chemical Physics Letters 2013, 585, 53-58.
Copyright 2013 Elsevier B.V.

Table 3
Structural parameters of octahedral $[VO_2(H_2O)_4]^+$ and bipyramidal $[VO_2(H_2O)_3]^+$ (all in Å).

Method	Octahedral $[VO_2(H_2O)_4]^+$			Bipyramidal$[VO_2(H_2O)_3]^+$	
	V...O(H_2O equatorial)[a]	V...O(H_2O axial)[a]	V–O[a]	V...O(H_2O)[a]	V–O[a]
B3LYP/6-311G**/SMD[b]	2.09	2.30	1.60	2.11	1.60
B3LYP/6-311+G**/SMD[b]	2.10	2.32	1.61	2.11	1.60
BP86/I[c]	2.13	2.28	1.61	2.10	1.61
B3LYP/QZ4P/COSMO[d]	–	–	–	2.11	1.64
LAXS[e]	2.00	2.22	1.63	–	–

[a] Average value.
[b] This work.
[c] Buhl et al. [17].
[d] Vijayakumar et al. [49].
[e] Krakowiak et al. [21].

Table 4
Binding energies of water ligands to central vanadium cations calculated at B3LYP/6-311G** and B3LYP/6-311+G** (in parenthesis) level of theory (all in kcal/mol).

Structure	ΔE[a]	ΔE_{ZPE}[b]
$[V(H_2O)_6]^{2+}$	−58.52(−54.10)	−56.06(−51.73)
$[V(H_2O)_6]^{3+}$	−113.77(−108.27)	−110.99(−105.58)
$[VO(H_2O)_5]^{2+}$	−67.44(−62.34)	−64.68(−59.66)
$[VO_2(H_2O)_3]^+$	−50.20(−45.51)	−47.41(−42.74)
$[VO_2(H_2O)_4]^+$	−42.83(−37.88)	−40.12(−35.23)

[a] Binding energy based on uncorrected total electronic energies.
[b] Binding energy based on ZPE corrected total electronic energies.

Table 5
Atomic charges calculated by ChelpG method at B3LYP/6-311G**/SMD and B3LYP/6-311+G**/SMD (in parenthesis) level of theory.

Structure	V	O	O(H_2O)[a]	H(H_2O)[a]
$[V(H_2O)_6]^{2+}$	1.72(1.93)	–	-0.89_5(−0.97)	0.47(0.49)
$[V(H_2O)_6]^{3+}$	2.05(1.77)	–	−0.86(−0.76)	0.51(0.48)
$[VO(H_2O)_5]^{2+}$	1.80(1.87)	-0.61_5(-0.64_5)	-0.80_5(−0.80)	0.48(0.48)
$[VO_2(H_2O)_3]^+$	1.79(1.78$_5$)	−0.70(−0.71)[a]	−0.75(−0.74)	0.48(0.47)
$[VO_2(H_2O)_4]^+$	1.70(1.78)	−0.69(−0.72)[a]	−0.76(−0.75)	0.46_5(0.46)

[a] Average value.

3. Results and discussion

The first hydration shell structures for the vanadium ions obtained from the approach described above are illustrated in Figure 1. The V^{2+} and V^{3+} cations (Figure 1a and b) are hydrated with six water molecules and both have an octahedral structure that matches well with the previous studies [15,36]. The gas structures for V^{2+} and V^{3+} show T_h and S_6 point group symmetries, respectively. However, the solution phase structures are slightly distorted and don't possess point group symmetries. Further structural analysis indicates that the trivalent vanadium complex is more distorted compared to the divalent as the charge density is higher on the former. For the VO^{2+} ion (Figure 1c) the first hydration shell consists of five water molecules with an octahedral structure. Also, the distance of the axial water molecule from the central vanadium ion is longer than the average distance to the equatorial water molecules. Moreover, the equatorial plane in VO^{2+} is distorted as a result of the repulsion caused by the oxo-oxygen atoms of VO^{2+}. Interestingly, as shown in Figure 1, there are two different structures for the fourth cation, aqua-VO_2^+. The reason is the presence of two local minima for the tetra-hydrated VO_2^+ complex. One with four water molecules inside the first hydration shell which had an octahedral structure (Figure 1d) and the other with three water molecules inside the first hydration shell and one water molecule outside of the shell (Figure 1e). Hence, this structure is bipyramidal as the first hydration shell structure is trigonal bipyramidal. The free energy of the bipyramidal structure at 298 K was determined to be lower than that of the octahedral complex by 7.3 kcal/mol at the B3LYP/6-311G** level of theory (8.6 kcal/mol with inclusion of diffuse functions) and therefore the bipyramidal is the most stable structure for aqua-VO_2^+. However, this does not imply that the octahedral structure doesn't exist in solution, but does imply that there is a population distribution for the bipyramidal and octahedral structures at 298 K as previously found in CPMD results [17].

The structural bond lengths are summarized and compared with the literature values in Table 1 for V^{2+} and V^{3+}, Table 2 for VO^{2+} and Table 3 for VO_2^+. The first two rows of Table 1 (the results of the present work) show that the distance between oxygen atom of water and V^{2+} is 0.11 Å longer than that of V^{3+} which is very close to the 0.14 Å found experimentally by Cotton et al. [36]. This is expected as the charge density of V^{3+} is higher than V^{2+} and therefore in a V^{3+} complex the ligands will bind closer to the ion and will increase the ligand-field splitting parameter, Δ. In all cases, the inclusion of the diffuse function to heavy atoms in the calculations resulted in longer bond length. Also, in all of these aqua-complexes, the experimental bond lengths are slightly shorter than the computational values except for VO^{2+} (see Table 2) with the covalent V–O bond 0.02 Å shorter than the experimental value. This may be attributed to the fact that the X-ray diffraction (XRD) measurements take place in the solid phase and our calculations are in solution phase or it may be the effect of counter ion which is not considered in these *ab initio* calculations. For the VO_2^+, our results reported in Table 3 are in the range of 0.04 Å of the literature computational values. Experimental results were only found for the octahedral structure with bond lengths in the range of 0.09 Å of our results. It is noteworthy that the difference between the equatorial and axial waters bond lengths in both experimental and computational values are fixed and about 0.22 Å.

The binding energies of water molecules to central vanadium cations is calculated for the above structures and presented in Table 4. As expected, the binding energy for V^{3+} is larger and twice that of V^{2+} as a result of the higher atomic charge density on V^{3+} ion. The value for VO^{2+} is close to V^{2+} while the lowest binding energy belongs to the two VO_2^+ complexes. Also, the small and close binding energies of bipyramidal and octahedral VO_2^+ may promote the interchange between the two structures in solution as stated above.

Partial atomic charges calculated by the ChelpG method are shown in Table 5. The charge on V^{2+} is 1.72 (1.93 when diffuse function are included) which is close to its formal charge. But for V^{3+} it is 2.05 (1.77 with diffuse function) which is only two thirds of its formal charge. The atomic charges on oxygen and water of these two ions are very close to each other and in 0.13 of atomic charges of a bulk water molecule. The inclusion of diffuse function on the V^{2+} complex resulted in higher atomic charges on all the

Reprinted with permission from Chemical Physics Letters 2013, 585, 53-58.
Copyright 2013 Elsevier B.V.

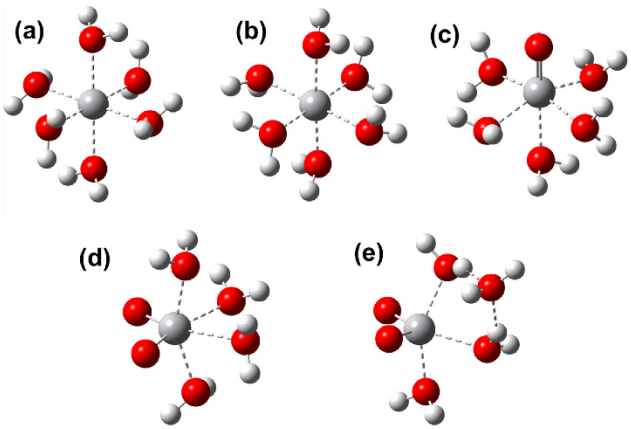


Figure 1. First hydration shell structures of vanadium ions at B3LYP6-311 + G**/SMD level of theory: (a) V^{2+} hydrated with six water molecules with octahedral structure; (b) V^{3+} hydrated with six water molecules with octahedral structure; (c) VO^{2+} hydrated with five water molecules, the equatorial plane in VO^{2+} is distorted as a result of the oxo-oxygen repulsion; (d) Octahedral structure of VO_2^+ hydrated with four water molecules; (e) Trigonal bipyramidal structure of VO_2^+ hydrated with three water molecules inside the first hydration shell and one water molecule outside of the shell. The free energy of bipyramidal at 298 K is 8.6 kcal/mol lower than octahedral and therefore bipyramidal structure is the most stable structure for aqua-VO_2^+.

atoms, while it had a reverse effect on the V^{3+} complex. For VO^{2+} and VO_2^+ complexes the atomic charges on the vanadium and oxo-oxygen atoms are slightly higher with the inclusion of diffuse functions while they are lower on both the oxygen and hydrogen atoms of the water molecules.

It is important to choose an appropriate inner-shell structure in applying the quasi-chemical method to the vanadium cations. The choice of the inner-shell structure depends on the definition of an appropriate inner-shell boundary which involves quite a bit of subtlety and has been the topic of a couple of publications [37,38]. Based on the results of the *ab initio* calculations on the hydration of the four cations, we chose the most stable aqua-complex for each cation and used it as the inner-shell structure in the quasi-chemical approach. Therefore, the six water coordinated octahedral structure for V^{2+} and V^{3+}, the five water coordinated structure for VO^{2+}, and the three water coordinated trigonal bipyramidal structure for VO_2^+ were selected. The calculated free energies of hydration based on Eq. (2) for the cations along with available experimental information are listed in Table 6. The calculated values for V^{2+} and V^{3+} ions are very close to the experimental information (within 1% of the experimental values). Previous quasi-chemical derived solvation free energies of several first transition row metal cations have also been found to agree well with experimental values [34,39,40]. Despite the fact that the calculated and experimental values are in the same range and in good agreement, one should notice that the solvation free energy of highly charged species may have significant uncertainty [41]. However, as there were no experimental information for the hydration energies of VO^{2+} and VO_2^+, the calculated values may be used as an estimate for these two cations.

Table 6
Calculated free energy of hydration of vanadium cations using quasi-chemical approach compared with available experimental information (all in kcal/mol).

Cation	ΔG_{calc}	ΔG_{exp}
V^{2+}	−440.0	−436.2[a]
V^{3+}	−1018.8	−1008.6[a]
VO^{2+}	−457.2	–[b]
VO_2^+	−184.4	–[b]

[a] Marcus [50].
[b] Not reported in the literature.

By progressively adding water molecules to the inner-shell structure (molecular *aufbau* approach [42]) we may monitor the ion's excess chemical potential versus its coordination number and determine the coordination state at which the dominant contribution to the thermodynamics of hydration is obtained [43]. The results of the *aufbau* approach on the four vanadium cations using the quasi-chemical approach are presented in Figure 2. As depicted, with varying the number of water molecules inside the inner-shell the free energy of cations (showed by circles) change, which signifies the importance of chemical structure around the cation in its solvation phenomena. From Figure 2 it is clear that for both V^{2+} and V^{3+} cations the octahedral structure is the most stable form in solution and contributes the most to the hydration thermodynamics. This coordination number is consistent with our previous *ab initio* results. However, the prediction of quasi-chemical theory for the coordination number of VO^{2+} and VO_2^+ ions is 4 and 2, respectively, which differs than our *ab initio* results by one. This result signifies that the majority of the solvation thermodynamics is captured by $VO^{2+}(H_2O)_4$ and $VO_2^+(H_2O)_2$, while it is the hexa-hydrate structures for V^{2+} and V^{3+} cations. Previous studies [44] show that the compatibility of the *aufbau* approach and *ab initio* results usually occurs for ions with high charge densities, in our case V^{2+} and V^{3+} and not for VO^{2+} and VO_2^+. However, the primitive quasi-chemical approximation with the choice of a proper inner-shell boundary provides good results and it is confirmed with the case of the thermodynamics of CO_2 solvation [37].

Additional useful information derived by the quasi-chemical treatment of the ions is the portion of each contribution to the total free energy of solvation. In Figure 2, triangles represent the chemical contribution to the total free energy of solvation that comes from inner-shell structure calculations. This contribution is increased by the addition of water molecules to the cluster. In contrast, the outer-shell contribution which is shown by squares is decreased by adding water molecules to the coordination shell of cluster. Previous studies suggest that the ligand desolvation free energy is the reason for this decrease [45,46]. The chemical portion of the free energy of hydration for the most stable structure is about 64% for V^{2+}, 59% for V^{3+}, 60% for VO^{2+}, and 67% for VO_2^+.

Reprinted with permission from Chemical Physics Letters 2013, 585, 53-58.
Copyright 2013 Elsevier B.V.

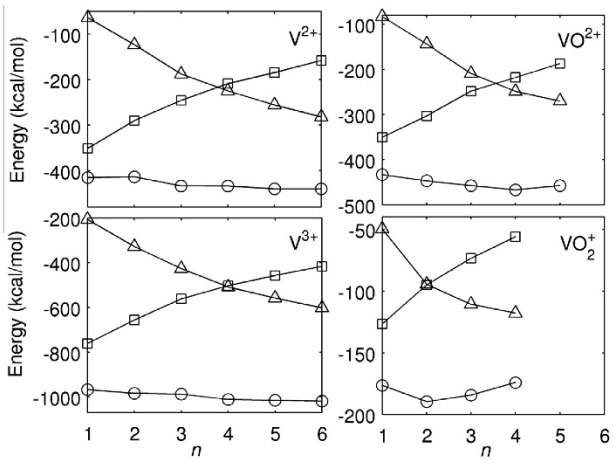


Figure 2. Quasi-chemical contributions of the solvation free energy of aqueous V^{2+}, V^{3+}, VO^{2+}, and VO_2^+ versus n number of water molecules inside the inner-shell structure. The calculations performed at the B3LYP/6-311 + G(2d,p)//B3LYP/6-311G** level of theory and the outer-shell contributions are assessed using the SMD universal dielectric continuum model. Triangles represent inner-shell contribution (first two terms in Eq. (2)) and squares are outer-shell contribution (last two terms in Eq. (2)) to the total free energy of solvation. Circles are the total free energy of solvation predicting $n = 6$ as the most probable inner-shell occupancy for V^{2+} and V^{3+}, $n = 4$ for VO^{2+} and $n = 2$ for VO_2^+.

Hence, the local chemical effects form more than half of the hydration phenomena for the structures with the most stable coordination number. As the major contribution to the ion solvation is due to the inner-shell structure, there might be a relationship between the binding energies of the ligands and the free energy of solvation, as the ratios of binding energies and free energies of solvation between different cations are fairly similar.

4. Conclusions

The first hydration shell structures of the vanadium cations commonly employed in VRFBs were determined with electronic structure calculations. The results indicated that for the V^{2+} and V^{3+} cations the hexa-aqua octahedral structures and for the VO^{2+} the penta-aqua octahedral complexes are the most stable structures while for the VO_2^+ the tri-hydrated bipyramidal structures is the ground state. Structural parameters including: bond lengths and partial atomic charges were also computed. The calculated bond lengths were found to be in close agreement to available experimental values.

The free energies of solvation for the four vanadium cations in bulk water were determined using a quasi-chemical theory. The calculated free energies were close to the experimental values for V^{2+} and V^{3+} and therefore the results can be used for VO^{2+} and VO_2^+ ions for which no experimental information is currently available. The contribution of inner-shell and outer-shell effects to the total free energies varying the number of ligands inside the inner-shell were illustrated and discussed. The results showed that the inner-shell contribution is increased by addition of water molecules to the cluster but the outer-shell contribution is decreased. Hence, the ligands lose favorable hydration free energy in binding to the ion as the number of ligands is increased in the coordination shell. It can be concluded that in the most stable structure of a solvated ion the local chemical effects form the majority of the hydration phenomena.

Acknowledgements

This work was supported by the EPSCoR program of the National Science Foundation under the TNSCORE program with NSF EPS_1004083. Helpful discussions with Dr. Dilip Asthagiri (JHU) are gratefully acknowledged.

References

[1] M. Skyllas-Kazacos, D. Kasherman, D.R. Hong, M. Kazacos, J. Power Sources 35 (1991) 399.
[2] X.F. Li, H.M. Zhang, Z.S. Mai, H.Z. Zhang, I. Vankelecom, Energy Environ. Sci. 4 (2011) 1147.
[3] M. Skyllas-Kazacos, M. Rychick, R. Robins, All-vanadium Redox Battery, US Patent 4786567, Unisearch Limited, Australia, 1988.
[4] P. Zhao, H.M. Zhang, H.T. Zhou, J. Chen, S.J. Gao, B.L. Yi, J. Power Sources 162 (2006) 1416.
[5] L. Li et al., Adv. Energy Mater. 1 (2011) 306.
[6] F. Rahman, M. Skyllas-Kazacos, J. Power Sources 189 (2009) 1212.
[7] M. Vijayakumar, L.Y. Li, Z.M. Nie, Z.G. Yang, J.Z. Hu, Phys. Chem. Chem. Phys. 14 (2012) 10233.
[8] E. Wiedemann, A. Heintz, R.N. Lichtenthaler, J. Membr. Sci. 141 (1998) 215.
[9] J.Q. Chen, B.B. Wang, J.C. Yang, Solvent Extr. Ion Exch. 27 (2009) 312.
[10] S. Quezado, J.C.T. Kwak, M. Falk, Can. J. Chem. 62 (1984) 958.
[11] T. Xue, R.B. Longwell, K. Osseoasare, J. Membr. Sci. 58 (1991) 175.
[12] K.M. Cable, K.A. Mauritz, R.B. Moore, J. Polym. Sci., Part B: Polym. Phys. 33 (1995) 1065.
[13] H. Montgomery, R.V. Chastain, J.J. Natt, A.M. Witkowska, E.C. Lingafelter, Acta Cryst. 22 (1967) 775.
[14] C.J. Ballhausen, B.F. Djurinskij, K.J. Watson, J. Am. Chem. Soc. 90 (1968) 3305.
[15] F.A. Cotton, L.R. Falvello, C.A. Murillo, I. Pascual, A.J. Schultz, M. Tomas, Inorg. Chem. 33 (1994) 5391.
[16] C.V. Grant, W. Cope, J.A. Ball, G.G. Maresch, B.J. Gaffney, W. Fink, R.D. Britt, J. Phys. Chem. B 103 (1999) 10627.
[17] M. Buhl, M. Parrinello, Chem. Eur. J. 7 (2001) 4487.
[18] M. Benmelouka, S. Messaoudi, E. Furet, R. Gautier, E. Le Fur, J.Y. Pivan, J. Phys. Chem. A 107 (2003) 4122.
[19] C. Kritayakornupong, J. Comput. Chem. 30 (2009) 2777.
[20] M. Vijayakumar et al., J. Power Sources 195 (2010) 7709.
[21] J. Krakowiak, D. Lundberg, I. Persson, Inorg. Chem. 51 (2012) 9598.
[22] M. Vijayakumar et al., J. Membr. Sci. 366 (2011) 325.
[23] L.R. Pratt, R.A. Laviolette, Mol. Phys. 94 (1998) 909.
[24] L.R. Pratt, S.B. Rempe, AIP Conf. Proc. 492 (1999) 172.
[25] M.J. Frisch et al., Gaussian 09, Revision A.01, Wallingford, CT, 2009.
[26] A.D. Becke, J. Chem. Phys. 98 (1993) 5648.
[27] P.C. Hariharan, J.A. Pople, Theor. Chim. Acta 28 (1973) 213.
[28] A.V. Marenich, C.J. Cramer, D.G. Truhlar, J. Phys. Chem. B 113 (2009) 6378.
[29] A.D. Mclean, G.S. Chandler, J. Chem. Phys. 72 (1980) 5639.
[30] C.M. Breneman, K.B. Wiberg, J. Comput. Chem. 11 (1990) 361.
[31] T.L. Beck, M.E. Paulaitis, L.R. Pratt, The Potential Distribution Theorem and the Statistical Thermodynamics of Molecular Solutions, Cambridge University Press, 2006.
[32] D. Asthagiri, P.D. Dixit, S. Merchant, M.E. Paulaitis, L.R. Pratt, S.B. Rempe, S. Varma, Chem. Phys. Lett. 485 (2010) 1.
[33] D.M. Rogers, D. Jiao, L.R. Pratt, S.B. Rempe, Ann. Rep. Comp. Chem. 8 (2012) 71.

Reprinted with permission from Chemical Physics Letters 2013, 585, 53-58.
Copyright 2013 Elsevier B.V.

[34] S.B. Rempe, L.R. Pratt, G. Hummer, J.D. Kress, R.L. Martin, A. Redondo, J. Am. Chem. Soc. 122 (2000) 966.
[35] P. Grabowski, D. Riccardi, M.A. Gomez, D. Asthagiri, L.R. Pratt, J. Phys. Chem. A 106 (2002) 9145.
[36] F.A. Cotton, L.R. Falvello, R. Llusar, E. Libby, C.A. Murillo, W. Schwotzer, Inorg. Chem. 25 (1986) 3423.
[37] D. Jiao, S.B. Rempe, J. Chem. Phys. 134 (2011) 224506.
[38] D. Sabo, D. Jiao, S. Varma, L.R. Pratt, S.B. Rempe, Annu. Rep. Prog. Chem., Sect. C: Phys. Chem. 109 (2013) 266.
[39] D. Asthagiri, L.R. Pratt, M.E. Paulaitis, S.B. Rempe, J. Am. Chem. Soc. 126 (2004) 1285.
[40] D. Jiao, K. Leung, S.B. Rempe, T.M. Nenoff, J. Chem. Theory Comput. 7 (2011) 485.
[41] D. Asthagiri, L.R. Pratt, Chem. Phys. Lett. 371 (2003) 613.
[42] S. Merchant, D. Asthagiri, J. Chem. Phys. 130 (2009) 195102.
[43] S. Merchant, J.K. Shah, D. Asthagiri, J. Chem. Phys. 134 (2011) 124514.
[44] S. Merchant, P.D. Dixit, K.R. Dean, D. Asthagiri, J. Chem. Phys. 135 (2011) 054505.
[45] S. Varma, S.B. Rempe, Biophys. J. 93 (2007) 1093.
[46] S. Varma, S.B. Rempe, J. Am. Chem. Soc. 130 (2008) 15405.
[47] R. Akesson, L.G.M. Pettersson, M. Sandstrom, U. Wahlgren, J. Am. Chem. Soc. 116 (1994) 8691.
[48] F.A. Cotton, C.K. Fair, G.E. Lewis, G.N. Mott, F.K. Ross, A.J. Schultz, J.M. Williams, J. Am. Chem. Soc. 106 (1984) 5319.
[49] M. Vijayakumar, L.Y. Li, G. Graff, J. Liu, H.M. Zhang, Z.G. Yang, J.A. Hu, J. Power Sources 196 (2011) 3669.
[50] Y. Marcus, J. Chem. Soc., Faraday Trans. 87 (1991) 2995.

Reprinted with permission from Journal of Physical Chemistry A 2015, 119, 5749-5761.
Copyright 2015 American Chemical Society.

THE JOURNAL OF PHYSICAL CHEMISTRY A

Article

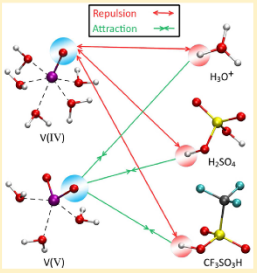
pubs.acs.org/JPCA

Effect of Sulfuric and Triflic Acids on the Hydration of Vanadium Cations: An *ab Initio* Study

Fatemeh Sepehr and Stephen J. Paddison*

Department of Chemical & Biomolecular Engineering, University of Tennessee, Knoxville, Tennessee 37996, United States

ABSTRACT: Vanadium redox flow batteries (VRFBs) may be a promising solution for large-scale energy storage applications, but the crossover of any of the redox active species V^{2+}, V^{3+}, VO^{2+}, and VO_2^+ through the ion exchange membrane will result in self-discharge of the battery. Hence, a molecular level understanding of the states of vanadium cations in the highly acidic environment of a VRFB is needed. We examine the effects of sulfuric and triflic (CF_3SO_3H) acids on the hydration of vanadium species as they mimic the electrolyte and functional group of perfluorosulfonic acid (PFSA) membranes. Hybrid density functional theory in conjunction with a continuum solvation model was utilized to obtain the local structures of the hydrated vanadium cations in proximity to H_2SO_4, CF_3SO_3H, and their conjugate anions. The results indicate that none of these species covalently bond to the vanadium cations. The hydration structure of V^{3+} is more distorted than that of V^{2+} in an acidic medium. The oxo-group of VO_2^+ is protonated by either acid, in contrast to VO^{2+} which is not protonated. The atomic partial charge of the four oxidation states of vanadium varies from +1.7 to +2.0. These results provide the local solvation structures of vanadium cations in the VRFBs environment that are directly related to the electrolytes stability and diffusion of vanadium ions into the membrane.



INTRODUCTION

Recently, there has been an increased interest in redox flow batteries (RFBs) in order to transpire the substitution of fossil fuels with renewable energy sources such as solar and wind. Having the power and energy decoupled, these batteries can store electrical energy in the form of chemical energy on a multi-megawatt scale. Particularly, all-vanadium redox flow batteries (VRFBs) are of interest for grid-scale electrical energy storage due to long lifespan, fast response, and no inherent cross-contamination.[1] The VRFB has vanadium cations at four different oxidation states as its electroactive species. The four vanadium cations are solvated in a concentrated sulfuric acid solution as the supporting electrolyte. The V^{3+}/V^{2+} couple at the negative electrolyte tank and the VO^{2+}/VO_2^+ couple at the positive tank. They are separated by an ion exchange membrane that only allows the permeation of one type of ion (i.e., cation or anion) in order to complete the electrical circuit.[2]

In general, VRFBs have low energy density and therefore need large electrolyte tanks which limit their application to stationary storage.[3,4] The energy density of the battery depends on the concentration of the vanadium solution. Hence, increasing the vanadium concentration results in a favorable energy density increase for the battery. However, the concentration of vanadium ions is limited by poor stability of electrolytes and precipitation. In fact, all four vanadium cations form precipitates by increasing the vanadium concentration in a sulfuric acid solution. The stability of the electrolytes is also affected by the concentration of sulfuric acid, solution temperature, and the state of charge of the battery.[5−7] The stability of VO_2^+ in sulfuric acid is limited by V_2O_5 precipitation at high temperatures (>40 °C) and high vanadium concentration (>2 M).[8] Although the VO_2^+ concentration can be increased through the addition of sulfuric acid to the solution, the increase in acid concentration is limited by the stability of the VO^{2+} species, as both VO_2^+ and VO^{2+} species are present in the positive electrolyte.[7] In contrast to the VO_2^+ ion, the V^{2+}, V^{3+}, and VO^{2+} solutions are stabilized by increasing the temperature and decreasing the sulfuric acid concentration,[5,7] which makes the design of VRFB electrolytes challenging. Inorganic and organic agents have been added in an effort to stabilize the electrolytes.[6,9−12] The stability of the vanadyl solution V(IV) at low temperatures can be improved by addition of stabilizing agents; however, the effect of stabilizers should be considered on both the V(IV) and V(V) solutions as they coexist at the positive electrolyte. Furthermore, since the crossover of stabilizing agents through the membrane is possible, their effects should be considered on all four vanadium cations simultaneously.[6,11]

Membranes used in VRFBs are classified as either cation exchange or anion exchange depending on the type of ion they permeate. Both types of membranes must exhibit low permeability to the vanadium ions, high proton or sulfate conductivity, good thermal and chemical stability, good mechanical integrity, and low cost.[1,3] Usually, the imperfect ion selectivity of the cation exchange membrane results in vanadium cation crossover that causes electrolyte contamination and capacity loss of the battery as well as a decrease in conductivity of membrane.[1,13−15] In addition, the unexpected diffusion of sulfuric acid into Nafion has been reported.[16−18]

Received: February 23, 2015
Revised: May 7, 2015
Published: May 8, 2015

ACS Publications © 2015 American Chemical Society

DOI: 10.1021/acs.jpca.5b01794
J. Phys. Chem. A 2015, 119, 5749−5761

Reprinted with permission from Journal of Physical Chemistry A 2015, 119, 5749-5761.
Copyright 2015 American Chemical Society.

Hence, there is ongoing research on the development of new membranes and membrane treatment methods to decrease solvent and vanadium ion transport across the membrane.[19−22] One of the most widely used cation exchange membranes for VRFBs is the perfluorosulfonic acid (PFSA) membrane, Nafion. In the presence of water Nafion phase separates into a porous hydrophobic matrix with nanoscale domains of water. The water domains are lined with sulfonate groups.[23−27] In a VRFB environment protons and vanadium cations permeate through the water domains. Although the mobility of the vanadium cations is much lower than that of a proton, over time the crossover of vanadium cations results in capacity loss and electrolyte contamination.[13,28,29] Hence, because Nafion is a stable membrane for VRFBs,[30] it is important to understand the diffusion of vanadium ions through this material in order to provoke novel materials that exhibit reduced vanadium crossover.

Under the high ionic strength environment of a VRFB, understanding of the nature of hydrated vanadium cations and their local interactions with the solvent and membrane is crucial and beneficial to optimizing the design and modification of electrolytes and membranes. Although there has been some work done understanding the preferred structure of the vanadium cations, their hydration free energies, electrolyte stability, and the nature of diffused vanadium in the membrane,[8,31−38] a molecular level investigation on the interaction of vanadium cations in sulfuric acid electrolyte and PFSA membranes is warranted. This work seeks to unravel the local interactions and molecular structures of the hydrated vanadium cations in close proximity to sulfuric acid (H_2SO_4) and trifluoromethanesulfonic acid (CF_3SO_3H). These two acids are selected because they exist in the electrolyte and PFSA membrane of a VRFB.

We begin with a brief description of the computational methods used to determine the hydration of vanadium cations in proximity to sulfuric and triflic acids. This is followed by a presentation of the results and discussion on the local structure of the four vanadium cations in the presence of the strong acids. Finally, the significant findings are summarized in the conclusions section.

■ COMPUTATIONAL METHODS

Electronic structure calculations were performed on each of the hydrated cations in the presence of an acid molecule using the Gaussian 09 suite of programs.[39] The introduction of an acid to each of the four vanadium cations was performed beginning from three different initial starting positions. In the first set of geometry optimizations, the acid molecule was placed adjacent to the hydrated vanadium cation. In the second set, one of the water molecules of the hydration shell was replaced by an acid molecule and placed at a different position in the cluster. Under the third set of conditions the acid molecule was forced to coordinate with the central vanadium ion, while all the water molecules in the first hydration shell remained coordinated with the vanadium cation. It should be noted that the total number of initial starting geometries generated for each set of conditions often exceeded several hundred due to the steric and symmetry of the ions and molecules.

After generating the initial coordinates, optimizations were carried out over all degrees of freedom by conjugate gradient methods without symmetry constraints using density functional theory (DFT) invoking Becke's three-parameter functional (B3LYP)[40−42] and the 6-31G**[43−45] split-valence basis set. The V^{2+} and V^{3+} cations were considered to be of high spin state in the open shell calculations.[46,47] The resulting structures were then refined with optimizations performed with the larger 6-311G** basis set[48] and were followed by a frequency calculation at the same level of theory to confirm local minima and facilitate correction for zero-point energies (ZPEs). Subsequently, a universal solvation model[49] (implemented in Gaussian 09 as SMD) was utilized to optimize all of the resulting structures with the solvent dielectric constant of water (ε = 78). The B3LYP/6-311G** model chemistry along with the SMD continuum solvation model was chosen because we determined[37] that it predicts the structures of the vanadium cations in bulk water and the associated hydration free energies in good agreement with the experimental values.[35,50−54] The importance of using a dielectric continuum solvation model in correctly accounting for the hydration effects of the vanadium cations was previously substantialized.[37,55,56]

The vanadium cations were hydrated by their first hydration shell, and only one acid or ion was added to each cluster. Hence, the water molecules in the first hydration shell of the vanadium cations were treated explicitly while the additional effects of the solvent (second and third hydration shells) were included implicitly through the SMD model. The addition of an explicit second hydration shell, acid molecules, or ions was deemed to be unnecessary from a practical computational stand point. It is worth noting that a recent computational study determined that the explicit solvation of the first and second hydration shells around Cu^{2+} were needed for an accurate estimation of the reaction free energies.[57] This is in contrast to the hydration of vanadium cations where it was found that explicit inclusion of only the first hydration shell was sufficient to correctly predict both the structural and thermodynamic properties.[37]

Among all the optimized structures obtained from the many different initial geometries, the structures with the lowest energy were selected as the global minimum. In order to test whether a different treatment of the dispersion forces would affect the results, optimizations were performed using MP2 on V^{3+} in proximity to sulfuric acid. The results were essentially identical to the B3LYP results with only minor structural changes. For the other clusters, only single point MP2 calculations were performed on the B3LYP optimized structures. It was found that even with MP2 the B3LYP determined global minima structures were still the lowest energy configurations. Partial atomic charges were also computed using the ChelpG scheme[58] with the inclusion of the SMD solvation model. A local interaction analysis of the oxo-species was undertaken by mapping the electrostatic potential energies onto a 0.002 electron density isosurface.

Since both H_2SO_4 and CF_3SO_3H are very strong acids, the dissociation of the proton in water is expected. Therefore, in the calculations not only the acids (H_2SO_4, CF_3SO_3H) but also their conjugate anions (HSO_4^-, SO_4^{2-}, $CF_3SO_3^-$) were considered. Moreover, due to the high proton concentrations in a VRFB medium, the local interactions between the hydrated proton and the vanadium cations were also investigated.

In order to probe the effects of the dielectric permittivity of the aqueous acids, optimizations were undertaken with dielectric constants set to ε = 50 and ε = 20. Although the energy differences between the global and local minima were dependent on the solvent dielectric constant, the selected global minima remained unchanged. Only minor structural changes were observed, and the overall results were found to be

DOI: 10.1021/acs.jpca.5b01794
J. Phys. Chem. A 2015, 119, 5749−5761

Reprinted with permission from Journal of Physical Chemistry A 2015, 119, 5749-5761.
Copyright 2015 American Chemical Society.

independent to the change of solvent dielectric constant from 78 to 20.

RESULTS AND DISCUSSION

V^{2+} Cation. The fully optimized configurations of a hydrated V^{2+} ion in proximity to (a) sulfuric acid, (b) triflic acid, (c) bisulfate, (d) triflate, and (e, f) sulfate are shown in Figure 1. The mean V···O(H_2O) distance for water molecules in the primary hydration shell are reported in Table 1 while other distances including the vanadium−sulfur are shown in Figure 1. The mean and standard deviation of the OVO angles are reported in Table 2. In Figure 1 the V^{2+} adopts a hexacoordinated octahedral structure in the presence of all acids and anions with a slight angle deviation (<3°) from 90°. This strong tendency of the V^{2+} cation to form hexacoordinated complexes is also seen in solid state by crystallographic measurements of $[V(H_2O)_6]SO_4$, $[V(H_2O)_6](SiF_6)_2$, and Tutton salt of $(NH_4)_2[V(H_2O)_6](SO_4)_2$ by Cotton et al.[54,59] and $[V(H_2O)_6](CF_3SO_3)_2$ by Holt et al.[60] Moreover, the QM/MM-MD and quasi-chemical theory studies revealed that the V^{2+} prefers a hexacoordinating structure in liquid water.[37,46]

Among all the structures illustrated in Figure 1, no covalent bond formed between the vanadium cation and the acids/anions. The metal cation acts as a Lewis acid and accepts electron density from the oxygen atom of either a water or an acid molecule (the latter acting as a Lewis base). Since the shared electrons are only from the Lewis base, the bonds are dipolar or coordinate and may undergo ligand substitution reactions.

Table 3 shows partial atomic charges on the vanadium and water molecules in the primary hydration shell both in pure water and in the presence of the acids or anions (studied in this work). The partial charge on the vanadium atom varies from +1.7 to +1.8, which is less than its formal charge of +2. The neighboring water molecules are not charge neutral and carry a positive partial charge indicating that a small portion of the positive charge on the V^{2+} cation disperses on its ligands.

In the presence of molecular acids as shown in Figures 1a,b it is observed that one of the water molecules in the primary hydration shell is replaced by the acid. However, the direct interaction of the oxygen atom of the acid with the cation does not change the hexacoordinated octahedral structure of the V^{2+} ion. The distances between the oxygen atom of the acid (which is in direct interaction with V^{2+}) and the vanadium ion are 2.31 and 2.23 Å for the sulfuric and triflic acids, respectively (see Figures 1a,b). These distances are 0.13 and 0.04 Å longer than the average V···O(H_2O) distances in each configuration (see Table 1).

The interaction between the molecular acids and the V^{2+} ion affects the extent of dissociation of the acids. It can be seen from Figures 1a,b that the sulfuric acid does not dissociate and only forms hydrogen bonds with the water, whereas the triflic acid undergoes dissociation forming a hydronium ion. This is due to the fact that CF_3SO_3H acid is a stronger acid than H_2SO_4 and hence has a higher propensity to transfer a proton. The displaced water molecule in the sulfuric acid complex (Figure 1a) forms two hydrogen bonds: one with the hydration shell and the other with the sulfuric acid that results in only stretching of the HO_3SO−H bond. However, in the triflic acid complex (Figure 1b) the displaced H_2O (now H_3O^+) is only hydrogen bonded with the acid. The S···V^{2+} distances are similar for both acids (≈3.5 Å) as either acid coordinates directly with V^{2+}.

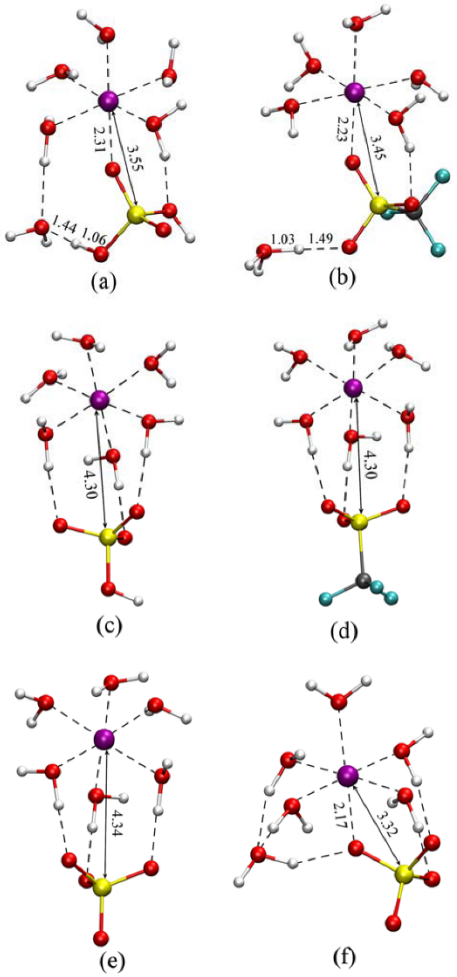


Figure 1. Fully optimized configurations at the B3LYP/6-311G**/SMD level of theory for the hydrated V^{2+} cation in proximity to (a) H_2SO_4, (b) CF_3SO_3H, (c) HSO_4^-, (d) $CF_3SO_3^-$, and (e) SO_4^{2-}. The geometry in (f) is a local minimum in proximity to sulfate with 0.3 kcal/mol higher energy than the configuration in (e). The atomic color scheme used in the figures: oxygen (red), hydrogen (white), vanadium (purple), sulfur (yellow), carbon (gray), and fluorine (cyan). In the figures distances are in angstroms, two-tone solid lines present covalent bonds, and dashed lines show coordinate bonds and hydrogen bonds (hydrogen bond criterion 1.1 Å < O···H < 2.5 Å).

The global minimum energy structures for the interaction of the bisulfate and triflate anions with hydrated V^{2+} are shown in Figures 1c,d. In contrast to the two acid conformations (Figures 1a,b) in the presence of the bisulfate and triflate (Figures 1c,d) the primary hydration shell consists of all six water molecules, and the anions do not enter and are only hydrogen bonded to the primary hydration shell. Obviously, the S···V^{2+} distance is

DOI: 10.1021/acs.jpca.5b01794
J. Phys. Chem. A 2015, 119, 5749−5761

Reprinted with permission from Journal of Physical Chemistry A 2015, 119, 5749-5761.
Copyright 2015 American Chemical Society.

Table 1. Vanadium−Oxygen Distance for Optimized Structures Shown in Figures 1−4 (All Values in Å)

	V^{2+}	V^{3+}	VO^{2+}			VO_2^+	
species	V···O(H_2O)[a]	V···O(H_2O)[a]	V−O_{oxo}	V···O(H_2O equatorial)[a]	V···O(H_2O axial)	V−O_{oxo}[a]	V···O(H_2O)[a]
H_2SO_4	2.18	2.07	1.56	2.07	3.57	1.64	2.04
CF_3SO_3H	2.19	2.07	1.56	2.08	7.76	1.64	2.05
HSO_4^-	2.20	2.08	1.56	2.06	3.94	1.60	2.10
$CF_3SO_3^-$	2.19	2.07	1.56	2.06	3.58	1.60	2.10
SO_4^{2-}	2.19	2.09	1.57	2.09	3.26	1.61	1.92
water[b]	2.19	2.09	1.57	2.10	2.35	1.60[c,d]	2.11,[c] 2.20[d]

[a]Mean value. [b]Taken from ref 37. [c]Bipyramidal. [d]Octahedral.

Table 2. OVO Angles for Hydrated Vanadium Cations (All Values in deg)

environment	V^{2+} ∠OVO[a]	V^{3+} ∠OVO[a]	VO^{2+} $\angle O_{oxo}VO$[b]	VO_2^+ $\angle O_{oxo}VO_{oxo}$[c]
H_2SO_4	90.0 ± 2.9	90.0 ± 2.7	105.1 ± 1.7	103.3
CF_3SO_3H	90.0 ± 0.8	90.0 ± 2.0	105.4 ± 2.4	103.8
HSO_4^-	90.0 ± 2.9	90.1 ± 5.2	104.3 ± 2.2	106.7
$CF_3SO_3^-$	90.0 ± 2.5	90.0 ± 3.8	105.2 ± 1.3	107.7
SO_4^{2-}	90.0 ± 1.9	90.0 ± 3.6	107.3 ± 6.5	108.1
water[d]	90.0 ± 1.2	90.0 ± 0.8	99.2 ± 2.4	107.3,[e] 105.8[f]

[a]Mean value and standard deviation of the angles in octahedral structure. [b]Mean value and standard deviation of the angles between oxo-oxygen, vanadium, and oxygen of equatorial ligands of oxo-vanadium(IV). [c]Angle between oxo-oxygen, vanadium, and oxo-oxygen of dioxo-vanadium(V). [d]Taken from ref 37. [e]Bipyramidal. [f]Octahedral.

greater for the anions (4.3 Å) than for the acids (ca. 3.5 Å) because the anions do not directly interact with the cation and only interact with V^{2+} through the primary hydration shell. From a consideration of only the electrostatics one expects closer association of the anions to V^{2+}. However, the presence of the high dielectric constant solvent (i.e., water $\varepsilon = 78$) and the hydrogen bonds between the anions and hydration shell that increase structural stability results in the dissociation of the hydrated V^{2+} cation from HSO_4^- and $CF_3SO_3^-$ anions and prevents formation of contact ion pairs. The former contributes more significantly because in the absence of a solvation model (i.e., in the gas phase), the most stable structures are with the anions occupying the primary hydration shell and directly interacting with V^{2+}.

We obtained two conformations of very similar energy for the interaction of hydrated V^{2+} with sulfate. These are shown in Figures 1e,f. The structure in Figure 1e with the SO_4^{2-} outside of the primary hydration shell is 0.3 kcal/mol lower in energy

Table 3. Computed Atomic Partial Charges on Vanadium, Oxygen, and Water Molecules in the Primary Hydration Shell Using ChelpG Scheme

environment		V^{2+}	V^{3+}	VO^{2+}	VO_2^+
H_2SO_4	V	1.778	1.851	1.850	1.825
	H_2O[a]	0.036	0.184	0.176	0.228
	O(H_2O)[b]	−0.952	−0.825	−0.797	−0.752
	O_{oxo}			−0.605	−0.777,[c] −0.455
CF_3SO_3H	V	1.749	1.995	1.792	1.940
	H_2O[a]	0.044	0.169	0.178	0.208
	O(H_2O)[b]	−0.914	−0.855	−0.826	−0.813
	O_{oxo}			−0.574	−0.774,[c] −0.465
HSO_4^-	V	1.700	1.889	1.816	1.798
	H_2O[a]	0.026	0.159	0.146	0.163
	O(H_2O)[b]	−0.913	−0.836	−0.814	−0.812
	O_{oxo}			−0.612	−0.771, −0.631
$CF_3SO_3^-$	V	1.799	2.057	2.031	1.861
	H_2O[a]	0.025	0.139	0.129	0.153
	O(H_2O)[b]	−0.947	−0.880	−0.924	−0.853
	O_{oxo}			−0.652	−0.745, −0.692
SO_4^{2-}	V	1.729	2.044	1.899	1.810
	H_2O[a]	0.011	0.098	0.093	0.139
	O(H_2O)[b]	−0.940	−0.889	−0.894	−0.857
	O_{oxo}			−0.666	−0.776, −0.740
water[d]	V	1.719	2.054	1.801	1.805,[e] 1.703[f]
	H_2O[a]	0.047	0.158	0.179,[g] 0.097[h]	0.161,[e] 0.167[f]
	O(H_2O)[b]	−0.895	−0.859	−0.797,[g] −0.838[h]	−0.783[e], −0.763[f]
	O_{oxo}			−0.615	(−0.702, −0.697),[e] (−0.702, −0.671)[f]

[a]Average total charge on water molecules in the primary hydration shell of vanadium. [b]Average atomic charge on oxygen atom of water molecules in the primary hydration shell of vanadium. [c]Protonated oxo-oxygen. [d]Taken from ref 37. [e]Bipyramidal. [f]Octahedral. [g]Equatorial water molecules. [h]Axial water molecule.

DOI: 10.1021/acs.jpca.5b01794
J. Phys. Chem. A 2015, 119, 5749−5761

Reprinted with permission from Journal of Physical Chemistry A 2015, 119, 5749-5761.
Copyright 2015 American Chemical Society.

than Figure 1f with the sulfate directly interacting to V^{2+} at 2.17 Å. Hence, the former is taken to be the global minimum. We further investigated both structures by adding up to two additional water molecules and optimizing the structures. However, the results indicate that even with as many as seven or eight water molecules the two configurations still have very similar energy difference. This suggested that the probability for both configurations occurring is roughly equal. This small energy difference between the two lowest energy conformations was only observed for the hydrated V^{2+} with SO_4^{2-}. All other cation−anion complexes reported in this work are at least 1.1 kcal/mol more stable than the next lowest energy minima.

V^{3+} Cation. The results for the V^{3+} cation are shown in Figure 2. Similar to V^{2+}, V^{3+} also exhibits a hexacoordinated octahedral structure in accordance with previous experimental and computational studies.[35,37,53,55,61−65] However, the octahedral angles deviate more significantly from 90° when compared to V^{2+} (see Table 2), indicating that the structure is more distorted in the presence of the acids/anions when compared to V^{2+}.

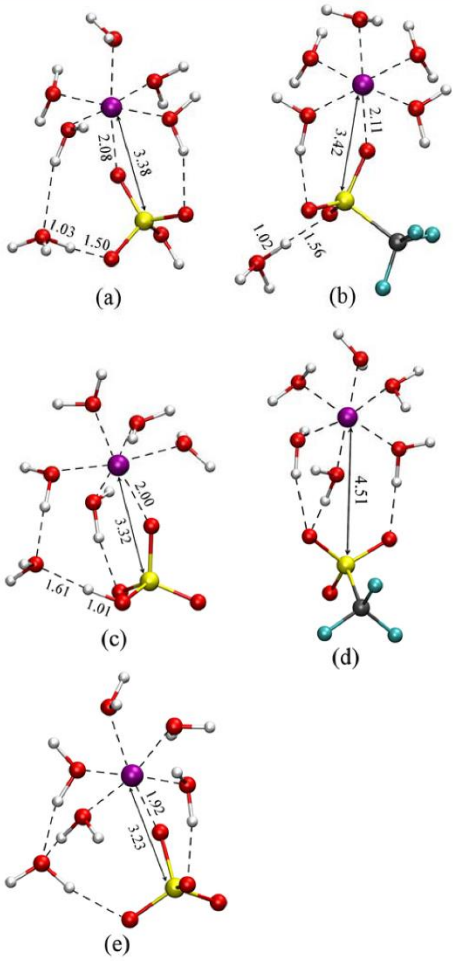


Figure 2. Fully optimized configurations at the B3LYP/6-311G**/SMD level of theory for the hydrated V^{3+} cation in proximity to (a) H_2SO_4, (b) CF_3SO_3H, (c) HSO_4^-, (d) $CF_3SO_3^-$, and (e) SO_4^{2-}.

In Figures 2a,b both acid molecules (H_2SO_4 and CF_3SO_3H) displace one water molecule from the primary hydration shell. The bond distances between the oxygen atom of the acid and V^{3+} are 2.08 and 2.11 Å for sulfuric and triflic acids, respectively (Figures 2a,b), and are longer than the average V···O(H_2O) distances in each configuration (see Table 1). Comparing to V^{2+}, both sulfuric and triflic acids associate closer to V^{3+}, implying a stronger interaction between the acids and the cation. Previously, we reported that the V^{3+} cation has the greatest solvation free energy and associated water binding energy among the four vanadium cations and almost twice the value for the V^{2+} ion.[37] However, the atomic charge on V^{3+} (reported in Table 3) varies from +1.9 to +2.1 (formal charge of +3), which is slightly greater than the atomic charge on the V^{2+} ion. Consequently, the electron donor ligands around the V^{3+} carry a relatively high positive charge to compensate the difference between the formal charge of the V^{3+} ion and the actual charge residing on the atom. The charges on the water molecules as reported in Table 3 vary from +0.1 to +0.18 and are an order of magnitude greater than those of V^{2+}. This considerable charge transfer observed indicates that the coordinate bonds between the metal and ligands for the V^{3+} cation are stronger resulting in the closer association of the acids to V^{3+}.

Both H_2SO_4 and CF_3SO_3H with the V^{3+} cation dissociate and form H_3O^+ with the displaced water (Figures 2a,b), whereas only the stronger acid, CF_3SO_3H, dissociates with the V^{2+} cation. This again is due to the higher charge transfer to the ligands for V^{3+} than V^{2+} and facilitates proton dissociation by both acids.

Figures 2c−e illustrate the anions interacting with the hydrated V^{3+} cation. It can be seen that both HSO_4^- and SO_4^{2-} enter the hydration shell and coordinate directly with vanadium, but $CF_3SO_3^-$ does not enter the shell forming hydrogen bonds with the water molecules. The formation of contact ion pairs between V^{3+} and SO_4^{2-} has been observed previously, both experimentally and computationally.[34] The structure of the V^{3+} cation with triflate as the counteranion is in agreement with the crystallography results of Cotton et al.[53] in solid state and NMR studies of Hugi et al.[62] in solution. In the previous case involving V^{2+}, the anions dissociated and did not form contact ion pairs. We primarily attribute this to the ability of the solvent to dissociate the ions. However, in the case of the V^{3+} cation two out of the three anions (i.e., bisulfate and sulfate) form contact ion pairs. This suggests that the high electrostatic interaction between the positive and negative ions may overcome the ion dissociation effect of the solvent. This only takes place for the bisulfate and sulfate anions and not triflate. This may be explained by considering the following: (1) triflate is the conjugate base of a very strong acid owing to the electron withdrawing by the trifluoromethyl group, and (2) V^{3+} transfers a high positive charge to its ligands as discussed above (i.e., electrons are transferred from anion to cation) that is not feasible for triflate with the strong electron withdrawing group of trifluoromethyl. Table 4 also shows that in most cases the charge residing on $CF_3SO_3^-$ is more negative compared to HSO_4^-.

DOI: 10.1021/acs.jpca.5b01794
J. Phys. Chem. A 2015, 119, 5749−5761

Reprinted with permission from Journal of Physical Chemistry A 2015, 119, 5749-5761.
Copyright 2015 American Chemical Society.

Table 4. Computed Atomic Partial Charges on Sulfur, Oxygen Atoms of Acid/Anion, and Negative Fragment Using ChelpG Scheme

environment		V^{2+}	V^{3+}	VO^{2+}	VO_2^+
H_2SO_4	S	1.592	1.402	1.429	1.488
	O	−0.704[a]	−0.660[b]	−0.647[a]	−0.722[b]
	negative fragment (H_2SO_4 or HSO_4^-)	−0.120[c]	−0.679[d]	−0.099[c]	−0.851[d]
CF_3SO_3H	S	1.357	1.189	1.352	1.059
	O[a]	−0.736	−0.653	−0.711	−0.666
	negative fragment ($CF_3SO_3^-$)	−0.889	−0.752	−0.815	−0.918
HSO_4^-	S	1.361	1.437	1.467	1.467
	O[b]	−0.686	−0.695	−0.734	−0.730
	negative fragment (HSO_4^-)	−0.858	−0.805	−0.972	−0.925
$CF_3SO_3^-$	S	0.952	1.162	1.099	1.079
	O[a]	−0.648	−0.675	−0.683	−0.674
	negative fragment ($CF_3SO_3^-$)	−0.948	−0.890	−0.934	−0.933
SO_4^{2-}	S	1.509	1.571	1.555	1.500
	O[a]	−0.825	−0.796	−0.798	−0.750
	negative fragment (SO_4^{2-})	−1.792	−1.614	−1.637	−0.977[d]

[a]Average atomic charges of all oxygen atoms of acid/anion. [b]Average atomic charges of the three oxygen atoms of acid/anion that are not protonated. [c]H_2SO_4 [d]HSO_4^-

VO^{2+} Cation. Figure 3 shows the results of the VO^{2+} cation in proximity to the acids and anions. The structural distances and angles are reported in Tables 1 and 2. Vanadium in the aqua-vanadyl ion adopts a hexacoordinated structure in pure water.[31,37,66] However, the calculation results in Figures 3a−d show that in close proximity to the acids/anions the axial water in the *trans* position relative to VO is replaced with either an acid or anion. Although the acids or anions are in the axial position, their distance from VO^{2+} is greater than 4 Å (as a result of the high dielectric solvent); therefore, the acids or anions are not considered coordinating with vanadyl, and vanadium becomes pentacoordinated. The solidity of the VO_{oxo} entity in Figure 3 is in accordance with the fact that vanadyl is the most stable diatomic ion[67] present in both solution and solid phases with a strong covalent bond between vanadium and oxo-oxygen.[68,69] In Figure 3 there are no interactions with the oxo-oxygen, and also none of the minimum-energy geometries obtained for the VO^{2+} show any interactions within 3 Å of the oxo-oxygen. Previously, Ballhausen and Gray presented a molecular orbital bonding scheme for vanadyl ion in which the oxygen 2p orbitals are used in σ-bonding with the metal and only the nonbonding sp_σ hybrid remains, which is energetically unsuited for bonding.[68] This explains the high stability and absence of any interactions of the oxo-oxygen observed in our results.

Table 3 reports the partial atomic charge on vanadium in the range of +1.8 to +2.0, which is much less than its formal charge of +4. The charge on the oxo-oxygen atom is about −0.6, which gives a total charge of +1.2 to +1.4 on the VO_{oxo} instead of formal charge of +2. Hence, the water ligands are positively charged as were for the V^{2+} and V^{3+} cations. The charge on the water ligands of VO^{2+} is in the same order of V^{3+} and almost an order of magnitude greater than that of V^{2+}.

In Figures 3a−d the presence of the acids or anions decreases the $V-O_{oxo}$ bond by 0.01 Å and also displaces the axial water molecule.[37] The triflic and triflate associate closer to the VO^{2+} cation than the sulfuric and sulfate. The same trend was followed by the V^{2+} cation in Figure 1; however, the V···S distances were shorter as a result of stronger interactions and contact ion pairs. Figures 3a−d represent the high propensity of axial water replacement by acids/anions. However, this replacement does not result in a strong contact ion pair formation but a weak interaction between the hydrated vanadyl and acids/anions. Recently, a combined experimental and theoretical analysis of core-level vanadium and sulfur K-edge spectroscopy revealed that both contact ion pair and solvent share interactions between diffusing vanadyl ion, and sulfonic sites of Nafion are probable.[70] However, authors stated that different factors may result in preference of one over the other.

The extent of dissociation of the acids interacting with VO^{2+} (Figures 3a,b) is similar to that of the V^{2+} cation. Triflic acid again dissociates completely and forms a hydronium ion, whereas the sulfuric acid does not dissociate with only a slight stretching of the OH bond due to hydrogen bonding with the displaced H_2O. Based on our previous work, the V^{2+} and VO^{2+} cations have very similar hydration free energies (−440.0 and −457.2 kcal/mol, respectively) and binding energies to the water molecules (−56.1 and −64.7 kcal/mol, respectively).[37] Thus, despite the fact that V^{2+} and VO^{2+} have quite different structures, they have very similar hydration free energies, binding energies, and proton dissociation behavior.

The interaction of VO^{2+} with sulfate (Figure 3e) forms a rather different structure which is still pentacoordinated but has the sulfate anion in one of the equatorial positions. The distance between the oxygen atom of the sulfate and vanadium is 1.97 Å which is shorter than the average V···O(H_2O equatorial) distance (see Table 1) and indicates a stronger interaction with SO_4^{2-}. This structure is similar to the crystallographic measurements of Ballhausen et al.[52] The equatorial and axial water molecules that are displaced from the primary hydration shell are hydrogen bonded with the remaining equatorial water molecules of the hydration shell. In Figure 3e, the oxo-oxygen bond is 1.57 Å, which is similar to the structure in bulk water. In all the other VO^{2+} clusters (Figures 3a−d) this bond is decreased to 1.56 Å as a result of displacement of the axial water. In addition, the sulfate cluster has the longest mean V···O(H_2O equatorial) (see Table 1). Hence, the direct coordination of oxo-vanadium(IV) with the sulfate anion (a strong electron donor group) increases both the covalent $V-O_{oxo}$ and dipolar V···O(H_2O equatorial) bonds. Among all the acids or anions examined, only the sulfate forms an ion pair with VO^{2+}.

DOI: 10.1021/acs.jpca.5b01794
J. Phys. Chem. A 2015, 119, 5749−5761

Reprinted with permission from Journal of Physical Chemistry A 2015, 119, 5749-5761.
Copyright 2015 American Chemical Society.

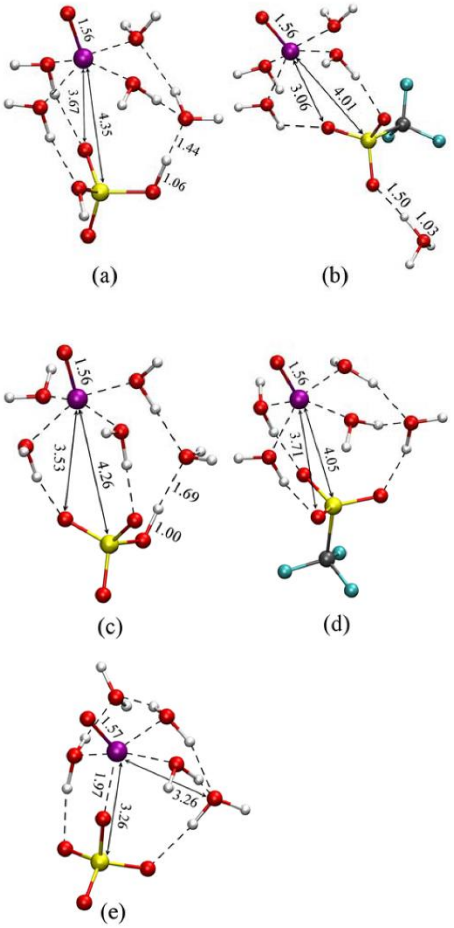


Figure 3. Fully optimized configurations at the B3LYP/6-311G**/SMD level of theory for the hydrated VO^{2+} cation in proximity to (a) H_2SO_4, (b) CF_3SO_3H, (c) HSO_4^-, (d) $CF_3SO_3^-$, and (e) SO_4^{2-}.

In Figure 3, the four equatorial ligands are located in a plane lower than vanadium, similar to the hydrated VO^{2+} in pure water or dilute solutions.[35,37,66] The angles between the oxo-oxygen, vanadium, and the oxygen atoms of the equatorial ligands are presented in Table 2. The $\angle O_{oxo}VO$ are increased by 5−6° in the presence of the acids/anions. The water molecule in the axial position (the weakest ligand in the primary hydration shell) in all cases is displaced by either an acid or anion with the result that the number of coordinating ligands for VO^{2+} is decreased by one. Hence, the $\angle O_{oxo}VO$ increases to stabilize oxo-vanadium(IV). These observations are similar to recent experimental results.[35] These authors reported that the presence of a space demanding oxygen-donor ligand removes the axial ligand and reduces the vanadium coordination number to five, which consequently increases the $\angle O_{oxo}VO$.

VO_2^+ Cation. Figure 4 shows the results of the VO_2^+ cation (vanadate) in proximity to the studied acids and anions. The

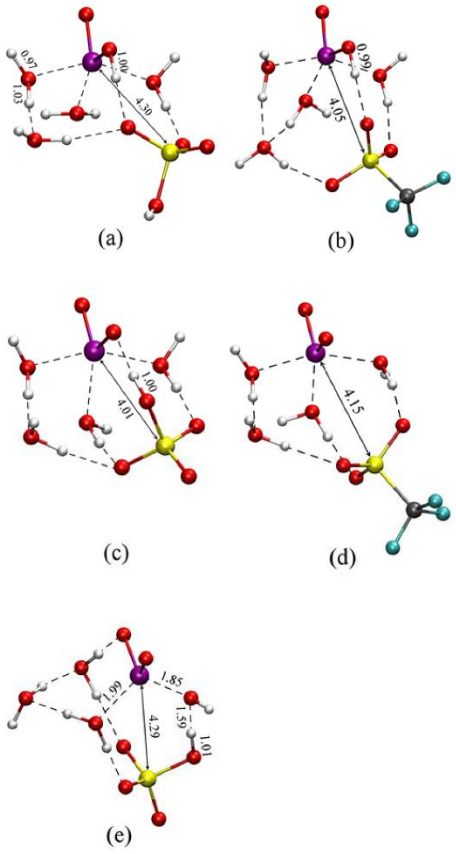


Figure 4. Fully optimized configurations at the B3LYP/6-311G**/SMD level of theory for the hydrated VO_2^+ cation in proximity to (a) H_2SO_4, (b) CF_3SO_3H, (c) HSO_4^-, (d) $CF_3SO_3^-$, and (e) SO_4^{2-}.

mean vanadium−oxygen distances and $\angle O_{oxo}VO_{oxo}$ for the illustrated clusters are reported in Tables 1 and 2. It is known that the solution acidity and total concentration of vanadium determine the form of the vanadium species in the +5 oxidation state.[71] In highly acidic solutions it generally exists in the form of a hydrated VO_2^+ cation, consistent with the results shown in Figure 4. Both penta- and hexahydrated structures have been reported for the hydrated VO_2^+.[37,56,72−74] However, the results from the electronic structure calculations (illustrated in Figure 4) suggest that VO_2^+ only adopts a pentacoordinated bipyramidal structure (except for sulfate in Figure 4e which has a tetracoordinated structure). We found no cases where the hexacoordinated octahedral is more stable than the bipyramidal. In fact, during the optimizations many of the initial octahedral geometries transformed into bipyramidal conformations. Also, among all the local minima those clusters with an octahedral conformation (not shown) were observed to have an energy at

DOI: 10.1021/acs.jpca.5b01794
J. Phys. Chem. A 2015, 119, 5749−5761

Reprinted with permission from Journal of Physical Chemistry A 2015, 119, 5749-5761.
Copyright 2015 American Chemical Society.

least 7 kcal/mol higher than those with a bipyramidal structure. This was also observed in our previous study of the VO_2^+ cation in bulk water.[37] The higher stability of the pentacoordinated VO_2^+ in comparison to the octahedral structure was also reported in previous electronic structure calculations and CPMD simulations.[8,37,56,74,75]

Figures 4a and 4b show the interaction of sulfuric and triflic acid on the hydrated VO_2^+ cation, respectively. In these two clusters, the acidic proton fully dissociates and protonates one of the oxo-oxygen atoms to form $[VO(OH)(H_2O)_3]^{2+}$ and the conjugate anion. In proximity to sulfuric acid (Figure 4a), in addition to protonation of the oxo-oxygen, a stretched hydrogen−oxygen bond with 1.03 Å length is observed for one of the water ligands. Deprotonation of the hydrated dioxovanadium cation and formation of a hydroxyl group may eventually result in inorganic polymerization and precipitation as reported previously by others.[8,56,71] The protonation of the positively charged oxo-species is unique to the VO_2^+ cation. As mentioned in the previous section, the oxo-vanadium(IV) is not protonated in the presence of either acid. Further investigations of the cation in proximity to a hydronium ion were performed, and the results are presented in the following section.

The interaction of VO_2^+ with the bisulfate anion is shown in Figure 4c. As mentioned before, the cation has a pentacoordinated bipyramidal structure. The proton of the bisulfate anion is hydrogen bonded to one of the oxo-oxygen atoms of VO_2^+. However, no dissociation or protonation of the oxo-group occurs. In Figure 4d, the cation with the triflate anion adopts a bipyramidal hydration structure, and $CF_3SO_3^-$ does not enter the primary hydration shell of the dioxo-vanadium(V). For the sulfate anion (see Figure 4e), a tetracoordinated vanadium structure is obtained. This structure has two oxo-oxygen atoms, one water ligand at 1.99 Å, and a hydroxyl group at 1.85 Å from the vanadium cation. The hydroxyl group is formed by deprotonation of a water ligand and transfer of the dissociated proton to the sulfate to form the bisulfate anion shown in Figure 4e. The other two water molecules are expelled from the primary hydration shell. The water deprotonation in proximity to the sulfate anion (now bisulfate) results in the formation of an active hydroxyl group that can be followed by oxolation condensation and formation of precipitates.[8,56,76] Madic et al.[77] reported the formation of dimeric species of aqua-dioxo-vanadium(V) involving HSO_4^- or SO_4^{2-} ions in concentrated sulfuric acid solutions that may polymerize at temperatures above 20 °C. The interaction of VO_2^+ with SO_4^{2-} ions and the formation of the complex illustrated in Figure 4e could be the initiation of precipitation.

The reduction of the vanadium coordination number to four, protonation of the oxo-oxygen, and deprotonation of a water ligand to form hydroxyl were also observed in CPMD simulations by Sadoc et al.[56] Although Sadoc et al. did not include counterions in their simulation box, they did witness the protonation of the oxo-groups at 300 K and in acidic medium at 500 K. They also observed hydroxyl formation through deprotonation of water at the higher temperature. Protonation of the vanadium(V) species under moderate acidic solutions has been well studied experimentally,[73,78] but for the VO_2^+ species the protonation has been only observed in simulations.

Table 3 reports that the partial charge on vanadium ranges from +1.7 to +1.9, which is significantly lower than its formal charge of +5. The negative charge on the oxo-oxygen varies between −0.5 and −0.8 depending on the environment and whether it is protonated or not. The water molecules in the hydration shell, as expected, are not charge neutral and carry the highest positive charge when coordinating with VO_2^+.

Vanadium Cations in Proximity to H_3O^+. DFT calculations using the procedure described in the Computational Methods section were first undertaken in a vacuum. However, none of the calculations converged except for clusters with VO_2^+ ion. In fact, the calculations showed that the V^{2+}, V^{3+}, and VO^{2+} cations actually repel a hydronium ion in the gas phase, whereas for the VO_2^+ ion the hydronium ion interacted with the oxo-group and the proton was shared with one of the oxo-oxygen atoms. To obtain an optimized geometry for hydrated V^{2+}, V^{3+}, and VO^{2+} cations, the gas phase optimization step was eliminated and the dielectric continuum model (SMD) was undertaken in the initial optimization.

The structures for the two oxo-species (VO^{2+} and VO_2^+ cations) with an added H_3O^+ are presented in Figure 5. The

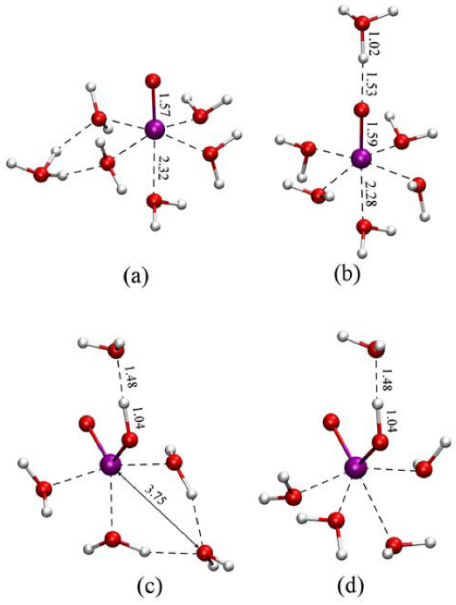


Figure 5. Hydrated vanadyl and vanadate cations in proximity to a hydronium ion: (a) hydrated VO^{2+} and H_3O^+; (b) hydrated VO^{2+} and H_3O^+ (2.91 kcal/mol higher energy than (a)); (c) hydrated bipyramidal VO_2^+ and H_3O^+; (d) hydrated octahedral VO_2^+ and H_3O^+ (8.21 kcal/mol higher energy than (c)).

interaction of either a V^{2+} or V^{3+} cation with a hydronium ion is very similar to Figure 5a, and since they are less important to the discussion here, their structures are not shown. The conformation in Figure 5a with the hydronium ion not interacting with the oxo-oxygen is more stable than the configuration in Figure 5b by 2.9 kcal/mol, indicating that the interaction of a proton with the oxo-oxygen of VO^{2+} cation is not favorable. This is in agreement with the molecular orbital bonding scheme of Ballhausen and Gray.[68] Therefore, as

DOI: 10.1021/acs.jpca.5b01794
J. Phys. Chem. A 2015, 119, 5749−5761

Reprinted with permission from Journal of Physical Chemistry A 2015, 119, 5749-5761.
Copyright 2015 American Chemical Society.

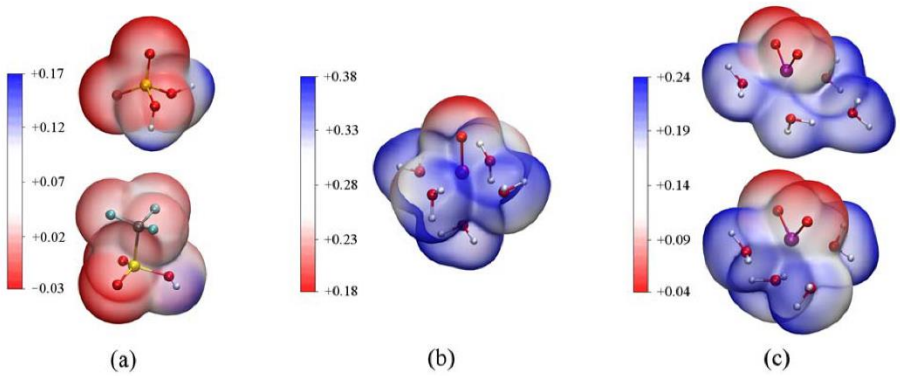


Figure 6. Electrostatic potential energies mapped onto electron density isosurface at 0.002 isovalue for (a) H_2SO_4 (top) and CF_3SO_3H (bottom) acids, (b) hydrated VO^{2+} cation, and (c) hydrated bipyramidal VO_2^+ cation (top) and hydrated octahedral VO_2^+ cation (bottom). The red and blue colors on the map are indicative of the electron-rich and electron-deficient areas, respectively. The color scale bars show electrostatic potential energies in hartree.

observed in Figures 3 and 5, the VO_{oxo} entity in the VO^{2+} cation is very stable.

The interaction of a hydronium ion with the VO_2^+ cation is shown in Figures 5c and 5d for bipyramidal and octahedral conformations, respectively. The bipyramidal VO_2^+ (Figure 5c) is more stable by 8.21 kcal/mol than the octahedral. In both conformations the hydronium ion protonates the oxo-oxygen similar to the interaction of the acids with the VO_2^+ species shown in Figures 4a,b. Hence, the interaction of the oxo-group of VO_2^+ with hydronium ion or acids is quite different than that of the VO^{2+} species, despite the fact that they both carry a positive total charge. Further insight into the reasons behind these results is given by the electrostatic potential maps in the following section.

Electrostatic Potential Maps. Electrostatic potential maps were computed and are shown for each acid and both the VO^{2+} and VO_2^+ cations in Figure 6. The higher electrostatic potential values indicate electron deficiencies (colored as blue), and the lower potentials represent electron-rich areas (shown in red). It is clear from Figure 6a that the acidic protons have a potential value of about +0.17 hartree. The oxo-groups (shown in Figures 6b,c) are electron-rich. In general, the electron-deficient areas with the higher potentials interact with the electron-rich areas with the lower potentials. In Figure 6c both bipyramidal and octahedral VO_2^+ species have potentials about +0.04 hartree on their oxo-oxygen atoms (electron-rich areas), which is smaller than the potentials on the acidic protons. Hence, the interaction of the acids with oxo-oxygen atoms of the VO_2^+ cation is favorable as indicated earlier. However, for the VO^{2+} cation (Figure 6b) the oxo-oxygen has a higher potential value (ca. +0.18 hartree) than the acidic hydrogen potentials (+0.17 hartree). This indicates that there are no interactions and even a slight repulsion between the oxo-oxygen atom and the acidic protons. Hence, the interaction of the acids or H_3O^+ is not favorable for the VO^{2+} cation, in agreement with its high stability,[67] whereas the inverse behavior is expected for the VO_2^+ cation with a probable protonation.

Hydrated V^{n+} in an Acidic Environment. For almost all the vanadium cations, the presence of either acid or anion decreases the V···O(H_2O) distance (see Table 1). The atomic partial charge on the vanadium atom is between +1.7 and +2.0 for all oxidation states either in water or in an acidic environment. The cations impose a partial positive charge on their ligands. The atomic charge on the sulfur atom (see Table 4) is always lower for CF_3SO_3H and $CF_3SO_3^-$ than observed for H_2SO_4 and HSO_4^-. This is because of the presence of the highly electron withdrawing, trifluoromethyl, group. Comparing the partial charge on the negative anion (Table 4), it is evident that the triflate anion is more negatively charged than the bisulfate anion. This is anticipated as $CF_3SO_3^-$ is the more stable conjugate base. The only exception is in the case of VO^{2+} where the bisulfate has a charge of −0.972 and triflate has −0.934 (structures shown in Figures 3c and 3d, respectively). This anomaly is likely due to the differences in the hydrogen bonding. The bisulfate (Figure 3c) is hydrogen bonded to the oxygen atom of a water molecule and therefore receives some electron density from the water. However, $CF_3SO_3^-$ (see Figure 3d) is only hydrogen bonded to the water molecules and therefore loses some electron density and becomes less negative than HSO_4^-.

The preparation of a vanadium solution usually involves the presence of excess sulfate as the counterion in the system. Hence, the addition of sulfuric acid to the system increases the concentration of both bisulfate and hydrated protons and decreases the sulfate concentration already present in the system (Le Chatelier's principle). The stability of the V^{2+}, V^{3+}, and VO^{2+} cations in a sulfuric acid solution decreases as the sulfuric acid concentration is increased. The electronic structure calculations indicated the presence of unfavorable interactions between H_3O^+ and each of the V^{2+}, V^{3+}, and VO^{2+} cations. Hence, at high acid concentrations the increased electrostatic repulsion between the hydrated protons and vanadium cations is responsible for the electrolyte instability. This unfavorable interaction between the protons and the oxo-group of VO^{2+} may be related to the proton mobility reduction reported for VO^{2+} in Nafion.[18]

The addition of sulfuric acid stabilizes the VO_2^+ solution, in contrast to the other oxidation states of vanadium. Rahman et al.[7] reported that the increase of the VO_2^+ concentration in the electrolyte is tied to the increase in the concentration of sulfuric

DOI: 10.1021/acs.jpca.5b01794
J. Phys. Chem. A 2015, 119, 5749−5761

Reprinted with permission from Journal of Physical Chemistry A 2015, 119, 5749-5761.
Copyright 2015 American Chemical Society.

acid. The electronic structure calculations indicate that the protons favorably interact and protonate the oxo-group of the VO_2^+ cation; therefore, upon the addition of sulfuric acid to the electrolyte there will be no strong repulsion effect. In the VO_2^+ section, it was revealed that the hydrated VO_2^+ cation is fairly stable in the presence of HSO_4^- (Figure 4c), whereas it forms a highly reactive hydroxyl group in proximity to SO_4^{2-} that can initiate precipitation (Figure 4e). Hence, by increasing the sulfuric acid concentration, the ratio of HSO_4^- to SO_4^{2-} increases, thereby stabilizing the hydrated VO_2^+. Our *ab initio* results confirm the previous observant on the stability of the VO_2^+ cation at low pH values.[71] However, it limits the extent of dissociation of the acid and the ratio of HSO_4^- to SO_4^{2-}.

Oriji et al. measured the electronic state of the VO^{2+} ions in sulfuric acid at concentrations greater than 5 M and observed that there is no noticeable change in the UV−vis spectra.[79] Figure 3 shows weak interactions and no covalent bond formation with VO^{2+} which indicate that the electronic state of the VO_{oxo} entity does not change in an acidic environment. Therefore, the UV−vis spectra did not change regardless of the increase in the acid concentration. In contrast to VO^{2+}, the authors observed shift in the main absorption band of VO_2^+ depending on the sulfuric acid concentration which indicates the nearest neighbor of VO_2^+ atom is affected by the sulfuric acid concentration.[79] Our calculations suggest protonation of the VO_2^+ cation in proximity to acidic protons as illustrated in Figures 4 and 5. As the protonation of the oxo-oxygen affects the nearest neighbor of VO_2^+ atom, therefore the shift in the UV−vis spectra is due to the protonation of the VO_2^+ cation at high acid concentrations. Conversely, the oxo-oxygen in the VO^{2+} cation does not interact, and consequently there is no change in its UV−vis spectra.

Among all the acids and anions examined, the triflate anion, on average, resides the farthest distance from a vanadium cation. The triflate anion does not directly interact with the cation and only forms hydrogen bonds with the water molecules in the primary hydration shell. This propensity of triflate to interact with the cations through their hydration shell has also been observed for triflate interacting with protons using static and dynamic *ab initio* studies[80,81] as well as crystallographic and NMR studies of vanadium cations with the triflate as the counterion.[35,53,60,62,82] Hence, the triflate ion has the least effect on the destabilization of the hydrated vanadium cations and may serve as a stabilizing agent similar to methanesulfonic acid (CH_3SO_3H) which has already been shown to stabilize VRFB electrolytes.[11]

The reaction energy associated with the interaction of triflic acid with each of the vanadium cations, i.e., $E(V^{n+}(\text{tri}^-\text{ic})\text{-}(H_2O)_{n-1}) + E(H_2O) - E(V^{n+}(H_2O)_n) - E(\text{triflic})$, is always negative for the structures shown in this work: −10.1, −7.6, −10.6, and −28.6 kcal/mol for V^{2+}, V^{3+}, VO^{2+}, and VO_2^+, respectively. Similar behavior is observed for the interaction of triflate with vanadium cations with −11.0, −13.0, −16.9, and −16.8 kcal/mol. This suggests that each of the vanadium cations favorably interacts with the perfluorosulfonic acid group, consistent with the permeation of all four vanadium cations through a PFSA membrane.[83,84] However, in the actual VRFB where all four vanadium cations simultaneously exist in the system, Vijayakumar et al. reported the presence of only the VO^{2+} species inside Nafion membranes.[32] Whether the prevalence of VO^{2+} in the membrane is a result of oxidation and reduction of the diffused species with each other[85] or the ever present VO^{2+} cation in all battery electrolytes is still unknown.[86] The local solvation results presented in this work do not remove the ambiguity on the prevalence of VO^{2+} in the membrane.

■ CONCLUSIONS

The local hydration structures of the four vanadium cations in proximity to sulfuric and triflic acids and their conjugate anions were elucidated through extensive electronic structure calculations. It was determined that for all four species the vanadium cations does not bind covalently to any of the acids or anions. However, the formation of contact ion pairs is possible and is promoted in the vicinity of a proton. The presence of either an acid or anion in the majority of cases decreased the V···O(H_2O) distance compared to that of the cation in bulk water. The structure of the V^{3+} ion is more distorted than V^{2+} when in the presence of any of the acids or anions. No interaction of a proton with the oxo-group of the VO^{2+} cation was observed. However, protonation of the oxo-group of the VO_2^+ cation was observed. The partial atomic charge on the vanadium cation for all oxidation states was computed to be between +1.7 and +2.0, significantly lower than the formal oxidation state.

The electrostatic repulsion between hydrated protons and V^{2+}, V^{3+}, and VO^{2+} cations under acidic conditions decreased the stability of their solutions. However, for VO_2^+, the protons interact with the oxo-groups, and therefore the repulsion effect was determined not to be important. Our results indicate that the VO_2^+ species is stable in the presence of HSO_4^- while it forms new complexes with SO_4^{2-} that can deprotonate and form hydroxyl which can subsequently precipitate. Hence, the stability of the VO_2^+ cation at low pH is linked to the proton concentration and the ratio of HSO_4^- to SO_4^{2-} in the solution.

The interaction of all four vanadium cations with CF_3SO_3H (the protogenic group of a PFSA ionomer) was found to be energetically favorable: all cations retained their primary hydration shell and did not form covalent bonds with the acid. However, in the vicinity of a hydrated proton the V^{2+} and V^{3+} cations formed contact ion pairs with CF_3SO_3H. The reduced proton mobility in PFSA membranes with absorbed VO^{2+} may be due to the unfavorable interaction of the oxo-group of VO^{2+} and hydrated protons. The triflate anion, in general, did not form a contact ion pair with any of the vanadium cationic species.

■ AUTHOR INFORMATION

Corresponding Author

*Fax +1 865 974 2026; e-mail spaddison@utk.edu (S.J.P.).

Notes

The authors declare no competing financial interest.

■ ACKNOWLEDGMENTS

This work was supported by the EPSCoR program of the National Science Foundation under the TNSCORE program with NSF EPS_1004083.

■ REFERENCES

(1) Skyllas-Kazacos, M. Secondary Batteries - Flow Systems| Vanadium Redox-Flow Batteries. In *Encyclopedia of Electrochemical Power Sources*; Garche, J., Ed.; Elsevier: Amsterdam, 2009; pp 444–453.

(2) Skyllas-Kazacos, M.; Rychick, M.; Robins, R. All-Vanadium Redox Battery. U.S. Patent 4,786,567, Nov 22, 1988.

DOI: 10.1021/acs.jpca.5b01794
J. Phys. Chem. A 2015, 119, 5749−5761

Reprinted with permission from Journal of Physical Chemistry A 2015, 119, 5749-5761.
Copyright 2015 American Chemical Society.

(3) Parasuraman, A.; Lim, T. M.; Menictas, C.; Skyllas-Kazacos, M. Review of Material Research and Development for Vanadium Redox Flow Battery Applications. *Electrochim. Acta* **2013**, *101*, 27−40.
(4) Weber, A. Z.; Mench, M. M.; Meyers, J. P.; Ross, P. N.; Gostick, J. T.; Liu, Q. H. Redox Flow Batteries: A Review. *J. Appl. Electrochem.* **2011**, *41*, 1137−1164.
(5) Skyllas-Kazacos, M.; Menictas, C.; Kazacos, M. Thermal Stability of Concentrated V(V) Electrolytes in the Vanadium Redox Cell. *J. Electroanal. Chem.* **1996**, *143*, L86−L88.
(6) Skyllas-Kazacos, M.; Peng, C.; Cheng, M. Evaluation of Precipitation Inhibitors for Supersaturated Vanadyl Electrolytes for the Vanadium Redox Battery. *Electrochem. Solid-State Lett.* **1999**, *2*, 121−122.
(7) Rahman, F.; Skyllas-Kazacos, M. Vanadium Redox Battery: Positive Half-Cell Electrolyte Studies. *J. Power Sources* **2009**, *189*, 1212−1219.
(8) Vijayakumar, M.; Li, L. Y.; Graff, G.; Liu, J.; Zhang, H. M.; Yang, Z. G.; Hu, J. A. Towards Understanding the Poor Thermal Stability of V^{5+} Electrolyte Solution in Vanadium Redox Flow Batteries. *J. Power Sources* **2011**, *196*, 3669−3672.
(9) Skyllas-Kazacos, M.; Kazacos, M. Stabilized Vanadium Electrolyte Solutions for All-Vanadium Redox Cells and Batteries. U.S. Patent 6,562,514, May 13, 2003.
(10) Kazacos, M.; Skyllas-Kazacos, M. High Energy Density Vanadium Electrolyte Solutions, Methods of Preparation Thereof and All-Vanadium Redox Cells and Batteries Containing High Energy Vanadium Electrolyte Solutions. U.S. Patent 7,078,123, July 18, 2006.
(11) Zhang, J. L.; Li, L. Y.; Nie, Z. M.; Chen, B. W.; Vijayakumar, M.; Kim, S.; Wang, W.; Schwenzer, B.; Liu, J.; Yang, Z. G. Effects of Additives on the Stability of Electrolytes for All-Vanadium Redox Flow Batteries. *J. Appl. Electrochem.* **2011**, *41*, 1215−1221.
(12) Li, S.; Huang, K. L.; Liu, S. Q.; Fang, D.; Wu, X. W.; Lu, D.; Wu, T. Effect of Organic Additives on Positive Electrolyte for Vanadium Redox Battery. *Electrochim. Acta* **2011**, *56*, 5483−5487.
(13) Wiedemann, E.; Heintz, A.; Lichtenthaler, R. N. Transport Properties of Vanadium Ions in Cation Exchange Membranes: Determination of Diffusion Coefficients Using a Dialysis Cell. *J. Membr. Sci.* **1998**, *141*, 215−221.
(14) Chen, J. Q.; Wang, B. B.; Yang, J. C. Adsorption and Diffusion of $VO^{2+}$and VO_2^+ across Cation Membrane for All-Vanadium Redox Flow Battery. *Solvent Extr. Ion Exch.* **2009**, *27*, 312−327.
(15) Tang, Z.; Keith, R. E.; Aaron, D. S.; Lawton, J. S.; Papandrew, A. B.; Zawodzinski, T. A. Proton Exchange Membrane Performance Characterization in VRFB. *ECS Trans.* **2012**, *41*, 25−34.
(16) Verbrugge, M. W.; Hill, R. F. Experimental and Theoretical Investigation of Perfluorosulfonic Acid Membranes Equilibrated with Aqueous Sulfuric Acid Solutions. *J. Phys. Chem.* **1988**, *92*, 6778−6783.
(17) Verbrugge, M. W.; Hill, R. F. Ion and Solvent Transport in Ion-Exchange Membranes. II. A Radiotracer Study of the Sulfuric-Acid, Nafion-117 System. *J. Electrochem. Soc.* **1990**, *137*, 893−899.
(18) Tang, Z. J.; Svoboda, R.; Lawton, J. S.; Aaron, D. S.; Papandrew, A. B.; Zawodzinski, T. A. Composition and Conductivity of Membranes Equilibrated with Solutions of Sulfuric Acid and Vanadyl Sulfate. *J. Electrochem. Soc.* **2013**, *160*, F1040−F1047.
(19) Mohammadi, T.; Skyllas-Kazacos, M. Characterization of Novel Composite Membrane for Redox Flow Battery Applications. *J. Membr. Sci.* **1995**, *98*, 77−87.
(20) Mohammadi, T.; Skyllas-Kazacos, M. Preparation of Sulfonated Composite Membrane for Vanadium Redox Flow Battery Applications. *J. Membr. Sci.* **1995**, *107*, 35−45.
(21) Sukkar, T.; Skyllas-Kazacos, M. Modification of Membranes Using Polyelectrolytes to Improve Water Transfer Properties in the Vanadium Redox Battery. *J. Membr. Sci.* **2003**, *222*, 249−264.
(22) Li, X. F.; Zhang, H. M.; Mai, Z. S.; Zhang, H. Z.; Vankelecom, I. Ion Exchange Membranes for Vanadium Redox Flow Battery (VRB) Applications. *Energy Environ. Sci.* **2011**, *4*, 1147−1160.
(23) Kreuer, K. D.; Portale, G. A Critical Revision of the Nano-Morphology of Proton Conducting Ionomers and Polyelectrolytes for Fuel Cell Applications. *Adv. Funct. Mater.* **2013**, *23*, 5390−5397.
(24) Kreuer, K. D. Ion Conducting Membranes for Fuel Cells and other Electrochemical Devices. *Chem. Mater.* **2014**, *26*, 361−380.
(25) Rubatat, L.; Rollet, A. L.; Gebel, G.; Diat, O. Evidence of Elongated Polymeric Aggregates in Nafion. *Macromolecules* **2002**, *35*, 4050−4055.
(26) Li, J.; Park, J. K.; Moore, R. B.; Madsen, L. A. Linear Coupling of Alignment with Transport in a Polymer Electrolyte Membrane. *Nat. Mater.* **2011**, *10*, 507−511.
(27) Wang, C.; Krishnan, V.; Wu, D. S.; Bledsoe, R.; Paddison, S. J.; Duscher, G. Evaluation of the Microstructure of Dry and Hydrated Perfluorosulfonic Acid Ionomers: Microscopy and Simulations. *J. Mater. Chem. A* **2013**, *1*, 938−944.
(28) Sukkar, T.; Skyllas-Kazacos, M. Water Transfer Behaviour across Cation Exchange Membranes in the Vanadium Redox Battery. *J. Membr. Sci.* **2003**, *222*, 235−247.
(29) Mohammadi, T.; Chieng, S. C.; Skyllas-Kazacos, M. Water Transport Study across Commercial Ion Exchange Membranes in the Vanadium Redox Flow Battery. *J. Membr. Sci.* **1997**, *133*, 151−159.
(30) Prifti, H.; Parasuraman, A.; Winardi, S.; Lim, T. M.; Skyllas-Kazacos, M. Membranes for Redox Flow Battery Applications. *Membranes* **2012**, *2*, 275−306.
(31) Vijayakumar, M.; Burton, S. D.; Huang, C.; Li, L. Y.; Yang, Z. G.; Graff, G. L.; Liu, J.; Hu, J. Z.; Skyllas-Kazacos, M. Nuclear Magnetic Resonance Studies on Vanadium(IV) Electrolyte Solutions for Vanadium Redox Flow Battery. *J. Power Sources* **2010**, *195*, 7709−7717.
(32) Vijayakumar, M.; Bhuvaneswari, M. S.; Nachimuthu, P.; Schwenzer, B.; Kim, S.; Yang, Z. G.; Liu, J.; Graff, G. L.; Thevuthasan, S.; Hu, J. Z. Spectroscopic Investigations of The Fouling Process on Nafion Membranes in Vanadium Redox Flow Batteries. *J. Membr. Sci.* **2011**, *366*, 325−334.
(33) Li, L. Y.; Kim, S.; Wang, W.; Vijayakumar, M.; Nie, Z. M.; Chen, B. W.; Zhang, J. L.; Xia, G. G.; Hu, J. Z.; Graff, G.; et al. A Stable Vanadium Redox-Flow Battery with High Energy Density for Large-Scale Energy Storage. *Adv. Energy Mater.* **2011**, *1*, 394−400.
(34) Vijayakumar, M.; Li, L. Y.; Nie, Z. M.; Yang, Z. G.; Hu, J. Z. Structure and Stability of Hexa-Aqua V(III) Cations in Vanadium Redox Flow Battery Electrolytes. *Phys. Chem. Chem. Phys.* **2012**, *14*, 10233−10242.
(35) Krakowiak, J.; Lundberg, D.; Persson, I. A Coordination Chemistry Study of Hydrated and Solvated Cationic Vanadium Ions in Oxidation States +III, +IV, and +V in Solution and Solid State. *Inorg. Chem.* **2012**, *51*, 9598−9609.
(36) Vijayakumar, M.; Wang, W.; Nie, Z. M.; Sprenkle, V.; Hu, J. Z. Elucidating the Higher Stability of Vanadium(V) Cations in Mixed Acid Based Redox Flow Battery Electrolytes. *J. Power Sources* **2013**, *241*, 173−177.
(37) Sepehr, F.; Paddison, S. J. The Solvation Structure and Thermodynamics of Aqueous Vanadium Cations. *Chem. Phys. Lett.* **2013**, *585*, 53−58.
(38) Vijayakumar, M.; Nie, Z.; Walter, E.; Hu, J.; Liu, J.; Sprenkle, V.; Wang, W. Understanding Aqueous Electrolyte Stability through Combined Computational and Magnetic Resonance Spectroscopy: A Case Study on Vanadium Redox Flow Battery Electrolytes. *ChemPlusChem* **2015**, *80*, 428−437.
(39) Frisch, M. J.; Trucks, G. W.; Schlegel, H. B.; Scuseria, G. E.; Robb, M. A.; Cheeseman, J. R.; Scalmani, G.; Barone, V.; Mennucci, B.; Petersson, G. A.; et al. *Gaussian 09, Revision A.01*; Gaussian, Inc.: Wallingford, CT, 2009.
(40) Lee, C. T.; Yang, W. T.; Parr, R. G. Development of the Colle-Salvetti Correlation-Energy Formula into a Functional of the Electron-Density. *Phys. Rev. B: Condens. Matter Mater. Phys.* **1988**, *37*, 785−789.
(41) Becke, A. D. Density-Functional Thermochemistry. III. The Role of Exact Exchange. *J. Chem. Phys.* **1993**, *98*, 5648−5652.
(42) Becke, A. D. A New Mixing of Hartree-Fock and Local Density-Functional Theories. *J. Chem. Phys.* **1993**, *98*, 1372−1377.
(43) Ditchfield, R.; Hehre, W. J.; Pople, J. A. Self-Consistent Molecular-Orbital Methods. IX. An Extended Gaussian-Type Basis for

DOI: 10.1021/acs.jpca.5b01794
J. Phys. Chem. A 2015, 119, 5749−5761

Reprinted with permission from Journal of Physical Chemistry A 2015, 119, 5749-5761.
Copyright 2015 American Chemical Society.

Molecular-Orbital Studies of Organic Molecules. *J. Chem. Phys.* **1971**, *54*, 724−728.
(44) Hehre, W. J.; Ditchfield, R.; Pople, J. A. Self-Consistent Molecular-Orbital Methods. 12. Further Extensions of Gaussian-Type Basis Sets for Use in Molecular-Orbital Studies of Organic-Molecules. *J. Chem. Phys.* **1972**, *56*, 2257−2261.
(45) Hariharan, P. C.; Pople, J. A. Influence of Polarization Functions on Molecular-Orbital Hydrogenation Energies. *Theor. Chim. Acta* **1973**, *28*, 213−222.
(46) Loeffler, H. H.; Yague, J. I.; Rode, B. M. QM/MM-MD Simulation of Hydrated Vanadium(II) Ion. *Chem. Phys. Lett.* **2002**, *363*, 367−371.
(47) Rotzinger, F. P. Performance of Molecular Orbital Methods and Density Functional Theory in the Computation of Geometries and Energies of Metal Aqua Ions. *J. Phys. Chem. B* **2005**, *109*, 1510−1527.
(48) McLean, A. D.; Chandler, G. S. Contracted Gaussian Basis Sets for Molecular Calculations. I. Second Row Atoms, Z = 11−18. *J. Chem. Phys.* **1980**, *72*, 5639−5648.
(49) Marenich, A. V.; Cramer, C. J.; Truhlar, D. G. Universal Solvation Model Based on Solute Electron Density and on a Continuum Model of the Solvent Defined by the Bulk Dielectric Constant and Atomic Surface Tensions. *J. Phys. Chem. B* **2009**, *113*, 6378−6396.
(50) Montgomery, H.; Chastain, R. V.; Natt, J. J.; Witkowska, A. M.; Lingafelter, E. C. The Crystal Structure of Tutton's Salts. VI. Vanadium(II), Iron(II) and Cobalt(II) Ammonium Sulfate Hexahydrates. *Acta Crystallogr.* **1967**, *22*, 775−780.
(51) Marcus, Y. Thermodynamics of Solvation of Ions Part 5. Gibbs Free Energy of Hydration at 298.15 K. *J. Chem. Soc., Faraday Trans.* **1991**, *87*, 2995−2999.
(52) Ballhausen, C. J.; Djurinskij, B. F.; Watson, K. J. The Polarized Absorption Spectra of Three Crystalline Polymorphs of $VOSO_4 \cdot 5H_2O$. *J. Am. Chem. Soc.* **1968**, *90*, 3305−3309.
(53) Cotton, F. A.; Fair, C. K.; Lewis, G. E.; Mott, G. N.; Ross, F. K.; Schultz, A. J.; Williams, J. M. Precise Structural Characterizations of the Hexaaquovanadium(III) and Diaquohydrogen Ions. X-Ray and Neutron Diffraction Studies of $[V(H_2O)_6][H_5O_2](CF_3SO_3)_4$. *J. Am. Chem. Soc.* **1984**, *106*, 5319−5323.
(54) Cotton, F. A.; Falvello, L. R.; Llusar, R.; Libby, E.; Murillo, C. A.; Schwotzer, W. Synthesis and Characterization of Four Vanadium-(II) Compounds, Including Vanadium(II) Sulfate Hexahydrate and Vanadium(II) Saccharinates. *Inorg. Chem.* **1986**, *25*, 3423−3428.
(55) Benmelouka, M.; Messaoudi, S.; Furet, E.; Gautier, R.; Le Fur, E.; Pivan, J. Y. Density Functional Investigation of Hydrated V(II) and V(III) Ions: Influence of the Second Coordination Sphere; Water Exchange Mechanism. *J. Phys. Chem. A* **2003**, *107*, 4122−4129.
(56) Sadoc, A.; Messaoudi, S.; Furet, E.; Gautier, R.; Le Fur, E.; Le Polles, L.; Pivan, J. Y. Structure and Stability of VO_2^+ in Aqueous Solution: A Car-Parrinello and Static ab Initio Study. *Inorg. Chem.* **2007**, *46*, 4835−4843.
(57) Bryantsev, V. S.; Diallo, M. S.; Goddard, W. A. Computational Study of Copper(II) Complexation and Hydrolysis in Aqueous Solutions Using Mixed Cluster/Continuum Models. *J. Phys. Chem. A* **2009**, *113*, 9559−9567.
(58) Breneman, C. M.; Wiberg, K. B. Determining Atom-Centered Monopoles from Molecular Electrostatic Potentials. The Need for High Sampling Density in Formamide Conformational Analysis. *J. Comput. Chem.* **1990**, *11*, 361−373.
(59) Cotton, F. A.; Daniels, L. M.; Murillo, C. A.; Quesada, J. F. Hexaaqua Dipositive Ions of the First Transition Series: New and Accurate Structures; Expected and Unexpected Trends. *Inorg. Chem.* **1993**, *32*, 4861−4867.
(60) Holt, D. G. L.; Larkworthy, L. F.; Povey, D. C.; Smith, G. W.; Leigh, G. J. Facile Synthesis of Complexes of Vanadium(II) and the Crystal and Molecular Structures of Hexaaquavanadium(II) Trifluoromethylsulphonate. *Inorg. Chim. Acta* **1990**, *169*, 201−205.
(61) Rotzinger, F. P. Mechanism of Water Exchange for the Di- and Trivalent Metal Hexaaqua Ions of the First Transition Series. *J. Am. Chem. Soc.* **1997**, *119*, 5230−5238.
(62) Hugi, A. D.; Helm, L.; Merbach, A. E. Water Exchange on Hexaaquavanadium(III): a Variable-Temperature and Variable-Pressure ^{17}O-NMR Study at 1.4 and 4.7 T. *Helv. Chim. Acta* **1985**, *68*, 508−521.
(63) Kallies, B.; Meier, R. Electronic Structure of 3d $[M(H_2O)_6]^{3+}$ Ions from Sc^{III} to Fe^{III}: A Quantum Mechanical Study Based on DFT Computations and Natural Bond Orbital Analyses. *Inorg. Chem.* **2001**, *40*, 3101−3112.
(64) Tregenna-Piggott, P. L. W.; Spichiger, D.; Carver, G.; Frey, B.; Meier, R.; Weihe, H.; Cowan, J. A.; McIntyre, G. J.; Zahn, G.; Barra, A. L. Structure and Bonding of the Vanadium(III) Hexa-Aqua Cation. 1. Experimental Characterization and Ligand-Field Analysis. *Inorg. Chem.* **2004**, *43*, 8049−8060.
(65) Kritayakornupong, C. Structural and Dynamical Properties of the V^{3+} Ion in Dilute Aqueous Solution: An *ab initio* QM/MM Molecular Dynamics Simulation. *J. Comput. Chem.* **2009**, *30*, 2777−2783.
(66) Grant, C. V.; Cope, W.; Ball, J. A.; Maresch, G. G.; Gaffney, B. J.; Fink, W.; Britt, R. D. Electronic Structure of the Aqueous Vanadyl Ion Probed by 9 and 94 GHz EPR and Pulsed ENDOR Spectroscopies and Density Functional Theory Calculations. *J. Phys. Chem. B* **1999**, *103*, 10627−10631.
(67) Selbin, J. The Chemistry of Oxovanadium(IV). *Chem. Rev.* **1965**, *65*, 153−175.
(68) Ballhausen, C. J.; Gray, H. B. The Electronic Structure of the Vanadyl Ion. *Inorg. Chem.* **1962**, *1*, 111−122.
(69) Winkler, J. R.; Gray, H. B. *Molecular Electronic Structures of Transition Metal Complexes I*; Springer: Berlin, 2011; Vol. *142*, pp 17−28.
(70) Vijayakumar, M.; Govind, N.; Li, B.; Wei, X.; Nie, Z.; Thevuthasan, S.; Sprenkle, V.; Wang, W. Aqua-Vanadyl Ion Interaction with Nafion Membranes. *Front. Energy Res.* **2015**, DOI: 10.3389/fenrg.2015.00010.
(71) Vanadium, Niobium and Tantalum. In *Chemistry of the Elements*, Greenwood, N. N., Earnshaw, A., Eds.; Butterworth-Heinemann: Oxford, 1997; pp 976−1001.
(72) Harnung, S. E.; Larsen, E.; Pedersen, E. J. Structure of Monovanadates in Aqueous-Solution. *Acta Chem. Scand.* **1993**, *47*, 674−682.
(73) Cruywagen, J. J.; Heyns, J. B. B.; Westra, A. N. Protonation Equilibria of Mononuclear Vanadate: Thermodynamic Evidence for the Expansion of the Coordination Number in VO_2^+. *Inorg. Chem.* **1996**, *35*, 1556−1559.
(74) Bühl, M.; Parrinello, M. Medium Effects on ^{51}V NMR Chemical Shifts: A Density Functional Study. *Chem.—Eur. J.* **2001**, *7*, 4487−4494.
(75) Zhang, Y. Ab Initio Study of Low pH Vanadium (V). M.S. Thesis, Saint Mary's University, Halifax, Canada, March 2012.
(76) Wang, Z. L.; Kang, Z. C. *Functional and Smart Materials: Structural Evolution and Structure Analysis*; Plenum Press: New York, 1998.
(77) Madic, C.; Begun, G. M.; Hahn, R. L.; Launay, J. P.; Thiessen, W. E. Dimerization of Aquadioxovanadium(V) Ion in Concentrated Perchloric and Sulfuric Acid Media. *Inorg. Chem.* **1984**, *23*, 469−476.
(78) Gharib, F.; Sayadian, M.; Shame, A.; Mobasher-Moghaddam, M. Formation Equilibria of Vanadium(V) Species in Different Ionic Media: Salt Effect and Protonation Constant. *J. Mol. Liq.* **2008**, *138*, 9−13.
(79) Oriji, G.; Katayama, Y.; Miura, T. Investigation on V(IV)/V(V) Species in a Vanadium Redox Flow Battery. *Electrochim. Acta* **2004**, *49*, 3091−3095.
(80) Wang, C.; Clark, J. K.; Kumar, M.; Paddison, S. J. An ab initio Study of the Primary Hydration and Proton Transfer of CF_3SO_3H and $CF_3O(CF_2)_2SO_3H$: Effects of the Hybrid Functional and Inclusion of Diffuse Functions. *Solid State Ionics* **2011**, *199*, 6−13.
(81) Hayes, R. L.; Paddison, S. J.; Tuckerman, M. E. Proton Transport in Triflic Acid Pentahydrate Studied via Ab Initio Path Integral Molecular Dynamics. *J. Phys. Chem. A* **2011**, *115*, 6112−6124.

DOI: 10.1021/acs.jpca.5b01794
J. Phys. Chem. A 2015, 119, 5749−5761

Reprinted with permission from Journal of Physical Chemistry A 2015, 119, 5749-5761.
Copyright 2015 American Chemical Society.

(82) Magnussen, M.; Brock-Nannestad, T.; Bendix, J. Pentaaquaoxovanadium(IV) bis(trifluoromethanesulfonate). *Acta Crystallogr., Sect. C: Cryst. Struct. Commun.* **2007**, *63*, M51−M53.
(83) Sun, C. X.; Chen, J.; Zhang, H. M.; Han, X.; Luo, Q. T. Investigations on Transfer of Water and Vanadium Ions across Nafion Membrane in an Operating Vanadium Redox Flow Battery. *J. Power Sources* **2010**, *195*, 890−897.
(84) Xi, J. Y.; Wu, Z. H.; Teng, X. G.; Zhao, Y. T.; Chen, L. Q.; Qiu, X. P. Self-Assembled Polyelectrolyte Multilayer Modified Nafion Membrane with Suppressed Vanadium Ion Crossover for Vanadium Redox Flow Batteries. *J. Mater. Chem.* **2008**, *18*, 1232−1238.
(85) Tang, A.; Bao, J.; Skyllas-Kazacos, M. Thermal Modelling of Battery Configuration and Self-Discharge Reactions in Vanadium Redox Flow Battery. *J. Power Sources* **2012**, *216*, 489−501.
(86) Lawton, J. S.; Aaron, D. S.; Tang, Z. J.; Zawodzinski, T. A. Qualitative Behavior of Vanadium Ions in Nafion Membranes Using Electron Spin Resonance. *J. Membr. Sci.* **2013**, *428*, 38−45.

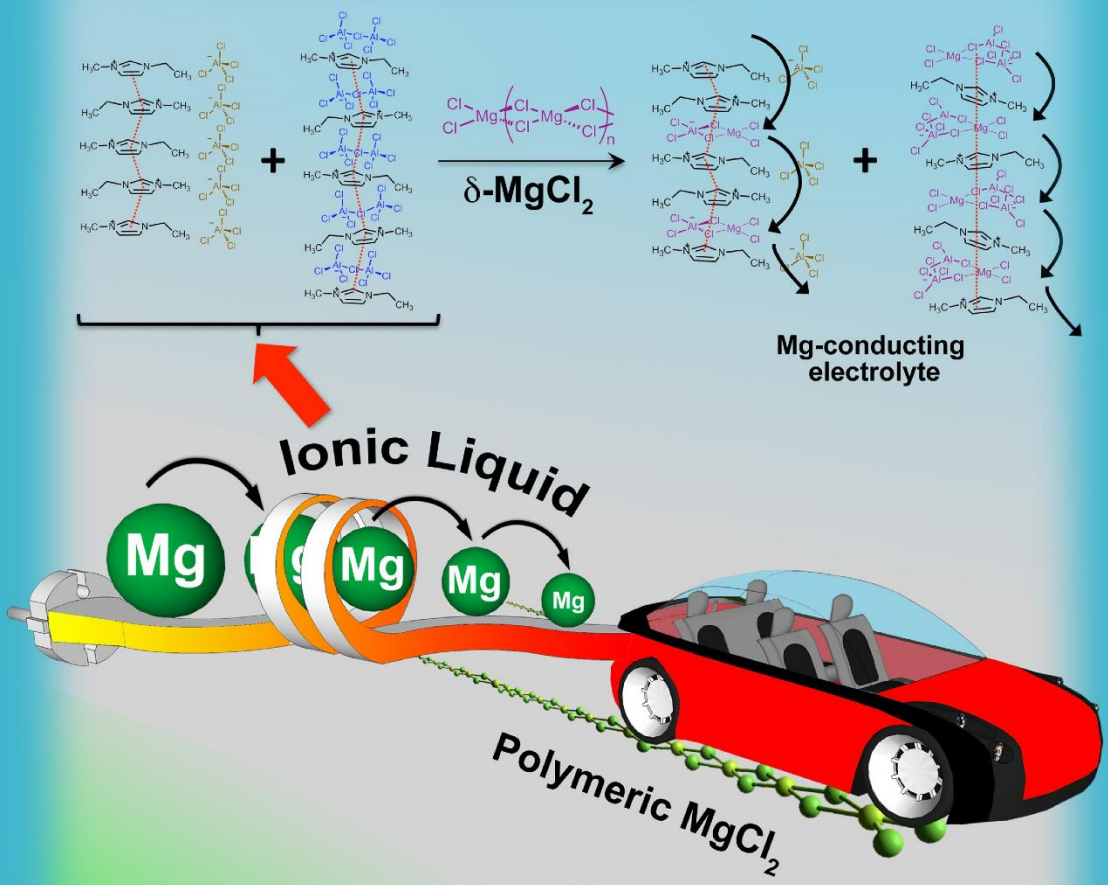
DOI: 10.1021/acs.jpca.5b01794
J. Phys. Chem. A 2015, 119, 5749−5761

Reprinted with permission from ChemSusChem 2015, 8, 3069-3076.
Copyright 2015 Wiley-VCH Verlag GmbH & Co.

CHEMISTRY & SUSTAINABILITY

CHEMSUSCHEM

ENERGY & MATERIALS



18/2015

Cover Picture:
V. Di Noto et al.
A Key concept in Magnesium Secondary Battery Electrolytes

A Journal of
ChemPubSoc Europe

WILEY-VCH www.chemsuschem.org

Reprinted with permission from ChemSusChem 2015, 8, 3069-3076.
Copyright 2015 Wiley-VCH Verlag GmbH & Co.
ChemPubSoc Europe
DOI: 10.1002/cssc.201500339
CHEMSUSCHEM Full Papers



A Key concept in Magnesium Secondary Battery Electrolytes

Federico Bertasi,[a, b] Chaminda Hettige,[c] Fatemeh Sepehr,[d] Xavier Bogle,[e] Gioele Pagot,[a, b] Keti Vezzù,[b, f] Enrico Negro,[a, b] Stephen J. Paddison,[d] Steve G. Greenbaum,[e] Michele Vittadello,[c] and Vito Di Noto*[a, b]

A critical roadblock toward practical Mg-based energy storage technologies is the lack of reversible electrolytes that are safe and electrochemically stable. Here, we report on high-performance electrolytes based on 1-ethyl-3-methylimidazolium chloride (EMImCl) doped with $AlCl_3$ and highly amorphous δ-$MgCl_2$. The phase diagram of the electrolytes reveals the presence of four thermal transitions that strongly depend on salt content. High-level density functional theory (DFT)-based electronic structure calculations substantiate the structural and vibrational assignment of the coordination complexes. A 3D chloride-concatenated dynamic network model accounts for the outstanding redox behaviour and the electric and magnetic properties, providing insight into the conduction mechanism of the electrolytes. Mg anode cells assembled using the electrolytes were cyclically discharged at a high rate (35 mA g^{-1}), exhibiting an initial capacity of 80 mA h g^{-1} and a steady-state voltage of 2.3 V.

Introduction

Mg power sources[1–4] are a promising alternative to Li batteries,[5–7] but they are far from reaching their full potential in practical applications. Existing electrolytes based on ethereal solvents and organomagnesium compounds[8–11] are inadequate for meeting the needs of functional devices in portable electronics and transportation applications. Electrolytes based on inorganic Mg salts have been proposed, showing improvements in terms of stability, volatility and corrosiveness of the materials.[12–15]

The possibility of synthesising high-performance polymer electrolytes with $MgCl_2$ has been previously ruled out in the literature because of the high lattice energy of the α and β forms of this salt.[16] However, $MgCl_2$ can be prepared in a form called δ-$MgCl_2$, which is characterised by high crystallographic disorder, reactivity and solubility.[3,17] The unconventional properties of this salt result from the presence of a metastable nanoribbon or polymeric structures with concatenating $MgCl_2$ repeating units, in which the Mg atoms are bridged together by chloride bridges. The preparation of polymer electrolytes using this salt has yielded Mg^{2+}-conducting materials with conductivities as high as 10^{-4} S cm^{-1} at room temperature.[3] These studies have led to the first Mg-polymer batteries.[18]

Ionic liquids (ILs) have been investigated for the preparation of electrolytes for Mg batteries because, in addition to having high thermal and electrochemical stability, they exhibit negligible vapour pressure and are non-flammable.[19–21] Furthermore, ILs enable the use of oxide-based cathodic materials, which show a superior specific capacity and operating voltage with respect to conventional Chevrel-phase materials.[22] However, it has been reported that Mg electrodes are generally reactive toward imidazolium-based ILs.[23] In addition, Mg developed a blocking passivation layer impervious to the transport of ions in the few ILs that appeared to be electrochemically stable.[23] These observations dampened earlier interest in 1-ethyl-3-methylimidazolium chloride (EMImCl)/$AlCl_3$ melts partially neutralised with conventional $MgCl_2$,[24,25] which were closely studied because of their intriguing Lewis acid–base properties defined in terms of the ratio $R = n_{AlCl_3}/n_{EMImCl}$. A melt is defined as

[a] Dr. F. Bertasi, Dr. G. Pagot, Dr. E. Negro, Prof. V. Di Noto
Department of Chemical Sciences
University of Padua
Via Marzolo 1, 35131 Padua (Italy)
E-mail: vito.dinoto@unipd.it
[b] Dr. F. Bertasi, Dr. G. Pagot, Dr. K. Vezzù, Dr. E. Negro, Prof. V. Di Noto
Department of Industrial Engineering
Section of Chemistry for Technology
University of Padua
Via Gradenigo 6/a, 35131 Padua (Italy)
[c] Dr. C. Hettige, Prof. M. Vittadello
Energy Nanotechnology and Materials Chemistry Lab
Medgar Evers College and Graduate Center of the City University of New York
1638 Bedford Avenue, Brooklyn, NY 11225 (USA)
[d] F. Sepehr, Prof. S. J. Paddison
Department of Chemical and Biomolecular Engineering
University of Tennessee
419 Dougherty Engineering Bldg. Knoxville, TN 37996-2200 (USA)
[e] Dr. X. Bogle, Prof. S. G. Greenbaum
Department of Physics
Hunter College and Graduate Center of the City University of New York
695 Park Avenue, New York, NY 10021 (USA)
[f] Dr. K. Vezzù
Veneto Nanotech S.C.p.a.
Via San Crispino 106, I-35129 Padua (Italy)

Supporting Information for this article is available on the WWW under http://dx.doi.org/10.1002/cssc.201500339.

© 2015 Wiley-VCH Verlag GmbH & Co. KGaA, Weinheim

Reprinted with permission from ChemSusChem 2015, 8, 3069-3076.
Copyright 2015 Wiley-VCH Verlag GmbH & Co.

basic, neutral, or acidic, if R is less than, equal to, or more than 1, respectively. The introduction of $MgCl_2$ minimises the concentration of the $Al_2Cl_7^-$ dimeric species (strong Lewis acids) in favour of the monomeric species $AlCl_4^-$ concatenated to $MgCl_2$.

ILs containing $EMIm^+$ cations and various anions including Cl^-, BF_4^- and AsF_6^- have been thoroughly characterised using low-temperature single-crystal X-ray diffraction.[26,27] These materials crystallise in layered structures in which $EMIm^+$ cations are stacked, thus forming one-dimensional pillars, together with parallel (in the case of Cl^-) or intercalated anionic stacking (in the case of BF_4^- and AsF_6^-) depending on the anion size. An alternating anion and cation sequence is observed perpendicular to the direction of the pillars. The structural characteristics of these ILs are key features in understanding the ion–ion interactions within the ILs, IL–salt interactions and the properties of the resulting IL-based electrolytes.

Results and Discussion

In this study, we synthesised 3D chloride-concatenated dynamic Mg-ion conducting electrolytes by reacting $EMImCl/(AlCl_3)_{1.5}$ with δ-$MgCl_2$. The resulting systems have the general formula $(EMImCl/(AlCl_3)_{1.5})/(\delta\text{-}MgCl_2)_x$, with molar ratio $x = n_{\delta\text{-}MgCl_2}/n_{IL}$, $0 \leq x \leq 0.20$, and $R > 1$. Four concentrations were explored that ranged from pure chloroaluminate IL, $EMImCl/(AlCl_3)_{1.5}$, to a saturated solution of δ-$MgCl_2$ with $x = 0.2$ (Table 1). Higher δ-$MgCl_2$ concentrations cannot be obtained because of the limited solubility of δ-$MgCl_2$ in the IL. Furthermore, the use of IL with an $AlCl_3$/EMImCl molar ratio higher than 1.5 leads (higher $EMImCl/AlCl_3$ ratio) lead to a general decrease in the electrochemical performance as shown in Figure S1 in the Supporting Information. As x increases, the viscosity of the samples increases substantially, changing from a liquid to a paste-like material.

Table 1. Composition of $(EMImCl/(AlCl_3)_{1.5})/(\delta\text{-}MgCl_2)_x$ electrolytes.

Sample	IL [wt%]	δ-$MgCl_2$ [wt%]	$x = n_{\delta\text{-}MgCl_2}/n_{IL}$ [a]	$y = n_{Mg}/n_{AlCl_3}$ [b]
IL	100	0	0	–
2	98.7	1.3	0.05	0.033
1	98.0	2.0	0.08	0.052
0	94.9	5.1[c]	0.20	0.130

[a] n_{IL} is the moles of $EMImCl/(AlCl_3)_{1.5}$, determined by ICP-AES spectroscopy. [b] n_{Mg} is the moles of Mg determined by ICP-AES spectroscopy. [c] Saturated.

Thermogravimetric analysis (TGA) shows that $EMImCl/(AlCl_3)_{1.5}$ is thermally stable up to 500 °C (Figure S2). The main bulk decomposition of the IL occurs at 530 °C, demonstrating that these electrolytes are endowed with excellent thermal stability and negligible volatility. These properties are crucial for the development of practical Mg batteries with better performance than the state-of-the-art, which is limited by the use of volatile and flammable ethereal solvents.[28]

Differential scanning calorimetry (DSC; Figures 1 and 2) revealed that the glass transition temperatures (T_g) of these materials are between −100 and −90 °C because of an order–disorder event involving $EMIm^+$ cations and chloroaluminate anion stacks. The exothermic crystallisation (T_c) associated with the reorganisation of $EMIm^+$ cations was measured between −70 and −50 °C. Two melting events, T_{m1} and T_{m2}, were detected at −20 and 60 °C corresponding to A′ and B′ crystalline domains, respectively. The values of T_g, T_c, T_{m1} and T_{m2} depend on the concentration of δ-$MgCl_2$ modulating the relative abundance of $AlCl_4^-$ and $Al_2Cl_7^-$, the concentration of the Mg–chloroaluminate complexes, and the flexibility of the $EMIm^+$ cationic stacks. The resulting phase diagram (Figure 2) indicates that

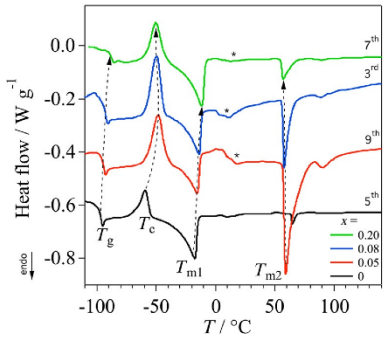


Figure 1. Differential Scanning Calorimetry profiles of $(EMImCl/(AlCl_3)_{1.5})/(\delta\text{-}MgCl_2)_x$ with $0 \leq x \leq 0.20$. The glass transition temperature (T_g), an exothermic crystallisation event (T_c), and melting events (T_{m1} and T_{m2}) are indicated.

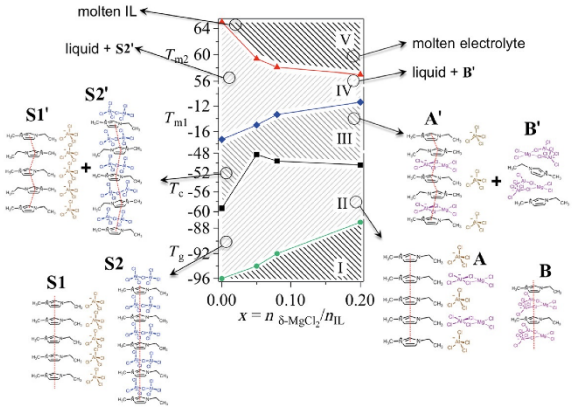


Figure 2. Illustrated phase diagram of $(EMImCl/(AlCl_3)_{1.5})/(\delta\text{-}MgCl_2)_x$ electrolytes.

© 2015 Wiley-VCH Verlag GmbH & Co. KGaA, Weinheim

Reprinted with permission from ChemSusChem 2015, 8, 3069-3076.
Copyright 2015 Wiley-VCH Verlag GmbH & Co.

there are five distinct regions. Region I is a rigid phase below the T_g. In region II, there are two types of structures at lower x values: S1, in which the $EMIm^+$ cations are packed parallel to the $AlCl_4^-$ anions, both in one-dimensional pillars; and S2, in which more sterically hindered $Al_2Cl_7^-$ anions intercalate within $EMIm^+$ cationic stacks. At higher concentrations, the A phase corresponds to the basic structure S1 with anionic species consisting of $MgCl_2$ concatenated to $AlCl_4^-$ units whereas the B phase corresponds to a similar anionic complexation involving the structure S2. In region III, at lower x we find structures S1′ and S2′, in which the original one-dimensional cationic pillars reorganise to a more thermodynamically favoured zig–zag stacking. The complexation of S1′ and S2′ by δ-$MgCl_2$ at higher x yields phases A′ and B′, respectively. In region IV, at lower x values liquid S1′ is mixed with solid S2′ whereas at higher x values liquid A′ is mixed with solid B′. S1′ and A′ melt first because there is less cross-linking with $AlCl_4^-$ as opposed to $Al_2Cl_7^-$. In region V, the systems are completely molten.

Density functional theory (DFT) electronic structure calculations were undertaken to determine the atomic scale structures of the $EMIm^+$ cation interacting with $AlCl_4^-$, $Al_2Cl_7^-$ and $MgCl_2$ (Figure 3). Based on these results, it is inferred that the anion is highly likely to occupy the front position (position 2) around the imidazolium ring, rather than the side (1, 3) and back positions (4, 5).

Upon addition of $MgCl_2$ and $(MgCl_2)_2$ units to the optimised structures, the nearest anion to $EMIm^+$ is Mg chloride rather than Al chloride anions, in all cases. This is a consequence of the more polarised Mg–Cl bond compared to the Al–Cl bond, and is confirmed by the electrostatic potential maps on the electron isodensity surface of $[AlCl_4MgCl_2]^-$ and $[Al_2Cl_7MgCl_2]^-$ concatenated complexes. These maps (Figure S3) show a more negative electrostatic potential and, therefore, a more electron rich area on Mg-bonded chloride rather than Al-bonded chloride. Analysing the energetics of these systems, we find that the binding energy of $MgCl_2$ to the $EMImAlCl_4$ structure is 5 and 7 kcal mol^{-1} lower than its binding to the $EMImAl_2Cl_7$ structure after addition of one and two units of $MgCl_2$, respectively. This indicates that in the presence of $MgCl_2$ the $AlCl_4^-$ concatenated complexes are more energetically favoured compared to those based on $Al_2Cl_7^-$ complexes. However, the binding energy results were not conclusive, hence the vibrational frequencies were also analysed.

Experimental IR and Raman spectra of the electrolytes (Figure 4) combined with the computed vibrational frequencies (Tables S1 and S2) and the related correlative assignments[29–32] support the interpretation of the thermal data. The Raman spectra show that the intensity of the band at 350 cm^{-1} (Figure 4C, blue peak) attributed to the stretching mode of $AlCl_4^-$ increases at a higher concentration of Mg salt buffer whereas the intensity of the band at 311 cm^{-1} (Figure 4C, yellow peak), related to the Al–Cl–Al symmetrical stretching mode of $Al_2Cl_7^-$, decreases. Therefore, the concentration of $AlCl_4^-$ units prevails at higher x values. Frequencies derived from the ab initio calculations confirm that the presence of $MgCl_2$ does not affect our conclusions based on the ratio of $AlCl_4^-$ and $Al_2Cl_7^-$ peak intensities. Moreover, the peak intensities at 156, 310, 331 and 385 cm^{-1} in the far IR region decrease with increasing Mg salt concentration. The calculated vibrational modes of these peaks correlate well with the vibrations of the $Al_2Cl_7^-$ species, in agreement with the finding that their concentration decreases with the addition of Mg salt to the system. As the concentration of δ-$MgCl_2$ increases, new peaks appear in the far IR spectrum (highlighted blue, yellow and green in Figure 4D). Interestingly, the calculated frequencies for structures containing $EMIm^+$, $AlCl_4^-$, $Al_2Cl_7^-$ and $MgCl_2$ (see Figure 3A, B, C, D) do not show any vibrational modes between 242 and 296 cm^{-1}. However, addition of a second or third concatenated $MgCl_2$ unit to the system (see Figure 3E and F) results in the appearance of new vibrational modes for Mg chloride structures. Thus, the appearance of the green

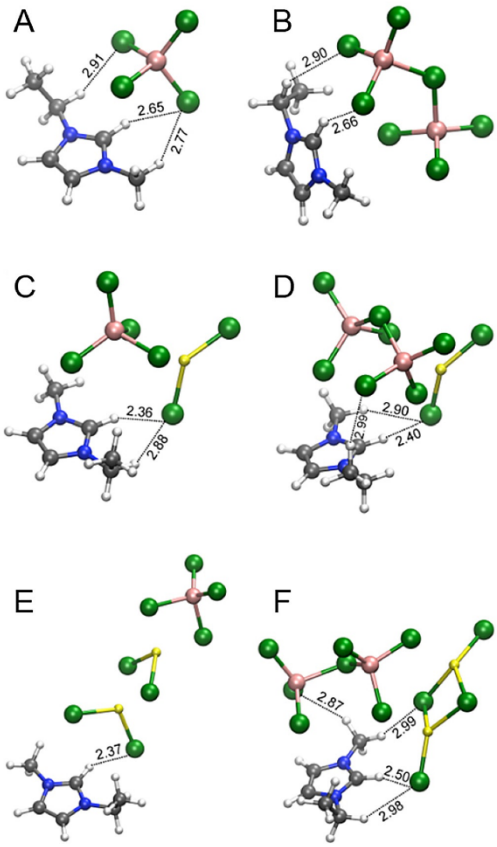


Figure 3. Optimised geometries of the ionic liquid complexes determined at the B3LYP/6-311G** level of theory. Structures of A) $EMImAlCl_4$, B) $EMImAl_2Cl_7$, C) $EMImAlCl_4$ with $MgCl_2$, D) $EMImAl_2Cl_7$ with $MgCl_2$, E) $EMImAlCl_4$ with $(MgCl_2)_2$, and F) $EMImAl_2Cl_7$ with $(MgCl_2)_2$. Colour code: Cl atoms, green; Al atoms, pink; Mg atoms, yellow; C atoms, grey; N atoms, blue; H atoms, white. Distances are only shown between Cl and H atoms that have a bond distance of less than 3 Å.

© 2015 Wiley-VCH Verlag GmbH & Co. KGaA, Weinheim

Reprinted with permission from ChemSusChem 2015, 8, 3069-3076.
Copyright 2015 Wiley-VCH Verlag GmbH & Co.

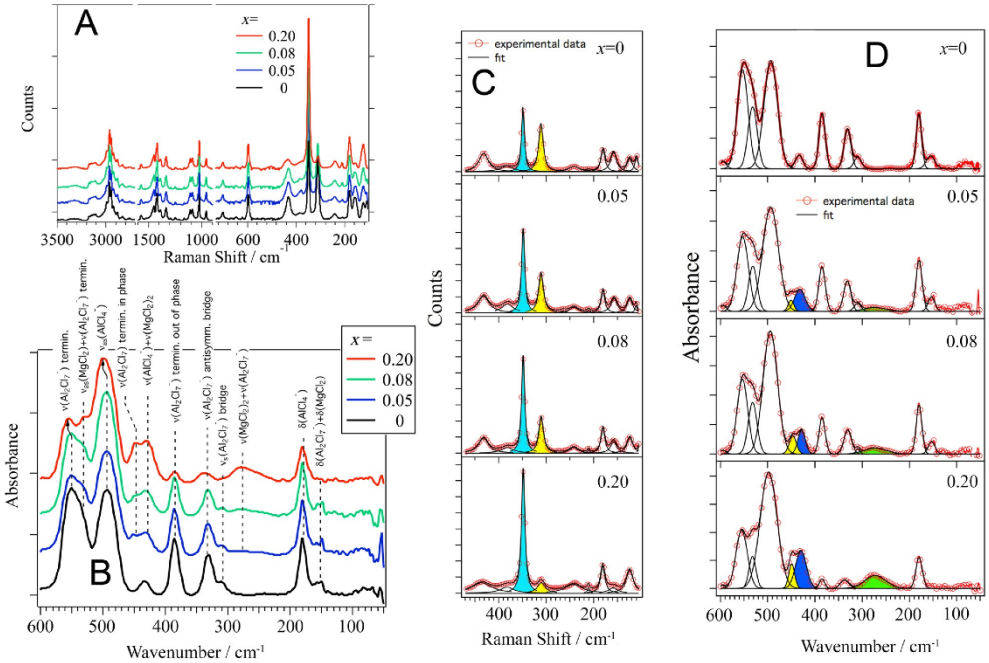


Figure 4. Vibrational spectra of $(EMImCl/(AlCl_3)_{1.5})/(\delta\text{-}MgCl_2)_x$ electrolytes and spectral assignment. A) Raman spectra of $(EMImCl/(AlCl_3)_{1.5})/(\delta\text{-}MgCl_2)_x$ with $0 \le x \le 0.20$. B) Far infrared spectra of the $(EMImCl/(AlCl_3)_{1.5})/(\delta\text{-}MgCl_2)_x$ with band assignment in accordance with the literature and ab initio calculated vibrational modes. C) Gaussian decomposition of the Raman spectra in (A) in the region between 100 and 480 cm^{-1}; The intensity of the band corresponding to the stretching of the monomeric species $AlCl_4^-$ (blue) increases at higher concentrations of the Mg salt buffer, whereas the intensity of the band attributed to the stretching of the dimeric species $Al_2Cl_7^-$ (yellow) decreases. D) Gaussian decomposition of the far IR spectrum (B); the intensities of the bands corresponding to the vibrations of polymeric $MgCl_2$ species (green) and Mg–Cl–Al stretching modes (blue and yellow) increase at higher concentrations of the Mg salt buffer. The fractional area analysis of the far IR spectra is provided in Figure S4.

peaks in Figure 4 D is a result of the presence of $(MgCl_2)_n$, $n > 1$. Furthermore, the growth of the blue peak at 430 cm^{-1} and the appearance of the yellow peak at 450 cm^{-1} is attributed to the Mg–Cl–Al and Cl–Mg–Cl vibrational modes. Combining this result with the previous finding that the concentration of the $Al_2Cl_7^-$ species is reduced by the addition of $\delta\text{-}MgCl_2$ salt, it is concluded that: a) at low Mg concentrations ($x < 0.05$) both $AlCl_4^-$ and $Al_2Cl_7^-$ concatenated anionic complexes (A and B phase) dominate and b) at higher Mg concentration ($x \ge 0.05$) the equilibrium is shifted toward phase A chain complexes because of a decrease in the concentration of $Al_2Cl_7^-$ and higher concentrations of concatenated complexes (phase A) involving Al–Cl–Mg and Cl–Mg–Cl bridges.

Cyclic voltammetry measurements (Figure 5) with Pt and Mg as working electrodes indicate that the threshold potential for Al deposition shifts toward more negative values as the concentration of $Al_2Cl_7^-$ decreases. In the presence of Mg concatenated species, a clear cathodic peak is observed at approximately −200 mV with a deposition overpotential lower than 100 mV. An asymmetric anodic peak is present at 400 mV which is assigned to the stripping of the co-deposited Mg–Al alloy.[33] On average, the electrolytes show a potential window of about 2.7 V, considerably lower than the 3.9 V observed in melts buffered with conventional $MgCl_2$.[24] The anodic limit (2.2 V) is owing to the $AlCl_4^-$ oxidation yielding Cl_2[24] whereas the cathodic stability (−0.5 V) is limited by electrolyte degradation. Mg deposition on Mg at 25 mV s^{-1} (Figure S5 B) occurs at two distinct potentials: −100 and −200 mV. In accordance with the literature,[34] the peak at −100 mV is probably associated with the $Mg^{2+} \rightarrow [MgCl]^+$ reduction process whereas that at −200 mV corresponds to the $[MgCl]^+ \rightarrow Mg^0$ reduction process.

The ability of the proposed electrolytes to effectively deposit Al/Mg alloys at −0.4 V was studied by analysing the alloy layer electrodeposited on a Pt working electrode by inductively-coupled plasma atomic emission spectroscopy (ICP-AES). The electrodeposited alloy layer is prepared using an $(EMImCl/(AlCl_3)_{1.5})/(\delta\text{-}MgCl_2)_{0.08}$ electrolyte by means of potentiostatic methods as described in the Experimental Section. This electrolyte is the best compromise between high conductivity (Figure S6) and $\delta\text{-}MgCl_2$ concentration. The results show that the deposited layer presents an Al/Mg molar ratio, $\phi = n_{Al}/n_{Mg}$, of 29.9, which is consistent with the ϕ value of 18.8 characterising the $(EMImCl/(AlCl_3)_{1.5})/(\delta\text{-}MgCl_2)_{0.08}$ electrolyte. This evidence

© 2015 Wiley-VCH Verlag GmbH & Co. KGaA, Weinheim

Reprinted with permission from ChemSusChem 2015, 8, 3069-3076.
Copyright 2015 Wiley-VCH Verlag GmbH & Co.

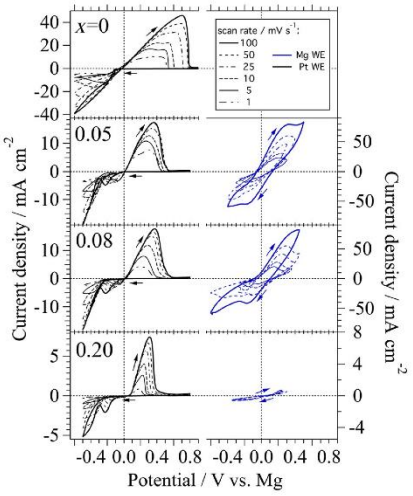


Figure 5. Cyclic voltammograms of the ionic liquid electrolytes hosting Mg ions, $(EMImCl/(AlCl_3)_{1.5})/(\delta\text{-}MgCl_2)_x$; voltammograms in black (left side) were obtained with Pt working electrodes; voltammograms in blue (right side) were obtained with Mg working electrodes. Mg pseudo-reference electrodes and counter electrodes were used in all experiments and measurements were recorded at scan rates in the range 1–100 mV s^{-1}.

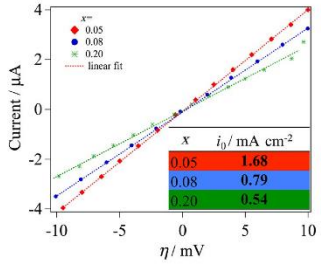


Figure 6. Exchange current of $(EMImCl/(AlCl_3)_{1.5})/(\delta\text{-}MgCl_2)_x$.

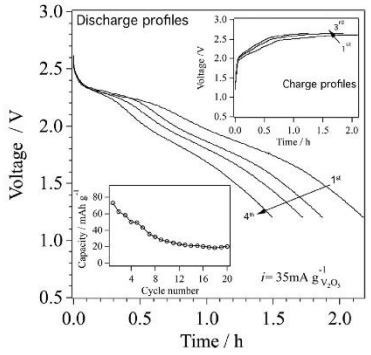


Figure 7. Voltage discharge profiles of a proof of concept prototype coin cell composed of Mg as the anode, $(EMImCl/(AlCl_3)_{1.5})/(\delta\text{-}MgCl_2)_{0.08}$ as the electrolyte, and V_2O_5 as the cathode; the inset shows the corresponding charge profiles; the rate of charge and discharge was 35 mA g^{-1}.

proves that: a) both Al and Mg alloys are effectively deposited on Pt at −0.4 V (vs. Mg); and b) the composition of the electrolytic solutions plays a crucial role in modulating the stoichiometry of the obtained electrodeposited alloy layer.

Furthermore, Figure 5 shows that the ex situ cyclability of the electrolyte is significantly influenced by the viscosity of the electrolyte, which rises as the concentration of δ-$MgCl_2$ in the electrolyte increases, thus reducing the mobility of the free species. This phenomenon is easily justified by considering that for δ-$MgCl_2$ the concentration of the anionic species able to interact with the H atom at the C2 position increases, thus raising the density of the hydrogen bond networks that protect the C2–H bond. Exchange currents i_0 in the range 0.54–1.68 mA cm^{-2} at 25 °C were recorded (Figure 6), revealing a decrease with higher Mg concentration.

A proof-of-concept prototype coin cell was assembled using Mg as the anode, $(EMImCl/(AlCl_3)_{1.5})/(\delta\text{-}MgCl_2)_{0.08}$ as electrolyte, and V_2O_5 as the cathode (Figure 7). Vanadium oxide is very suitable because of its low solubility in pristine chloroaluminate ILs (≤0.005 M).[35] Two plateaus are present in the discharge profiles at 2.3 and 1.7 V at a rate of 35 mA g^{-1}. After 10 cycles the remaining specific capacity is approximately 20 mA h g^{-1}. The capacity fade is attributed to a non-optimised cathode. The observed low practical specific capacity (about 20 mA h g^{-1}) is in agreement with the literature for V_2O_5-based cathode materials operating with completely anhydrous electrolytes.[2]

A Chevrel-phase cathode[36] was also tested, showing very poor cycling performance because of the solubility of Mo_6S_8 in acidic melts[37] such as those present in the electrolytes proposed here. This evidence supports the use of $(EMImCl/(AlCl_3)_{1.5})/(\delta\text{-}MgCl_2)_x$ electrolytes with oxide-based cathode materials with high specific capacity and operating voltage.

Broadband electrical spectroscopy (BES; Figures 8, S6, S7, and S8) was used to identify polarisation (σ) and dielectric relaxations in the systems (f). The polarisation events are related to the formation of cationic and anionic nanoclusters with different permittivities (ε). σ_1 corresponds to the bulk conductivity of the electrolytes. It is the only polarisation event below T_g, and exhibits Arrhenius behaviour, thus revealing a hopping mechanism with the activation energy increasing from 3.6 to 56 kJ mol^{-1} as the Mg concentration is increased.

Above T_g, the three interdomain polarisation events, σ_i, correspond to mesoscale heterogeneities of the systems and show a Vogel–Tamman–Fulcher (VTF) behaviour, indicating that the dynamics of IL stacks assist the conduction mechanism. We hypothesise that delocalisation bodies (DBs)[38] of different sizes, composed of cationic aggregates, provide the counter-charges for the mostly anionic migration. Long-range migration occurs when anionic species are exchanged between different DBs, assisted by the segmental motion of mi-

© 2015 Wiley-VCH Verlag GmbH & Co. KGaA, Weinheim

Reprinted with permission from ChemSusChem 2015, 8, 3069-3076.
Copyright 2015 Wiley-VCH Verlag GmbH & Co.

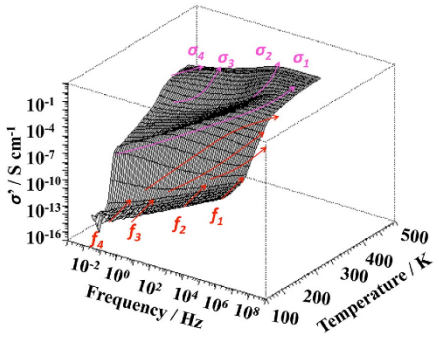


Figure 8. Real part of the conductivity surfaces obtained by broadband electrical spectroscopy of $(EMImCl/(AlCl_3)_{1.5})/(\delta\text{-}MgCl_2)_{0.20}$ as a function of temperature and frequency.

cellar $EMIm^+$ aggregates (f_1, f_2), and local fluctuation of the cations (f_3, f_4). Similarly, a broad distribution of Mg sites is detected in the electrolytes at lower temperatures by the appearance of a broad resonance peak in the ^{25}Mg NMR spectra (Figure 9), which narrows at higher temperature in proximity of T_{m1} because of rapid motion and site exchange, in agreement with the thermal analysis.

Above the melting point of $(EMImCl/(AlCl_3)_{1.5})/(\delta\text{-}MgCl_2)_x$ (regions IV and V), the activation energy of the most intense polarisation phenomena, σ_1 and σ_2, decreases with x (Figure S8). As the $\delta\text{-}MgCl_2$ concentration rises the extension of the concatenated network rises, facilitating the long-range charge migration of Mg species. Below the crystallisation temperature (regions I and II) the activation energy of f_1, f_2, f_3, and f_4 relaxation events show an overall increase with x (Figure S8). This indicates that with the increase of x: a) the fluctuation of cationic and anionic aggregates is inhibited, thus confirming that $\delta\text{-}MgCl_2$ is extending the concatenated network; and b) the segmental motion of the charged aggregates plays a crucial role in modulating the long-range charge transfer mechanism of the Mg species.

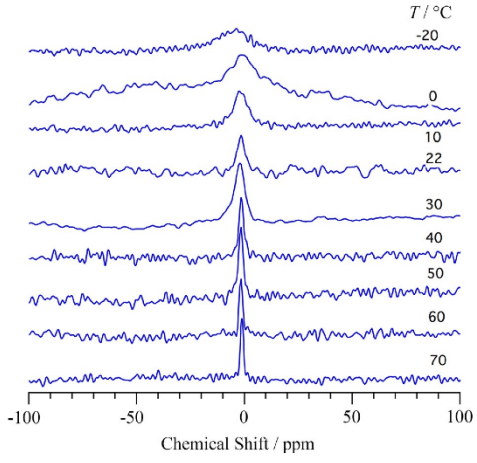


Figure 9. Temperature dependence of the ^{25}Mg NMR spectra of $(EMImCl/(AlCl_3)_{1.5})/(\delta\text{-}MgCl_2)_{0.08}$.

Conclusions

High-performance electrolytes with the formula $(EMImCl/(AlCl_3)_{1.5})/(\delta\text{-}MgCl_2)_x$, $0 \le x \le 0.20$ were synthesised and thoroughly characterised. Thermal analysis allowed us to gain insight into structural changes induced by variations in temperature and composition of these systems. DFT-based calculations elucidated the geometrical, electronic and vibrational characteristics of the coordination complexes formed between $EMIm^+$ and monomeric ($AlCl_4^-$) or dimeric ($Al_2Cl_7^-$) aluminium chloride species. The interactions of these complexes with $MgCl_2$ were also explored. Vibrational spectroscopy provided information about the shift in the equilibrium between $AlCl_4^-$ and $Al_2Cl_7^-$, which depends on the Mg salt concentration. The presence of spectral bands associated with chlorine bridges involving both Al and Mg atoms supported the existence of concatenated structures in the electrolyte systems. These structural features were compatible with the relatively uniform distribution of Mg sites observed by NMR spectroscopy. Electrochemical measurements indicated superior charge and discharge characteristic of the electrolyte and its highly reversible behaviour. Electrical spectroscopy data were compatible with the presence of positively charged delocalisation bodies composed of $EMIm^+$ aggregates, assisting the long-range migration of chlorides and concomitant metal–cation motion in the opposite direction. The cycling behaviour at a high rate ($35\ mA\,g^{-1}$) of a preliminary prototype based on a Mg anode, the electrolyte, and a non-optimised V_2O_5 cathode showed an initial capacity of $80\ mAh\,g^{-1}$ and a steady-state voltage of 2.3 V.

In summary, these results led us to conclude that the fluxional nature of chlorine bridges in concatenated complexes allow for rapid migration of Mg and possibly Al ions by breaking and forming Mg–Cl ($327.6\ kJ\,mol^{-1}$) and Al–Cl ($511.3\ kJ\,mol^{-1}$) bonds.[39] The concatenated anion channels delimited by micellar cationic aggregates of $EMIm^-$ enable an ion pump mechanism in which Mg and Al percolate to and from the anode without disrupting the IL network and without compromising the electrochemical reversibility. The possible co-deposition of Mg and Al is not a disadvantage for practical applications in future power sources based on the proposed electrolyte systems.

Experimental Section

Synthesis of the IL-based electrolytes: $\delta\text{-}MgCl_2$ was prepared by reacting Mg powder and 1-chlorobutane (Sigma–Aldrich) as reported elsewhere.[3] The ionic liquid $EMImCl/(AlCl_3)_{1.5}$ (io-li-tec USA) was vacuum dried at 105 °C for 168 h. $\delta\text{-}MgCl_2$ was dissolved in $EMImCl/(AlCl_3)_{1.5}$ to saturation (5.1% *w/w*). Dilution with further

© 2015 Wiley-VCH Verlag GmbH & Co. KGaA, Weinheim

Reprinted with permission from ChemSusChem 2015, 8, 3069-3076.
Copyright 2015 Wiley-VCH Verlag GmbH & Co.

$EMImCl/(AlCl_3)_{1.5}$ yielded the $(EMImCl/(AlCl_3)_{1.5})/(\delta\text{-}MgCl_2)_x$ electrolytes. All materials were stored and manipulated under Ar.

Inductively coupled plasma atomic emission spectroscopy: ICP-AES measurements were performed using a SPECTRO Arcos spectrometer with EndOnPlasma torch. The samples were digested using hot aqua regia. The emission lines at 279.079 and 308.215 nm were used to determine the concentration of Mg and Al, respectively. The sample used to determine the composition of the electrodeposited layer was prepared by immersing a Pt electrode in the $(EMImCl/(AlCl_3)_{1.5})/(\delta\text{-}MgCl_2)_{0.08}$ electrolytic solution and applying a constant voltage of −0.4 V versus Mg for 20 min. A deposit (2.28 mg) formed and was washed carefully with anhydrous toluene and dissolved using a 5% HNO_3 solution.

Thermogravimetric analysis: TGA measurements were performed using a TGA 2950 thermobalance (TA Instruments) under N_2. The heating rate was modulated from 0.001 to 50 °C min^{-1} depending on the first derivative of the weight loss. Samples were loaded on a Pt pan under an inert atmosphere.

Differential scanning calorimetry: DSC measurements were performed using a Modulated DSC (MDSC) 2920 instrument (TA instruments) equipped with a liquid N_2 cooling system. DSC profiles were measured from −110 to 140 °C, at a heating rate of 3 °C min^{-1}, by loading a weighed aliquot of sample inside a hermetically sealed Al pan.

Vibrational spectroscopy: Raman spectra were recorded using a Thermo Scientific NICOLET 6700 spectrometer equipped with a NXR-FT Raman spectrometer module. Samples were sealed in quartz tubes analysed with 25 000 scans at a resolution of 2 cm^{-1}. The excitation laser wavelength was 1064 nm. Fourier transform far infrared (FT-FIR) spectra were measured using a Nicolet Nexus spectrometer in transmission mode with a resolution of 2 cm^{-1} in the range 50–600 cm^{-1}. The samples were prepared in a cell with polyethylene windows and sealed inside an Ar dry box. Each spectrum was obtained by averaging 1000 scans.

Electronic structure calculations: First-principles-based electronic structure calculations were performed using the Gaussian 09 suite of programs.[40] Density functional theory (DFT) with Becke's 3-parameter hybrid functional (B3LYP)[41] was used with the 6-31G** split valence basis set[42] with no symmetry constraint. The resulting structures were then refined with optimisations performed using a larger basis set 6-311G**,[43] and frequency calculations at the same level of theory were performed to confirm the resulting stationary points as local minima. To minimise the effect of systematic errors in calculated vibrational frequencies, all of the calculated frequencies were scaled by 1.04 except for cationic vibrations, which were not scaled. This factor was used to match the experimental and calculated $AlCl_4$ characteristic peak at 350 cm^{-1}. We used this factor to scale the vibrational frequencies that involve only Cl, Mg and Al atoms. This factor is close to the scaling factors obtained using the scaled quantum mechanical (SQM) method for organic molecules containing C, H, N, O, S, P and Cl atoms[44] (i.e., 1.04 for stretching of non C and H vibrations).

Electrochemical measurements: Cyclic voltammetry measurements were performed with a VSP Bio-Logic 5-channel potentiostat/galvanostat. A three-electrode configuration was used at room temperature (22 °C). The working electrode was either Mg or Pt with a nominal surface area of 0.7 cm^2. The counter electrode and the reference electrode were both Mg. The deposition and stripping of Mg and Al from the electrolyte solutions were recorded at scan rates in the range of 1–100 mV s^{-1} until steady state was achieved. The exchange current density was determined using Mg or Pt working electrodes by cycling the potential in a narrow potential window at approximately 0 V at 1 mV s^{-1}. Battery cycling was conducted on coin cell prototypes comprised of $Mg/[(EMImCl/(AlCl_3)_{1.5})/(\delta\text{-}MgCl_2)_{0.08}]/V_2O_5$ using a Maccor 2300 test station.

Broadband electrical spectroscopy: Measurements were conducted using a broadband electrical spectrometer (BES) in the frequency range 10 mHz–10 MHz using a Novocontrol Alpha-A analyser over the temperature range −80–160 °C. The temperature was controlled with precision greater than ±0.2 °C using a custom-built cryostat operating with an N_2 gas jet heating and cooling system. The sample was sandwiched between two circular Pt electrodes kept apart by a separator comprised of optical fibres (d = 0.126 mm) inside a sealed cylindrical Teflon cell closed in a glove box filled with Ar and maintained under Ar during the measurements.

NMR measurements: The individual samples were packed into 4 mm Bruker rotors which were then hermetically sealed under Ar using Kel-F inserts and a Kel-F drive tip. The ^{25}Mg NMR spectra were obtained using a Bruker 750 MHz wide bore UltraStabilized spectrometer at a frequency of 45.91 MHz. An aqueous solution of 1 M $MgCl_2$ was used as an external reference and set to 0 ppm. A variable temperature study was conducted across a temperature range of 253–343 K. Dry N_2 gas was employed as the carrier gas and a (90°–90°) Hahn-Echo pulse sequence was employed to minimise the intensity of acoustic ringing artefacts typical of low γ nuclei.

Acknowledgements

This work was conducted with support from "Progetto Strategico Maestra" of The University of Padova Italy (V.D. PI) and Academic Excellence Award # 90827-00 (M.V. PI). M.V. and C.H. are thankful to President William Pollard, Provost Howard Johnson, and President Rudolph Crew for financial support. The NMR Program at Hunter College is supported by a single investigator grant from the Basic Energy Sciences Division of the U.S. Department of Energy (No. DE-SC0005029). S.G.G. is a member of the New York Structural Biology Center. The NMR data collected at NYSBC was made possible by a grant from NYSTAR. The DFT calculations were supported by the U.S. Army Research Office under Contract No. W911NF-07-1-0085.

Keywords: batteries · conduction mechanism · electrolytes · ionic liquids · magnesium

[1] T. D. Gregory, R. J. Hoffman, R. C. Winterton, *J. Electrochem. Soc.* **1990**, *137*, 775–780.
[2] P. Novák, J. Desilvestro, *J. Electrochem. Soc.* **1993**, *140*, 140–144.
[3] V. Di Noto, S. Lavina, D. Longo, M. Vidali, *Electrochim. Acta* **1998**, *43*, 1225–1237.
[4] M. Piccolo, G. A. Giffin, K. Vezzù, F. Bertasi, P. Alotto, M. Guarnieri, V. Di Noto, *ChemSusChem* **2013**, *6*, 2157–2160.
[5] J. B. Goodenough, K.-S. Park, *J. Am. Chem. Soc.* **2013**, *135*, 1167–1176.
[6] J. Hassoun, K.-S. Lee, Y.-K. Sun, B. Scrosati, *J. Am. Chem. Soc.* **2011**, *133*, 3139–3143.
[7] J. Wang, L. Yin, H. Jia, H. Yu, Y. He, J. Yang, C. W. Monroe, *ChemSusChem* **2014**, *7*, 563–569.

© 2015 Wiley-VCH Verlag GmbH & Co. KGaA, Weinheim

Reprinted with permission from ChemSusChem 2015, 8, 3069-3076.
Copyright 2015 Wiley-VCH Verlag GmbH & Co.

[8] D. Aurbach, I. Weissman, Y. Gofer, E. Levi, *Chem. Rec.* **2003**, *3*, 61 – 73.
[9] C. Liebenow, Z. Yang, P. Lobitz, *Electrochem. Commun.* **2000**, *2*, 641 – 645.
[10] Y.-S. Guo, F. Zhang, J. Yang, F.-F. Wang, Y. NuLi, S. Hirano, *Energy Environ. Sci.* **2012**, *5*, 9100 – 9106.
[11] J. Muldoon, C. B. Bucur, T. Gregory, *Chem. Rev.* **2014**, *114*, 11683 – 11720.
[12] R. E. Doe, R. Han, J. Hwang, A. J. Gmitter, I. Shterenberg, H. D. Yoo, N. Pour, D. Aurbach, *Chem. Commun.* **2014**, *50*, 243 – 245.
[13] I.-T. Kim, K. Yamabuki, M. Morita, H. Tsutsumi, N. Yoshimoto, *J. Power Sources* **2015**, *278*, 340 – 343.
[14] T. Liu, Y. Shao, G. Li, M. Gu, J. Hu, S. Xu, Z. Nie, X. Chen, C. Wang, J. Liu, *J. Mater. Chem. A* **2014**, *2*, 3430 – 3438.
[15] M. E. Spahr, P. Novák, O. Haas, R. Nesper, *J. Power Sources* **1995**, *54*, 346 – 351.
[16] L. L. Yang, A. R. McGhie, G. C. Farrington, *J. Electrochem. Soc.* **1986**, *133*, 1380 – 1385.
[17] M. Vittadello, P. E. Stallworth, F. M. Alamgir, S. Suarez, S. Abbrent, C. M. Drain, V. Di Noto, S. G. Greenbaum, *Inorg. Chim. Acta* **2006**, *359*, 2513 – 2518.
[18] V. Di Noto, M. Fauri, Magnesium-Based Primary (Non Rechargeable) and Secondary (Rechargeable) Batteries, **2000**, PCT/EP00/07221.
[19] T. Kakibe, J. Hishii, N. Yoshimoto, M. Egashira, M. Morita, *J. Power Sources* **2012**, *203*, 195 – 200.
[20] Y. NuLi, J. Yang, P. Wang, *Appl. Surf. Sci.* **2006**, *252*, 8086 – 8090.
[21] M. A. Navarra, J. Manzi, L. Lombardo, S. Panero, B. Scrosati, *ChemSusChem* **2011**, *4*, 125 – 130.
[22] P. Novák, R. Imhof, O. Haas, *Electrochim. Acta* **1999**, *45*, 351 – 367.
[23] N. Amir, Y. Vestfrid, O. Chusid, Y. Gofer, D. Aurbach, *J. Power Sources* **2007**, *174*, 1234 – 1240.
[24] P. Koronaios, R. A. Osteryoung, *J. Electrochem. Soc.* **1999**, *146*, 2995 – 2999.
[25] J. Fuller, R. T. Carlin, R. A. Osteryoung, P. Koronaios, R. Mantz, *J. Electrochem. Soc.* **1998**, *145*, 24 – 28.
[26] C. J. Dymek, D. A. Grossie, A. V. Fratini, W. Adams, *J. Mol. Struct.* **1989**, *213*, 25 – 34.
[27] K. Matsumoto, R. Hagiwara, Z. Mazej, P. Benkič, B. Žemva, *Solid State Sci.* **2006**, *8*, 1250 – 1257.
[28] J. Muldoon, C. B. Bucur, A. G. Oliver, T. Sugimoto, M. Matsui, H. S. Kim, G. D. Allred, J. Zajicek, Y. Kotani, *Energy Environ. Sci.* **2012**, *5*, 5941 – 5950.
[29] S. Takahashi, L. a. Curtiss, D. Gosztola, N. Koura, M.-L. Saboungi, *Inorg. Chem.* **1995**, *34*, 2990 – 2993.
[30] S. A. Katsyuba, E. E. Zvereva, A. Vidis, P. J. Dyson, *J. Phys. Chem. A* **2007**, *111*, 352 – 370.
[31] K. Nakamoto, *Infrared and Raman Spectra of Inorganic and Coordination Compounds*, Wiley, New York, USA, **1986**.
[32] C. J. Dymek, J. S. Wilkes, M.-A. Einarsrud, H. A. Øye, *Polyhedron* **1988**, *7*, 1139 – 1145.
[33] M. Morimitsu, N. Tanaka, M. Matsunaga, *Chem. Lett.* **2000**, 1028 – 1029.
[34] G. G. Perrault, *Encyclopedia Of Electrochemistry Of The Elements, Vol. VIII*, Marcel Dekker Inc., New York, **1978**.
[35] D. M. Ryan, T. L. Riechel, T. Welton, *J. Electrochem. Soc.* **2002**, *149*, A371 – A378.
[36] G. S. Suresh, M. D. Levi, D. Aurbach, *Electrochim. Acta* **2008**, *53*, 3889 – 3896.
[37] B. L. Tremillon, G. S. Picard, in *Molten Salt Chem.—An Introd. Sel. Appl.* (Eds.: G. Mamantov, R. Marassi), D. Reidel Publishing Company, Dordrecht, Holland, **1987**.
[38] V. Di Noto, M. Piga, G. A. Giffin, K. Vezzù, T. A. Zawodzinski, *J. Am. Chem. Soc.* **2012**, *134*, 19099 – 19107.
[39] J. A. Kerr in *CRC Handb. Chem. Phys. 81st ed.* (Ed.: D. R. Lide), CRC Press, Boca Raton, FL, USA, **2000**.
[40] Gaussian 09, Revision A.1, M. J. Frisch, G. W. Trucks, H. B. Schlegel, G. E. Scuseria, M. A. Robb, J. R. Cheeseman, G. Scalmani, V. Barone, B. Mennucci, G. A. Petersson, H. Nakatsuji, M. Caricato, X. Li, H. P. Hratchian, A. F. Izmaylov, J. Bloino, G. Zheng, J. L. Sonnenberg, M. Hada, M. Ehara, K. Toyota, R. Fukuda, J. Hasegawa, M. Ishida, T. Nakajima, Y. Honda, O. Kitao, H. Nakai, T. Vreven, J. A. Montgomery, Jr., J. E. Peralta, F. Ogliaro, M. Bearpark, J. J. Heyd, E. Brothers, K. N. Kudin, V. N. Staroverov, R. Kobayashi, J. Normand, K. Raghavachari, A. Rendell, J. C. Burant, S. S. Iyengar, J. Tomasi, M. Cossi, N. Rega, J. M. Millam, M. Klene, J. E. Knox, J. B. Cross, V. Bakken, C. Adamo, J. Jaramillo, R. Gomperts, R. E. Stratmann, O. Yazyev, A. J. Austin, R. Cammi, C. Pomelli, J. W. Ochterski, R. L. Martin, K. Morokuma, V. G. Zakrzewski, G. A. Voth, P. Salvador, J. J. Dannenberg, S. Dapprich, A. D. Daniels, Ö. Farkas, J. B. Foresman, J. V. Ortiz, J. Cioslowski, and D. J. Fox, Gaussian, Inc., Wallingford CT, **2009**.
[41] A. D. Becke, *J. Chem. Phys.* **1993**, *98*, 5648 – 5652.
[42] P. C. Hariharan, J. A. Pople, *Theor. Chim. Acta* **1973**, *28*, 213 – 222.
[43] A. D. McLean, G. S. Chandler, *J. Chem. Phys.* **1980**, *72*, 5639 – 5648.
[44] S. Katsyuba, E. Vandyukova, *Chem. Phys. Lett.* **2003**, *377*, 658 – 662.

Received: March 6, 2015
Revised: April 20, 2015
Published online on September 2, 2015

© 2015 Wiley-VCH Verlag GmbH & Co. KGaA, Weinheim

Reprinted with permission from ChemSusChem 2015, 8, 3069-3076.
Copyright 2015 Wiley-VCH Verlag GmbH & Co.

CHEMISTRY & SUSTAINABILITY
CHEMSUSCHEM
ENERGY & MATERIALS

Supporting Information

A Key concept in Magnesium Secondary Battery Electrolytes

Federico Bertasi,[a, b] Chaminda Hettige,[c] Fatemeh Sepehr,[d] Xavier Bogle,[e] Gioele Pagot,[a, b] Keti Vezzù,[b, f] Enrico Negro,[a, b] Stephen J. Paddison,[d] Steve G. Greenbaum,[e] Michele Vittadello,[c] and Vito Di Noto*[a, b]

cssc_201500339_sm_miscellaneous_information.pdf

Reprinted with permission from ChemSusChem 2015, 8, 3069-3076.
Copyright 2015 Wiley-VCH Verlag GmbH & Co.

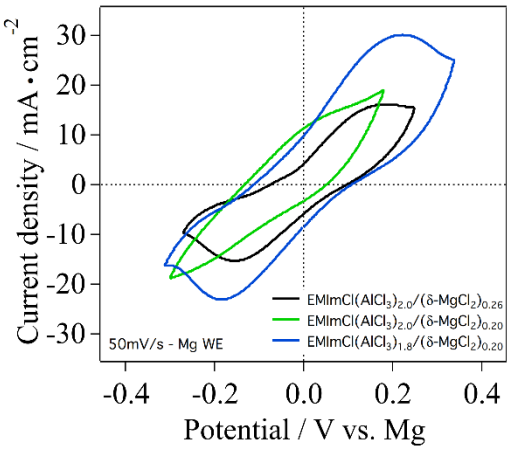


Figure S1. Deposition-stripping performance for samples with $AlCl_3$:EMImCl ratio higher that 1.5 and x≥0.2. WE: Mg, CE: Mg, Ref: Mg, scan rate 50mVs^{-1}.

Reprinted with permission from ChemSusChem 2015, 8, 3069-3076.
Copyright 2015 Wiley-VCH Verlag GmbH & Co.

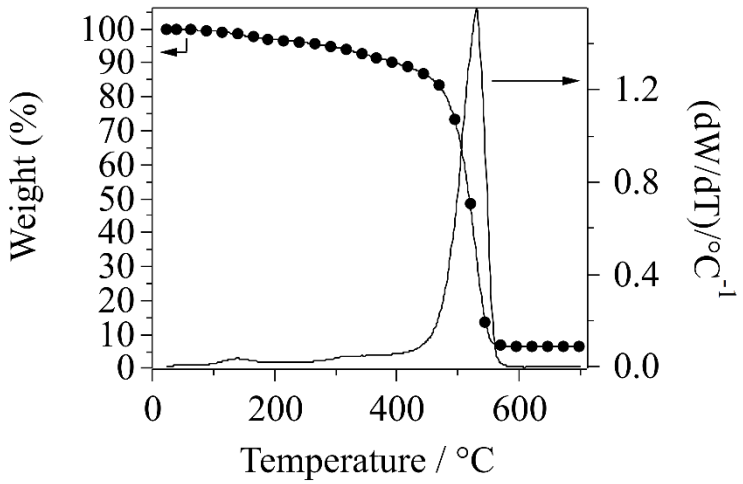


Figure S2. Thermogravimetric analysis for pristine EMImCl/$(AlCl_3)_{1.5}$ ionic liquid.

Reprinted with permission from ChemSusChem 2015, 8, 3069-3076.
Copyright 2015 Wiley-VCH Verlag GmbH & Co.

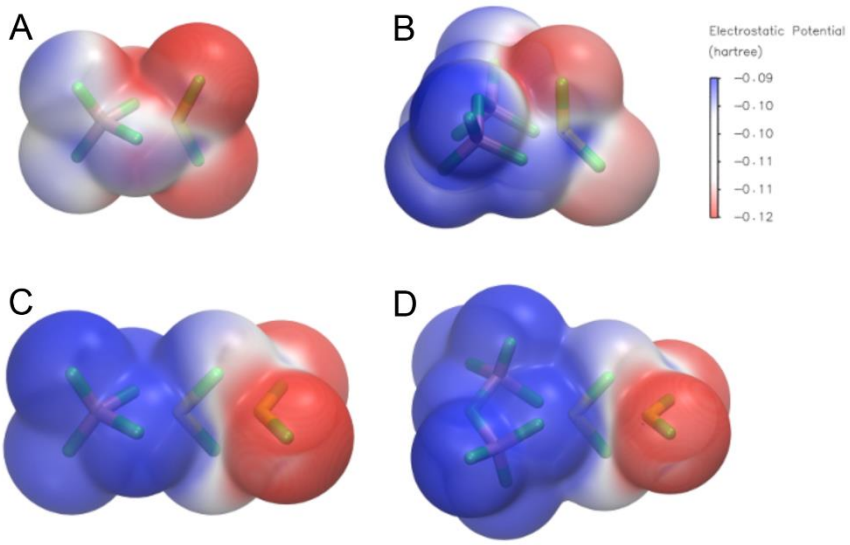


Figure S3. Electrostatic potential map on total electron density isosurface. A) $[AlCl_4MgCl_2]^-$ complex. B) $[Al_2Cl_7MgCl_2]^-$ complex. C) $[AlCl_4(MgCl_2)_2]^-$ complex. D) $[Al_2Cl_7(MgCl_2)_2]^-$ complex. These maps show a more negative electrostatic potential and therefore more electron rich area on magnesium bonded chloride rather than aluminium bonded chloride. Colour code for atoms: chlorine, green; aluminium, pink; magnesium, yellow.

Reprinted with permission from ChemSusChem 2015, 8, 3069-3076.
Copyright 2015 Wiley-VCH Verlag GmbH & Co.

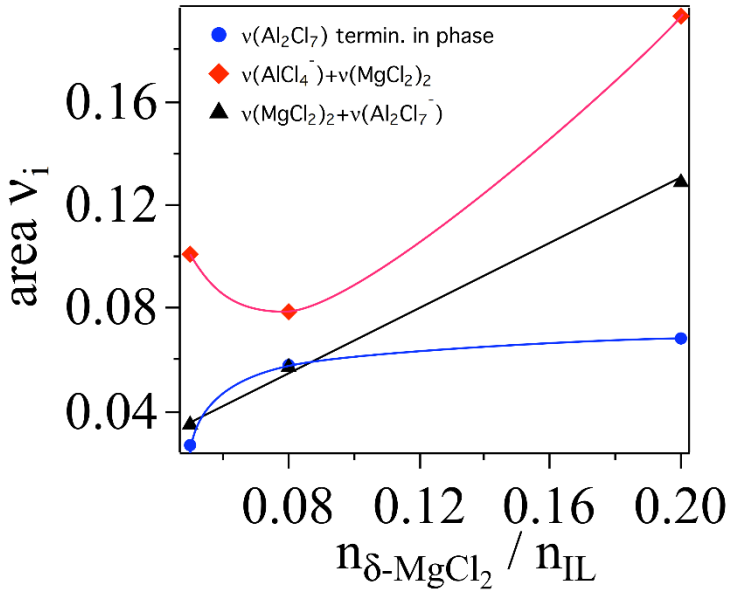


Figure S4. Fractional area analysis of far infrared spectra of $[EMIm/(AlCl_3)_{1.5}]/(\delta\text{-}MgCl_2)_x$ electrolytes. Semi-quantitative analysis of the fractional area of the far IR spectrum in Figure 3D.

Reprinted with permission from ChemSusChem 2015, 8, 3069-3076.
Copyright 2015 Wiley-VCH Verlag GmbH & Co.

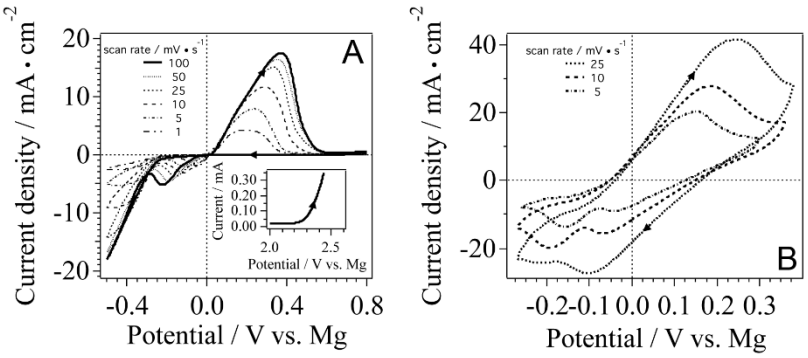


Figure S5. Details of cyclic voltammetry of $[EMIm/(AlCl_3)_{1.5}]/(\delta\text{-}MgCl_2)_{0.08}$ electrolyte. A) Pt working electrode. B) Mg ribbon working electrode.

Reprinted with permission from ChemSusChem 2015, 8, 3069-3076.
Copyright 2015 Wiley-VCH Verlag GmbH & Co.

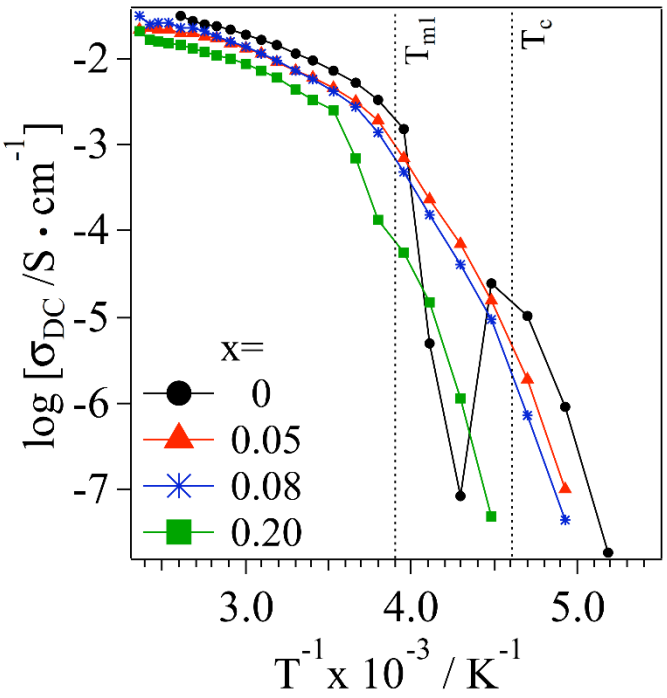


Figure S6. Temperature-dependence of direct current conductivity profiles of $[EMIm/(AlCl_3)_{1.5}]/(\delta\text{-}MgCl_2)_x$ electrolytes.

Reprinted with permission from ChemSusChem 2015, 8, 3069-3076.
Copyright 2015 Wiley-VCH Verlag GmbH & Co.

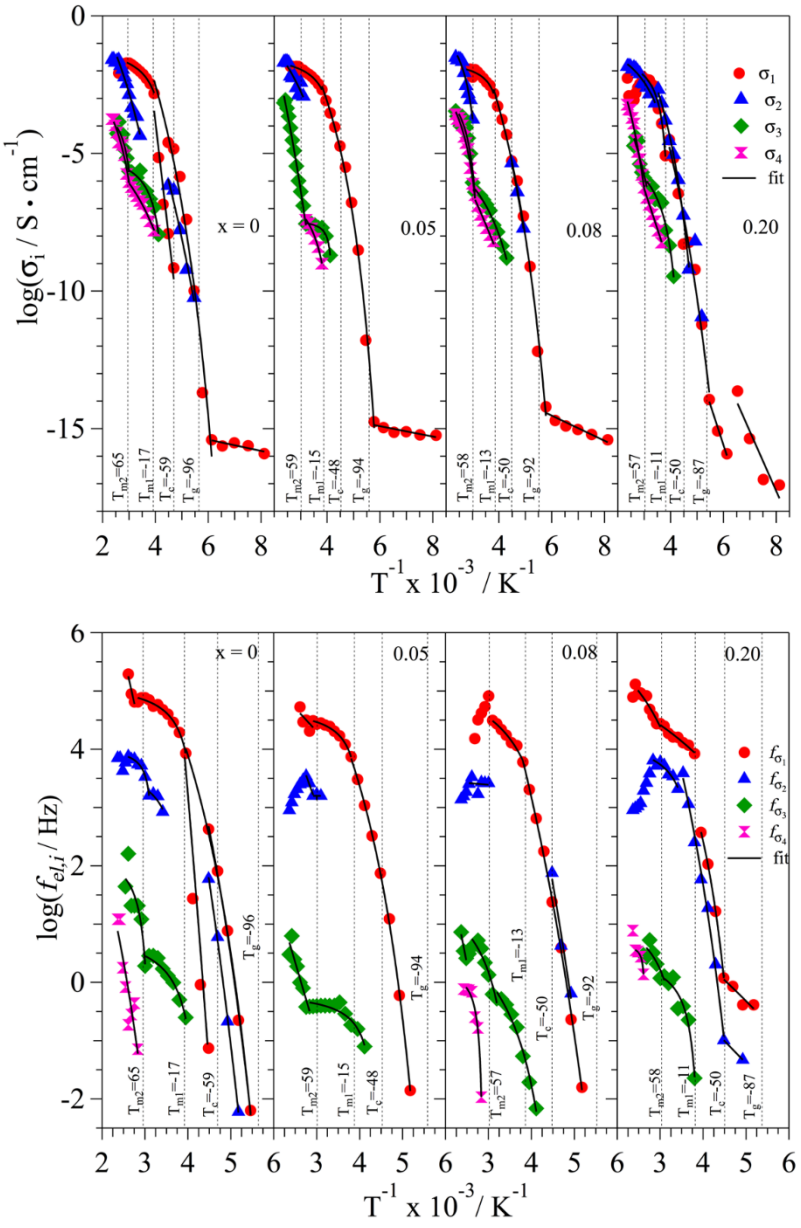


Figure S7. Temperature-dependence of broadband electrical parameters of [EMIm/$(AlCl_3)_{1.5}$]/$(\delta\text{-}MgCl_2)_x$ electrolytes.

Reprinted with permission from ChemSusChem 2015, 8, 3069-3076.
Copyright 2015 Wiley-VCH Verlag GmbH & Co.

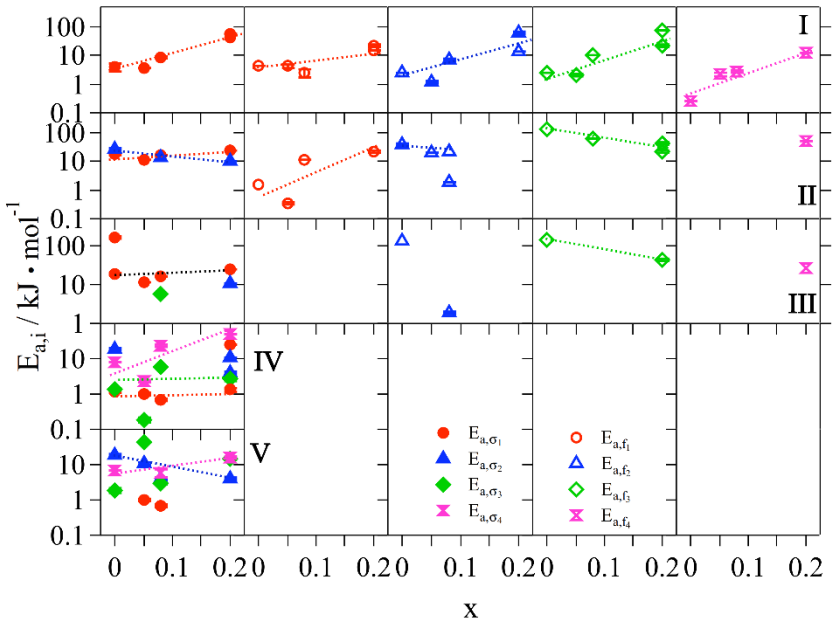


Figure S8. Activation energies vs. x for relaxation and polarization phenomena. I, II, III, IV, V are the temperature regions delimited by the $[EMIm/(AlCl_3)_{1.5}]/(\delta\text{-}MgCl_2)_x$ thermal transitions, detected by DSC analysis.

Reprinted with permission from ChemSusChem 2015, 8, 3069-3076.
Copyright 2015 Wiley-VCH Verlag GmbH & Co.

Table S1. Ab initio vibrational frequencies for $EMImAlCl_4$ and $EMImAl_2Cl_7$ in the far infrared region compared to experimental Raman and IR frequencies for $EMImCl(AlCl_3)_{1.5}$.

Structure	Calculated frequencies (cm^{-1}) at B3LYP/6-311G**	Experimental frequencies (cm^{-1})		Assignment [a]
		Raman	IR	
$AlCl_4^-$ + $EMIm^+$ ≡ Figure 2A	182	181[26], 179	180	$\delta(AlCl_4^-)$
	190			$\delta(AlCl_4^-)$
	242[b] IR inactive	241[26], 240		γ(N-Me)[27]
	350 IR inactive	350[26], 348		$\nu(AlCl_4^-)$[29]
	375[b] IR inactive	383[26], 385		γ(N-Et)
	431[b]	431		r(N-Et), r(N-Me)[27]
	477 Raman inactive			$\nu_{as}(AlCl_4^-)$
	488 Raman inactive		493	$\nu_{as}(AlCl_4^-)$
	561 Raman inactive		551	$\nu(AlCl_4^-)$
$Al_2Cl_7^-$ + $EMIm^+$ ≡ Figure 2B	156,162	157[26],156		$\delta(Al_2Cl_7^-)$
	189			$\delta(Al_2Cl_7^-)$ termin.
	241[b] IR inactive	24[26],240		γ(N-Me)[27]
	314	310[26], 311	310	$\nu_s(Al_2Cl_7^-)$ bridge
	342 weak Raman		331	$\nu_{as}(Al_2Cl_7^-)$ bridge[30]
	380[b] IR inactive	383[26], 385		γ(N-Et)
	393	383[26], 385	385	$\nu(Al_2Cl_7^-)$ termin, out of phase
	427[b]	432[26], 431		r(N-Et), r(N-Me)[27]
	448	432[26], 431	433	$\nu(Al_2Cl_7^-)$ termin., in phase
	538		536	$\nu(Al_2Cl_7^-)$ termin.
	576,586	566[26]		$\nu(Al_2Cl_7^-)$ termin.

[a] ν stretching, δ bending, r rocking, γ out of plane, s symmetric, as antisymmetric.
[b] Calculated frequency is not scaled.

(26) Dymek, C. J.; Grossie, D. A.; Fratini, A. V.; Wade Adams, W. *J. Mol. Struct.* **1989**, *213*, 25.
(27) Matsumoto, K.; Hagiwara, R.; Mazej, Z.; Benkič, P.; Žemva, B. *Solid State Sci.* **2006**, *8*, 1250.
(29) Takahashi, S.; Curtiss, L. a.; Gosztola, D.; Koura, N.; Saboungi, M.-L. *Inorg. Chem.* **1995**, *34*, 2990.
(30) Katsyuba, S. A.; Zvereva, E. E.; Vidis, A.; Dyson, P. J. *J. Phys. Chem. A* **2007**, *111*, 352.

Reprinted with permission from ChemSusChem 2015, 8, 3069-3076.
Copyright 2015 Wiley-VCH Verlag GmbH & Co.

Table S2. Ab initio vibrational frequencies for $[EMImAlCl_4](MgCl_2)_{1,2}$ and $[EMImAl_2Cl_7](MgCl_2)_{1,2}$ in the far infrared region compared to experimental Raman and IR frequencies for $[EMImCl(AlCl_3)_{1.5}](\delta\text{-}MgCl_2)_{0.2}$.

Structure	Calculated frequencies (cm^{-1}) At B3LYP/6-311G**	Experimental frequencies (cm^{-1}) Raman	Experimental frequencies (cm^{-1}) IR	Assignment [a]
$AlCl_4^-$+EMIm$^+$+$MgCl_2$ ($AlCl_4^-$+EMIm$^+$+2$MgCl_2$) ≡ Figure 2C (Figure 2E)	177(172)	180	180	$\delta(AlCl_4^-)$
	193			$\delta(AlCl_4^-)$, $\delta(MgCl_2)$
	(209)	210	210	$\delta(AlCl_4^-)$, $\delta((MgCl_2)_2)$
	237	237		scissoring $AlCl_4^-$ next to Mg
	241[b] (240[b])	237		γ(N-Me)
	(245)			$\nu((MgCl_2)_2)$
	(256, 267) Raman inactive		277	$\nu((MgCl_2)_2)$
	(271)		277	$\nu((MgCl_2)_2)$
	342			$\nu_s(MgCl_2)$
	351(343) weak IR, strong Raman	348		$\nu(AlCl_4^-)$
	381[b] IR inactive (383[b])			γ(N-Et)
	(388,392) Raman inactive		385	$\nu((MgCl_2)_2)$
	(419,426,436) Raman inactive		430,447	$\nu(AlCl_4^-)$, $\nu((MgCl_2)_2)$
	428[b] (430[b])	433		r(N-Et), r(N-Me)
	450 Raman inactive		447	$\nu_{as}(AlCl_4^-)$
	511 Raman inactive		499	$\nu_{as}(AlCl_4^-)$, $\nu_{as}(MgCl_2)$
	(522)			$\nu_s(AlCl_4^-)$
	528(606)			$\nu(AlCl_4^-)$
$Al_2Cl_7^-$+ EMIm$^+$+ $MgCl_2$ ($Al_2Cl_7^-$+EMIm$^+$+2$MgCl_2$) ≡ Figure 2D (Figure 2F)	164(168)	150	150	$\delta(Al_2Cl_7^-)$, $\delta(MgCl_2)$
	179(176)	180	180	$\delta(Al_2Cl_7^-)$, $\delta(MgCl_2)$
	197(201)			$\delta(Al_2Cl_7^-)$, $\delta(MgCl_2)$
	240[b] (239[b])	237		γ(N-Me)
	(247, 253)		277	$\nu(MgCl_2)_2$
	(266) Raman inactive		277	$\nu(MgCl_2)_2$
	(297)	310		$\nu(Al_2Cl_7^-)$,$\nu(MgCl_2)_2$
	320	310		$\nu_s(Al_2Cl_7^-)$ bridge
	328		337	$\nu_s(MgCl_2)$
	347		337	$\nu_{as}(Al_2Cl_7^-)$ bridge
	(347)	348		$\nu(Al_2Cl_7^-)$
	(360)			$\nu((MgCl_2)_2)$
	366[b] (381[b]) IR inactive			γ(N-Et)
	386(389)		385	$\nu(Al_2Cl_7^-)$ termin., out of phase
	439[b] (429[b])	433		r(N-Et), r(N-Me)
	447(447)	433	430	$\nu(Al_2Cl_7^-)$ termin.
	(477, 491) Raman inactive		447,499	$\nu((MgCl_2)_2)$
	(517)			$\nu((MgCl_2)_2)$
	521		528	$\nu(Al_2Cl_7^-)$ termin.
	529		528	$\nu_{as}(MgCl_2)$
	(552)		555	$\nu(Al_2Cl_7^-)$ termin.
	591,609(588,600)			$\nu(Al_2Cl_7^-)$ termin.

[a] ν stretching, δ bending, r rocking, γ out of plane, s symmetrical, as antisymmetric.
[b] Calculated frequency is not scaled.

Reprinted with permission from Chemical Physics Letters 2016, 645, 20-26.
Copyright 2016 Elsevier B.V.
Chemical Physics Letters 645 (2016) 20–26

Contents lists available at ScienceDirect

Chemical Physics Letters

journal homepage: www.elsevier.com/locate/cplett

Dissipative Particle Dynamics interaction parameters from *ab initio* calculations

Fatemeh Sepehr, Stephen J. Paddison*

Department of Chemical & Biomolecular Engineering, University of Tennessee, Knoxville, TN 37996, USA

ARTICLE INFO

Article history:
Received 11 September 2015
In final form 16 December 2015
Available online 23 December 2015

ABSTRACT

Dissipative Particle Dynamics (DPD) is a commonly employed coarse-grained method to model complex systems. Presented here is a pragmatic approach to connect atomic-scale information to the meso-scale interactions defined between the DPD particles or beads. Specifically, electronic structure calculations were utilized for the calculation of the DPD pair-wise interaction parameters. An implicit treatment of the electrostatic interactions for charged beads is introduced. The method is successfully applied to derive the parameters for a hydrated perfluorosulfonic acid ionomer with absorbed vanadium cations.

© 2015 Elsevier B.V. All rights reserved.

1. Introduction

Dissipative Particle Dynamics (DPD) is a meso-scale simulation technique that was first introduced by Hoogerbrugge and Koelman [1]. Further developments by Español and Warren included the stochastic differential equations and conservation of energy [2,3]. The method describes the system in terms of soft particles, or beads, whose motion is governed by certain collision rules [4]. The soft particles, or beads, represent groups of atoms or molecules in the system. The use of simplified potentials and the grouping of the atoms into particles permit simulations of large systems over long time-scales that are either impossible or difficult to perform in all atom methods such as molecular dynamics (MD) [5]. Since its development, the original formulation of DPD has been successfully applied to model a large variety of systems including: block copolymers [6,7], surfactant solutions [8], bilayer membranes [9], and ionomers [10–12].

The reliability of DPD simulations depends on the proper translation of the atomic-scale into the meso-scale interaction parameters. There have been different methods for the derivation of the interaction parameters between the various types of beads in order to link the actual physical system to the fictitious DPD particles. The most widely used method was introduced by Groot and Warren through mapping onto Flory–Huggins theory [4]. They used the Flory–Huggins χ-parameter to define the interactions between different components of the system. The χ-parameter may be related to the solubility [13] or approximated from mixing energy calculations using a Monte Carlo approach [12,14]. However, χ is not available for every substance, and there are cases where the calculations via mixing energy are not fruitful. For instance, if the beads contain a net electrostatic charge both the solubility and mixing energy approximations fail to give a suitable value for χ and consequently the interaction parameters. Some authors have set the parameters based on the nature of the chemical groups that are lumped into each bead or the phase separation behavior of the system [15–17]. This technique requires a thorough understanding of the materials, specific experimental, and simulation results. Others started with MD simulations and extracted an effective coarse-grained potential, requiring the meso-scale simulations to match the structural data or pair-correlation functions of the atomistic simulations [18–20].

Groot developed a smeared-charge approach for the treatment of electrostatic interactions in which the charge is distributed within a sphere rather than being only on a point [21]. The inclusion of this long-range interaction increases the computational cost and violates the basic principle of DPD (that only considers the interactions to be short range). Therefore, it is necessary to provide a method for defining the interaction parameters that is versatile, does not rely on the experimental information, and still fits into the simple original DPD framework to ensure the expected high computational efficiency. The aim of this letter is to introduce a parameterization method that is capable of capturing the various types of interactions including strong electrostatics while preserving the simple form of the DPD potentials and high computational efficiency of the method.

In the following the overall DPD framework is briefly described (for a more detailed and complete description of the method the reader is referred elsewhere [1–4,22]). We then present a pragmatic

* Corresponding author.
E-mail address: spaddison@utk.edu (S.J. Paddison).

http://dx.doi.org/10.1016/j.cplett.2015.12.032
0009-2614/© 2015 Elsevier B.V. All rights reserved.

Reprinted with permission from Chemical Physics Letters 2016, 645, 20-26.
Copyright 2016 Elsevier B.V.

approach that uses ab initio electronic structure calculations for the development of the conservative interaction parameters. The average pairwise potentials derived from these quantum chemical calculations ensure the perseverance of the original framework. Finally, the parameterization method is applied to a system of interest, which consists of a hydrated perfluorosulfonic acid ionomer with absorbed ionic species.

2. DPD framework

The time evolution of the interacting particles is governed by Newton's equations of motion that are integrated using a modified velocity-Verlet algorithm [4]. The dimensionless equations of motion in the Hamiltonian form are:

$$\frac{dr_i}{dt} = v_i, \quad \frac{dv_i}{dt} = f_i \tag{1}$$

the r_i and v_i are the position and velocity of the ith particle and f_i is the net force acting on that particle. The net force contains three non-bonded terms. Bonded terms may also be included in order to make the simulation of polymers viable.

$$f_i = \sum_{j \neq i} \left(F_{ij}^C + F_{ij}^D + F_{ij}^R\right) + f_i^{bonded} \tag{2}$$

The first three terms in the summation: F_{ij}^C, F_{ij}^D, and F_{ij}^R conservative, dissipative, and random forces which are the non-bonded components and are typically formulated as follows:

$$F_{ij}^C = a_{ij}(1 - r_{ij})n_{ij} \tag{3}$$

$$F_{ij}^D = -\gamma_{ij}(1 - r_{ij})^2(n_{ij}.v_{ij})n_{ij} \tag{4}$$

$$F_{ij}^R = \sigma_{ij}(1 - r_{ij})\xi_{ij}\frac{1}{\sqrt{\Delta t}}n_{ij} \tag{5}$$

These forces are pairwise and in the direction of $\mathbf{n}_{ij} = (r_i - r_j)/|r_{ij}|$ which is the unit vector toward the centers of particles i and j. The cut off distance for all the non-bonded forces is r_c, the length-scale, which is linked to physical units based on the system of study and degree of coarse-graining. The relative position and velocities are defined as $r_{ij} = r_i - r_j$ and $v_{ij} = v_i - v_j$. a_{ij} is the interaction parameter between two beads and is material or chemical compositional specific and therefore must be determined for each system. The dissipation constant, γ_{ij}, and the noise amplitude, σ_{ij}, are related by $\sigma_{ij} = \sqrt{\gamma_{ij} 2k_B T}$ to control the temperature fluctuations as dictated by the fluctuation-dissipation theorem [2]. The dissipation constant has a typical value of 4.5 [4,12,14]. ξ_{ij} is a symmetric Gaussian random number with zero mean and unit variance chosen independently for each pair of interacting particles at each time step (Δt). The last term in Eq. (2) comes from the bonded potentials defined to describe polymeric systems. Beads of a polymer are usually connected to their nearest neighbor beads by harmonic springs [4,6]. However, another spring term to describe the second nearest neighbor beads may also be added in order to improve the structural properties of a polymer chain [19,23,24].

In this formulation, the only material parameters to be determined for the system of interest are the conservative interaction parameters, a_{ij}, and bonded potentials if present. It has been previously shown that the relative interactions affect the phase behavior of the system and not the absolute values [25,26]. Recent studies also underline the use of different like bead interactions for different bead types (i.e., $a_{ii} \neq a_{jj}$) and its effect on the correct prediction of phase behavior and local densities [27,28]. Hence, it is important to find the relative amount of the interactions between all pairs of beads (either like or unlike) as accurate as possible.

3. Parameterization of the conservative force

The conservative interaction potential is assumed to consist of two terms in the quadratic form:

$$U_{ij}^C = U_{ij}^R + U_{ij}^{ex} = \begin{cases} \frac{a_{ij}}{2}(1 - r_{ij})^2, & r_{ij} < 1 \\ 0, & r_{ij} \geq 1 \end{cases} \tag{6}$$

where $U_{ij}^R = \frac{a^R}{2}(1 - r_{ij})^2$ and $U_{ij}^{ex} = \frac{a_{ij}^{ex}}{2}(1 - r_{ij})^2$ (this implies $a_{ij} = a^R + a_{ij}^{ex}$). The first term is the reference potential and is related to the compressibility of a reference material. The second term is the excess interaction and contains the information regarding the relative interactions among the beads excess to the reference. The intention is to reproduce the experimental compressibility of one pure reference material and then to obtain all the other interactions (either like or unlike) relative to this reference. The reference bead is a charge neutral species in the system with known experimental compressibility. The a^R is then obtained by matching the simulated compressibility of pure reference to that of the experiment, similar to the remarkable work by Groot and Warren (see Section IV of Ref. [4]).

The excess energy may be related to the interaction energy of the two beads which can be calculated using electronic structure calculations.

$$U_{ij}^{\text{int}} = U_{(i+j)} - U_{(i)} - U_{(j)} \tag{7}$$

where U_{ij}^{int} is the interaction energy and is obtained by subtracting the ab initio calculated electronic energy of the isolated beads (i.e., $U_{(i)}$ and $U_{(j)}$) from that of the interacting beads (i.e., $U_{(i+j)}$; the total electronic energy of a system containing the two interacting beads i and j). In order to correctly sample the interaction energy, $U_{(i+j)}$ should be calculated and averaged over many different spatial configurations of the two beads. Figure 1 illustrates the six spatial degrees of freedom that are varied in order to consider all the probable configurations of two objects in a three dimensional space. By varying these six geometric parameters, many different configurations are generated and consequently the interaction energies are fitted to a quadratic function of r_{ij} (the distance between the centers of mass of beads i and j). Overall, the procedure is similar to the derivation of classical two-body pair potentials from quantum chemical calculations [29–31]. However, in this case the calculations are performed on two large clusters of atoms or molecules (the selected beads with full atomistic resolution) instead of two atoms

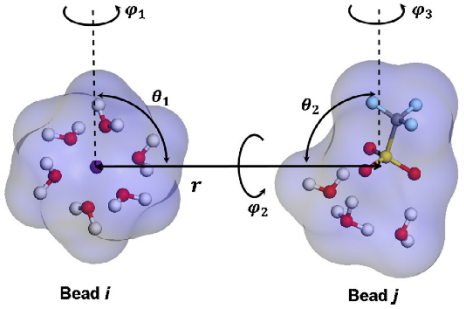


Figure 1. The six degrees of freedom that contribute different configurations to the two objects (beads). The atomic structures of the beads ***i*** and ***j*** are arbitrary. The angles can vary as $\mathbf{0^\circ \leq \theta \leq 180^\circ}$ and $\mathbf{0^\circ \leq \phi \leq 360^\circ}$ for each configuration. The lower limit for the $\mathbf{r}_{ij}$ is when the beads start to overlap and the upper limit is the cut off distance $\mathbf{r}_c$.

Reprinted with permission from Chemical Physics Letters 2016, 645, 20-26.
Copyright 2016 Elsevier B.V.

or small molecules and also the functional form of the potential is only a simple quadratic from.

The least squares method is used to fit the calculated interaction energies onto the quadratic functional form. A high quality fit is not expected to be achieved because the simple quadratic form of the potential is not sufficient to completely explain the interaction of the two clusters of atoms. However, the use of more sophisticated potentials is not utilized in order to maintain the linear functional form of the conservative force and consequently the high speed and efficiency of the DPD simulations. In practice, addition of a constant to the quadratic form improves the fit quality. This improvement is significant and necessary for the charged beads and minor for those that are charge neutral. Hence, the practical form of the interaction energy becomes:

$$U_{ij}^{\text{int}} = \frac{a_{ij}^{\text{int}}}{2}(1 - r_{ij})^2 + b_{ij}^{\text{int}} \tag{8}$$

Because b_{ij}^{int} is usually negligible for charge neutral beads but has a large value for charged beads, it may be considered as the contribution of electrostatic interactions.

The next step is to map the fitted parameters, a_{ij}^{int} and b_{ij}^{int}, to the meso-scale parameter a_{ij}^{ex}. The excess parameter of the reference bead should go to zero because the excess energy is defined as the excess to the reference. Hence, the calculated a_{RR}^{int} is scaled to a negligible value. The fitted parameters for all the beads (either like or unlike) are also scaled with this factor in order to maintain the correlation between the calculated energies as it affects the phase behavior of the system. The fitted parameter, b_{ij}^{int}, vanishes in the derivative of energy and consequently in the force. In order to keep its effect in the final force we assume that this interaction decays quadratically from the center of particle becoming zero at the cut off distance, similar to the U_{ij}^{R} and U_{ij}^{ex} potentials. Hence:

$$a_{ij}^{ex} = a_{ij}^{\text{int}*} + b_{ij}^{\text{int}**} \tag{9}$$

where the stars indicate that the fitted parameters are scaled. The double star in the superscript of b_{ij}^{int} denotes that its scaling differs to that of a_{ij}^{int} by r_c^2, as their units are different. Eq. (9) applies to both $i=j$ and $i \neq j$, so depending on the $a_{ii}^{\text{int}*}$ and b_{ii}^{int**} values the like bead interactions (a_{ii}) differ for different bead types. The importance of having different like bead interactions has been substantiated recently [27,28].

The treatment of electrostatics via the b_{ij}^{int**} parameter in the conservative force with a cut off distance at r_c does not violate the domain decomposition scheme of the DPD method. However, this assumption is only reasonable when the charge screening effect is strong (i.e., short Debye length and high ionic strength) and as a result the long range electrostatic interactions vanish at distances around the cut off. This limitation is only for the systems with charged beads otherwise this constraint is irrelevant. It is also important to note that the excess energy is a meso-scale quantity corresponding to both overlapping and non-overlapping configurations of the two beads. During the mapping we relate it to the atomistic interaction energy in the inter-bead distance where two beads are not overlapping and up to the cut off distance, r_c. Because the ab initio energy of an overlapping configuration is either impossible to converge or extremely high (i.e., far beyond the soft particle treatment) the excess energy in the overlapping region is covered by extrapolating the energy of the non-overlapping configurations.

4. A case study

Hydrated Nafion with absorbed vanadium cations (V^{2+} and V^{3+}) is selected to be studied as it is the most widely used perfluorosulfonic acid ionomer in vanadium redox flow battery (VRFB) systems. The membrane of a VRFB is designed to only permeate hydronium, however vanadium cations cross over due to imperfect permeability of Nafion [32]. Therefore, investigation of the morphology, phase separation and diffusion of vanadium cations is critical to the improved design of these systems. Although DPD simulations had been previously performed on hydrated Nafion systems [12,14,19,33–35], but they lack the effect of the vanadium cations. The presence of charged vanadium species in the system requires special treatment of conservative interactions so the above parameterization method is selected to define the DPD interactions.

Table 1
Selected bead types, their structures, and volumes.

Bead Type	Structure[a]	Volume[b] (Å^3)
A	[F](CF$_2$)$_6$[F]	291.8
B	[CF$_3$]OCF$_2$CF(CF$_3$)OCF$_2$[F]	279.7
C	[F]CF$_2$SO$_3^-$ + H$_3$O$^+$ + (H$_2$O)$_2$	224.0
C^{-1}	[F]CF$_2$SO$_3^-$ + (H$_2$O)$_3$	225.1
W	(H$_2$O)$_8$	241.1
H$^+$	(H$_2$O)$_8$ + H$_3$O$^-$	229.2
V^{2+}	V^{2+} + (H$_2$O)$_6$[c]	212.8
V^{3+}	V^{3+} + (H$_2$O)$_6$[c]	203.0

[a] The atoms in brackets are added to stabilize the structures and facilitate DFT calculations. Only fluorine and carbon atoms are added to prevent changes in the chemical nature of the selected beads.
[b] Volumes are calculated by creating Connolly surfaces via Atom Volumes and Surfaces tool in Materials Studio [50].
[c] Structure taken from Sepehr and Paddison [40].

4.1. Coarse-graining of particles

The choice of the particles is based on the requirement for similar volumes and distinct chemical nature of different beads. Selected bead types, their structures, and volumes are listed in Table 1. The structure of all bead types were optimized using density functional theory (DFT) at the B3LYP/6-311G** level [36–38] using the GAUSSIAN 09 suite of programs [39] and reported in the Supplementary data. Our previous studies indicate that the V^{2+} and V^{3+} cations have a tight first hydration shell and they tend to retain it even in acidic environment [40,41]. Therefore, distinct bead types were defined for the V^{2+} and V^{3+} cations including their first hydration shells. The rest of the beads were selected to have their volume as close to them as possible. Eight water molecules were lumped together to form a W bead. The backbone of Nafion ionomer was represented by A type bead and contained six CF_2 units. The side chain was represented by two different bead types: B type bead representing the perfluoroether link, and C type bead representing the protogenic group. The C bead, sulfonic acid group with three water molecules, was selected similar to the previous work on hydrated PFSA membranes [14]. A negatively charged particle, C^{-1} bead, was introduced containing a sulfonate anion and three water molecules. Hydronium ion bead, H^+, was defined by lumping a hydronium ion (H_3O^+) and seven water molecules. The number of positively and negatively charged beads may interchange in order to maintain the electroneutrality in a simulation system.

4.2. Conservative interaction parameters

In order to apply the parameterization method introduced in Section 3 the interaction energies were calculated using DFT at B3LYP/3-21G* level [36,37,42–44] and the excess energies were obtained for all pairs of beads. The counterpoise method of Boys and Bernardi [45] was employed to compute the effect of basis set superposition error on the computed energies of a pair of beads. The calculated error was determined to be less than 3% of the computed excess energy and therefore negligible. Over 16 000

Reprinted with permission from Chemical Physics Letters 2016, 645, 20-26.
Copyright 2016 Elsevier B.V.

Table 2
DFT-derived conservative interaction parameters.

	$\left(a_{ij},\ a_{ij}^{int^*}\ b_{ij}^{int**}\right)$	A	B	C	C^{-1}	W	H^+	V^{2+}	V^{3+}
A	**34.6** (12.0, −2.4)								
B	**32.0** (8.7, −1.7)	**28.4** (4.2, −0.8)							
C	**38.5** (16.1, −2.6)	**31.7** (8.3, −1.6)	**29.9** (6.3, −1.4)						
C^{-1}	**39.7** (17.6, −2.9)	**33.7** (10.8, −2.1)	**32.9** (10.2, −2.3)	**43.7** (14.2, 4.5)					
W	**37.9** (16.1, −3.2)	**28.4** (4.3, −0.9)	**25.9** (1.3, −0.4)	**27.6** (1.7, 0.9)	**24.9** (0.0, −0.1)				
H^+	**37.0** (15.1, −3.1)	**27.5** (3.2, −0.7)	**25.7** (1.1, −0.4)	**19.1** (0.4, −6.3)	**25.4** (0.7, −0.3)	**33.1** (1.3, 6.8)			
V^{2+}	**34.9** (13.7, −3.8)	**25.3** (-0.9, −0.6)	**24.4** (−0.2, −0.4)	**7.3** (−2.3, −15.4)	**24.3** (−0.4, −0.3)	[a]	**56.6** (3.5, 28.1)		
V^{3+}	**27.4** (6.8, −4.4)	**23.8** (1.4, −2.6)	**19.6** (0.4, −6.0)	**−13.1** (−1.0, −37.1)	**18.0** (0.2, −7.2)	–[a]	–[a]	**96.3** (8.0,63.3)	

[a] The interaction is not calculated as the simulated systems does not include the pair.

different configurations were considered for each pairs. The calculated energies were fitted using the least squares method to Eq. (8) to obtain a_{ij}^{int} and b_{ij}^{int}. The energies were equally weighted during the least squares procedure, however values above an energy threshold were excluded as they correspond to the overlapping configurations. The water was selected as the reference material and a^R was set to 25 based on the experimental compressibility [4]. The a_{WW}^{int} was scaled to a negligible value. The scaling factor was chosen to be r_c^{-3} and the rest of a_{ij}^{int} and b_{ij}^{int} values were scaled accordingly. The scaled values of fitted parameters are reported in Table 2 with the final a_{ij} values calculated based on Eq. (9).

Table 2 shows the like bead interaction between the W beads a_{WW} = 24.9 which is very close to the desired value of 25.0. The interaction parameters between A, B, and C beads are in qualitative agreement with those of Wu et al. [14] which were related to the Flory–Huggins χ-parameter (they calculated χ using the Blends module in Materials Studio which approximates it from the mixing energy calculated using a Monte Carlo approach). The self-repulsion is calculated as 33.1, 56.6, and 96.3 for H^+, V^{2+}, and V^{3+} beads, respectively. This indicates that the like bead repulsion increases as the charge of the bead is increased. Note that the b_{ij}^{int**} is almost negligible for neutral beads and has a large value for the charged ones, confirming that it represents the electrostatics. Overall, the derived interaction parameters are physically meaningful and compare well with previous literature values.

It is worth noting that by increasing the number of molecules lumped into one bead the repulsion parameter is generally increased [4,5]. However, we used a^R = 25 (derived for one water molecule lumped into one bead) for our system of interest to prevent the solidification artifact observed in large degrees of coarse-graining [46]. This also increases the simulation speed as the required time step for softer beads is greater. The use of softer beads is a common practice [11,14,19] and it is in fact the relative amount of the interactions that matters to the behavior of the system [25,26]. Therefore, the use of a smaller a^R is acceptable and it does not affect the rest of the mapping and relative interactions.

4.3. Bonded interaction parameters

The rigidity of the ionomer chain influences the distribution of the distance between the side chain groups and consequently affects the phase separation and morphology of the hydrated ionomer. For the Nafion chain two bonded potentials were defined. A harmonic spring potential between neighboring connected beads and an angular potential between three consecutive beads, $f_i^{Bonded} = f_i^S + f_i^A$. The spring force experienced by bead i is: $f_i^S = -\partial U^S/\partial r_i$, where U^S is the total spring potential.

$$U^S = \sum_{all\ bonds} \frac{1}{2} K_b (r_b - r_b^0)^2 \tag{10}$$

with K_b, r_b, and r_b^0 being the spring modulus, bond length, and equilibrium bond length, respectively. Similarly, the angle force is obtained from the total angular potential defined as:

$$U^A = \sum_{all\ angles} K_a (1 - \cos(\theta_a - \theta_a^0)) \tag{11}$$

where θ is the angle between three neighboring beads.

In order to find the bonded interaction parameters, K_b, K_a, r_b^0, and θ_a^0, the structure of Nafion chain in a DPD simulation was matched to that of a corresponding MD simulation for a model system, similar to previous studies [19,47]. Because the MD calculations are limited in the time and length-scales, a smaller system is chosen as the prototype. MD simulations were undertaken for a three dimensional periodic system of hydrated Nafion in NVT ensemble. The number of water molecules in the system corresponded to the hydration level ($\lambda = (H_2O)/(-SO_3^-)$) of 18 and the Nafion chains contained 15 repeating units. More details on the MD simulations may be found in a recent work by Cui and Paddison [48]. The DPD bonded parameters were tuned until the structure of the coarse-grained molecules were close to those of the MD system. Table 3 summarizes the bonded parameters obtained via fitting to MD results. Figure 2 shows the structural improvements for using the fitted parameters over the default bonded potential used in previous simulations [4,10,11,14,49]. The stiffness parameters are deliberately set to values that qualitatively match the bond distance and angles. If we decide to exactly replicate the MD structures the K_b and K_a values become too large which consequently requires much shorter

Table 3
Bonded interaction parameters obtained by fitting to the structures from MD simulation results.

Bond	K_b	r_b^0	Angle	K_a	θ_a^0
A–A	100	0.65	A–A–A	5	135
A–B	100	0.55	A–A–B	10	100
B–C	100	0.5	A–B–C	10	135
B–C [1]	100	0.5	A–B–C [1]	10	135

Reprinted with permission from Chemical Physics Letters 2016, 645, 20-26.
Copyright 2016 Elsevier B.V.

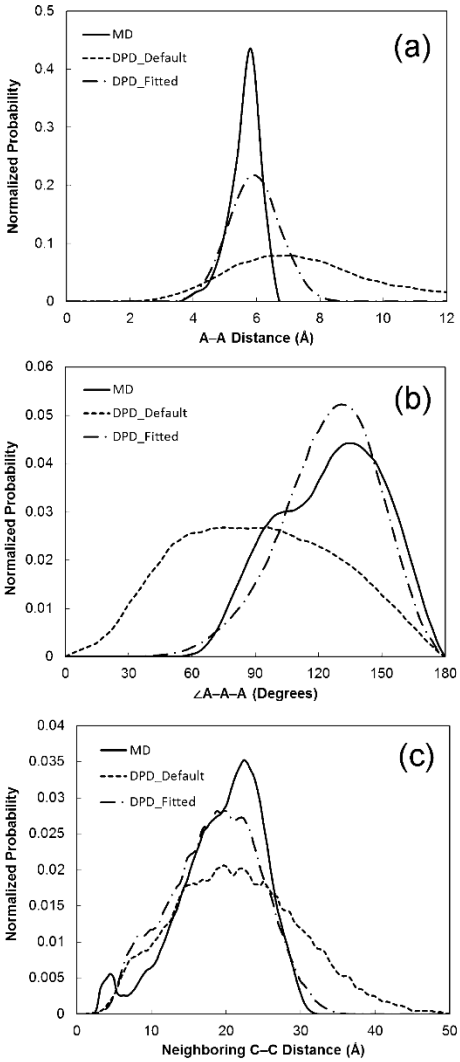


Figure 2. Distribution of: (a) bond distance between connected A beads; (b) angle between three consecutive A beads; (c) distance between two neighboring C beads in each Nafion chain. In order to compare atomistic chain structures from MD simulations to those of DPD, each Nafion chain was dissected into fragments equivalent to the selected beads and the center of mass of each fragment was considered as the position of the representing bead. The solid lines are the MD simulation results. The dashed lines are the corresponding DPD system with conservative interaction parameters from Table 2 and the default set of bonded interactions $\left(f_i^{Bonded} = 4.0r_b\right)$. The dash-dots are the corresponding DPD system with both bonded and non-bonded interactions from Tables 2 and 3.

time steps and decreases simulation efficiency [19,47]. Hence, a reasonable bond and angle distribution is deemed to be suitable.

4.4. DPD simulations

Simulations were performed on the systems of hydrated Nafion or hydrated Nafion with diffused V^{n+} cation ($n = 2 or 3$) at three

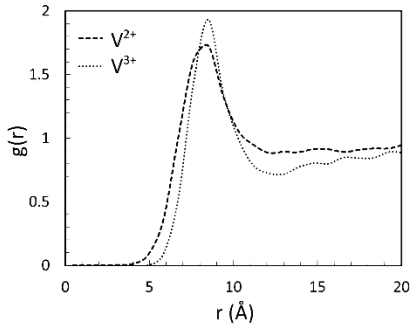


Figure 3. Radial distribution functions of vanadium beads at $\lambda = 6$. The dashed line is for the system of hydrated Nafion with absorbed V^{2+} species and the dotted line is for the system of hydrated Nafion with absorbed V^{3+} species.

hydration levels ($\lambda = 6$, 12, and 18). Nafion chains were selected to have the equivalent weight (EW) of 1115 and consist of 112 repeating units corresponding to the molecular weight of 124 928 g/mol. In order to keep the electro-neutrality of the system upon addition of the vanadium cations, hydronium ions have been removed and C beads were replaced by C^{-1}. The mass-, length-, and energy-scales were set according to the method of Groot and Warren [4]. Considering the mass and volume of the reference bead (W) and the common value of 3 for the density, the length- and time-scales are determined to be $r_c \cong 8.96$ Å and $r_c\sqrt{m/k_BT} \cong 6.83$ ps, respectively (see [14] for more details). A three dimensional unit cell of side length 40 (35.8 nm) was chosen containing around 192 000 DPD beads. The time step was set to 0.02 (136.6 fs) and the systems were equilibrated for at least 30 000 steps (4.08 ns).

Figure 3 shows the radial distribution functions (RDFs) for hydrated Nafion systems containing either V^{2+} or V^{3+}. The V^{3+} RDF shows a stronger peak compared to V^{2+} and the onset of the curve is shifted to the right. This suggests that the V^{3+} species has stronger self-repulsion. This is consistent with and is in fact a consequence of the greater repulsion parameter a_{ii} of V^{3+} than V^{2+}. However, the effect becomes weaker as the hydration level increases (see supplementary data for other hydration levels).

The RDFs of water beads are shown in Figure 4. The first peak of the system containing V^{3+} is slightly stronger than V^{2+} and both are stronger than pure hydrated Nafion. The presence of vanadium cations also shifts the peak to the left. Hence, water clusters are more compact and structured in the systems containing V^{2+} and V^{3+}. This effect is evident at the lowest hydration level but is hardly noticeable at the highest. Similar behavior was recently observed in MD simulations [48]. The pair correlation functions were stronger and shifted to the left for water molecules with addition of vanadium cations to the system. They also reported decreasing peak height with increasing water content. However, the peaks are much stronger in MD than in DPD. This is due to the coarse graining effect and the use of large DPD beads which screens some of the effects. However, the observed behavior in the DPD simulation results is still outstanding.

The sulfonate RDFs are shown in Figure 5 at $\lambda = 12$. The RDF peaks are clearly stronger and shifted to the right as a result of vanadium cations. It indicates that the sulfonate groups are brought closer together in presence of the cationic vanadium species. The effects are more significant for V^{3+} and are lessened at higher hydration levels (see Supplementary data). Similar behavior was also reported in the MD simulations [48].

Reprinted with permission from Chemical Physics Letters 2016, 645, 20-26.
Copyright 2016 Elsevier B.V.

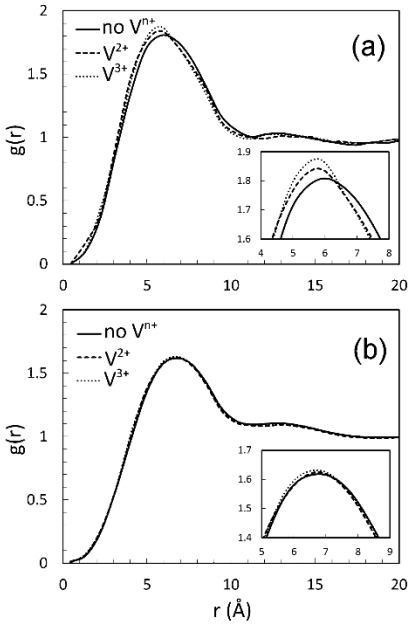


Figure 4. Radial distribution functions of water beads at two different hydration levels: (a) $\lambda = 6$; and (b) $\lambda = 18$. The insets are magnification of the first peak in each graph. The solid line is for the system of hydrated Nafion, the dashed line has absorbed V^{2+}, and the dotted line has absorbed V^{3+}.

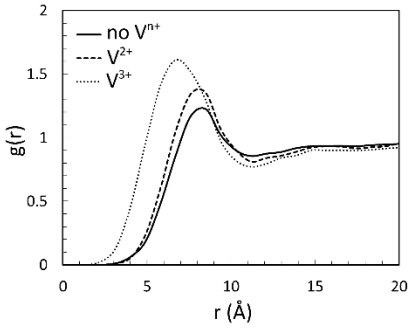


Figure 5. Radial distribution functions of sulfonate beads at $\lambda = 12$. The solid line is for the system of hydrated Nafion, the dashed line has absorbed V^{2+}, and the dotted line has absorbed V^{3+}.

5. Conclusions

We have presented a new method for the parameterization of DPD conservative interactions. The conservative potential was assumed to be composed of two terms: reference and excess potentials. The reference potential was obtained from the experimental compressibility of a selected reference material. The excess term was related to the ab initio calculated interaction energy between two beads. Several different spatial configurations were considered to correctly sample the interaction energy. The ab initio energies were fitted onto a quadratic function of inter-particle distance. A mapping procedure was implemented to scale the fitted parameters and obtain the conservative force parameters. The electrostatic interactions were considered implicitly through the conservative force parameters (the b_{ij}^{int**} term). The absence of a separate electrostatic potential term significantly improves the computational efficiency over previous treatments of the electrostatics.

The method was applied to systems consisting of hydrated Nafion ionomer and diffused vanadium cations. The conservative interaction parameters were derived using the method described above and the bonded potentials were parameterized by comparing to a prototype classical MD simulated system. The simulations were performed using the derived parameters and the results were in agreement with recent MD simulations, confirming the credibility of the parameterization method.

Acknowledgements

This work was supported by the National Science Foundation under the TNSCORE program with NSF EPS_1004083. Authors would like to thank Dr. Shengting Cui (of our department) for providing the classical MD conformations.

Appendix A. Supplementary data

Supplementary data associated with this article can be found, in the online version, at doi:10.1016/j.cplett.2015.12.032.

References

[1] P.J. Hoogerbrugge, J. Koelman, Europhys. Lett. 19 (1992) 155.
[2] P. Español, P.B. Warren, Europhys. Lett. 30 (1995) 191.
[3] P. Español, Europhys. Lett. 40 (1997) 631.
[4] R.D. Groot, P.B. Warren, J. Chem. Phys. 107 (1997) 4423.
[5] R.D. Groot, K.L. Rabone, Biophys. J. 81 (2001) 725.
[6] R.D. Groot, T.J. Madden, J. Chem. Phys. 108 (1998) 8713.
[7] X.R. Cao, G.Y. Xu, Y.M. Li, Z.Q. Zhang, J. Phys. Chem. A 109 (2005) 10418.
[8] Y. Li, P. Zhang, F.L. Dong, X.L. Cao, X.W. Song, X.H. Cui, J. Colloid Interface Sci. 290 (2005) 275.
[9] J.C. Shillcock, R. Lipowsky, J. Phys.: Condens. Matter 18 (2006) S1191.
[10] C. Wang, S.J. Paddison, Soft Matter 10 (2014) 819.
[11] D.S. Wu, S.J. Paddison, J.A. Elliott, S.J. Hamrock, Langmuir 26 (2010) 14308.
[12] S. Yamamoto, S.A. Hyodo, Polym. J. (Tokyo, Jpn.) 35 (2003) 519.
[13] A. Maiti, J. Wescott, P. Kung, Mol. Simul. 31 (2005) 143.
[14] D.S. Wu, S.J. Paddison, J.A. Elliott, Energy Environ. Sci. 1 (2008) 284.
[15] J.C. Shillcock, R. Lipowsky, J. Chem. Phys. 117 (2002) 5048.
[16] S. Yamamoto, Y. Maruyama, S. Hyodo, J. Chem. Phys. 117 (2002) 2990.
[17] A. Alexeev, W.E. Uspal, A.C. Balazs, ACS Nano 2 (2008) 1117.
[18] D. Reith, H. Meyer, F. Muller-Plathe, Macromolecules 34 (2001) 2335.
[19] A. Vishnyakov, A.V. Neimark, J. Phys. Chem. B 118 (2014) 11353.
[20] W. Tschop, K. Kremer, J. Batoulis, T. Burger, O. Hahn, Acta Polym. 49 (1998) 61.
[21] R.D. Groot, J. Chem. Phys. 118 (2003) 11265.
[22] E. Moeendarbary, T.Y. Ng, M. Zangeneh, Int. J. Appl. Mech. 1 (2009) 737.
[23] M.T. Lee, A. Vishnyakov, A.V. Neimark, J. Phys. Chem. B 117 (2013) 10304.
[24] A. Vishnyakov, D.S. Talaga, A.V. Neimark, J. Phys. Chem. Lett. 3 (2012) 3081.
[25] C.M. Wijmans, B. Smit, R.D. Groot, J. Chem. Phys. 114 (2001) 7644.
[26] M. Kranenburg, J.P. Nicolas, B. Smit, Phys. Chem. Chem. Phys. 6 (2004) 4142.
[27] G. Kacar, E.A.J.F. Peters, G. de With, EPL 102 (2013) 40009.
[28] K.P. Travis, M. Bankhead, K. Good, S.L. Owens, J. Chem. Phys. 127 (2007) 014109.
[29] H.H. Loeffler, J.I. Yague, B.M. Rode, Chem. Phys. Lett. 363 (2002) 367.
[30] Y. Inada, A.M. Mohammed, H.H. Loeffler, B.M. Rode, J. Phys. Chem. A 106 (2002) 6783.
[31] C. Kritayakornupong, J.I. Yague, B.M. Rode, J. Phys. Chem. A 106 (2002) 10584.
[32] E. Wiedemann, A. Heintz, R.N. Lichtenthaler, J. Membr. Sci. 141 (1998) 215.
[33] G. Dorenbos, K. Morohoshi, J. Mater. Chem. 21 (2011) 13503.
[34] R. Jorn, G.A. Voth, J. Phys. Chem. C 116 (2012) 10476.
[35] J.T. Wescott, Y. Qi, L. Subramanian, T.W. Capehart, J. Chem. Phys. 124 (2006).
[36] C.T. Lee, W.T. Yang, R.G. Parr, Phys. Rev. B: Condens. Matter Mater. Phys. 37 (1988) 785.
[37] A.D. Becke, J. Chem. Phys. 98 (1993) 5648.
[38] A.D. McLean, G.S. Chandler, J. Chem. Phys. 72 (1980) 5639.
[39] M.J. Frisch, G.W. Trucks, H.B. Schlegel, G.E. Scuseria, M.A. Robb, J.R. Cheeseman, G. Scalmani, V. Barone, B. Mennucci, G.A. Petersson, H. Nakatsuji, M. Caricato, X. Li, H.P. Hratchian, A.F. Izmaylov, J. Bloino, G. Zheng, J.L. Sonnenberg, M. Hada, M. Ehara, K. Toyota, R. Fukuda, J. Hasegawa, M. Ishida, T. Nakajima, Y. Honda, O. Kitao, H. Nakai, T. Vreven, J.A. Montgomery, J.E. Peralta, F. Ogliaro, M. Bearpark, J.J. Heyd, E. Brothers, K.N. Kudin, V.N. Staroverov, R. Kobayashi, J. Normand, K. Raghavachari, A. Rendell, J.C. Burant, S.S. Iyengar, J. Tomasi, M. Cossi, N. Rega, J.M. Millam, M. Klene, J.E. Knox, J.B. Cross, V. Bakken, C. Adamo, J. Jaramillo, R. Gomperts, R.E. Stratmann, O. Yazyev, A.J. Austin, R. Cammi, C. Pomelli, J.W.

Reprinted with permission from Chemical Physics Letters 2016, 645, 20-26.
Copyright 2016 Elsevier B.V.

Ochterski, R.L. Martin, K. Morokuma, V.G. Zakrzewski, G.A. Voth, P. Salvador, J.J. Dannenberg, S. Dapprich, A.D. Daniels, Farkas, J.B. Foresman, J.V. Ortiz, J. Cioslowski, D.J. Fox, Gaussian 09, Revision A.01, Gaussian Inc., Wallingford, CT, 2009.
[40] F. Sepehr, S.J. Paddison, Chem. Phys. Lett. 585 (2013) 53.
[41] F. Sepehr, S.J. Paddison, J. Phys. Chem. A 119 (2015) 5749.
[42] K.D. Dobbs, W.J. Hehre, J. Comput. Chem. 8 (1987) 861.
[43] M.S. Gordon, J.S. Binkley, J.A. Pople, W.J. Pietro, W.J. Hehre, J. Am. Chem. Soc. 104 (1982) 2797.
[44] J.S. Binkley, J.A. Pople, W.J. Hehre, J. Am. Chem. Soc. 102 (1980) 939.
[45] S.F. Boys, F. Bernardi, Mol. Phys. 19 (1970) 553.
[46] I.V. Pivkin, G.E. Karniadakis, J. Chem. Phys. 124 (2006).
[47] V. Ortiz, S.O. Nielsen, D.E. Discher, M.L. Klein, R. Lipowsky, J. Shillcock, J. Phys. Chem. B 109 (2005) 17708.
[48] S. Cui, S.J. Paddison, J. Phys. Chem. C 119 (2015) 12848.
[49] D.S. Wu, S.J. Paddison, J.A. Elliott, Macromolecules 42 (2009) 3358.
[50] Materials Studio, Accelrys Inc., San Diego, CA, USA, 2005.

Reprinted with permission from Chemical Physics Letters 2016, 645, 20-26.
Copyright 2016 Elsevier B.V.

Dissipative Particle Dynamics Interaction Parameters from *Ab Initio* Calculations

Fatemeh Sepehr and Stephen J. Paddison*

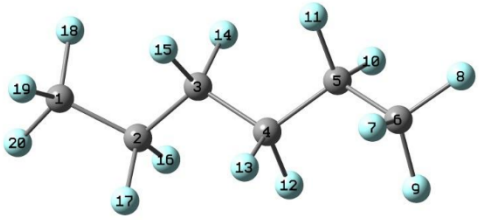
Department of Chemical & Biomolecular Engineering, University of Tennessee, Knoxville, TN 37996, U.S.A.

* Corresponding author.
E-mail address: spaddison@utk.edu (S. J. Paddison).

Reprinted with permission from Chemical Physics Letters 2016, 645, 20-26.
Copyright 2016 Elsevier B.V.

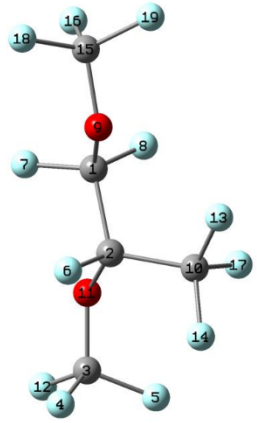
The structures of different bead types used to simulate the hydrated Nafion system with diffused vanadium cations and sulfuric acid. The atomic structures were optimized using density functional theory (DFT) at the B3LYP/6-311G** level using the Gaussian 09 suite of programs. The structures of V^{2+} and V^{3+} beads are taken from "F. Sepehr and S. J. Paddison, *Chem. Phys. Lett.* 585 (2013) 53" and are not shown here again.

Bead A



Label	Atom	x	y	z
1	C	0	0	0
2	C	0	0	1.55304
3	C	1.418454	0	2.19187
4	C	1.420007	0.372114	3.706107
5	C	2.731281	-0.02518	4.442878
6	C	2.913324	0.650737	5.829235
7	F	3.177542	1.953472	5.687298
8	F	3.937522	0.06873	6.46366
9	F	1.804807	0.50398	6.567973
10	F	2.729716	-1.36244	4.633257
11	F	3.793361	0.317829	3.675671
12	F	0.388175	-0.25654	4.315925
13	F	1.249618	1.710698	3.812977
14	F	1.947962	-1.23638	2.040851
15	F	2.191053	0.896695	1.5351
16	F	-0.65777	-1.10553	1.964917
17	F	-0.67223	1.101472	1.964226
18	F	0.806955	-0.96354	-0.46526
19	F	0.409378	1.181892	-0.47181
20	F	-1.24496	-0.23014	-0.43291

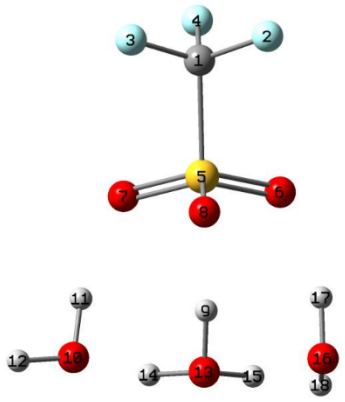
Bead B



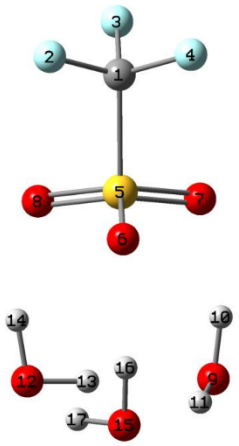
Label	Atom	x	y	z
1	C	0	0	0
2	C	0	0	1.570501
3	C	1.85809	0	3.173355
4	F	1.26402	-0.92981	3.920183
5	F	1.748616	1.176233	3.798153
6	F	-0.56662	-1.16251	1.98774
7	F	0.925539	-0.86614	-0.4403
8	F	0.34136	1.225352	-0.44623
9	O	-1.26532	-0.3627	-0.40548
10	C	-0.83089	1.171615	2.197929
11	O	1.353827	0.055838	1.889805
12	F	3.144917	-0.29421	3.048187
13	F	-2.04337	1.250126	1.642435
14	F	-0.98671	0.950953	3.508608
15	C	-1.6233	-0.48125	-1.75608
16	F	-0.61307	-0.12291	-2.57677
17	F	-0.20469	2.336741	2.0258
18	F	-1.87112	-1.7901	-1.97514
19	F	-2.60161	0.421324	-1.98137

Reprinted with permission from Chemical Physics Letters 2016, 645, 20-26.
Copyright 2016 Elsevier B.V.

Bead C



Bead C^{-1}

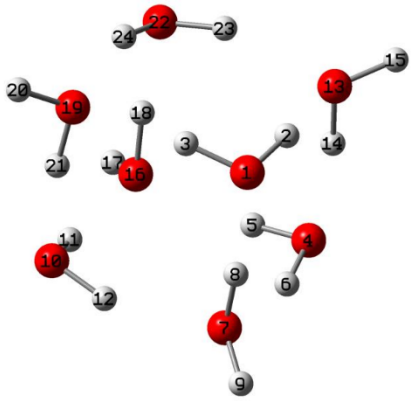


Label	Atom	x	y	z
1	C	0	0	0
2	F	0	0	1.331341
3	F	1.258299	0	-0.43898
4	F	-0.61746	-1.09561	-0.43962
5	S	-0.8907	1.519062	-0.63463
6	O	-2.25787	1.430972	-0.08217
7	O	-0.80546	1.431401	-2.1092
8	O	-0.09539	2.652593	-0.06845
9	H	-0.61507	4.08495	-0.45743
10	O	-0.93283	3.888569	-3.27121
11	H	-0.88328	2.929028	-3.05126
12	H	-0.15741	4.087437	-3.80554
13	O	-1.1637	4.815754	-0.91299
14	H	-1.06728	4.583158	-1.91061
15	H	-2.12936	4.593369	-0.63647
16	O	-3.42512	3.909563	-0.1655
17	H	-3.18353	2.970826	0.003965
18	H	-4.187	3.888797	-0.75333

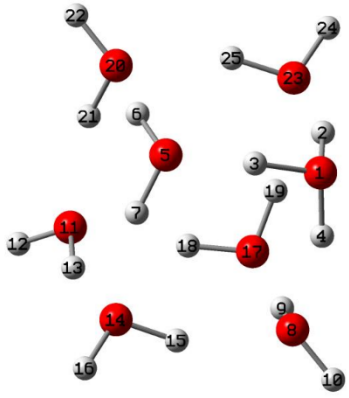
Label	Atom	x	y	z
1	C	0	0	0
2	F	0	0	1.34383
3	F	1.279845	0	-0.4098
4	F	-0.56175	-1.14995	-0.40998
5	S	-0.9262	1.483008	-0.67525
6	O	-2.28716	1.308309	-0.12743
7	O	-0.81671	1.311918	-2.13864
8	O	-0.17477	2.629519	-0.12388
9	O	-2.21692	3.542543	-3.38761
10	H	-1.69488	2.747637	-3.18709
11	H	-2.98773	3.450321	-2.79565
12	O	-1.46738	5.060332	-1.08047
13	H	-1.52661	4.724547	-1.99528
14	H	-0.90724	4.397253	-0.64323
15	O	-3.89595	3.548908	-1.07099
16	H	-3.55736	2.72989	-0.67207
17	H	-3.2044	4.200617	-0.84728

Reprinted with permission from Chemical Physics Letters 2016, 645, 20-26.
Copyright 2016 Elsevier B.V.

Bead W



Bead H^+



Label	Atom	x	y	z
1	O	0	0	0
2	H	0	0	0.975999
3	H	0.945866	0	-0.24038
4	O	-0.40906	-3.13343	2.164185
5	H	0.465605	-3.56465	2.126172
6	H	-0.68507	-3.06746	1.230393
7	O	-0.70066	-2.49711	-0.54969
8	H	-0.52933	-1.52225	-0.4138
9	H	-1.45742	-2.57253	-1.13775
10	O	2.001292	-3.13468	-0.93293
11	H	2.180625	-3.56763	-0.07697
12	H	1.028226	-3.06909	-0.97003
13	O	0.239645	-0.62359	2.721172
14	H	-0.07672	-1.56455	2.608652
15	H	-0.20877	-0.26463	3.492059
16	O	2.288525	-3.78773	1.778302
17	H	2.850517	-4.43052	2.220104
18	H	2.620395	-2.88127	2.03542
19	O	2.697084	-0.62429	-0.43875
20	H	3.336036	-0.26507	-1.06074
21	H	2.510508	-1.56494	-0.71888
22	O	2.933581	-1.26489	2.28004
23	H	2.087084	-0.89842	2.598514
24	H	3.03092	-0.89863	1.38071

Label	Atom	x	y	z
1	O	-0.30346	-1.92125	-1.107
2	H	-1.06379	-1.79269	-0.46937
3	H	-0.24487	-1.01042	-1.68887
4	H	0.53821	-1.95895	-0.55957
5	O	-0.15376	0.260942	-2.23947
6	H	-0.84318	0.818504	-1.82592
7	H	0.700745	0.651878	-1.96875
8	O	1.789009	-1.50922	0.418418
9	H	1.291394	-1.18832	1.232811
10	H	2.446653	-2.15717	0.697056
11	O	0.319884	2.113263	1.078376
12	H	0.527948	2.940891	1.52651
13	H	1.066605	1.909949	0.475502
14	O	2.085988	0.987926	-0.73594
15	H	2.25237	0.100194	-0.35185
16	H	2.932488	1.330582	-1.04532
17	O	0.233567	-0.49315	2.228693
18	H	0.238446	0.473684	2.12285
19	H	-0.67511	-0.77159	2.034771
20	O	-1.879	1.4469	-0.3935
21	H	-1.2022	1.869385	0.183021
22	H	-2.56561	2.10205	-0.56314
23	O	-2.11206	-1.09156	0.630717
24	H	-2.96303	-1.49393	0.839754
25	H	-2.2785	-0.17493	0.318185

Reprinted with permission from Chemical Physics Letters 2016, 645, 20-26.
Copyright 2016 Elsevier B.V.

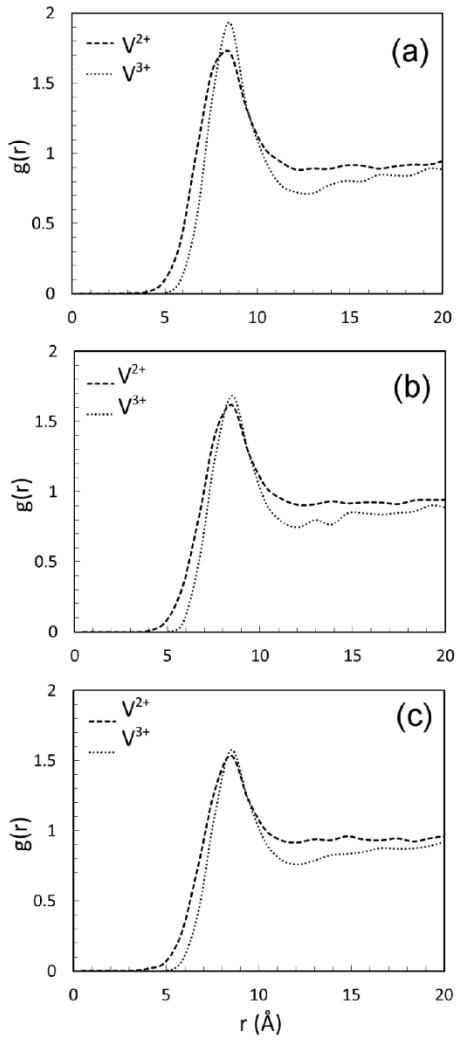


Figure S1. Radial distribution functions of vanadium beads at three hydration levels: (a) $\lambda = 6$; (b) $\lambda = 12$; and (c) $\lambda = 18$. The dashed line is for the system of hydrated Nafion with absorbed V^{2+} species and the dotted line is for the system of hydrated Nafion with absorbed V^{3+} species.

Reprinted with permission from Chemical Physics Letters 2016, 645, 20-26.
Copyright 2016 Elsevier B.V.

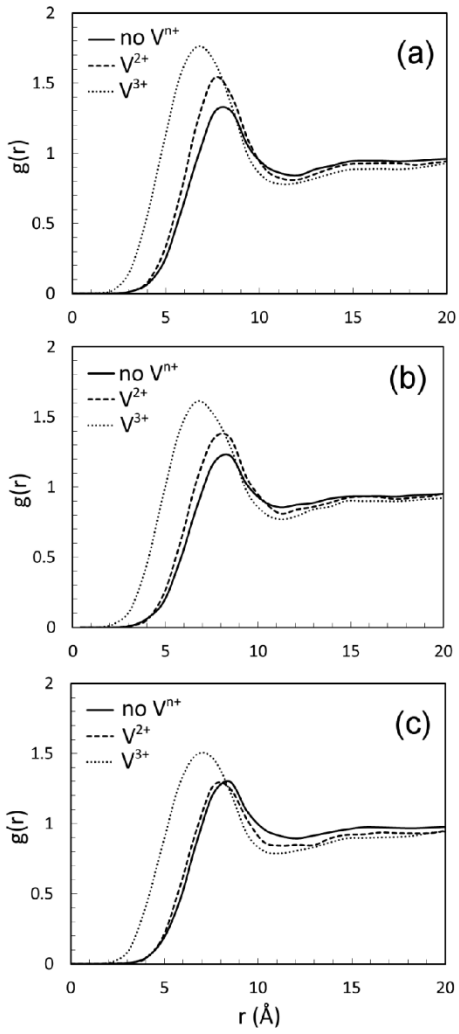
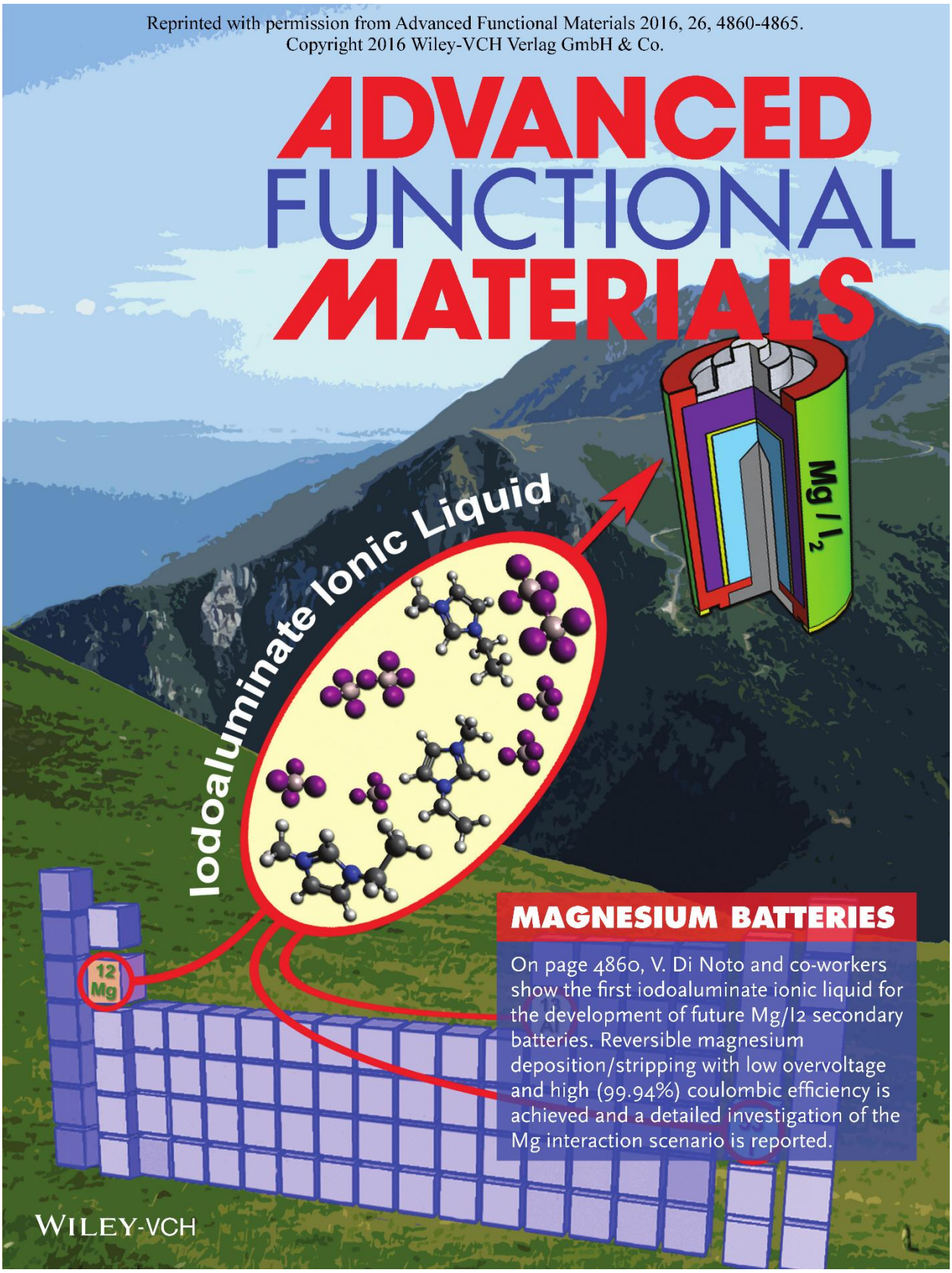


Figure S2. Radial distribution functions of sulfonate beads at three hydration levels: (a) $\lambda = 6$; (b) $\lambda = 12$; and (c) $\lambda = 18$. The solid line is for the system of hydrated Nafion, the dashed line has absorbed V^{2+}, and the dotted line has absorbed V^{3+}.

Reprinted with permission from Advanced Functional Materials 2016, 26, 4860-4865.
Copyright 2016 Wiley-VCH Verlag GmbH & Co.



Reprinted with permission from Advanced Functional Materials 2016, 26, 4860-4865.
Copyright 2016 Wiley-VCH Verlag GmbH & Co.

ADVANCED FUNCTIONAL MATERIALS
www.afm-journal.de
www.MaterialsViews.com

FULL PAPER

Toward a Magnesium-Iodine Battery

*Federico Bertasi, Fatemeh Sepehr, Gioele Pagot, Stephen J. Paddison, and Vito Di Noto**

The quest for new electrolyte and cathode materials is a crucial point for beyond-lithium-ion energy storage systems. Following this, an electrolyte for secondary magnesium batteries based on a new iodoaluminate ionic liquid and δ-MgI_2 is reported. Promising electrochemical performance in terms of Mg plating-stripping, coulombic efficiency, and conductivity, demonstrates the potential of this iodine-based system for future Mg secondary batteries.

1. Introduction

Magnesium batteries are promising electrochemical energy storage devices which can provide a viable alternative to lithium-ion batteries.[1–3] Currently, state-of-the-art electrolytes based on organo–Mg complexes, notwithstanding their excellent electrochemical performance, present serious safety issues associated with flammability and corrosivity.[4] Furthermore, they only operate if coupled with Chevrel-phase cathodic materials,[5] which possess energy densities that are too low (≈130 mAh g^{-1}) to be practical.[6]

Room-temperature ionic liquids (RTILs) are key materials for the development of new energy storage and conversion systems.[7,8] In the past decade several relevant properties such as their negligible vapor pressure, non-flammability, and high room-temperature conductivity were explored in order to obtain safer and better performing devices.[9–11]

Following this, the use of ILs as electrolytes for secondary magnesium batteries[12–14] could give rise to a breakthrough in the field of Mg energy storage systems, in which the development of efficient electrolytes is probably the most critical issue to be addressed.[15,16] Furthermore, the use of ILs could enable the use of high-voltage cathodic materials (such as oxides) with a distinct enhancement of the energy density.[7,17–20]

Nevertheless, especially in the case of IL based electrolytes for Mg batteries, a fundamental understanding of the relation between Mg-ion speciation and the long-range charge transfer mechanism is still an ongoing research activity. Similarly, several crucial points including the solid-electrolyte interphase (SEI) structure, details of formation, and the conductivity mechanism are still unknown.[21]

It was recently shown that in the case of chloroaluminate ILs,[22] reversible Mg/Al codeposition could be achieved with very low (i.e., <0.2 V vs Mg) overvoltages.[23]

Hence, we report for the first time in this paper the synthesis and characterization of a new iodoaluminate ionic liquid[24] for application in secondary magnesium batteries. It is shown that, with respect to our recent work on similar chloroaluminate systems,[23] it is possible to achieve a reversible Mg/Al codeposition with a Mg content on the electrodeposited layer that is four times higher with a higher coulombic efficiency (C.E.) (up to 99.94%). These findings demonstrate that by simply changing the halogen atom in haloaluminate ILs it is possible to modulate several electrochemical features such as: conductivity, C.E., overvoltage for deposition-stripping, and composition of the deposited layer; indeed, this clearly opens new possibilities in the field of IL-based electrolytes for Mg battery applications.

Furthermore, the use of iodide-based electrolytes enables the possibility of iodine-based cathodes, which are very appealing due to their low cost and high specific capacity of I_2.[25] Indeed, in agreement with the equilibrium $I_2 + I^- \Leftrightarrow I_3^-$ and $I_3^- + 2e^- \Leftrightarrow 3I^-$, ($E^0 = 0.536$ vs SHE) an iodine cathode, coupled with a magnesium anode ($Mg \Leftrightarrow Mg^{2+} + 2e^-$, $E^0 = -2.38$ V vs SHE) could lead to a 2.9 V Mg/I_2 secondary battery. Nevertheless, to the best of our knowledge no iodide-based RTIL for secondary Mg batteries have ever been reported in the literature.

2. Results and Discussion

A new iodoaluminate IL ($EMImAlI_4$) was prepared by reacting 1-ethyl-3-methylimidazolium iodide (EMImI) (T_m (melting temperature) = 86 °C) with aluminum iodide (T_m = 189 °C) at a 1:1 molar ratio. This reaction leads to the formation of a new RTIL showing a T_m = −12 °C, a glass transition event (T_g) at −60 °C and a crystallization exothermic peak at −20 °C (see Figure S1, Supporting Information). $EMImAlI_4$ consists of a highly hygroscopic, homogeneous transparent liquid. Indeed, $EMImAlI_4$ when open to air reacts violently with the moisture producing Al_2O_3 and hydrogen iodide. On the other hand, in totally anhydrous conditions $EMImAlI_4$ shows an excellent thermal stability, as confirmed by differential scanning calorimetry (DSC) profiles which show reversible thermal transitions up to 130 °C.

δ-MgI_2 is obtained by direct reaction of *n*-iodobutane with metallic Mg in strictly anhydrous conditions as described elsewhere.[26] Following this, a family of four electrolytes with the general formula: $EMImAlI_4/(\delta\text{-}MgI_2)_x$ and $0 \le x \le 0.023$ was thereby obtained by diluting the saturated

Dr. F. Bertasi, G. Pagot, Prof. V. Di Noto
Department of Industrial Engineering
Section of Chemistry for Technology and Energy
Department of Chemical Sciences
University of Padova
Via Marzolo 1, I-35131 Padova, Italy
E-mail: vito.dinoto@unipd.it
F. Sepehr, Prof. S. J. Paddison
Department of Chemical and Biomolecular Engineering
University of Tennessee
Knoxville, TN 37996, USA

DOI: 10.1002/adfm.201601448

© 2016 WILEY-VCH Verlag GmbH & Co. KGaA, Weinheim

Reprinted with permission from Advanced Functional Materials 2016, 26, 4860-4865.
Copyright 2016 Wiley-VCH Verlag GmbH & Co.

$EMImAlI_4/(\delta\text{-}MgI_2)_{0.023}$ solution. It is observed that the viscosity of $EMImAlI_4/(\delta\text{-}MgI_2)_x$ electrolytes increases on x reaching, at high $\delta\text{-}MgI_2$ concentration, a consistence similar to that of a honey-like solution.

The structure and local interactions of $EMImAlI_4/(\delta\text{-}MgI_2)_x$ electrolytes were determined using density functional theory (DFT) based calculations in conjunction with the vibrational spectroscopy measurements (IR and Raman). Calculations performed at the B3LYP/6-311G** level enabled the identification of the various species in the electrolyte and the assignment of the vibrational spectra. The experimental and calculated vibrational spectra of the EMImI system do not show any characteristic vibrations in the far IR (FIR) region (see Figure S3, Supporting Information). The experimental Raman spectrum of pristine $EMImAlI_4$ shows two strong peaks at 146 and 140 cm^{-1} (see **Figure 1**a), which are characteristic of the AlI_4^- and $Al_2I_7^-$ anions, respectively, in agreement with the computed frequencies (see the Supporting Information) and prior work.[27,28] Hence, $EMIm^+$ cationic species and both AlI_4^- and $Al_2I_7^-$ anions exist in the pristine IL despite the stoichiometric formulation of $EMImAlI_4$.

Figure 1a shows that the ratio of the peak intensity at 140 cm^{-1} to the one at 146 cm^{-1} decreases upon addition of the $\delta\text{-}MgI_2$ salt. These two peaks, according to the DFT calculations, are still assigned to the vibrations of AlI_4^- and $Al_2I_7^-$ anions even in the presence of MgI_2. Hence, the increase in the ratio of the intensities of the two peaks suggests that the concentration of AlI_4^- anions increases and the equilibrium $2AlI_4^- \Leftrightarrow Al_2I_7^- + I^-$ (Figure 1c) shifts to the left with the increase of $\delta\text{-}MgI_2$ concentration. Similar relationship between the peak intensities of chloroaluminate anions and their concentrations has been observed previously.[23] The increase in the AlI_4^- concentration on x is associated to the formation of an anionic complex with bridging iodide atoms as witnessed by the

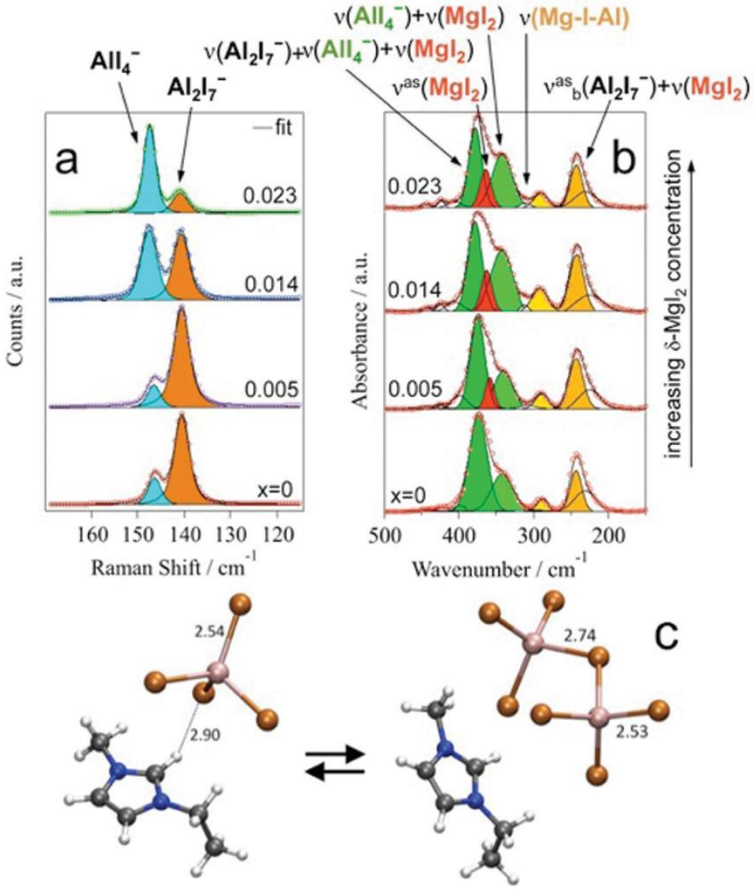


Figure 1. Vibrational spectra of $EMImAlI_4/(\delta\text{-}MgI_2)_x$ with $0 \le x \le 0.023$. a) FT-Raman spectra of $EMImAlI_4/(\delta\text{-}MgI_2)_x$; b) Far infrared spectra of $EMImAlI_4/(\delta\text{-}MgI_2)_x$ with band assignments based on B3LYP/6-311G** calculations; c) Equilibrium between monomeric and dimeric iodoaluminate anions.

© 2016 WILEY-VCH Verlag GmbH & Co. KGaA, Weinheim

Reprinted with permission from Advanced Functional Materials 2016, 26, 4860-4865.
Copyright 2016 Wiley-VCH Verlag GmbH & Co.

ADVANCED FUNCTIONAL MATERIALS
www.afm-journal.de
www.MaterialsViews.com

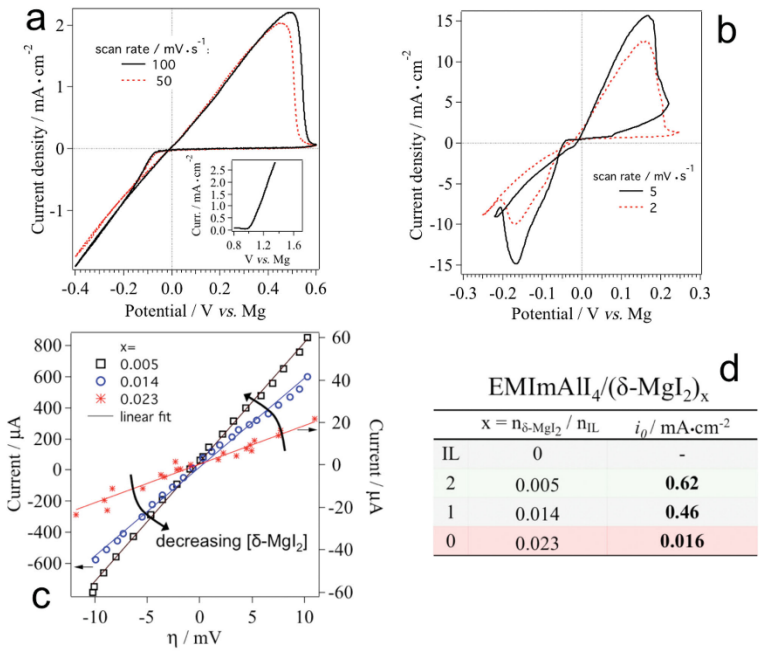


Figure 2. Mg deposition/stripping performance for $EMImAlI_4/(\delta\text{-}MgI_2)_x$ with $x = 0.005$. Measurements obtained using: a) Pt working electrode and b) Mg working electrode; c) Exchange current density measurements of $EMImAlI_4/(\delta\text{-}MgI_2)_x$ with $0 \le x \le 0.023$; d) Exchange current density results (n_{Mg} and n_{IL} are the moles of Mg and $EMImAlI_4$, respectively).

presence of the stretching band ν(Mg—I—Al) at 312 cm^{-1} in the FIR spectra (Figure 1b and Supporting Information). Therefore, at low δ-MgI_2 concentration ($x = 0.005$) $[Al_2I_7MgI_2]^-$ anionic complexes (α) are predominant, while for $x > 0.005$ the concentration of $[AlI_4MgI_2]^-$ anionic complexes (β) increases together with the concentration of Mg—I—Al bridges. The detailed interaction scenario and magnesium speciation as a function of x are reported in Figure S2 (Supporting Information).

The capability of the electrolytes to reversibly deposit Mg was assessed by cyclic voltammetry measurements using a three-electrode configuration. Results are reported in **Figure 2** for $EMImAlI_4/(\delta\text{-}MgI_2)_{0.005}$ which shows the best performance in terms of current densities and overvoltages. Measurements are performed using Pt (Figure 2a) and Mg (Figure 2b) working electrodes (WEs). The electrochemical stability window (ESW) of $EMImAlI_4/(\delta\text{-}MgI_2)_{0.005}$ is measured using linear sweep voltammetry as reported in the inset of Figure 2a.

In the case of Mg deposition on Pt, the electrolytes show a cathodic wave at −0.100 V versus Mg associated with the Mg plating and an anodic peak centered at +0.500 V versus Mg due to the stripping process. Reversible deposition and stripping can also be obtained using a Mg WE as witnessed in Figure 2b. In this case, the cathodic wave onset corresponds to −0.05 V versus Mg while the anodic peak is centered at +0.150 V versus Mg, thus demonstrating the compatibility of the proposed electrolytes with a magnesium anode, which reduces the overvoltage for oxidation and reduction. The peak current densities (I_{max}) in the case of the Mg WE are one order of magnitude higher with respect to the Pt WE thus demonstrating faster kinetics at the electrode. Figure 2b also confirms that the SEI growth on the Mg electrode does not inhibit its reversible redox behavior. It is also observed that on Mg concentration in both deposition and stripping events: (a) I_{max} decreases in the order I_{max} ($x = 0.005$) > I_{max} ($x = 0.014$) > I_{max} ($x = 0.023$) (see Figure S7, Supporting Information); while (b) no significant difference in the peak positions is detected. This behavior confirms that in ILs on δ-MgI_2 concentration the degree of 3D concatenation phenomena rises, reducing the conductivity and increasing the viscosity of the proposed electrolytes. Furthermore, the shape of the CV profiles at both low ($V \approx -0.2$ V vs Mg) and high ($V > 0.2$ V vs Mg) potentials (see Figure S7, Supporting Information) suggests that the δ-MgI_2 concentration plays a crucial role in modulating the electrochemical stability window and the SEI formation mechanism and structure.

The measured exchange current densities are reported in Figure 2d. The values range from 0.016 to 0.620 mA cm^{-2} on x. In agreement with the interaction scenario reported in Figure S2 (Supporting Information) for $x = 0.005$, MgI_2 is mostly coordinated by the $Al_2I_7^-$ dimers which increases the mobility of the Mg based species and accordingly, i_0. At higher δ-MgI_2 concentrations ($x > 0.005$), the concentration of stable

© 2016 WILEY-VCH Verlag GmbH & Co. KGaA, Weinheim

Reprinted with permission from Advanced Functional Materials 2016, 26, 4860-4865.
Copyright 2016 Wiley-VCH Verlag GmbH & Co.

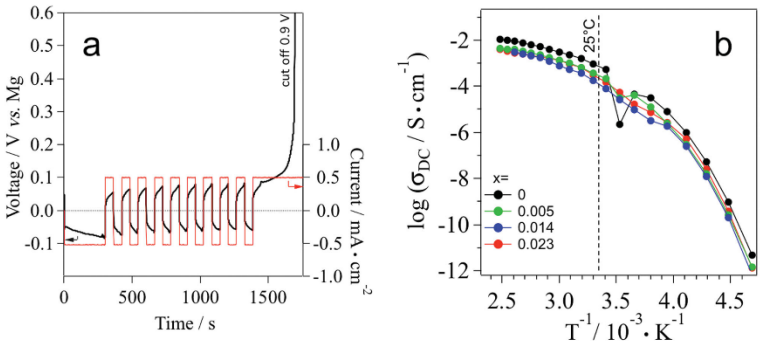


Figure 3. a) Average coulombic efficiency evaluation for $EMImAlI_4/(\delta\text{-}MgI_2)_{0.005}$; b) Arrhenius plot for $EMImAlI_4/(\delta\text{-}MgI_2)_x$ electrolytes.

$[AlI_4MgI_2]^-$-concatenated complexes increases, inhibiting the charge injection processes at the electrode.

The cycling performance as well as the average coulombic efficiency of the proposed electrolytes are evaluated by galvanostatic cycling.[29] Representative results are reported in **Figure 3**a for $EMImAlI_4/(\delta\text{-}MgI_2)_{0.005}$ revealing the best compromise between high conductivity, low viscosity, and Mg concentration. This electrolyte shows an average coulombic efficiency of 99.94%, which was the highest among the proposed materials. An overvoltage for Mg deposition/stripping of ±50 mV versus Mg is measured when a current density of 500 μA cm^{-2} is used. A negligible shift in the overvoltage was also observed for at least ten cycles, demonstrating excellent reversible behavior.

In order to fully characterize the electrodeposited layer obtained from the $EMImAlI_4/(\delta\text{-}MgI_2)_{0.005}$ electrolyte, ICP-AES measurements were performed after a potentiostatic deposition at −0.3 V versus Mg on a large (10 mm^2) Pt foil electrode. After 40 min, 1.18 mg are deposited and the ICP-AES measurements revealed a $\phi = n_{Al}/n_{Mg}$ molar ratio of 8. In principle, due to the higher standard potential of the Al^{3+}/Al couple with respect to Mg^{2+}/Mg, the Al deposition should not take place with the present electrolytes. On the contrary, Al reduction and co-deposition with Mg are probably induced by the presence of $\delta\text{-}MgI_2$ salt.[23,30]

In comparison with our recent prior work[23] with a chloroaluminate-based IL where a ϕ = 29.7 and C.E. of 98.5% were obtained, the use of this new iodoaluminate electrolyte resulted in an increase in the Mg concentration on the electrodeposited layer by a factor of 4 (ϕ = 8). This evidence clearly opens new perspectives in the field of haloaluminate ionic liquids for secondary Mg batteries. Indeed, by changing the nature of the halogen atoms in haloaluminate systems several electrochemical properties such as coulombic efficiency, conductivity, and Mg content on the deposited layer can easily be controlled and optimized.

Broadband electrical spectroscopy (BES) measurements (Figure 3b) demonstrate a RT conductivity higher than 10^{-4} S cm^{-1} for all the materials with activation energies comprised between 6 and 17 kJ mol^{-1}. The highest RT conductivity value (3.0×10^{-4} S cm^{-1}) is obtained for $EMImAlI_4/(\delta\text{-}MgI_2)_{0.005}$ due to both its low viscosity and high concentration of $Al_2I_7^-$ anions. This can be easily understood by considering the large steric hindrance and charge delocalization of $Al_2I_7^-$ with respect to the AlI_4^- anions. Figure 3b also shows a drop in the conductivity at about 283 K. This phenomenon, which is typically observed in imidazolium[23] and pyrrolidinium[31] ILs, is associated to the structural features of the pristine $EMImAlI_4$ material. In details this event is ascribed to an order–disorder transition, which is observed when stacks of imidazolium cations are present at low temperature in the IL (see Figures S1 and S6, Supporting Information). It is expected that a higher degree of interaction between cation and anion stacks acts to decrease the IL conductivity. This effect at high $\delta\text{-}MgI_2$ concentration is less pronounced owing to the presence in $EMImAlI_4/(\delta\text{-}MgI_2)_x$ of an extended density of cross-links along the stacks, which occurs when a high concentration of iodide-concatenated Mg—Al complexes are present in bulk materials. A detailed discussion of the electrolyte conductivity mechanism will be discussed in a forthcoming publication.

3. Conclusions

A family of electrolytes with the general formula $EMImAlI_4/(\delta\text{-}MgI_2)_x$ are prepared using a new iodoaluminate RTIL obtained by reacting EMImI with AlI_3. Vibrational spectroscopy measurements coupled with DFT calculations elucidate the interactions between organic and inorganic moieties in the materials as well as the ion speciation as a function of the $\delta\text{-}MgI_2$ content. The concentration of AlI_4^- and $Al_2I_7^-$ anions as a function of the Mg content revealed the presence of two concatenated Mg—Al anionic complexes α and β with bridging iodine atoms. Electrochemical characterizations in terms of Mg deposition and stripping and average coulombic efficiency measurements reveal very promising performance. A high reversibility and compatibility with the Mg anode is demonstrated together with a high conductivity (3×10^{-4} S cm^{-1} for $EMImAlI_4/(\delta\text{-}MgI_2)_{0.005}$ at 25 °C). These results clearly indicate that iodoaluminate ionic liquids are a very promising class of materials for application in secondary magnesium batteries. Furthermore, for the first time, they may enable the use of

 © 2016 WILEY-VCH Verlag GmbH & Co. KGaA, Weinheim

Reprinted with permission from Advanced Functional Materials 2016, 26, 4860-4865.
Copyright 2016 Wiley-VCH Verlag GmbH & Co.

I^-/I_3^- -based cathode thus opening new perspectives in the field of secondary Mg batteries.

4. Experimental Section

Synthesis of $EMImAlI_4$ Ionic Liquid and $EMImAlI_4/(\delta\text{-}MgI_2)_x$ Electrolytes: $EMImAlI_4$ was prepared by direct reaction of EMImI (io-li-tec USA) with AlI_3 (Aldrich) under strictly anhydrous conditions at 80 °C. $\delta\text{-}MgI_2$ was prepared by reacting Mg powder (50 mesh, Aldrich) with anhydrous *n*-iodobutane (Aldrich) as reported elsewhere.[26] The $EMImAlI_4/(\delta\text{-}MgI_2)_x$ electrolytes were prepared by diluting a $\delta\text{-}MgI_2$ saturated mother solution. Prior to use, EMImI and *n*-iodobutane were dried by standard methods. All manipulations and characterizations were performed inside an Ar-filled dry-box (MBraun) (O_2, H_2O < 1 ppm).

Inductively Coupled Plasma Atomic Emission Spectroscopy: Mg and Al concentrations were measured using a SPECTRO Arcos ICP-AES spectrometer. Samples were previously digested using concentrated aqua regia. The 279.079 nm and 308.215 nm Mg and Al emission lines, respectively, were used to determine the concentration of the two elements in the electrolytes. The ICP-AES measurement of the electrodeposited layer obtained from $EMImAlI_4/(\delta\text{-}MgI_2)_{0.005}$ electrolyte was performed after removing the excess of $EMImAlI_4/(\delta\text{-}MgI_2)_{0.005}$ from the Pt electrode by washing with freshly distilled toluene. The deposited layer was then dissolved using a diluted HNO_3 solution.

Differential Scanning Calorimetry: DSC measurements were performed using a Q20 DSC (TA instruments) with a scanning rate of 3 °C min^{-1}. A known amount of sample was loaded on hermetically sealed alodined aluminum pans, prior to measure.

Vibrational Spectroscopy: Far-infrared spectra were obtained using a Nexus spectrometer (Thermo Scientific) with a 4 cm^{-1} resolution after sandwiching each sample between two polyethylene windows. Raman spectra were measured using a NXR-FT Raman module (Thermo Scientific) with a 1064 nm excitation line. For both the Raman and FIR measurements the spectra were obtained by averaging 500 scans.

Electrochemical Measurements: CV profiles were obtained using a VSP Bio-Logic potentiostat/galvanostat. Mg deposition/stripping measurements were carried out using either Pt or Mg WE and both Mg counter (CE) and reference (RE) electrodes. The average coulombic efficiency was measured after an initial deposition of 0.18 C cm^{-2} followed by nine 0.03 C cm^{-2} cycles with a current density of 0.5 mA cm^{-2}. The final stripping step was cut off at +0.9 V versus Mg. Exchange current density measurements are performed at a scan rate of 0.1 mV s^{-1} and normalized respect to the WE geometrical area.

Broadband Electrical Spectroscopy: Conductivity measurements were performed using a Novocontrol Alpha-A analyzer in the −100 ÷ 130 °C temperature range, every 10 °C with an accuracy higher than ±0.5 °C. A home-made hermetic Teflon cell was prepared inside an Ar-filled glove box and then kept under N_2 atmosphere during the measurement.

Computational Methods: DFT calculations with Becke's three-parameter hybrid functional (B3LYP)[32] were performed using GAUSSIAN 09.[33] For H, C, N, Mg, and Al atoms the 6-311G** split valence basis set and for I atom an all electrons basis set supplemented for iodine[34] was used. The optimizations were performed over all degrees of freedom with no symmetry constraints and tight convergence criteria. Frequency calculations at the same level of theory were done to confirm the resulting stationary points as local minima. To minimize the effect of systematic errors in calculated vibrational frequencies all of the calculated frequencies were scaled by 1.04 except for cationic vibrations, which were not scaled. This was similar to the scaling factor used in a previous work[23] on $\delta\text{-}MgCl_2$ based IL systems and also the scaling factor obtained using SQM method for organic molecules containing C, H, N, O, S, P, and Cl atoms.[35]

Supporting Information

Supporting Information is available from the Wiley Online Library or from the author.

Acknowledgements

F.B., G.P., and V.D.N. are grateful for financial support to the strategic project "MAESTRA" of the University of Padova. F.S. and S.J.P. acknowledge support by the Army Research Office under Contract No. W911NF-07-1-0085. A typo in the name of F.S. was corrected on 18.07.2016.

Received: March 21, 2016
Revised: May 6, 2016
Published online: May 30, 2016

[1] F. Cheng, J. Liang, Z. Tao, J. Chen, *Adv. Mater.* **2011**, *23*, 1695.
[2] J. Liu, J.-G. Zhang, Z. Yang, J. P. Lemmon, C. Imhoff, G. L. Graff, L. Li, J. Hu, C. Wang, J. Xiao, G. Xia, V. V. Viswanathan, S. Baskaran, V. Sprenkle, X. Li, Y. Shao, B. Schwenzer, *Adv. Funct. Mater.* **2013**, *23*, 929.
[3] J. Xie, C. Li, Z. Cui, X. Guo, *Adv. Funct. Mater.* **2015**, *25*, 6519.
[4] P. Saha, M. K. Datta, O. I. Velikokhatnyi, A. Manivannan, D. Alman, P. N. Kumta, *Prog. Mater. Sci.* **2014**, *66*, 1.
[5] D. Aurbach, G. S. Suresh, E. Levi, A. Mitelman, O. Mizrahi, O. Chusid, M. Brunelli, *Adv. Mater.* **2007**, *19*, 4260.
[6] J. Muldoon, C. B. Bucur, T. Gregory, *Chem. Rev.* **2014**, *114*, 11683.
[7] C. Liu, F. Li, L.-P. Ma, H.-M. Cheng, *Adv. Mater.* **2010**, *22*, E28.
[8] M. Armand, F. Endres, D. R. MacFarlane, H. Ohno, B. Scrosati, *Nat. Mater.* **2009**, *8*, 621.
[9] *Electrochemical Aspects of Ionic Liquids* (Ed: H. Ohno), Wiley, Hoboken, NJ **2005**.
[10] Y. Lu, S. K. Das, S. S. Moganty, L. A. Archer, *Adv. Mater.* **2012**, *24*, 4430.
[11] N. Byrne, P. C. Howlett, D. R. MacFarlane, M. Forsyth, *Adv. Mater.* **2005**, *17*, 2497.
[12] Y. NuLi, J. Yang, P. Wang, *Appl. Surf. Sci.* **2006**, *252*, 8086.
[13] T. Kakibe, J. Hishii, N. Yoshimoto, M. Egashira, M. Morita, *J. Power Sources* **2012**, *203*, 195.
[14] G. T. Cheek, W. E. O'Grady, S. Z. El Abedin, E. M. Moustafa, F. Endres, *J. Electrochem. Soc.* **2008**, *155*, D91.
[15] J. Muldoon, C. B. Bucur, A. G. Oliver, T. Sugimoto, M. Matsui, H. S. Kim, G. D. Allred, J. Zajicek, Y. Kotani, *Energy Environ. Sci.* **2012**, *5*, 5941.
[16] G. Vardar, A. E. S. Sleightholme, J. Naruse, H. Hiramatsu, D. J. Siegel, C. W. Monroe, *ACS Appl. Mater. Interfaces* **2014**, *6*, 18033.
[17] P. Novák, R. Imhof, O. Haas, *Electrochim. Acta* **1999**, *45*, 351.
[18] J. Hassoun, S. Panero, P. Reale, B. Scrosati, *Adv. Mater.* **2009**, *21*, 4807.
[19] M. M. Huie, D. C. Bock, E. S. Takeuchi, A. C. Marschilok, K. J. Takeuchi, *Coord. Chem. Rev.* **2015**, *287*, 15.
[20] G. Pagot, F. Bertasi, G. Nawn, E. Negro, G. Carraro, D. Barreca, C. Maccato, S. Polizzi, V. Di Noto, *Adv. Funct. Mater.* **2015**, *25*, 4032.
[21] M. Piccolo, G. A. Giffin, K. Vezzù, F. Bertasi, P. Alotto, M. Guarnieri, V. Di Noto, *ChemSusChem* **2013**, *6*, 2157.
[22] F. Endres, D. MacFarlane, A. Abbott, *Electrodeposition from Ionic Liquids*, Wiley-VCH, Weinheim, Germany **2008**.
[23] F. Bertasi, C. Hettige, F. Sepehr, X. Bogle, G. Pagot, K. Vezzù, E. Negro, S. J. Paddison, S. G. Greenbaum, M. Vittadello, V. Di Noto, *ChemSusChem* **2015**, *8*, 3069.
[24] F. Bertasi, C. Hettige, S. G. Greenbaum, M. Vittadello, V. Di Noto, *US Patent 61/900522*, **2013**.
[25] C. Liebenow, K. Lühder, P. Lobitz, H. Füllbier, *J. Power Sources* **1993**, *41*, 299.
[26] M. Vittadello, D. I. Waxman, P. J. Sideris, Z. Gan, K. Vezzù, E. Negro, A. Safari, S. G. Greenbaum, V. Di Noto, *Electrochim. Acta* **2011**, *57*, 112.

© 2016 WILEY-VCH Verlag GmbH & Co. KGaA, Weinheim

Reprinted with permission from Advanced Functional Materials 2016, 26, 4860-4865.
Copyright 2016 Wiley-VCH Verlag GmbH & Co.

[27] G. M. Begun, C. R. Boston, G. Torsi, G. Mamantov, *Inorg. Chem.* **1971**, *10*, 886.
[28] A. Manteghetti, A. Potier, *Spectrochim. Acta, Part A* **1982**, *38*, 141.
[29] D. Aurbach, Y. Gofer, J. Langzam, *J. Electrochem. Soc.* **1989**, *136*, 3198.
[30] M. Morimitsu, N. Tanaka, M. Matsunaga, *Chem. Lett.* **2000**, *29*, 1028.
[31] G. A. Giffin, J. Tannert, S. Jeong, W. Uhl, S. Passerini, *J. Phys. Chem. C* **2015**, *119*, 5878.
[32] A. D. Becke, *J. Chem. Phys.* **1993**, *98*, 5648.
[33] M. J. Frisch, G. W. Trucks, H. B. Schlegel, G. E. Scuseria, M. A. Robb, J. R. Cheeseman, G. Scalmani, V. Barone, B. Mennucci, G. A. Petersson, H. Nakatsuji, M. Caricato, X. Li, H. P. Hratchian, A. F. Izmaylov, J. Bloino, G. Zheng, J. L. Sonnenberg, M. Hada, M. Ehara, K. Toyota, R. Fukuda, J. Hasegawa, M. Ishida, T. Nakajima, Y. Honda, O. Kitao, H. Nakai, T. Vreven, J. A. Montgomery, J. E. Peralta, F. Ogliaro, M. Bearpark, J. J. Heyd, E. Brothers, K. N. Kudin, V. N. Staroverov, R. Kobayashi, J. Normand, K. Raghavachari, A. Rendell, J. C. Burant, S. S. Iyengar, J. Tomasi, M. Cossi, N. Rega, J. M. Millam, M. Klene, J. E. Knox, J. B. Cross, V. Bakken, C. Adamo, J. Jaramillo, R. Gomperts, R. E. Stratmann, O. Yazyev, A. J. Austin, R. Cammi, C. Pomelli, J. W. Ochterski, R. L. Martin, K. Morokuma, V. G. Zakrzewski, G. A. Voth, P. Salvador, J. J. Dannenberg, S. Dapprich, A. D. Daniels, Ö. Farkas, J. B. Foresman, J. V. Ortiz, J. Cioslowski, D. J. Fox, J. A. Montgomery Jr., *Gaussian 09, Rev A.1* **2009**.
[34] M. N. Glukhovtsev, A. Pross, M. P. McGrath, L. Radom, *J. Chem. Phys.* **1995**, *103*,1878.
[35] S. Katsyuba, E. Vandyukova, *Chem. Phys. Lett.* **2003**, *377*, 658.

 © 2016 WILEY-VCH Verlag GmbH & Co. KGaA, Weinheim

Reprinted with permission from Advanced Functional Materials 2016, 26, 4860-4865.
Copyright 2016 Wiley-VCH Verlag GmbH & Co.

Copyright WILEY-VCH Verlag GmbH & Co. KGaA, 69469 Weinheim, Germany, 2016.

ADVANCED FUNCTIONAL MATERIALS

Supporting Information

for *Adv. Funct. Mater.,* DOI: 10.1002/adfm.201601448

Toward a Magnesium-Iodine Battery

*Federico Bertasi, Fatemeh Sepher, Gioele Pagot, Stephen J. Paddison, and Vito Di Noto**

Reprinted with permission from Advanced Functional Materials 2016, 26, 4860-4865.
Copyright 2016 Wiley-VCH Verlag GmbH & Co.

WILEY-VCH

Copyright WILEY-VCH Verlag GmbH & Co. KGaA, 69469 Weinheim, Germany, 2013.

Supporting Information

Towards a Magnesium-Iodine Battery

*Federico Bertasi, Fatemeh Sepher, Gioele Pagot, Stephen J. Paddison and Vito Di Noto**

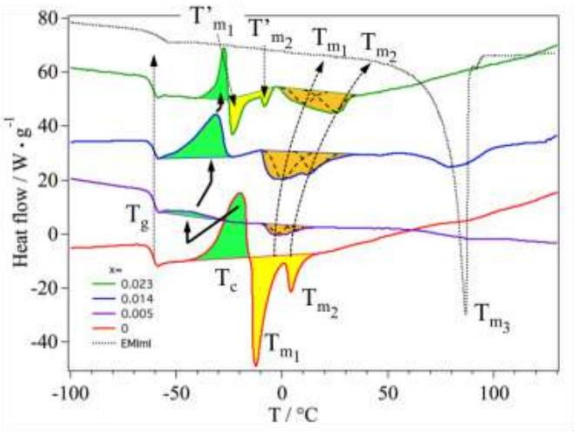


Figure S1. DSC measurements for $EMImAlI_4/(\delta\text{-}MgI_2)_x$ with $0 < x < 0.023$. (T_g, glass transition event; T_c, crystallization exothermic peak; $T_{m,i}$ melting temperature).

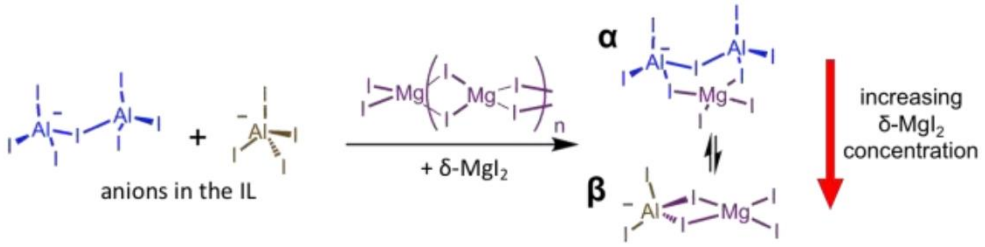


Figure S2. Mg interaction scenario as a function of *x*.

Reprinted with permission from Advanced Functional Materials 2016, 26, 4860-4865.
Copyright 2016 Wiley-VCH Verlag GmbH & Co.

DFT Calculations

Computational Method:

The experimental vibrational IR spectrum of the EMImI system, model clusters of EMImI, and $[EMImI_3]^{-2}$ were optimized and analysed using the described computational method. Similar calculations were performed on model clusters of $EMImAlI_4$ and $EMImAl_2I_7$ to compare with the experimental vibrational IR and Raman spectra of the equimolar pristine ionic liquid, $EMImAlI_4$. For each ionic cluster the optimizations were performed beginning from different initial starting positions and the lowest energy structure was selected and used for further investigation. In order to investigate the effect of δ-MgI_2 salt, monomeric and dimeric magnesium iodide were added to the $EMImAlI_4$ and $EMImAl_2I_7$ clusters and optimized. The vibrational spectra of the resulting clusters were compared to the IR and Raman spectra of $EMImAlI_4/(\delta\text{-}MgI_2)_{0.023}$.

Diffuse functions for hydrogen and heavy atoms, including iodine, were added to the $EMImAlI_4/MgI_2$ and $EMImAl_2I_7/MgI_2$ clusters. It was found that the optimized structures change insignificantly and vibrational frequencies shift by only one or two wavenumbers. As the effect of diffuse functions was determined to be negligible for the vibrational analysis, they were not included in the calculations in favour of computational efficiency.

Assignment of IR spectrum of EMImI:

The optimized structures for EMImI and $[EMImI_3]^{2-}$ clusters are shown in Figure S3 and the vibrational frequencies are reported in Table S1. The result shows that both EMImI and $[EMImI_3]^{2-}$ clusters explain the experimental spectra of EMImI at the far IR region. At the near IR region, the $[EMImI_3]^{2-}$ cluster better predicts the carbon-hydrogen vibrations. However, both calculated and experimental spectra do not show any characteristic vibrational band in the Far IR region.

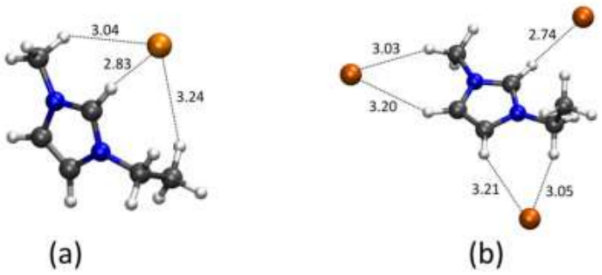


Figure S3. DFT optimized geometries. (a) Structure of EMImI; (b) Structure of $[EMImI_3]^{2-}$. Colour code: iodine, orange; carbon, grey; nitrogen, blue; hydrogen, white. Distances are in Å.

Assignment of IR and Raman spectra of pristine $EMImAlI_4$:

Reprinted with permission from Advanced Functional Materials 2016, 26, 4860-4865.
Copyright 2016 Wiley-VCH Verlag GmbH & Co.

Figure S5 shows the optimized structures and Table S2 summarizes the experimental and calculated vibrational frequencies in the far IR region. In the experimental Raman spectrum of $EMImAlI_4$, there are two strong peaks at 146 and 140 cm^{-1} which are characteristic of the AlI_4^- and $Al_2I_7^-$ anions, respectively. The calculated frequencies (see Table S2) show two peaks at 144 and 138 cm^{-1} with strong Raman intensities for $EMImAlI_4$ and $EMImAl_2I_7$ clusters, respectively.

The far IR spectrum of $EMImAlI_4$ shows a strong peak at 242 cm^{-1}. Calculated frequencies for the $EMImAlI_4$ cluster only show an out of plane vibrational mode for the ethyl group of the cation at 243 cm^{-1}. This vibrational mode is usually weak (similar to the IR peak of EMImI at 244 cm^{-1}) and cannot explain the strong peak observed at 242 cm^{-1}. The asymmetrical stretching of the Al–I–Al bridge in the $EMImAl_2I_7$ cluster appears at 245 cm^{-1} with a high IR intensity which corresponds to the strong peak at 242 cm^{-1}.

The peak at 291 cm^{-1} is related to the cation vibrations at 296 and 297 cm^{-1}. However, the IR intensity of this vibrational mode is not high enough to fully describe the observed peak at 291 cm^{-1}. The $EMImAl_2I_7$ cluster shows symmetrical stretching of $Al_2I_7^-$ at 300 cm^{-1} which is related to the experimentally observed peak at 291 cm^{-1}.

Overall, the Raman peak at 146 cm^{-1} is an indication of the presence of the AlI_4^- species and the Raman peak at 140 cm^{-1} and IR peaks at 242 and 291 cm^{-1} indicate the presence of $Al_2I_7^-$. Hence, the pristine IL ($EMImAlI_4$) contains both AlI_4^- and $Al_2I_7^-$ anionic species.

The observed peak at 341 cm^{-1} can only be related to the stretching vibrational mode of AlI_4^- at 331 cm^{-1} in the $EMImAlI_4$ cluster. The peaks at 359 and 374 cm^{-1} are assigned to the stretching modes of both AlI_4^- and $Al_2I_7^-$.

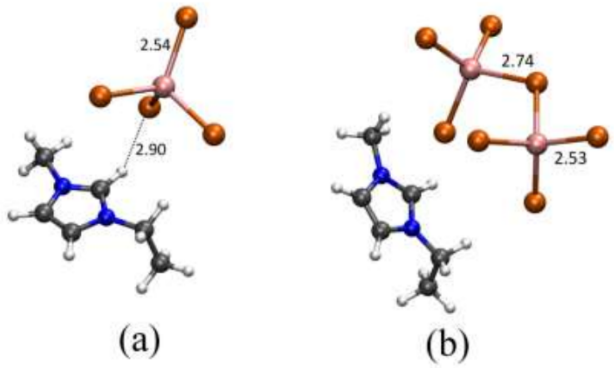


Figure S4. B3LYP/6-311G** optimized structures. (a) $EMImAlI_4$; (b) $EMImAl_2I_7$. Colour code: iodine, orange; aluminium, pink; carbon, grey; nitrogen, blue; hydrogen, white. Distances between the iodine and hydrogen atoms are only shown when less than 3 Å.

Reprinted with permission from Advanced Functional Materials 2016, 26, 4860-4865.
Copyright 2016 Wiley-VCH Verlag GmbH & Co.

Assignment of IR and Raman spectra of $EMImAlI_4/(\delta\text{-}MgI_2)_{0.023}$:

Addition of δ-MgI_2 to $EMImAlI_4$ changes the intensity of the two Raman peaks of the AlI_4^- and $Al_2I_7^-$ anions (146 cm^{-1}/140 cm^{-1}). Increasing the concentration of δ-MgI_2 increases the ratio of the intensity of AlI_4^- to $Al_2I_7^-$. The Raman peak at 146 cm^{-1} related to the AlI_4^- anionic species is also blue shifted to 147 cm^{-1} in $EMImAlI_4/(\delta\text{-}MgI_2)_{0.023}$. The same behaviour is observed in the calculated frequencies for the stretching mode of AlI_4^- (shifts from 144 to 146 cm^{-1}) upon addition of MgI_2 to the $EMImAlI_4$ cluster (see Table S3).

In Table S3, both clusters containing $(MgI_2)_2$ species have vibrational modes with high intensity at wavenumbers that are inactive in the experimental IR and Raman spectra (at 268 cm^{-1} for $EMImAlI_4/(MgI_2)_2$ and at 258 and 261 cm^{-1} for $EMImAl_2I_7/(MgI_2)_2$. Similar high intensity bands appear in the vibrational spectra of $EMImAlI_4/(MgI_2)_3$ and $EMImAl_2I_7/(MgI_2)_3$ clusters (result not shown). Hence, the computational frequency analysis disregards the presence of dimeric and trimeric magnesium iodide in the IL system.

The $EMImAl_2I_7/MgI_2$ cluster has vibrational modes due to the stretching of the Mg–I bonds at 210 cm^{-1} with relatively high IR and Raman intensity and also at 260 cm^{-1} with high IR intensity that do not appear in the experimental spectra. Hence, the presence of the $EMImAl_2I_7/MgI_2$ species in the $EMImAlI_4/(\delta\text{-}MgI_2)_{0.023}$ system is ruled out or at least negligible due to the absence of these vibrational modes in the experimental IR and Raman spectra.

The peak at 341 cm^{-1} is related to the stretching mode of AlI_4^- and MgI_2 in both the $EMImAlI_4$ and $EMImAlI_4/MgI_2$ clusters while the 374 cm^{-1} peak is assigned to the $EMImAlI_4$, $EMImAl_2I_7$, and $EMImAlI_4/MgI_2$ clusters. The ratio of the intensity of the two bands of the experimental spectra at 341 and 374 cm^{-1} increases as the concentration of δ-MgI_2 is increased. This is in agreement with the increase of the $EMImAlI_4$ and $EMImAlI_4/MgI_2$ species upon addition of δ-MgI_2 to the system.

The $[EMImAlI_4MgAlI_4]^+$ cluster shows similar vibrational frequencies to the $EMImAlI_4/MgI_2$ cluster with only minor differences. In addition to the known Raman vibration of $\nu(AlI_4^-)$ at 146 cm^{-1} it also shows a strong Raman peak at 138 cm^{-1} for the same vibrational mode corresponding to the AlI_4^- anion positioned farther from the $EMIm^+$ cation. Hence, the experimental Raman peak at 140 cm^{-1} could be assigned to both $EMImAl_2I_7$ and $[EMImAlI_4MgAlI_4]^+$ clusters.

The $[EMImAlI_4MgAlI_4]^+$ cluster has a strong IR peak at 431 cm^{-1} which can be assigned to the experimentally observed peak at 443 cm^{-1}. Among all the calculated clusters, it is only $[EMImAlI_4MgAlI_4]^+$ that shows any vibrations near the observed peak at 443 cm^{-1}. However, this peak also exists in the spectra of $EMImAlI_4$ (which has no Mg present) and its intensity only becomes greater with addition of the δ-MgI_2 salt. Hence, the presence of the $[EMImAlI_4MgAlI_4]^+$ species based on the vibrational frequency at 431 cm^{-1} is not certain.

The $[EMImAlI_4MgAlI_4]^+$ cluster has a very strong IR peak at 299 cm^{-1}. The experimental spectra have only a weak peak at 291 cm^{-1}. In conclusion, the presence of the $[EMImAlI_4MgAlI_4]^+$ clusters in the solution is not likely. However, its existence may not be rejected if its concentration is assumed to be much lower than the other species.

Reprinted with permission from Advanced Functional Materials 2016, 26, 4860-4865.
Copyright 2016 Wiley-VCH Verlag GmbH & Co.

The DFT calculations suggest that the pristine IL, (i.e., $EMImAlI_4$ system) contains both AlI_4^- and $Al_2I_7^-$ species. Addition of the buffering δ-MgI_2 salt to the pristine IL results in an increase in the ratio of AlI_4^- to $Al_2I_7^-$. The added δ-MgI_2 salt is dissolved in the system forming the $EMImAlI_4/MgI_2$ species. It is found that the MgI_2 salt favours interaction with the IL in the form of a monomer rather than either a dimer or trimer.

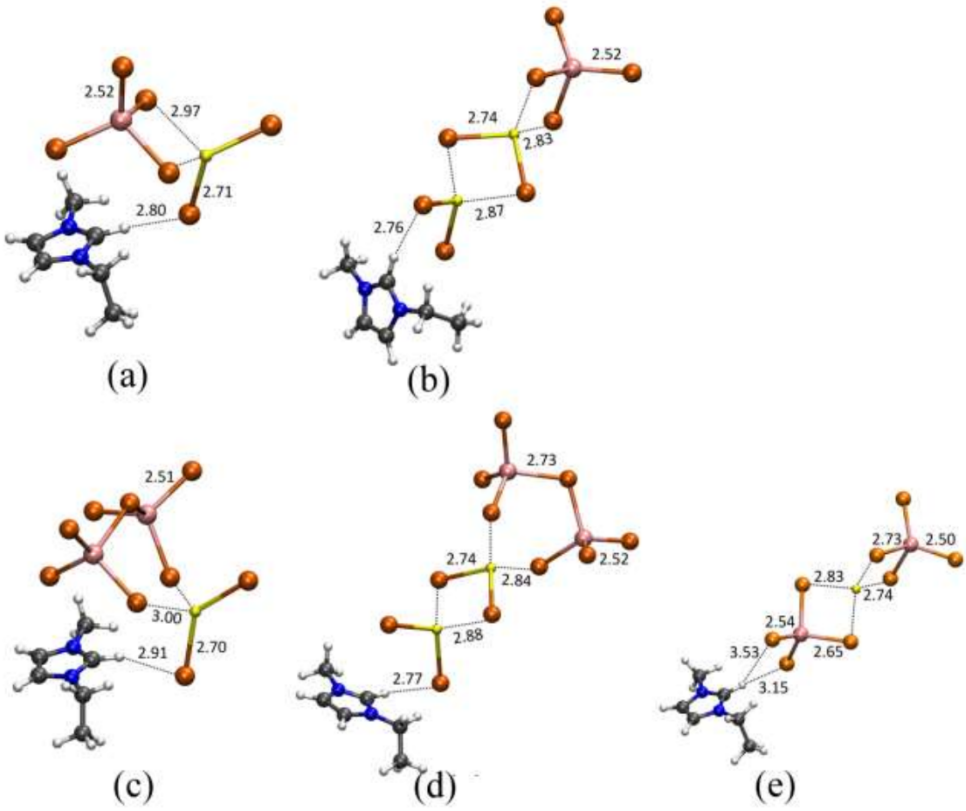


Figure S5. B3LYP/6-311G** optimized structures. (a) $EMImAlI_4$ moiety with MgI_2; (b) $EMImAlI_4$ moiety with $(MgI_2)_2$; (c) $EMImAl_2I_7$ moiety with MgI_2; (d) $EMImAl_2I_7$ moiety with $(MgI_2)_2$; and (e) the $[EMImAlI_4MgAlI_4]^+$ cluster. Colour code: iodine, orange; aluminium, pink; magnesium, yellow; carbon, grey; nitrogen, blue; hydrogen, white. Distances between iodine and hydrogen are only shown where less than 3 Å except for (e).

Reprinted with permission from Advanced Functional Materials 2016, 26, 4860-4865.
Copyright 2016 Wiley-VCH Verlag GmbH & Co.

WILEY-VCH

Table S1. Experimental vibrational spectra of EMImI and calculated vibrational modes for EMImI and $[EMImI_3]^{2-}$ clusters in cm^{-1}.

Experiment[a] EMImI		Computation EMImI	Computation $[EMImI_3]^{2-}$	Assignment[b]
IR	Raman	Freq. (I_{IR}, I_{Ra})[c]	Freq. (I_{IR}, I_{Ra})[c]	
		54(2.9, 1.1)	66(1.1, 0.8)	Cat-An
			76(7.6, 0.5)	Cat-An
75(s)			77(31.4, 0.7)	Cat-An
		72(2.6, 0.5)		tors(N-Et)
88(s)		92(0.4, 3.6)	100(4.8, 3.4)	tors(N-Me)
		112(14.1, 0.6)		tors(N-Me), γ(N-Et)
150(w)		164(4.5, 3.5)	132(1.0, 0.5)	γ(N-Et)
		221(0.3, 1.0)	201(0.1, 1.4)	tors(C-CH_3)
244(w)		243(2.9, 4.4)	234(1.4, 1.4)	γ(N-Me)
298(w)		293(0.1, 2.7)	296(4.1, 0.7)	δ(N-Me), δ(N-Et)
		391(2.9, 2.5)	398(1.2, 2.0)	γ(N-Et)
		426(0.7, 1.3)	426(5.2, 2.4)	r(N-Me), r(N-Et)
595(w)		600(2.8, 9.9)	598(0.5, 2.2)	δ(N1-C2-N3)

[a] Labels in parenthesis are experimental IR intensities: w, weak; m, medium; s, strong.
[b] Labels: δ, bending; r, rocking; γ, out of plane; tors, torsion; Cat-An, vibrations in which the imidazolium cation oscillates around the anion.
[c] Values in parenthesis are calculated IR intensities (km/mole) and Raman scattering activities ($Å^4$/AMU).

Reprinted with permission from Advanced Functional Materials 2016, 26, 4860-4865.
Copyright 2016 Wiley-VCH Verlag GmbH & Co.

Table S2. Experimental vibrational spectra of $EMImAlI_4$ and calculated vibrational modes of $EMImAlI_4$ and $EMImAl_2I_7$ clusters in cm^{-1}.

Experiment[a] $EMImAlI_4$		Computation		Assignment[b]
		$EMImAlI_4$	$EMImAl_2I_7$	
IR	Raman	Freq. (I_{IR}, I_{Ra})[c]	Freq. (I_{IR}, I_{Ra})[c]	
		48(0.3, 1.9)	48(0.4, 0.8)	Cat-An
		59(1.4, 2.1)	58(3.9, 1.6)	Cat-An
		68(0.9, 0.1)	65(0.2, 1.2)	Cat-An, tors(N-Et)
		74(7.2, 1.0)	70(6.1, 2.1)	Cat-An
			73(3.2, 3.8)	Cat-An
			77(1.2, 2.6)	Cat-An, tors(N-Et)
		78(0.5, 2.4)	78(1.2, 1.4)	Cat-An, $\delta(AlI_4^-)$, $\delta(Al_2I_7^-)$
		81(0.6, 2.5)		$\delta(AlI_4^-)$
		89(9.5, 4.5)	89(3.9, 1.2)	$\delta(AlI_4^-)$, $\delta_t(Al_2I_7^-)$, tors(N-Et), tors(N-Me)
			94(0.1,0.9)	$\delta_b(Al_2I_7^-)$, $\delta_t(Al_2I_7^-)$
		100(0.3, 0.8)	103(0.1, 1.6)	tors(N-Me)
146(w)		137(0.9, 4.9)	137(0.6, 4.0)	γ(N-Et)
	140(s)		138(0.3, 18.4)	$\nu^s_b(Al_2I_7^-)$, $\nu^s_t(Al_2I_7^-)$
	146(s)	144(0.3, 10.6)		$\nu(AlI_4^-)$
			146(3.7, 0.7)	$\nu^{as}_b(Al_2I_7^-)$, $\nu^s_t(Al_2I_7^-)$, γ(N-Et)
		208(0.2, 0.2)	208(0.4, 0.2)	tors(C-CH_3)
230		243(1.9, 1.5)	238(35.0, 1.4)	γ(N-Me)
242(s)			245(170.5, 1.3)	$\nu^{as}_b(Al_2I_7^-)$, γ(N-Me)
		297(1.5, 0.7)	296(1.8, 0.8)	δ(N-Me), δ(N-Et)
291(w)			300(26.0, 3.0)	$\nu^s_b(Al_2I_7^-)$
		319(97.3, 0.8)		$\nu(AlI_4^-)$
341(m)		331(104.1, 1.0)		$\nu(AlI_4^-)$
359(sh, m)			356(30.5, 0.7)	$\nu^{as}_t(Al_2I_7^-)$
			362(144.4, 0.5)	$\nu_t(Al_2I_7^-)$
374(vs)		379(141.3, 1.5)	383(103.5, 2.1)	$\nu(AlI_4^-)$, $\nu_t(Al_2I_7^-)$
			392(176.0, 5.0)	$\nu_t(Al_2I_7^-)$
		390(0.2, 3.3)	389(0.2, 3.3)	γ(N-Et)
424(w)		423(1.3, 1.8)	425(0.8, 2.4)	r(N-Me), r(N-Et)
443(w)				
594(w)		594(2.5, 3.9)	594(2.4, 3.3)	δ(N1-C2-N3)

[a] Labels in parenthesis are experimental IR and Raman intensities: w, weak; m, medium; s, strong; v, very; sh, shoulder; br, broad.

[b] Labels: ν, stretching; δ, bending; r, rocking; γ, out of plane; tors, torsion; s, symmetrical; as, antisymmetrical; t, terminal; b, bridge; Cat-An, vibrations in which the imidazolium cation oscillates around the anion.

[c] Values in parenthesis are calculated IR intensities (km/mole) and Raman scattering activities ($Å^4$/AMU)

Reprinted with permission from Advanced Functional Materials 2016, 26, 4860-4865.
Copyright 2016 Wiley-VCH Verlag GmbH & Co.

WILEY-VCH

Table S3. Experimental vibrational spectra of $EMImAlI_4/(\delta\text{-}MgI_2)_{0.023}$ and calculated vibrational modes for $EMImAlI_4/MgI_2$, $EMImAlI_4/(MgI_2)_2$, $EMImAl_2I_7/MgI_2$, $EMImAl_2I_7/(MgI_2)_2$, and $[EMImAlI_4MgAlI_4]^+$ clusters in cm^{-1}.

Experiment[a] $EMImAlI_4/(\delta\text{-}MgI_2)_{0.023}$		Computation					Assignment[b]
		$EMImAlI_4/MgI_2$	$EMImAlI_4/(MgI_2)_2$	$EMImAl_2I_7/MgI_2$	$EMImAl_2I_7/(MgI_2)_2$	$[EMImAlI_4MgAlI_4]^+$	
IR	Raman	Freq. (I_{IR}, I_{Ra})[c]	Freq. (I_{IR}, I_{Ra})[c]	Freq. (I_{IR}, I_{Ra})[c]	Freq. (I_{IR}, I_{Ra})[c]	Freq. (I_{IR}, I_{Ra})[c]	
						46(0.1, 3.5)	Cat-An, τ(Al-I_2), τ(Mg-I_2)
					47(0.5, 0.4)	51(1.2, 1.1)	tors(N-Et)
		49(0.8, 1.0)	47(0.1, 2.2)	47(1.7, 1.8)			Cat-An
			53(0.4, 1.4)	53(0.4, 1.2)	50(0.4, 0.9)		Cat-An
		56(0.8, 0.4)	56(0.8, 1.2)	55(0.6, 0.4)	55(0.3, 0.8)		Cat-An, r($(MgI_2)_2$)
		59(5.0, 1.8)	60(2.8, 0.3)	60(1.7, 1.1)	59(0.6, 2.9)	60(6.7, 0.6)	Cat-An
			67(0.8, 0.6)	65(3.2, 2.3)	64(3.1, 2.1)		Cat-An
					67(1.6, 0.8)		Cat-An
		75(4.9, 2.2)	72(1.7, 1.3)	72(5.0, 0.7)			Cat-An
						75(0.9, 3.3)	δ(AlI_4^-), tors(N-Me)
			77(0.3, 1.6)	78(0.5, 1.6)	76(1.1, 3.0)	76(0.2, 3.0)	δ(AlI_4^-), δ($Al_2I_7^-$)
					77(21.5, 1.3)		Cat-An
			79(0.0, 2.1)			77(0.4, 1.9)	δ(AlI_4^-)
			79(21.7, 2.7)				Cat-An
		80(1.7, 1.4)				79(0.2, 0.2)	Cat-An, δ(AlI_4^-), δ(MgI_2)
				84(0.7, 1.5)	83(4.0, 3.4)		δ($Al_2I_7^-$), δ(MgI_2), tors(N-Me)
					86(1.3, 0.6)		δ_t($Al_2I_7^-$)
		89(1.8, 3.1)					Cat-An, δ(AlI_4^-), δ(MgI_2)
			93(0.0, 4.1)				δ(AlI_4^-), δ($(MgI_2)_2$), tors(N-Me)
				93(1.4, 2.5)			δ($Al_2I_7^-$), δ(MgI_2), tors(N-Me)
			93(2.8, 1.4)	98(0.7, 1.5)	94(0.2, 0.6)	98(0.2, 4.6)	tors(N-Me)
					96(0.0, 0.5)		δ($Al_2I_7^-$), δ($(MgI_2)_2$)
				100(2.4, 2.1)			δ($Al_2I_7^-$), δ(MgI_2), tors(N-Me)

Reprinted with permission from Advanced Functional Materials 2016, 26, 4860-4865.
Copyright 2016 Wiley-VCH Verlag GmbH & Co.

WILEY-VCH

Experiment[a] $EMImAlI_4/(\delta\text{-}MgI_2)_{0.023}$		Computation					Assignment[b]
		$EMImAlI_4/MgI_2$	$EMImAlI_4/(MgI_2)_2$	$EMImAl_2I_7/MgI_2$	$EMImAl_2I_7/(MgI_2)_2$	$[EMImAlI_4MgAlI_4]^+$	
IR	Raman	Freq. (I_{IR}, I_{Ra})[c]	Freq. (I_{IR}, I_{Ra})[c]	Freq. (I_{IR}, I_{Ra})[c]	Freq. (I_{IR}, I_{Ra})[c]	Freq. (I_{IR}, I_{Ra})[c]	
		106(6.5, 2.0)	109(0.5, 2.0)				$\delta(AlI_4^-)$, $\nu(MgI_2)$, $\nu((MgI_2)_2)$
					107(0.6, 0.9)		$\nu((MgI_2)_2)$
			120(1.5, 3.4)		115(1.8, 6.9)		$\delta(AlI_4^-)$, $\nu((MgI_2)_2)$
						121(0.6, 0.5)	$\nu^s(MgI_4^{2-})$, δ(Al-I)
		129(2.5, 0.7)					tors(N-Me)
						133(1.6, 2.5)	tors(N-Me), γ(N-Et)
		133(8.1, 0.8)					ν(Mg-I-Al), tors(N-Me), γ(N-Et)
				139(0.5, 15.9)	138(0.1, 16.1)		$\nu^s_b(Al_2I_7^-)$, $\nu^s_t(Al_2I_7^-)$, ν(Mg-I)
						138(11.6, 11.2)[d]	$\nu(AlI_4^-)$, tors(N-Me), γ(N-Et)
	140(m)						$\nu^s_b(Al_2I_7^-)$, $\nu^s_t(Al_2I_7^-)$ from $EMImAl_2I_7$
			144(0.7, 3.8)	140(1.7, 0.8)	143(1.8, 4.9)		γ(N-Et)
				143(1.3, 1.6)			ν(Mg-I-Al)
					145(4.3, 0.4)		$\nu^{as}_b(Al_2I_7^-)$, $\nu^s_t(Al_2I_7^-)$
146(w)		145(0.2, 2.4)					tors(N-Me), γ(N-Et)
	147(s)	146(0.7, 10.9)	144(3.3, 13.6)			146(0.7, 14.9)[c]	$\nu(AlI_4^-)$
				153(21.9, 2.6)			ν(Mg-I)
			185(9.7, 1.0)		184(7.0, 0.7)		$\nu((MgI_2)_2)$
			189(1.1, 0.2)			192(3.5, 0.5)	ν(Mg-I-Al)
						203(6.1, 0.3)	ν(Mg-I-Al)
					206(0.1, 0.4)		$\nu_t(Al_2I_7^-)$, ν(Mg-I)
				210(106.0, 8.3)			$\nu(MgI_2)$
		212(0.1, 0.2)	214(1.0, 0.7)	207(0.4, 0.2)	207(0.2, 0.2)	209(0.2, 0.2)	tors(C-CH_3)
229(m, b)		235(125.1, 4.4)					$\nu(MgI_2)$
242(s)							$\nu^{as}_b(Al_2I_7^-)$ from $EMImAl_2I_7$
242(s)		242(3.2, 1.6)	241(1.4, 2.4)	237(2.8, 1.6)	238(2.6, 2.0)	236(1.6, 1.5)	γ(N-Me)

Reprinted with permission from Advanced Functional Materials 2016, 26, 4860-4865.
Copyright 2016 Wiley-VCH Verlag GmbH & Co.

WILEY-VCH

Experiment[a] $EMImAlI_4/(\delta\text{-}MgI_2)_{0.023}$		Computation					Assignment[b]
		$EMImAlI_4/MgI_2$	$EMImAlI_4/(MgI_2)_2$	$EMImAl_2I_7/MgI_2$	$EMImAl_2I_7/(MgI_2)_2$	$[EMImAlI_4MgAlI_4]^+$	
IR	Raman	Freq. (I_{IR}, I_{Ra})[c]	Freq. (I_{IR}, I_{Ra})[c]	Freq. (I_{IR}, I_{Ra})[c]	Freq. (I_{IR}, I_{Ra})[c]	Freq. (I_{IR}, I_{Ra})[c]	
				260(179.2, 0.5)	258(192.3, 0.0)		$\nu^{as}{}_b(Al_2I_7^-)$, ν(Mg-I)
			268 (365.1, 1.4)		261(422.8, 3.5)		$\nu((MgI_2)_2)$
			284(64.8, 0.0)		284(28.1, 0.6)		$\nu((MgI_2)_2)$
			293(35.2, 0.0)			294(72.8, 0.1)	ν(Mg-I), ν(Al-I)
					294(22.7, 1.3)		$\nu((MgI_2)_2)$, $\nu_t(Al_2I_7^-)$
			301(115.1, 0.3)		301(44.1, 1.2)		$\nu(AlI_4^-)$, $\nu^s{}_b(Al_2I_7^-)$, ν(Mg-I)
					301(63.9, 0.5)		$\nu^s{}_b(Al_2I_7^-)$, ν(Mg-I)
291(w)		296(18.4, 0.3)	294(2.0, 0.2)	295(1.1, 0.6)	294(0.4, 1.0)	293(0.5, 0.4)	δ(N-Me), δ(N-Et)
						299(495.8, 0.3)	ν(Mg-I-Al)
312(sh,vw)		308(58.3, 0.3)					δ(N-Me), δ(N-Et), ν(Mg-I-Al)
			308(105.3, 0.2)				$\nu((MgI_2)_2)$, ν(Al-I)
				309(48.6, 2.2)			$\nu^s{}_b(Al_2I_7^-)$
						311(71.4, 0.1)	ν(Mg-I), ν(Al-I)
				339(46.0, 0.8)	340(150.2, 1.2)		$\nu_t(Al_2I_7^-)$
						341(7.2, 1.3)	ν(Mg-I), ν(Al-I)
				347(151.8, 2.4)	343(39.3, 3.5)		$\nu_t(Al_2I_7^-)$
341(sh, m)		344(110.5, 1.1)	351(65.8, 1.8)				$\nu(AlI_4^-)$, ν(Mg-I)
						361(87.2, 1.9)	ν(Mg-I), ν(Al-I)
360(sh, m)		362(91.7, 1.3)		373(90.1, 1.5)			$\nu^{as}(MgI_2)$
						384(94.0, 0.5)	$\nu^{as}(AlI_2)$
		390(0.7, 2.7)	380(0.3, 3.4)	378(1.2, 1.5)	376(0.2, 4.8)	385(0.4, 1.8)	γ(N-Et)
				392(87.8, 2.6)			$\nu_t(Al_2I_7^-)$, γ(N-Et)
374(vs)		392(146.9, 1.8)					$\nu(AlI_4^-)$, $\nu(MgI_2)$
			406(116.7, 2.4)				$\nu(AlI_4^-)$
				406(170.1, 4.1)	411(159.4, 1.2)		$\nu_t(Al_2I_7^-)$

Reprinted with permission from Advanced Functional Materials 2016, 26, 4860-4865.
Copyright 2016 Wiley-VCH Verlag GmbH & Co.

WILEY-VCH

Experiment[a]		Computation					Assignment[b]
$EMImAlI_4/(\delta\text{-}MgI_2)_{0.023}$		$EMImAlI_4/MgI_2$	$EMImAlI_4/(MgI_2)_2$	$EMImAl_2I_7/MgI_2$	$EMImAl_2I_7/(MgI_2)_2$	$[EMImAlI_4MgAlI_4]^+$	
IR	Raman	Freq. (I_{IR}, I_{Ra})[c]	Freq. (I_{IR}, I_{Ra})[c]	Freq. (I_{IR}, I_{Ra})[c]	Freq. (I_{IR}, I_{Ra})[c]	Freq. (I_{IR}, I_{Ra})[c]	
					413(75.0, 4.6)		$\nu_t(Al_2I_7^-)$
424(w)		424(1.6, 1.2)	430(1.0, 0.9)	431(0.7, 2.3)	434(1.0, 2.1)	424(1.0, 1.0)	r(N-Me), r(N-Et)
443(w)						431(115.8, 3.2)	$\nu^{as}(AlI_2)$
593(w)		596(2.7, 3.8)	598(0.1, 5.1)	595(2.1, 2.5)	596(7.7, 6.8)	593(1.1, 4.0)	δ(N1-C2-N3)

[a] Labels in parenthesis are experimental IR and Raman intensities: w, weak; m, medium; s, strong; v, very; sh, shoulder; br, broad.
[b] Labels: ν, stretching; δ, bending; r, rocking; γ, out of plane; tors, torsion; τ, twisting; s, symmetrical; as, antisymmetrical; t, terminal; b, bridge; Cat-An, vibrations in which the imidazolium cation oscillates around the anion.
[c] Values in parenthesis are calculated IR intensities (km/mole) and Raman scattering activities ($Å^4$/AMU).
[d] This vibrational mode involves one of the AlI_4^- anions in the $[EMImAlI_4MgAlI_4]^+$ cluster which is farther to the $EMIm^+$ cation.
[e] This vibrational mode involves one of the AlI_4^- anions in the $[EMImAlI_4MgAlI_4]^+$ cluster which is closer to the $EMIm^+$ cation.

Reprinted with permission from Advanced Functional Materials 2016, 26, 4860-4865.
Copyright 2016 Wiley-VCH Verlag GmbH & Co.

WILEY-VCH

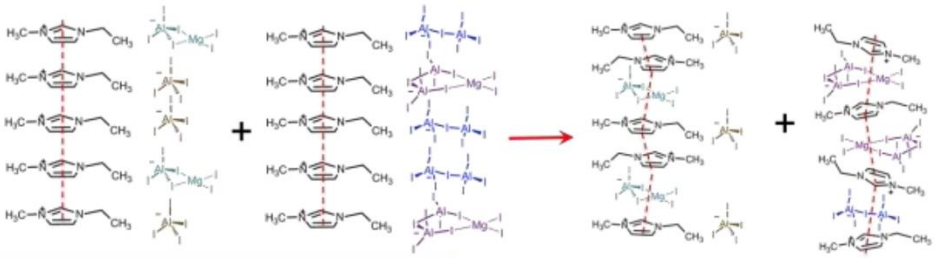


Figure S6. Scheme of the T_C thermal transition.

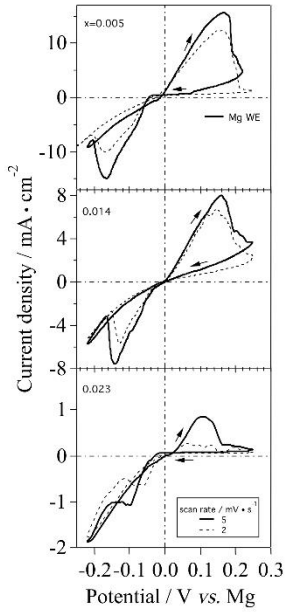


Figure S7. CV experiments for $EMImAlI_4/(\delta\text{-}MgI_2)_x$.

To be submitted for publication in Macromolecules.

Meso-Scale Simulations of Anion Exchange Membranes Based on Quaternary Ammonium Tethered Triblock Copolymers

Fatemeh Sepehr,[†] Hongjun Liu,[†] Chulsung Bae,[‡] Mark E. Tuckerman,[§] Michael A. Hickner,[∥] and Stephen J. Paddison*,[†]

[†] Department of Chemical & Biomolecular Engineering, University of Tennessee, Knoxville, Tennessee 37996, United States

[‡] Department of Chemistry and Chemical Biology, New York State Center for Polymer Synthesis, Rensselaer Polytechnic Institute, Troy, New York 12180, United States

[§] Department of Chemistry and Courant Institute, New York University, New York City, New York 10003, United States

[∥] Department of Materials Science and Engineering, The Pennsylvania State University, University Park, Pennsylvania 16802, United States

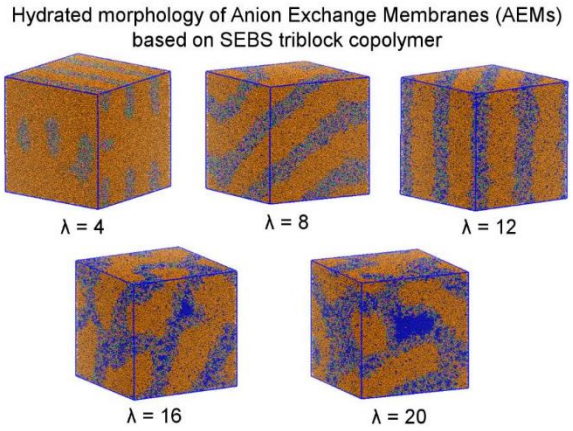
KEYWORDS: SEBS, Dissipative Particle Dynamics (DPD), Morphology, Alkaline Fuel Cell, Electrolyte, Hydroxide, Chloride

ABSTRACT: The hydrated morphology of either proton exchange membranes (PEMs) or anion exchange membranes (AEMs) determines many aspects of species transport. The present work seeks to understand the morphology and microstructure of a triblock copolymer, polystyrene-b-poly(ethylene-co-butylene)-b-polystyrene (SEBS), functionalized with alkyl-substituted quaternary ammonium groups. Meso-scale dissipative particle dynamics (DPD) simulations were utilized and parameterized by reproducing the experimental morphology of the SEBS copolymer. It was found that the AEM (i.e., quaternary ammonium-functionalized SEBS) phase separates into a functionalized polystyrene-rich phase that is hydrophilic and a hydrophobic phase consisting of the SEBS midblocks. The morphology was controlled by the water content and was transformed from perforated and interconnected lamellae to perfect lamellae and then to disordered bicontinuous domains by increasing the hydration level (λ) from 4 to 20. The hydrophilic phase swelled upon the hydration of the membrane consistent with AFM phase imaging of a similar SEBS-based ionomer. Domains exclusively consisting of water were formed at high levels of hydration (λ = 16 and 20) within the hydrophilic phase. Changing the anion from OH^- to Cl^- resulted in larger water domains at the highest hydration levels.

Meso-Scale Simulations of Anion Exchange Membranes Based on Quaternary Ammonium Tethered Triblock Copolymers

Fatemeh Sepehr,[†] Hongjun Liu,[†] Chulsung Bae,[‡] Mark E. Tuckerman,[§] Michael A. Hickner,[∥] and Stephen J. Paddison*[,†]

for Table of Content use only



I. INTRODUCTION

Anion exchange membrane (AEM) fuel cells have received extensive attention in recent years due to facile oxygen reduction reaction at high pH which enables the cell to operate with little or no platinum catalyst, thereby significantly reducing the cost.[1-2] AEMs are generally polymers functionalized by cationic groups capable of conducting hydroxide ions. A critical limitation in commercializing AEMs for fuel cell application is their low chemical stability under highly corrosive alkaline conditions.[1-4] The cationic groups may be decomposed by OH^- that results in degradation of the polymer, reduced ion exchange capacity, and lower conductivity of the membrane.

Several chemically stable AEMs using the triblock copolymer: polystyrene-b-poly(ethylene-co-butylene)-b-polystyrene (SEBS), functionalized by various benzyl- and alkyl-substituted quaternary ammonium groups have recently been developed.[5-7] The SEBS backbone provides good chemical and mechanical stability to the membrane due to its robust structure, high molecular weight, and elastomeric units. It is known that the morphology of the SEBS copolymer depends on the block compositions.[8-11] Hence, the phase-separated morphology of SEBS-based AEMs may be tailored to achieve high anion conductivity by varying the block composition in the SEBS copolymer.

Fundamental understanding of transport in AEMs is still in its infancy,[12] in contrast to PEMs which have been systematically studied for many years.[13] Quantum chemical calculations[14-16] and molecular dynamics simulations[17-20] have previously been used to determine the structure and stability of the anion exchange functional groups as well as the transport mechanism of OH^- in AEMs, similar to what has been done for PEMs.[21-25] These techniques provide valuable information at the atomic and molecular scales, however they are inadequate to explore the

morphological aspects due to the length and time scale limitations. Meso-scale simulations may provide a better understanding of the morphological features of AEMs as has been previously demonstrated for PEMs.[26-31]

There are no prior molecular-level simulations of the morphology of AEMs. For example, the morphology of SEBS has been the subject of a number of studies,[9-11,32-33] and a number of SEBS-based AEMs have been reported.[5-7] However, their correlation of morphology with ion conductivity is not well understood. This work aims to understand the morphology and microstructure of a chemically stable AEM based on SEBS by using meso-scale dissipative particle dynamics (DPD) simulations. A broad range of hydration levels are examined and the effect of another anion (Cl^-) is studied in addition to OH^-, as membranes are usually prepared and studied in a halogen precursor form.[6-7] Although the chemical structure of SEBS has ethylethylene and butylene repeating units randomly distributed in the middle block, we used a simplified structure with polyethylene unit for simulation (see Figure 1).

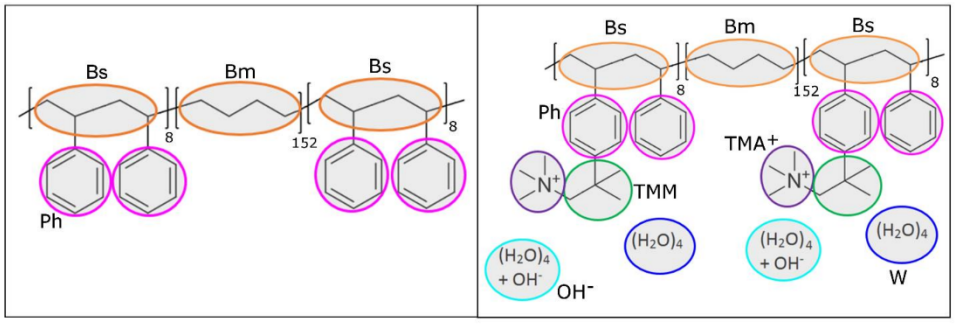
This paper is organized as follows: the simulation method is described and the coarse-grained model is briefly explained. The results and discussion section begins with a presentation of the simulated morphology of the SEBS triblock copolymer. Subsequently, the morphology of the hydrated AEM is presented and the effects of varying the water content and associated anion (OH^- vs Cl^-) are discussed. Finally, the conclusions section summarizes key findings.

II. SIMULATION METHOD

The DPD,[34-36] simulation method, was selected as it has been successfully utilized to model the morphology of PEMs.[26-31] The theoretical background and a review of the methodology is reported elsewhere.[34-37] The following presents the coarse-grained model and the simulation set up for the

study of the SEBS copolymer and the hydrated AEM. Further details on the calculation of the meso-scale interactions and simulation parameters are provided in the Supporting Information.

Coarse-Grained Model. Similar volume particles corresponding to distinct chemical groups were selected. Figure 1 shows the coarse-grained models of the SEBS triblock copolymer and the hydrated AEM in the alkaline form. Selected bead types, their chemical structure, and corresponding volume are listed in Table 1. This level of coarse-graining was chosen to enable future examination of various desired microstructural changes. The SEBS was also modeled in order to benchmark the bonded interaction parameters for the DPD simulations (see the Supporting Information).



(a) (b)

Figure 1. Coarse-grained model of: (a) SEBS triblock copolymer; and (b) hydrated AEM in alkaline form. Each circle represents the selected chemical group or collection of atoms for a particular bead and is distinguished with a different color. The midblock of SEBS is modeled as polyethylene instead of the poly(ethylene-co-butylene) for simplicity.

The polystyrene block of the SEBS copolymer was modeled by two different bead types: a Bs bead representing two polymerized vinyl groups, $(CH_2CH_2)_2$; and a Ph bead representing the phenyl group. The midblock was considered to be polyethylene instead of the poly(ethylene-co-butylene) for simplicity and was modeled with a Bm bead consisting of two vinyl groups (identical

to Bs). Although the Bs and Bm beads are chemically identical, one of them represents the backbone of a more rigid polymer (polystyrene) and the other a flexible elastomer. The model incorporates these characteristic properties through the careful choice of the bonded parameters distinguishing the flexibility of the end and mid block polymers (see the Supporting Information).

Table 1. Selected bead type, chemical structure, and volume.

Bead Type	Structure[a]	Volume[b] (Å^3)
Bs, Bm	[H](CH$_2$CH$_2$)$_2$[H]	125.5
Ph	C$_6$H$_4$[H$_2$]	129.7
TMM	[H]C(CH$_3$)$_2$CH$_2$[H]	124.8
TMA$^+$	[H]N(CH$_3$)$_3^+$	121.8
W	(H$_2$O)$_4$	120.1
OH$^-$	OH$^-$ (H$_2$O)$_4$	134.6
Cl$^-$	Cl$^-$ (H$_2$O)$_3$	125.0

[a] The atoms in brackets were added to stabilize the structures and facilitate DFT calculations. Only hydrogen atom was added to prevent changes in the chemical nature of the beads; [b] Volumes were calculated by creating Connolly surfaces with the Atom Volumes & Surfaces tool in Materials Studio.[38]

The TMA$^+$ bead represents the trimethyl ammonium (TMA) cationic group and bears a single positive charge. Two negatively charged particles: OH$^-$ bead to model the alkaline form; and Cl$^-$ bead for the chloride precursor form were introduced in the system to be simulated. The OH$^-$ bead consists of a hydroxide ion and four water molecules (i.e., OH$^-$ (H$_2$O)$_4$), while the Cl$^-$ bead consists of a chloride anion and three water molecules (i.e., Cl$^-$ (H$_2$O)$_3$). The hydrated structures of the OH$^-$ and Cl$^-$ beads were taken from structures reported in the literature,[39-40] and satisfying the similar volume criterion. A water bead, W, was taken to consist of four water molecules.

A recent parameterization method[31] based on explicit consideration of the atomic-scale interactions was utilized to derive the meso-scale conservative interactions. The interaction energies were calculated using DFT based electronic structure calculations and the DPD conservative interaction parameters were obtained for all pairs of beads. Harmonic spring and angular potentials were considered between the connected beads. The bonded interactions were tuned until the simulations of SEBS reproduced the experimental morphology of the copolymer.[8,41] These parameters were further used in the simulation of the hydrated AEMs. The Supporting Information describes the parameterization and reports the calculated parameters.

Simulations. The large scale atomic/molecular massively parallel simulator (LAMMPS) software package[42] employing a DPD style was used to perform all the simulations. The PACKMOL package[43] and VMD program[44] were used to generate random initial configurations and visualize the results, respectively. A three dimensional periodic unit cell of side length 60 DPD length units (42.7 nm) was chosen. With a density of 3 there were 648000 DPD particles in the simulation box. The time step was set to 0.01 DPD time units (38 fs) and systems were equilibrated for 70 million steps (2.68 μs).

The SEBS macromolecules were constructed with a molecular weight of 11840 g/mol with the composition of polystyrene, i.e., end blocks, being 29.63 mol%. All chains had equal molecular weight or a polydispersity index of 1.0. This simulated system is quite similar to molecular weight property of experimental SEBS except for chain length. For example, a commercial SEBS synthesized by anionic polymerization has M_n = 105,000 g/mol, a polydispersity index of 1.04, and polystyrene content of 30 mol%.[7] In the pure SEBS system there were 3240 macromolecules of SEBS and therefore, only Bs, Ph, and Bm beads were placed in the simulation box.

The AEM ionomers had the same number of repeating units as SEBS, but 50% of the styrene was functionalized with the TMM and TMA^+ beads. Every other styrene group was functionalized as shown in Figure 1 (b), however in experiment they are randomly functionalized. The effect of water content was explored by simulating various degrees of hydration. The hydration level in these systems ranged from $\lambda = 4 - 20$, where $\lambda \equiv \frac{H_2O}{TMA^+}$, i.e., water molecules per cationic functional group. The systems consisted of water, OH^- or Cl^- anions, and more than 2000 macromolecules depending on the hydration level. The number of positively and negatively charged beads were set to maintain the electroneutrality of the system.

III. RESULTS AND DISCUSSION

SEBS Triblock Copolymer. Figure 2 presents the simulated morphology of the SEBS copolymer. Only the polystyrene end blocks (those modeled with Bs and Ph beads) are shown in this figure for clear illustration of the morphology. The mid blocks are modeled by the Bm beads (not shown in the figure) and occupy the empty spaces between the cylinders. The end and mid blocks of the SEBS clearly phase separate. The polystyrene units form cylinders in a hexagonal orientation and are contained within the matrix of the midblocks. The simulated hexagonal cylindrical morphology is in agreement with the previous experimental and simulation studies.[8-11,41,45]

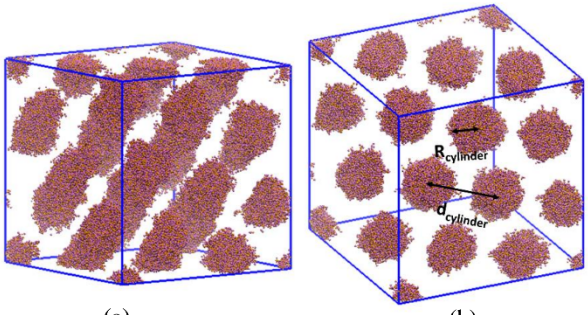


Figure 2. Simulated morphology of the SEBS triblock copolymer. Only the polystyrene end blocks, i.e., the Bs and Ph beads, are shown for clarity. (a) and (b) show two different views of the hexagonal cylindrical morphology. $R_{cylinder}$ is the cylinder radius and $d_{cylinder}$ is the intercylinder distance. The orange and mauve spheres illustrate the Bs and Ph beads, respectively. The simulation box is shown in blue.

The polystyrene radial distribution function (RDF) is shown in Figure 3. The distance at which the RDF reaches one for the second time is considered to be twice the cylinder radius ($2R_{cylinder}$) and the position of the next peak is the intercylinder distance ($d_{cylinder}$).[11] The DPD simulation results suggest that $R_{cylinder} = 3.1$ nm and $d_{cylinder} = 15.6$ nm (see Figure 3). Experimental measurements based on small angle X-ray scattering (SAXS) determined $R_{cylinder} = 7.5$ nm and $d_{cylinder} = 29.5$ nm.[8] The difference between the values from the DPD simulations and the scattering experiments may be due to the selected molecular weight of the macromolecule. The molecular weight of the real SEBS macromolecule is about an order of magnitude larger than that simulated. The ratio of the cylinder radius to the intercylinder distance for the DPD simulations is 0.20 and compares favorably with the experimental value of 0.25.

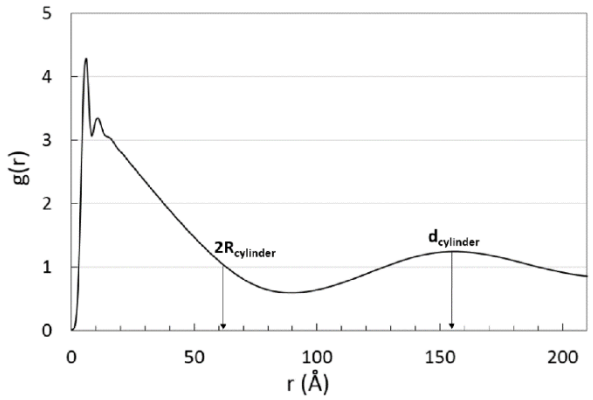


Figure 3. The polystyrene (i.e., BsPh – BsPh) RDF of the SEBS triblock copolymer. The position of the second point with the unit function value is twice the cylinder radius ($2R_{cylinder}$) and the position of the next peak is the intercylinder distance ($d_{cylinder}$).

Hydrated AEM. Figure 4 shows the simulated morphology of the hydrated ionomer, the SEBS triblock copolymer functionalized by TMA cationic groups, in the alkaline form at a hydration number of $\lambda = 8$. The AEM ionomer strongly phase separates into a lamellae morphology with alternating layers of the functionalized polystyrene end blocks (consisting of Bs, Ph, TMM, and TMA^+) and the polyethylene midblocks (Bm). The lamellae morphology is generally perforated and interconnected.

Figures 4 (d) and (e) show the distribution of the ionic species, i.e., the TMA^+ and OH^- beads. The distribution of the TMA^+ beads resembles that of the polystyrene end blocks in Figure 4 (b) which is expected as they are chemically bonded to each other. The oppositely charged beads, i.e., OH^-, are similarly distributed due to their strong attraction to the cationic sites.

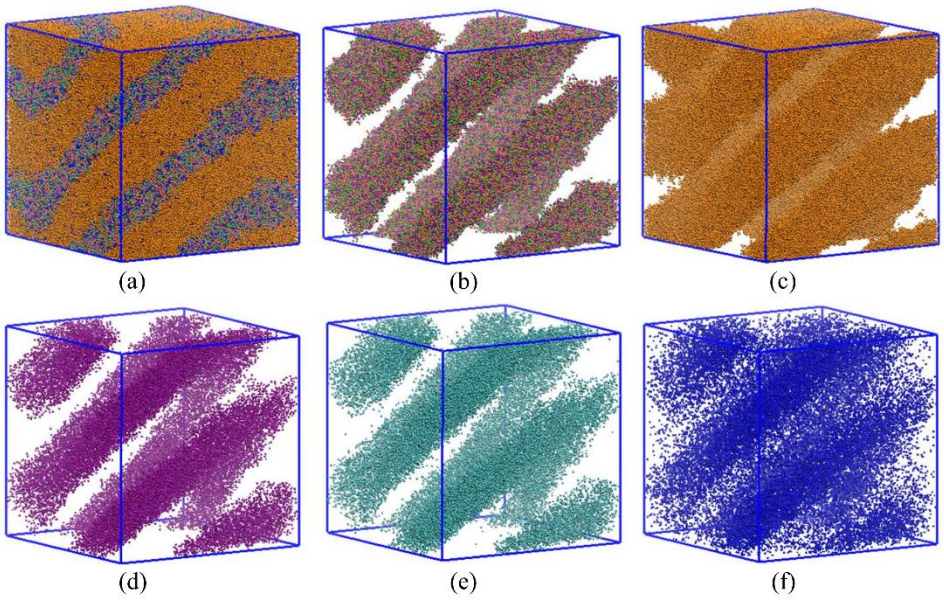


Figure 4. Simulated morphology of the hydrated AEM in the alkaline form at $\lambda = 8$. Each figure shows a specific bead type for clarity: (a) all beads; (b) Bs, Ph, TMM, and TMA^+; (c) Bm; (d) TMA^+; (e) OH^-; and (f) W. (a) shows a strong phase separation between the functionalized polystyrene end blocks and the midblocks that are shown separately in (b) and (c). (d) and (e) illustrate the distribution of ionic species and (d) shows that the majority of water are in the polystyrene phase with a few distributed in the midblock phase. Color code: Bs and Bm (orange); Ph (mauve); TMM (green); TMA^+ (purple); OH^- (cyan); and W (blue).

The ionic species and the majority of the water are in the functionalized polystyrene phase, with some water also distributed throughout the polyethylene phase. This distribution suggests that the hydrated AEM phase separates into a hydrophilic phase consisting of the end blocks and a hydrophobic phase consisting of the midblocks.

The computed RDFs are shown in Figure 5. The blue line is the BsPh – BsPh RDF corresponding to the polystyrene end blocks. The orange line corresponds to the midblocks and hence the hydrophobic phase. The RDF of the hydrophilic and hydrophobic phases is in red and shows a strong repulsion between the two phases as clearly shown in Figure 4.

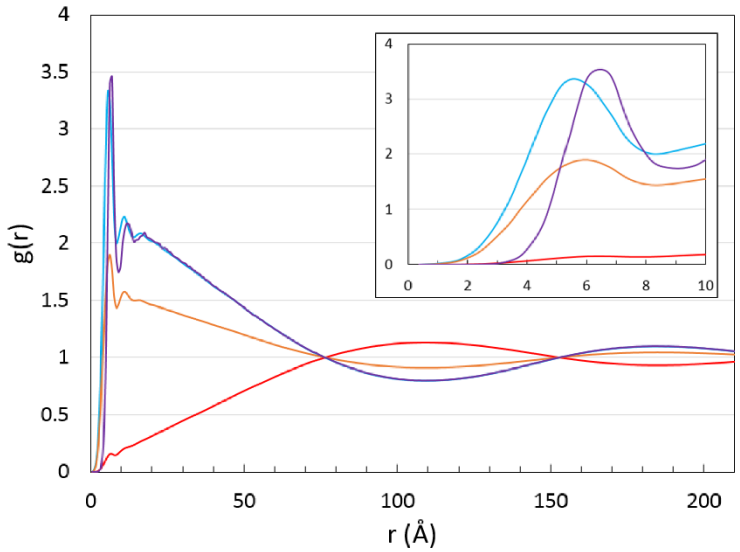


Figure 5. RDFs of the hydrated AEM in the alkaline form at $\lambda = 8$. The inset shows a magnification at short distances. Color scheme: BsPh – BsPh (blue); BsPh – Bm (red); Bm – Bm (orange); and TMA^+ – TMA^+ (purple).

The TMA^+ beads result in a similar RDF to the end blocks. The RDFs of the hydrophilic phase and TMA^+ closely resemble each other at distances greater than 20 Å, confirming that the TMA^+ groups are distributed within the hydrophilic phase. The TMA^+ – TMA^+ RDF (purple curve) is shifted to the right at very short distances in comparison to the hydrophilic phase (blue curve) (see the inset in Figure 5). This is due to the strong self-repulsion between the positively charged beads.

The Effect of Hydration. Figure 6 shows the morphology of the hydrated AEM in the alkaline form at five different hydration levels: $\lambda = 4$, 8, 12, 16, and 20. It is clear that the AEM ionomer sharply phase separates into hydrophilic and hydrophobic phases at all degrees of hydration. More importantly is the qualitative change in the morphology with increasing hydration. A perforated and interconnected lamellae morphology is exhibited at the lower water contents where $\lambda = 4$ and

8. The morphology is perfectly lamellae at $\lambda = 12$ and then becomes a disordered bicontinuous morphology at the highest hydration ($\lambda = 16$ and 20).

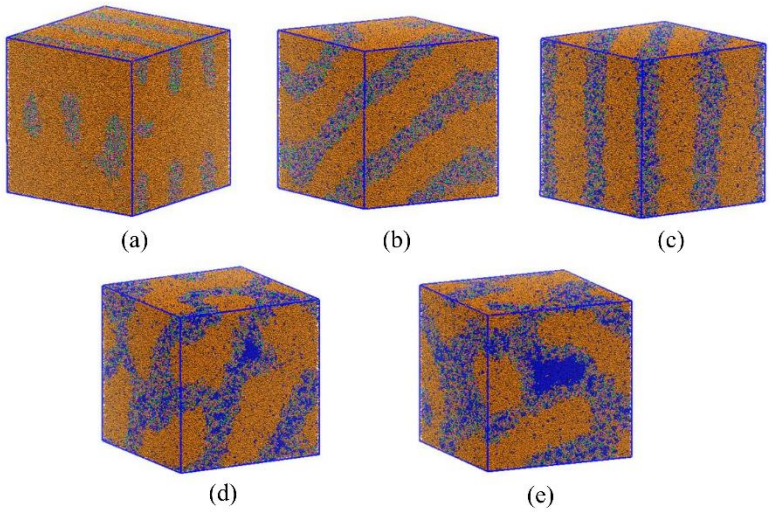


Figure 6. Simulated morphology of the hydrated AEM in the alkaline form for $\lambda =$: (a) 4; (b) 8; (c) 12; (d) 16; and (e) 20. All beads are shown and the color scheme is the same as in Figure 4. The ionomer phase separates into hydrophilic and hydrophobic phases at all hydration levels. As the hydration increases the morphology changes from perforated and interconnected lamellae ($\lambda =$ 4 and 8) to perfect lamellae ($\lambda = 12$) and then to disordered bicontinuous domains ($\lambda = 16$ and 20). Domains exclusively consisting of water are formed within the hydrophilic phase at the two highest water contents only.

Figure 7 shows the polystyrene RDFs for the systems displayed in Figure 6. It is clear that increasing the level of hydration increases the intensity of the first peak and decreases that of the second. This suggests that the polystyrene end blocks become more structured as water is added. The distance at which the RDF reaches unity (which was previousely related to the size of the domains[27]) increases through hydration indicating that the size of the hydrophilic phase grows. Recently, Sun *et al.* characterized the morphology of a similar SEBS-based ionomer functionalized with quaternary ammonium groups through atomic force microscopy (AFM) phase imaging.[6] They observed a clear phase separation between the hydrophilic functional styrene blocks and the

hydrophobic ethylene/butylene blocks. Their results revealed that the hydrophilic domains swell and become larger upon hydration in agreement with the results displayed in Figure 6.

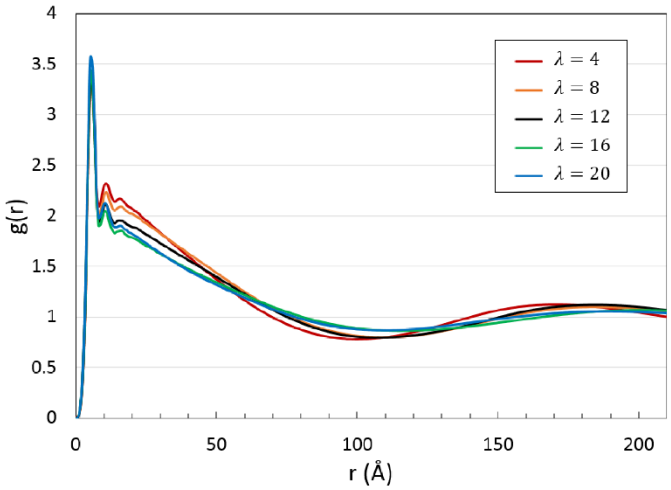
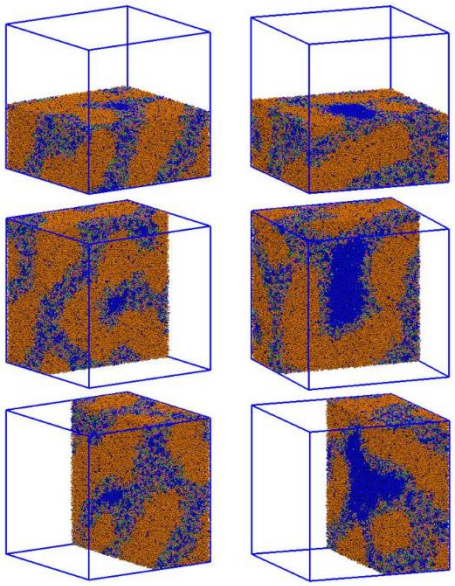


Figure 7. Polystyrene RDFs for the hydrated AEM in the alkaline form at five levels of hydration. Increasing the water content increases the intensity of the first peak and decreases that of the second. The distance at which the RDF reaches one increases through hydration indicating that the hydrophilic phase swells.

The blue domains observed in Figures 6 (d) and (e) correspond to the regions that only contain water (i.e., exclusively the W beads). Cross sections of the morphologies at $\lambda = 16$ and 20 are shown in Figure 8 for better visualization of the 3D extent. Several small domains of water are observed at $\lambda = 16$ and there is one large domain at $\lambda = 20$. The cross sections show that these clusters are three dimensional. The SAXS measurements of the sulfonated SEBS ionomers by Weiss *et al.* exhibited the formation of nano-scale ionic clusters dispersed within larger polystyrene domains that themselves were dispersed in a continuous elastomeric phase.[46]



(a) (b)

Figure 8. Cross sections of the morphologies (shown in Figures 6 (d) and (e)) in the xy, yz, and xz planes (top to bottom). (a) $\lambda = 16$; and (b) $\lambda = 20$. The exclusive water domains are within the hydrophilic phase and larger at the higher level of hydration. The cross sections reveal that the water domains are three dimensional.

Their experimental finding compares well with our simulations results. They both show the formation of nano domains within the polystyrene end block phase, although their ionomer was sulfonated and our system is functionalized with TMA.

The W –W RDFs at various levels of hydration are shown in Figure 9. The intensity of both peaks increases as the hydration increases suggesting that the water becomes more structured. The distance at which the RDF reaches a value of one is the same for $\lambda = 8$ and 12 which hardly showed any exclusive domains of water. However, this distance increases for $\lambda = 16$ and 20 as a result of the formation of exclusive water domains at these two levels of hydration. The formation

of large water domains and the extension of the RDF tail at the highest water contents were also observed in the 3M perfluorosulfonic acid ionomers.[27]

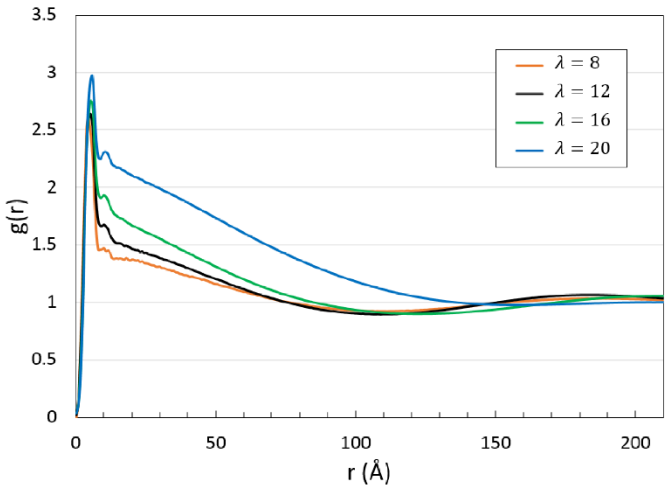


Figure 9. W – W RDFs for the hydrated AEM in the alkaline form at various degrees of hydration. Clearly, increasing the hydration intensifies the peaks. The distance at which the RDF reaches one is the same for $\lambda = 8$ and 12 and increases for $\lambda = 16$ and 20. This is due to the formation of domains that exclusively contain water. There are not sufficient W beads in the simulation box at $\lambda = 4$ to form a smooth curve and therefore this data is not shown.

The TMA^+ – OH^- RDFs for the hydrated AEM are shown in Figure 10. The intensity of the first peak increases with increasing hydration, whereas the second and third peaks decrease. Figure 10 (c) shows that the integrated number of OH^- is one at the vicinity of each TMA^+ bead and independent of the hydration level. This suggests that each TMA^+ bead is paired with one OH^- in its immediate vicinity. This value monotonically increases at longer distances (> 5 Å), however the rate of increase is lower at higher levels of hydration. This suggests that there are fewer number of OH^- beads around the TMA^+ cations as the water

content is increased and that the ionic pairs disperse throughout the hydrophilic phase as the ionomer swells upon hydration.

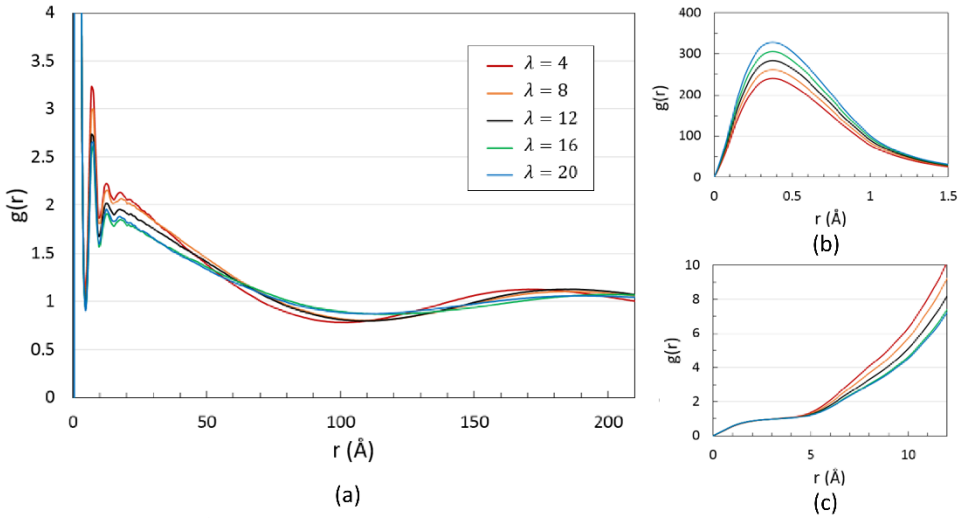


Figure 10. (a) $TMA^+ - OH^-$ RDFs for the hydrated AEM in the alkaline form at various levels of hydration. (b) An expanded view of the first peak seen in (a). (c) The integrated number of the OH^- beads around the TMA^+ beads. There is one OH^- in the immediate vicinity of each TMA^+. At a higher degree of hydration there are fewer numbers of OH^- around TMA^+ at r > 5 Å.

The Effect of Anion (OH^- versus Cl^-). The effect of changing the anion from hydroxide to chloride was also investigated, as the AEMs are usually prepared in a halogen precursor form, but tested in hydroxide form, so knowledge of both anions is informative. Similar simulations were performed using the Cl^- as the anion at five levels of hydration. Figure 11 shows the simulated morphology of the hydrated AEM system in the Cl^- precursor form at $\lambda = 8$.

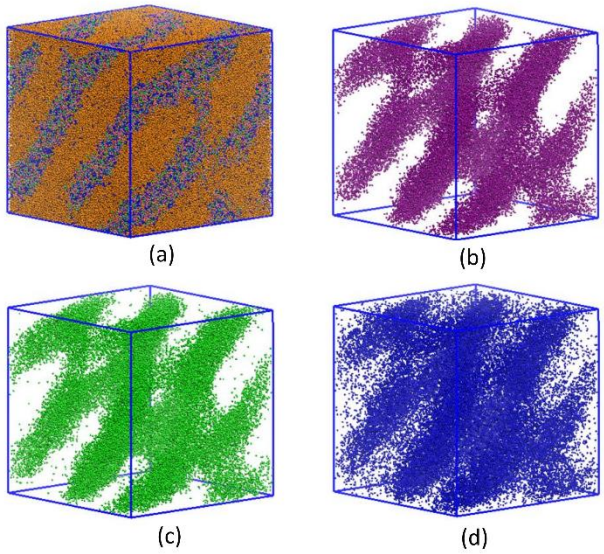


Figure 11. Simulated morphology of the hydrated AEM in the chloride form at $\lambda = 8$. Each figure shows a specific bead type for clarity: (a) all beads; (b) TMA^+; (c) Cl^-; and (d) W. The AEM ionomer shows phase separation similar to the alkaline form. Color code: Bs and Bm (orange); Ph (mauve); TMM (green); TMA^+ (purple); Cl^- (shamrock green); and W (blue).

The functionalized SEBS phase separates into a hydrophilic and a hydrophobic phase similar to the hydroxide form. Perforated interconnected lamellae morphology is formed and the Cl^- beads are positioned near the TMA^+ beads. The Cl^- precursor form shows similar morphological dependence to the water content as the hydroxide form (see Figure S1).

Figure 12 compares the W – W RDFs of the chloride and alkaline as a function of hydration. Increasing the hydration level increases the intensity of peaks in both chloride and alkaline forms. However, the RDF peaks have greater intensity with Cl^- in the system. The effect is more profound at the highest levels of hydration (i.e., $\lambda = 16$ and 20). The distance at which the RDF reaches a value of one substantially increases at $\lambda = 16$ indicating that much larger clusters of water are formed at this level of hydration in comparison to the hydroxide form.

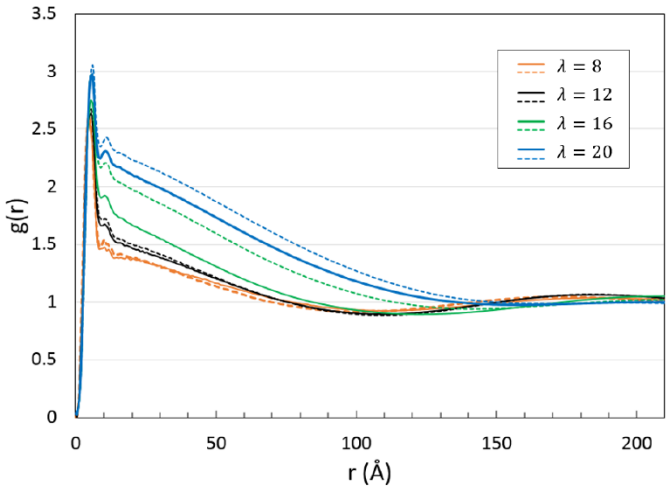


Figure 12. W – W RDFs for the hydrated AEM in the alkaline (solid lines) and chloride (dashed lines) forms at various levels of hydration. Changing the anion from OH^- to Cl^- results in negligible changes at $\lambda = 8$ and 12, however it significantly increases the peaks at $\lambda = 16$ and 20. The distance at which the RDF reaches one substantially increases at $\lambda = 16$.

Figure 13 confirms this finding as it clearly shows the presence of larger water domains in the chloride form. The chloride anion has higher preference for associating to TMA^+ when compared to the hydroxide (based on the *ab initio* calculated conservative interactions reported in Table S1) and OH^- prefers W more than Cl^- prefers W. The differences in the W and TMA^+ affinities affect the distribution of ions and water and results in larger water domains in the systems with chloride. Table 2 reports the diffusivities of the W, OH^-, and Cl^- beads at various levels of hydration calculated from the root mean square displacements. It is known that the DPD simulations are insufficient to quantitatively predict the diffusivities due to the intrinsic deficiencies of the method.[47] Hence, the values reported in this table may only serve as a qualitative or as a comparative measure in understanding the dynamics of the systems.

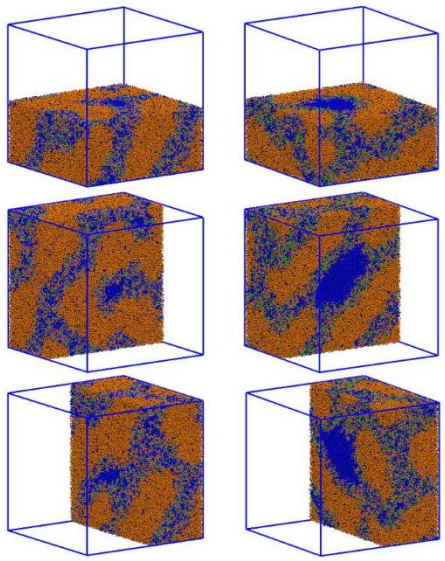


Figure 13. Cross sections of the hydrated AEM morphologies in the: xy (top), yz (middle), and xz (bottom) planes at $\lambda = 16$. (a) Alkaline form; and (b) chloride form. Changing the anion from OH^- to Cl^- results in larger exclusive domains of water.

Increasing the hydration level increases the diffusivities of both anions as expected. The simulation results indicate that the Cl^- beads have lower diffusivities than the OH^-. It is interesting that the DPD simulations correctly predicted the relative diffusivities of the OH^- and Cl^-, despite the fact that the transport mechanism of hydroxide ion[39,48] is obviously more complex than these simulations are able to capture. In fact, the deficiencies of the DPD model in including migration of the charge through individual proton transfer reactions were partially compensated by the derivation of meso-scale interactions obtained from the quantum chemical calculations.

The diffusivity of the W beads slightly decreases as the hydration level increases independent of the anion type. The diffusivities of both anions are lower than the W beads by an order of magnitude. However, the experimental diffusivities of OH^- in water[49-52] are larger than that of

H_2O.[53-54] As indicated earlier, this discrepancy is due to the deficiencies of the mesoscopic model in capturing the structural changes, hydrogen bond reorientation, and proton shuttling or hopping involved in the water and ion transport.

Table 2. Diffusivities of W, OH^-, and Cl^- beads at various hydration levels for the hydrated AEMs at the alkaline and chloride forms. Diffusivities are in $cm^2/s \times 10^4$.

Hydration Level	Hydroxide Form		Chloride Form	
(λ)	W	OH^-	W	Cl^-
4	1.72	0.31	1.73	0.27
8	1.67	0.34	1.70	0.29
12	1.62	0.35	1.66	0.30
16	1.62	0.36	1.61	0.31
20	1.56	0.38	1.53	0.31

IV. CONCLUSIONS

DPD simulations were performed to study the hydrated morphology and microstructure of an alkyl-substituted quaternary ammonium-functionalized SEBS triblock copolymer. The unfunctionalized SEBS base material was first simulated to benchmark the bonded interaction parameters by reproducing the experimental morphology of SEBS (i.e., hexagonal cylinders). The hydrated AEM was subsequently simulated employing a similar set of parameters and was observed to phase separate into a functionalized polystyrene-rich phase (hydrophilic) and a polyethylene phase (hydrophobic). The ionic species and majority of the water were distributed throughout the former phase, while some water was also in the latter.

The morphology was observed to be controlled by the degree of hydration and was transformed from perforated and interconnected lamellae at low water content (i.e., $\lambda = 4$ and 8) to perfect

lamellae ($\lambda = 12$) and then to disordered bicontinuous domains at the highest water contents (i.e., $\lambda = 16$ and 20). The hydrophilic phase swelled with hydration consistent with the AFM phase imaging of a similar SEBS-based ionomer. Domains exclusively consisting of water were formed at the high levels of hydration within the hydrophilic phase. Changing the associated anion from OH^- to Cl^- resulted in larger exclusive domains of water at the highest hydration levels. The diffusivities of water and ionic species were calculated and reported only as a comparative measure. The simulation results predict that the Cl^- ion is less mobile than OH^- with a slight increase in the diffusivity of both anions with increasing water content ($\frac{\Delta D}{\Delta \lambda} = 4.4$ and 2.5 $\frac{cm^2/_s \times 10^7}{H_2O/_{TMA^+}}$ for OH^- and Cl^-, respectively).

■ ASSOCIATED CONTENT

Supporting Information

The Supporting Information is available free of charge on the ACS Publications website including the parameterization of the conservative interactions; bonded potentials; and AEM morphologies in the chloride form as a function of hydration level.

■ AUTHOR INFORMATION

Corresponding Author

*Phone 865 974-2026; Fax 865 974 7076; e-mail: spaddison@utk.edu (S.J.P.).

Notes

The authors declare no competing financial interest.

■ ACKNOWLEDGMENTS

This work was supported by the National Science Foundation under CHE 1534355: "DMREF: Collaborative Research: Development of Design Rules for High Hydroxide Transport in Polymer Architectures."

■ REFERENCES

1. Merle, G.; Wessling, M.; Nijmeijer, K., Anion exchange membranes for alkaline fuel cells: A review. *Journal of Membrane Science* **2011,** *377*, 1-35.

2. Varcoe, J. R.; Atanassov, P.; Dekel, D. R.; Herring, A. M.; Hickner, M. A.; Kohl, P. A.; Kucernak, A. R.; Mustain, W. E.; Nijmeijer, K.; Scott, K.; Xu, T. W.; Zhuang, L., Anion-exchange membranes in electrochemical energy systems. *Energy & Environmental Science* **2014,** *7*, 3135-3191.

3. Hickner, M. A.; Herring, A. M.; Coughlin, E. B., Anion Exchange Membranes: Current Status and Moving Forward. *Journal of Polymer Science Part B-Polymer Physics* **2013,** *51*, 1727-1735.

4. Cheng, J.; He, G. H.; Zhang, F. X., A mini-review on anion exchange membranes for fuel cell applications: Stability issue and addressing strategies. *International Journal of Hydrogen Energy* **2015,** *40*, 7348-7360.

5. Zeng, Q. H.; Liu, Q. L.; Broadwell, I.; Zhu, A. M.; Xiong, Y.; Tu, X. P., Anion exchange membranes based on quaternized polystyrene-block-poly(ethylene-ran-butylene)-block-polystyrene for direct methanol alkaline fuel cells. *Journal of Membrane Science* **2010,** *349*, 237-243.

6. Sun, L.; Guo, J. S.; Zhou, J.; Xu, Q. M.; Chu, D.; Chen, R. R., Novel nanostructured high-performance anion exchange ionomers for anion exchange membrane fuel cells. *Journal of Power Sources* **2012,** *202*, 70-77.

7. Mohanty, A. D.; Ryu, C. Y.; Kim, Y. S.; Bae, C., Stable Elastomeric Anion Exchange Membranes Based on Quaternary Ammonium-Tethered Polystyrene-b-poly(ethylene-co-butylene)-b-polystyrene Triblock Copolymers. *Macromolecules* **2015,** *48*, 7085-7095.

8. Heck, B.; Arends, P.; Ganter, M.; Kressler, J.; Stuhn, B., SAXS and TEM studies on poly(styrene)-block-poly(ethene-co-but-1-ene)-block-poly(styrene) in bulk and at various interfaces. *Macromolecules* **1997,** *30*, 4559-4566.

9. Matsen, M. W.; Thompson, R. B., Equilibrium behavior of symmetric ABA triblock copolymer melts. *Journal of Chemical Physics* **1999,** *111*, 7139-7146.

10. Abu-Sharkh, B.; AlSunaidi, A., Morphology and conformation analysis of self-assembled triblock copolymer melts. *Macromolecular Theory and Simulations* **2006,** *15*, 507-515.

11. Tallury, S. S.; Spontak, R. J.; Pasquinelli, M. A., Dissipative particle dynamics of triblock copolymer melts: A midblock conformational study at moderate segregation. *Journal of Chemical Physics* **2014,** *141*.

12. Marino, M. G.; Melchior, J. P.; Wohlfarth, A.; Kreuer, K. D., Hydroxide, halide and water transport in a model anion exchange membrane. *Journal of Membrane Science* **2014,** *464*, 61-71.

13. Kreuer, K. D.; Paddison, S. J.; Spohr, E.; Schuster, M., Transport in proton conductors for fuel-cell applications: Simulations, elementary reactions, and phenomenology. *Chemical Reviews* **2004,** *104*, 4637-4678.

14. Chempath, S.; Boncella, J. M.; Pratt, L. R.; Henson, N.; Pivovar, B. S., Density Functional Theory Study of Degradation of Tetraalkylammonium Hydroxides. *Journal of Physical Chemistry C* **2010,** *114*, 11977-11983.

15. Castaneda, S.; Ribadeneira, R., Theoretical Description of the Structural Characteristics of the Quaternized SEBS Anion-Exchange Membrane Using DFT. *Journal of Physical Chemistry C* **2015,** *119*, 28235-28246.

16. Long, H.; Pivovar, B. S., Hydroxide Degradation Pathways for Substituted Benzyltrimethyl Ammonium: A DFT Study. *Ecs Electrochemistry Letters* **2015,** *4*, F13-F16.

17. Han, K. W.; Ko, K. H.; Abu-Hakmeh, K.; Bae, C.; Sohn, Y. J.; Jang, S. S., Molecular Dynamics Simulation Study of a Polysulfone-Based Anion Exchange Membrane in Comparison with the Proton Exchange Membrane. *Journal of Physical Chemistry C* **2014,** *118*, 12577-12587.

18. Takaba, H.; Shimizu, N.; Hisabe, T.; Alam, M. K., Modeling of transport mechanisms of OH- in electrolyte of alkaline fuel cell. *Computational Studies on Battery and Fuel Cell Materials* **2014,** *61*, 63-69.

19. Zhang, W. W.; van Duin, A. C. T., ReaxFF Reactive Molecular Dynamics Simulation of Functionalized Poly(phenylene oxide) Anion Exchange Membrane. *Journal of Physical Chemistry C* **2015,** *119*, 27727-27736.

20. Chen, C.; Tse, Y. L. S.; Lindberg, G. E.; Knight, C.; Voth, G. A., Hydroxide Solvation and Transport in Anion Exchange Membranes. *Journal of the American Chemical Society* **2016,** *138*, 991-1000.

21. Cui, S. T.; Liu, J. W.; Selvan, M. E.; Keffer, D. J.; Edwards, B. J.; Steele, W. V., A molecular dynamics study of a nafion polyelectrolyte membrane and the aqueous phase structure for proton transport. *Journal of Physical Chemistry B* **2007,** *111*, 2208-2218.

22. Elliott, J. A.; Paddison, S. J., Modelling of morphology and proton transport in PFSA membranes. *Physical Chemistry Chemical Physics* **2007,** *9*, 2602-2618.

23. Wang, C.; Clark, J. K.; Kumar, M.; Paddison, S. J., An ab initio study of the primary hydration and proton transfer of CF(3)SO(3)H and CF(3)O (CF(2))(2)SO(3)H: Effects of the hybrid functional and inclusion of diffuse functions. *Solid State Ionics* **2011,** *199*, 6-13.

24. Kumar, M.; Paddison, S. J., Side-chain degradation of perfluorosulfonic acid membranes: An ab initio study. *Journal of Materials Research* **2012,** *27*, 1982-1991.

25. Wang, C.; Paddison, S. J., Hydration and Proton Transfer in Highly Sulfonated Poly(phenylene sulfone) Ionomers: An Ab Initio Study. *Journal of Physical Chemistry A* **2013,** *117*, 650-660.

26. Yamamoto, S.; Hyodo, S. A., A computer simulation study of the mesoscopic structure of the polyelectrolyte membrane Nafion. *Polymer Journal* **2003,** *35*, 519-527.

27. Wu, D. S.; Paddison, S. J.; Elliott, J. A., A comparative study of the hydrated morphologies of perfluorosulfonic acid fuel cell membranes with mesoscopic simulations. *Energy & Environmental Science* **2008,** *1*, 284-293.

28. Wu, D. S.; Paddison, S. J.; Elliott, J. A., Effect of Molecular Weight on Hydrated Morphologies of the Short-Side-Chain Perfluorosulfonic Acid Membrane. *Macromolecules* **2009,** *42*, 3358-3367.

29. Vishnyakov, A.; Neimark, A. V., Self-assembly in nafion membranes upon hydration: Water mobility and adsorption isotherms. *Journal of Physical Chemistry B* **2014,** *118*, 11353-11364.

30. Wang, C.; Paddison, S. J., Mesoscale modeling of hydrated morphologies of sulfonated polysulfone ionomers. *Soft Matter* **2014,** *10*, 819-830.

31. Sepehr, F.; Paddison, S. J., Dissipative Particle Dynamics interaction parameters from ab initio calculations. *Chemical Physics Letters* **2016,** *645*, 20-26.

32. Sliozberg, Y. R.; Strawhecker, K. E.; Andzelm, J. W.; Lenhart, J. L., Computational and experimental investigation of morphology in thermoplastic elastomer gels composed of AB/ABA blends in B-selective solvent. *Soft Matter* **2011,** *7*, 7539-7551.

33. Chantawansri, T. L.; Sirk, T. W.; Sliozberg, Y. R., Entangled triblock copolymer gel: Morphological and mechanical properties. *Journal of Chemical Physics* **2013,** *138*.

34. Hoogerbrugge, P. J.; Koelman, J., Simulating microscopic hydrodynamic phenomena with dissipative particle dynamics. *Europhysics Letters* **1992,** *19*, 155-160.

35. Español, P.; Warren, P. B., Statistical mechanics of dissipative particle dynamics. *Europhysics Letters* **1995,** *30*, 191-196.

36. Groot, R. D.; Warren, P. B., Dissipative particle dynamics: Bridging the gap between atomistic and mesoscopic simulation. *Journal of Chemical Physics* **1997,** *107*, 4423-4435.

37. Moeendarbary, E.; Ng, T. Y.; Zangeneh, M., Dissipative particle dynamics: Introduction, methodology and complex fluid applications - a review. *International Journal of Applied Mechanics* **2009,** *1*, 737-763.

38. MaterialsStudio *Materials Studio*, Accelrys Inc., San Diego, CA, USA, **2005**.

39. Tuckerman, M. E.; Marx, D.; Parrinello, M., The nature and transport mechanism of hydrated hydroxide ions in aqueous solution. *Nature* **2002,** *417*, 925-929.

40. Ge, L.; Bernasconi, L.; Hunt, P., Linking electronic and molecular structure: insight into aqueous chloride solvation. *Physical Chemistry Chemical Physics* **2013,** *15*, 13169-13183.

41. Sugimoto, M.; Sakai, K.; Aoki, Y.; Taniguchi, T.; Koyama, K.; Ueda, T., Rheology and Morphology Change with Temperature of SEBS/Hydrocarbon Oil Blends. *Journal of Polymer Science Part B-Polymer Physics* **2009,** *47*, 955-965.

42. Plimpton, S., Fast Parallel Algorithms for Short-Range Molecular-Dynamics. *Journal of Computational Physics* **1995,** *117*, 1-19.

43. Martinez, L.; Andrade, R.; Birgin, E. G.; Martinez, J. M., PACKMOL: A Package for Building Initial Configurations for Molecular Dynamics Simulations. *Journal of Computational Chemistry* **2009,** *30*, 2157-2164.

44. Humphrey, W.; Dalke, A.; Schulten, K., VMD: Visual molecular dynamics. *Journal of Molecular Graphics & Modelling* **1996,** *14*, 33-38.

45. Chantawansri, T. L.; Duncan, A. J.; Ilavsky, J.; Stokes, K. K.; Berg, M. C.; Mrozek, R. A.; Lenhart, J. L.; Beyer, F. L.; Andzelm, J. W., Phase Behavior of SEBS Triblock Copolymer Gels. *Journal of Polymer Science Part B-Polymer Physics* **2011,** *49*, 1479-1491.

46. Weiss, R. A.; Sen, A.; Pottick, L. A.; Willis, C. L., Block Copolymer Ionomers: Thermoplastic Elastomers Possessing two Distinct Physical Networks. *Polymer Communications* **1990,** *31*, 220-223.

47. Groot, R. D.; Madden, T. J., Dynamic simulation of diblock copolymer microphase separation. *Journal of Chemical Physics* **1998,** *108*, 8713-8724.

48. Marx, D.; Chandra, A.; Tuckerman, M. E., Aqueous Basic Solutions: Hydroxide Solvation, Structural Diffusion, and Comparison to the Hydrated Proton. *Chemical Reviews* **2010,** *110*, 2174-2216.

49. Halle, B.; Karlstrom, G., Prototropic Charge Migration in Water .1. Rate Constants in Light and Heavy-Water and in Salt Solution from O-17 Spin Relaxation. *Journal of the Chemical Society-Faraday Transactions Ii* **1983,** *79*, 1031-1046.

50. Atkins, P.; de Paula, J., *Atkins' Physical Chemistry*. 7th ed.; Oxford University Press, Oxford, **2002**.

51. Tuckerman, M. E.; Chandra, A.; Marx, D., Structure and dynamics of OH-(aq). *Accounts of Chemical Research* **2006,** *39*, 151-158.

52. Lee, S. H.; Rasaiah, J. C., Proton transfer and the mobilities of the H+ and OH- ions from studies of a dissociating model for water. *Journal of Chemical Physics* **2011,** *135*.

53. Mills, R., Self-Diffusion in Normal and Heavy-Water in Range 1-45 Degrees. *Journal of Physical Chemistry* **1973,** *77*, 685-688.

54. Krynicki, K.; Green, C. D.; Sawyer, D. W., Pressure and Temperature-Dependence of Self-Diffusion in Water. *Faraday Discussions* **1978,** *66*, 199-208.

Supporting Information

Meso-Scale Simulations of Anion Exchange Membranes Based on Quaternary Ammonium Tethered Triblock Copolymers

Fatemeh Sepehr,[†] Hongjun Liu,[†] Chulsung Bae,[‡] Mark E. Tuckerman,[§] Michael A. Hickner,[∥] and Stephen J. Paddison*[,†]

[†] Department of Chemical & Biomolecular Engineering, University of Tennessee, Knoxville, Tennessee 37996, United States

[‡] Department of Chemistry and Chemical Biology, New York State Center for Polymer Synthesis, Rensselaer Polytechnic Institute, 110 8th Street, Troy, New York 12180, United States

[§] Department of Chemistry and Courant Institute, New York University, New York City, New York 10003, United States

[∥] Department of Materials Science and Engineering, The Pennsylvania State University, University Park, Pennsylvania 16802, United States

KEYWORDS: SEBS, Dissipative Particle Dynamics (DPD), Morphology, Alkaline Fuel Cell, Electrolyte, Hydroxide, Chloride

ABSTRACT: The hydrated morphology of either proton exchange membranes (PEMs) or anion exchange membranes (AEMs) determines many aspects of species transport. The present work seeks to understand the morphology and microstructure of a triblock copolymer, polystyrene-b-poly(ethylene-co-butylene)-b-polystyrene (SEBS), functionalized with alkyl-substituted quaternary ammonium groups. Meso-scale dissipative particle dynamics (DPD) simulations were utilized and parameterized by reproducing the experimental morphology of the SEBS copolymer. It was found that the AEM (i.e., quaternary ammonium-functionalized SEBS) phase separates into a functionalized polystyrene-rich phase that is hydrophilic and a hydrophobic phase consisting of the SEBS midblocks. The morphology was controlled by the water content and was transformed from perforated and interconnected lamellae to perfect lamellae and then to disordered bicontinuous domains by increasing the hydration level (λ) from 4 to 20. The hydrophilic phase swelled upon the hydration of the membrane consistent with AFM phase imaging of a similar SEBS-based ionomer. Domains exclusively consisting of water were formed at high levels of hydration (λ = 16 and 20) within the hydrophilic phase. Changing the anion from OH^- to Cl^- resulted in larger water domains at the highest hydration levels.

Coarse-Grained Model:

Conservative Interaction Parameters. A recent parameterization method[1] based on explicit consideration of the atomic-scale interactions was utilized to derive the conservative interactions. The structure of all bead types were optimized using density functional theory (DFT) at the B3LYP/6-311G** level[2-4] using the GAUSSIAN 09 suite of programs.[5] The interaction energies were calculated at the B3LYP/6-31G* level and the excess energies were obtained for all pairs of beads. Over 2000 different configurations were considered for each pair. The DPD particles in this work represent half the volume size of the particles used in a previous study employing this parameterization scheme.[1] Therefore, a larger basis set and fewer number of configurations were considered in this work. The calculated energies were fitted to:

$$U_{ij}^{int} = \frac{a_{ij}^{int}}{2}(1 - r_{ij})^2 + b_{ij}^{int} .$$

where U_{ij}^{int} is the interaction energy obtained from DFT calculations and a_{ij}^{int} and b_{ij}^{int} are the fitting parameters. The a_{ij}^{int} and b_{ij}^{int} were calculated using the least squares method with the energies equally weighted. Values above an energy threshold were excluded as they correspond to the overlapping configurations.

The water was selected as the reference material and a^R was set to 25 based on the experimental compressibility.[6] The a_{WW}^{int} was scaled to a negligible value. The scaling factor was chosen to be $(2.28 \times r_c^2)^{-1}$ and the remainder of the a_{ij}^{int} and b_{ij}^{int} values were scaled accordingly. Utilizing the common value for the density, $\rho r_c^3 = 3$, and taking the volume of each water molecule as 30 Å^3, the length scale was determined to be: $r_c \cong 7.11$ Å.

The a_{ij} values were calculated for the selected bead types and their values are reported in Table S1. Interaction parameters were not calculated if the simulated systems did not contain the specific pair of beads. This table shows a strong repulsive interaction between the SEBS copolymer beads (i.e., Bs, Ph, and Bm) and the W bead consistent with their hydrophobic nature.

Table S1. Calculated conservative interaction parameters.

a_{ij}	Bs, Bm	Ph	TMM	TMA^+	W	OH^-	Cl^-
Bs, Bm	30.28						
Ph	35.02	30.53					
TMM	29.24	27.74	26.03				
TMA^+	27.52	27.31	25.59	65.79			
W	35.57	33.44	27.46	26.61	25.01		
OH^-	34.80	30.05	27.88	–15.02	27.34	65.68	
Cl^-	32.22	30.50	29.34	–16.65	28.17	–	73.99

The identical chemical structures of the Bs and Bm beads results in the same conservative interaction parameters. The Bs bead represents the backbone of a more rigid polymer (polystyrene), whereas the Bm bead models a flexible elastomer. This was incorporated into the model by careful choice of the bonded parameters distinguishing the flexibility of the end and mid block polymers (see the following).

Bonded Interaction Parameters. Harmonic spring and angular potentials were considered between the connected beads of polymer. The harmonic spring potential between two connected neighboring beads was defined as:

$$U^S = \sum_{all\ bonds} \frac{1}{2} K_b (r_b - r_b^0)^2 ,$$

with K_b, r_b, and r_b^0 being the spring modulus, bond length, and equilibrium bond length, respectively. The angular potential between three connected neighboring beads was defined as:

$$U^A = \sum_{all\ angles} K_a (1 - \cos(\theta_a - \theta_a^0)) ,$$

where K_a is the angular modulus, θ is the angle between the three beads, and θ^0 is its equilibrium value. Among all the possible angles only four and six angles were considered for the simulation of the SEBS and hydrated AEM, respectively (see Table S2).

Several initial values for the bonded potential parameters (K_b, K_a, r_b^0, and θ_a^0) were used based on the flexibility of the polymers. The polystyrene end blocks are stiffer than the elastomeric midblocks, hence more rigid parameters were used for the former. The parameters were further refined until the expected experimental morphology of SEBS, i.e., hexagonal cylindrical,[7-8] was reproduced. The first four rows of Table S2 report the bonded interaction parameters corresponding to the hexagonal cylindrical morphology of SEBS that were also used in the simulation of the hydrated AEMs.

The AEM ionomer has cationic functional groups attached to the end blocks and therefore two additional types of bonds and angles were required for the coarse-grained model. There were no structural information to benchmark these parameters, hence values close to those of SEBS were selected.

Table S2. Bonded interaction parameters for simulating the SEBS triblock copolymer and hydrated AEMs. The first four rows define the bonded parameters for the SEBS and all for the AEM.

Bond	K_b	r_b^0	Angle	K_a	θ_a^0
Bs – Bs	30	0.7	Bs – Bs – Bs	15	150
Bs – Ph	30	0.7	Bs – Bs – Bm	10	150
Bs – Bm	30	0.7	Bs – Bm – Bm	1	90
Bm – Bm	20	0.7	Bm – Bm – Bm	1	90
Ph – TMA^+	30	0.7	Bs – Ph – TMM	1	90
TMM – TMA^+	20	0.7	Ph – TMM – TMA^+	1	90

The Effect of Anion (OH^- versus Cl^-):

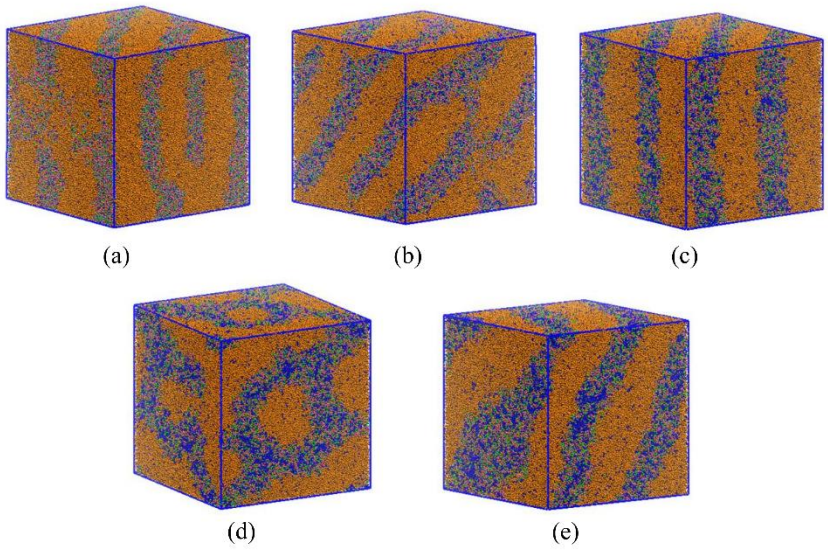


Figure S1. Simulated morphology of the hydrated AEM in the chloride form for water contents, where λ is: (a) 4; (b) 8; (c) 12; (d) 16; and (e) 20. All beads are shown and the color scheme is the same as in Figure 11. The ionomer phase separates into hydrophilic and hydrophobic phases at all hydration levels. Similar to the alkaline form, the morphology changes by increasing the water content and exclusive domains of water are formed within the hydrophilic phase at the two highest values of λ.

■ REFERENCES

1. Sepehr, F.; Paddison, S. J., Dissipative particle dynamics interaction parameters from *ab initio* calculations. *Chemical Physics Letters* **2016,** *645*, 20-26.

2. Becke, A. D., Density-functional thermochemistry. III. The role of exact exchange. *Journal of Chemical Physics* **1993,** *98*, 5648-5652.

3. McLean, A. D.; Chandler, G. S., Contracted Gaussian Basis Sets for Molecular Calculations. I. Second Row Atoms, Z=11-18. *Journal of Chemical Physics* **1980,** *72*, 5639-5648.

4. Lee, C. T.; Yang, W. T.; Parr, R. G., Development of the Colle-Salvetti correlation-energy formula into a functional of the electron density. *Physical Review B* **1988,** *37*, 785-789.

5. Frisch, M. J.; Trucks, G. W.; Schlegel, H. B.; Scuseria, G. E.; Robb, M. A.; Cheeseman, J. R.; Scalmani, G.; Barone, V.; Mennucci, B.; Petersson, G. A.; Nakatsuji, H.; Caricato, M.; Li, X.; Hratchian, H. P.; Izmaylov, A. F.; Bloino, J.; Zheng, G.; Sonnenberg, J. L.; Hada, M.; Ehara, M.; Toyota, K.; Fukuda, R.; Hasegawa, J.; Ishida, M.; Nakajima, T.; Honda, Y.; Kitao, O.; Nakai, H.; Vreven, T.; Montgomery, J. A.; Peralta, J. E.; Ogliaro, F.; Bearpark, M.; Heyd, J. J.; Brothers, E.; Kudin, K. N.; Staroverov, V. N.; Kobayashi, R.; Normand, J.; Raghavachari, K.; Rendell, A.; Burant, J. C.; Iyengar, S. S.; Tomasi, J.; Cossi, M.; Rega, N.; Millam, J. M.; Klene, M.; Knox, J. E.; Cross, J. B.; Bakken, V.; Adamo, C.; Jaramillo, J.; Gomperts, R.; Stratmann, R. E.; Yazyev, O.; Austin, A. J.; Cammi, R.; Pomelli, C.; Ochterski, J. W.; Martin, R. L.; Morokuma, K.; Zakrzewski, V. G.; Voth, G. A.; Salvador, P.; Dannenberg, J. J.; Dapprich, S.; Daniels, A. D.; Farkas; Foresman, J. B.; Ortiz, J. V.; Cioslowski, J.; Fox, D. J., Gaussian 09, Revision A.01. Gaussian 09, Revision A.01, Wallingford CT, 2009.

6. Groot, R. D.; Warren, P. B., Dissipative particle dynamics: Bridging the gap between atomistic and mesoscopic simulation. *Journal of Chemical Physics* **1997,** *107*, 4423-4435.

7. Heck, B.; Arends, P.; Ganter, M.; Kressler, J.; Stuhn, B., SAXS and TEM studies on poly(styrene)-block-poly(ethene-co-but-1-ene)-block-poly(styrene) in bulk and at various interfaces. *Macromolecules* **1997,** *30*, 4559-4566.

8. Sugimoto, M.; Sakai, K.; Aoki, Y.; Taniguchi, T.; Koyama, K.; Ueda, T., Rheology and Morphology Change with Temperature of SEBS/Hydrocarbon Oil Blends. *Journal of Polymer Science Part B-Polymer Physics* **2009,** *47*, 955-965.

To be submitted for publication in Solid State Ionics.

The Primary Hydration and Proton Transfer of Acids: An *ab initio* Study

*Fatemeh Sepehr and Stephen J. Paddison**

Department of Chemical & Biomolecular Engineering, University of Tennessee, Knoxville, Tennessee 37996

*Author to whom correspondence should be addressed. Fax: +1 865 974 2026.

E-mail address: spaddison@utk.edu (S.J. Paddison).

Abstract

Acids dissolved in solution or tethered to a polymer backbone play an important role in the performance of the electrolytes utilized in energy storage and conversion technologies. The relative acidity and acid-base interactions are influential in the design of advanced electrolyte materials such as acid-base complexes and electrospun ionomers that involving two or more types of acids. Here we present a first principles based study of the primary hydration and proton transfer of ten acid molecules commonly employed in electrolytes. Clusters consisting of a single molecule with up to five water molecules were considered and the effect of a dielectric continuum solvation model was explored. For CF_3SO_3H, FSO_3H, CH_3SO_3H, H_2SO_4, HNO_3, HF, H_3PO_2, H_3PO_3, H_3PO_4, and $CF_3SO_2NHSO_2CF_3$ acids a minimum number of 3, 3, 3, 4, 5, >5, 5, >5, >5, and 3 water molecules were required, respectively, to effect proton transfer in the gas phase. It was determined that stronger acids or clusters with a continuum solvation model require fewer number of water molecules to first witness proton dissociation. The hydronium ion further separated from the conjugate anion as the number of water molecules was increased. Potential energy surface scans indicated that the proton transfer energetics are controlled by the hydration structure, acid strength, and the continuum solvation model. The calculated energy barrier to transfer a proton from HF to a water molecule was determined 27 kcal/mol, more than twice the barrier for all the other acids (10 - 16 kcal/mol). This fundamental study may serve the purpose of designing or screening novel electrolytes featuring one or more of these acids.

Keywords: Proton Transfer, Hydrated Acidity, Bis(trifluoromethane)sulfonimide, Phosphinic, Phosphonic, Phosphoric

1. Introduction

Fuel cells [1-3] and redox flow batteries (RFBs) [4,5] are currently under investigation to fulfill the requirements of efficient and sustainable energy storage and conversion technologies. The discovery of high-performance stable electrolytes that are relatively cheap and versatile is crucial to these technologies and necessitates a comprehensive understanding of the materials [3,6-8].

The most widely used proton exchange membrane (PEM) electrolytes utilized in fuel cells and redox flow batteries are perfluorosulfonic acid (PFSA) membranes (perfluorinated polymers functionalized by sulfonic acid groups) due to their high proton conductivity and substantial thermal and mechanical stability [6]. The high cost, limited operating temperatures, and poor insulation to methanol fuels [7] associated with these membranes have led to extensive research on finding alternative materials either by modifying the PFSAs (e.g., replacing the sulfonic acid group with bis(trifluoromethane)sulfonimide ($CF_3SO_2NHSO_2CF_3$) [9] or phosphonic acid [10]) or developing advanced materials, e.g.: hydrocarbon polymers functionalized by acidic groups [11,12]; phosphoric/sulfuric/nitric acid-doped polybenzimidazole (acid/PBI) [13-15]; and electrospun nanofiber composites [16-23].

The electrolytes utilized in fuel cells and RFBs often include acids dissolved in a solution or tethered to a polymer backbone. The properties of electrolyte membranes are directly related to the acid strength and propensity of the acidic groups to transfer the proton to the water absorbed within the membrane. Hence, the relative acidity and acid-base interactions [24] are influential in the design and performance of advanced electrolyte materials that involve two or more types of acids. Hence, a comparative study of acid strength including the primary hydration structure is a first step in the design of electrolytes. This work aims to provide a fundamental understanding of

the relative acidity and proton transfer to serve the purpose of designing or screening novel electrolytes featuring one or more of these acids.

This paper is organized as follows. The first section briefly describes the utilized computational methods. Then, the primary hydrated structures of ten acid molecules commonly used in electrolytes: CF_3SO_3H; FSO_3H; CH_3SO_3H; H_2SO_4; HNO_3; HF; H_3PO_2; H_3PO_3; H_3PO_4; and $CF_3SO_2NHSO_2CF_3$ are presented in the results section. Proton dissociation is discussed and the effect of a dielectric continuum solvation model is explored. The potential energy surface scans of the hydrated acids are analyzed to understand the relative proton transfer energetics. Finally, the significant findings are summarized in the conclusions section.

2. Computational Methods

Electronic structure calculations were performed using the GAUSSIAN 09 suite of programs [25]. Geometries were optimized using DFT with Becke's 3-parameter hybrid functional (B3LYP)[26-28] and the 6-31G** split valence basis set [29] without imposing any symmetry constraints. The resulting structures were then refined with optimizations performed with the larger 6-311G** basis set [30]. Frequency calculations at the same level of theory were performed to confirm local minima. The SMD solvation model [31] was subsequently applied to all the optimized structures with water selected as the solvent.

The B3LYP functional and the Pople's split valence basis set were selected in this study to enable comparison of the results with previous computational studies of these acids [32-45]. This level of theory has proven successful in providing relative information on the primary hydration, proton dissociation, and interactions of various imide, sulfonic, and phosphonic acid groups [32,36,46,47]. This work does not evaluate the validity or preeminence of DFT over other

computational methods, but rather seeks to provide a fundamental and relative understanding of the hydration and proton transfer of the acids.

Minimum energy structures of the ten acid molecules were obtained using the described methodology. One to five water molecules were subsequently added to the optimized structures of each acid from different initial starting positions and full optimizations (over all degrees of freedom) were performed. The lowest energy structure for each system was selected as the ground state hydrated structure for that particular acid.

Potential energy surface (PES) scans were performed on the optimized structures of the acids with one to three water molecules. The length of the covalent OH bond between the transferring proton and the oxygen was increased incrementally in steps of 0.02 Å. In the case of $CF_3SO_2NHSO_2CF_3$ and HF the NH and FH bond lengths are scanned, respectively. The length of the OH bond (or NH or FH) was the only fixed parameter and the optimizations were performed over all other degrees of freedom without symmetry constraints at each step of the scan. A reverse set of scans were also performed by decreasing the OH bond with the same incremental steps starting from the geometry obtained at the last step of the original scan. The configuration with the lower energy at a similar OH bond length was selected from the original and reverse scans to plot the energy profiles.

3. Results and Discussion

3.1. Hydration of the Acids

Figures 1 to 10 show the fully optimized structures for the ten acids in both gas phase and solvated with the SMD model. All distances are reported in Å and covalent bonds between hydrogen and oxygen atoms are shown when $O - H \leq 1.10$ Å. Figure 1a shows that a single isolated

triflic acid molecule does not dissociate in the gas phase until three water molecules are added to the cluster, in agreement with the computational studies by Paddison et al [34,37] and other authors [48]. However, it dissociates in the vicinity of only one water molecule when the SMD model is applied on the hydrated system as shown in Figure 1b. This clearly reveals the effect of a dielectric medium on stabilizing the conjugate base ($CF_3SO_3^-$) and the propensity of the acid to dissociate.

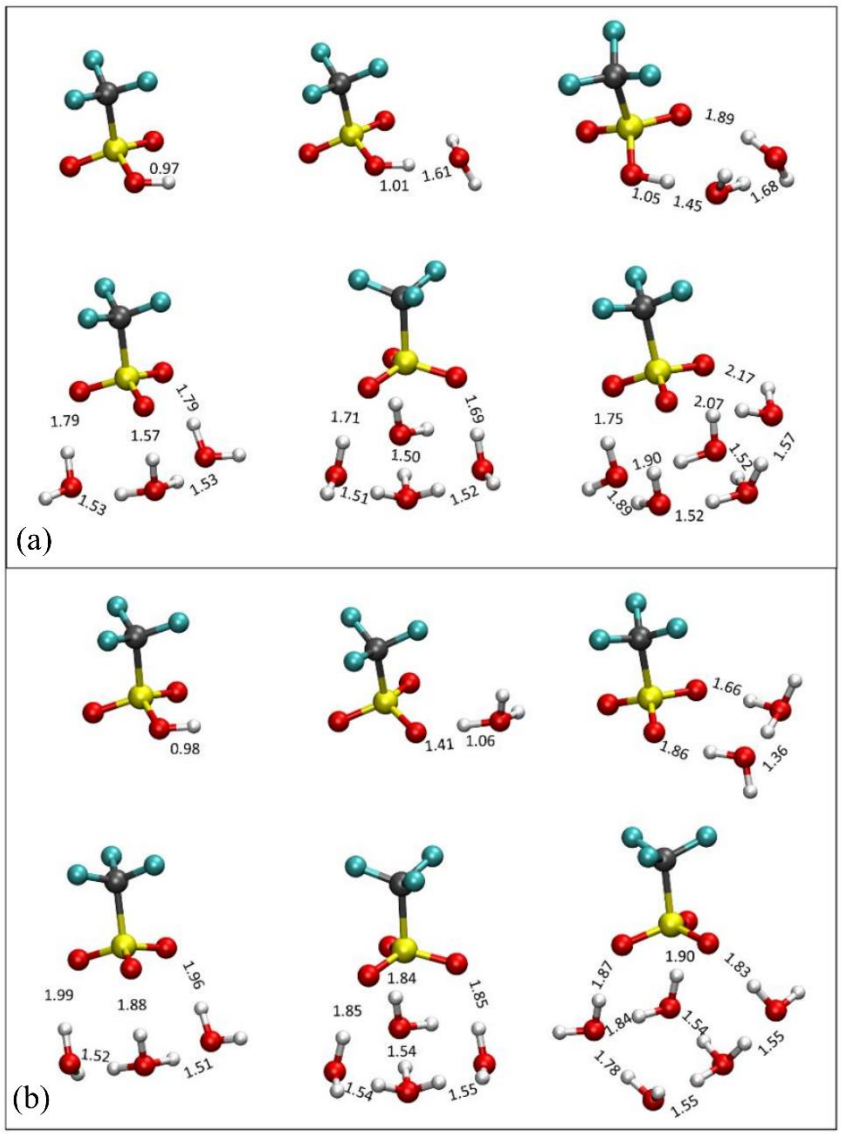


Figure 1. Fully optimized structures of CF_3SO_3H with from zero to five water molecules at the B3LYP/6-311G** level of theory: (a) gas phase structures, proton dissociation occurs after three water molecules are added; (b) structures with the SMD model, proton dissociates after only one water molecule is added. The atomic color scheme in Figures 1 to 10 is: oxygen (red), hydrogen (white), sulfur (yellow), carbon (gray), fluorine (cyan), nitrogen (blue), phosphor (orange).

Similar behavior is observed for the other acids, with dissociation occurring with a fewer number of water molecules when the dielectric continuum solvation model is included. Table 1 reports the number of water molecules required to first witness proton dissociation for each of the acids.

Table 1. The number of water molecules required to effect dissociation of a proton in the gas phase and SMD solvated systems. The acids are ordered based on the acid strength (i.e., pK_a values and gas phase acidities).

Acid	pK_a		Gas	SMD
	value	reference		
$CF_3SO_2NHSO_2CF_3$	[a]		3	2
CF_3SO_3H	−14.7	[49]	3	1
FSO_3H	−6.4	[50]	3	1
H_2SO_4	−3.0	[51]	4	3
CH_3SO_3H	−1.9	[50,52]	3	2
HNO_3	−1.3	[51]	5	3
H_3PO_2	+1.24	[53]	5	>5
H_3PO_3	+1.26	[53]	>5	>5
H_3PO_4	+2.15	[53]	>5	>5
HF	+3.17	[54]	>5	>5

[a] Not reported in the literature.

The three sulfonic acids shown in Figures 1 to 3 form similar hydrogen bond networks. In a prior study, Li et al [43] performed quantum chemical calculations on the clusters of $XSO_3H{-}(H_2O)_n$, n = 1−4 and X = F, Cl, and Br, and reported accumulation of water molecules around the hydroxyl group of XSO_3H promoting the proton transfer and stabilizing the resulting hydronium cation. They also observed the spontaneous transfer of a proton from the acid to water with three or four water molecules in the gas phase in agreement with our results.

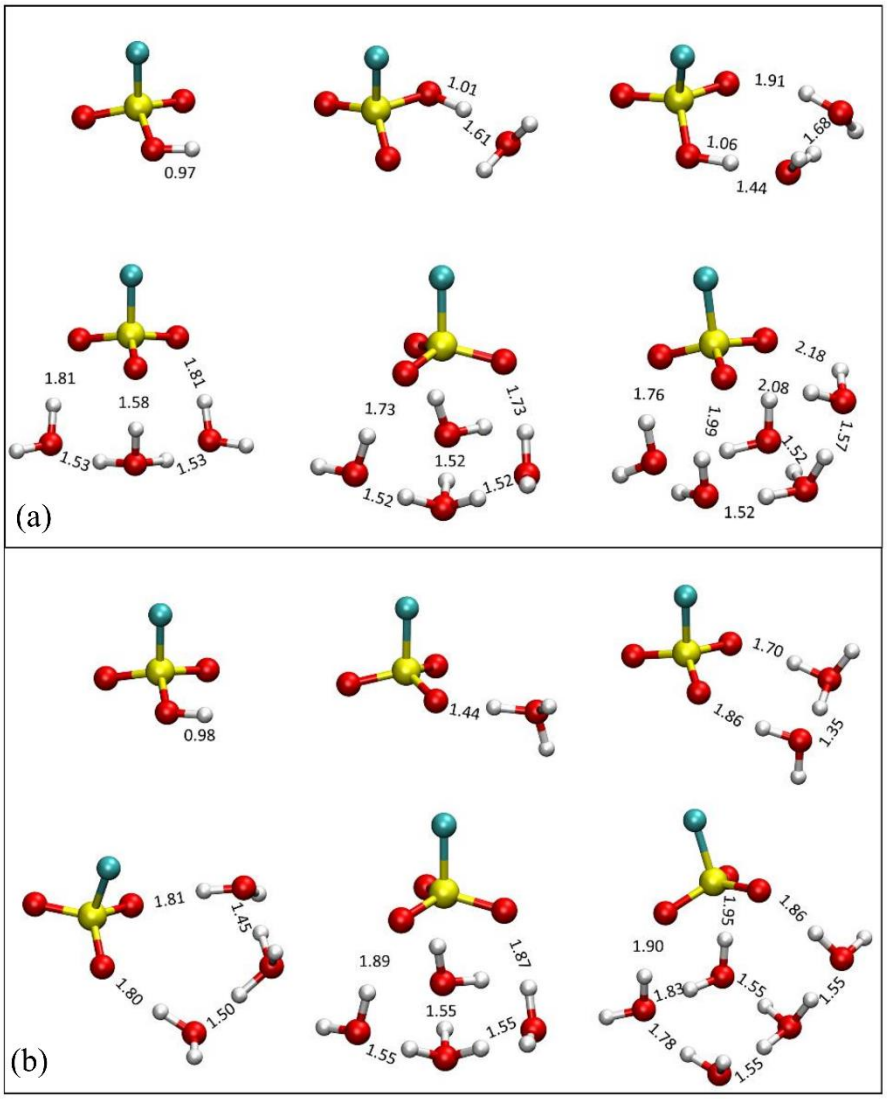


Figure 2. Fully optimized structures of FSO_3H with from zero to five water molecules at the B3LYP/6-311G** level of theory: (a) gas phase structures, proton dissociation occurs after three water molecules are added; (b) structures with the SMD model, proton dissociates after only one water molecule is added.

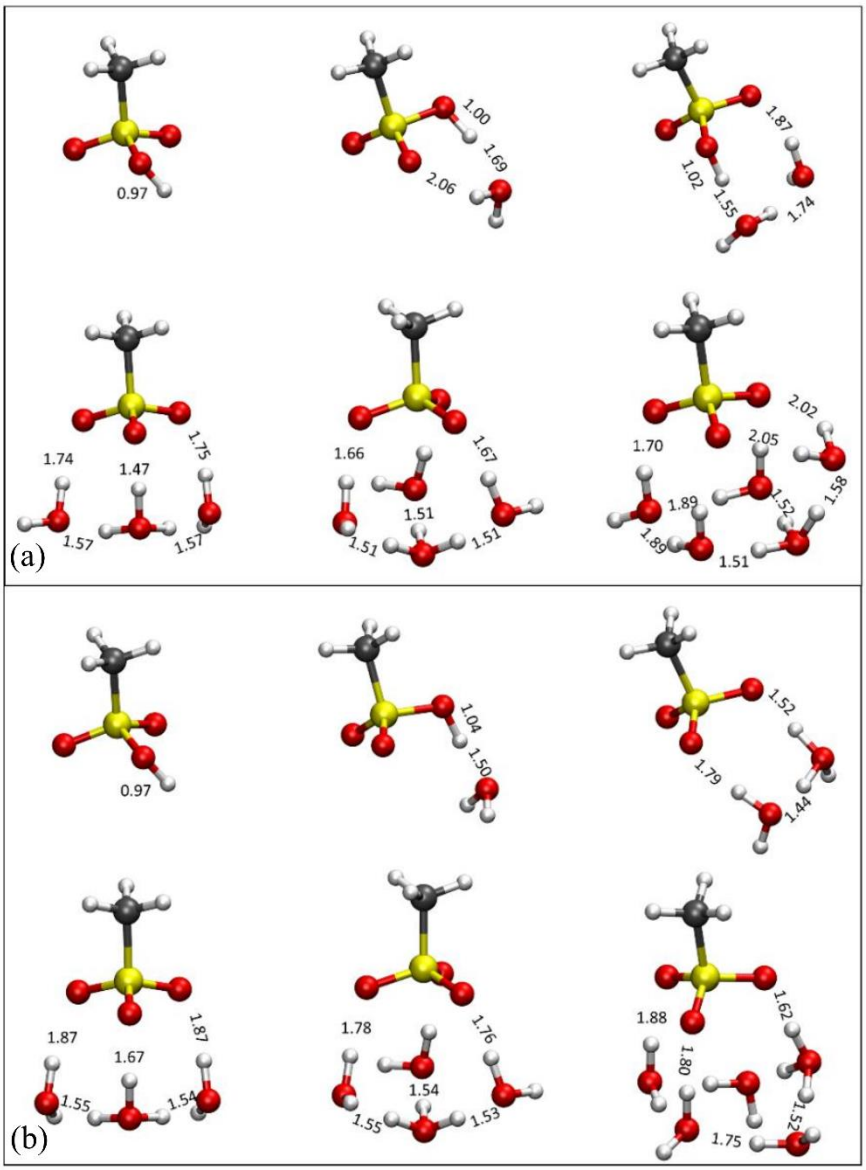


Figure 3. Fully optimized structures of CH_3SO_3H with from zero to five water molecules at the B3LYP/6-311G** level of theory: (a) gas phase structures, proton dissociation occurs after three water molecules are added; (b) structures with the SMD model, proton dissociates after only two water molecules are added.

A prior study of CH_3SO_3H with one to five water molecules using B3LYP/6-311++G** level of theory determined that proton transfer occurs when four water molecules are added in the gas phase [42]. Their results are confirmed with our calculations upon the addition of diffuse functions. The diffuse functions were not included in our calculations in favor of the computational efficiency and also because the effects were determined negligible on the confirmation of hydrated CF_3SO_3H [34] (the most widely used acid in electrolytes).

The hydrated structure of sulfuric acid shown in Figure 4 is in agreement with previous calculations [55,56]. There are some discrepancies in the literature regarding the position of the water molecules in the most stable hydrated clusters and whether the water molecules bind to the acid molecule from one side or both sides [40,55,57]. The structure of the $H_2SO_4(H_2O)_2$ cluster shown in Figure 4a is in agreement with recent semiempirical calculations that reproduce the proton transfer observed in this system [56]. The authors in this work also found that the first proton transfer occurs in clusters consisting of four water molecules, in agreement with the present work.

Figure 5 shows the hydrated structures for HNO_3. Successive hydrogen bonds forming ring structure are observed in both the gas phase and SMD solvated molecules in agreement with previous computational work [44,58]. The acidic proton is transferred to water in the gas phase when five water molecules are in the cluster consistent with previous MP2 and B3LYP results [44]. The minimum energy structures in Figure 6 do not show a proton transfer as a result of the weak acidity of HF in water. Gas phase computational studies of hydrated clusters of HF employing DFT and MP2 indicate that more than seven [45] or ten [59] water molecules are required in order to first witness proton dissociation.

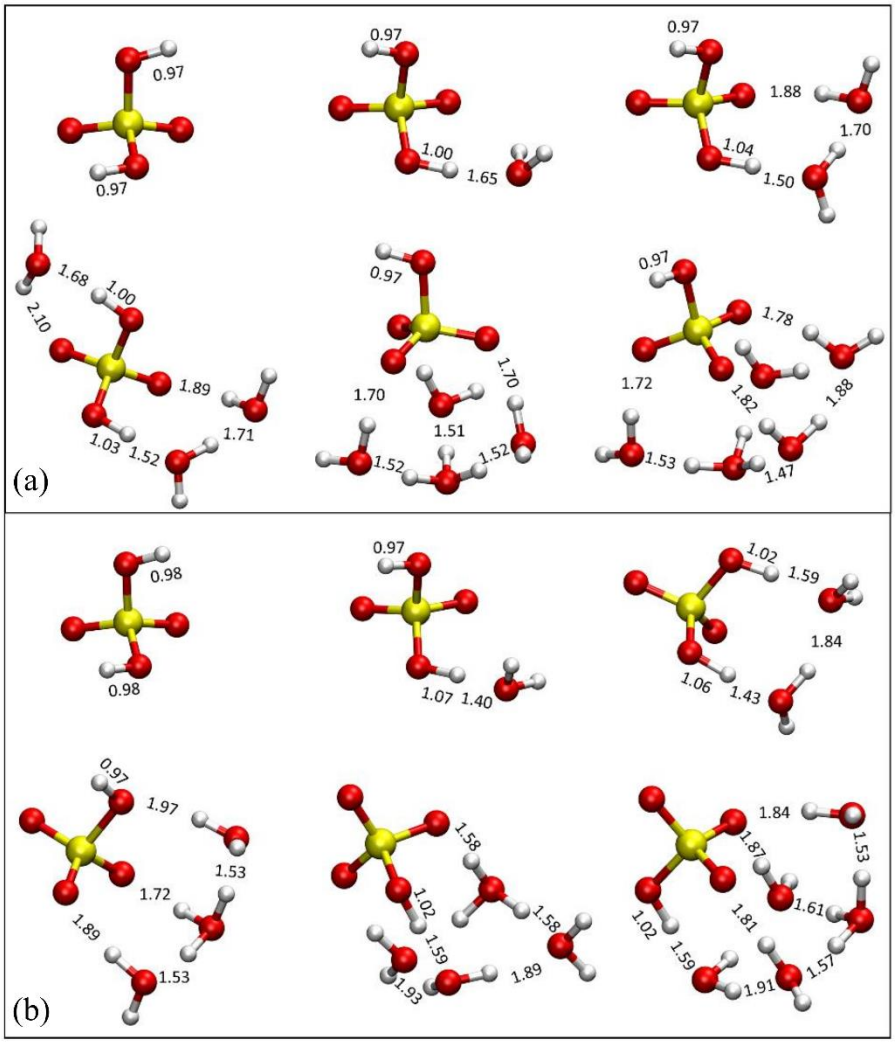


Figure 4. Fully optimized structures of H_2SO_4 with from zero to five water molecules at the B3LYP/6-311G** level of theory: (a) gas phase structures, proton dissociation occurs after four water molecules are added; (b) structures with the SMD model, proton dissociates after three water molecules are added. In all structures, the water molecules bind to one side of the acid. The only exception is the gas phase with three water molecules.

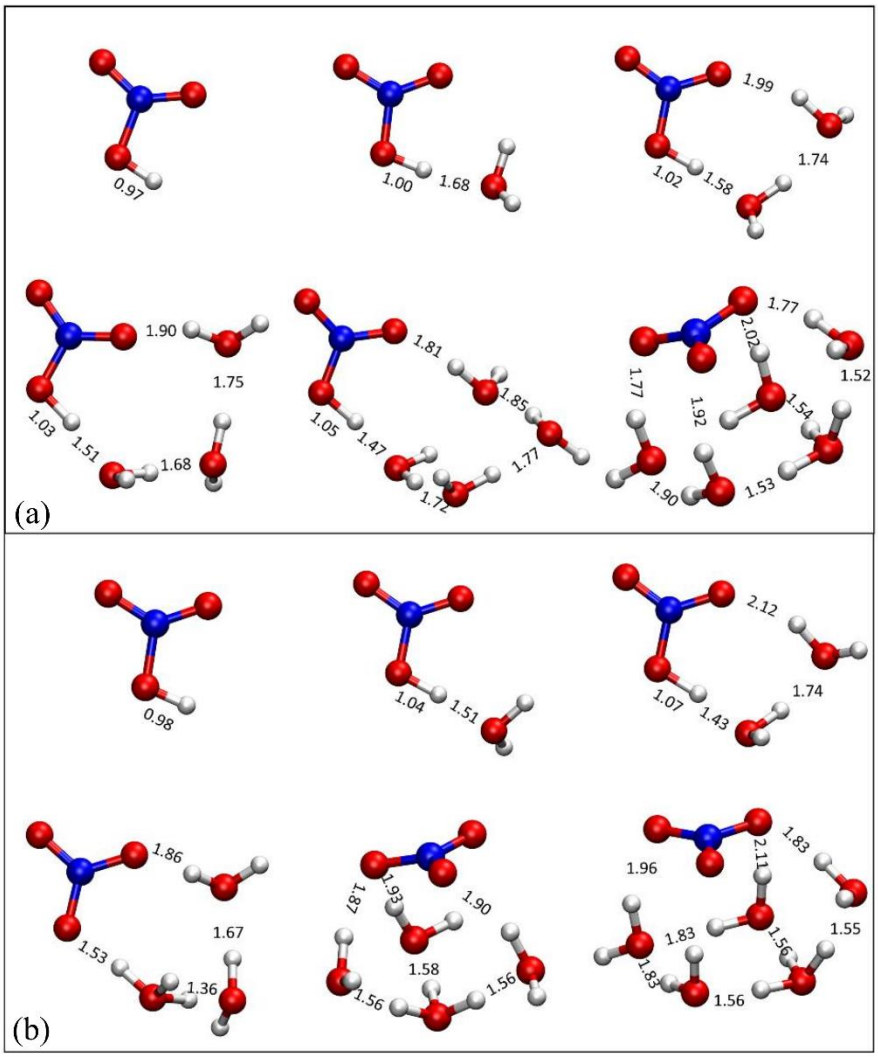


Figure 5. Fully optimized structures of HNO_3 with from zero to five water molecules at the B3LYP/6-311G** level of theory: (a) gas phase structures, proton dissociation occurs after five water molecules are added; (b) structures with the SMD model, proton dissociates after only three water molecules are added.

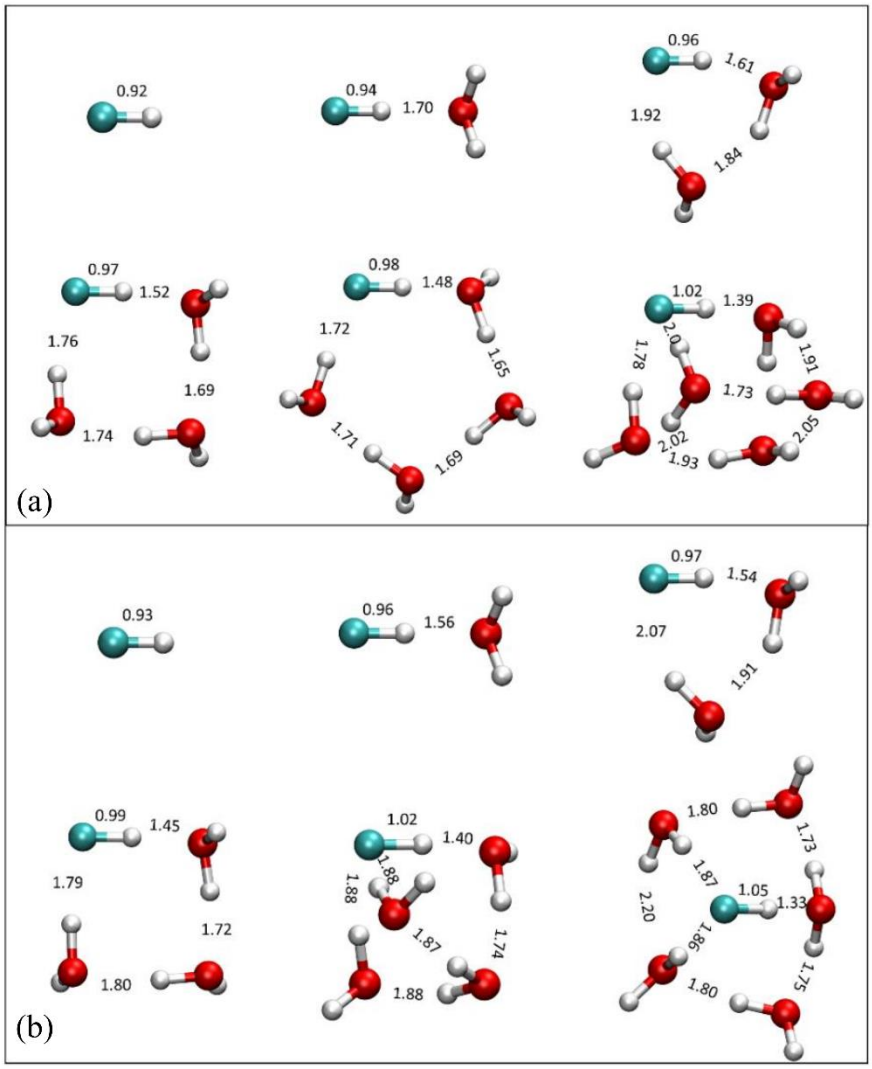


Figure 6. Fully optimized structures of HF with from zero to five water molecules at the B3LYP/6-311G** level of theory: (a) gas phase structures; (b) structures with the SMD model. No proton dissociation occurs in agreement with the weak acidity of HF.

An important observation is the relation between the acid strength and the number of water molecules required to effect proton dissociation forming the conjugate anion and hydrated proton. The gas phase acidities of the strong acids studied in this work may be ranked as follows: $CF_3SO_2NHSO_2CF_3 > CF_3SO_3H > FSO_3H > H_2SO_4 > CH_3SO_3H > HNO_3$, based on measurements using the pulsed FT ion cyclotron resonance (ICR) equilibrium constant method [60] and the pK_a values (see Table 1). The gas phase calculations are in agreement with this ranking except for H_2SO_4 which requires four water molecules to dissociate in the gas phase, more than that of the CH_3SO_3H acid. This may be due to the diprotic nature of the acid.

The weak acids in this study: $H_3PO_2 > H_3PO_3 > H_3PO_4 > HF$ (ranked based on the pK_a values in Table 1) do not dissociate even with the addition of five water molecules. The only exception is H_3PO_2 which is the strongest among these weak acids. It dissociates in the gas phase when five water molecules are added (see Figure 7a).

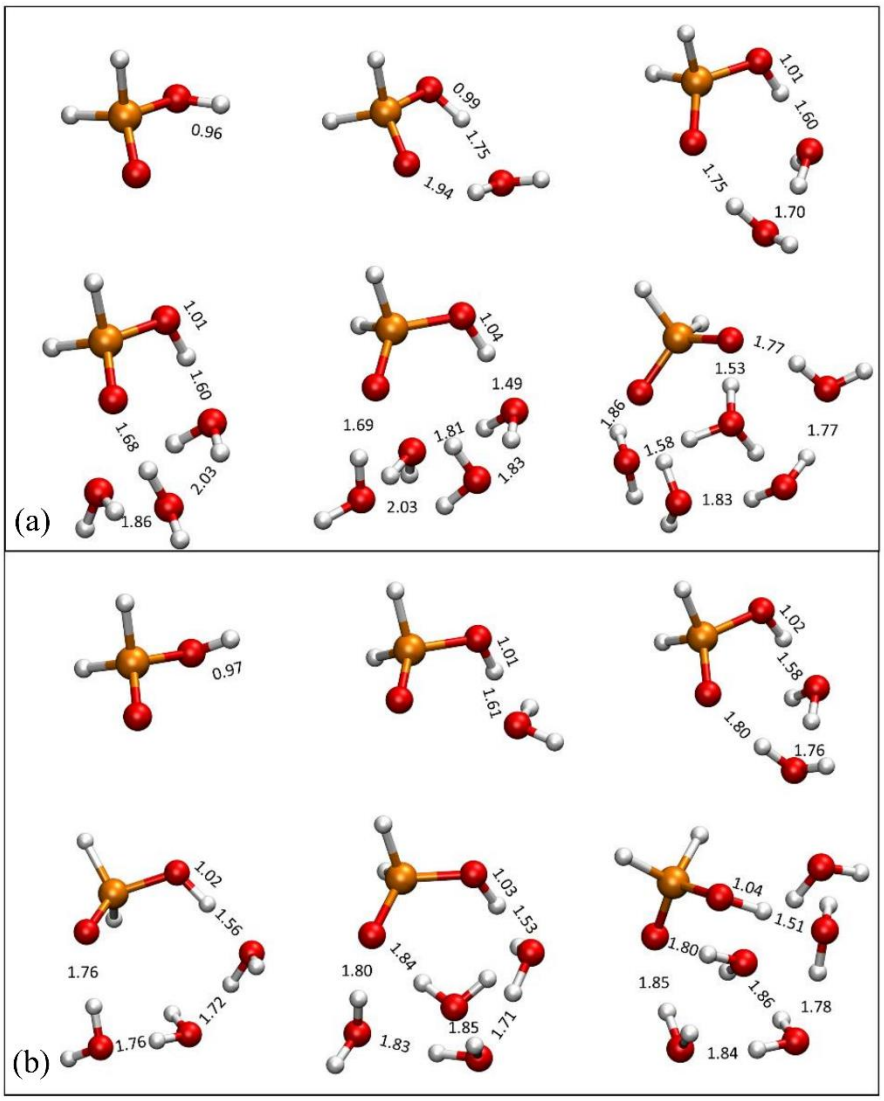


Figure 7. Fully optimized structures of H_3PO_2 with from zero to five water molecules at the B3LYP/6-311G** level of theory: (a) gas phase structures; (b) structures with the SMD model. No proton dissociation occurs, except in the gas phase with five added water molecules.

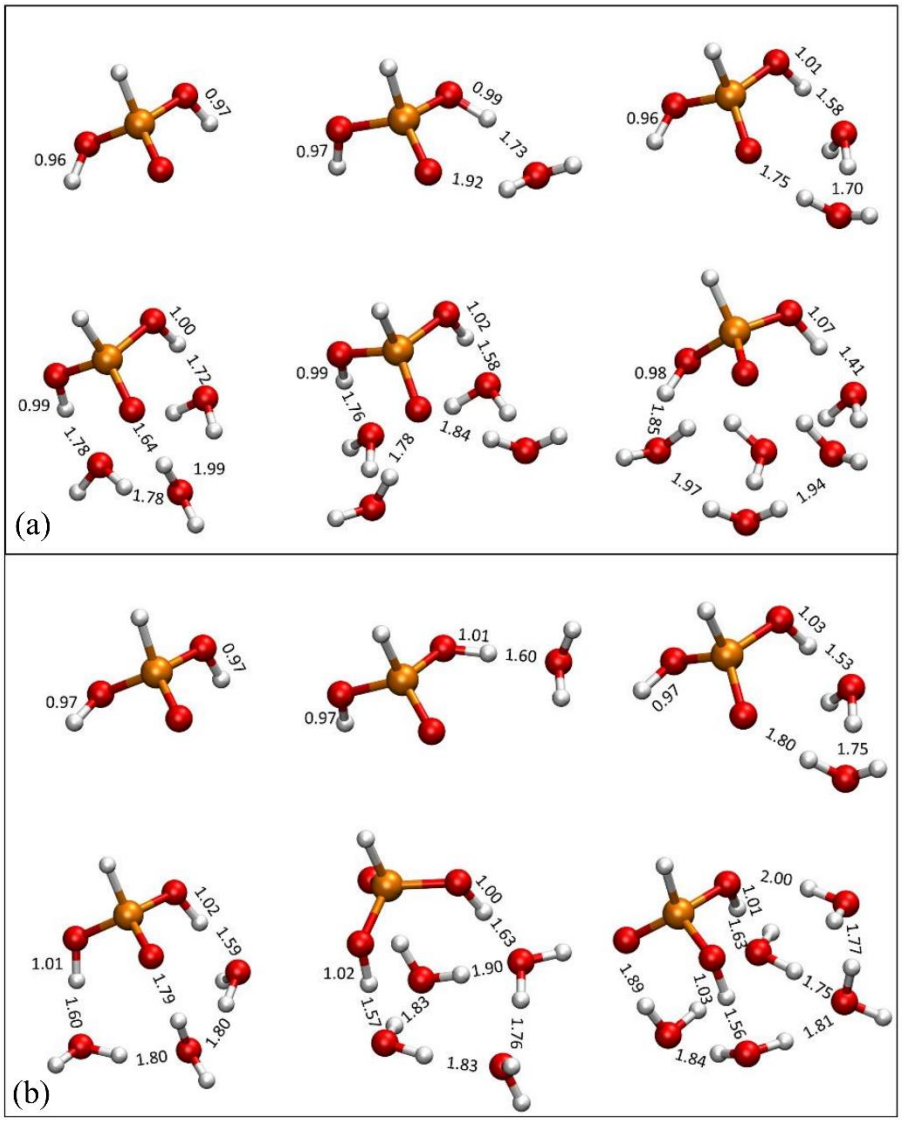


Figure 8. Fully optimized structures of H_3PO_3 with from zero to five water molecules at the B3LYP/6-311G** level of theory: (a) gas phase structures; (b) structures with the SMD model. No proton dissociation occurs.

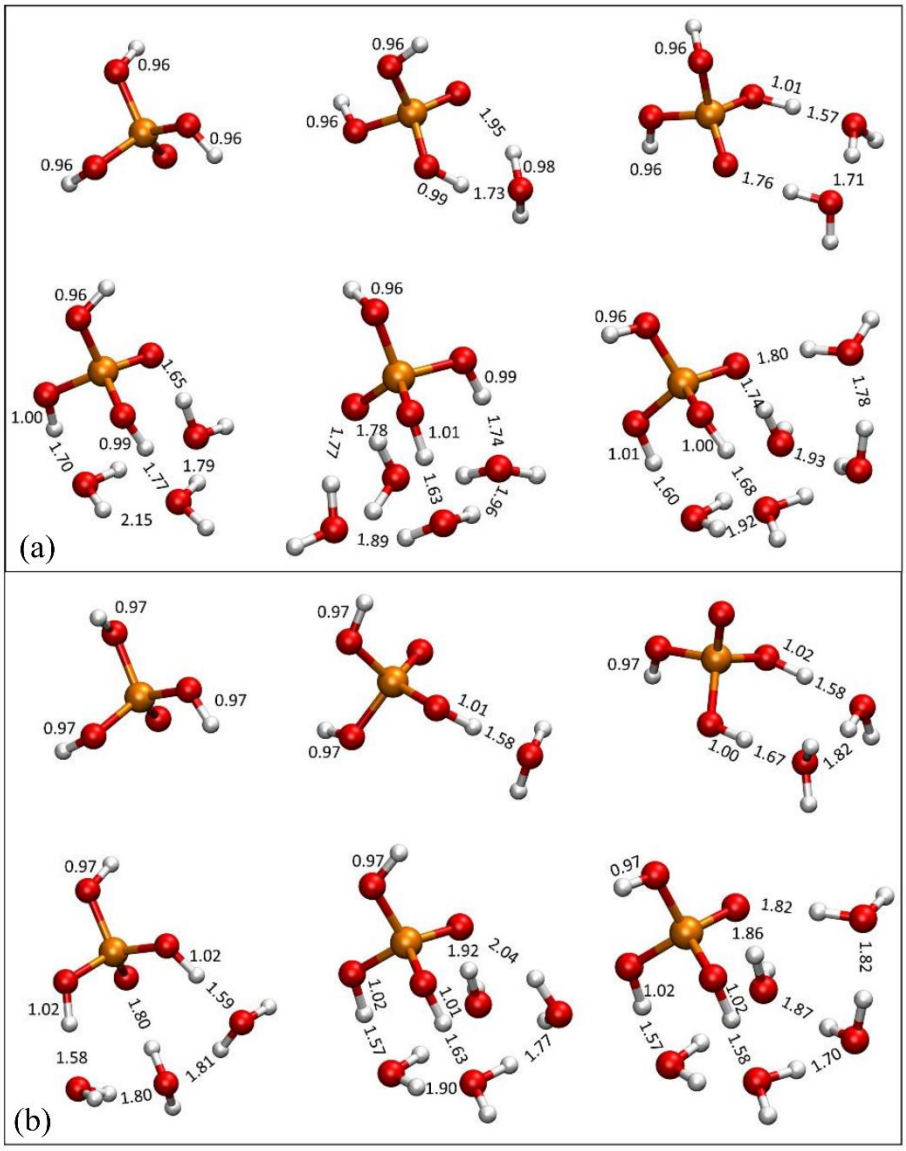


Figure 9. Fully optimized structures of H_3PO_4 with from zero to five water molecules at the B3LYP/6-311G** level of theory: (a) gas phase structures; (b) structures with the SMD model. No proton dissociation occurs.

The hydrated structures for the $CF_3SO_2NHSO_2CF_3$ acid are shown in Figure 10. The gas phase structures dissociate when three or more water molecules are added to the system in agreement with the literature using the same level of theory [32]. Figure 10b shows that in the SMD solvated clusters the proton is transferred to water in the vicinity of two or more water molecules. The experimental gas phase acidities indicate that this imide acid is stronger than either CF_3SO_3H or FSO_3H [60]. However, the calculations using the SMD solvation model show that CF_3SO_3H and FSO_3H require only one water molecule to transfer a proton. This may be due to the solvent effects that change the relative acid strengths, implying that the gas phase acidities are not transferable to the liquid phase or solvent.

Adding more water molecules to the dissociated systems in the gas phase results in further separation of the hydronium ion from the conjugate anion. This implies that the solvent separated ion pairs are more stable than the contact ion pairs and reflects the propensity of the hydronium ion to delocalize the excess charge over the water molecules [32,37]. This behavior is also observed in the SMD solvated structures with some deviations.

The reported structures in this work may only serve as a relative measure of the propensity of the acids to dissociate and transfer a proton in the vicinity of a few water molecules and therefore may not be the exact hydration structures. Only one acid and a few water molecules were present in each cluster and therefore the findings are not general, because the presence of additional acid molecules or anhydrous conditions will certainly affect the results. One example is the energetics of proton transfer in anhydrous or neat phosphoric acid (the highest proton conducting substance) which decreases by increasing the number of phosphoric acids in the cluster [61].

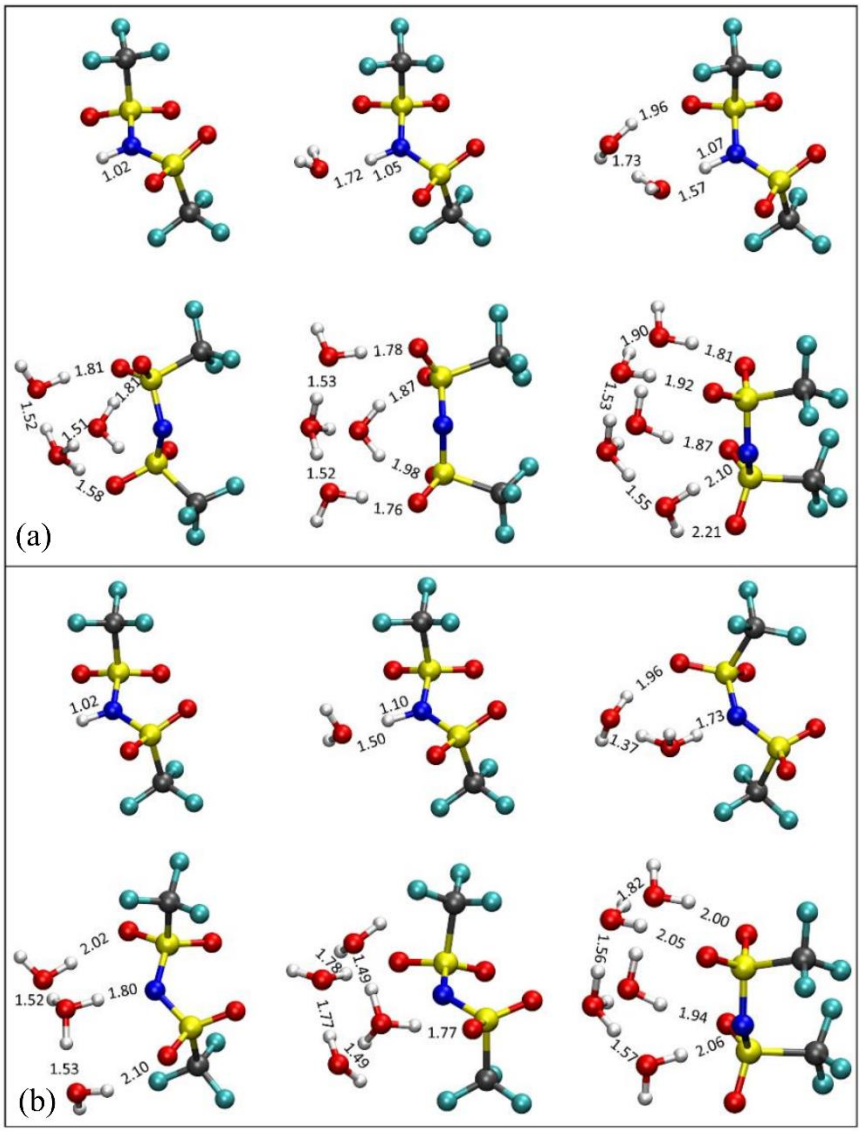


Figure 10. Fully optimized structures of $CF_3SO_2NHSO_2CF_3$ with from zero to five water molecules at the B3LYP/6-311G** level of theory: (a) gas phase structures, proton dissociation occurs after three water molecules are added (nitrogen is not involved in the hydrogen bond network); (b) structures with the SMD model, proton dissociates after only two water molecules are added (nitrogen is involved in the hydrogen bond network).

3.2. Proton Transfer

Figure 11 to 14 show the relative energy profiles with respect to the optimized structures shown previously. The relative energy profiles are plotted as a function of the distance between the scanned proton and the oxygen/ nitrogen/ or fluorine atom of the acid. These plots may be categorized into four groups corresponding to the distinct behavior as the OH (or NH or FH) distance is increased: (1) the relative energy continuously increases from zero to a positive value; (2) the relative energy continuously decreases from a positive value to zero; (3) first the relative energy increases to an extremum and then decays; and (4) the changes in the relative energy are negligible (smaller than 2 kcal/mol).

The first type of scan occurs when the hydrated structure with the acid molecule is more stable than the dissociated form and as the proton is separated from the acid the configuration becomes energetically unfavorable. The opposite occurs in second class, i.e., the dissociated form is more stable than the molecular acid and when the proton is near the acid the relative energy is high and dramatically decreases when the proton is moved away from the acid. The third type of scans occur when the molecular acid is more stable (similar to the first case) but during the scan another proton is transferred to the acid, from either the hydronium ion or a water molecule. This secondary proton transfer is denoted a 'back transfer' in the literature [46]. The fourth type corresponds to the case where the energy difference between the dissociated and the molecular form is less than 2 kcal/mol. Hence, the energy penalty for transferring a proton from or to the acid is negligible.

Figure 11 compares the proton transfer scans for the three sulfonic acids with one to three water molecules. The three acids in the gas phase show back transfer of a proton with one and two water molecules (type 3) and a decreasing scan is observed with three water molecules (type 2). This is because of the acids do not dissociate in the gas phase until three water molecules are added.

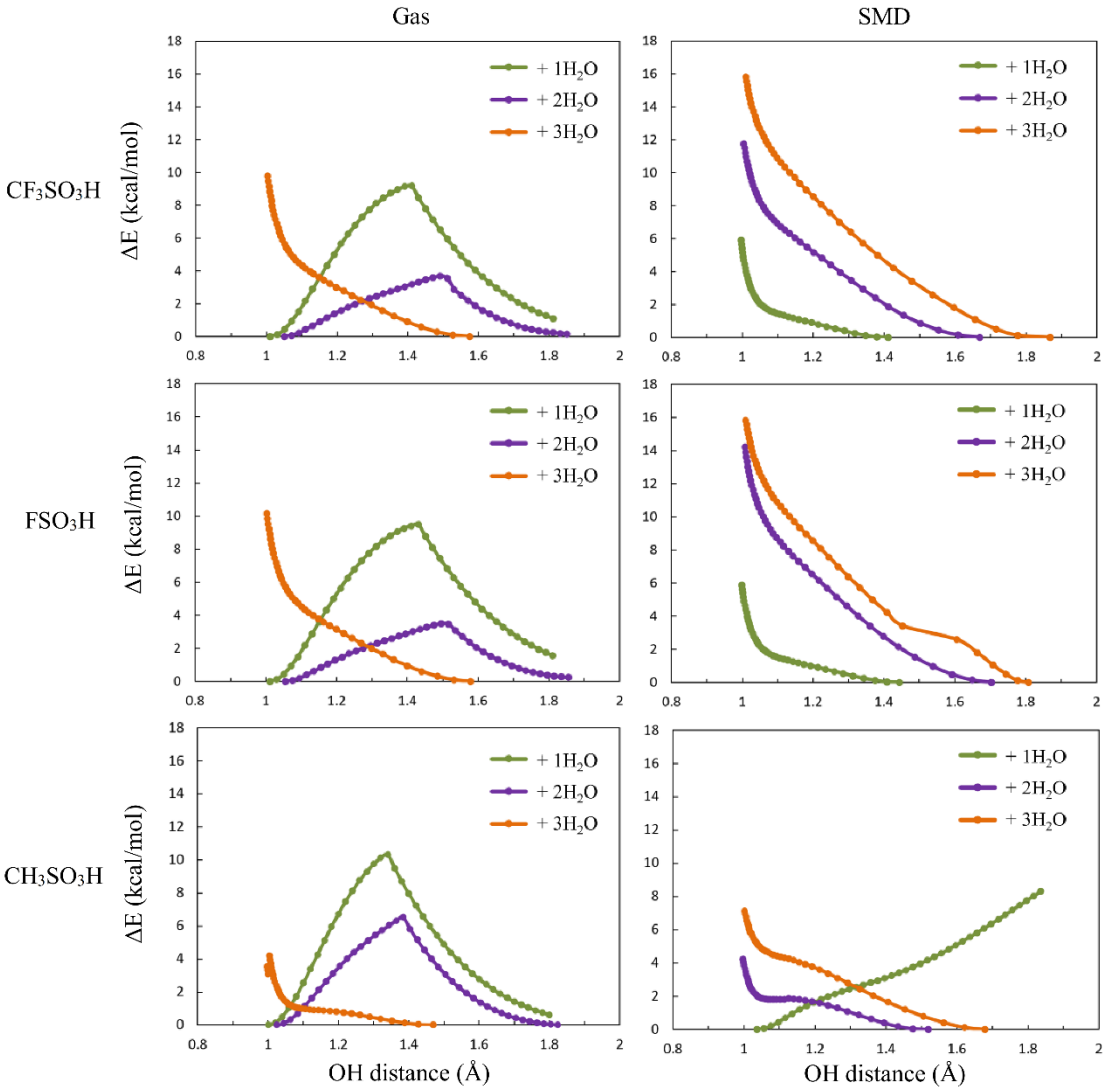


Figure 11. The relative energy profiles of PES scans for: CF_3SO_3H, FSO_3H, and CH_3SO_3H. The gas phase results are shown in the left panel and the results with the SMD model are displayed in the right panel. The extremum plots in the gas phase correspond to the back transfer events indicating that the molecular acid is more stable than the ionized form. The gas phase results are similar, because the proton dissociation occurs after three water molecules are added. The SMD results for CF_3SO_3H and FSO_3H are similar to each other and different to those for CH_3SO_3H, as the formers require only one water molecule to effect proton dissociation. The right panel scans do not show a back transfer of a proton, because the formed hydronium ion is stabilized by the continuum solvation model.

The solvated structures (the right panel in Figure 11) do not show a back transfer of a proton and the relative energy decreases as the OH distance is increased (type 2). The absence of a back transfer suggests that the formed hydronium ion is stabilized by the continuum solvation model. The CH_3SO_3H acid with one water molecule does not dissociate (see Figure 3b) and therefore the energy simply increases with increasing OH distance (type 1). The energy penalty for moving the proton closer to the acid increases as the number of water molecules is increased in the SMD model scans. This implies that the clusters consisting of more water molecules have a higher propensity to remain in the ionized (dissociated) form.

Figure 12 shows the proton transfer scans for three of the inorganic acids: H_2SO_4; HNO_3; and HF. The gas phase scans show back transfer of a proton to the acids in all cases. An extra proton transfer scan for the HNO_3 acid with four water molecules was also performed for further verification. The energy barrier at the extremum points decreases as the number of water molecules is increased. The acid strength is inversely related to the energy barriers and hence the values for HF (the weakest acid) are much greater than those for H_2SO_4 and HNO_3.

The right panels in Figure 12 show that the transfer of a proton to one water molecule is unfavorable for all three acids (type 1) and as the acid strength decreases the energy penalty increases. The H_2SO_4 and HNO_3 acids with two water molecules show type 4 behavior, implying a negligible energy barrier to transfer a proton. As both H_2SO_4 and HNO_3 dissociate with three water molecules with the SMD model, the energy simply decreases with increasing OH distance (see the right panel of Figure 12). The weakest acid, HF, exhibits a back transfer with either two or three added water molecules and the energy barriers are lower than their corresponding values in the gas phase.

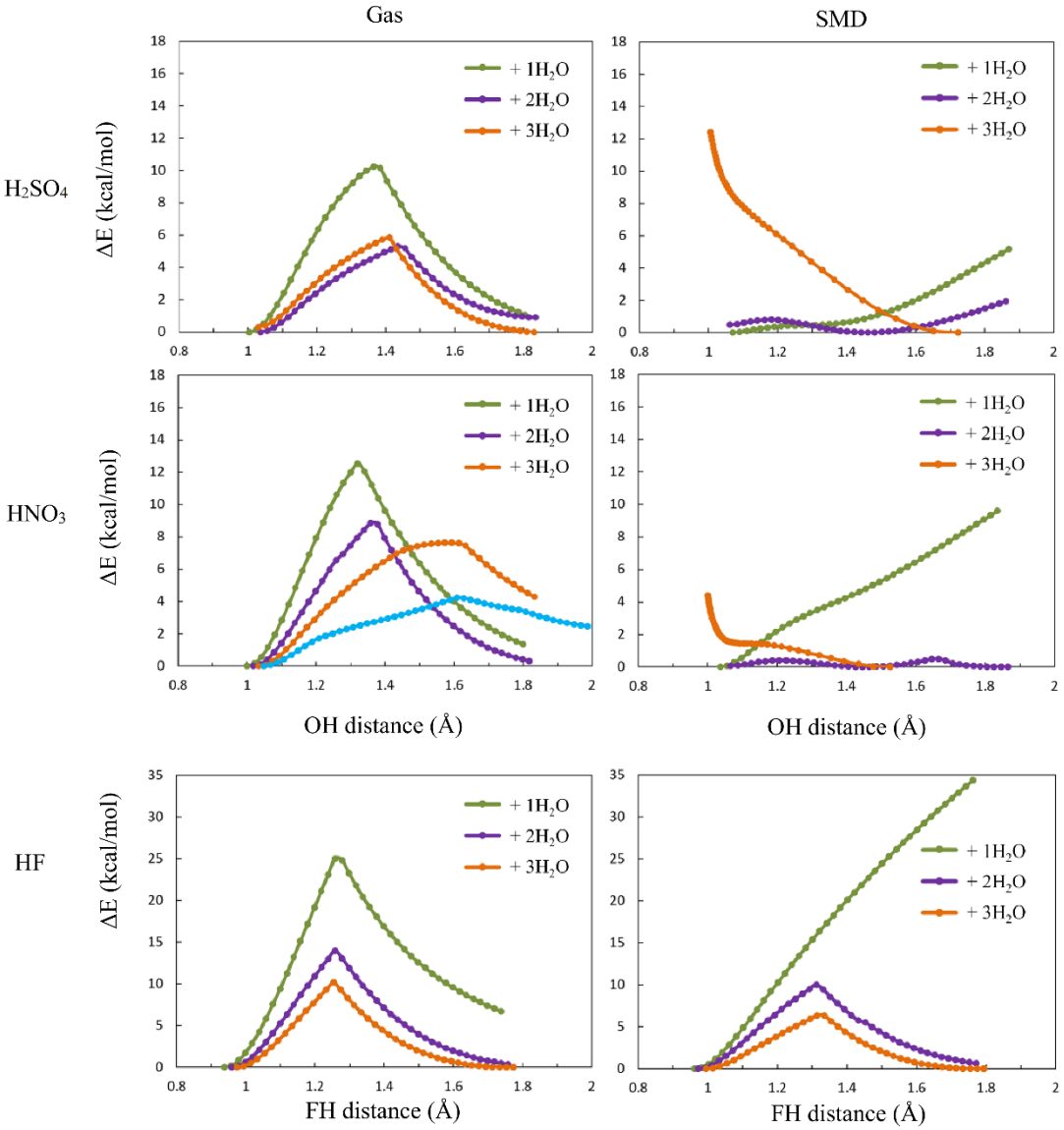


Figure 12. The relative energy profiles of PES scans for: H_2SO_4, HNO_3, and HF. The gas phase results are shown in the left panel and the results with the SMD model are displayed in the right panel. The gas phase results exhibit back transfer of a proton indicating that the molecular acid is more stable than the ionized form. The energy barrier to move a proton away from the acid is inversely related to the number of water molecules and the acid strength. The weakest acid, HF, has the highest energy barriers. The relative energy axis is plotted from 0 to 18 kcal/mol for all acids except for HF (from 0 to 35 kcal/mol).

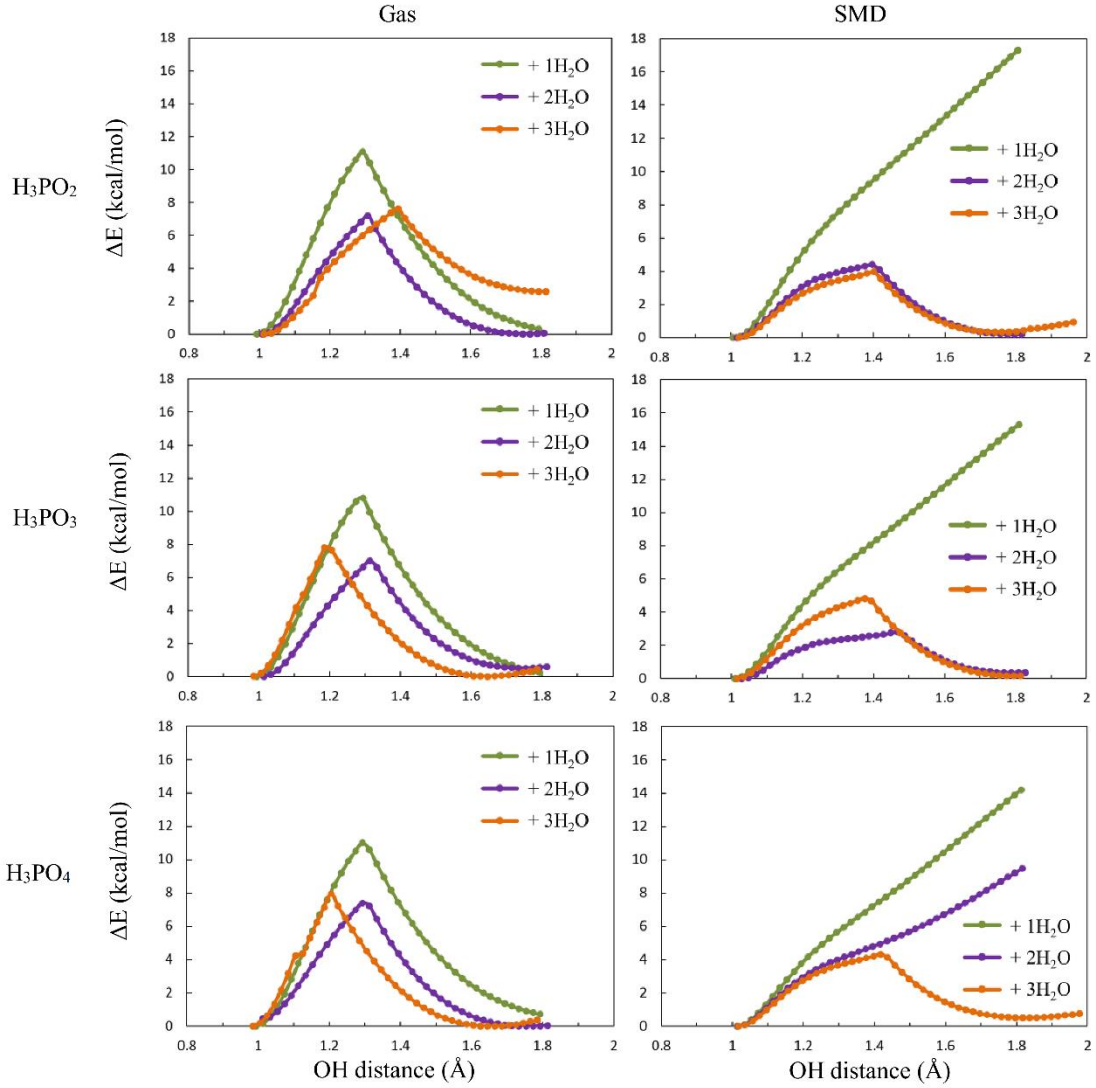


Figure 13. The relative energy profiles of PES scans for: H_3PO_2, H_3PO_3, and H_3PO_4. The gas phase results are shown in the left panel and the results with the SMD model are displayed in the right panel. Only a back transfer or an increasing scan is observed, because the proton dissociation is not favored by any of these weak acids. The proton transfer energetics are similar for these acids in agreement with their similar acidity and pK_a values listed in Table 1.

The scan plots of the three phosphor based acids are shown in Figure 13. These acids do not dissociate when up to three water molecules are added either in the gas phase or in a solvent. They all have a proton back transferred to them in the gas phase similar to the HF acid. The proton transfer behavior for the SMD solvated scans is also similar to those of HF. However, the energy barriers and penalties are much lower than HF.

Figure 14 plots the proton transfer scans for the imide acid, $CF_3SO_2NHSO_2CF_3$. The acid with one water molecule shows a back transfer in the gas phase; the secondary proton is transferred to an oxygen atom of the acid. Type 2 behavior is observed for this strong acid with three water molecules in the gas phase and with two and three when solvated with the SMD model, consistent with the structures shown in Figure 10. The acid and three water molecules in the gas phase form a hydrogen bond network that does not involve the nitrogen atom (see Figure 10a). Hence, the proton transfer scan was performed by transferring a proton to the oxygen atom of the acid.

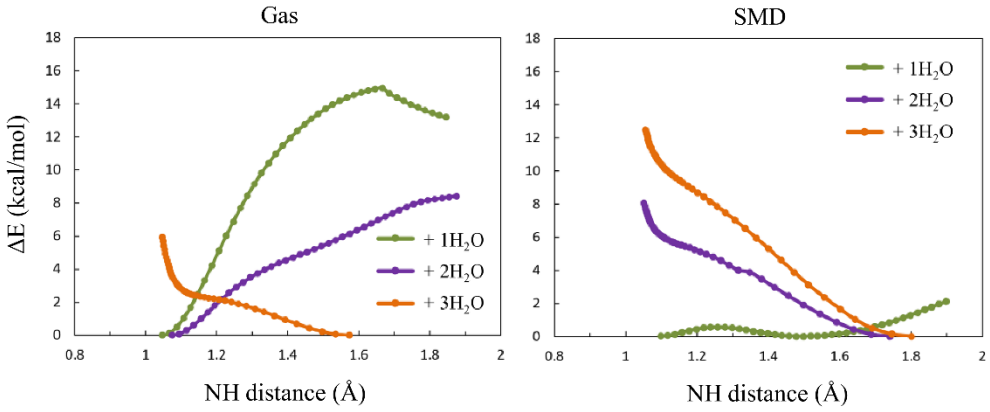


Figure 14. The relative energy profiles of PES scans for $CF_3SO_2NHSO_2CF_3$. The gas phase results are shown in the left panel and the results with the SMD model are displayed in the right panel. In the gas phase with one water molecule, the secondary proton is transferred to an oxygen atom of the acid. The gas phase structure of this acid with three water molecules does not involve hydrogen bonding with nitrogen as shown in Figure 10 (a). Hence the proton was transferred to an oxygen atom of the acid, i.e., the orange plot in the left panel shows OH distance rather than NH. The proton dissociation occurs after two water molecules are added to the SMD solvated structures, however the proton transfer energetics is negligible with one water molecule.

4. Conclusions

The primary hydration of ten acids commonly employed in electrolytes was investigated using quantum chemical calculations in order to provide a fundamental understanding of their hydrated acidity and proton transfer in comparison to each other. It was determined that fewer number of water molecules were required to dissociate a proton from the stronger acids. The number of water molecules required to first witness proton dissociation was decreased upon the addition of a solvation model through stabilizing the conjugate ions. It was observed that the hydronium ion further separated from the conjugate anion as the number of water molecules was increased. This was explained by the solvent separated ion pairs being more stable than the contact ion pairs.

PES scans were performed to analyze the relative proton transfer. It was determined that the proton transfer energetics are controlled by the structure of the hydrated acid, the acid strength, and the continuum solvation model. The energy barrier for moving a proton away from the acid was inversely related to the acid strength. The propensity of proton dissociation was higher when the solvation model was applied. The results provide a fundamental understanding of the relative acidity and proton transfer of common acids employed in electrolyte solutions and membrane electrolytes.

Acknowledgements

This work was supported by the EPSCoR program of the National Science Foundation under the TNSCORE program with NSF EPS_1004083.

References

[1] A. Kirubakaran, S. Jain, R.K. Nema, Renewable Sustainable Energy Rev. 13 (9) (2009) 2430-2440.

[2] A.B. Stambouli, E. Traversa, Renewable Sustainable Energy Rev. 6 (3) (2002) 295-304.

[3] S.J. Peighambardoust, S. Rowshanzamir, M. Amjadi, Int. J. Hydrogen Energy 35 (17) (2010) 9349-9384.

[4] A.Z. Weber, M.M. Mench, J.P. Meyers, P.N. Ross, J.T. Gostick, Q.H. Liu, J. Appl. Electrochem. 41 (10) (2011) 1137-1164.

[5] M. Skyllas-Kazacos, In: J. Garche, Editor, Encyclopedia of Electrochemical Power Sources, Elsevier, Amsterdam (2009), p.444-453.

[6] B. Smitha, S. Sridhar, A.A. Khan, J. Membr. Sci. 259 (1-2) (2005) 10-26.

[7] J. Roziere, D.J. Jones, Annu. Rev. Mater. Res. 33 (2003) 503-555.

[8] X.F. Li, H.M. Zhang, Z.S. Mai, H.Z. Zhang, I. Vankelecom, Energy Environ. Sci. 4 (4) (2011) 1147-1160.

[9] S.E. Creager, J.J. Sumner, R.D. Bailey, J.J. Ma, W.T. Pennington, D.D. DesMarteau, Electrochem. Solid-State Lett. 2 (9) (1999) 434-436.

[10] S.V. Kotov, S.D. Pedersen, W.M. Qiu, Z.M. Qiu, D.J. Burton, J. Fluorine Chem. 82 (1) (1997) 13-19.

[11] C.H. Fujimoto, M.A. Hickner, C.J. Cornelius, D.A. Loy, Macromolecules 38 (12) (2005) 5010-5016.

[12] P.X. Xing, G.P. Robertson, M.D. Guiver, S.D. Mikhailenko, K.P. Wang, S. Kaliaguine, J. Membr. Sci. 229 (1-2) (2004) 95-106.

[13] J.T. Wang, R.F. Savinell, J. Wainright, M. Litt, H. Yu, Electrochim. Acta 41 (2) (1996) 193-197.

[14] O. Savadogo, B. Xing, J. New Mater. Electrochem. Syst. 3 (4) (2000) 343-347.

[15] J.S. Wainright, J.T. Wang, D. Weng, R.F. Savinell, M. Litt, J. Electrochem. Soc. 142 (7) (1995) L121-L123.

[16] S. Cavaliere, S. Subianto, I. Savych, D.J. Jones, J. Roziere, Energy Environ. Sci. 4 (12) (2011) 4761-4785.

[17] M.M. Hasani-Sadrabadi, I. Shabani, M. Soleimani, H. Moaddel, J. Power Sources 196 (10) (2011) 4599-4603.

[18] I. Shabani, M.M. Hasani-Sadrabadi, V. Haddadi-Asl, M. Soleimani, J. Membr. Sci. 368 (1-2) (2011) 233-240.

[19] R. Takemori, H. Kawakami, J. Power Sources 195 (18) (2010) 5957-5961.

[20] J.B. Ballengee, P.N. Pintauro, J. Electrochem. Soc. 158 (5) (2011) B568-B572.

[21] H. Chen, J.D. Snyder, Y.A. Elabd, Macromolecules 41 (1) (2008) 128-135.

[22] S. Subianto, S. Cavaliere, D.J. Jones, J. Roziere, Polym. Electrolyte Fuel Cells 11 41 (1) (2011) 1517-1520.

[23] Y.F. Yao, B.K. Guo, L.W. Ji, K.H. Jung, Z. Lin, M. Alcoutlabi, H. Hamouda, X.W. Zhang, Electrochem. Commun. 13 (9) (2011) 1005-1008.

[24] D. Wu, T.W. Xu, L. Wu, Y.H. Wu, J. Power Sources 186 (2) (2009) 286-292.

[25] M.J. Frisch, G.W. Trucks, H.B. Schlegel, G.E. Scuseria, M.A. Robb, J.R. Cheeseman, G. Scalmani, V. Barone, B. Mennucci, G.A. Petersson, H. Nakatsuji, M. Caricato, X. Li, H.P. Hratchian, A.F. Izmaylov, J. Bloino, G. Zheng, J.L. Sonnenberg, M. Hada, M. Ehara, K. Toyota, R. Fukuda, J. Hasegawa, M. Ishida, T. Nakajima, Y. Honda, O. Kitao, H. Nakai, T. Vreven, J.A.

Montgomery, J.E. Peralta, F. Ogliaro, M. Bearpark, J.J. Heyd, E. Brothers, K.N. Kudin, V.N. Staroverov, R. Kobayashi, J. Normand, K. Raghavachari, A. Rendell, J.C. Burant, S.S. Iyengar, J. Tomasi, M. Cossi, N. Rega, J.M. Millam, M. Klene, J.E. Knox, J.B. Cross, V. Bakken, C. Adamo, J. Jaramillo, R. Gomperts, R.E. Stratmann, O. Yazyev, A.J. Austin, R. Cammi, C. Pomelli, J.W. Ochterski, R.L. Martin, K. Morokuma, V.G. Zakrzewski, G.A. Voth, P. Salvador, J.J. Dannenberg, S. Dapprich, A.D. Daniels, Farkas, J.B. Foresman, J.V. Ortiz, J. Cioslowski, D.J. Fox, Gaussian 09, Revision A.01, Gaussian 09, Revision A.01, Wallingford CT (2009).

[26] C.T. Lee, W.T. Yang, R.G. Parr, Phys. Rev. B: Condens. Matter Mater. Phys. 37 (2) (1988) 785-789.

[27] A.D. Becke, J. Chem. Phys. 98 (7) (1993) 5648-5652.

[28] A.D. Becke, J. Chem. Phys. 98 (2) (1993) 1372-1377.

[29] P.C. Hariharan, J.A. Pople, Theor. Chim. Acta 28 (3) (1973) 213-222.

[30] A.D. McLean, G.S. Chandler, J. Chem. Phys. 72 (10) (1980) 5639-5648.

[31] A.V. Marenich, C.J. Cramer, D.G. Truhlar, J. Phys. Chem. B 113 (18) (2009) 6378-6396.

[32] J.K. Clark, S.J. Paddison, M. Eikerling, M. Dupuis, T.A. Zawodzinski, J. Phys. Chem. A 116 (7) (2012) 1801-1813.

[33] J.K. Clark, S.J. Paddison, S.J. Hamrock, Phys. Chem. Chem. Phys. 14 (47) (2012) 16349-16359.

[34] C. Wang, J.K. Clark, M. Kumar, S.J. Paddison, Solid State Ionics 199 (2011) 6-13.

[35] C. Wang, S.J. Paddison, J. Phys. Chem. A 117 (3) (2013) 650-660.

[36] S.J. Paddison, J. New Mater. Electrochem. Syst. 4 (4) (2001) 197-207.

[37] M. Eikerling, S.J. Paddison, T.A. Zawodzinski, J. New Mater. Electrochem. Syst. 5 (1) (2002) 15-23.

[38] J.A. Elliott, S.J. Paddison, Phys. Chem. Chem. Phys. 9 (21) (2007) 2602-2618.

[39] S.J. Paddison, T.A. Zawodzinski, Solid State Ionics 113 (1998) 333-340.

[40] A.R. Bandy, J.C. Ianni, J. Phys. Chem. A 102 (32) (1998) 6533-6539.

[41] T. Loerting, K.R. Liedl, J. Phys. Chem. A 105 (21) (2001) 5137-5145.

[42] S.J. Li, W. Qian, F.M. Tao, Chem. Phys. Lett. 438 (4-6) (2007) 190-195.

[43] S.J. Li, F.M. Tao, R.N. Gu, Chem. Phys. Lett. 426 (1-3) (2006) 1-7.

[44] J.R. Scott, J.B. Wright, J. Phys. Chem. A 108 (47) (2004) 10578-10585.

[45] S.Y. Re, J. Phys. Chem. A 105 (42) (2001) 9725-9735.

[46] C. Wang, S.J. Paddison, Phys. Chem. Chem. Phys. 12 (4) (2010) 970-981.

[47] S.J. Paddison, K.D. Kreuer, J. Maier, Phys. Chem. Chem. Phys. 8 (39) (2006) 4530-4542.

[48] T. Ishimoto, T. Ogura, M. Koyama, Comput. Theor. Chem. 975 (1-3) (2011) 92-98.

[49] A. Trummal, L. Lipping, I. Kaljurand, I.A. Koppel, I. Leito, J. Phys. Chem. A 120 (20) (2016) 3663-3669.

[50] J.P. Guthrie, Can. J. Chem. 56 (17) (1978) 2342-2354.

[51] I.M. Kolthoff, Treatise on Analytical Chemistry, Interscience Encyclopedia, Inc., New York (1959).

[52] A. Albert, E.P. Serjeant, Ionization constants of acids and bases, Methuen, London (1962).

[53] J.W. Larson, M. Pippin, Polyhedron 8 (4) (1989) 527-530.

[54] D.C. Harris, Quantitative Chemical Analysis (Eighth Edition), W. H. Freeman and Company, New York (2010).

[55] S. Re, Y. Osamura, K. Morokuma, J. Phys. Chem. A 103 (18) (1999) 3535-3547.

[56] S. Sugawara, T. Yoshikawa, T. Takayanagi, M. Shiga, M. Tachikawa, J. Phys. Chem. A 115 (42) (2011) 11486-11494.

[57] H. Arstila, K. Laasonen, A. Laaksonen, J. Chem. Phys. 108 (3) (1998) 1031-1039.

[58] P.R. McCurdy, W.P. Hess, S.S. Xantheas, J. Phys. Chem. A 106 (33) (2002) 7628-7635.

[59] S. Odde, B.J. Mhin, K.H. Lee, H.M. Lee, P. Tarakeshwar, K.S. Kim, J. Phys. Chem. A 110 (25) (2006) 7918-7924.

[60] I.A. Koppel, R.W. Taft, F. Anvia, S.Z. Zhu, L.Q. Hu, K.S. Sung, D.D. Desmarteau, L.M. Yagupolskii, Y.L. Yagupolskii, N.V. Ignatev, N.V. Kondratenko, A.Y. Volkonskii, V.M. Vlasov, R. Notario, P.C. Maria, J. Am. Chem. Soc. 116 (7) (1994) 3047-3057.

[61] L. Vilciauskas, S.J. Paddison, K.D. Kreuer, J. Phys. Chem. A 113 (32) (2009) 9193-9201.

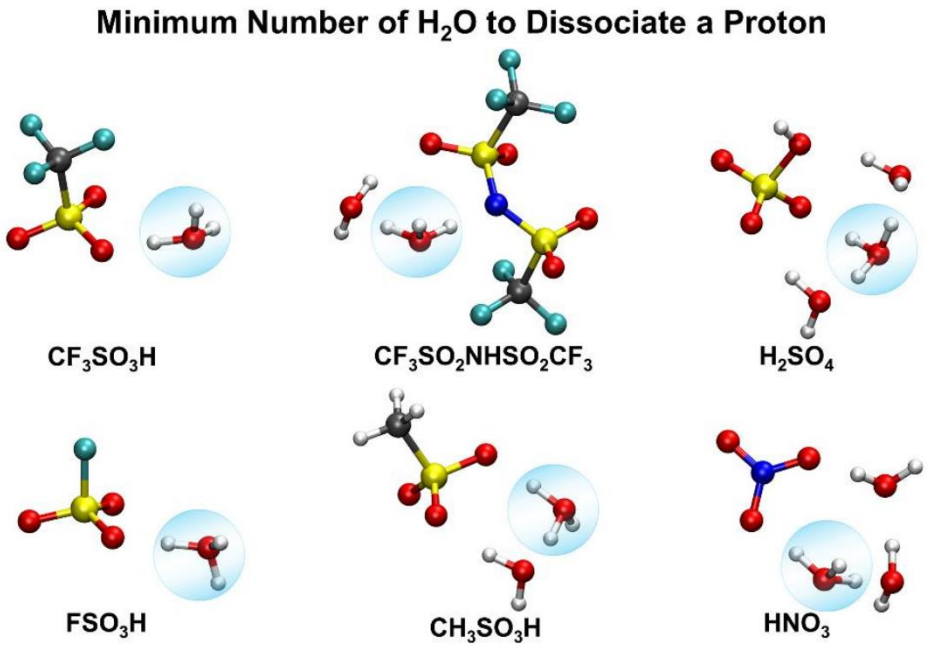


Table of Content Image (TOC)

33

Vita

Fatemeh began her college education in 2004 at Amirkabir University of Technology (Tehran Polytechnic). She graduated with high honors in 2008 and received B.Sc. degrees in polymer engineering and mechanical engineering. During her M.Sc. at Amirkabir University, she studied the rheological properties of polymer nanocomposites using several experimental characterization techniques (linear/non-linear viscoelastic measurements and measuring extrusion). She started her Ph.D. in fall 2011 at the University of Tennessee. Her interdisciplinary research involves molecular modeling and simulations of electrolyte materials for energy storage and conversion technologies.